A Network Approach for Strapdown Inertial Kinematic Gravimetry

M. Assumpció Termens

UNIVERSITAT POLITÈCNICA
DE CATALUNYA
BARCELONATECH

Programme: Applied Mathematics
Doctoral Supervisor: Dr. Ismael Colomina

Barcelona, 2013

Al meu padrí Estanislau (q.e.p.d.).

Als meus pares, Jordi (q.e.p.d.) i Ramona.

The important thing is not to stop questioning. Curiosity has its own reason for existing. One cannot help but be in awe when he contemplates the mysteries of eternity, of life; of the marvelous structure of reality. It is enough if one tries merely to comprehend a little of this mystery every day. Never lose a holy curiosity.

Albert Einstein

Acknowledgements

There are several people I would like to thank for helping me complete these studies. Taking the risk of unintentionally not mentioning someone, I would like to thank all the people who encouraged and supported me during the undertaking of this thesis.

To Dr. Ismael Colomina, who introduced me to geodesy and who gave me the opportunity to pursue PhD study. His support and expertise have been invaluable.

To all my colleagues at the Institut Cartogràfic de Catalunya (ICC), for their unforgettable support and help. To share knowledge and thoughts with them was always constructive. Furthermore, most of the work done is dependent on the data, the computing facilities and the technical library and software of the ICC.

To the colleagues at the Geomatics Institute, for their support and help, especially relating to simulated test data.

To Prof. Carl Christian Tscherning (University of Copenhague), Prof. Fernando Sansò (Politecnico de Milano), Dr. René Forsberg (KMS) and Dr. Jan Škaloud (EPF Lausanne), for their thoughtful comments and suggestions.

Finally, on a more personal note, I would like to express appreciation to my family and friends who have been so supportive.

To Ignasi, who was carrying his Ph.D. at the same time as me. Thank you for his unforgettable friendship and for sharing happiness, sadness, satisfaction and frustation, during all this time.

Last, but no least, I would like to express my deepest gratitude to my family. Love, encouragement, support and patience from Mum, Dad (he had been very proud to see it), Montse, Jordi, Alba and Txell have truly made my fulfillment of this Ph.D. possible.

Barcelona, 2013 A. T.

Abstract

Compared to the conventional ground measurement of gravity, airborne gravimetry is more efficient and cost-effective. Especially, the combination of GPS and INS is known to show very good performances recovering the gravity signal in the range of medium frequencies (1–100 km).

The processing of airborne gravity data traditionally consists of various independent steps, such as filtering, gridding and adjustment of misfits at crossover points. Each of these steps may introduce errors that accumulate in the course of processing.

Mainly, the extraction of gravity anomalies from airborne strapdown INS gravimetry has been based on the state-space approach (SSA), which has many advantages but displays a serious disadvantage, namely, its very limited capacity to handle space correlations (like the rigorous treatment of crossover points).

This dissertation explores an alternative approach through the well known geodetic network approach, where the INS differential mechanisation equations are interpreted as observation equations of a least-squares parameter estimation problem.

In numerical terms, the INS equations are solved by a finite difference method where the initial/boundary values are substituted with the appropriated observation equations. The author believes that the above approach has some advantages that are on worth exploring; mainly, that modelling the Earth gravity field can be more rigorous than with the SSA and that external information can be better exploited.

It is important to remark that this approach cannot be applied to real-time navigation. However, here we are not trying to solve a navigation problem but a geodetic one.

A discussion of the different ways to handle with the associated system of linear equations will be described and some practical results from simulated data are presented and discussed.

Resum

En comparació amb la gravimetria terrestre, la gravimetria aerotransportada és més eficient i rendible. Especialment, la combinació de INS i GPS és ben coneguda per mostrar molts bons resultats al recuperar el senyal de la gravetat en el rang de freqüències mitjanes (1–100 km).

L'extracció de les anomàlies de gravetat a partir de gravimetria aerotransportada SINS s'ha basat principalment en l'aproximació SSA, que té molts avantatges, però que mostra un greu inconvenient, a saber, la capacitat molt limitada per tractar les correlacions espacials (com el tractament rigorós dels punts d'encreuament o cross-overs).

Aquesta tesi examina una alternativa a través de la coneguda aproximació en xarxes extensament usada en geodèsia, en el que les equacions diferencials de mecanització del INS s'interpreten com equacions d'observació d'un problema d'estimació de paràmetres per mínims-quadrats.

En termes numèrics, les equacions de mecanització INS es resolen per un mètode de diferències finites, on els valors inicials de frontera se substitueixen per equacions d'observació. L'autora considera que l'enfocament exposat té algunes avantatges que val la pena explorar; sobretot, la modelització del camp gravitatori terrestre pot ser més rigorós que amb SSA i les equacions d'observació poden ser explotades millor.

És important assenyalar que aquest enfocament no es pot aplicar a la navegació en temps real. Tanmateix, en aquest cas no es tracta de resoldre un problema de navegació, sino un de geodèsic.

En aquesta dissertació es presentaran diferents maneres de tractar aquest sistema d'equacions lineals i es mostraran alguns resultats pràctics a partir de dades simulades.

Resumen

En comparación con la gravimetría terrestre, la gravimetría aerotransporta es más eficiente y rentable. Especialmente, la combinación de INS y GPS es bién conocida por mostrar muy buenos resultados recuperando la gravedad en el rango de frecuencias medias (1–100 km).

La extracción de las anomalías de gravedad aerotransportada SINS se ha basado fundamentalmente en el enfoque SSA, que aunque tiene muchas ventajas muestra un inconveniente grave, a saber, su capacidad muy limitada de manejar las correlaciones espaciales (como el tratamiento riguroso de crossovers).

Esta tesis examina una alternativa a través de la conocida aproximación de redes ampliamente usada en Geodesia, en el que las ecuaciones de mecanización INS se interpretan como las ecuaciones de observación de un problema de estimación de paràmetros por mínimos cuadrados.

En términos numéricos, las ecuaciones INS se resuelven por un método de diferencias finitas, donde los valores iniciales de frontera se sustituyen por las ecucaciones de observación apropiadas. La autora considera que el enfoque expuesto tiene algunas ventajas que valen la pena explorar, sobretodo que la modelización del campo gravitatorio terrestre puede realizarse de una manera más rigurosa que con SSA y que las ecuaciones de observación externas y/o auxiliares pueden explotarse mejor.

Es importante mencionar que, actualmente, este enfoque no puede aplicarse a la navegación en tiempo real. Sin embargo, aquí no se trata de resolver un problema de navegación, sino uno de geodésico.

En esta disertación se presentan diferentes maneras de tractar el sistema lineal de ecuaciones asociado y se muestran algunos resultados prácticos a partir de datos simulados.

Contents

List of Figures

List of Tables

List of acronyms

ACX	Ajust Combinat de Xarxes
AGMASCO	Airborne Geoid Mapping System for Coastal Oceanography
AR	AutoRegressive process
AUSLIG	Australian Surveying and Land Information Group (now Geoscience Australia)
b-frame	Body Frame
bps	bits per second
C/A code	Coarse Acquisition Code
CDMA	Code Division Multiple Access
CHAMP	CHAllenging Minisatellite Payload
COMPASS	BeiDou-2
CORS	Continously Operating Reference Station
CUPT	Coordinate Update PoinT
CPU	Central Processing Unit
DGPS	Differential Global Positioning System
DTM	Digital Terrain Model
e-frame	Conventional Terrestrial (or Earth Fixed) Frame
ECEF	Earth Centered Earth Fixed
EGM2008	Earth Gravitational Model 2008
EGM96	Earth Gravitational Model 1996
EGNOS	European Geostationary Navigation Overlay System
EIGEN	European Improved Gravity model of the Earth bye New Techniques
EKF	Extended Kalman Filter
ESA	European Space Agency
EU	European Union
FIR	Finite Impulse Response (for a discrete-time filter)
GAGAN	GPS And GEO Augmented Navigation
GBAS	Ground Based Augmentation System
GDT	Gravity Disturbance's changes with respect to Time
GEO	GEostationary Orbit
GeoCat	Geoide de Catalunya
GeoTeX	Geodesia, Teledeteccio en Xarxes
GLONASS	GLObal'naya NAvigatsionnaya Sputnikovaya Sistema
GM	Gauss-Markov model

GNSS	Global Navigation Satellite Systems
GOCE	Gravity field and steady-state Ocean Circulation Explorer
GPS	Global Positioning System
GRACE	Gravity Recovery And Climate Experiment
GRAS	Ground-based Regional Augmentation System (Australia)
GRS80	Geodetic Reference System 1980
GUPT	Gravity Update PoinT
ICC	Institut Cartografic de Catalunya
ICGEM	International Centre for Global Earth Models
`i`-frame	Operational Inertial Frame
IG	Institut of Geomatics
IIR	Infinite Impulse Response (for a discrete-time filter)
IMU	Inertial Measurement Unit
INS	Inertial Navigation System
I/O	Input/Output
ITC	Inertial Technology Center in Moscow
ITG	Institute of Theoretical Geodesy
KBR	K-Band Ranging
KFS	Kalman Filtering and Smoothing
KMS	Kort & Matrikelstyrelsen (Danish Geodata Agency)
`l`-frame	Local-level Frame
LORAN-C	LOng RAnge Navigation
LRF-III	Honeywell Laseref III inertial navigation unit
LS	Least Squares
MEO	Medium Earth Orbit
mGal	milliGal = one thousandth of a Gal = $1 \times 10^{-5} m/s^2$
MSAS	Multi-Functional Satellite Augmentation System
NA	Network Approach
NAVSTAR	NAVigation Satellite Timing And Ranging
NRL	US Naval Research Lab
ODE	Ordinary Differential Equation
OS Net	Ordnance Survey GNSS Network
OSU	Ohio State University
OTF	On The Fly
PSD	Power Spectral Density
QZSS	Quasi-Zenith Satellite System
`r`-frame	Reference Frame (for aircraft motion)
RAM	Random Access Memory
RISG	Rotation Invariant Scalar Gravimetry
RLG	Ring Laser Gyro
RMS	Root Mean Square
SA	Selective Availability

SBAS	Satellite Based Augmentation System
SDE	Stochastic Differential Equation
SI	Systeme Internationale (units)
SINS	Strapdown Inertial Navigation System
SISG	Strapdown Inertial Scalar Gravimetry
SRTM	Shuttle Radar Topographic Mission
SSA	State-Space Approach
VUPT	Velocity Update PoinT
WAAS	Wide Area Augmentation System
XOVER	Crossover point
ZUPT	Zero Velocity Update PoinT

1 Introduction

1.1 Background

The determination of the Earth's gravity field is one of the most important areas in geodesy for the determination of the geoid and for the prediction of dynamical parameters of low Earth-orbiting satellites. In addition, gravity information is important for many scientific and engineering areas such as geophysical exploration and navigation, and in studying geophysical phenomena of the Earth. Traditionally, the gravity signal is determined by measuring its magnitude with a gravimeter and the deflections of the vertical, defined by the difference of the directions between the natural gravity and normal gravity vector, by astronomical observations. Although this produces highly accurate gravity vector information, it is extremely expensive and time consuming.

Due to recent satellite technology, it is possible to determine the gravity field using satellite observations, mostly in the form of satellite altimetry. Now there are available different refined global gravity models based on terrestrial gravity and satellite data, e.g. EGM2008 ([25]), EGM96 ([77]) or EIGEN ([26]). Hence the long wavelength gravity signal can be obtained by using a global model — as it has seen in Jekeli [61] and in Rapp [90]. According to a study by Jekeli [64], however, the shorter-wavelength signatures of the global model are either poorly modelled or only moderately well known in the global model.

The purpose of aerial gravimetry is to recover the Earth's gravity field on the medium-frequency gravity signal, which then fills the gap between the terrestrial gravity field measurements and global gravity models in the wavelengths between 1 and 100–200 km ([55]).

Measurements from GRACE ([113]), CHAMP ([91]) and GOCE ([92]) gravity mapping are expected to provide revolutionary improvement in our knowledge of the Earth's static gravity field and its temporal component. Especially, the accuracy of the mean geoid will be about 1 cm at a wavelength of 100 km or longer (primarily by GOCE). The accuracy and resolution from these missions, however, are still not good enough for geophysical exploration in which 1 mGal over less than 10 km is required ([93]). In addition, there will be polar gaps with radius

of 700 km due to the sun-synchronised orbits for GOCE. Therefore, even after these missions, airborne gravimetry will still play an important role in improving the model for the earth's gravity field.

As a matter of fact, the Inertial Navigation System (INS) was introduced as a surveying instrument in the late 1960's, and immediately it was noticed that the potential of INS for precise positioning was limited by the unknown anomalous gravity field.

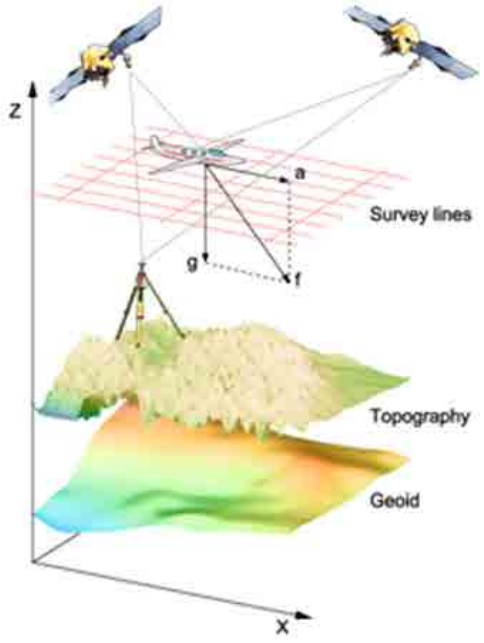

Figure 1.1: Principle of airborne gravimetry (Source: TUDelft).

Conversely, this means that the anomalous 3D gravity field could be recovered from the INS instrument if accurate kinematic positions and/or velocities were known and the system errors were kept small.

The important issue in gravity recovery using INS is the separation of the gravitational acceleration from kinematic acceleration as well as from instrumental errors. The kinematic acceleration can be separated from the sensed acceleration of INS by using a different sensor such as GPS. The separation between the gravitational acceleration and system errors from INS can be achieved by introducing external information, e.g. ZUPT (Zero Velocity Update Point, [118]). Although this semi-kinematic method has been successfully used in many cases, it is still inefficient and expensive for the exploration of large areas.

Obviously, an alternative way of determining the kinematic position and velocity was necessary to perform mobile, especially airborne, gravity surveys. Moritz proposed in 1967 ([79]) the

combination of INS and a gravity gradiometer, and simulation studies on such a combination showed promising results. Because of the high cost of the gradiometers, however, other combinations such as the combination of INS with a radio navigation system, LORAN-C, were investigated.

Clearly, the advent of the Global Positioning System (GPS), providing high accuracy position and velocity, created revolutionary progress in the area of airborne gravimetry. At that time, Schwarz ([97]) compared different kinematic methods for airborne gravimetry with combinations of GPS, INS and gradiometers.

Compared to the other positioning instruments, GPS is inexpensive and the accuracy of the vehicle acceleration from GPS is generally sufficient for airborne gravimetry.

INS/GPS gravimetry is mainly affected by two error sources: short term GPS-derived acceleration errors and long term INS inertial sensor errors ([104]).

For geoid determination applications, short term errors — i.e., the noise of GPS-derived accelerations — have been identified as one of the limiting factors of the technique ([3], [9], [16], [17], [18], [20], [44], [47], [60], [61], [62], [63], [66], [100], [102], [103], [104], [106], [108], [111]). Fortunately, the situation will likely improve significantly with the GPS modernisation programme and the advent of the European global navigation satellite system Galileo, because of its higher signal-to-noise ratio and with the subsequent use of hybrid Galileo/GPS receivers.

The correct measurement of gravity with INS/GPS gravimetry depends on the correct separation of the INS/GPS errors from the actual variations of the gravity field itself. This separation is, in principle, feasible because of the different characteristics of the two signals: errors of the inertial sensors can be reasonably modelled as time functions, whereas the variations of the gravity field are, strictly, spatial functions[1]. An improvement of the calibration of inertial sensors may be seen as an improvement of the long wavelength errors of INS/GPS gravimetry. By doing so, we are not only achieving an overall improvement of INS/GPS gravimetry but, in particular, we are extending its spectral window of applicability. This extension might be instrumental to the integrated use of GOCE gravimetry and INS/GPS gravimetry as the sole means of gravimetry for geoid determination.

There have been various studies ([61], [76], [103]) on the feasibility of INS/GPS gravimetry in both time and spectral domains. This research has shown that the gravity disturbance can be recovered with errors, defined by wavelengths, in the order of (RMS) ± 1–2 mGal using a high-accuracy INS within a spectral window of 10–200 km.

The main challenge in INS/GPS gravimetry is the low signal to noise ratio of the system. Typically, the gravity disturbance vector does not exceed 100 mGal in each component over distances of about 100 km, while the noise level of the system is much higher ([52]). Analysis

[1] Understandably, so far, most of the research has focused on the INS/GPS short wavelength errors as the practical use of the technique and its competitiveness with traditional terrestrial gravimetry is bounded by, moderate to high, precision and resolution thresholds.

and simulations were conducted by many investigators, mainly applying a low pass filter on the signal to reduce the system noises and extract the optimal gravity signatures in INS/GPS airborne gravimetry. In addition, the development as well as the analysis of the INS error model has been investigated theoretically, and tested throughout simulations. Recently, some test flights have been also carried out to determine the feasibility and to assess the accuracy in airborne gravimetry. It has been shown that 1 mGal accuracy in GPS acceleration and 2–3 mGal of accuracy in the vertical gravity component can be achieved ([127]).

1.2 Problem statement and objectives

There are two main techniques in airborne gravimetry based on accelerometer measurements, namely scalar gravimetry and vector gravimetry. Gravity gradiometry may be considered as the third type, where the observations are gradients of gravity. Scalar gravimetry determines either the vertical component or the magnitude of the gravity anomaly vector while vector gravimetry aims at recovering the full gravity anomaly vector in all three dimensions.

Currently, airborne gravimetry is conducted using either sea/air gravimeters on a Schuler-tuned stabilised platform for scalar gravimetry, or with an Inertial Navigation System — mainly strapdown INS and we will refer to it as INS/GPS gravimetry — for scalar or vector gravimetry. In both cases, the separation of the gravitational and kinematic accelerations from the system errors is crucial in estimating the gravity field. Results of scalar airborne gravity survey using gravimeters, modified for the higher dynamics of the aircraft, in Greenland, Antarctica and Switzerland show that an accuracy of 3–5 mGal and a resolution of 10 km wavelength is achievable with current technology ([1], [2], [7], [11], [12], [14], [31], [34], [35], [36], [38], [39], [40], [43], [57], [67], [68], [70], [71], [72], [73], [74], [78],[87], [109], [116], [120],[125], [127]). The main error source in these cases was insufficient platform stabilisation. Another test using the ITC-2 inertial platform system ([93]) showed that an accuracy of 1 mGal with resolution of 2–3 km is achievable.

Unlike the stabilised systems, there is no physical stabilising platform in a strapdown system. Instead, the inertial sensors are physically bolted down to the vehicle so that the measured data in the IMU instrumental (know as *body*) frame are transformed to the local level frame or ECEF frame (e-frame) computationally. The advantage of the strapdown INS is its smaller size, lower cost and more operational flexibility. It has been shown that the performance of the INS/GPS systems is comparable to that of the airborne gravimeter ([45], [46]).

The traditional way of analyzing the determination of gravity using the INS/GPS signal is to integrate the error dynamic equations or the dynamic equations of the INS system, and model the gravity disturbance and the INS errors as stochastic processes ([33], [49], [61], [62], [76], [122]). The a priori stochastic information of the INS errors, such as biases and scale factors, are obtained from the manufacturer's specifications and from further extensive and tricky calibration and field testing based modelling.

Remember that a dynamical system can be considered to be a rule for time evolution on a state space. The above described method is known as State-space Approach (SSA) and it is an optimal procedure for real-time applications. But this method cannot use all the existing observational information contained in a survey because it has a serious disadvantage trying to deal with space correlations — measurements involving states at different times. A good example of this limited capacity is the difficulty of a rigorous treatment of crossover points.

The key to overcome such limitations is to look at the system as stochastic differential equations (SDE) that, through discretisation, leads to a geodetic network widely used in geodesy, photogrammetry and remote sensing. The discretisation of dynamic observation models together with static (auxiliary) observation models and further network least-squares adjustment will be referred to as the Network Approach (NA).

There are two basic objectives in this dissertation:

- to prove the feasibility of the NA for the rigorous determination of the gravity field using INS/GPS techniques;
- to show that the above use of NA methodology shall provide, within the essential limitations of the technology, a procedure to simultaneously calibrate the INS sensors and estimate the anomalous gravity field.

There is a central idea in this dissertation: the use of the Network Approach allows the use of information — observations — that the State-space Approach cannot take, thus facilitating the achievement of the two above objectives.

1.3 Thesis Outline

One of the main objectives of this research is to investigate algorithms to better calibrate the systematic errors of the inertial sensors. More specifically, the research of an alternative geodetic procedure to the traditional Kalman filtering and smoothing borrowed from navigation. The advantage of the *new* procedure is that it can assimilate all the information available in a gravimetric (aerial) mission; from ground gravity control to the crossover or multiple-flight-line conditions, among other observational information types. The proposed procedure is nothing else than *geodesy as usual* in that we redefine the INS/GPS gravimetry problem as a network adjustment problem — early studies can be seen at [32] for least-squares methods in land-based and helicopter-based inertial gravimetry. In a more general perspective, the use of the NA procedure as a genuine geodetic method for non real-time navigation and positioning problems has been proposed in [22] and [23].

This thesis is divided as follows:

- Chapter 2 reviews the concept of airborne gravimetry.
- Chapter 3 covers the concept of the NA method. In this chapter, the dynamic and static observation models that can be assimilated by the NA for INS/GPS gravimetry are reviewed. Their implantation in the `GeoTeX/ACX` program is described. As well, some implementation issues of NA are discussed: limitations found and future improvements.
- Chapters 4 and 5 present the experimental results of the NA concept. The experiments use INS simulated data and demonstrate that the proposed NA procedure works.
- Chapter 6 summarises the main contributions of this study and provides suggestions and recommendations for further research.

2 Airborne Gravimetry Review

Measuring the Earth's gravity field is one of the most important activities in geodesy, especially for the determination of the geoid and the prediction of dynamic orbits of satellites. In addition, many scientific and engineering disciplines need gravity information for exploration and navigation and for investigation of geophysical phenomena. Although satellite technology makes possible to determine the gravity field, the shorter-wavelength signatures have been poorly modelled or only moderately well known in the high-degree expansions, such as the globals models EGM96 or EIGEN. Therefore, airborne gravimetry can play a very important role in recovering the Earth's gravity field in the range of medium to high frequencies, which then fills the gap between the terrestrial gravity field measurements and global gravity models in the wavelengths between 1 and 100–200 km.

2.1 The beginnings

Discussions on the possibility of measuring gravity in airborne mode were taking place in the geophysical exploration community about 60 years ago. Hammer ([54]) mentioned that he considered it as an *impossible dream* at that time. Given the state of airborne gravity today, the perspective of the dreamers has been the realistic one. In this section, an attempt will be made to trace the major phases of this development.

To understand the initial skepticism with respect to airborne gravity methods, a brief discussion of the mathematical model of kinematic gravimetry will be helpful. The formula for kinematic gravimetry in a local geodetic reference frame ([65]) is of the form

$$\underline{g} = \dot{\underline{v}} + (2\Omega_{ie} + \Omega_{el})\underline{v} - \underline{f} \tag{2.1}$$

where $\underline{g}$ is the gravity vector, $\underline{v}$ is the aircraft velocity vector, Ω_{ie} is the Earth rotation rate in skew-symmetric matrix form, Ω_{el} is the vehicle rate referenced to the ellipsoid and $\underline{f}$ is a vector of accelerometer measurements obtained from an orthogonal sensor triad aligned to the local astronomic system. The dot above a vector indicates time differentiation, i.e. the

first term on the right-hand side of the Equation (2.1), $\underline{\dot{v}}$, is the airplane acceleration vector. The second term is the well-known Coriolis effect, which is due to measurements in a rotating coordinate frame.

When comparing this equation to the model for stationary terrestrial gravimetry, there are some obvious differences, as well as some that are not so obvious:

- An obvious difference is the presence of the first and second term on the right-hand side of Equation (2.1). They will disappear when the system is in stationary mode because both terms are dependent on sensor motion. In stationary mode, i.e. in the case of no sensor motion, the accelerometer triad only senses gravity as a reaction force. Thus, the effect of vehicle motion on the accuracy of the gravity measurement is an obvious difference that has to be taken into account. Because accurate determination of carrier motion plays such a key role in the implementation of the Equation (2.1), this approach is sometimes called motion-aided gravimetry.
- A difference that is not as obvious is the requirement of determining the local vertical for the moving sensor system. Since all quantities in Equation (2.1) are given in the same reference frame the acceleration measurements $\underline{f}$ have to be made in that frame or have to be transformed to it. This means that ways have to be found to align the z-axis of the measurement frame $\underline{f}$ to the local vertical while the system is moving. In more general terms, the orientation of the measurement frame with respect to a well-known ECEF frame has to be known as a function of time. In stationary mode, this is easily achieved by using a level bubble. In kinematic mode, it is a difficult problem to solve.

This implementation of kinematic gravimetry must therefore solve two major tasks:

- The separation of gravitational acceleration from non-gravitational acceleration, i.e. forming the difference $\underline{\dot{v}} - \underline{g}$.
- The determination of sensor orientation for a moving measurement system.

The first task requires the measurement of vehicle acceleration at the same level of accuracy as the gravity measurement itself. The second task requires some form of platform stabilisation, either by mechanical or by computational means. It was mainly the first requirement that defeated the early attempts at implementing airborne gravimetry at the level of accuracy required for exploration applications.

To determine gravity with an accuracy of 1 mGal, the first term of the right-hand side of Equation (2.1) must be zero within an accuracy of 10^{-5} m s^{-2} or must be measurable within that accuracy. In practical terms this means that vehicle velocity must be either kept constant within rather narrow bounds or measured with extremely high accuracy. Keeping the velocity constant to this level is quite impossible for airplane trajectories. Realistic values for airplane

acceleration in a non-turbulent environment are between 0.1–0.3 m s^{-2}, i.e. between 10000–30000 mGal. Measuring airplane acceleration with an accuracy of a few mGal was simply not possible in the fifties, even if fairly long filtering periods were allowed.

The impossibility to realise this dream with sufficient accuracy for geophysical applications is probably the major reason why the geodetic community can claim first experimental results in this field. Recognising that high-resolution surveys were not possible with the available technology, attention shifted to applications, which did not require such high resolution. The determination of mean gravity anomalies for blocks ($1^\circ \times 1^\circ$), which were needed for a homogeneous global gravity coverage, seemed to be a suitable application. A first experiment — with this goal in mind — was conducted in 1958 by the Airforce Cambridge Research Center. Its results were reported by Thompson [115]. A LaCoste and Romberg sea surface gravimeter with some minor modifications was used in this test. Although successful in its main goal — to determine mean gravity anomalies with an accuracy of 10 mGal or better for $1^\circ \times 1^\circ$ blocks — it also showed very clearly that technical problems had to be overcome to make this an operational procedure:

- dynamic stability of the airplane required to stay within the measurement range of the gravimeter used[1],
- accuracy of the navigation data[2],
- filtering of high-frequency airplane accelerations,
- the magnitude of the Eötvös effect[3] and its accurate determination with the velocity information available.

The gravity measurements were averaged over 5' intervals which corresponded to a half-wavelength resolution of about 50 km at the given airplane speed of 150–200 m/s. The accuracy of the filtered gravity estimate at flight level was about 10 mGal. Since this test was performed as a feasibility study, it included a number of features not ordinarily available under operational conditions, as for instance the theodolite tracking system. The experiment showed, however, in which areas improvements were needed to realise the *impossible dream*.

Tests with a similar objective were carried out by Fairchild Aerial Surveys in May 1959 and by Fairchild LaCoste Gravity Surveys under contract to the Army Map Service in May 1961. Results of these tests are reported by Nettleton in [82] and [83], respectively. The LaCoste and Romberg system was used again, but some improvements had been made based on the previous test. In addition, the flying altitude was lower in this case — about 3.6 km — as was

[1] High flying altitudes of 6–9 km were deemed necessary.

[2] Navigation data was provided by Askania tracking cameras on the ground and a Doppler navigation system on the airplane.

[3] The Eötvös correction is due to the `ECEF`-type of Earth frame rotation and defined in Section 2.2 by the last two terms on the right-hand side of the Equation (2.2). This correction is affected by uncertainties in the navigation systems, in terms of course, speed and position errors.

the flight speed. The averaging period was only 3 min. All of this resulted in a half-wavelength resolution of about 16 km and in an accuracy of about 10 mGal in the first test and 6–7 mGal in the second. Compared to the initial test, the navigation equipment used in these tests was more standard and the comparison with ground truth in the 1961 test was based on a much larger sample. The considerable improvement in wavelength resolution was obviously due to the lower flight speed and the shorter averaging interval. These variables played a decisive role in the further development of airborne gravity techniques.

At the end of this first period, the *impossible dream* seemed not that impossible any more. Improvements in the determination of airplane motion, a careful tuning of the gravity filters applied and the use of carriers that could fly at very low speed seemed to be the main parameters for a further improvement of accuracy and resolution.

2.2 GPS and the solution of the motion problem

Although the initial tests of motion-aided gravimetry did not offer great promise for exploration, limited testing continued in the early 1970's to investigate the use of airborne techniques for oil exploration. In this phase and in much of the subsequent work, the modified LaCoste and Romberg sea surface gravimeter was used. It represents a scalar approach to airborne gravimetry in which the magnitude of gravity is measured by aligning a high-accuracy accelerometer to the local vertical. Such a sensor mimics the function of a stationary gravimeter. It yields a measurement of specific force f_u in the direction of the local vertical. Writing the third equation of formula (2.1) explicitly

$$g = f_u - \dot{v}_u + \left(v_e \left(R_n + h\right)^{-1} + 2\omega_{ie} \cos\phi\right) v_e + {v_n}^2 \left(R_m + h\right)^{-1} \tag{2.2}$$

results in the mathematical model for such a sensor. In this equation, f_u is the upward component of specific force measured along the local vertical; (v_e, v_n, v_u) are the east, north and upward component of the vehicle velocity $\underline{v}$; R_m and R_n are the meridian and prime vertical radii of curvature of the geodetic reference ellipsoid; ω_{ie} is the rotation rate of the Earth, and ϕ and h are ellipsoidal latitude and height, respectively.

The difference between the first two terms on the right-hand side gives essentially the magnitude of gravity, while the other two terms are measurement corrections due to the ECEF-type of Earth frame rotation. They are usually called the Eötvös correction.

To get g with an accuracy of 1 mGal, each of the terms on the right-hand side has to be determined with an accuracy of better than 1 mGal. This is clearly impossible for the vertical acceleration term $\dot{v}_u$ and the specific force term f_u measured by the stabilised gravimeter if point measurements are required. Even the computation of the Eötvös correction at this level of accuracy requires a velocity error smaller than 0.05 m/s in the third term. Considering the measurement systems available in the 1960's to determine motion in space, there was ample reason to call airborne gravimetry an impossible dream for exploration. It is to the credit of

the early investigators that they did not give up on this dream. They eventually succeeded in solving most of the problems by combining a careful error model analysis, customised filtering methods and optimal operational procedures.

The approximate solution of this problem in a damped-platform environment was achieved by determining the difference $\dot{v}_u - f_u$ within a certain band-limited region and making the Eötvös correction with the highest possible accuracy. Band-limitation was achieved by an elaborate system of filters and feedback loops, which for instance disregarded gravity information in the high frequency band when separating horizontal carrier acceleration from the acceleration effects due to platform tilt; Brozena did a good discussion in [10]. The resulting gravity solution is therefore low-pass filtered and its accuracy is strongly dependent on the accuracy of the motion data.

Recognising that the accuracy of carrier motion determination was a major problem, a number of improvements were made to ensure adequate measurement systems and smooth flight conditions. They included laser or radar altimeter systems for vertical acceleration determination, local navigation systems using range and range-rate measurements to known master stations and the use of flight-stabilised helicopters under optimal operational conditions (e.g. night flights, low speed). An overview of the results of the early experiments was published by Gumert in [50]. They renewed the interest of the exploration community in the further development of these methods, as it can be seen in [54]. During the 1980's Carson and Gumert looked out a number of patents on airborne gravity surveying, which started the pioneering work of Carson Geophysics as a company offering world-wide airborne gravity services for exploration. Over the years, this company has improved their system by paying careful attention to the operational conditions under which scalar gravimeters work best when used in moving mode (see for instance [51]).

The arrival of GPS as an operational procedure provided a major impetus to airborne gravimetry. This was not only due to the vastly improved positioning accuracy, but also because work on a world-wide scale without any special installations for obtaining precise trajectory information was now possible. The potential of using differential GPS — DGPS — measurements for airplane acceleration determination had been recognised early in the development of GPS applications (see [8], [69] and [98]). By using carrier phase data to obtain the velocity and position vectors of the airplane trajectory, the acceleration can be determined from either one of these vectors by time differentiation. Thus, the three vector variables needed for motion-aided scalar gravimetry, namely $\underline{r}$, $\underline{v}$, $\underline{\dot{v}}$ can be determined with high accuracy. While the velocity and position accuracy are fully sufficient to determine the Eötvös correction to better than 0.5 mGal, the acceleration determination still shows errors of several hundred mGal for the individual measurement, due to the amplification of measurement noise by time differentiation. Since gravity changes slowly in horizontal direction, filtering $\dot{v}_u - f_u$ over predetermined time periods will reduce the noise in the acceleration measurements to the desired level and provide a low-pass filtered approximation of the gravity spectrum.

In a number of geophysical and geodetic applications, the determination of the gravity field rather than the high-accuracy determination of individual points is of primary importance. What is often needed is the estimation of a specific spectral band of the gravity field. This band differs from one application to the next. For exploration, the high-frequency spectrum of the gravity field is of interest, while for geoid determination the low and medium frequency range is far more important. To obtain an optimal estimate of this band, bandpass filtering methods are used to extract this information from the measurements by minimising the noise in the data. The band for which the gravity signal can be reliably determined from airborne gravity data is often called the spectral window of airborne gravimetry (see [107]). A discussion of suitable filtering methods can be found in [17] and [52].

Besides providing accurate airplane motion determination for high resolution exploration surveys, DGPS also opened the door to airborne gravity surveys of continental extent. Pioneering work in this application has been done by the US Naval Research Lab (NRL) under the leadership of John Brozena. The survey of Greenland, done in cooperation with the Danish National Survey and Cadastre (KMS), was the first example of a successful gravity survey of continental extent (see for instance [11]). It showed many features of geophysical interest unknown at that time. A total of about 200000 line km were flown at a height of about 4 km in a large and stable military airplane at flight speeds between 370–450 km h^{-1}. Scalar gravity systems of the damped platform type were used in conjunction with differential GPS. The low-pass filtering of the data resulted in a RMS accuracy of 3–5 mGal as determined from crossover points and of 5 mGal as determined from comparison with sparse upward continued data; for details see [13] and [34]. Work of this type is continuing with smaller aircrafts in the Arctic and in the Antarctic, resulting in crossover RMS values of about 2 mGal; see for instance [15] and [37]. Similar geophysical problems were also studied in the European AGMASCO campaign; see [116].

2.3 Gravity gradiometry and the emergence of kinematic geodesy

It was about a decade after the initial experiments that a new method of airborne gravity sensing was proposed and investigated. The technology to be developed was a gravity gradiometer system that would allow the measurement of the full tensor of gravity gradients in the airborne environment. When combined with a highly accurate inertial navigation system, it could provide an autonomous navigation capability over long periods of time. The use of such a system for gravity determination in airborne mode was the major objective of the research done at the Ohio State University (OSU). Conceptually, it is quite different from the previous approach and is commonly called gravity gradiometry.

Instead of determining gravity by forming the difference between specific force measurements and airplane acceleration, gravity gradients are introduced as a new set of observables. Thus, aircraft acceleration has not to be modelled with as high an accuracy as before. Instead, gravity gradients measured by the gradiometer are used to determine a first approximation of the

gravity vector, which is used to correct the aircraft accelerometer output for the effect of gravity. Airplane velocity is then obtained by integrating the corrected accelerometer measurements. Equation (2.1) is therefore re-written as a differential equation for airplane velocity and coupled with the differential equation for gravity vector. Expressing all variables again in the local frame (l-frame), one obtains two sets of differential equations in the following form

$$\begin{aligned} \dot{\underline{v}} &= \underline{f} - (2\Omega_{ie} + \Omega_{el})\underline{v} + \underline{g} \\ \dot{\underline{g}} &= (\underline{G} - \Omega_{ie}\Omega_{ie})\underline{v} - \Omega_{el}\underline{g} \end{aligned} \tag{2.3}$$

where the observations or measurements are $\underline{f}$, the specific force; and $\underline{G}$, the gravity gradient tensor. The parameters are $\underline{v}$, the vehicle velocity; and $\underline{g}$, the gravity.

As can be seen from the equations, two systems are coupled, i.e. aircraft velocity $\underline{v}$ is needed to solve the differential equations for $\underline{g}$ and $\underline{g}$ is needed to determine aircraft velocity. Moritz ([79], [80]) proposed to solve these equations in an iterative scheme. Although appropriate for the geodetic applications where post-mission processing is possible, it is obviously not the appropriate method for the general navigation problem. Schwarz ([99]) later proposed a Kalman filter scheme for the real-time solution of this problem. Moritz ([79]) coined the term kinematic geodesy for this area of research. After the initial work on the mathematical models for airborne gravity gradiometry, it took almost 20 years before an actual system could be tested. The complexity of the system concept and the extreme sensor accuracy and stability to be achieved were major reasons for the long development time. When the system was finally operational, GPS had arrived and a much simpler solution could be implemented using aircraft velocity determined by DGPS together with the gradiometer measurements.

Gravity gradients have high power in the short-wavelength part of the gravity spectrum. They are therefore well suited for applications where the resolution of the high-frequency gravity spectrum is the major concern, as for instance in oil and mineral exploration. They are not as well suited for applications where the complete gravity spectrum is required, as for instance in geoid determination. In this application, the medium and long wavelength have to be determined by other means, because biases in the gravity gradiometer sensors will quickly generate major errors in low frequencies. This, and the high cost of the system, were the major reasons why airborne gravity gradiometry has not become a geodetic production method. Results have been reported in [5], [58] and [119] among others. Although airborne gravity gradiometry did not become an important geodetic tool, it has greatly advanced the theory of kinematic methods in geodesy and has prepared the way for satellite gravity gradiometry as a means for the determination of the global gravity field.

2.4 The use of inertial systems in airborne gravimetry

Airborne gravity systems used until the mid-1990's were all of the type described above, scalar systems with a damped platform to stabilise the gravity sensor. Most of them were modified

versions of the LaCoste and Romberg sea surface gravity system. In the mid-1990's work started at the University of Calgary to use off-the-shelf inertial systems in combination with DGPS for airborne gravimetry. There were several reasons why this step was taken. Besides size and cost, the main conceptual reason for using INS/GPS was the damped platform did not allow the complete elimination of the effect of horizontal accelerations on gravity. Stabilisation of the gravity sensor in these systems is therefore always approximate and performance degrades in turns and in situations where long-periodic dynamics affected the system.

To overcome such problems, either a Schuler-tuned platform had to be employed or a strap-down inertial system (SINS) could be used. The first solution was pursued in cooperation with O. Salychev from the Inertial Technology Center (ITC) in Moscow and with Sander Geophysics of Ottawa. The second solution was developed at the University of Calgary in cooperation with Intermap Technologies in Calgary. A brief description of the different concepts and their advantages and drawbacks will be given in the following. For details, the given references could be consulted.

Both, the Schuler-tuned stable platform system and the SINS are three-dimensional in nature and are therefore suitable for vector gravimetry, i.e. the determination of the magnitude and orientation of the gravity vector. All experiments conducted so far have shown that the accuracy of the deflections of the vertical, which can be determined from the vector orientation, is almost one order of magnitude poorer than the determination of the magnitude of gravity. This is largely due to drift effects of the horizontal gyros. To keep this section consistent with the previous ones, only the scalar case will be discussed. For readers interested in vector gravimetry, [61], [101] and [124] are recommended.

The difference between the two system concepts is the stabilisation of the gravity sensor. In a stable platform system the stabilisation is done mechanically, while in a SINS it is done numerically. Thus, in a stable platform system the local-level system is implemented by the gimbaled stable element. In a SINS the transformation matrix between the accelerometer frame and the `l`-frame is computed at very high speed as a function of time. The advantage of the Schuler-tuned system is that it automatically eliminates all effects of horizontal accelerations on the gravity measurements and that it has a simple error model when operated in a `l`-frame. Disadvantages are the difficulty to obtain orientation parameters from the read-out and often difficulty to obtain the information needed to accurately model the errors in the feedback loops. The SINS has the advantage that it is a fully digital system where all numerical operations are under full control of the operator. This gives enormous flexibility in trying different solution approaches. Its error model is more complicated because of the significant rotational dynamics, but its sensors are designed for a wide range of dynamical conditions and there is no danger of reaching the limits of the sensor range on a typical airborne gravity mission. The integration with DGPS is straightforward. Other advantages of the SINS are price, size and power requirements.

The model for the three-axes stable platform system is given by Equation (2.1), thus a full

vector solution is possible. The first system tested was the Russian ITC-2, which had been developed by combining a standard Schuler-tuned aircraft platform with a newly designed high-precision vertical accelerometer as the gravity sensor. Thus, stabilisation was done in this case by a Schuler-tuned inertial platform, while the magnitude of gravity was sensed by an especially built accelerometer. The installation and balancing of this additional sensor required very intricate procedures. The system was tested in 1993 and 1994 in the Calgary area. Results achieved by using a deterministic filtering method designed by Salychev in [95] indicate that a half-wavelength resolution of 2–3 km with an accuracy of 1 mGal or better is achievable. Detailed results are given in [94] and in [95].

The second system tested, named AIRGrav, is a stable platform system that has been specifically developed for airborne gravimetry by Sander Geophysics in Ottawa. For a description of the AIRGrav system and first results see [30]. This system has some unique features, as for instance the design of the gimbals is in such a way that the accelerometers can be tumbled and a calibration can be easily performed at the beginning and the end of the survey. Note that no special gravity sensor is used in this case. The vertical accelerometer takes on this function. First results with the instrument are excellent. It shows essentially no drift over several hours of flight and achieves a half-wavelength resolution of about 2 km with an accuracy of better than 1 mGal for a flight speed of 45 m/s. It can be expected that these results will improve with increasing operational experience.

To get the model for strapdown inertial system, Equation (2.1) has to be modified, because the accelerometer triad now has an arbitrary orientation and has to be transformed to the `l`-frame. Thus the specific force vector f^b measured in the body frame is now multiplied by the transformation matrix $\underline{R}$ to be rotated in the `l`-frame. Equation (2.1) therefore takes the form

$$\underline{g} = \dot{\underline{v}} + (2\Omega_{ie} + \Omega_{el})\underline{v} - \underline{R}f^b \tag{2.4}$$

The use SINS for airborne gravimetry was pursued at the University of Calgary from about 1995 onwards. A standard Honeywell LaserRef III system was made available by Intermap Technologies in Calgary. Tests with this system were done over the Canadian Rocky Mountains, in Greenland and in a test area close to Ottawa. First results were reported by Wei in [127] for a very rough area of the Canadian Rocky Mountains, showing a half-wavelength resolution of about 5 km with an accuracy of 2–3 mGal at a flight speed of about 120 m/s. Since resolution is dependent on aircraft speed, it can be improved by using a slower airplane. This was confirmed by test flights in Ottawa area where a half-wavelength of 2 km with an accuracy of 1–1.5 mGal were achieved for a flight speed of 45 m/s. In contrast to the AIRGrav system, which uses the same accelerometers, the Honeywell system shows considerable accelerometer drifts. They are most likely due to temperature effects because the AIRGrav accelerometers are temperature controlled, while the LaserRef III accelerometers are not.

An interesting modification of the standard SINS approach to airborne gravimetry is the

so-called RISG approach, see [24], where the acronym stands for Rotation Invariant Scalar Gravimetry. In this case, the magnitude of gravity is computed by combining the three specific force outputs with the three aircraft acceleration components without the use of the gyro measurements. The advantages of such a system are obvious. Instead of a full strapdown inertial system, only an accelerometer triad is needed. This results in a system of very small dimensions (5 cm^3) that is conceptually simple and low cost. A comparison of such a system with a standard SINS is given by Wei in [126] where error modelling and results are discussed. At this point in time, using the same measurements, results from the RISG approach are typically 15–20 % poorer than from the SINS approach. The reason for this difference was not clear.

The use of INS for airborne gravimetry has resulted in at least three operational systems. In side-by-side tests on the same aircraft, their performance compared very well to the LaCoste and Romberg system. In general, wavelength resolution was better, performance in turns was more regular and accuracy for the AIRGrav system was higher; for details see [19]. Taking into account the advantages such systems have in size, power requirements and cost, it can be expected that their use in airborne gravimetry will increase.

2.5 State of the art

Available airborne gravity systems have been used for gravity survey of continental extent (tectonics), for geoid determination and for geophysical exploration. To characterise the status of airborne gravity, a brief discussion of current results in geoid determination and geophysical exploration and and outlook on possible improvements will conclude the chapter.

Results published in [110] show that airborne gravity data from a 100 km × 100 km area flown at 10 km profile spacing with an average velocity of about 100 m/s are sufficient to determine a relative geoid with a standard deviation of 2 cm. The term *relative geoid* refers to a band-limited geoid with half-wavelength between 10–100 km. The standard deviation is computed from the undulation differences with respect to the geoid derived in the same area from ground gravity data. Taking into account that currently gravity satellite missions — such as GRACE, CHAMP and GOCE — are designed to improve low and medium wavelength accuracy to a cumulative geoid error of 1 cm for all wavelength above 100 km, the goal of achieving the cm-geoid appears to be possible. By combining results from the dedicated satellite missions with airborne gravity data at 5 km spacing, the band-limited spectrum for the cm-geoid is covered with sufficient accuracy. Thus, absolute geoid accuracy at the cm-level can be reached if the gravity satellite missions achieve their goal combined with airborne gravity data in areas where cm-accuracy is needed.

The use of airborne gravity data for geoid determination has typically been considered as a two step process. In the first step the gravity disturbances were downward continued from flight level to the ground by inverting Poisson's integral and in the second step they were integrated to obtain geoidal undulations using Hotine's integral; see for instance [84] or [128]. In these

papers, an alternative approach is also discussed, where integration at flight level is done first with subsequent downward continuation of the undulations determined at flight level. In both cases, downward continuation is considered as the crucial step for geoid accuracy. A number of papers have therefore been devoted to this topic. This method which essentially reduces the airborne data problem to a standard boundary value problem may not be the most accurate, nor the most efficient way to approach this problem.

In 2002, Novak ([85]) proposed an alternative approach, which takes into account the characteristics of the data acquisition process. The two features that are important to formulate are the nearly constant altitude at which the data are acquired and their band limitation due to the filtering process. The first is used to formulate a spherical initial-value problem for the anomalous potential at R (reference sphere) and $R+h$ (flight altitude reference sphere). The second allows to band-limit the integral kernel of the resulting solution to a range where its divergence will not affect the accuracy of the numerical solution adversely. The combination of these two features results in a one-step procedure. Numerical model studies have shown that this solution has sub-centimeter accuracy for the whole range of operational parameters that have been used in airborne gravimetry and is superior in accuracy and efficiency when compared to other solutions of this problem.

It might be possible to extend this methodology to topographic effects and to the treatment of satellite gravity gradiometry data. This would result in a powerful algorithm to the simultaneous treatment of airborne and satellite gravity data and their errors.

The requirements of exploration geophysics are more difficult to meet because they require both high accuracy and high resolution. Precision is largely a function of the length of the filtering interval, i.e. as filtering time increases, so does accuracy. Resolution is the product of vehicle speed and time interval. Since the speed of airborne vehicles has a definite lower limit, the time interval is also the decisive parameter to achieve high resolution. In this case, the behavior is opposite: as time increases, resolution decreases. This causes the difficulties when one attempts to increase accuracy and resolution at the same time. The main obstacle in reaching the requirements for exploration applications[4] is the noise in the DGPS-determined vehicle acceleration. Typically, it is close to the noise in the estimated gravity data as determined from independent observations. This indicates that in comparison the INS-noise is largely negligible. Similarly, DGPS noise and the estimated gravity noise at flight level vary in an almost linear fashion. Thus, flight conditions for high-accuracy work have to be chosen in such a way that they are done at times of low DGPS noise, i.e. at times of low ionospheric activity at night or in the early morning.

At this point, it appears that the main limitation in improving accuracy and resolution of airborne gravimetry is due to the accuracy of motion determination (or isolation) of the system sensors. The critical component seems to be the determination of aircraft acceleration

[4] Usually the requirements for exploration applications is a half-wavelength resolution of about 1 km with a standard deviation of 0.5–1.0 mGal

by DGPS. There are a number of ways in which a solution of this problem can be approached:

- The first and obvious one is the reduction of DGPS noise. This could most likely be achieved by using better clocks inside the GPS receiver and by optimising operational conditions to avoid high-noise environments (high ionospheric activity, multi-path environment).

- Supplementing DGPS by a low-noise relative height sensor would be a second approach. Barometric altimeters have been proposed and used for this purpose. Results at this point are not convincing and the theoretical problem of combining two very different height systems has not been solved at the required level of accuracy.

- A third approach would be to better define the signature to be detected, e.g. the signature of oil-bearing geological features. In that case, filters could be designed that make use of this information and are capable of finding such signatures in a high-noise environment. Although such an approach may be possible for certain geological features, it may not be suitable as a general approach.

- Finally, a system design could be considered that does not require a low-noise acceleration estimate. Gravity gradiometry is a possible candidate and recent results achieved in mineral exploration show that the required resolution is definitely there. There may be a problem, however, in detecting anything but shallow subsurface features with such an instrument. Thus, it may be necessary to combine airborne gravity gradiometry with airborne gravimetry to observe the required spectrum with sufficient accuracy. This would make for a very expensive system.

A proposal by Brown ([6]) for a dynamic absolute gravity system has great potential in increasing the measurement accuracy of the gravity sensor, but seems to require trajectory information of the same accuracy to make the aircraft motion corrections. Thus, the accuracy of the gravity estimate will be determined by the accuracy of the motion corrections rather than the accuracy of the gravity sensor.

There is no doubt that airborne gravimetry has become an operational method. When comparing the initial results of 10 mGal accuracy at a half-wavelength of 50 km to the results from the AIGRav system ([19]) of about 0.3 mGal accuracy at a half-wavelengths of 8 km or 1 mGal accuracy at a half-wavelenghts of 1 km, a great improvement can be observed in each of the parameters.

2.6 Outlook

It appears that, at the end, the motion determination problem — which plagued the early implementation of the idea — is the limiting factor for high accuracy and resolution in airborne

gravimetry. But in the coming years, with many more operational Global Navigation Satellite System (GNSS) signals, systems and frequencies, this will not be true.

GNSS is the standard generic term for satellite navigation systems that provide autonomous positioning with global coverage. GNSS allows small electronic receivers to determine their location to within a few meters using time signals transmitted along a line-of-sight by radio from satellites.

For the last 20 years, the term GNSS has been synonymous with the GPS. The United States NAVSTAR Global Positioning System (GPS) is the only fully functional, fully available GNSS. It consists of up to 32 medium Earth orbit satellites in 6 different orbital planes, with the exact number of satellites varying as older satellites are retired and replaced. Operational since 1978 and globally available since 1994, GPS is currently the world's most utilised satellite navigation system.

Of course, GPS was not the only GNSS available. The formerly Soviet, and now Russian, GLObal'naya NAvigatsionnaya Sputnikovaya Sistema (GLONASS) was a fully functional navigation constellation — 24 satellites with 21 used for transmitting signals and 3 for on-orbit spares, deployed in 3 orbital planes — in 1995. But the system rapidly fell into disrepair with the collapse of the Russian economy, leading to gaps in coverage an only partial availability. Beginning in 2001, Russia committed to restoring the system, and in recent years has diversified, introducing the Indian government as a partner, and accelerated the program with a goal of restoring global coverage. Now, the GLONASS system consists of 22 satellites, of which 17 are operational, 2 are in maintenance, 2 are in commissioning phase and 1 is in decommissioning phase.[5] The system requires 18 satellites for continuous navigation services covering the entire territory of the Russian Federation and 24 satellites to provide services worldwide.

China has indicated it will expand its regional navigation system, called Beidou[6] into a truly global satellite navigation system; a program that has been called COMPASS (or Beidou-2). The COMPASS system will be a constellation of 35 satellites, which include 5 geostationary orbit (GEO) satellites and 30 medium Earth orbit (MEO) satellites, that will offer complete coverage of the globe.

The European Union (EU) and the European Space Agency (ESA) agreed on March 2002 to introduce their own alternative to GPS, called the Galileo positioning system ([42]). Galileo is an alternative and complementary to GPS and GLONASS. The full constellation will consist of 30 satellites deployed in 3 orbital planes (9 operational satellites and one active spare per orbital plane). The system is scheduled to be operational by 2013 and it is intended to provide more precise measurements than available through GPS [7] or GLONASS including the altitude

[5] $http://www.glonass-ianc.rsa.ru/pls/htmldb/f?p=202:20:14637162736231801312::NO$

[6] The Beidou Navigation System is a project by China to develop an independent satellite navigation system. The current Beidou-1 system — made up to 4 satellites — is experimental and has limited coverage and application.

[7] Galileo will be accurate down to the meter range.

above sea level and better positioning services at high altitudes. The political aim is to provide and independent positioning system upon which European countries can rely even in times of war or political disagreement, since Russia or EEUU could disable the use of their systems — through encryption — by others.

The significance and value of the GNSS is recognised by a larger and larger audience. The existence of different fully operational GNSS systems — see Table 2.1 — will provide substantial benefits to civilian users worldwide.

Satellite Navigation systems:	
Global	GPS (EEUU), GLONASS (Russia),
	Galileo (EU), COMPASS (China).
Regional	QZSS (Japan), IRNSS (India), Beidou (China).
Satellite Based Augmentation Sytems (SBAS):	
Global	Omnistar, StarFire.
Regional	WAAS (EEUU), EGNOS (Europe),
	MSAS (Japan), GAGAN (India).
Ground Based Augmentation Systems (GBAS):	
Continental	GRAS (Australia), US DGPS Service (EEUU).
Regional	CORS (EEUU), AUSLIG (Australia)
Local	CATNET, ERGPS (Spain), OS Net (Great Britain)

Table 2.1: Classification of GNSS systems with examples of realisations.

This large increase in satellites will benefit not only single-point accuracy but also position reliability and the ability of GNSS user equipment to resolve integer ambiguities when using carrier phase tracking techniques. With more independent but compatible GNSS available, users will be able to exploit this situation by using only one system, by checking one o more systems for the others and by combining observations. The benefits of more GNSS signals in space include improved availability, particularly in urban canyons and steep terrain in which signals can be blocked, as well as greater accuracy (phase-positioning to the 0–5 cm level). Gains in precision are usually associated with the improved satellite geometry of combined GNSS constellations, which reduces the dilution of precision (DOP) and the latter factor's multiplicative effect on ranging errors. However, the redundant observations possible with more satellites also enable receivers in carrier-phase tracking mode to average measurement noise more effectively and, consequently, to make the position solution more precise.

At this point, remember that the determination of the anomalous gravity by inertial techniques depends on the capacity to separate the errors of the system — INS and GNSS errors — of the effects of the gravitational field. In this section, it has been shown that the existence of different GNSS systems improves the accuracy of motion determination. As GNSS errors decrease, the study of algorithms to better calibrate the systematic INS errors has to be increase. Note that this study is one of the main objectives of this dissertation.

3 INS/GNSS gravimetry: geodesy as usual

Remember that, currently, airborne gravimetry is conducted using either sea-air gravimeters on a stabilised platform for scalar gravimetry or with an INS for scalar or vector gravimetry. On the other hand, there are many different designs of INS with different performance characteristics, but they fall generally into two categories: gimbaled or stabilised platform techniques and strapdown. In all cases the GPS — GNSS, in next future — provides accurate kinematic acceleration and the separation of the gravitational acceleration from the system errors is crucial. Results from airborne gravity surveys using modified gravimeters and GPS in Greenland, Antarctica and Switzerland show that an accuracy of 3–5 mGal and a resolution of 10 km is achievable with current technology ([13], [34]). For a local stabilised system, [93], an ITC-2 inertial platform system was tested and showed that an accuracy of 1 mGal with a resolution of 2–3 km is achievable. Unlike the above two systems, there is no physically stabilised platform in the strapdown case. Instead, the strapdown inertial sensors are physically bolted to the vehicle and the measured data in the body frame[1] (b-frame) are transformed to the local-level frame (l-frame) computationally. The advantages of the strapdown system are its smaller size, lower cost and greater operational flexibility ([61]). In [48] it has been shown that the performance of the strapdown INS is comparable to that of the stabilised airborne gravimeter.

The traditional way of determining the gravity disturbance components using the INS/GNSS data is: first, to integrate the navigation equations associated with an INS, and second, to model the INS errors and gravity disturbances as stochastic processes ([28], [33], [49], [61], [76], [122]). GNSS positions and/or velocities are used as updates in a Kalman filter estimation of the errors, including the gravity disturbances and the calculations are done in the navigation frame (l-frame).

Alternatively, the gravity disturbance vector can be obtained directly by differencing the GNSS and INS sensed accelerations, [59], which is analogous to conventional airborne scalar gravimetry using gravimeters, [9].

[1] In strapdown systems the inertial sensors are mounted rigidly onto the device (ie. body of the host vehicle) and measure *body* acceleration. More information in Appendix B.

In INS/GNSS gravimetry, the separation of the INS/GNSS errors from the variations of the gravity field is obtained by the use of appropriate models for the IMU sensor systematic errors and for the gravity field anomalies. Given the INS mechanisation equations, the IMU calibration equations and the gravity field variation equations (sic), the SSA generates “optimal" estimates for the IMU trajectory (position, velocity and attitude), for the IMU errors and for the gravity field differences with respect to some reference gravity model.

In INS/GNSS gravimetry, the SSA approach ([123]) is essentially of the form

$$\begin{array}{rcl} \dot{\underline{r}}^{\mathtt{e}} & = & \underline{v}^{\mathtt{e}} \\ \dot{\underline{v}}^{\mathtt{e}} & = & \underline{R}^{\mathtt{e}}_{\mathtt{b}} \left(\underline{f}^{\mathtt{b}} + \underline{w}^{\mathtt{b}}_{f} \right) - 2 \left[\underline{\omega}^{\mathtt{e}}_{\mathtt{ie}} \times \right] \underline{v}^{\mathtt{e}} + \underline{g}^{\mathtt{e}}(\underline{r}^{\mathtt{e}}) \\ \dot{\underline{R}}^{\mathtt{e}}_{\mathtt{b}} & = & \underline{R}^{\mathtt{e}}_{\mathtt{b}} \left[\left(\underline{\omega}^{\mathtt{b}}_{\mathtt{ib}} + \underline{w}^{\mathtt{b}}_{\omega} \right) \times \right] - \left[\underline{\omega}^{\mathtt{e}}_{\mathtt{ie}} \times \right] \underline{R}^{\mathtt{e}}_{\mathtt{b}} \end{array} \tag{3.1}$$

where

- $\underline{r}^{\mathtt{e}}$ and $\underline{v}^{\mathtt{e}}$ are the position and velocity vectors in the ECEF frame (e-frame);
- $\underline{R}^{\mathtt{e}}_{\mathtt{b}}$ is the transformation matrix form the body frame (b-frame) to the e-frame;
- $\underline{\omega}^{\mathtt{e}}_{\mathtt{ie}} = (0,0,\omega_{\mathtt{e}})^T$ where $\omega_{\mathtt{e}}$ is the rate of Earth rotation;
- $\underline{g}^{\mathtt{e}}$ is the gravity vector as a function of $\underline{r}^{\mathtt{e}}$;
- $\underline{w}^{\mathtt{b}}_{f}$ and $\underline{w}^{\mathtt{b}}_{\omega}$ are white-noise processes of the specific force $\underline{f}^{\mathtt{b}}$ and angular velocities $\underline{\omega}^{\mathtt{b}}_{\mathtt{ib}}$ inertial observations respectively.

The numerical solution of this system can take many different forms which may be model-based or not (see [53]).

One approach could be: the output of the stochastic dynamical system defined by the INS mechanisation equations is Kalman-filtered and -smoothed with the GPS-derived positions and/or velocities (see [96], [104], [117], [123]).

Some of the active groups working on these problems employ the following two-step procedure: in a first stage, FIR filtering or something similar to take care of time-dependent errors, and in a second stage, a crossover adjustment to take care of the spatial structure of the gravity field.

The problem is, however, that the SSA *optimal* estimates are not the best estimates because the SSA cannot use all the observational information contained in an aerial survey. It is an optimal procedure for real-time applications. But it has a serious disadvantage, namely, its very-limited to no-capacity of dealing with space correlations — measurements involving states at different times. An example of this limited capacity is the difficulty of a rigorous treatment of crossover points.

The key to overcome the SSA limitations is to look at the system (3.1) as stochastic differential equations (SDE) that, through discretisation, leads to a time dependent geodetic network as discussed in [22], [23] and [114], for geodetic, photogrammetric and remote sensing applications.

3.1 Time dependent networks

A time dependent network ([22], [23]) is a network[2] such that some of its parameters are time dependent; i.e., that some of its parameters are stochastic processes. A time dependent network can be seen as a classical network that incorporates stochastic processes and dynamic models. A classical network can be seen as a particular case of a time dependent network.

To solve a time dependent network is to perform an optimal estimation of its parameters which may include some stochastic processes. Optimality in estimating a stochastic process means to estimate the best expectation function $\widehat{x}(t)$ in the sense of having minimal $E(\|x-\widehat{x}\|^2)$.

In the classical network adjustment theory it is well known that the network — its observations, parameters and their relationships — is completely defined by the set of observation equations

$$f(l+v,x)=0 \tag{3.2}$$

where

- l is usually the outcome of a measurement (or observation),
- v is a normally distributed random variable of null expectation (or residual), and
- x is an unknown random variable (or parameter).

Similarly, the time dependent network is completely defined by the set of its static and dynamic observation equations. A static observation equation or model is an equation of the type

$$f_s(t,l+v,x(t))=0 \tag{3.3}$$

where

- v is a normally distributed variable of null expectation,
- t is a time value, and
- $x(t)$ is an unknown stochastic process.

[2] In geomatics, a network is a set of instruments, observations and parameters that are inter-related through mathematical models. The mathematical models are the observation equations.

A dynamic observation equation — equivalently, a dynamic observation model or a stochastic dynamic model — is an equation of the type

$$f_d(t, l(t) + \omega(t), x(t), \dot{x}(t)) = 0 \tag{3.4}$$

where

- $\omega(t)$ is a white noise process, and
- $\dot{x}(t)$ is the time derivative of $x(t)$.

For the sake of simplicity in notation, the term $x(t)$ stands for time independent parameters (random variables) and for time dependent parameters (stochastic processes). We note, that Equation (3.4) is a stochastic differential equation (SDE) and that $\dot{x}(t)$ is not a conventional time derivative but a time derivative of a stochastic process. The theory ([86]) and the numerical solution ([75]) of SDEs are, today, active fields of research in mathematics.

In more global terms, we will refer to the family of static observation equations as the network static model and to the family of dynamic observation equations as the network dynamic model. Needless to say, a classical network is a particular case of a time dependent network.

The actual situation is the increasing availability of time series of measurements and the increasing use of time dependent information and the usual reaction is to resort from the classical least-squares network adjustment (the network approach, NA) to Kalman-filtering and smoothing (KFS), known as the state-space approach (SSA). However, while Kalman filtering is the tool of choice for real-time applications it cannot take advantage of observation equations relating parameters at different time epochs. Moreover, extended and non-linear KFS requires that the dynamic observation equation be of the form

$$\dot{x}(t) = f_d(t, l(t) + \omega(t), x(t)) \tag{3.5}$$

which is restrictive as compared to the formulation of Equation (3.4).

In practice, the solution of a time dependent network over a time interval $[0, T]$ requires a time discretisation $(t_i)_{i=0,\dots,n}$ with $0 = t_0 < t_1 < \cdots < t_i < \cdots < t_n = T$, which in the simplest equidistant case has a time step size δ ($\delta = T/n$).

Given the time discretisation $(t_i)_{i=0,\dots,n}$, if we put $l_i = l(t_i)$, $v_i = v(t_i)$, $\omega_i = \omega(t_i)$ and $x_i = x(t_i)$, then the static observation in Equation (3.3) may be writen in the form

$$f_s(l_i + v_i, x_i) = 0,$$

and the dynamic observation Equation (3.4) in the form

$$f_d(t_i, l_i + \omega_i, x_i, \dot{x}_i) = 0.$$

Recall that the discretisation of the dynamic observation models together with the static observation models and further network least-squares adjustment will be referred to as the network approach (NA).

The simplest heuristic approach to the solution of the network is based on the numerical approximation of $\dot{x}_i$ by a linear combination of a subset $\{x_{i-p},\ldots,x_i,\ldots,x_{i+q}\}$ of the time discretisation $\{x_0,\ldots,x_n\}$ of the stochastic process $x(t)$

$$f_d(t_i, l_i+\omega_i, x_i, \sum_{j=i-p}^{i+q} \alpha_j x_j) = 0.$$

Numerically speaking, once this is done, we are back to the situation of a static observation equation and, therefore, to the situation of a classical static network. See Appendix D for more information about the approach used in this dissertation.

3.2 The NA approach

In general, the Network Approach (NA) has some potential advantages compared to State-Space Approach (SSA): parameters may be related by observations regardless of time; covariance information can be computed selectively; and variance component estimation can be performed. In the context of INS/GNSS gravimetry the author believes that some of the NA potential advantages are significant:

- modelling of the Earth gravity field can be more rigorous than with the SSA;
- external observational information can be better exploited; and
- more information for further geoid determination can be produced.

The main drawback of NA is that it cannot be applied to real-time INS/GNSS navigation but this is certainly not an issue for a geodetic gravimetric task.

In this section, the dynamic and static observation models that can be assimilated by the NA for INS/GNSS gravimetry are reviewed. The set of dynamic observation models corresponds to what is called *the system model* in stochastic modelling and estimation. Analogously, the set of static observation models corresponds to what is called *the measurement model*. In the context of time dependent networks ([22]) the expressions *dynamic observation model* and *static observation model* are used to highlight the fact that we build our network from observations that contribute to the estimation of parameters either through dynamic or static equations.

In INS/GNSS gravimetry there are, essentially, two main models. One model is the system of the INS mechanisation equations and the other model expresses the *continuity* of gravity along the aircraft trajectory.

The mathematical model associated to SINS navigation is given by the well-known mechanisation equations (3.1), that are usually extended with the angular rate sensors and accelerometers calibration states and models.

The accelerometer and gyro sensor errors of a SINS consist of two parts: a deterministic part — biases and scale factors — which is determined by calibration and then removed from the raw measurements, and a random part, which is correlated over time and is basically due to the variations in the SINS sensor bias terms.

Therefore, these random errors are modelled stochastically so that they can be included in the SINS error model. For most of the SINS systems, a first-order Gauss-Markov model with a fairly large correlation time is usually used to described these errors. However, by studying the autocorrelation sequences of the noise components at the outputs of inertial sensors, Nassar ([81]) determined that a first-order Gauss-Markov is not adequate to model such noise behavior and offered an alternative method to model the inertial sensor noise as a higher order autoregressive (AR) process. But now, to fix the ideas and for the sake of simplicity we restrict intentionally the calibration states to time dependent biases

$$\begin{array}{rcl}
\dot{\underline{r}}^{\mathsf{e}} & = & \underline{v}^{\mathsf{e}} \\
\dot{\underline{v}}^{\mathsf{e}} & = & \underline{R}^{\mathsf{e}}_{\mathsf{b}}\left(\underline{f}^{\mathsf{b}} + \underline{a}^{\mathsf{b}}\right) - 2\left[\underline{\omega}^{\mathsf{e}}_{\mathsf{ie}}\times\right]\underline{v}^{\mathsf{e}} + \underline{g}^{\mathsf{e}}(\underline{r}^{\mathsf{e}}) \\
\dot{\underline{R}}^{\mathsf{e}}_{\mathsf{b}} & = & \underline{R}^{\mathsf{e}}_{\mathsf{b}}\left[\left(\underline{\omega}^{\mathsf{b}}_{\mathsf{ib}} + \underline{o}^{\mathsf{b}}\right)\times\right] - \left[\underline{\omega}^{\mathsf{e}}_{\mathsf{ie}}\times\right]\underline{R}^{\mathsf{e}}_{\mathsf{b}} \\
\dot{\underline{o}}^{\mathsf{b}} & = & F_{gyr}(\underline{o}^{\mathsf{b}}) \\
\dot{\underline{a}}^{\mathsf{b}} & = & F_{acc}(\underline{a}^{\mathsf{b}})
\end{array} \tag{3.6}$$

where F_{gyr} and F_{acc} are the calibration model functions of the angular rate sensors ($\underline{o}^{\mathsf{b}}$) and accelerometers biases ($\underline{a}^{\mathsf{b}}$). (Needless to say, the calibration functions and the calibration states depend on the type of sensors.)

The system (3.6) can be extended with a new mathematical model — GDT model — that shows the changes of the gravity disturbance along the trajectory of a moving vehicle with respect to time.

Traditionally, gravity disturbance is modelled as an stochastic process ([49], [61], [62], [76], [121], [33], [27]). Usually, the models for the gravity field assume ergodicity and, hence, stationarity and some isotropic covariance function that depends on two parameters: variance and the correlation distance. For details or forms of the covariance models see [122], [61], [76], [33] and [27]. Now, to fix the ideas and for the sake of simplicity, it is possible to consider $\delta\underline{g}^{\mathsf{e}}$ as a random walk: $\delta\dot{\underline{g}}^{\mathsf{e}} = \underline{w}$.

Finally, the dynamic observation models formed by the SINS mechanisation equations (3.6) including also the GDT model are

$$
\begin{aligned}
&\text{VEL:} && \dot{\underline{r}}^{\mathsf{e}} = \underline{v}^{\mathsf{e}} + \underline{w}_0^{\mathsf{e}} \\
&\text{FB:} && \dot{\underline{v}}^{\mathsf{e}} = \underline{R}_{\mathsf{b}}^{\mathsf{e}} \left(\underline{f}^{\mathsf{b}} + \underline{w}_f^{\mathsf{b}} + \underline{a}^{\mathsf{b}} \right) - 2 \left[\underline{\omega}_{\mathtt{ie}}^{\mathsf{e}} \times \right] \underline{v}^{\mathsf{e}} + \delta \underline{g}^{\mathsf{e}} + \underline{\gamma}^{\mathsf{e}}(\underline{r}^{\mathsf{e}}) \\
&\text{WIB:} && \dot{\underline{R}}_{\mathsf{b}}^{\mathsf{e}} = \underline{R}_{\mathsf{b}}^{\mathsf{e}} \left[\left(\underline{\omega}_{\mathtt{ib}}^{\mathsf{b}} + \underline{w}_{\omega}^{\mathsf{b}} + \underline{o}^{\mathsf{b}} \right) \times \right] - \left[\underline{\omega}_{\mathtt{ie}}^{\mathsf{e}} \times \right] \underline{R}_{\mathsf{b}}^{\mathsf{e}} \\
&\text{OB:} && \dot{\underline{o}}^{\mathsf{b}} = F_{gyr}(\underline{o}^{\mathsf{b}} + \underline{w}_o^{\mathsf{b}}) \\
&\text{AB:} && \dot{\underline{a}}^{\mathsf{b}} = F_{acc}(\underline{a}^{\mathsf{b}} + \underline{w}_a^{\mathsf{b}}) \\
&\text{GDT:} && \delta \dot{\underline{g}}^{\mathsf{e}} = \underline{w}_g^{\mathsf{e}}
\end{aligned}
\tag{3.7}
$$

These models are time dependent equations such as Equation (3.4), where $\underline{\ell}(t) = (\underline{f}^{\mathsf{b}}, \underline{\omega}_{\mathtt{ib}}^{\mathsf{b}})^T$ and $\underline{x}(t) = (\underline{r}^{\mathsf{e}}, \underline{v}^{\mathsf{e}}, \underline{R}_{\mathsf{b}}^{\mathsf{e}}, \delta \underline{g}^{\mathsf{e}}, \underline{a}^{\mathsf{b}}, \underline{o}^{\mathsf{b}})^T$ and $\underline{w}_0^{\mathsf{e}}$, $\underline{w}_f^{\mathsf{b}}$, $\underline{w}_{\omega}^{\mathsf{b}}$, $\underline{w}_o^{\mathsf{b}}$, $\underline{w}_a^{\mathsf{b}}$, $\underline{w}_g^{\mathsf{e}}$ are the process noises.

The static observation models, that usually have been considered, are the coordinate update point (CUPT), the velocity update point (VUPT), the gravity update point (GUPT) and the crossover points (XOVER) models. Here, they are defined briefly, and later in section 3.4 they will be described in detail:

- **CUPT model**. A coordinate update is a point where the position of the platform is known from an independent procedure (usually GPS). The CUPT equation is $\underline{p}_0^{\mathsf{e}} + \underline{w}_p^{\mathsf{e}} = \underline{r}^{\mathsf{e}}$.

- **VUPT model**. If instead of the position the velocity is known, the associated equation is $\underline{v}_0^{\mathsf{e}} + \underline{w}_v^{\mathsf{e}} = \underline{v}^{\mathsf{e}}$.

  A good example of the VUPT model is shown in [29]. Farrell studied an extensive set of flight-validated methods. One is the improvement of INS/GNSS integration with placement of tags for velocity and attitude adjustments. Sequential changes in carrier phase can adjust dynamics only, with velocity history feedforward to the position estimator for integration into a priori position, adjusted by pseudoranges only.

  The zero velocity update (ZUPT) is based on $\underline{v}^{\mathsf{e}} = 0$ and it is widely used in terrestrial inertial surveying. But, in a gravimetric flight, it can only be applied at the beginning and at the end of the survey.

  A ZUPT point is as a particular case of a VUPT one where $\underline{v}_0^{\mathsf{e}} = 0$.

- **GUPT model**. If gravity is known in some point of the trajectory, the following equation is obtained: $\underline{g}_0 + \underline{w}_g = \| \delta \underline{g}^{\mathsf{e}} + \underline{\gamma}^{\mathsf{e}}(\underline{r}^{\mathsf{e}}) \|$.

- **XOVER model**. In airborne gravimetry, the data acquisition profiles are usually chosen to form a network with a sufficient number of crossings, which are known as crossovers. The difference of the computed gravities at these points gives a quality control of the survey. These differences are due to the difference of the flight altitudes, as well as other bias sources. Classically, after the application of low pass filtering, a post-processing adjustment is applied to make the system gravity disturbance estimates self-consistent; i.e. measurements taken at the same location at different times give the same value.

  The adjustment is based on the use of crossover point differences in gravity disturbance estimates between flight lines. Each flight line used in the crossover adjustment is considered to have a separate slope and bias term.

  From [56, Equation (4–16)], we have

  $$g^{\mathsf{e}}(P) = g^{\mathsf{e}}(Q) - \frac{\partial g}{\partial h}\left(h_Q - h_P\right),$$

  where $\frac{\partial g}{\partial h} = -0.0848$ mGal/m.

  It is important to note that, sometimes, the gravity data will be computed at a lower frequency than navigation data. All the parameters associated to one crossover have been related to the same value of gravity. The crossover point has been generalised to the concept of a crossover area.

  On the other hand, in a ZUPT point gravity can be considered as a constant function. For times t_n and t_{n+1}, $\underline{g}^{\mathsf{e}}_n$ and $\underline{g}^{\mathsf{e}}_{n+1}$ are the same. Consequently, it can be considered as a crossover.

Remember that dynamic observation equations are Stochastic Differential Equations (SDE). They arise naturally from real-life Ordinary Differential Equations (ODE) whose coefficients are only approximately known because they are measured by instruments or deduced from other data subject to random errors. The initial or boundary conditions may be also known just randomly. In these situations, we would expect that the solution of the problem be a stochastic process.

Like in ODE theory, certain classes of SDE have solutions that can be found analytically using various formulas, and other classes — the vast majority of them — have no analytic solution. There are several numerical techniques to solve SDE; see [75]. All of them are based on their correct stochastic discretisation which is not a trivial issue.

3.3 The `GeoTeX` software package

The observation equations of this research has been implemented into the existing `GeoTeX` software system of the ICC — which includes the `GeoTeX/ACX` computer program [21] — that has been used for all the computations.

3.3.1 General description

GeoTeX/ACX is a general geodetic and photogrammetric point determination system which is able to deal with any type of geometric functional model. It is suited for research as well as for production purposes and can be easily extended to incorporate new models. GeoTeX has been developed by the ICC since 1988 and it is still currently used for research and production.

In GeoTeX/ACX it is relatively easy to add a new functional model. The user is allowed to define observable and parameter new data types. That addition takes only the formal definition of the observable and of the new parameters involved (definition of the particular observable and parameter data type), the codding of the observation equations and their jacobian matrices, and a subsequent compilation and generation of the new executable. Only a limited knowledge of the software is needed for the extension of the models.

GeoTeX adopts a simple adjustment oriented point of view: the main data types are observables, parameters and sensors.

An observable is defined as

$$\langle p_1 \dots p_i \rangle \langle s_1 \dots s_j \rangle \langle a_1 \dots a_k \rangle \langle o_1 \dots o_l \rangle \langle c_1 \dots c_m \rangle$$

where

- $p_1 \dots p_i$ are the identifiers of the parameters involved in the observational model,
- $s_1 \dots s_j$ the identifiers of the instruments used,
- $a_1 \dots a_k$ auxiliary information (time, meteorological data, etc.),
- $o_1 \dots o_l$ the actual observed amounts, and
- $c_1 \dots c_m$ some representation of the covariance matrix.

Analogously, the abstract types parameter and sensor follow the same philosophy.

3.3.2 Functional model implementation

When the user wants to implement a new model, she/he has just to edit some table-files where she/he can define the abstract types for observations, sensors and parameters. Then, she/he has to program a FORTRAN subroutine for the observation equations and their derivatives according to certain calling conventions; this subroutine is added to the GeoTeX/ACX object module library and a new executable module is generated. So, the user needs to know very few about the program and just nothing about discrete and I/O modules.

GeoTeX/ACX supports the following model: $l = f(x)$ or $l - f(x) = 0$. Then the linearised model is:

$$l - f(x_0) - Df(x_0) \cdot \Delta x = 0.$$

And the error equation is:

$$v + l - f(x_0) - Df(x_0) \cdot \Delta x = 0.$$

Therefore, the partial misclosure vector m is computed as $m = l - f(x_0)$, and the partial design matrix J as $J = -Df(x_0) = D\langle f, x_0 \rangle$.

Last, the residual vector v has to be computed as $v = -m - J \cdot \widehat{\Delta x}$, where, recall, $\widehat{\Delta x}$ are the adjusted corrections obtained in the solution of the normal equations.

3.3.3 Software used in this thesis

Since its creation in 1988, GeoTeX/ACX has been improved several times. Now, for this research, it has been moved from FORTRAN77-static to FORTRAN90-dynamic memory 32-bit implementation.

Static allocation is simple from the compiler's perspective because all that is needed is to create a list of variables that need allocation and lay them down in memory one after the other. A run-time advantage of static allocation is that it is usually easy and fast to access a fixed address and statically allocated data can be used from anywhere in the program. But static allocation has disadvantages too. Here the most important one is that you have to recompile the program every time you need to increase the dimension of the arrays.

Dynamic allocation is the complete opposite of static allocation. The big advantage of dynamic allocation is that the program can decide at run time how much memory to get, making it possible that programs can accommodate problems of any size. The user is limited only by the total amount of virtual memory available to the process: a little less than 2GB in 32-bit Windows.

To take advantage of previous work, GeoTeX/ACX allocates and deallocates array information in files. When an array is deallocated, all its structure is stored in a temporal binary file, and when it has to be used later, all this structure is read faster (allocate). This practice is provisional and it can increase actual device I/O as well as CPU time. However some years ago, this device I/O was a big problem. Now, with improvement of hardware systems, the problem seems to disappear. For the purposes of this research and to be able to compute the entire network, having plenty of available virtual memory is more important than increasing the CPU time. But for production purposes of the ICC, both factors — managing big-size networks rapidly — have the same importance: GeoTeX/ACX has to adjust big networks in few minutes.

It seems more reasonable to migrate GeoTeX/ACX from 32-bit into 64-bit implementation. The 64-bit operating systems offer greater power, reliability and scalability. First and foremost, a 64-bit machine can address more memory directly without using complex indexing or register-addressing schemes. Because internal memory is several orders of magnitude faster than storage, combining a 64-bit processing architecture with more RAM lets a processor pull more data into memory and operate on it directly, increasing performance manifold. A 64-bit file system also can improve disk management.

The move to 64 bits will primarily help users who need to access very large data stores. While some 64-bit machines can process both 64-bit and 32-bit instructions, and translators exist to convert 32-bit programs to slow but functional 64-bit programs, a 64-bit machine needs a 64-bit operating system and 64-bit applications to deliver optimum results.

Sun gives this analogy to describe the difference between a 32-bit operating environment and a 64-bit operating environment:

> *A 32-bit addressing space can keep track of the name and address of every person who has lived in the United States since 1997, a 64-bit addressing space can keep track of the name and address of every person who has ever lived in the world, from the beginning of time.*

The capability to accommodate huge quantities of memory, combined with far greater efficiency at managing high-bandwidth I/O, give 64-bit systems scalability advantages that 32-bit technology can not match.

The next step, if 64-bit environment is to be outdone, would be to move GeoTeX/ACX to supercomputing technologies. The use of computational power of the center's parallel machines might be a possibility[3].

All the computations done in this dissertation — see Chapter 4 — has been computed with GeoTeX/ACX (now a 32-bit program) running in a 64-bit platform[4].

3.4 Observation equations

In this section, the INS/GNSS differential mechanisation equations are interpreted as observation equations to be used in a least-squares parameter estimation problem. In numerical terms, the equations are solved by a finite difference method where the initial/boundary values are substituted with the appropriate observation equations.

[3] Since 2005, there is the Barcelona Supercomputing Center (BSC). It is the national supercomputing facility in Spain and BSC manages Marenostrum, the most powerful supercomputer in Europe. BSC focuses in Computer Sciences, Life Sciences and Earth Sciences. Following this multidisciplinary approach, BSC brings together researchers, high performance computing experts and cutting-edge supercomputing technologies.

[4] Windows Server 2003 Enterprise Edition. Service Pack 1. Intel (R) Xeon (TM) MP. CPU 3 GHz with 8 processors and Physical Address Extension. 4 GB RAM / 30 GB PF.

There are several finite difference methods that could be used, but the discussion is limited to the simplest one: the explicit midpoint method or leap-frog method. This method is described in the function `deriva1` in Appendix D. In this research, it is used to illustrate the use of NA for INS/GNSS gravimetry and that the previous equations — the dynamic and the static — can be transformed into a finite set of observation equations.

It is important to consider the rates of the parameters to be estimated. These rates are related to the frequency of the observations: if an IMU is working at a given frequency, then the parameters $\underline{r}^{\mathsf{e}}$, $\underline{v}^{\mathsf{e}}$, $\underline{q}$ will be estimated at the same frequency, but $\delta\underline{g}^{\mathsf{e}}$ and $\underline{a}^{\mathsf{b}}$, $\underline{o}^{\mathsf{b}}$ would be determined at given different rates.

To determine a parameter at time t_n with the unknowns referred at a different rate, it is necessary to interpolate these unknowns at the desired time. There are many interpolation methods to be applied. Depending on the method, the associated functional model would be more or less complex.

A simple one may be the linear interpolation method:

$$y[n] = \left(\frac{t[n] - t_x[m]}{t_x[m+1] - t_x[m]}\right) \cdot x[m+1] + \left(\frac{t_x[m+1] - t[n]}{t_x[m+1] - t_x[m]}\right) \cdot x[m]$$

where $t[n] \in [t_x[m], t_x[m+1][$. For each $y[n]$ value, two unknowns parameters — $x[m]$ and $x[m+1]$ — should be determined.

But, in this work, we consider the following interpolation method that keeps the number of unknowns to be determined:

$$y[n] = \begin{cases} x[m] & t[n] \in \left[t_x[m], \frac{t_x[m]+t_x[m+1]}{2}\right[\\ \\ x[m+1] & t[n] \in \left[\frac{t_x[m]+t_x[m+1]}{2}, t_x[m+1]\right] \end{cases}$$

The equations can be discretised and afterwards written as

$$\underline{\ell} + \underline{w} = F(x),$$

where $\underline{\ell}$ are the observations (in our case $\underline{f}^{\mathsf{b}}$, $\underline{\omega}^{\mathsf{b}}_{\mathtt{ib}}$), $\underline{w}$ are the residuals of $\underline{\ell}$ and $\underline{x}$ are the parameters to be determined: $\underline{r}^{\mathsf{e}}$, $\underline{v}^{\mathsf{e}}$, $\delta\underline{g}^{\mathsf{e}}$, $\underline{a}^{\mathsf{b}}$, $\underline{o}^{\mathsf{b}}$, $\underline{q}$.

In this section, the stochastic models associated to the inertial sensor errors and the gravity anomaly are particularly relevant.

As mentioned in Section 3.2, $\delta\underline{g}^{\mathsf{e}}$ is modelled as a random process: $\delta\dot{\underline{g}}^{\mathsf{e}} = \underline{w}$.

The accelerometer — $\underline{a}^{\mathsf{b}}$ — and gyro — $\underline{o}^{\mathsf{b}}$ — sensor errors of a strapdown INS (SINS) consist of two parts: a constant (or deterministic) part and a stochastic (or random) part. The

deterministic part includes biases and scale factors, which are determined by calibration and then removed from the raw measurements. The stochastic part is basically due to the random variations of the SINS sensor errors (biases) over time.

The inertial sensor random errors can be expressed as: white noise, random constant (random bias), random walk, Gauss-Markov (first and higher orders) or periodic random processes. For most of the navigation-grade SINS systems (angular rate drift 0.005–0.01 $^\circ\,\mathrm{h}^{-1}$), a first order Gauss-Markov model (GM) is used to describe the random errors associated with inertial sensors. This is also true for low-cost inertial systems (angular rate drift 100–1000 $^\circ\,\mathrm{h}^{-1}$) although sometimes a white noise process instead of a first order GM is used.

Here, to fix the ideas and for the sake of simplicity, the inertial sensor models — $\underline{o}^{\mathtt{b}}$ and $\underline{a}^{\mathtt{b}}$ — are also considered as random walk processes.

In this dissertation, several observational models have been implemented into the `GeoTeX/ACX` program and they are described in this section. Table 3.1 describes the related parameters or unknowns to be determined.

Parameter type	aux.	x (par.)	Dimension	Remarks
RE-P	t	$\underline{r}^{\mathtt{e}}$	3×1	(1)
VE-P	t	$\underline{v}^{\mathtt{e}}$	3×1	(2)
Q-P	t	$\underline{q}$	4×1	(3)
OB-P	t	$\underline{o}^{\mathtt{b}}$	3×1	(3)
AB-P	t	$\underline{a}^{\mathtt{b}}$	3×1	(3)
DG-P	t	$\delta\underline{g}$	3×1	(4)
G-P	t	$\underline{g}$	3×1	(4)
GRAVITY-P	t	gg	3×1	(5)
AOFF-P		$\underline{d}^{\mathtt{b}}$	3×1	(3)

Table 3.1: INS/GNSS gravimetry parameters implemented in GeoTeX/ACX: (1) Cartesian coordinates in `e` -frame referred to IMU. (2) `ECEF` system (`e` -frame) referred to IMU. (3) `b` -frame. (4) `e` -frame or `l` -frame depends on the context. (5) $gg = (g,\eta,\zeta)$. (5) $\mathrm{gg}(gg) = (g\sin\zeta, g\sin\eta, g\cos\theta)$.

3.4.1 VEL: Velocity vector model

The velocity vector is defined as the time derivative of the position vector: $v = \dot{r}$.

If we put $\Delta t_r = t_r[n] - t_r[n-1]$, then the equation associated to this model is

$$\underline{v}^{\mathtt{e}}[n] = D\left\langle \underline{r}^{\mathtt{e}}[n], t \right\rangle = (\Delta t_r)^{-1} \left(\underline{r}^{\mathtt{e}}[n] - \underline{r}^{\mathtt{e}}[n-1] \right) \tag{3.8}$$

Concept	#	Notation	Constants	Frame
Observables	1	$\underline{0}$		
$\underline{0}$	3	$0[i]$		$\mathtt{e}$
Parameter Groups	3	$\underline{r}^{\mathtt{e}}[n-1], \underline{r}^{\mathtt{e}}[n], \underline{v}^{\mathtt{e}}[n]$		
$\underline{r}^{\mathtt{e}}[n-1]$	3	$\mathtt{re}[n-1\|i]$	$t_r[n-1]$	$\mathtt{e}$
$\underline{r}^{\mathtt{e}}[n]$	3	$\mathtt{re}[n\|i]$	$t_r[n]$	$\mathtt{e}$
$\underline{v}^{\mathtt{e}}[n]$	3	$\mathtt{ve}[n\|i]$	$t_r[n]$	$\mathtt{e}$

Table 3.2: VEL model.

And the associated observation functional model is

$$\begin{array}{l} \text{VEL}: \\ \quad R^3 \times R^3 \times R^3 \longrightarrow R^3 \\ \quad \underline{r}^{\mathtt{e}}[n-1], \underline{r}^{\mathtt{e}}[n], \underline{v}^{\mathtt{e}}[n] \longmapsto \underline{0} \end{array}$$

$$0[i] = \mathtt{re}[n|i] - \mathtt{re}[n-1|i] - \Delta t_r \, \mathtt{ve}[n|i]$$

Derivatives

$$\begin{aligned} D\left\langle 0[i], \mathtt{re}[n-1|j] \right\rangle &= -\delta_{ij} \\ D\left\langle 0[i], \mathtt{re}[n|j] \right\rangle &= \delta_{ij} \\ D\left\langle 0[i], \mathtt{ve}[n|j] \right\rangle &= -\Delta t_r \, \delta_{ij} \end{aligned}$$

where δ_{ij} is the Dirac's function, defined as:

$$\delta_{ij} = \begin{cases} 1 & i = j \\ 0 & i \neq j \end{cases} \tag{3.9}$$

3.4.2 WIB: INS angular rate vector model

A strapdown INS is physically bolted to the frame of the vehicle to be navigated. It is convenient for an understanding of the strapdown mechanisation to think of the accelerations and angular rates as being sensed in the body frame, or b-frame. The orientation must now be accomplished completely by computations, using gyro data, that transform the accelerometer output from the sensor frame to the navigation frame. In the strapdown mode, this transformation is accomplished computationally, where the rates sensed by the gyros are combined with the computed rates of the arbitrary frame a—that should serve as navigation frame (e-frame or l-frame)— to yield the transformation $\underline{R}_{\mathtt{b}}^{a}$ that converts the sensed accelerations to the navigation frame.

One procedure to determine the transformation matrix is to solve the differential equation for the associated Euler angles. The solution to this equation may be performed numerically using an integrator such as the Runge-Kutta algorithm. This procedure can led to difficulties when the differential equation becomes singular. In fact, most inertial navigation algorithms employ quaternions to solve the equation. The use of quaternions offers a very robust method to compute the transformation matrix under any circumstances.

If the determination of the transformation matrix $\underline{R}_{\mathtt{b}}^{\mathtt{e}}$ is formulated, the differential equation to be solved is given by

$$\dot{\underline{R}}_{\mathtt{b}}^{\mathtt{e}} = \underline{R}_{\mathtt{b}}^{\mathtt{e}} \cdot \underline{\Omega}_{\mathtt{eb}}^{\mathtt{b}},$$

where the off-diagonal elements of $\underline{\Omega}_{\mathtt{eb}}^{\mathtt{b}}$ are the components of the angular rates $\underline{\omega}_{\mathtt{eb}}^{\mathtt{b}}$.

The equivalent differential equation in terms of quaternions is given by the Equation (G.1):

$$\dot{\underline{q}} = \frac{1}{2} \cdot \underline{M}_{\underline{q}} \cdot \underline{\omega}_{\mathtt{eb}}^{\mathtt{b}}.$$

Rewritting the equations we have

$$(\Delta t_r)^{-1} \cdot \Big(\underline{q}[n] - \underline{q}[n-1]\Big) = \frac{1}{2} \cdot \underline{M}_{\underline{q}[n]} \cdot \Big(\underline{\omega}_{\mathtt{ib}}^{\mathtt{b}}[n] + \underline{o}^{\mathtt{b}}[n] - \underline{R}_{\mathtt{b}}^{\mathtt{e}\,T}[n]\underline{\omega}_{\mathtt{ie}}^{\mathtt{e}}\Big).$$

Isolating the INS angular rates, $\underline{\omega}_{\mathtt{ib}}^{\mathtt{b}}$, the equation becomes

$$\underline{\omega}_{\mathtt{ib}}^{\mathtt{b}}[n] = -\underline{o}^{\mathtt{b}}[n] + \underline{R}_{\mathtt{b}}^{\mathtt{e}\,T}[n] \cdot \underline{\omega}_{\mathtt{ie}}^{\mathtt{e}} + 2(\Delta t_r)^{-1} \cdot \Big(\underline{M}_{\underline{q}[n]}\Big)^{T} \cdot \Big(\underline{q}[n] - \underline{q}[n-1]\Big),$$

where $\Delta t_r = t_r[n] - t_r[n-1]$.

Concept	#	Notation	Constants	Frame
Observables	1	$\underline{\omega}^{\mathtt{b}}_{\mathtt{ib}}[n]$		
$\underline{\omega}^{\mathtt{b}}_{\mathtt{ib}}[n]$	3	$\omega^{\mathtt{b}}_{\mathtt{ib}}[n\|i]$		
Parameter Groups	3	$\underline{o}^{\mathtt{b}}[n]$, $\underline{q}[n-1]$, $\underline{q}[n]$		
$\underline{o}^{\mathtt{b}}[n]$	3	$\mathtt{ob}[\mathtt{n}\|\mathtt{i}]$	$t_c[n]$	$\mathtt{b}$
$\underline{q}[n-1]$	4	$\mathtt{q}[\mathtt{n}-1\|\mathtt{i}]$	$t_r[n-1]$	
$\underline{q}[n]$	4	$\mathtt{q}[\mathtt{n}\|\mathtt{i}]$	$t_r[n]$	

Table 3.3: WIB model.

Then, the functional model is

$$\begin{array}{l}\text{WIB}: \\ \quad R^3 \times R^4 \times R^4 \quad \longrightarrow \quad R^3 \\ \quad \underline{o}^{\mathtt{b}}[n], \underline{q}[n-1], \underline{q}[n] \quad \longmapsto \quad \underline{\omega}^{\mathtt{b}}_{\mathtt{ib}}[n]\end{array}$$

$$\begin{array}{rcl}\omega^{\mathtt{b}}_{\mathtt{ib}}[n|i] & = & -\mathtt{ob}[n|i] + \omega_{\mathtt{e}} \cdot \mathtt{rbe}[n|3,i] + \\ & & +2(\Delta t_r)^{-1} \cdot \sum_{s=1}^{4} \mathtt{mq}[n|s,i] \cdot \big(\mathtt{q}[n|s] - \mathtt{q}[n-1|s]\big)\end{array} \tag{3.10}$$

and $\mathtt{rbe}[n] = \mathtt{rbe}(\mathtt{q}[\mathtt{n}])$ is defined in Appendix F and $\mathtt{mq}[n] = \mathtt{mq}(\mathtt{q}[\mathtt{n}])$ is defined by Equation (G.3).

Derivatives

$$\begin{array}{rcl} D\left\langle \omega^{\mathtt{b}}_{\mathtt{ib}}[n|i], \mathtt{ob}[n|j] \right\rangle & = & -\delta_{ij} \\ D\left\langle \omega^{\mathtt{b}}_{\mathtt{ib}}[n|i], \mathtt{q}[n-1|k] \right\rangle & = & -2(\Delta t_r)^{-1} \cdot \mathtt{mq}[n|k,i] \\ D\left\langle \omega^{\mathtt{b}}_{\mathtt{ib}}[n|i], \mathtt{q}[n|k] \right\rangle & = & \omega_{\mathtt{e}} \cdot D\mathtt{rbe}[n|3,i,k] + 2(\Delta t_r)^{-1} \cdot \mathtt{mq}[n|k,i] + \\ & + & 2(\Delta t_r)^{-1} \cdot \sum_{s=1}^{4} D\mathtt{mq}[n|s,i,k] \cdot \big(\mathtt{q}[n|s] - \mathtt{q}[n-1|s]\big) \end{array}$$

where δ_{ij} is the Dirac's function defined by Equation (3.9).

3.4.3 FB-DGE: INS acceleration vector model

According to Equation (3.7), we have

$$\underline{\dot{v}}^{\mathtt{e}}[n] = \underline{R}^{\mathtt{e}}_{\mathtt{b}}[n] \cdot \left(\underline{f}^{\mathtt{b}}[n] + \underline{a}^{\mathtt{b}}[n]\right) - 2\left[\underline{\omega}^{\mathtt{e}}_{\mathtt{ie}}\times\right]\underline{v}^{\mathtt{e}}[n] + \delta\underline{g}^{\mathtt{e}}[n] + \underline{\gamma}^{\mathtt{e}}(\underline{r}^{\mathtt{e}}[n])$$

and considering $\underline{\dot{v}}^{\mathtt{e}}[n]$ as

$$\underline{\dot{v}}^{\mathtt{e}}[n] = (\Delta t_r)^{-1} \cdot \left(\underline{r}^{\mathtt{e}}[n] - \underline{r}^{\mathtt{e}}[n-1]\right),$$

then the equation associated to this model is

$$(\Delta t_r)^{-1} \cdot \left(\underline{r}^{\mathtt{e}}[n] - \underline{r}^{\mathtt{e}}[n-1]\right) =$$

$$\underline{R}^{\mathtt{e}}_{\mathtt{b}}[n] \cdot \left(\underline{f}^{\mathtt{b}}[n] + \underline{a}^{\mathtt{b}}[n]\right) - 2\left[\underline{\omega}^{\mathtt{e}}_{\mathtt{ie}}\times\right]\underline{v}^{\mathtt{e}}[n] + \delta\underline{g}^{\mathtt{e}}[n] + \underline{\gamma}^{\mathtt{e}}(\underline{r}^{\mathtt{e}}[n])$$

where $\Delta t_r = t_r[n] - t_r[n-1]$.

Isolating the accelerometer observation $\underline{f}^{\mathtt{b}}[n]$, we obtain

$$\begin{aligned}\underline{f}^{\mathtt{b}}[n] &= -\underline{a}^{\mathtt{b}}[n] + \underline{R}^{\mathtt{e}\,T}_{\mathtt{b}}[n] \cdot \left\{(\Delta t_r)^{-1}\left(\underline{r}^{\mathtt{e}}[n] - \underline{r}^{\mathtt{e}}[n-1]\right) - \right.\\ &- \left. \delta\underline{g}^{\mathtt{e}}[n] - \underline{\gamma}^{\mathtt{e}}(\underline{r}^{\mathtt{e}}[n]) + 2\left[\underline{\omega}^{\mathtt{e}}_{\mathtt{ie}}[n]\times\right]\underline{v}^{\mathtt{e}}[n]\right\}.\end{aligned}$$

Concept	#	Notation	Constants	Frame
Observables	1	$\underline{f}^{\mathtt{b}}[n]$		
$\underline{f}^{\mathtt{b}}[n]$	3	$\underline{f}^{\mathtt{b}}[n\|i]$		b
Parameter Groups	6	$\underline{a}^{\mathtt{b}}[n]$, $\underline{q}[n]$, $\underline{r}^{\mathtt{e}}[n]$, $\underline{v}^{\mathtt{e}}[n-1]$, $\underline{v}^{\mathtt{e}}[n]$, $\delta\underline{g}^{\mathtt{e}}[n]$		
$\underline{a}^{\mathtt{b}}[n]$	3	ab$[n\|i]$	$t_c[n]$	b
$\underline{q}[n]$	4	q$[n\|i]$	$t_r[n]$	b
$\underline{r}^{\mathtt{e}}[n]$	3	re$[n\|i]$	$t_r[n]$	e
$\underline{v}^{\mathtt{e}}[n-1]$	3	ve$[n-1\|i]$	$t_r[n-1]$	e
$\underline{v}^{\mathtt{e}}[n]$	3	ve$[n\|i]$	$t_r[n]$	e
$\delta\underline{g}^{\mathtt{e}}[n]$	3	δge$[n\|i]$	$t_g[n]$	e

Table 3.4: FB-DGE model.

Then the associated observation functional model is

FB-DGE :

$$\begin{array}{lcl} R^3 \times R^4 \times R^3 \times R^3 \times R^3 \times R^3 & \longrightarrow & R^3 \\ \underline{a}^{\mathtt{b}}[n], \underline{q}[n], \underline{r}^{\mathtt{e}}[n], \underline{v}^{\mathtt{e}}[n-1], \underline{v}^{\mathtt{e}}[n], \delta\underline{g}^{\mathtt{e}}[n] & \longmapsto & \underline{f}^{\mathtt{b}}[n] \end{array}$$

$$\underline{f}^{\mathtt{b}}[n|i] = -\mathtt{ab}[n|i] + \sum_{k=1}^{3} \mathtt{rbe}[n|k,i] \cdot W[k] \tag{3.11}$$

where $\mathtt{gne}[n] = \mathtt{gne}(\mathtt{re}[n])$ is computed using formulas described by Equation (C.17), $\mathtt{rbe}[n] = \mathtt{rbe}(\mathtt{q}[n])$ by Equation (F.7) and

$$\begin{aligned} W[k] &= -\delta\mathtt{ge}[n|k] - \mathtt{gne}[n|k] + \\ &+ (\Delta t_r)^{-1} \cdot (v[n|k] - v[n-1|k]) + 2 \textstyle\sum_{s=1}^{3} \underline{\Omega}^{\mathtt{e}}_{\mathtt{ie}}[k,s] \cdot \mathtt{ve}[n|s]. \end{aligned}$$

Derivatives

$$\begin{aligned}
D\left\langle \underline{f}^{\mathtt{b}}[n|i], \mathtt{ab}[n|j] \right\rangle &= -\delta_{ij} \\
D\left\langle \underline{f}^{\mathtt{b}}[n|i], \mathtt{q}[n|k] \right\rangle &= \textstyle\sum_{s=1}^{3} D\mathtt{rbe}[n|s,i,k] \cdot W[s] \\
D\left\langle \underline{f}^{\mathtt{b}}[n|i], \mathtt{re}[n|j] \right\rangle &= \textstyle\sum_{s=1}^{3} \mathtt{rbe}[n|s,i] \cdot D\left\langle W[s], \mathtt{re}[n|j] \right\rangle \\
D\left\langle \underline{f}^{\mathtt{b}}[n|i], \mathtt{ve}[n-1|j] \right\rangle &= \textstyle\sum_{s=1}^{3} \mathtt{rbe}[n|s,i] \cdot D\left\langle W[s], \mathtt{ve}[n-1|j] \right\rangle \\
D\left\langle \underline{f}^{\mathtt{b}}[n|i], \mathtt{ve}[n|j] \right\rangle &= \textstyle\sum_{s=1}^{3} \mathtt{rbe}[n|s,i] \cdot D\left\langle W[s], \mathtt{ve}[n|j] \right\rangle \\
D\left\langle \underline{f}^{\mathtt{b}}[n|i], \delta\mathtt{ge}[n|j] \right\rangle &= \textstyle\sum_{s=1}^{3} \mathtt{rbe}[n|s,i] \cdot D\left\langle W[s], \delta\mathtt{ge}[n|j] \right\rangle
\end{aligned}$$

where

$$\begin{aligned}
D\left\langle W[i], \mathtt{re}[n|j] \right\rangle &= -D\left\langle \mathtt{gne}[n|i], \mathtt{re}[n|j] \right\rangle = -D\mathtt{gne}[n|i,j] \\
D\left\langle W[i], \mathtt{ve}[n-1|j] \right\rangle &= -(\Delta t_r)^{-1}\, \delta_{ij} \\
D\left\langle W[i], \mathtt{ve}[n|j] \right\rangle &= (\Delta t_r)^{-1}\, \delta_{ij} + 2\, \underline{\Omega}^{\mathtt{e}}_{\mathtt{ie}}[i,j] \\
D\left\langle W[i], \delta\mathtt{ge}[n|j] \right\rangle &= -\delta_{ij}
\end{aligned}$$

Finally, the associated derivatives are

$$
\begin{aligned}
D\left\langle \underline{f}^{\mathtt{b}}[n|i], \mathtt{ab}[n|j] \right\rangle &= -\delta_{ij} \\
D\left\langle \underline{f}^{\mathtt{b}}[n|i], \mathtt{q}[n|k] \right\rangle &= \textstyle\sum_{s=1}^{3} D\mathtt{rbe}[n|s,i,k] \cdot W[s] \\
D\left\langle \underline{f}^{\mathtt{b}}[n|i], \mathtt{re}[n|j] \right\rangle &= -\textstyle\sum_{s=1}^{3} \mathtt{rbe}[n|s,i] \cdot D\mathtt{gne}[n|s,j] \\
D\left\langle \underline{f}^{\mathtt{b}}[n|i], \mathtt{ve}[n-1|j] \right\rangle &= -(\Delta t_r)^{-1} \textstyle\sum_{s=1}^{3} \mathtt{rbe}[n|s,i]\, \delta_{sj} \\
D\left\langle \underline{f}^{\mathtt{b}}[n|i], \mathtt{ve}[n|j] \right\rangle &= \textstyle\sum_{s=1}^{3} \mathtt{rbe}[n|s,i] \left\{ (\Delta t_r)^{-1} \delta_{sj} + 2\, \underline{\Omega}^{\mathtt{e}}_{\mathtt{ie}}[s,j] \right\} \\
D\left\langle \underline{f}^{\mathtt{b}}[n|i], \delta\mathtt{ge}[n|j] \right\rangle &= -\textstyle\sum_{s=1}^{3} \mathtt{rbe}[n|s,i]\, \delta_{sj}
\end{aligned}
$$

where δ_{ij} is the Dirac's function, defined by Equation (3.9), $D\mathtt{rbe}$ is defined in Appendix F and $D\mathtt{gne}$ in C.3.2.

3.4.4 FB-DGN: INS acceleration vector model

This model is a variation of FB-DGE model, which has been described in Section 3.4.3. Here the gravity disturbance parameter is referred to the `l`-frame (usually `NED`-frame), instead of the `e`-frame.

Concept	#	Notation	Constants	Frame
Observables	1	$\underline{f}^{\mathtt{b}}[n]$		
$\underline{f}^{\mathtt{b}}[n]$	3	$\underline{f}^{\mathtt{b}}[n\|i]$		`b`
Parameter Groups	6	$\underline{a}^{\mathtt{b}}[n],\underline{q}[n],\underline{r}^{\mathtt{e}}[n],\underline{v}^{\mathtt{e}}[n-1],\underline{v}^{\mathtt{e}}[n],\delta\underline{g}^{\mathtt{e}}[n]$		
$\underline{a}^{\mathtt{b}}[n]$	3	$\mathtt{ab}[n\|i]$	$t_c[n]$	`b`
$\underline{q}[n]$	4	$\mathtt{q}[n\|i]$	$t_r[n]$	
$\underline{r}^{\mathtt{e}}[n]$	3	$\mathtt{re}[n\|i]$	$t_r[n]$	`e`
$\underline{v}^{\mathtt{e}}[n-1]$	3	$\mathtt{ve}[n-1\|i]$	$t_r[n-1]$	`e`
$\underline{v}^{\mathtt{e}}[n]$	3	$\mathtt{ve}[n\|i]$	$t_r[n]$	`e`
$\delta\underline{g}^{\mathtt{l}}[n]$	3	$\delta\mathtt{gl}[n\|i]$	$t_g[n]$	`l`

Table 3.5: FB-DGN model.

Now, the associated observation functional model is

$$
\begin{array}{l}
\text{FB-DGN}: \\
\quad R^3 \times R^4 \times R^3 \times R^3 \times R^3 \times R^3 \quad \longrightarrow \quad R^3 \\
\quad \underline{a}^{\mathtt{b}}[n], \underline{q}[n], \underline{r}^{\mathtt{e}}[n], \underline{v}^{\mathtt{e}}[n-1], \underline{v}^{\mathtt{e}}[n], \delta\underline{g}^{\mathtt{l}}[n] \quad \longmapsto \quad \underline{f}^{\mathtt{b}}[n]
\end{array}
$$

$$
\underline{f}^{\mathtt{b}}[n|i] = -\mathtt{ab}[n|i] + \sum_{k=1}^{3} \mathtt{rbe}[n|k,i]\; W[k] \tag{3.12}
$$

where

$$
\begin{aligned}
W[k] \;&=\; -\textstyle\sum_{s=1}^{3} \mathtt{rle}[n|k,s]\, \delta\mathtt{gl}[n|s] - \mathtt{gne}[n|k] + \\
&+\; (\Delta t_r)^{-1}\, (v[n|k] - v[n-1|k]) + 2\, \textstyle\sum_{s=1}^{3} \underline{\Omega}^{\mathtt{e}}_{\mathtt{ie}}[k,s]\, \mathtt{ve}[n|s],
\end{aligned}
$$

$\mathtt{gne}[n] = \mathtt{gne}(\mathtt{re}[n])$ is computed using Equation (C.17), $\mathtt{rle}[n] = \mathtt{rle}(\mathtt{re}[n])$ is defined in Appendix B and $\mathtt{rbe}[n] = \mathtt{rbe}(\mathtt{q}[n])$ is computed from Equation (F.7).

Derivatives

$$
\begin{aligned}
D\left\langle \underline{f}^{\mathtt{b}}[n|i], \mathtt{ab}[n|j] \right\rangle &= -\delta_{ij} \\
D\left\langle \underline{f}^{\mathtt{b}}[n|i], \mathtt{q}[n|k] \right\rangle &= \sum_{s=1}^{3} D\mathtt{rbe}[n|s,i,k]\, W[s] \\
D\left\langle \underline{f}^{\mathtt{b}}[n|i], \mathtt{re}[n|j] \right\rangle &= \sum_{s=1}^{3} \mathtt{rbe}[n|s,i]\, D\left\langle W[s], \mathtt{re}[n|j] \right\rangle \\
D\left\langle \underline{f}^{\mathtt{b}}[n|i], \mathtt{ve}[n-1|j] \right\rangle &= \sum_{s=1}^{3} \mathtt{rbe}[n|s,i]\, D\left\langle W[s], \mathtt{ve}[n-1|j] \right\rangle \\
D\left\langle \underline{f}^{\mathtt{b}}[n|i], \mathtt{ve}[n|j] \right\rangle &= \sum_{s=1}^{3} \mathtt{rbe}[n|s,i]\, D\left\langle W[s], \mathtt{ve}[n|j] \right\rangle \\
D\left\langle \underline{f}^{\mathtt{b}}[n|i], \delta\mathtt{gl}[n|j] \right\rangle &= \sum_{s=1}^{3} \mathtt{rbe}[n|s,i]\, D\left\langle W[s], \delta\mathtt{gl}[n|j] \right\rangle
\end{aligned}
$$

where

$$
\begin{aligned}
D\left\langle W[i], \mathtt{re}[n|j] \right\rangle &= -D\left\langle \delta\mathtt{ge}[n|i], \mathtt{re}[n|j] \right\rangle - D\mathtt{gne}[n|i,j] \\
D\left\langle W[i], \mathtt{ve}[n-1|j] \right\rangle &= -(\Delta t_r)^{-1}\, \delta_{ij} \\
D\left\langle W[i], \mathtt{ve}[n|j] \right\rangle &= (\Delta t_r)^{-1}\, \delta_{ij} + 2\, \underline{\Omega}^{\mathtt{e}}_{\mathtt{ie}}[i,j] \\
D\left\langle W[i], \delta\mathtt{gl}[n|j] \right\rangle &= -D\left\langle \delta\mathtt{ge}[n|i], \delta\mathtt{gl}[n|j] \right\rangle
\end{aligned}
$$

and

$$
\begin{aligned}
D\left\langle \delta\mathtt{ge}[n|i], \mathtt{re}[n|j] \right\rangle &= \sum_{s=1}^{3} D\mathtt{rle}[n|i,s,j]\, \delta\mathtt{gl}[n|s] \\
D\left\langle \delta\mathtt{ge}[n|i], \delta\mathtt{gl}[n|j] \right\rangle &= \mathtt{rle}[n|i,j]
\end{aligned}
$$

and δ_{ij} is the Dirac's function, defined by Equation (3.9).

3.4.5 FB-GG: INS acceleration vector model

This model is a variation of the FB models described in Sections 3.4.3 and 3.4.4. Here, the gravity vector parameter is referred to the `l`-frame (`NED`-frame) and expressed as $gg = (g\,\sin\zeta, g\,\sin\eta, g\,\cos\theta)^T$, where g is the magnitude of gravity, (η,ζ) are the deflections of the vertical and $\theta = \left(\eta^2+\zeta^2\right)^{\frac{1}{2}}$.

Concept	#	Notation	Constants	Frame
Observables	1	$\underline{f}^{\mathtt{b}}[n]$		
$\underline{f}^{\mathtt{b}}[n]$	3	$\underline{f}^{\mathtt{b}}[n\|i]$		`b`
Parameter Groups	6	$\underline{a}^{\mathtt{b}}[n]$,$\underline{q}[n]$,$\underline{r}^{\mathtt{e}}[n]$, $\underline{v}^{\mathtt{e}}[n-1]$,$\underline{v}^{\mathtt{e}}[n]$,$gg[n]$		
$\underline{a}^{\mathtt{b}}[n]$	3	$\mathtt{ab}[n\|i]$	$t_c[n]$	`b`
$\underline{q}[n]$	4	$\mathtt{q}[n\|i]$	$t_r[n]$	
$\underline{r}^{\mathtt{e}}[n]$	3	$\mathtt{re}[n\|i]$	$t_r[n]$	`e`
$\underline{v}^{\mathtt{e}}[n-1]$	3	$\mathtt{ve}[n-1\|i]$	$t_r[n-1]$	`e`
$\underline{v}^{\mathtt{e}}[n]$	3	$\mathtt{ve}[n\|i]$	$t_r[n]$	`e`
$gg[n]$	3	$gg[n\|i]$	$t_g[n]$	

Table 3.6: FB-GG model.

The associated observation functional model is

$$
\begin{array}{l}
\text{FB-GG}: \\
\quad R^3 \times R^4 \times R^3 \times R^3 \times R^3 \times R^3 \quad \longrightarrow \quad R^3 \\
\quad \underline{a}^{\mathtt{b}}[n], \underline{q}[n], \underline{r}^{\mathtt{e}}[n], \underline{v}^{\mathtt{e}}[n-1], \underline{v}^{\mathtt{e}}[n], gg[n] \quad \longmapsto \quad \underline{f}^{\mathtt{b}}[n]
\end{array}
$$

$$
\underline{f}^{\mathtt{b}}[n|i] = -\mathtt{ab}[n|i] + \sum_{k=1}^{3} \mathtt{rbe}[n|k,i]\; W[k] \tag{3.13}
$$

where

$$
\begin{aligned}
W[k] \;&=\; -\textstyle\sum_{s=1}^{3} \mathtt{rle}[n|k,s]\; \mathtt{gg}[n|s] + \\
&+\; (\Delta t_r)^{-1}\,(v[n|k] - v[n-1|k]) + 2\,\textstyle\sum_{s=1}^{3} \underline{\Omega}^{\mathtt{e}}_{\mathtt{ie}}[k,s]\; \mathtt{ve}[n|s],
\end{aligned}
$$

$\mathtt{gg}[n] = \mathtt{gg}(gg[n])$ is defined in Section C.20, $\mathtt{rle}[n] = \mathtt{rle}(\mathtt{re}[n])$ is defined in Appendix B and $\mathtt{rbe}[n] = \mathtt{rbe}(\mathtt{q}[n])$ is computed from Equation (F.7).

Derivatives

$$
\begin{aligned}
D\left\langle \underline{f}^{\mathtt{b}}[n|i], \mathtt{ab}[n|j] \right\rangle &= -\delta_{ij} \\
D\left\langle \underline{f}^{\mathtt{b}}[n|i], \mathtt{q}[n|k] \right\rangle &= \sum_{s=1}^{3} D\mathtt{rbe}[n|s,i,k]\, W[s] \\
D\left\langle \underline{f}^{\mathtt{b}}[n|i], \mathtt{re}[n|j] \right\rangle &= \sum_{s=1}^{3} \mathtt{rbe}[n|s,i]\, D\left\langle W[s], \mathtt{re}[n|j] \right\rangle \\
D\left\langle \underline{f}^{\mathtt{b}}[n|i], \mathtt{ve}[n-1|j] \right\rangle &= \sum_{s=1}^{3} \mathtt{rbe}[n|s,i]\, D\left\langle W[s], \mathtt{ve}[n-1|j] \right\rangle \\
D\left\langle \underline{f}^{\mathtt{b}}[n|i], \mathtt{ve}[n|j] \right\rangle &= \sum_{s=1}^{3} \mathtt{rbe}[n|s,i]\, D\left\langle W[s], \mathtt{ve}[n|j] \right\rangle \\
D\left\langle \underline{f}^{\mathtt{b}}[n|i], gg[n|j] \right\rangle &= \sum_{s=1}^{3} \mathtt{rbe}[n|s,i]\, D\left\langle W[s], gg[n|j] \right\rangle
\end{aligned}
$$

where

$$
\begin{aligned}
D\left\langle W[i], \mathtt{re}[n|j] \right\rangle &= -D\left\langle \mathtt{ge}[n|i], \mathtt{re}[n|j] \right\rangle \\
D\left\langle W[i], \mathtt{ve}[n-1|j] \right\rangle &= -(\Delta t_r)^{-1}\, \delta_{ij} \\
D\left\langle W[i], \mathtt{ve}[n|j] \right\rangle &= (\Delta t_r)^{-1}\, \delta_{ij} + 2\, \underline{\Omega}^{\mathtt{e}}_{\mathtt{ie}}[i,j] \\
D\left\langle W[i], gg[n|j] \right\rangle &= -D\left\langle \mathtt{ge}[n|i], gg[n|j] \right\rangle \\
\\
D\left\langle \mathtt{ge}[n|i], \mathtt{re}[n|j] \right\rangle &= \sum_{s=1}^{3} D\mathtt{rle}[n|i,s,j]\, \mathtt{gg}[n|s] \\
D\left\langle \mathtt{ge}[n|i], gg[n|j] \right\rangle &= \sum_{s=1}^{3} \mathtt{rle}[n|i,s]\, D\mathtt{gg}[n|s,j]
\end{aligned}
$$

and δ_{ij} is the Dirac's function, defined by Equation (3.9).

3.4.6 Q-NORM: Quaternion dependency model

As it is described in Appendix F, the definition of the quaternion parameters in Equation (F.3) implies that the four quaternion components (q_1, q_2, q_3, q_4) are not independent, because of the following relationship

$$q_1^2 + q_2^2 + q_3^2 + q_4^2 = 1$$

Concept	#	Notation	Constants	Frame
Observables	1	0		
Parameter Groups	1	$\underline{q}[n]$		
$\underline{q}[n]$	4	$\mathtt{q[n\|i]}$	$t_r[n]$	

Table 3.7: Q-NORM model.

Then, the equation associated to the functional model is

$$\begin{aligned} &\text{Q-NORM}: \\ &\quad R^4 \longrightarrow R \\ &\quad \underline{q}[n] \longmapsto 0 \end{aligned}$$

$$0 = 1 - \sum_{k=1}^{4} \mathtt{q[n|k]}^2 \tag{3.14}$$

Derivatives

$$D\left\langle 0, \mathtt{q[n|j]} \right\rangle = -2\mathtt{q[n|j]}$$

3.4.7 OB: Gauss-Markov gyro drift vector model

Usually, through laboratory and field calibrations gyro drifts can be determined by means of correction parameters for the gyro error models. Thus, the sensor measurements can be compensated. However, systematic errors do *survive* the calibration procedures or just appear during the mission probably due to environmental factors. The variation of the remaining systematic sensor errors are random. Therefore, the sensor errors can be modelled by stochastic processes. In the following $\underline{o}^{\mathtt{b}}$ are interpreted as the remaining systematic sensor errors for the gyro measurement errors and are called gyro drifts.

The gyro drifts $\underline{o}^{\mathtt{b}}$ are usually correlated and can be modelled by first-order Gauss-Markov processes of the form:

$$\dot{\underline{o}}^{\mathtt{b}} = \kappa_\omega \, \underline{o}^{\mathtt{b}} + \underline{w}_o^{\mathtt{b}}$$

where κ_ω are diagonal matrices containing reciprocals of the time correlation parameters of the processes and $\underline{w}_o^{\mathtt{b}}$ the vector containing white noise. Gyro drifts equations are given in the body frame and are thus independent of the computational reference frame.

The equations associated to this functional model, a 1st order Gauss-Markov, are

$$\begin{array}{l} \text{OB}: \\ \quad R^3 \times R^3 \longrightarrow R^3 \\ \quad \underline{o}^{\mathtt{b}}[n-1], \underline{o}^{\mathtt{b}}[n] \longmapsto \underline{0} \end{array}$$

$$0[i] = \mathtt{ob}[n-1|i] - (1 + \kappa_\omega \, \Delta t_c) \; \mathtt{ob}[n|i] \tag{3.15}$$

where $\Delta t_c = t_c[n+1] - t_c[n-1]$.

Concept	#	Notation	Constants	Frame
Observables	1	$\underline{0}$		
$\underline{0}$	3	$0[i]$		b
Sensors	1	IMU		
IMU	4	$(\omega_b, \kappa_\omega, a_b, \kappa_a)^T$		
Parameter Groups	2	$\underline{o}^{\mathtt{b}}[n-1], \underline{o}^{\mathtt{b}}[n]$		
$\underline{o}^{\mathtt{b}}[n-1]$	3	ob[n−1|i]	$t_c[n-1]$	b
$\underline{o}^{\mathtt{b}}[n]$	3	ob[n|i]	$t_c[n]$	b

Table 3.8: First order Gauss-Markov OB model.

Derivatives

$$
\begin{aligned}
D\left\langle 0[i], \mathtt{ob}[n-1|j]\right\rangle &= \delta_{ij} \\
D\left\langle 0[i], \mathtt{ob}[n|j]\right\rangle &= -(1+\kappa_\omega\,\Delta t_c)\;\delta_{ij}
\end{aligned}
$$

where δ_{ij} is the Dirac's function, defined by Equation (3.9).

3.4.8 OB: Random Walk gyro drift vector model

As mentioned before, $\underline{o}^{\mathtt{b}}$ can be expressed as first Gauss-Markov process. But here, for the sake of simplicity, $\underline{o}^{\mathtt{b}}$ may be considered a random walk process:

$$\underline{\dot{o}}^{\mathtt{b}} = \underline{w}_o^{\mathtt{b}}$$

where $\underline{w}_o^{\mathtt{b}}$ is a zero-mean, white noise process with covariance function, $q\delta(\tau)$.

Considering the definition of derivative of $\underline{o}^{\mathtt{b}}$, we have

$$(\Delta t_c)^{-1} \cdot \left(\underline{o}^{\mathtt{b}}[n] - \underline{o}^{\mathtt{b}}[n-1]\right) = \underline{w}_o^{\mathtt{b}}.$$

Concept	#	Notation	Constants	Frame
Observables	1	$\underline{0}$		
$\underline{0}$	3	$0[i]$		$\mathtt{b}$
Parameter Groups	2	$\underline{o}^{\mathtt{b}}[n-1], \underline{o}^{\mathtt{b}}[n]$		
$\underline{o}^{\mathtt{b}}[n-1]$	3	$\mathtt{ob[n-1\|i]}$	$t_c[n-1]$	$\mathtt{b}$
$\underline{o}^{\mathtt{b}}[n]$	3	$\mathtt{ob[n\|i]}$	$t_c[n]$	$\mathtt{b}$

Table 3.9: Random Walk OB model.

The equations associated to this *simple* functional model are

$$\begin{aligned} &\text{OB}: \\ &\quad R^3 \times R^3 \longrightarrow R^3 \\ &\quad \underline{o}^{\mathtt{b}}[n-1], \underline{o}^{\mathtt{b}}[n] \longmapsto \underline{0} \end{aligned}$$

$$0 = 0[i] = \mathtt{ob}[n-1|i] - \mathtt{ob}[n|i] \tag{3.16}$$

where $\Delta t_c = t_c[n] - t_c[n-1]$.

Derivatives

$$\begin{aligned} D\langle 0[i], \mathtt{ob}[n-1|j]\rangle &= \delta_{ij} \\ D\langle 0[i], \mathtt{ob}[n|j]\rangle &= -\delta_{ij} \end{aligned}$$

where δ_{ij} is the Dirac's function, defined by Equation (3.9).

3.4.9 AB: Gauss-Markov accelerometer bias model

Similar to the random walk INS-OB model, which has been described in Section 3.4.7, accelerometer biases $\underline{a}^{\mathtt{b}}$ are usually correlated and can be modelled by first-order Gauss-Markov processes of the form

$$\dot{\underline{a}}^{\mathtt{b}} = -\kappa_a \, \underline{a}^{\mathtt{b}} + \underline{w}_a^{\mathtt{b}}$$

where κ_a are diagonal matrices containing reciprocals of the time correlation parameters of the processes and $\underline{w}_a^{\mathtt{b}}$ the vector containing white noise.

The equations associated to this model are

$$\begin{aligned} &\text{AB}: \\ &\quad R^3 \times R^3 \quad \longrightarrow \quad R^3 \\ &\quad \underline{a}^{\mathtt{b}}[n-1], \underline{a}^{\mathtt{b}}[n] \quad \longmapsto \quad \underline{0} \end{aligned}$$

$$0[i] = \mathtt{ab}[n-1|i] - (1 + \kappa_a \, \Delta t_c) \; \mathtt{ab}[n|i] \tag{3.17}$$

where $\Delta t_c = t_c[n+1] - t_c[n-1]$.

Concept	#	Notation	Constants	Frame
Observables	1	$\underline{0}$		
$\underline{0}$	3	$0[i]$		b
Sensors	1	IMU		
IMU	4	$(\omega_b, \kappa_\omega, a_b, \kappa_a)^T$		
Parameter Groups	2	$\underline{a}^{\mathtt{b}}[n-1]$,$\underline{a}^{\mathtt{b}}[n]$		
$\underline{a}^{\mathtt{b}}[n-1]$	3	ab[n−1|i]	$t_c[n-1]$	b
$\underline{a}^{\mathtt{b}}[n]$	3	ab[n|i]	$t_c[n]$	b

Table 3.10: First order Gauss-Markov AB model.

Derivatives

$$\begin{aligned} D\langle 0[i], \mathtt{ab}[n-1|j] \rangle &= \delta_{ij} \\ D\langle 0[i], \mathtt{ab}[n|j] \rangle &= -(1 + \kappa_a \, \Delta t_c) \; \delta_{ij} \end{aligned}$$

where δ_{ij} is the Dirac's function, defined by Equation (3.9).

3.4.10 AB: Random Walk accelerometer bias model

Similar to the random walk OB model, which has been described in Section 3.4.8, for the sake of simplicity, accelerometer biases are modeled as a random walk:

$$(\Delta t_c)^{-1} \left(\underline{a}^{\mathtt{b}}[n] - \underline{a}^{\mathtt{b}}[n-1]\right) = \underline{w}_a^{\mathtt{b}}$$

Concept	#	Notation	Constants	Frame
Observables	1	$\underline{0}$		
$\underline{0}$	3	$0[i]$		b
Parameter Groups	2	$\underline{a}^{\mathtt{b}}[n-1], \underline{a}^{\mathtt{b}}[n]$		
$\underline{a}^{\mathtt{b}}[n-1]$	3	ab[n−1|i]	$t_c[n-1]$	b
$\underline{a}^{\mathtt{b}}[n]$	3	ab[n|i]	$t_c[n]$	b

Table 3.11: Random Walk AB model.

If $\Delta t_c = t_c[n] - t_c[n-1]$, the equations associated to the functional model are

$$\begin{aligned} &\text{AB}: \\ &\quad R^3 \times R^3 \longrightarrow R^3 \\ &\quad \underline{a}^{\mathtt{b}}[n-1], \underline{a}^{\mathtt{b}}[n] \longmapsto \underline{0} \end{aligned}$$

$$0[i] = \mathtt{ab}[n-1|i] - \mathtt{ab}[n|i] \tag{3.18}$$

Derivatives

$$\begin{aligned} D\left\langle 0[i], \mathtt{ab}[n-1|j]\right\rangle &= \delta_{ij} \\ D\left\langle 0[i], \mathtt{ab}[n|j]\right\rangle &= -\delta_{ij} \end{aligned}$$

where δ_{ij} is the Dirac's function, defined by Equation (3.9).

3.4.11 GDT-DGN: Stochastic gravity disturbance model

As mentioned in Section 3.2, traditionally, the gravity disturbance is modelled as an stochastic process. These models assume, usually, ergodicity, stationarity and some isotropic covariance function that depends on variance and correlation distance. One of the often used models is the Gauss-Markov process, but here to illustrate the approach with a simple functional model, we consider that $\delta\underline{g}$ is a random walk process (as it has been described in Sections 3.4.8 and 3.4.10):

$$\dot{\delta\underline{g}} = \underline{w}_g.$$

Concept	#	Notation	Constants	Frame
Observables	1	$\underline{0}$		
$\underline{0}$	3	$0[i]$		$\mathtt{l}$
Parameter Groups	2	$\delta\underline{g}^{\mathtt{l}}[n-1]$,$\delta\underline{g}^{\mathtt{l}}[n]$		
$\delta\underline{g}^{\mathtt{l}}[n-1]$	3	$\delta\mathtt{gl}[\mathtt{n}-1\vert\mathtt{i}]$	$t_g[n-1]$	$\mathtt{l}$
$\delta\underline{g}^{\mathtt{l}}[n]$	3	$\delta\mathtt{gl}[\mathtt{n}\vert\mathtt{i}]$	$t_g[n]$	$\mathtt{l}$

Table 3.12: GDT-DGN model.

The equations associated to the functional model are

$$\begin{aligned}
&\text{GDT-DGN}: \\
&\quad R^3 \times R^3 \longrightarrow R^3 \\
&\quad \delta\underline{g}^{\mathtt{l}}[n-1], \delta\underline{g}^{\mathtt{l}}[n] \longmapsto \underline{0}
\end{aligned}$$

$$0[i] = \delta\mathtt{gl}[\mathtt{n}-1\vert\mathtt{i}] - \delta\mathtt{gl}[\mathtt{n}\vert\mathtt{i}] \tag{3.19}$$

Derivatives

$$D\left\langle 0[i], \delta\mathtt{gl}[\mathtt{n}-1\vert\mathtt{j}]\right\rangle = \delta_{ij}$$

$$D\left\langle 0[i], \delta\mathtt{gl}[\mathtt{n}\vert\mathtt{j}]\right\rangle = -\delta_{ij}$$

where δ_{ij} is the Dirac's function, defined by Equation (3.9).

3.4.12 GDT-DGE: Stochastic gravity disturbance model

The model, here, is a variation of GDT-DGN model described in Section 3.4.11, where the gravity field is referred to the `e`-frame instead of the `l`-frame.

GDT-DGE :

$$\begin{array}{lcl} R^3 \times R^3 \times R^3 \times R^3 & \longrightarrow & R^3 \\ \underline{r}^{\mathtt{e}}[n-1], \underline{r}^{\mathtt{e}}[n], \delta\underline{g}^{\mathtt{e}}[n-1], \delta\underline{g}^{\mathtt{e}}[n] & \longmapsto & \underline{0} \end{array}$$

$$0[i] = \delta\mathtt{gl}[\mathtt{n}-1|\mathtt{i}] - \delta\mathtt{gl}[\mathtt{n}|\mathtt{i}] \tag{3.20}$$

where

$$\delta\mathtt{gl}[\mathtt{s}|\mathtt{i}] = \sum_{\mathtt{k}=1}^{3} \mathtt{rle}[\mathtt{s}|\mathtt{k},\mathtt{i}]\, \delta\mathtt{ge}[\mathtt{s}|\mathtt{k}],$$

and $\mathtt{rle}[s] = \mathtt{rle}(\mathtt{re}[s])$ is defined in Appendix B.

Concept	#	Notation	Constants	Frame
Observables	1	$\underline{0}$		
$\underline{0}$	3	$0[i]$		`NED`
Parameter Groups	4	$\underline{r}^{\mathtt{e}}[n-1]$, $\underline{r}^{\mathtt{e}}[n]$, $\delta\underline{g}^{\mathtt{e}}[n-1]$,$\delta\underline{g}^{\mathtt{e}}[n]$		
$\underline{r}^{\mathtt{e}}[n-1]$	3	$\mathtt{re}[\mathtt{n}-1\|\mathtt{i}]$	$t_r[n-1]$	`e`
$\underline{r}^{\mathtt{e}}[n]$	3	$\mathtt{re}[\mathtt{n}\|\mathtt{i}]$	$t_r[n]$	`e`
$\delta\underline{g}^{\mathtt{e}}[n-1]$	3	$\delta\mathtt{ge}[\mathtt{n}-1\|\mathtt{i}]$	$t_g[n-1]$	`e`
$\delta\underline{g}^{\mathtt{e}}[n]$	3	$\delta\mathtt{ge}[\mathtt{n}\|\mathtt{i}]$	$t_g[n]$	`e`

Table 3.13: GDT-DGE model.

Finally, the equations of the functional model, $\forall i = 1 \div 3$, are

$$0[i] = \sum_{k=1}^{3} \mathtt{rle}[n-1|k,i]\, \delta\mathtt{ge}[\mathtt{n}-1|\mathtt{k}] - \sum_{\mathtt{k}=1}^{3} \mathtt{rle}[\mathtt{n}|\mathtt{k},\mathtt{i}]\, \delta\mathtt{ge}[\mathtt{n}|\mathtt{k}] \tag{3.21}$$

Derivatives

$$\begin{array}{lcl} D\langle 0[i], \mathtt{re}[\mathtt{n}-1|\mathtt{j}]\rangle & = & \sum_{k=1}^{3} D\mathtt{rle}[n-1|k,i,j]\, \delta\mathtt{ge}[\mathtt{n}-1|\mathtt{k}] \\ D\langle 0[i], \mathtt{re}[\mathtt{n}|\mathtt{j}]\rangle & = & -\sum_{k=1}^{3} D\mathtt{rle}[n|k,i,j]\, \delta\mathtt{ge}[\mathtt{n}|\mathtt{k}] \\ D\langle 0[i], \delta\mathtt{ge}[\mathtt{n}-1|\mathtt{j}]\rangle & = & \mathtt{rle}[n-1|j,i] \\ D\langle 0[i], \delta\mathtt{ge}[\mathtt{n}|\mathtt{j}]\rangle & = & -\mathtt{rle}[n|j,i] \end{array}$$

3.4.13 GDT-GG: Stochastic gravity disturbance model

If the gravity field in `l`-frame is expressed as gg, the functional model associated to GDT-DGN model — described in Section 3.4.11 — is defined as

$$\begin{aligned}
&\text{GDT-GG}: \\
&\quad R^3 \times R^3 \times R^3 \times R^3 \longrightarrow R^3 \\
&\quad \underline{r}^{\mathtt{e}}[n-1], \underline{r}^{\mathtt{e}}[n], gg[n-1], gg[n] \longmapsto \underline{0}
\end{aligned}$$

$$0[i] = \mathtt{gg}[n-1|i] - \mathtt{gnn}[n-1|i] - \mathtt{gg}[n|i] + \mathtt{gnn}[n|i] \tag{3.22}$$

where $\mathtt{gg}[n] = \mathtt{gg}(gg[n])$ is defined in Section C.3.3 and $\mathtt{gnn}[n] = \mathtt{gnn}(\mathtt{re}[n])$ is computed in Section C.3.1.

Concept	#	Notation	Constants	Frame
Observables	1	$\underline{0}$		
$\underline{0}$	3	$0[i]$		`l`
Parameter Groups	4	$\underline{r}^{\mathtt{e}}[n-1]$, $\underline{r}^{\mathtt{e}}[n]$,$gg[n-1]$,$gg[n]$		
$\underline{r}^{\mathtt{e}}[n-1]$	3	$\mathtt{re}[\mathtt{n}-1\|\mathtt{i}]$	$t_g[n-1]$	`e`
$\underline{r}^{\mathtt{e}}[n]$	3	$\mathtt{re}[\mathtt{n}\|\mathtt{i}]$	$t_g[n]$	`e`
$gg[n-1]$	3	$gg[n-1\|i]$	$t_g[n-1]$	
$gg[n]$	3	$gg[n\|i]$	$t_g[n]$	

Table 3.14: GDT-GG model.

Derivatives

$$\begin{aligned}
D\langle 0[i], \mathtt{re}[\mathtt{n}-1|\mathtt{j}]\rangle &= -D\mathtt{gnn}[n-1|i,j] \\
D\langle 0[i], \mathtt{re}[\mathtt{n}|\mathtt{j}]\rangle &= D\mathtt{gnn}[n|i,j] \\
D\langle 0[i], gg[n-1|j]\rangle &= D\mathtt{gg}[n-1|i,j] \\
D\langle 0[i], gg[n|j]\rangle &= -D\mathtt{gg}[n|i,j]
\end{aligned}$$

3.4.14 GDT1-DGN: Stochastic gravity disturbance magnitude model

The magnitude form of GDT-DGN model which is described in Section 3.4.11 is defined by the following functional model.

$$\begin{aligned}&\text{GDT1-DGN}:\\ &\quad R^3 \times R^3 \longrightarrow R\\ &\quad \delta\underline{g}^{\mathtt{l}}[n-1], \delta\underline{g}^{\mathtt{l}}[n] \longmapsto 0\end{aligned}$$

$$0 = \|\delta\underline{g}^{\mathtt{l}}[n-1]\| - \|\delta\underline{g}^{\mathtt{l}}[n]\| \tag{3.23}$$

where

$$\|\delta\underline{g}^{\mathtt{l}}[s]\| = \left[\sum_{k=1}^{3} \delta\mathtt{gl}[\mathtt{s}|\mathtt{k}]^2\right]^{\frac{1}{2}}$$

Concept	#	Notation	Constants	Frame
Observables	1	0		
Parameter Groups	2	$\delta\underline{g}^{\mathtt{l}}[n-1]$,$\delta\underline{g}^{\mathtt{l}}[n]$		
$\delta\underline{g}^{\mathtt{l}}[n-1]$	3	$\delta\mathtt{gl}[\mathtt{n}-1|\mathtt{i}]$	$t_g[n-1]$	$\mathtt{l}$
$\delta\underline{g}^{\mathtt{l}}[n]$	3	$\delta\mathtt{gl}[\mathtt{n}|\mathtt{i}]$	$t_g[n]$	$\mathtt{l}$

Table 3.15: GDT1-DGN model.

Derivatives

$$D\langle 0, \delta\mathtt{gl}[\mathtt{n}-1|\mathtt{j}]\rangle = \delta\mathtt{gl}[\mathtt{n}-1|\mathtt{j}] \cdot \|\delta\underline{\mathtt{g}}^{\mathtt{l}}[\mathtt{n}-1]\|^{-1}$$

$$D\langle 0, \delta\mathtt{gl}[\mathtt{n}|\mathtt{j}]\rangle = -\delta\mathtt{gl}[\mathtt{n}|\mathtt{j}] \cdot \|\delta\underline{\mathtt{g}}^{\mathtt{l}}[\mathtt{n}]\|^{-1}$$

3.4.15 GDT1-DGE: Stochastic gravity disturbance magnitude model

As a variant of the model DGT1-DGN described in Section 3.4.14 with the gravity disturbance vector in the e-frame, the following functional model holds

$$\begin{aligned}&\text{GDT1-DGE}:\\ &\quad R^3 \times R^3 \longrightarrow R\\ &\quad \delta\underline{g}^{\mathtt{e}}[n-1], \delta\underline{g}^{\mathtt{e}}[n] \longmapsto 0\end{aligned}$$

$$0 = \|\delta\underline{g}^{\mathtt{e}}[n-1]\| - \|\delta\underline{g}^{\mathtt{e}}[n]\| \tag{3.24}$$

where

$$\|\delta\underline{g}^{\mathtt{e}}[s]\| = \left[\sum_{k=1}^{3} \delta\mathtt{ge[s|k]}^2\right]^{\frac{1}{2}}$$

Concept	#	Notation	Constants	Frame
Observables	1	0		
Parameter Groups	2	$\delta\underline{g}^{\mathtt{e}}[n-1]$,$\delta\underline{g}^{\mathtt{e}}[n]$		
$\delta\underline{g}^{\mathtt{e}}[n-1]$	3	$\delta\mathtt{ge[n-1|i]}$	$t_g[n-1]$	e
$\delta\underline{g}^{\mathtt{e}}[n]$	3	$\delta\mathtt{ge[n|i]}$	$t_g[n]$	e

Table 3.16: GDT1-DGE model.

Derivatives

$$\begin{aligned}D\langle 0, \delta\mathtt{ge[n-1|j]}\rangle &= \delta\mathtt{ge[n-1|j]} \cdot \|\delta\underline{\mathtt{g}}^{\mathtt{e}}\mathtt{[n-1]}\|^{-1}\\ D\langle 0, \delta\mathtt{ge[n|j]}\rangle &= -\delta\mathtt{ge[n|j]} \cdot \|\delta\underline{\mathtt{g}}^{\mathtt{e}}\mathtt{[n]}\|^{-1}\end{aligned}$$

3.4.16 CUPT: Coordinate Update Point model

A Coordinate Update Point (CUPT) is a position which is obtained from independent procedures (i.e. from GNSS techniques).

It is important to note that the GNSS antenna is located at a different place that the IMU sensor. We call $\underline{d}^{\mathtt{b}}$ the antenna offset between the IMU sensor and the GNSS antenna in the b-frame, which is measured accurately by surveying techniques.

Taking into account the antenna offset and the position of the IMU sensor, in the e-frame, the CUPT position may be defined as

$$\widetilde{X} = \underline{r}^{\mathtt{e}} + \underline{R}^{\mathtt{e}}_{\mathtt{b}} \cdot \underline{d}^{\mathtt{b}} \tag{3.25}$$

Concept	#	Notation	Constants	Frame
Observables	1	$\widetilde{X}$		
$\widetilde{X}$	3	$X[i]$		e
Parameter Groups	3	$\underline{q}[n]$, $\underline{r}^{\mathtt{e}}[n]$, $\underline{d}^{\mathtt{b}}$		
$\underline{q}[n]$	4	q[n|i]	$t_r[n]$	
$\underline{r}^{\mathtt{e}}[n]$	3	re[n|i]	$t_r[n]$	e
$\underline{d}^{\mathtt{b}}$	3	db[n|i]		b

Table 3.17: CUPT model.

And the associated functional model is

$$\begin{aligned} &\text{CUPT}: \\ &\quad R^4 \times R^3 \times R^3 \quad \longrightarrow \quad R^3 \\ &\quad \underline{q}[n], \underline{r}^{\mathtt{e}}[n], \underline{d}^{\mathtt{b}} \quad \longmapsto \quad \widetilde{X} \end{aligned}$$

$$X[i] = \mathtt{re[n|i]} + \sum_{\mathtt{s}=1}^{3} \mathtt{rbe[n|i,s]} \cdot \mathtt{db[s]} \tag{3.26}$$

Derivatives

$$\begin{aligned} D\langle X[i], \mathtt{q[n|k]} \rangle &= \textstyle\sum_{s=1}^{3} D\mathtt{rbe}[n|i,s,k] \cdot \mathtt{db[s]} \\ D\langle X[i], \mathtt{re[n|j]} \rangle &= \delta_{ij} \\ D\langle X[i], \mathtt{db[n|j]} \rangle &= \mathtt{rbe[n|i,j]} \end{aligned}$$

where δ_{ij} is the Dirac's function, defined by Equation (3.9).

3.4.17 CUPTX: Coordinate Update Point model

The model is a small variation of the CUPT model described in Section 3.4.16. Here, the antenna offset $\underline{d}^{\mathtt{b}}$ is considered a constant of the model.

The Equation (3.25) is still valid

$$\widetilde{X} = \underline{r}^{\mathtt{e}} + \underline{R}^{\mathtt{e}}_{\mathtt{b}} \cdot \underline{d}^{\mathtt{b}} \tag{3.27}$$

Concept	#	Notation	Constants	Frame
Observables	1	$\widetilde{X}$		
$\widetilde{X}$	3	$X[i]$	$\underline{d}^{\mathtt{b}}$	e
Parameter Groups	2	$\underline{q}[n]$, $\underline{r}^{\mathtt{e}}[n]$		
$\underline{q}[n]$	4	q[n|i]	$t_r[n]$	
$\underline{r}^{\mathtt{e}}[n]$	3	re[n|i]	$t_r[n]$	e

Table 3.18: CUPTX model.

And the equations associated functional model are

$$\begin{aligned} &\text{CUPTX}: \\ &\quad R^4 \times R^3 \longrightarrow R^3 \\ &\quad \underline{q}[n], \underline{r}^{\mathtt{e}}[n] \longmapsto \widetilde{X} \end{aligned}$$

$$X[i] = \mathtt{re[n|i]} + \sum_{\mathtt{s}=1}^{3} \mathtt{rbe[n|i,s]} \cdot \mathtt{db[s]} \tag{3.28}$$

Derivatives

$$\begin{aligned} D\langle X[i], \mathtt{q[n|k]} \rangle &= \textstyle\sum_{s=1}^{3} D\mathtt{rbe}[n|i,s,k] \cdot \mathtt{db[s]} \\ D\langle X[i], \mathtt{re[n|j]} \rangle &= \delta_{ij} \end{aligned}$$

where δ_{ij} is the Dirac's function, defined by Equation (3.9).

3.4.18 VUPT: Velocity Update model

If, instead of the position, the velocity is known and the Equation (3.25) is differentiated, then the associated equation is

$$\widetilde{V} = \dot{\widetilde{X}} = \underline{\dot{t}}^{\mathtt{e}} + \underline{\dot{R}}^{\mathtt{e}}_{\mathtt{b}} \cdot \underline{d}^{\mathtt{b}}$$

Considering Equations (3.7), (F.7) and (3.10), the above equation can be transformed as follows:

$$\widetilde{V} = \underline{v}^{\mathtt{e}} + \underline{R}^{\mathtt{e}}_{\mathtt{b}} \cdot \underline{\Omega}^{\mathtt{b}}_{\mathtt{eb}} \cdot \underline{d}^{\mathtt{b}} = \underline{v}^{\mathtt{e}} + \underline{R}^{\mathtt{e}}_{\mathtt{b}} \cdot \left[\underline{\omega}^{\mathtt{b}}_{\mathtt{eb}} \times\right] \underline{d}^{\mathtt{b}}.$$

If the Equations (G.1) — $\underline{\dot{q}} = \frac{1}{2}\underline{M}_{\underline{q}}\,\underline{\omega}^{\mathtt{b}}_{\mathtt{eb}}$ — and (G.2) are taken into account, we obtain:

$$\widetilde{V} = \underline{v}^{\mathtt{e}} + 2\underline{R}^{\mathtt{e}}_{\mathtt{b}}[(\underline{M}^{T}_{\underline{q}}\underline{\dot{q}}) \times \underline{d}^{\mathtt{b}}] \tag{3.29}$$

The Zero Velocity Update (ZUPT), which is widely used in terrestrial inertial surveying, may be considered as a particular case of a VUPT model where $\widetilde{V} = 0$.

Concept	#	Notation	Constants	Frame
Observables	1	$\widetilde{V}$		
$\widetilde{V}$	3	$V[i]$		e
Parameter Groups	4	$\underline{q}[n-1]$, $\underline{q}[n]$, $\underline{v}^{\mathtt{e}}[n]$, $\underline{d}^{\mathtt{b}}$		
$\underline{q}[n-1]$	4	q[n−1|i]	$t_r[n-1]$	
$\underline{q}[n]$	4	q[n|i]	$t_r[n]$	
$\underline{v}^{\mathtt{e}}[n]$	3	ve[n|i]	$t_r[n]$	e
$\underline{d}^{\mathtt{b}}$	3	db[n|i]		b

Table 3.19: VUPT model.

The equations associated to the functional model are

$$\begin{aligned} &\text{VUPT}: \\ &\quad R^4 \times R^4 \times R^3 \times R^3 \quad \longrightarrow \quad R^3 \\ &\quad \underline{q}[n-1], \underline{q}[n], \underline{v}^{\mathtt{e}}[n], \underline{d}^{\mathtt{b}} \quad \longmapsto \quad \widetilde{V} \end{aligned}$$

$$V[i] = \mathtt{ve}[n|i] + 2\sum_{s=1}^{3} \mathtt{rbe}[\mathtt{n}|\mathtt{i},\mathtt{s}] \cdot \mathtt{Z}[\mathtt{s}] \tag{3.30}$$

where

$$
\begin{aligned}
Z[s] &= \textstyle\sum_{m=1}^{3} M[s,m]\,\mathtt{db[m]} \\
M &= \begin{pmatrix} 0 & -W[3] & W[2] \\ W[3] & 0 & -W[1] \\ -W[2] & W[1] & 0 \end{pmatrix} \\
W[s] &= (\Delta t_r)^{-1} \textstyle\sum_{m=1}^{4} \mathtt{mq[n|m,s]} \cdot \big(\mathtt{q[n|m]} - \mathtt{q[n-1|m]}\big).
\end{aligned}
$$

Derivatives

$$
\begin{aligned}
D\big\langle V[i], \mathtt{q[n-1|k]} \big\rangle &= 2\textstyle\sum_{s=1}^{3} \mathtt{rbe[n|i,s]} \cdot \mathtt{D}\big\langle \mathtt{Z[s]}, \mathtt{q[n-1|k]} \big\rangle \\
D\big\langle V[i], \mathtt{q[n|k]} \big\rangle &= 2\textstyle\sum_{s=1}^{3} D\mathtt{rbe}[n|i,s,k] \cdot Z[s] + \\
&+ 2\textstyle\sum_{s=1}^{3} \mathtt{rbe[n|i,s]} \cdot \mathtt{D}\big\langle \mathtt{Z[s]}, \mathtt{q[n|k]} \big\rangle \\
D\big\langle V[i], \mathtt{ve[n|j]} \big\rangle &= \delta_{ij} \\
D\big\langle V[i], \mathtt{db[n|j]} \big\rangle &= 2\textstyle\sum_{s=1}^{3} \mathtt{rbe[n|i,s]} \cdot \mathtt{D}\big\langle \mathtt{Z[s]}, \mathtt{db[n|j]} \big\rangle
\end{aligned}
$$

where

$$
\begin{aligned}
D\big\langle Z[s], \mathtt{q[n-1|k]} \big\rangle &= \textstyle\sum_{m=1}^{3} D\big\langle M[s,m], \mathtt{q[n-1|k]} \big\rangle\, \mathtt{db[m]} \\
D\big\langle Z[s], \mathtt{q[n|k]} \big\rangle &= \textstyle\sum_{m=1}^{3} D\big\langle M[s,m], \mathtt{q[n|k]} \big\rangle\, \mathtt{db[m]} \\
D\big\langle Z[s], \mathtt{db[j]} \big\rangle &= M[s,j]
\end{aligned}
$$

$$
D\big\langle M, \mathtt{q[r|k]} \big\rangle = \begin{pmatrix} 0 & -D\big\langle W[3], \mathtt{q[r|k]} \big\rangle & D\big\langle W[2], \mathtt{q[r|k]} \big\rangle \\ D\big\langle W[3], \mathtt{q[r|k]} \big\rangle & 0 & -D\big\langle W[1], \mathtt{q[r|k]} \big\rangle \\ -D\big\langle W[2], \mathtt{q[r|k]} \big\rangle & D\big\langle W[1], \mathtt{q[r|k]} \big\rangle & 0 \end{pmatrix}
$$

$$
\begin{aligned}
D\big\langle W[s], \mathtt{q[n-1|k]} \big\rangle &= -(\Delta t_r)^{-1}\, \mathtt{mq[n|k,s]} \\
D\big\langle W[s], \mathtt{q[n|k]} \big\rangle &= (\Delta t_r)^{-1}\, \mathtt{mq[n|k,s]} + \\
&+ (\Delta t_r)^{-1} \textstyle\sum_{m=1}^{4} D\mathtt{mq[n|m,s,k]}\, \big(\mathtt{q[n|m]} - \mathtt{q[n-1|m]}\big)
\end{aligned}
$$

and δ_{ij} is the Dirac's function, defined by Equation (3.9).

3.4.19 VUPTX: Velocity Update model

If the antenna offset $\underline{d}^{\mathtt{b}}$ is regarded as an auxiliary constant, the associated equation of VUPT model of Section 3.4.18 is

$$\widetilde{V} = \underline{v}^{\mathtt{e}} + 2\underline{R}^{\mathtt{e}}_{\mathtt{b}} \cdot [(\underline{M}^{T}_{\underline{q}}\dot{\underline{q}}) \times \underline{d}^{\mathtt{b}}] \tag{3.31}$$

Concept	#	Notation	Constants	Frame
Observables	1	$\widetilde{V}$		
$\widetilde{V}$	3	$V[i]$	$\underline{d}^{\mathtt{b}}$	e
Parameter Groups	3	$\underline{q}[n-1]$, $\underline{q}[n]$, $\underline{v}^{\mathtt{e}}[n]$		
$\underline{q}[n-1]$	4	q[n−1|i]	$t_r[n-1]$	
$\underline{q}[n]$	4	q[n|i]	$t_r[n]$	
$\underline{v}^{\mathtt{e}}[n]$	3	ve[n|i]	$t_r[n]$	e

Table 3.20: VUPTX model.

And the associated functional model is

$$\begin{array}{l} \text{VUPTX}: \\ \quad R^4 \times R^4 \times R^3 \quad \longrightarrow \quad R^3 \\ \quad \underline{q}[n-1], \underline{q}[n], \underline{v}^{\mathtt{e}}[n] \quad \longmapsto \quad \widetilde{V} \end{array}$$

$$V[i] = \mathtt{ve}[n|i] + 2\sum_{s=1}^{3} \mathtt{rbe}[\mathtt{n}|\mathtt{i},\mathtt{s}] \cdot \mathtt{Z}[\mathtt{s}] \tag{3.32}$$

where

$$\begin{aligned} Z[s] &= \textstyle\sum_{m=1}^{3} M[s,m] \cdot \mathtt{db}[\mathtt{m}], \\ M &= \begin{pmatrix} 0 & -W[3] & W[2] \\ W[3] & 0 & -W[1] \\ -W[2] & W[1] & 0 \end{pmatrix} \\ W[s] &= (\Delta t_r)^{-1} \textstyle\sum_{m=1}^{4} \mathtt{mq}[\mathtt{n}|\mathtt{m},\mathtt{s}] \left(\mathtt{q}[\mathtt{n}|\mathtt{m}] - \mathtt{q}[\mathtt{n}-1|\mathtt{m}]\right) \end{aligned}$$

Derivatives

$$
\begin{aligned}
D\langle V[i], \mathtt{q[n-1|k]}\rangle &= 2\sum_{s=1}^{3} \mathtt{rbe[n|i,s]} \cdot \mathtt{D}\langle \mathtt{Z[s]}, \mathtt{q[n-1|k]}\rangle \\
D\langle V[i], \mathtt{q[n|k]}\rangle &= 2\sum_{s=1}^{3} D\mathtt{rbe}[n|i,s,k] \cdot Z[s] + \\
&+ 2\sum_{s=1}^{3} \mathtt{rbe[n|i,s]} \cdot \mathtt{D}\langle \mathtt{Z[s]}, \mathtt{q[n|k]}\rangle \\
D\langle V[i], \mathtt{ve[n|j]}\rangle &= \delta_{ij}
\end{aligned}
$$

where

$$
\begin{aligned}
D\langle Z[s], \mathtt{q[n-1|k]}\rangle &= \sum_{m=1}^{3} D\langle M[s,m], \mathtt{q[n-1|k]}\rangle \, \mathtt{db[m]} \\
D\langle Z[s], \mathtt{q[n|k]}\rangle &= \sum_{m=1}^{3} D\langle M[s,m], \mathtt{q[n|k]}\rangle \, \mathtt{db[m]}
\end{aligned}
$$

$$
D\langle M, \mathtt{q[r|k]}\rangle = \begin{pmatrix}
0 & -D\langle W[3], \mathtt{q[r|k]}\rangle & D\langle W[2], \mathtt{q[r|k]}\rangle \\
D\langle W[3], \mathtt{q[r|k]}\rangle & 0 & -D\langle W[1], \mathtt{q[r|k]}\rangle \\
-D\langle W[2], \mathtt{q[r|k]}\rangle & D\langle W[1], \mathtt{q[r|k]}\rangle & 0
\end{pmatrix}
$$

$$
\begin{aligned}
D\langle W[s], \mathtt{q[n-1|k]}\rangle &= -(\Delta t_r)^{-1} \mathtt{mq[n|k,s]} \\
D\langle W[s], \mathtt{q[n|k]}\rangle &= (\Delta t_r)^{-1} \mathtt{mq[n|k,s]} + \\
&+ (\Delta t_r)^{-1} \sum_{m=1}^{4} D\mathtt{mq}[\mathtt{n|m,s,k}] \left(\mathtt{q[n|m]} - \right. \\
&- \left. \mathtt{q[n-1|m]}\right)
\end{aligned}
$$

and δ_{ij} is the Dirac's function, defined by Equation (3.9).

3.4.20 DG-OBS: Gravity disturbance magnitude model

Usually, the magnitude of the gravity disturbance (or the gravity anomaly), in the e-frame ($\delta\underline{g}^{\mathtt{e}}[n]$) or l-frame ($\delta\underline{g}^{\mathtt{l}}[n]$), is known and the gravity vector has to be computed in the e-frame or l-frame. The associated functional model is

$$\begin{aligned}&\text{DG-OBS}:\\ &\quad R^3 \longrightarrow R\\ &\quad \delta\underline{g}[n] \longmapsto \widetilde{\delta\underline{g}}\end{aligned}$$

$$\widetilde{\delta\underline{g}} = \mathtt{dgnorm} \tag{3.33}$$

where

$$\mathtt{dgnorm} = \left[\sum_{i=1}^{3} \delta\mathrm{g}[n|i]^2\right]^{\frac{1}{2}}.$$

Concept	#	Notation	Constants	Frame
Observables	1	$\widetilde{\delta\underline{g}}$		
Parameter Groups	1	$\delta\underline{g}[n]$		
$\delta\underline{g}[n]$	3	$\delta\mathrm{g}[\mathtt{n}\|\mathtt{i}]$	$t_g[n]$	e or l

Table 3.21: DG-OBS model.

Derivatives

$$D\left\langle \widetilde{\delta\underline{g}}, \delta\mathrm{g}[\mathtt{n}|\mathtt{j}] \right\rangle = \mathtt{dgnorm}^{-1} \cdot \delta\mathrm{g}[\mathtt{n}|\mathtt{j}]$$

3.4.21 DG-OBS-GG: Gravity disturbance magnitude model

This is a variation of the DG-OBS model described in Section 3.4.20. Here, the gravity parameters to be computed in the `l`-frame are expressed as $gg = (g, \eta, \zeta)^T$. The associated functional model is

$$\begin{array}{l}\text{DG-OBS-GG}: \\ \quad R^3 \times R^3 \longrightarrow R \\ \quad \underline{r}^{\mathtt{e}}[n], gg[n] \longmapsto \widetilde{\delta \underline{g}}\end{array}$$

$$\widetilde{\delta \underline{g}} = \delta \underline{g} \tag{3.34}$$

where

$$\begin{aligned}\delta \underline{g} &= \left[\textstyle\sum_{i=1}^{3} \delta \mathtt{g[n|i]}^2\right]^{\frac{1}{2}}, \\ \delta \mathtt{g[n]} &= \mathtt{gg}[n] - \mathtt{gne}[n],\end{aligned}$$

$\mathtt{gg}[n] = \mathtt{gg}(gg[n])$ is computed using the Equation (C.20) and $\mathtt{gne}[n] = \mathtt{gne}(\mathtt{re}[n])$ is computed using the Equation (C.19).

Concept	#	Notation	Constants	Frame
Observables	1	$\widetilde{\delta \underline{g}}$		
Parameter Groups	2	$\underline{r}^{\mathtt{e}}[n], gg[n]$		
$\underline{r}^{\mathtt{e}}[n]$	3	$\mathtt{re}[n\|i]$	$t_r[n]$	$\mathtt{e}$
$gg[n]$	3	$gg[n\|i]$	$t_g[n]$	

Table 3.22: DG-OBS-GG model.

Derivatives

$$\begin{aligned}D\left\langle \widetilde{\delta \underline{g}}, \mathtt{re[n|j]} \right\rangle &= (\delta \underline{g})^{-1} \textstyle\sum_{k=1}^{3} \delta \mathtt{g[n|k]}\, \mathtt{D}\left\langle \delta \mathtt{g[n|k]}, \mathtt{re[n|j]} \right\rangle \\ D\left\langle \widetilde{\delta \underline{g}}, gg[n|j] \right\rangle &= (\delta \underline{g})^{-1} \textstyle\sum_{k=1}^{3} \delta \mathtt{g[n|k]}\, \mathtt{D}\left\langle \delta \mathtt{g[n|k]}, \mathtt{gg[n|j]} \right\rangle\end{aligned}$$

where

$$\begin{aligned}D\left\langle \delta \mathtt{g[n|k]}, \mathtt{re[n|j]} \right\rangle &= -D\mathtt{gne}[n|k, j] \\ D\left\langle \delta \mathtt{g[n|k]}, \mathtt{gg[n|j]} \right\rangle &= D\mathtt{gg}[n|k, j]\end{aligned}$$

3.4.22 G-OBS: Gravity magnitude model

If instead of the gravity anomaly — as it has been defined in DG-OBS model in Section 3.4.20 — the gravity is known and the gravity vector is the parameter to be computed, the associated functional model is

$$\begin{aligned} &\text{G-OBS}: \\ &\quad R^3 \quad \longrightarrow \quad R \\ &\quad \underline{g}[n] \quad \longmapsto \quad \widetilde{\underline{g}} \end{aligned}$$

$$\widetilde{\underline{g}} = \texttt{gnorm} \tag{3.35}$$

where

$$\texttt{gnorm} = \left[\sum_{i=1}^{3} \mathrm{g}[n|i]^2 \right]^{\frac{1}{2}}.$$

Concept	#	Notation	Constants	Frame
Observables	1	$\widetilde{\underline{g}}$		
Parameter Groups	1	$\underline{g}[n]$		
$\underline{g}[n]$	3	$\mathrm{g}[n\|i]$	$t_g[n]$	`e` or `l`

Table 3.23: G-OBS model.

Derivatives

$$D\left\langle \widetilde{\underline{g}}, \mathrm{g}[n|j] \right\rangle = \texttt{gnorm}^{-1} \cdot \mathrm{g}[n|j]$$

3.4.23 GUPT-DGE: Gravity magnitude model

The model is a variation of the G-OBS model described in Section 3.4.22. Here, the associated parameters are position and gravity disturbance vectors in the e-frame. The associated functional model is

$$\underline{g}_0 = \|\delta\underline{g}^{\mathsf{e}} + \underline{\gamma}^{\mathsf{e}}(\underline{r}^{\mathsf{e}})\|$$

Concept	#	Notation	Constants	Frame
Observables	1	g_0		
Parameter Groups	2	$\underline{r}^{\mathsf{e}}[n]$, $\delta\underline{g}^{\mathsf{e}}[n]$		
$\underline{r}^{\mathsf{e}}[n]$	3	re[n|i]	$t_r[n]$	e
$\delta\underline{g}^{\mathsf{e}}[n]$	3	δge[n|i]	$t_g[n]$	e

Table 3.24: GUPT-DGE model.

The associated functional model is

$$\begin{aligned}&\text{GUPT-DGE}:\\ &\quad R^3 \times R^3 \longrightarrow R\\ &\quad \underline{r}^{\mathsf{e}}[n], \delta\underline{g}^{\mathsf{e}}[n] \longmapsto g_0\end{aligned}$$

$$g_0 = \texttt{gnorm} \tag{3.36}$$

with

$$\texttt{gnorm} = \left[\sum_{k=1}^{3} Z[k]^2\right]^{\frac{1}{2}},$$

and

$$Z[k] = \delta\texttt{ge[n|k]} + \texttt{gne[n|k]},$$

where gne[n] = gne(re[n]) is computed using the Equation (C.17).

Derivatives

$$D\langle g_0, \texttt{re[n|j]}\rangle = D\langle \texttt{gnorm}, \texttt{re[n|j]}\rangle$$

$$D\langle g_0, \delta\texttt{ge[n|j]}\rangle = D\langle \texttt{gnorm}, \delta\texttt{ge[n|j]}\rangle$$

where

$$
\begin{aligned}
D\langle \mathtt{gnorm}, \mathtt{re[n|j]} \rangle &= 2\,\mathtt{gnorm}^{-1} \cdot \textstyle\sum_{k=1}^{3} (Z[k]\, D\langle Z[k], \mathtt{re[n|j]} \rangle) \\
D\langle \mathtt{gnorm}, \delta\mathtt{ge[n|j]} \rangle &= 2\,\mathtt{gnorm}^{-1} \cdot \textstyle\sum_{k=1}^{3} (Z[k]\, D\langle Z[k], \delta\mathtt{ge[n|j]} \rangle) \\
\\
D\langle Z[k], \mathtt{re[n|j]} \rangle &= D\mathtt{gne[n|k,j]} \\
D\langle Z[k], \delta\mathtt{ge[n|j]} \rangle &= \delta_{kj}
\end{aligned}
$$

and δ_{ij} is the Dirac's function, defined by Equation (3.9).

3.4.24 GUPT-DGN: Gravity magnitude model

This model is a small variation of the GUPT-DGE model described in Section 3.4.23, where the gravity disturbance parameters have to be determined in the `l`-frame. The associated functional model is

$$\begin{array}{l}\text{GUPT-DGN}: \\ \quad R^3 \times R^3 \longrightarrow R \\ \quad \underline{r}^{\mathtt{e}}[n], \delta\underline{g}^{\mathtt{l}}[n] \longmapsto g_0\end{array}$$

$$g_0 = \mathtt{gnorm} \tag{3.37}$$

where

$$\begin{aligned}\mathtt{gnorm} &= \left[\textstyle\sum_{i=1}^{3} W[i]^2\right]^{\frac{1}{2}}, \\ W[i] &= \delta\mathtt{gl}[n|i] + \mathtt{gnn}[n|i],\end{aligned}$$

and $\mathtt{gnn}[n] = \mathtt{gnn}(\mathtt{re}[n])$ is defined in Section C.3.1.

Concept	#	Notation	Constants	Frame
Observables	1	g_0		
Parameter Groups	2	$\underline{r}^{\mathtt{e}}[n]$, $\delta\underline{g}^{\mathtt{l}}[n]$		
$\underline{r}^{\mathtt{e}}[n]$	3	$\mathtt{re}[n\|i]$	$t_r[n]$	`e`
$\delta\underline{g}^{\mathtt{l}}[n]$	3	$\delta\mathtt{gl}[n\|i]$	$t_g[n]$	`l`

Table 3.25: GUPT-DGN model.

Derivatives

$$\begin{aligned}D\langle g_0, \mathtt{re}[n|j]\rangle &= 2\,\mathtt{gnorm}^{-1} \cdot \textstyle\sum_{k=1}^{3} W[k]\, D\langle W[k], \mathtt{re}[n|j]\rangle \\ D\langle g_0, \delta\mathtt{gl}[n|j]\rangle &= 2\,\mathtt{gnorm}^{-1} \cdot \textstyle\sum_{k=1}^{3} W[k]\, D\langle W[k], \delta\mathtt{gl}[n|j]\rangle\end{aligned}$$

where

$$\begin{aligned}D\langle W[k], \mathtt{re}[n|j]\rangle &= D\mathtt{gnn}[n|k,j] \\ D\langle W[k], \delta\mathtt{gl}[n|j]\rangle &= \delta_{kj}\end{aligned}$$

and δ_{ij} is the Dirac's function, defined by Equation (3.9).

3.4.25 GUPT-GG: Gravity magnitude model

If the gravity parameters to be computed in the `l`-frame are expressed as gg described in Section C.3.3, here the model is a variation of the GUPT-DGN model described in Section 3.4.24. The associated functional model is

$$\begin{aligned} &\text{GUPT-GG}: \\ &\quad R^3 \longrightarrow R \\ &\quad gg[n] \longmapsto g_0 \end{aligned}$$

$$g_0 = \texttt{gnorm} \tag{3.38}$$

where

$$\texttt{gnorm} = \left[\sum_{k=1}^{3} \text{gg}[n|k]^2\right]^{\frac{1}{2}}$$

and $\text{gg}[n] = \text{gg}(gg[n])$ computed using the Equation (C.20).

Concept	#	Notation	Constants	Frame
Observables	1	g_0		
Parameter Groups	1	$gg[n]$		
$gg[n]$	3	$gg[n\|i]$	$t_g[n]$	

Table 3.26: GUPT-GG model.

Derivatives

$$D\left\langle g_0, \texttt{re}[n|j]\right\rangle = \texttt{gnorm}^{-1} \cdot \sum_{k=1}^{3} \text{gg}[n|k]\, D\text{gg}[n|k,j]$$

3.4.26 GUPTN-DGE model

The model is a variation of the GUPT-DGE model described in Section 3.4.23. Here, the magnitude of the gravity vector — the gravity — is considered as the sum of two magnitudes, the gravity disturbance (or anomaly) and the normal gravity, and the following equation can be considered

$$g_0 = \|\delta \underline{g}^{\mathtt{e}}\| + \|\underline{\gamma}^{\mathtt{e}}(\underline{r}^{\mathtt{e}})\|$$

where the associated parameters, in the e-frame, are the position and the gravity disturbance vectors.

Concept	#	Notation	Constants	Frame
Observables	1	g_0		
Parameter Groups	2	$\underline{r}^{\mathtt{e}}[n]$, $\delta \underline{g}^{\mathtt{e}}[n]$		
$\underline{r}^{\mathtt{e}}[n]$	3	re[n|i]	$t_r[n]$	e
$\delta \underline{g}^{\mathtt{e}}[n]$	3	δge[n|i]	$t_g[n]$	e

Table 3.27: GUPTN-DGE model.

The associated functional model is

$$\begin{array}{l} \text{GUPTN-DGE}: \\ \quad R^3 \times R^3 \longrightarrow R \\ \quad \underline{r}^{\mathtt{e}}[n], \delta \underline{g}^{\mathtt{e}}[n] \longmapsto g_0 \end{array}$$

$$g_0 = \mathtt{gnorm} + \mathtt{dgnorm} \tag{3.39}$$

where

$$\mathtt{dgnorm} = \left[\sum_{k=1}^{3} \delta \mathtt{ge}[\mathtt{n}|\mathtt{k}]^2\right]^{\frac{1}{2}},$$

$$\mathtt{gnorm} = \left[\sum_{k=1}^{3} \mathtt{gne}[n|k]^2\right]^{\frac{1}{2}},$$

and gne[n] = gne(re[n]) is computed using the Equation (C.17).

Derivatives

$$D\langle g_0, \mathtt{re}[\mathtt{n}|\mathtt{j}]\rangle = D\langle \mathtt{gnorm}, \mathtt{re}[\mathtt{n}|\mathtt{j}]\rangle$$

$$D\langle g_0, \delta\mathtt{ge}[\mathtt{n}|\mathtt{j}]\rangle = D\langle \mathtt{dgnorm}, \delta\mathtt{ge}[\mathtt{n}|\mathtt{j}]\rangle$$

where

$$D\langle \mathtt{gnorm}, \mathtt{re[n|j]} \rangle = \mathtt{gnorm}^{-1} \cdot \sum_{k=1}^{3} \mathtt{gne[n|k]}\, \mathtt{Dgne[n|k,j]}$$

$$D\langle \mathtt{dgnorm}, \delta\mathtt{ge[n|j]} \rangle = \mathtt{dgnorm}^{-1} \cdot \delta\mathtt{ge[n|j]}$$

3.4.27 GUPTN-DGN model

Equivalently to the GUPT-DGE and the GUPTN-DGE models, the model here is a variation of the GUPT-DGN model described in Section 3.4.24. If the gravity is known at some point — the magnitude is independent of the reference frame — the gravity disturbance vector is referenced to the `l`-frame and position vector in the `e`-frame, the associated functional model is

$$\begin{array}{l}\text{GUPTN-DGN}: \\ \quad \begin{array}{lcl} R^3 \times R^3 & \longrightarrow & R \\ \underline{r}^{\mathtt{e}}[n], \delta\underline{g}^{\mathtt{l}}[n] & \longmapsto & g_0 \end{array}\end{array}$$

$$g_0 = \mathtt{dgnorm} + \mathtt{gnnorm} \tag{3.40}$$

where

$$\mathtt{dgnorm} = \left[\sum_{k=1}^{3} \delta\mathtt{gl}[n|k]^2\right]^{\frac{1}{2}}$$

$$\mathtt{gnnorm} = \left[\sum_{k=1}^{3} \mathtt{gnn}[n|k]^2\right]^{\frac{1}{2}}$$

and $\mathtt{gnn}[n] = \mathtt{gnn}(\mathtt{re}[n])$ is defined in Section C.3.1.

Concept	#	Notation	Constants	Frame
Observables	1	g_0		
Parameter Groups	2	$\underline{r}^{\mathtt{e}}[n]$, $\delta\underline{g}^{\mathtt{l}}[n]$		
$\underline{r}^{\mathtt{e}}[n]$	3	$\mathtt{re}[n\|i]$	$t_r[n]$	`e`
$\delta\underline{g}^{\mathtt{l}}[n]$	3	$\delta\mathtt{gl}[n\|i]$	$t_g[n]$	`l`

Table 3.28: GUPTN-DGN model.

Derivatives

$$D\langle g_0, \mathtt{re}[n|j]\rangle = \mathtt{gnnorm}^{-1} \cdot \sum_{k=1}^{3} \mathtt{gnn}[n|k]\, D\mathtt{gnn}[n|k,j]$$

$$D\langle g_0, \delta\mathtt{gl}[n|j]\rangle = \mathtt{dgnorm}^{-1} \cdot \delta\mathtt{gl}[n|j]$$

3.4.28 DGUPT-GG: gravity disturbance model

If the gravity disturbance vector is known, in the `l`-frame, at some point of the trajectory and gravity parameters to be computed in the `l`-frame are expressed as gg, the following functional model is obtained.

$$\begin{aligned}
&\text{DGUPT-GG}: \\
&\quad R^3 \times R^3 \quad \longrightarrow \quad R^3 \\
&\quad \underline{r}^{\mathtt{e}}[n], gg[n] \quad \longmapsto \quad \widetilde{\delta \underline{g}^{\mathtt{l}}}
\end{aligned}$$

$$\widetilde{\delta \mathtt{gl}}[i] = \mathtt{gg}[n|i] - \mathtt{gnn}[n|i] \tag{3.41}$$

where $\mathtt{gg}[n] = \mathtt{gg}(gg[n])$ is defined in Section C.3.3 and $\mathtt{gnn}[n] = \mathtt{gnn}(\mathtt{re}[n])$ in Section C.3.1.

Concept	#	Notation	Constants	Frame
Observables	1	$\widetilde{\underline{g}^{\mathtt{l}}}$		
$\widetilde{\delta \underline{g}^{\mathtt{l}}}$	3	$\widetilde{\delta \mathtt{gl}}[n\|i]$	$t_g[n]$	`l`
Parameter Groups	2	$\underline{r}^{\mathtt{e}}[n]$, $gg[n]$		
$\underline{r}^{\mathtt{e}}[n]$	3	$\mathtt{re}[n\|i]$	$t_r[n]$	`e`
$gg[n]$	3	$gg[n\|i]$	$t_g[n]$	

Table 3.29: DGUPT-GG model.

Derivatives

$$D\left\langle \widetilde{\delta \mathtt{gl}}[n|i], \mathtt{re}[n|j] \right\rangle = -D\mathtt{gnn}[n|i,j]$$

$$D\left\langle \widetilde{\delta \mathtt{gl}}[n|i], gg[n|j] \right\rangle = D\mathtt{gg}[n|i,j]$$

3.4.29 XOVER-DGE: gravity's crossover model

In airborne gravimetry, the data acquisition profiles are usually chosen to form a network with a sufficient number of crossings, which are known as crossovers. An estimation of the gravity in airborne crossovers is used to verify the relative accuracy of the gravity data observed in the same position, but at different epochs, and to identify systematic errors. Crossovers do not test the measurements independently, but allow to detect possible systematic errors, to check the inherent accuracy o the sensor system and to give accuracy information, which may be helpul as input of other methods (i.e. collocation). The idea is to compare observed gravity data, when the airborne passes the same geographical position.

The airborne trajectory leads to a height difference at the crossovers. After having identified the crossovers, from [56, Equation (4–16)], we have:

$$g^{\mathsf{e}}(P) = g^{\mathsf{e}}(Q) - \frac{\partial g}{\partial h}\,(h_Q - h_P),$$

where $\frac{\partial g}{\partial h} = -0.0848$ mGal/m (see footnote[5]). This simple formula, although far from perfect, is often applied in practice.

Collecting terms, we obtain:

$$0 = g^{\mathsf{e}}(P - g^{\mathsf{e}}(Q) - \frac{\partial g}{\partial h}\,(h_P - h_Q),$$

The associated functional model is defined by

$$\begin{array}{l}\text{XOVER-DGE}: \\ \quad R^3 \times R^3 \times R^3 \times R^3 \times \\ \quad R^3 \times R^3 \times R^3 \times R^3 \qquad\qquad \longrightarrow \quad R \\ \quad \underline{r}^{\mathsf{e}}[n-1], \underline{r}^{\mathsf{e}}[n], \underline{r}^{\mathsf{e}}[m-1], \underline{r}^{\mathsf{e}}[m], \\ \quad \delta\underline{g}^{\mathsf{e}}[n-1], \delta\underline{g}^{\mathsf{e}}[n], \delta\underline{g}^{\mathsf{e}}[m-1], \delta\underline{g}^{\mathsf{e}}[m] \quad \longmapsto \quad 0\end{array}$$

Let $\underline{r}^{\mathsf{e}}[P] \in (\underline{r}^{\mathsf{e}}[n-1], \underline{r}^{\mathsf{e}}[n])$, $\underline{r}^{\mathsf{e}}[Q] \in (\underline{r}^{\mathsf{e}}[m-2], \underline{r}^{\mathsf{e}}[m])$, $\underline{r}^{\mathsf{e}}[P] = \underline{r}^{\mathsf{e}}[Q]$, $\delta\underline{g}^{\mathsf{e}}[P] \in (\delta\underline{g}^{\mathsf{e}}[n-1], \delta\underline{g}^{\mathsf{e}}[n])$ and $\delta\underline{g}^{\mathsf{e}}[Q] \in (\delta\underline{g}^{\mathsf{e}}[m-1], \delta\underline{g}^{\mathsf{e}}[m])$. Then, the equations associated to this model are

$$0 = \delta g_P + \gamma_P - \delta g_Q - \gamma_Q - \frac{\partial g}{\partial h}\,(h_P - h_Q) \tag{3.42}$$

[5] $\frac{\partial g}{\partial h} = \frac{\partial \gamma}{\partial h} + 4\pi k\rho$. With a density of $\rho = 2.67 g/cm^3$ and $k = 66.7 \times 10^{-9} c.g.s.$, we obtain: $\frac{\partial g}{\partial h} = -0.3086 + 0.2238 = -0.0848 gal/km = -0.0848 mGal/m$

Concept	#	Notation	Constants	Frame
Observables	1	0		
Auxiliary data	2	$t[P]$, $t[Q]$		
$t[P]$	1	t_P		
$t[Q]$	1	t_Q		
Parameter Groups	8	$\underline{r}^{\mathtt{e}}[n-1]$, $\underline{r}^{\mathtt{e}}[n]$, $\underline{r}^{\mathtt{e}}[m-1]$, $\underline{r}^{\mathtt{e}}[m]$, $\delta\underline{g}^{\mathtt{e}}[n-1]$, $\delta\underline{g}^{\mathtt{e}}[n]$, $\delta\underline{g}^{\mathtt{e}}[m-1]$, $\delta\underline{g}^{\mathtt{e}}[m]$		
$\underline{r}^{\mathtt{e}}[n-1]$	3	$\mathtt{re[n-1\|i]}$	$t_r[n-1]$	$\mathtt{e}$
$\underline{r}^{\mathtt{e}}[n]$	3	$\mathtt{re[n\|i]}$	$t_r[n]$	$\mathtt{e}$
$\underline{r}^{\mathtt{e}}[m-1]$	3	$\mathtt{re[m-1\|i]}$	$t_r[m-1]$	$\mathtt{e}$
$\underline{r}^{\mathtt{e}}[m]$	3	$\mathtt{re[m\|i]}$	$t_r[m]$	$\mathtt{e}$
$\delta\underline{g}^{\mathtt{e}}[n-1]$	3	$\delta\mathtt{ge[n-1\|i]}$	$t_g[n-1]$	$\mathtt{e}$
$\delta\underline{g}^{\mathtt{e}}[n]$	3	$\delta\mathtt{ge[n\|i]}$	$t_g[n]$	$\mathtt{e}$
$\delta\underline{g}^{\mathtt{e}}[m-1]$	3	$\delta\mathtt{ge[m-1\|i]}$	$t_g[m-1]$	$\mathtt{e}$
$\delta\underline{g}^{\mathtt{e}}[m]$	3	$\delta\mathtt{ge[m\|i]}$	$t_g[m]$	$\mathtt{e}$

Table 3.30: XOVER-DGE model.

where

$$\gamma_s = \left[\sum_{k=1}^{3} \mathtt{gne[s|k]}^2\right]^{1/2},$$

$$\delta g_s = \left[\sum_{k=1}^{3} \delta\mathtt{ge[s|k]}^2\right]^{1/2},$$

$\frac{\partial g}{\partial h} = -0.0848\frac{mGal}{m}$ and $\mathtt{gne[s]} = \mathtt{gne(re[s])}$ is computed using Equation (C.17).

Derivatives

$$
\begin{aligned}
D\langle 0, \mathtt{re[n-1|j]}\rangle &= D\langle \gamma_P, \mathtt{re[n-1|j]}\rangle - \tfrac{\partial g}{\partial h}\, D\langle h_P, \mathtt{re[n-1|j]}\rangle \\
D\langle 0, \mathtt{re[n|j]}\rangle &= D\langle \gamma_P, \mathtt{re[n|j]}\rangle - \tfrac{\partial g}{\partial h}\, D\langle h_P, \mathtt{re[n|j]}\rangle \\
D\langle 0, \mathtt{re[m-1|j]}\rangle &= -D\langle \gamma_Q, \mathtt{re[m-1|j]}\rangle + \tfrac{\partial g}{\partial h}\, D\langle h_Q, \mathtt{re[m-1|j]}\rangle \\
D\langle 0, \mathtt{re[m|j]}\rangle &= -D\langle \gamma_Q, \mathtt{re[m|j]}\rangle + \tfrac{\partial g}{\partial h}\, D\langle h_Q, \mathtt{re[m|j]}\rangle \\
D\langle 0, \delta\mathtt{ge[n-1|j]}\rangle &= D\langle \delta g_P, \delta\mathtt{ge[n-1|j]}\rangle \\
D\langle 0, \delta\mathtt{ge[n|j]}\rangle &= D\langle \delta g_P, \delta\mathtt{ge[n|j]}\rangle \\
D\langle 0, \delta\mathtt{ge[m-1|j]}\rangle &= -D\langle \delta g_Q, \delta\mathtt{ge[m-1|j]}\rangle \\
D\langle 0, \delta\mathtt{ge[m|j]}\rangle &= -D\langle \delta g_Q, \delta\mathtt{ge[m|j]}\rangle
\end{aligned}
$$

where

$$
\begin{aligned}
D\langle \gamma_P, \mathtt{re[n-1|j]}\rangle &= {\gamma_P}^{-1} \cdot \textstyle\sum_{k=1}^{3} \mathtt{gne[}P\mathtt{|}k\mathtt{]}\, D\langle \mathtt{gne[}P\mathtt{|}k\mathtt{]}, \mathtt{re[n-1|j]}\rangle \\
D\langle \gamma_P, \mathtt{re[n|j]}\rangle &= {\gamma_P}^{-1} \cdot \textstyle\sum_{k=1}^{3} \mathtt{gne[}P\mathtt{|}k\mathtt{]}\, D\langle \mathtt{gne[}P\mathtt{|}k\mathtt{]}, \mathtt{re[n|j]}\rangle \\
D\langle \gamma_Q, \mathtt{re[m-1|j]}\rangle &= {\gamma_Q}^{-1} \cdot \textstyle\sum_{k=1}^{3} \mathtt{gne[}Q\mathtt{|}k\mathtt{]}\, D\langle \mathtt{gne[}Q\mathtt{|}k\mathtt{]}, \mathtt{re[m-1|j]}\rangle \\
D\langle \gamma_Q, \mathtt{re[m|j]}\rangle &= {\gamma_Q}^{-1} \cdot \textstyle\sum_{k=1}^{3} \mathtt{gne[}Q\mathtt{|}k\mathtt{]}\, D\langle \mathtt{gne[}Q\mathtt{|}k\mathtt{]}, \mathtt{re[m|j]}\rangle
\end{aligned}
$$

$$
\begin{aligned}
D\langle \delta g_P, \delta\mathtt{ge[}n-1\mathtt{|}j\mathtt{]}\rangle &= {\delta g_P}^{-1} \cdot \textstyle\sum_{k=1}^{3} \delta\mathtt{ge[P|k]}\, \mathtt{D}\langle \delta\mathtt{ge[P|k]}, \delta\mathtt{ge[n-1|j]}\rangle \\
D\langle \delta g_P, \delta\mathtt{ge[}n\mathtt{|}j\mathtt{]}\rangle &= {\delta g_P}^{-1} \cdot \textstyle\sum_{k=1}^{3} \delta\mathtt{ge[P|k]}\, \mathtt{D}\langle \delta\mathtt{ge[P|k]}, \delta\mathtt{ge[n|j]}\rangle \\
D\langle \delta g_Q, \delta\mathtt{ge[}m-1\mathtt{|}j\mathtt{]}\rangle &= {\delta g_Q}^{-1} \cdot \textstyle\sum_{k=1}^{3} \delta\mathtt{ge[Q|k]}\, \mathtt{D}\langle \delta\mathtt{ge[Q|k]}, \delta\mathtt{ge[m-1|j]}\rangle \\
D\langle \delta g_Q, \delta\mathtt{ge[}m\mathtt{|}j\mathtt{]}\rangle &= {\delta g_Q}^{-1} \cdot \textstyle\sum_{k=1}^{3} \delta\mathtt{ge[Q|k]}\, \mathtt{D}\langle \delta\mathtt{ge[Q|k]}, \delta\mathtt{ge[m|j]}\rangle
\end{aligned}
$$

$$
\begin{aligned}
\delta\mathtt{ge[P|i]} &= cg_{n-1}\, \delta\mathtt{ge[n-1|i]} + \mathtt{cg_n}\, \delta\mathtt{ge[n|i]} \\
D\langle \delta\mathtt{ge[P|i]}, \delta\mathtt{ge[n-1|j]}\rangle &= cg_{n-1}\, \delta_{ij} \\
D\langle \delta\mathtt{ge[P|i]}, \delta\mathtt{ge[n|j]}\rangle &= cg_n\, \delta_{ij}
\end{aligned}
$$

$$\begin{aligned}
\delta\mathtt{ge}[\mathtt{Q}|\mathtt{i}] &= cg_{m-1}\,\delta\mathtt{ge}[\mathtt{m}-1|\mathtt{i}] + \mathtt{cg}_{\mathtt{m}}\,\delta\mathtt{ge}[\mathtt{m}|\mathtt{i}] \\
D\langle\delta\mathtt{ge}[\mathtt{Q}|\mathtt{i}],\delta\mathtt{ge}[\mathtt{m}-1|\mathtt{j}]\rangle &= cg_{m-1}\,\delta_{ij} \\
D\langle\delta\mathtt{ge}[\mathtt{Q}|\mathtt{i}],\delta\mathtt{ge}[\mathtt{m}|\mathtt{j}]\rangle &= cg_{m}\,\delta_{ij}
\end{aligned}$$

$$\begin{aligned}
D\langle\mathtt{gne}[P|k],\mathtt{re}[\mathtt{n}-1|\mathtt{j}]\rangle &= \textstyle\sum_{s=1}^{3} D\mathtt{gne}[P|k,s]\,D\langle\mathtt{re}[P|s],\mathtt{re}[n-1|j]\rangle \\
D\langle\mathtt{gne}[P|k],\mathtt{re}[\mathtt{n}|\mathtt{j}]\rangle &= \textstyle\sum_{s=1}^{3} D\mathtt{gne}[P|k,s]\,D\langle\mathtt{re}[P|s],\mathtt{re}[n|j]\rangle \\
D\langle\mathtt{gne}[Q|k],\mathtt{re}[\mathtt{m}-1|\mathtt{j}]\rangle &= \textstyle\sum_{s=1}^{3} D\mathtt{gne}[Q|k,s]\,D\langle\mathtt{re}[Q|s],\mathtt{re}[m-1|j]\rangle \\
D\langle\mathtt{gne}[Q|k],\mathtt{re}[\mathtt{m}|\mathtt{j}]\rangle &= \textstyle\sum_{s=1}^{3} D\mathtt{gne}[Q|k,s]\,D\langle\mathtt{re}[Q|s],\mathtt{re}[m|j]\rangle
\end{aligned}$$

$$\begin{aligned}
\mathtt{re}[P] &= cx_{n-1}\,\mathtt{re}[n-1] + cx_n\,\mathtt{re}[n] \\
D\langle\mathtt{re}[P|i],\mathtt{re}[n-1|j]\rangle &= cx_{n-1}\,\delta_{ij} \\
D\langle\mathtt{re}[P|i],\mathtt{re}[n|j]\rangle &= cx_n\,\delta_{ij}
\end{aligned}$$

$$\begin{aligned}
\mathtt{re}[Q] &= cx_{m-1}\,\mathtt{re}[m-1] + cx_m\,\mathtt{re}[m] \\
D\langle\mathtt{re}[Q|i],\mathtt{re}[m-1|j]\rangle &= cx_{m-1}\,\delta_{ij} \\
D\langle\mathtt{re}[Q|i],\mathtt{re}[m|j]\rangle &= cx_m\,\delta_{ij}
\end{aligned}$$

$$\begin{aligned}
D\langle h_P,\mathtt{re}[n-1|j]\rangle &= cx_{n-1}\,D\mathtt{getogc}[P|3,j] \\
D\langle h_P,\mathtt{re}[n|j]\rangle &= cx_n\,D\mathtt{getogc}[P|3,j] \\
D\langle h_Q,\mathtt{re}[m-1|j]\rangle &= cx_{m-1}\,D\mathtt{getogc}[Q|3,j] \\
D\langle h_Q,\mathtt{re}[m|j]\rangle &= cx_m\,D\mathtt{getogc}[Q|3,j]
\end{aligned}$$

$$
\begin{aligned}
cx_{n-1} &= (t_r[n] - t_P) \cdot (t_r[n] - t_r[n-1])^{-1} \\
cx_n &= (t_P - t_r[n-1]) \cdot (t_r[n] - t_r[n-1])^{-1} \\
cx_{m-1} &= (t_r[m] - t_Q) \cdot (t_r[m] - t_r[m-1])^{-1} \\
cx_m &= (t_Q - t_r[m-1]) \cdot (t_r[m] - t_r[m-1])^{-1} \\
cg_{n-1} &= (t_g[n] - t_P) \cdot (t_g[n] - t_g[n-1])^{-1} \\
cg_n &= (t_P - t_g[n-1]) \cdot (t_g[n] - t_g[n-1])^{-1} \\
cg_{m-1} &= (t_g[m] - t_Q) \cdot (t_g[m] - t_g[m-1])^{-1} \\
cg_m &= (t_Q - t_g[m-1]) \cdot (t_g[m] - t_g[m-1])^{-1}
\end{aligned}
$$

and where h_P, h_Q are computed applying `getogc` to `re`$[P]$ and `re`$[Q]$ respectively and `gne`$[P]$, `gne`$[Q]$ are computed using Equation (C.17) and δ_{ij} is the Dirac's function, defined by Equation (3.9).

3.4.30 XOVER-DGN: gravity's crossover model

This model is a variation on the XOVER-DGE model described in Section 3.4.29, where the gravity disturbance parameters are computed in the `l`-frame.

Concept	#	Notation	Constants	Frame
Observables	1	0		
Auxiliary Data	2	$t[P]$, $t[Q]$		
$t[P]$	1	t_P		
$t[Q]$	1	t_Q		
Parameter Groups	8	$\underline{r}^{\mathtt{e}}[n-1]$, $\underline{r}^{\mathtt{e}}[n]$, $\underline{r}^{\mathtt{e}}[m-1]$, $\underline{r}^{\mathtt{e}}[m]$, $\delta\underline{g}^{\mathtt{l}}[n-1]$, $\delta\underline{g}^{\mathtt{l}}[n]$, $\delta\underline{g}^{\mathtt{l}}[m-1]$, $\delta\underline{g}^{\mathtt{l}}[m]$		
$\underline{r}^{\mathtt{e}}[n-1]$	3	`re[n-1|i]`	$t_r[n-1]$	`e`
$\underline{r}^{\mathtt{e}}[n]$	3	`re[n|i]`	$t_r[n]$	`e`
$\underline{r}^{\mathtt{e}}[m-1]$	3	`re[m-1|i]`	$t_r[m-1]$	`e`
$\underline{r}^{\mathtt{e}}[m]$	3	`re[m|i]`	$t_r[m]$	`e`
$\delta\underline{g}^{\mathtt{l}}[n-1]$	3	δ`gl[n-1|i]`	$t_g[n-1]$	`l`
$\delta\underline{g}^{\mathtt{l}}[n]$	3	δ`gl[n|i]`	$t_g[n]$	`l`
$\delta\underline{g}^{\mathtt{l}}[m-1]$	3	δ`gl[m-1|i]`	$t_g[m-1]$	`l`
$\delta\underline{g}^{\mathtt{l}}[m]$	3	δ`gl[m|i]`	$t_g[m]$	`l`

Table 3.31: XOVER-DGN model.

The associated functional model is defined by

$$
\begin{array}{l}
\text{XOVER-DGN}: \\
\quad R^3\times R^3\times R^3\times R^3\times \\
\quad R^3\times R^3\times R^3\times R^3 \qquad\qquad \longrightarrow \quad R \\
\quad \underline{r}^{\mathtt{e}}[n-1],\underline{r}^{\mathtt{e}}[n],\underline{r}^{\mathtt{e}}[m-1],\underline{r}^{\mathtt{e}}[m], \\
\quad \delta\underline{g}^{\mathtt{l}}[n-1],\delta\underline{g}^{\mathtt{l}}[n],\delta\underline{g}^{\mathtt{l}}[m-1],\delta\underline{g}^{\mathtt{l}}[m] \quad \longmapsto \quad 0
\end{array}
$$

Let $\underline{r}^{\mathtt{e}}[P]\in(\underline{r}^{\mathtt{e}}[n-1],\underline{r}^{\mathtt{e}}[n])$, $\underline{r}^{\mathtt{e}}[Q]\in(\underline{r}^{\mathtt{e}}[m-2],\underline{r}^{\mathtt{e}}[m])$, $\underline{r}^{\mathtt{e}}[P]=\underline{r}^{\mathtt{e}}[Q]$, $\delta\underline{g}^{\mathtt{l}}[P]\in(\delta\underline{g}^{\mathtt{l}}[n-1],\delta\underline{g}^{\mathtt{l}}[n])$ and $\delta\underline{g}^{\mathtt{l}}[Q]\in(\delta\underline{g}^{\mathtt{l}}[m-1],\delta\underline{g}^{\mathtt{l}}[m])$. The equations associated to this model are

$$0=\delta g_P+\gamma_P-\delta g_Q-\gamma_Q-\frac{\partial g}{\partial h}\,(h_P-h_Q) \tag{3.43}$$

where, for $*=P,Q$,

$$
\begin{aligned}
\gamma_s &= \left[\textstyle\sum_{k=1}^{3}\mathtt{gnn[s|k]}^2\right]^{1/2}, \\
\delta g_s &= \left[\textstyle\sum_{k=1}^{3}\delta\mathtt{gl[s|k]}^2\right]^{1/2},
\end{aligned}
$$

$\frac{\partial g}{\partial h} = -0.0848 \frac{mGal}{m}$ and $\mathrm{gnn[s]} = \mathrm{gnn(re[s])}$ is computed using Equation (C.16).

Derivatives

$$
\begin{aligned}
D\langle 0, \mathrm{re[n-1|j]}\rangle &= D\langle \gamma_P, \mathrm{re[n-1|j]}\rangle - \tfrac{\partial g}{\partial h} D\langle h_P, \mathrm{re[n-1|j]}\rangle \\
D\langle 0, \mathrm{re[n|j]}\rangle &= D\langle \gamma_P, \mathrm{re[n|j]}\rangle - \tfrac{\partial g}{\partial h} D\langle h_P, \mathrm{re[n|j]}\rangle \\
D\langle 0, \mathrm{re[m-1|j]}\rangle &= -D\langle \gamma_Q, \mathrm{re[m-1|j]}\rangle + \tfrac{\partial g}{\partial h} D\langle h_Q, \mathrm{re[m-1|j]}\rangle \\
D\langle 0, \mathrm{re[m|j]}\rangle &= -D\langle \gamma_Q, \mathrm{re[m|j]}\rangle + \tfrac{\partial g}{\partial h} D\langle h_Q, \mathrm{re[m|j]}\rangle \\
D\langle 0, \delta\mathrm{gl[n-1|j]}\rangle &= D\langle \delta g_P, \delta\mathrm{gl[n-1|j]}\rangle \\
D\langle 0, \delta\mathrm{gl[n|j]}\rangle &= D\langle \delta g_P, \delta\mathrm{gl[n|j]}\rangle \\
D\langle 0, \delta\mathrm{gl[m-1|j]}\rangle &= -D\langle \delta g_Q, \delta\mathrm{gl[m-1|j]}\rangle \\
D\langle 0, \delta\mathrm{gl[m|j]}\rangle &= -D\langle \delta g_Q, \delta\mathrm{gl[m|j]}\rangle
\end{aligned}
$$

where

$$
\begin{aligned}
D\langle \gamma_P, \mathrm{re[n-1|j]}\rangle &= {\gamma_P}^{-1} \cdot \textstyle\sum_{k=1}^{3} \mathrm{gnn[P|k]}\, D\langle \mathrm{gnn[P|k]}, \mathrm{re[n-1|j]}\rangle \\
D\langle \gamma_P, \mathrm{re[n|j]}\rangle &= {\gamma_P}^{-1} \cdot \textstyle\sum_{k=1}^{3} \mathrm{gnn[P|k]}\, D\langle \mathrm{gnn[P|k]}, \mathrm{re[n|j]}\rangle \\
D\langle \gamma_Q, \mathrm{re[m-1|j]}\rangle &= {\gamma_Q}^{-1} \cdot \textstyle\sum_{k=1}^{3} \mathrm{gnn[Q|k]}\, D\langle \mathrm{gnn[Q|k]}, \mathrm{re[m-1|j]}\rangle \\
D\langle \gamma_Q, \mathrm{re[m|j]}\rangle &= {\gamma_Q}^{-1} \cdot \textstyle\sum_{k=1}^{3} \mathrm{gnn[Q|k]}\, D\langle \mathrm{gnn[Q|k]}, \mathrm{re[m|j]}\rangle
\end{aligned}
$$

$$
\begin{aligned}
D\langle \delta g_P, \delta\mathrm{gl}[n-1|j]\rangle &= {\delta g_P}^{-1} \cdot \textstyle\sum_{k=1}^{3} \delta\mathrm{gl[P|k]}\, \mathrm{D}\langle \delta\mathrm{gl[P|k]}, \delta\mathrm{gl[n-1|j]}\rangle \\
D\langle \delta g_P, \delta\mathrm{gl}[n|j]\rangle &= {\delta g_P}^{-1} \cdot \textstyle\sum_{k=1}^{3} \delta\mathrm{gl[P|k]}\, \mathrm{D}\langle \delta\mathrm{gl[P|k]}, \delta\mathrm{gl[n|j]}\rangle \\
D\langle \delta g_Q, \delta\mathrm{gl}[m-1|j]\rangle &= {\delta g_Q}^{-1} \cdot \textstyle\sum_{k=1}^{3} \delta\mathrm{gl[Q|k]}\, \mathrm{D}\langle \delta\mathrm{gl[Q|k]}, \delta\mathrm{gl[m-1|j]}\rangle \\
D\langle \delta g_Q, \delta\mathrm{gl}[m|j]\rangle &= {\delta g_Q}^{-1} \cdot \textstyle\sum_{k=1}^{3} \delta\mathrm{gl[Q|k]}\, \mathrm{D}\langle \delta\mathrm{gl[Q|k]}, \delta\mathrm{gl[m|j]}\rangle
\end{aligned}
$$

$$
\begin{aligned}
\delta\mathtt{gl[P|i]} &= cg_{n-1}\,\delta\mathtt{gl[n-1|i]} + \mathtt{cg_n}\,\delta\mathtt{gl[n|i]} \\
D\langle\delta\mathtt{gl[P|i]},\delta\mathtt{gl[n-1|j]}\rangle &= cg_{n-1}\,\delta_{ij} \\
D\langle\delta\mathtt{gl[P|i]},\delta\mathtt{gl[n|j]}\rangle &= cg_n\,\delta_{ij}
\end{aligned}
$$

$$
\begin{aligned}
\delta\mathtt{gl[Q|i]} &= cg_{m-1}\,\delta\mathtt{gl[m-1|i]} + \mathtt{cg_m}\,\delta\mathtt{gl[m|i]} \\
D\langle\delta\mathtt{gl[Q|i]},\delta\mathtt{gl[m-1|j]}\rangle &= cg_{m-1}\,\delta_{ij} \\
D\langle\delta\mathtt{gl[Q|i]},\delta\mathtt{gl[m|j]}\rangle &= cg_m\,\delta_{ij}
\end{aligned}
$$

$$
\begin{aligned}
D\langle\mathtt{gnn}[P|k],\mathtt{re[n-1|j]}\rangle &= \textstyle\sum_{s=1}^{3} D\mathtt{gnn}[P|k,s]\,D\langle\mathtt{re}[P|s],\mathtt{re}[n-1|j]\rangle \\
D\langle\mathtt{gnn}[P|k],\mathtt{re[n|j]}\rangle &= \textstyle\sum_{s=1}^{3} D\mathtt{gnn}[P|k,s]\,D\langle\mathtt{re}[P|s],\mathtt{re}[n|j]\rangle \\
D\langle\mathtt{gnn}[Q|k],\mathtt{re[m-1|j]}\rangle &= \textstyle\sum_{s=1}^{3} D\mathtt{gnn}[Q|k,s]\,D\langle\mathtt{re}[Q|s],\mathtt{re}[m-1|j]\rangle \\
D\langle\mathtt{gnn}[Q|k],\mathtt{re[m|j]}\rangle &= \textstyle\sum_{s=1}^{3} D\mathtt{gnn}[Q|k,s]\,D\langle\mathtt{re}[Q|s],\mathtt{re}[m|j]\rangle
\end{aligned}
$$

$$
\begin{aligned}
\mathtt{re}[P] &= cx_{n-1}\,\mathtt{re}[n-1] + cx_n\,\mathtt{re}[n] \\
D\langle\mathtt{re}[P|i],\mathtt{re}[n-1|j]\rangle &= cx_{n-1}\,\delta_{ij} \\
D\langle\mathtt{re}[P|i],\mathtt{re}[n|j]\rangle &= cx_n\,\delta_{ij}
\end{aligned}
$$

$$
\begin{aligned}
\mathtt{re}[Q] &= cx_{m-1}\,\mathtt{re}[m-1] + cx_m\,\mathtt{re}[m] \\
D\langle\mathtt{re}[Q|i],\mathtt{re}[m-1|j]\rangle &= cx_{m-1}\,\delta_{ij} \\
D\langle\mathtt{re}[Q|i],\mathtt{re}[m|j]\rangle &= cx_m\,\delta_{ij}
\end{aligned}
$$

$$
\begin{aligned}
D\langle h_P,\mathtt{re}[n-1|j]\rangle &= cx_{n-1}\,D\mathtt{getogc}[P|3,j] \\
D\langle h_P,\mathtt{re}[n|j]\rangle &= cx_n\,D\mathtt{getogc}[P|3,j] \\
D\langle h_Q,\mathtt{re}[m-1|j]\rangle &= cx_{m-1}\,D\mathtt{getogc}[Q|3,j] \\
D\langle h_Q,\mathtt{re}[m|j]\rangle &= cx_m\,D\mathtt{getogc}[Q|3,j]
\end{aligned}
$$

$$
\begin{aligned}
cx_{n-1} &= (t_r[n] - t_P) \cdot (t_r[n] - t_r[n-1])^{-1} \\
cx_n &= (t_P - t_r[n-1]) \cdot (t_r[n] - t_r[n-1])^{-1} \\
cx_{m-1} &= (t_r[m] - t_Q) \cdot (t_r[m] - t_r[m-1])^{-1} \\
cx_m &= (t_Q - t_r[m-1]) \cdot (t_r[m] - t_r[m-1])^{-1} \\
cg_{n-1} &= (t_g[n] - t_P) \cdot (t_g[n] - t_g[n-1])^{-1} \\
cg_n &= (t_P - t_g[n-1]) \cdot (t_g[n] - t_g[n-1])^{-1} \\
cg_{m-1} &= (t_g[m] - t_Q) \cdot (t_g[m] - t_g[m-1])^{-1} \\
cg_m &= (t_Q - t_g[m-1]) \cdot (t_g[m] - t_g[m-1])^{-1}
\end{aligned}
$$

where h_P, h_Q are computed applying `getogc` to `re`$[P]$ and `re`$[Q]$ respectively and `gnn`$[P]$, `gnn`$[Q]$ are computed using Equation (C.16) and δ_{ij} is the Dirac's function, defined by Equation (3.9).

3.4.31 XOVER-GG: gravity's crossover model

This model is a variation on the XOVER-DGE and XOVER-DGN models. Here, the gravity parameters in the `l`-frame are expressed as gg vector, defined in the Section C.3.3.

Concept	#	Notation	Constants	Frame
Observables	1	0		
Auxiliary Data	2	$t[P]$, $t[Q]$		
$t[P]$	1	t_P		
$t[Q]$	1	t_Q		
Parameter Groups	8	$\underline{r}^{\mathtt{e}}[n-1]$, $\underline{r}^{\mathtt{e}}[n]$, $\underline{r}^{\mathtt{e}}[m-1]$, $\underline{r}^{\mathtt{e}}[m]$, $gg[n-1]$, $gg[n]$, $gg[m-1]$, $gg[m]$		
$\underline{r}^{\mathtt{e}}[n-1]$	3	$\mathtt{re[n-1\|i]}$	$t_r[n-1]$	$\mathtt{e}$
$\underline{r}^{\mathtt{e}}[n]$	3	$\mathtt{re[n\|i]}$	$t_r[n]$	$\mathtt{e}$
$\underline{r}^{\mathtt{e}}[m-1]$	3	$\mathtt{re[m-1\|i]}$	$t_r[m-1]$	$\mathtt{e}$
$\underline{r}^{\mathtt{e}}[m]$	3	$\mathtt{re[m\|i]}$	$t_r[m]$	$\mathtt{e}$
$gg[n-1]$	3	$gg[n-1\|i]$	$t_g[n-1]$	
$gg[n]$	3	$gg[n\|i]$	$t_g[n]$	
$gg[m-1]$	3	$gg[m-1\|i]$	$t_g[m-1]$	
$gg[m]$	3	$gg[m\|i]$	$t_g[m]$	

Table 3.32: XOVER-GG model.

The associated functional model is defined by

$$
\begin{aligned}
&\text{XOVER-GG}: \\
&\quad R^3 \times R^3 \times R^3 \times R^3 \times \\
&\quad R^3 \times R^3 \times R^3 \times R^3 \qquad\qquad \longrightarrow \quad R \\
&\quad \underline{r}^{\mathtt{e}}[n-1], \underline{r}^{\mathtt{e}}[n], \underline{r}^{\mathtt{e}}[m-1], \underline{r}^{\mathtt{e}}[m], \\
&\quad gg[n-1], gg[n], gg[m-1], gg[m] \quad \longmapsto \quad 0
\end{aligned}
$$

Let $\underline{r}^{\mathtt{e}}[P] \in (\underline{r}^{\mathtt{e}}[n-1], \underline{r}^{\mathtt{e}}[n])$, $\underline{r}^{\mathtt{e}}[Q] \in (\underline{r}^{\mathtt{e}}[m-2], \underline{r}^{\mathtt{e}}[m])$, $\underline{r}^{\mathtt{e}}[P] = \underline{r}^{\mathtt{e}}[Q]$, $gg[P] \in (gg[n-1], gg[n])$ and $gg[Q] \in (gg[m-1], gg[m])$. The equations associated to this model are

$$0 = g_P - g_Q - \frac{\partial g}{\partial h}(h_P - h_Q) \tag{3.44}$$

where, for $* = P, Q$,

$$g_s = \left[\sum_{k=1}^{3} \mathtt{gg[s|k]}^2 \right]^{1/2},$$

$\frac{\partial g}{\partial h} = -0.0848 \frac{mGal}{m}$ and $\mathtt{gg[s]} = \mathtt{gg(gg[s])}$ is computed using Equation (C.20).

Derivatives

$$
\begin{aligned}
D\langle 0, \mathtt{re[n-1|j]}\rangle &= -\tfrac{\partial g}{\partial h}\, D\langle h_P, \mathtt{re[n-1|j]}\rangle \\
D\langle 0, \mathtt{re[n|j]}\rangle &= -\tfrac{\partial g}{\partial h}\, D\langle h_P, \mathtt{re[n|j]}\rangle \\
D\langle 0, \mathtt{re[m-1|j]}\rangle &= \tfrac{\partial g}{\partial h}\, D\langle h_Q, \mathtt{re[m-1|j]}\rangle \\
D\langle 0, \mathtt{re[m|j]}\rangle &= \tfrac{\partial g}{\partial h}\, D\langle h_Q, \mathtt{re[m|j]}\rangle \\
D\langle 0, gg[n-1|j]\rangle &= D\langle g_P, gg[n-1|j]\rangle \\
D\langle 0, gg[n|j]\rangle &= D\langle g_P, gg[n|j]\rangle \\
D\langle 0, gg[m-1|j]\rangle &= -D\langle g_Q, gg[m-1|j]\rangle \\
D\langle 0, gg[m|j]\rangle &= -D\langle g_Q, gg[m|j]\rangle
\end{aligned}
$$

where

$$
\begin{aligned}
D\langle g_P, gg[n-1|j]\rangle &= {g_P}^{-1} \cdot \textstyle\sum_{k=1}^{3} \mathrm{gg}[P|k]\; D\langle \mathrm{gg}[P|k], gg[n-1|j]\rangle \\
D\langle g_P, gg[n|j]\rangle &= {g_P}^{-1} \cdot \textstyle\sum_{k=1}^{3} \mathrm{gg}[P|k]\; D\langle \mathrm{gg}[P|k], gg[n|j]\rangle \\
D\langle g_Q, gg[m-1|j]\rangle &= {g_Q}^{-1} \cdot \textstyle\sum_{k=1}^{3} \mathrm{gg}[Q|k]\; D\langle \mathrm{gg}[Q|k], gg[m-1|j]\rangle \\
D\langle g_Q, gg[m|j]\rangle &= {g_Q}^{-1} \cdot \textstyle\sum_{k=1}^{3} \mathrm{gg}[Q|k]\; D\langle \mathrm{gg}[Q|k], gg[m|j]\rangle
\end{aligned}
$$

$$gg[P|i] = cg_{n-1}\, gg[n-1|i] + cg_n\, gg[n|i]$$

$$D\langle gg[P|i], gg[n-1|j]\rangle = cg_{n-1}\, \delta_{ij}$$

$$D\langle gg[P|i], gg[n|j]\rangle = cg_n\, \delta_{ij}$$

$$gg[Q|i] = cg_{m-1}\, gg[m-1|i] + cg_m\, gg[m|i]$$

$$D\langle gg[Q|i], gg[m-1|j]\rangle = cg_{m-1}\, \delta_{ij}$$

$$D\langle gg[Q|i], gg[m|j]\rangle = cg_m\, \delta_{ij}$$

$$
\begin{aligned}
D\langle \mathrm{gg}[P|k], gg[n-1|j]\rangle &= \textstyle\sum_{s=1}^{3} D\mathrm{gg}[P|k,s]\, D\langle gg[P|s], gg[n-1|j]\rangle \\
D\langle \mathrm{gg}[P|k], gg[n|j]\rangle &= \textstyle\sum_{s=1}^{3} D\mathrm{gg}[P|k,s]\, D\langle gg[P|s], gg[n|j]\rangle \\
D\langle \mathrm{gg}[Q|k], gg[m-1|j]\rangle &= \textstyle\sum_{s=1}^{3} D\mathrm{gg}[Q|k,s]\, D\langle gg[Q|s], gg[m-1|j]\rangle \\
D\langle \mathrm{gg}[Q|k], gg[m|j]\rangle &= \textstyle\sum_{s=1}^{3} D\mathrm{gg}[Q|k,s]\, D\langle gg[Q|s], gg[m|j]\rangle
\end{aligned}
$$

$$\mathtt{re}[P] = cx_{n-1}\,\mathtt{re}[n-1] + cx_n\,\mathtt{re}[n]$$

$$D\langle \mathtt{re}[P|i], \mathtt{re}[n-1|j]\rangle = cx_{n-1}\,\delta_{ij}$$

$$D\langle \mathtt{re}[P|i], \mathtt{re}[n|j]\rangle = cx_n\,\delta_{ij}$$

$$\mathtt{re}[Q] = cx_{m-1}\,\mathtt{re}[m-1] + cx_m\,\mathtt{re}[m]$$

$$D\langle \mathtt{re}[Q|i], \mathtt{re}[m-1|j]\rangle = cx_{m-1}\,\delta_{ij}$$

$$D\langle \mathtt{re}[Q|i], \mathtt{re}[m|j]\rangle = cx_m\,\delta_{ij}$$

$$
\begin{aligned}
D\langle h_P, \mathtt{re}[n-1|j]\rangle &= cx_{n-1}\, D\mathtt{getogc}[P|3,j] \\
D\langle h_P, \mathtt{re}[n|j]\rangle &= cx_n\, D\mathtt{getogc}[P|3,j] \\
D\langle h_Q, \mathtt{re}[m-1|j]\rangle &= cx_{m-1}\, D\mathtt{getogc}[Q|3,j] \\
D\langle h_Q, \mathtt{re}[m|j]\rangle &= cx_m\, D\mathtt{getogc}[Q|3,j]
\end{aligned}
$$

$$
\begin{aligned}
cx_{n-1} &= (t_r[n] - t_P) \cdot (t_r[n] - t_r[n-1])^{-1} \\
cx_n &= (t_P - t_r[n-1]) \cdot (t_r[n] - t_r[n-1])^{-1} \\
cx_{m-1} &= (t_r[m] - t_Q) \cdot (t_r[m] - t_r[m-1])^{-1} \\
cx_m &= (t_Q - t_r[m-1]) \cdot (t_r[m] - t_r[m-1])^{-1} \\
cg_{n-1} &= (t_g[n] - t_P) \cdot (t_g[n] - t_g[n-1])^{-1} \\
cg_n &= (t_P - t_g[n-1]) \cdot (t_g[n] - t_g[n-1])^{-1} \\
cg_{m-1} &= (t_g[m] - t_Q) \cdot (t_g[m] - t_g[m-1])^{-1} \\
cg_m &= (t_Q - t_g[m-1]) \cdot (t_g[m] - t_g[m-1])^{-1}
\end{aligned}
$$

where h_P, h_Q are computed applying `getogc` to `re`$[P]$ and `re`$[Q]$ respectively and gg$[P]$, gg$[Q]$ are computed using Equation (C.20) and δ_{ij} is the Dirac's function, defined by Equation (3.9).

3.4.32 RE-O: Coordinate Update pseudo-observation model

Table 3.1 describes the parameters to be determined. Particularly, position parameters are cartesian coordinates in the e -frame referred to IMU. If IMU positions are known, the associated functional model for this coordinate update point is a pseudo-observation

$$\underline{\widetilde{r}}^{\mathtt{e}} = \underline{r}^{\mathtt{e}}$$

Concept	#	Notation	Constants	Frame
Observables	1	$\underline{\widetilde{r}}^{\mathtt{e}}$		
$\underline{\widetilde{r}}^{\mathtt{e}}$	3	$\widetilde{\mathtt{re}}[i]$		e
Parameter Groups	1	$\underline{r}^{\mathtt{e}}[n]$		
$\underline{r}^{\mathtt{e}}[n]$	3	re[n|i]	$t_r[n]$	e

Table 3.33: RE-O model.

$$\begin{aligned} &\text{RE-O}: \\ &\quad R^3 \longrightarrow R^3 \\ &\quad \underline{r}^{\mathtt{e}}[n] \longmapsto \underline{\widetilde{r}}^{\mathtt{e}} \end{aligned}$$

$$\widetilde{\mathtt{re}}[i] = \mathtt{re}[\mathtt{n}|\mathtt{i}] \tag{3.45}$$

Derivatives

$$D\left\langle \widetilde{\mathtt{re}}[i], \mathtt{re}[n|j] \right\rangle = \delta_{ij}$$

where δ_{ij} is the Dirac's function, defined by Equation (3.9).

3.4.33 VE-O: Velocity Update pseudo-observation model

If instead of the position, the speed or velocity — referred to IMU — is also known, the associated equation model is also a pseudo-observation model.

$$\begin{array}{l}\text{VE-O}: \\ \quad R^3 \quad \longrightarrow \quad R^3 \\ \quad \underline{v}^{\mathtt{e}}[n] \quad \longmapsto \quad \widetilde{\underline{v}^{\mathtt{e}}}\end{array}$$

$$\widetilde{\mathtt{ve}}[i] = \mathtt{ve[n|i]} \tag{3.46}$$

Concept	#	Notation	Constants	Frame
Observables	1	$\widetilde{\underline{v}^{\mathtt{e}}}$		
$\widetilde{\underline{v}^{\mathtt{e}}}$	3	$\widetilde{\mathtt{ve}}[i]$		e
Parameter Groups	1	$\underline{v}^{\mathtt{e}}[n]$		
$\underline{v}^{\mathtt{e}}[n]$	3	ve[n|i]	$t_r[n]$	e

Table 3.34: VE-O model.

Derivatives

$$D\left\langle \widetilde{\mathtt{ve}}[i], \mathtt{ve[n|j]} \right\rangle = \delta_{ij}$$

where δ_{ij} is the Dirac's function, defined by Equation (3.9).

3.4.34 Q-O model

If quaternions are known, the associated pseudo-observation is defined by

$$\begin{aligned} &\text{Q-O}: \\ &\quad R^4 \longrightarrow R^4 \\ &\quad \underline{q}[n] \longmapsto \underline{\widetilde{q}} \end{aligned}$$

$$\widetilde{\mathtt{q}}[i] = \mathtt{q}[\mathtt{n}|\mathtt{i}] \tag{3.47}$$

Concept	#	Notation	Constants	Frame
Observables	1	$\underline{\widetilde{q}}$		
$\underline{\widetilde{q}}$	4	$\widetilde{\mathtt{q}}[i]$		
Parameter Groups	1	$\underline{q}[n]$		
$\underline{q}[n]$	4	$\mathtt{q}[\mathtt{n}\|\mathtt{i}]$	$t_r[n]$	

Table 3.35: Q-O model.

Derivatives

$$D\left\langle \widetilde{\mathtt{q}}[i], \mathtt{q}[\mathtt{n}|\mathtt{j}] \right\rangle = \delta_{ij}$$

where δ_{ij} is the Dirac's function, defined by Equation (3.9).

3.4.35 OB-O model

If the angular rate sensor ($\underline{o}^{\mathtt{b}}$) is known from IMU calibration procedures, the associated functional model is a pseudo-observation model

$$
\begin{aligned}
&\text{OB-O}: \\
&\quad R^3 \longrightarrow R^3 \\
&\quad \underline{o}^{\mathtt{b}}[n] \longmapsto \widetilde{\underline{o}^{\mathtt{b}}}
\end{aligned}
$$

$$\widetilde{\mathtt{ob}}[i] = \mathtt{ob[n|i]} \tag{3.48}$$

Concept	#	Notation	Constants	Frame
Observables	1	$\widetilde{\underline{o}^{\mathtt{b}}}$		
$\widetilde{\underline{o}^{\mathtt{b}}}$	3	$\widetilde{\mathtt{ob}}[i]$		b
Parameter Groups	1	$\underline{o}^{\mathtt{b}}[n]$		
$\underline{o}^{\mathtt{b}}[n]$	3	ob[n|i]	$t_c[n]$	b

Table 3.36: OB-O model.

Derivatives

$$D\left\langle \widetilde{\mathtt{ob}}[i], \mathtt{ob[n|j]} \right\rangle = \delta_{ij}$$

where δ_{ij} is the Dirac's function, defined by Equation (3.9).

3.4.36 AB-O model

If the accelerometer biases ($\underline{a}^{\mathtt{b}}$) of the IMU are known from calibration procedures, the associated functional model is a pseudo-observation model

$$
\begin{aligned}
&\text{AB-O}: \\
&\quad R^3 \longrightarrow R^3 \\
&\quad \underline{a}^{\mathtt{b}}[n] \longmapsto \widetilde{\underline{a}}^{\mathtt{b}}
\end{aligned}
$$

$$\widetilde{\mathtt{ab}}[i] = \mathtt{ab[n|i]} \tag{3.49}$$

Concept	#	Notation	Constants	Frame
Observables	1	$\widetilde{\underline{a}}^{\mathtt{b}}$		
$\widetilde{\underline{a}}^{\mathtt{b}}$	3	$\widetilde{\mathtt{ab}}[i]$		b
Parameter Groups	1	$\underline{a}^{\mathtt{b}}[n]$		
$\underline{a}^{\mathtt{b}}[n]$	3	ab[n|i]	$t_c[n]$	b

Table 3.37: AB-O model.

Derivatives

$$D\left\langle \widetilde{\mathtt{ab}}[i], \mathtt{ab[n|j]} \right\rangle = \delta_{ij}$$

where δ_{ij} is the Dirac's function, defined by Equation (3.9).

3.4.37 AOFF-O model

Usually, the antenna offset between the IMU sensor and the phase center of the GNSS antenna is measured. Its associated functional model — also a pseudo-observation — is defined as

$$\begin{aligned} &\text{AOFF-O}: \\ &\quad R^3 \quad \longrightarrow \quad R^3 \\ &\quad \underline{d}^{\mathtt{b}} \quad \longmapsto \quad \widetilde{\underline{d}^{\mathtt{b}}} \end{aligned}$$

$$\widetilde{\mathtt{db}}[i] = \mathtt{db}[i] \tag{3.50}$$

Concept	#	Notation	Constants	Frame
Observables	1	$\widetilde{\underline{d}^{\mathtt{b}}}$		
$\widetilde{\underline{d}^{\mathtt{b}}}$	3	$\widetilde{\mathtt{db}}[i]$		$\mathtt{b}$
Parameter Groups	1	$\underline{d}^{\mathtt{b}}$		
$\underline{d}^{\mathtt{b}}[n]$	3	$\mathtt{db}[i]$		$\mathtt{b}$

Table 3.38: AOFF-O model.

Derivatives

$$D\left\langle \widetilde{\mathtt{db}}[i], \mathtt{db}[j] \right\rangle = \delta_{ij}$$

where δ_{ij} is the Dirac's function, defined by Equation (3.9).

3.4.38 DG-O model

If the gravity disturbance vector is known, in the e-frame ($\delta\underline{g}^{\mathtt{e}}[n]$) or the l-frame ($\delta\underline{g}^{\mathtt{l}}[n]$), the associated functional model is

$$\begin{aligned}&\text{DG-O}:\\ &\quad R^3 \longrightarrow R^3\\ &\quad \delta\underline{g}[n] \longmapsto \widetilde{\delta\underline{g}}\end{aligned}$$

$$\widetilde{\delta\mathtt{g}}[i] = \delta\mathtt{g}[\mathtt{n}|\mathtt{i}] \tag{3.51}$$

Concept	#	Notation	Constants	Frame
Observables	1	$\widetilde{\delta\underline{g}}$		
$\widetilde{\delta\underline{g}}$	3	$\widetilde{\delta\mathtt{g}}[i]$		e or l
Parameter Groups	1	$\delta\underline{g}[n]$		
$\delta\underline{g}[n]$	3	$\delta\mathtt{g}[n\|i]$	$t_g[n]$	e or l

Table 3.39: DG-O model.

Derivatives

$$D\left\langle \widetilde{\delta\mathtt{g}}[i], \delta\mathtt{g}[\mathtt{n}|\mathtt{j}] \right\rangle = \delta_{ij}$$

where δ_{ij} is the Dirac's function, defined by Equation (3.9).

3.4.39 GRAVITY model

If the gravity magnitude and the deflections of the vertical are known, $gg = (g, \eta, \zeta)^T$, the associated functional model is

$$\begin{array}{l} \text{GRAVITY}: \\ \quad R^3 \longrightarrow R^3 \\ \quad gg[n] \longmapsto \widetilde{gg} \end{array}$$

$$\widetilde{gg}[i] = gg[n|i] \tag{3.52}$$

Concept	#	Notation	Constants	Frame
Observables	1	$\widetilde{gg}$		
$\widetilde{gg}$	3	$\widetilde{gg}[i]$		
Parameter Groups	1	$gg[n]$		
$gg[n]$	3	$gg[n|i]$	$t_g[n]$	

Table 3.40: GRAVITY model.

Derivatives

$$D\left\langle \widetilde{gg}[i], gg[n|j] \right\rangle = \delta_{ij}$$

where δ_{ij} is the Dirac's function, defined by Equation (3.9).

3.4.40 G-O model

If the gravity vector is known, in the e-frame ($\underline{g}^{\mathtt{e}}[n]$) or the l-frame ($\underline{g}^{\mathtt{l}}[n]$), the associated functional model is

$$\begin{aligned} &\text{G-O}: \\ &\quad R^3 \longrightarrow R^3 \\ &\quad \underline{g}[n] \longmapsto \widetilde{\underline{g}} \end{aligned}$$

$$\widetilde{\mathrm{g}}[i] = \mathrm{g}[n|i] \tag{3.53}$$

Concept	#	Notation	Constants	Frame
Observables	1	$\widetilde{\underline{g}}$		
$\widetilde{\underline{g}}$	3	$\widetilde{\mathrm{g}}[i]$		e or l
Parameter Groups	1	$\underline{g}[n]$		
$\underline{g}[n]$	3	$\mathrm{g}[n\|i]$	$t_g[n]$	e or l

Table 3.41: G-O model.

Derivatives

$$D\left\langle \widetilde{\mathrm{g}}[i], \mathrm{g}[n|j] \right\rangle = \delta_{ij}$$

where δ_{ij} is the Dirac's function, defined by Equation (3.9).

3.5 Final INS/GNSS gravimetric network

As a result of the preceding list of functional models, our problem can be reduced to the solution of a system of linear equations formed basically by the dynamic models VEL, FB, WIB, AB, OB, GDT and the static models CUPT, VUPT, GUPT-GG, GUPT-DGN, GUPT-DGE, GUPTN-DGN, GUPTN-DGE, XOVER-GG, XOVER-DGN and XOVER-DGE. The above mathematical models have been implemented in the `GeoTeX/ACX` software system ([21]). Tables 3.42, 3.43 and 3.44 display the observations — measurements l — and parameters — unknowns x — for each functional model.

Model	l	x
VEL	$\underline{0}$	$\underline{r}^{\mathtt{e}}[n-1]\ \underline{r}^{\mathtt{e}}[n]\ \underline{v}^{\mathtt{e}}[n]$
WIB	$\underline{\omega}^{\mathtt{b}}_{\mathtt{ib}}[n]$	$\underline{o}^{\mathtt{b}}[n]\ \underline{q}[n-1]\ \underline{q}[n]$
Q-NORM	0	$\underline{q}[n]$
OB	$\underline{0}$	$\underline{o}^{\mathtt{b}}[n-1]\ \underline{o}^{\mathtt{b}}[n]$
AB	$\underline{0}$	$\underline{a}^{\mathtt{b}}[n-1]\ \underline{a}^{\mathtt{b}}[n]$
FB-DGE	$\underline{f}^{\mathtt{b}}[n]$	$\underline{a}^{\mathtt{b}}[n]\ \underline{q}[n]\ \underline{r}^{\mathtt{e}}[n]\ \underline{v}^{\mathtt{e}}[n-1]\ \underline{v}^{\mathtt{e}}[n]\ \delta\underline{g}^{\mathtt{e}}[n]$
FB-DGN	$\underline{f}^{\mathtt{b}}[n]$	$\underline{a}^{\mathtt{b}}[n]\ \underline{q}[n]\ \underline{r}^{\mathtt{e}}[n]\ \underline{v}^{\mathtt{e}}[n-1]\ \underline{v}^{\mathtt{e}}[n]\ \delta\underline{g}^{\mathtt{l}}[n]$
FB-GG	$\underline{f}^{\mathtt{b}}[n]$	$\underline{a}^{\mathtt{b}}[n]\ \underline{q}[n]\ \underline{r}^{\mathtt{e}}[n]\ \underline{v}^{\mathtt{e}}[n-1]\ \underline{v}^{\mathtt{e}}[n]\ gg[n]$
GDT-DGE	$\underline{0}$	$\underline{r}^{\mathtt{e}}[n-1]\ \underline{r}^{\mathtt{e}}[n]\ \delta\underline{g}^{\mathtt{e}}[n-1]\ \delta\underline{g}^{\mathtt{e}}[n]$
GDT-DGN	$\underline{0}$	$\delta\underline{g}^{\mathtt{l}}[n-1]\ \delta\underline{g}^{\mathtt{l}}[n]$
GDT-GG	$\underline{0}$	$\underline{r}^{\mathtt{e}}[n-1]\ \underline{r}^{\mathtt{e}}[n]\ gg[n-1]\ gg[n]$
GDT1-DGE	0	$\delta\underline{g}^{\mathtt{e}}[n-1]\ \delta\underline{g}^{\mathtt{e}}[n]$
GDT1-DGN	0	$\delta\underline{g}^{\mathtt{l}}[n-1]\ \delta\underline{g}^{\mathtt{l}}[n]$

Table 3.42: NA models: SINS mechanisation equations.

Solving the system is to perform an optimal estimation of its parameters in the sense of least-squares. The method of least-squares is applied to the determination of the best values of a number of unknowns connected to the observed values by means of linear equations; i.e. solving the normal equations and estimating the precision of both the original observations and the calculated values of the unknowns .

In order to illustrate the structure of the normal equations matrix, let LOOP be an example of an INS/GNSS gravimetric mission. In fact, LOOP is one of the test data sets — CTRA — described in Chapter 4. Figure 3.1 displays the 700 s trajectory of the LOOP mission.

Let us consider that IMU data are collected at 20 Hz (50 Hz ≤ Hz(IMU) ≤ 400 Hz, typically in operational missions) and GPS data at 1 Hz (1 Hz ≤ Hz(GPS) ≤ 5 Hz). Navigation paramaters — $\underline{r}^{\mathtt{e}}$, $\underline{v}^{\mathtt{e}}$ and $\underline{q}$ — have to be computed at the same frequency as IMU data and sensor calibration

Model	l	x		
CUPT	$\widetilde{\underline{X}}$	$\underline{q}[n]$	$\underline{r}^{\mathsf{e}}[n]$	$\underline{d}^{\mathsf{b}}$
CUPTX	$\widetilde{\underline{X}}$	$\underline{q}[n]$	$\underline{r}^{\mathsf{e}}[n]$	
VUPT	$\widetilde{\underline{V}}$	$\underline{q}[n-1]$	$\underline{q}[n]$	
		$\underline{v}^{\mathsf{e}}[n]$	$\underline{d}^{\mathsf{b}}$	
VUPTX	$\widetilde{\underline{V}}$	$\underline{q}[n-1]$	$\underline{q}[n]$	$\underline{v}^{\mathsf{e}}[n]$
RE-O	$\widetilde{\underline{r}^{\mathsf{e}}}$	$\underline{r}^{\mathsf{e}}[n]$		
VE-O	$\widetilde{\underline{v}^{\mathsf{e}}}$	$\underline{v}^{\mathsf{e}}[n]$		
Q-O	$\widetilde{\underline{q}}$	$\underline{q}[n]$		
OB-O	$\widetilde{\underline{o}^{\mathsf{b}}}$	$\underline{o}^{\mathsf{b}}[n]$		
AB-O	$\widetilde{\underline{a}^{\mathsf{b}}}$	$\underline{a}^{\mathsf{b}}[n]$		
AOFF-O	$\widetilde{\underline{d}^{\mathsf{b}}}$	$\underline{d}^{\mathsf{b}}$		
DG-O	$\widetilde{\delta\underline{g}}$	$\delta\underline{g}[n]$		
GRAVITY	$\widetilde{gg}$	$gg[n]$		
G-O	$\widetilde{\underline{g}}$	$\underline{g}[n]$		

Table 3.43: NA models: static observations.

Model	l	x			
DG-OBS	$\widetilde{\delta\underline{g}}$	$\delta\underline{g}[n]$			
DG-OBS-GG	$\widetilde{\delta\underline{g}}$	$\underline{r}^{\mathsf{e}}[n]$	$gg[n]$		
G-OBS	$\widetilde{\underline{g}}$	$\underline{g}[n]$			
GUPT-DGE	g_0	$\underline{r}^{\mathsf{e}}[n]$	$\delta\underline{g}^{\mathsf{e}}[n]$		
GUPT-DGN	g_0	$\underline{r}^{\mathsf{e}}[n]$	$\delta\underline{g}^{\mathsf{l}}[n]$		
GUPT-GG	g_0	$gg[n]$			
GUPTN-DGE	g_0	$\underline{r}^{\mathsf{e}}[n]$	$\delta\underline{g}^{\mathsf{e}}[n]$		
GUPTN-DGN	g_0	$\underline{r}^{\mathsf{e}}[n]$	$\delta\underline{g}^{\mathsf{l}}[n]$		
DGUPT-GG	$\widetilde{\underline{g}^{\mathsf{l}}}$	$\underline{r}^{\mathsf{e}}[n]$	$gg[n]$		
XOVER-DGE	0	$\underline{r}^{\mathsf{e}}[n-1]$	$\underline{r}^{\mathsf{e}}[n]$	$\underline{r}^{\mathsf{e}}[m-1]$	$\underline{r}^{\mathsf{e}}[m]$
		$\delta\underline{g}^{\mathsf{e}}[n-1]$	$\delta\underline{g}^{\mathsf{e}}[n]$	$\delta\underline{g}^{\mathsf{e}}[m-1]$	$\delta\underline{g}^{\mathsf{e}}[m]$
XOVER-DGN	0	$\underline{r}^{\mathsf{e}}[n-1]$	$\underline{r}^{\mathsf{e}}[n]$	$\underline{r}^{\mathsf{e}}[m-1]$	$\underline{r}^{\mathsf{e}}[m]$
		$\delta\underline{g}^{\mathsf{l}}[n-1]$	$\delta\underline{g}^{\mathsf{l}}[n]$	$\delta\underline{g}^{\mathsf{l}}[m-1]$	$\delta\underline{g}^{\mathsf{l}}[m]$
XOVER-GG	0	$\underline{r}^{\mathsf{e}}[n-1]$	$\underline{r}^{\mathsf{e}}[n]$	$\underline{r}^{\mathsf{e}}[m-1]$	$\underline{r}^{\mathsf{e}}[m]$
		$gg[n-1]$	$gg[n]$	$gg[m-1]$	$gg[m]$

Table 3.44: NA models: gravimetric observations.

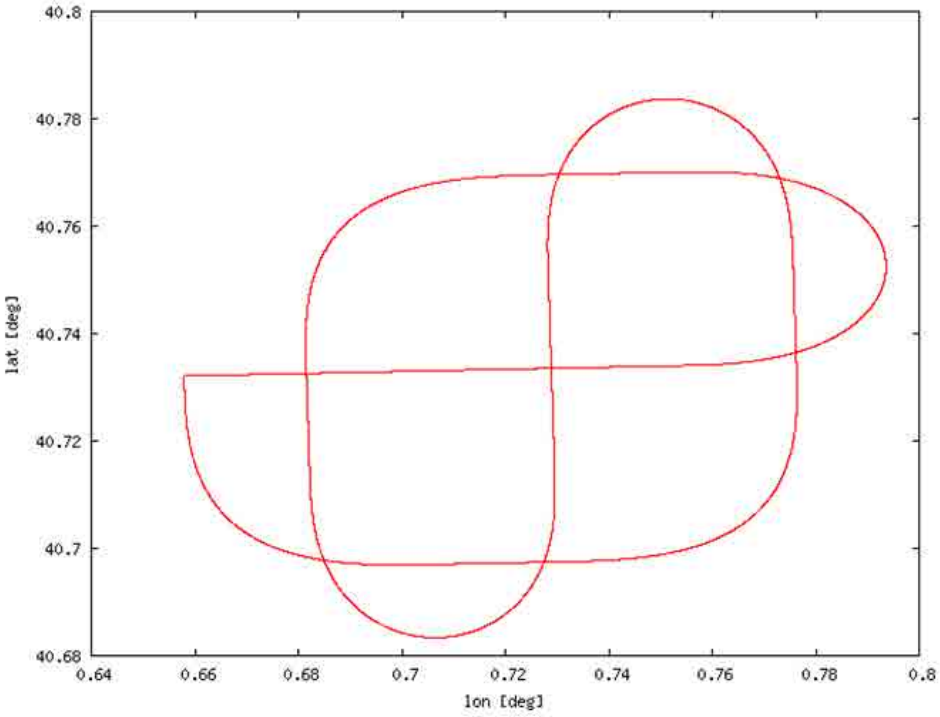

Figure 3.1: LOOP: Sample of a mission with crossovers.

parameters — $\underline{a}^{\mathsf{b}}$ and $\underline{o}^{\mathsf{b}}$ — and gravity parameters gg have to be determined at 0.1 Hz. The duration of the mission is 700 s.

Figure 3.2 shows the sparse structure of the normal equations matrix for LOOP sample. The system includes XOVER equations and GDT-perpendicular observations, where the gg parameters belong to different paths of the trajectory. As the XOVER model relates parameters that are far away, sparse non-zero elements (like points) are painted in the upper-left part of the matrix.

The normal equations matrix is large, however it is of the band-bordered type — Figure 3.2 — and we can apply sparse matrix techniques, fill-in reduction techniques and memory-to-disk paging to solve the system of linear equations. If this is done, the computational load is comparable to that of SSA. The NA computational load is equivalent to that of the SSA plus an additional penalty due to the accumulated crossovers in the band-border.

Initially, the expectation of all the parameters and their covariance will be known at the same frequency as the observed data at the highest frequency (usually IMU data). Consequently, the network's size — the size of the design and normal equations matrices — increases considerably. Table 3.45 displays this network size in some operational environments. In the next chapter, Tables 4.4, 4.15 and 4.40 also show it for the different tests carried out in this dissertation.

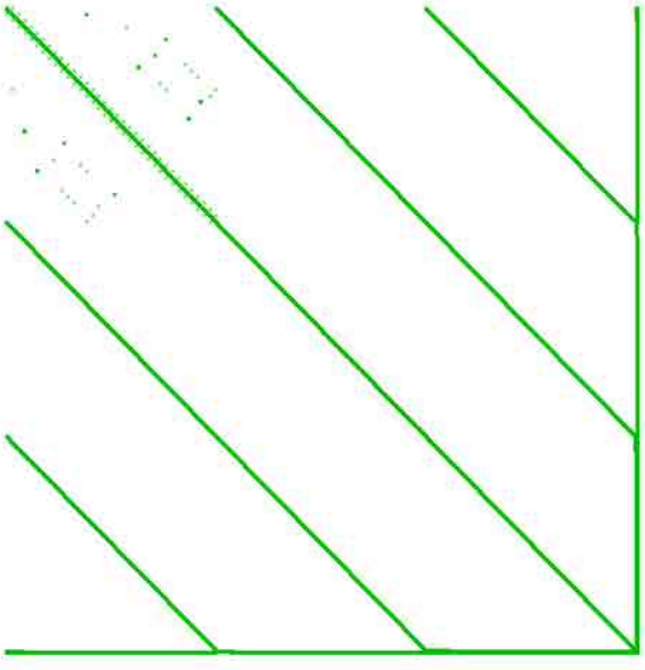

Figure 3.2: Structure of the LOOP normal equations matrix.

	Applanix	CASI	GeoMobil
IMU model	LN200	LTN101	LN200
Hz(IMU)	200	50	200
Hz(GPS)	10	1	5
t (s)	12 000	12 000	14 400
N_{IMU}	45 599 982	11 399 982	54 719 982
N_{GPS}	360 003	36 003	216 003
N_{aux}	720 000	180 000	
N^*_{eq}	45 959 985	11 435 985	54 935 985
N_{eq}	46 679 985	11 615 985	54 935 985
N_{par}	45 600 000	11 400 000	54 720 000
r^*_b	0.007 83	0.003 15	0.003 93
r_b	0.023 14	0.018 59	0.003 93

Table 3.45: Information data of some operational environments at the ICC: $N_{eq} = N^*_{eq} + N_{aux}$; $N^*_{eq} = N_{IMU} + N_{GPS}$; N_{aux} number of auxiliary observation equations; $r_b = (N_{eq} - N_{par}) \cdot (N_{eq})^{-1}$ (average redundancy) and $r^*_b = (N^*_{eq} - N_{par}) \cdot (N^*_{eq})^{-1}$ (average redundancy).

If it is necessary to reduce the size of the network, it is possible to take into account that some of the parameters — or unknowns — have a slow variation in time and subsets of them can be grouped. The number of unknows can be reduced considerably. For instance, it may be possible to compute $\underline{a}^{\mathsf{b}}$, $\underline{o}^{\mathsf{b}}$, $\delta\underline{g}^{\mathsf{e}}$ at the GPS receiver frequency and $\underline{r}^{\mathsf{e}}$, $\underline{v}^{\mathsf{e}}$ and $\underline{q}$ at the IMU frequency.

For the operational environments of Table 3.45, $Npar$ is reduced to half (19537200 in case 1, 6609600 in case 2, 26568000 in case 3 and 5288868 in case 4 respectively). A similar reduction has been applied in the LOOP sample and in all the computed tests (version $v9$ indicates parameter determination at IMU frequency, whereas version $v2$ is related to the described reduction) described in the next chapter and this reduction is displayed in Tables 4.4, 4.15 and 4.40.

The LOOP mission is only a sample. The structure and the size of the normal equations of the network will depend on every mission and will depend, specifically, on the complexity of the functional models used, on the *frequency* of the calibration parameters and on the sorting algorithm.

Table 3.45 also shows the small average redundancy — r_b — of the systems to be solved. The average redundancy is computed as

$$r_b = (N_{eq} - N_{par}) \cdot (N_{eq})^{-1}, \tag{3.54}$$

where $N_{eq} = N_{IMU} + N_{GPS} + N_{aux}$.

It is well-known that in least-squares adjustment, the more the redundancy increases the higher the accuracy of the network will be. Looking at Tables 3.45, 3.42, 3.43 and 3.44, the number of IMU data and GNSS (i.e. GPS) data cannot be increased without increasing the number of parameters to be determined. Taking a redundancy value r_b — $\frac{3}{10} \leq r_b < 1$ — as a desirable value to be obtained, the following relationship has to be considered

$$10 N_{par} \leq 7 N_{eq} \tag{3.55}$$

For example, in LOOP sample, if the duration of the mission may be T s, T Hz(IMU) measurements are collected for each IMU data and T Hz(GPS) measurements for GPS data. Whereas, T Hz(IMU) is the number of parameters that have to be computed for $\underline{r}^{\mathsf{e}}$, $\underline{v}^{\mathsf{e}}$ and $\underline{q}$; T Hz(cal) for $\underline{o}^{\mathsf{b}}$, $\underline{a}^{\mathsf{b}}$ and T Hz(gg) for gg. Therefore, N_{par} are defined as

$$\begin{aligned} N_{par} &= N_{\underline{r}^{\mathsf{e}}} + N_{\underline{v}^{\mathsf{e}}} + N_{\underline{q}} + N_{\underline{a}^{\mathsf{b}}} + N_{\underline{o}^{\mathsf{b}}} + N_{gg} + N_{\underline{d}^{\mathsf{b}}} = \\ &= 10\,T \cdot \mathrm{Hz(IMU)} + 6\,T \cdot \mathrm{Hz(cal)} + 3\,T \cdot \mathrm{Hz}(gg) + 3 \end{aligned} \tag{3.56}$$

where

$$
\begin{aligned}
N_{\underline{r}^{\mathsf{e}}} &= N_{\underline{v}^{\mathsf{e}}} = 3\,T\cdot\mathrm{Hz(IMU)},\\
N_{\underline{q}} &= 4\,T\cdot\mathrm{Hz(IMU)},\\
N_{\underline{a}^{\mathsf{b}}} &= N_{\underline{o}^{\mathsf{b}}} = 3\,T\cdot\mathrm{Hz(cal)},\\
N_{gg} &= 3\,T\cdot\mathrm{Hz}(gg)\,and\\
N_{\underline{d}^{\mathsf{b}}} &= 3.
\end{aligned}
$$

N_{eq} is defined as

$$
\begin{aligned}
N_{eq} &= N_{VEL} + N_{WIB} + N_{FB-GG} + N_{QNORM} + N_{AB} + N_{OB} +\\
&+ N_{GDT-GG} + N_{OB-O} + N_{AB-O} + N_{CUPT} + N_{AOFF} + N_{aux} =\\
&= 10\,T\cdot\mathrm{Hz(IMU)} + 12\,T\cdot\mathrm{Hz(cal)} + 3\,T\cdot\mathrm{Hz}(gg) +\\
&+ 3\,T\cdot\mathrm{Hz(GPS)} - 15 + N_{eq}^{aux}
\end{aligned}
$$

where

$$
\begin{aligned}
N_{VEL} &= N_{WIB} = N_{FB-GG} = 3\,(T\cdot\mathrm{Hz(IMU)} - 1),\\
N_{QNORM} &= 1\,T\cdot\mathrm{Hz(IMU)},\\
N_{AB} &= N_{OB} = 3\,(T\cdot\mathrm{Hz(cal)} - 1),\\
N_{GDT-GG} &= 3\,(T\cdot\mathrm{Hz}(gg) - 1),\\
N_{OB-O} &= N_{AB-O} = 3\,T\cdot\mathrm{Hz(cal)},\\
N_{CUPT} &= 3\,T\cdot\mathrm{Hz(GPS)},\\
N_{AOFF} &= 3\,and\\
N_{aux} &= N_{Q-O} + N_{GUPT-GG} + N_{XOVER-GG} + N_{GDT-GGp}.
\end{aligned}
$$

And Equation (3.55) becomes

$$
\begin{aligned}
7\,N_{aux} &\geq 30\,T\cdot\mathrm{Hz(IMU)} - 24\,T\cdot\mathrm{Hz(cal)} + 9\,T\cdot\mathrm{Hz}(gg) -\\
&- 21\,T\cdot\mathrm{Hz(GPS)} + 135
\end{aligned}
$$

It has been described above, for LOOP example where T = 700 s, that Hz(IMU) = 20 Hz, Hz(GPS) = 1 Hz, Hz(cal) = 0.1 Hz and Hz(gg) = 1 Hz. And so, the Equation (3.5), which fulfils $N_{aux} \geq 57772$, points out the need to increase the number of additional observation equations N_{aux}. Therefore, it would be advisable to use all the feasible information to increase N_{aux}.

As a model of how it should be done, think about some operational procedures, like a short warm-up period of static measurements for INS alignment. In such a case, the warm-up period can be considered as ZUPT models. If the warm-up location is also well-known — position, attitude and gravity are known — N_{aux} is

$$N_{aux} = N_{ZUPT} + N_{RE-O} + N_{Q-O} + N_{GRAVITY}.$$

If the same procedure is repeated at the end of the mission,

$$N_{aux} = 2\,(N_{ZUPT} + N_{RE-O} + N_{Q-O} + N_{GRAVITY}).$$

Survey's planning has to be investigated in detail to obtain more additional observational models and, by this means, to increase the amount of N_{aux}. Such additional models would be crossovers (repetition or/and intersection of mission lines), ZUPT intervals at the beginning and at the end of the survey, upwarded gravity, etc.

Finally, because the system is solved by the least-squares method, the covariance of a limited number of selected parameters may be determined. It is important to emphasise the possibility to compute the covariance of a limited number of selected parameters — perform a selective inversion of the normal matrix — and the variance component estimation. Here, the selected parameters will be the angular rate sensors biases ($\underline{o}^{\mathsf{b}}$), the accelerometers biases ($\underline{a}^{\mathsf{b}}$), the gravity disturbances (δg) and their covariances for further IMU calibration and geoid determination.

4 Computations

The aim of this chapter is to demonstrate that the NA approach works properly. In Chapter 3, the development of an adjustment method in genuinely geodetic post-process has been introduced. The INS mechanisation equations and other additional observation equations have been implemented into the ICC's `GeoTeX/ACX`program. As a result, the problem has been reduced to the solution of a system of linear equations in the sense of least-squares with large sparse band-bordered normal equations. Table 3.45 shows how large are such matrices for some operational environments at the ICC.

Since the current 32-bit version of `GeoTeX/ACX` cannot run such huge networks successfully, it is necessary to perform simulations based on real-life environments. Simulations provide well controlled data:

- to verify that the NA approach works,
- to validate the proposed functional models,
- to investigate the behavior of INS system errors for different types of IMU, from navigation ones to low-cost ones,
- to allow research works in the definition of a wide range of scenarios, the assessment of the performance of different sensors, and the configurations that better meet their mission and budget requirements.

The organisation of this chapter is as follows. First, the IMU simulator, which has been used, is described. Second, a description of each test configuration is given. Last, the outcome of the most relevant adjustments are discussed.

Before any discussion, it is interesting to remember that:

- All the *basic* computations — $\langle \texttt{TEST} \rangle$-$\langle IMU \rangle$-$v\left[\left\langle q \right\rangle\right]\langle Hz \rangle a1$, which are similar to Kalman Filtering — have not been compared with SSA ones.

- Although the gravity data are computed as gg (gravity and deflections of the vertical), in this chapter are presented as gravity disturbance vector in NED-frame as it is usual in most cases. The relationship between these kinds of parameter groups are described in Section C.3.3.
- All the network adjustments have been computed with 32-bit GeoTeX/ACX running in a 64-bit platforms.

The tables and figures that display the results of the simulations are located at the end of each test.

4.1 The IG-IMU simulator

The IMU simulator used in this research is a computer program developed at the Institute of Geomatics (IG) in the frame of the NAVEGA project for testing and validating navigation algorithms. This tool, which has been described by Parés in [88], emulates the behavior of standard IMUs with three linear accelerometers and three angular rate sensors in an orthogonal configuration.

The fundamentals of the IG-IMU simulator are the functional model that characterise the inertial motion (INS mechanisation equations), the stochastic models that characterise the IMU errors and the *geodetic* model that contextualises the previous models.

As any real IMU, the simulator delivers angular velocities and linear accelerations. Given a trajectory, i.e. a set of times, positions, velocities and attitudes, the system computes the signal that an IMU would measure if it were following the trajectory. After that, the signal is modified by adding a variety of errors, such as biases or scale factors. The order in which these errors are introduced to the IMU data — $IMU = (\omega, f)^T$ — is scale factor, bias, misalignment, random noise and quantisation. If IMU_{in} is the errorless signal (mechanisation equations), the output signal (also named corrupted signal) of the IG-IMU simulator are computed with the formulas of Appendix I:

$$IMU_{out} = \lfloor W_1 \rfloor \cdot quant \tag{4.1}$$

$$W_1 = quant^{-1} \cdot Err(W_{noise}) + \begin{pmatrix} 1 & -y_z & z_y \\ x_z & 1 & -z_x \\ -x_y & y_x & 1 \end{pmatrix} \cdot W_2$$

$$W_2 = \left[B_c + B_{rc} + B_{gm} + B_{rw} + \begin{pmatrix} 1 & B_{gs} \\ 0 & 1 \end{pmatrix} \cdot W_3 \right]$$

$$W_3 = (1 + S_c + S_{rc} + S_{gm} + S_{rw}) \cdot IMU_{in}$$

The use of the IG-IMU simulator has been limited to reproduce a simple behavior for a tactical-grade IMU and for a navigation-grade one. This simple behavior is obtained considering only the white noise error W_{noise} for both gyros $\underline{o}^{\mathsf{b}}$ and accelerometers $\underline{a}^{\mathsf{b}}$ errors. Table 4.1 shows the IMU data used in the IG-IMU simulator and in later computations, from a tactical and a navigation grade IMU respectively: bias repeatibility and white noise error.

From now on, the tactical-grade IMU will be known as LN200 and the navigation-grade as LTN101.

		LN200	LTN101	
IMU	Grade	Tactical	Navigation	
Gyro	Bias Rep.	1.0	0.01	$^{\circ}\,\mathrm{h}^{-1}$
	PSD_{noise}	0.04	0.001	$^{\circ}\,\mathrm{h}^{-frac12}$
Accel.	Bias Rep.	200.0	50.0	μg
	PSD_noise	50.0	10.0	mGal $\mathrm{Hz}^{-\frac{1}{2}}$

Table 4.1: Tests: LN200 and LTN101 simulator options.

In such a case, the output data of the IMU simulator — IMU_{out} — has been computed using the errorless signal IMU_{in} and assigning bias and scale factor constants randomly. Then, Equation (4.1) described in Appendix I becomes:

$$IMU_{out} = \alpha \cdot SENSOR_{noise} + B_c + (1 + S_c) \cdot IMU_{in}$$

where α is a random number, $SENSOR_{noise}$ is a function of the power spectral density of the random noise, B_c is the constant component of the bias and S_c is the constant component of the scale factor.

4.2 Tests description

This section presents the simulations which have been used to demonstrate that, using the preceding functional models defined in Section 3.4, the NA approach works.

The simulated platform consists of an strapdown IMU and two GPS receivers installed in a land vehicle. The GPS receivers and antennas are symmetrically located and their corresponding offsets $\underline{d}^{\mathsf{b}}$ have to be considered as $(1,0,-1)^T$ and $(-1,0,-1)^T$. The GPS data are collected at 1 Hz, while the IMU data are collected at 20 Hz.

Three different scenarios have been considered:

- STATIC: a non-dynamic scenario at 45 degree North latitude, 0 degree longitude and

0 m ellipsoidal height. The objective of this simple scenario is to validate the errorless signal and the implemented functional models.

- CIRCLE: the vehicle goes round 3 times a circular trajectory. The repetition of the trajectory will demonstrate that gravity determination is improved using additional information: the gravity value at one position is the same for each lap.

- CTRA: a more complex trajectory — similar to the one described in Figure 4.39 — that starts and ends in a known location.

For each scenario, a 20 Hz trajectory — times, positions, velocities and attitudes — has been defined and IMU data related to a tactical-grade (as LN200) and a navigation-grade (as LTN101) — see Table 4.1 — have been simulated. In all the tests, the platform moves at a constant speed during 15 min (700 s) approximately, and the attitude — α (roll), χ (pitch) and η (heading) — for each event is also considered constant equal to zero.

The gravity parameters are computed on trajectory level and related to the IMU location. Moreover, in real-life missions, the known gravity has to be upwarded previously. To avoid additional processes — upward and the posterior downward continuation of the computed gravity data — and errors, the simulated vehicle moves on a flatness ellipsoidal surface with an altitude of 0 m.

Several network configurations have been computed.Adjustments have been coded according to the following convention:

$$\langle \mathtt{TEST} \rangle\text{-}\langle IMU \rangle\text{-}v\big[\langle q \rangle\big]\langle Hz \rangle\langle \delta g_{NE} \rangle\langle method \rangle$$

where

- $\langle \mathtt{TEST} \rangle$ is the simulated scenario: STATIC, CIRCLE or CTRA.

- $\langle IMU \rangle$ is the type of IMU sensor. As mentioned, data from a tactical-grade (i.e. LN200) and a navigation-grade (i.e. LTN101)quality have been investigated.

- $\langle q \rangle$ — it is optional — indicates if prior knowledge of the vehicle's attitude exists at the beginning (t_0) and at the end (t_N) of the mission.

- $\langle Hz \rangle$ may be 2 or 9. If it is 9, all the parameters are computed at the IMU rate. If it is 2, some subsets of parameters — $\underline{o}^{\mathtt{b}}$, $\underline{a}^{\mathtt{b}}$, δg or gg — has been grouped.

- $\langle \delta g_{NE} \rangle$ indicates the prior knowledge of the horizontal gravity. Traditionally, the gravity vector has been related to the $\mathtt{l}$-frame, where only the vertical component is considered. An a indicates that no prior knowledge is considered and b indicates that, for all t, $\delta g_N(t) = \delta g_E(t) \approx 0$.

- $\langle method \rangle$ indicates which kind of auxiliary information is considered. An 1 indicates a basic network configuration similar to the Kalman filtering. If GDT-p (changes of the gravity disturbance of closed positions with respect to time) observations are added to the basic configuration, $\langle method \rangle = 2$. And if, moreover, XOVER observations are considered $\langle method \rangle = 2x$.

Figure 4.1 summarises the test convention. Remember that every test corresponds to a different network system configuration. For example, CIRCLE-LN200-vq9b2x means tactical-grade IMU simulated circular scenario with $\alpha_i = \chi_i = \eta_i = 0$, for $i = t_0, t_N$ and with prior knowledge of horizontal gravity, GDT-perpendicular and XOVER information where all the parameters are computed at 20 Hz.

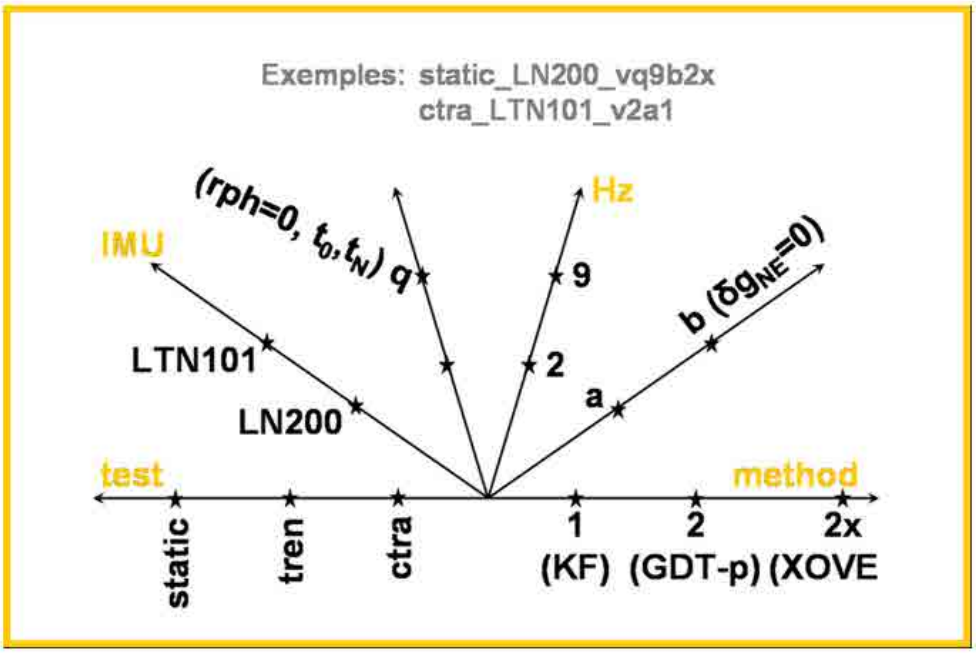

Figure 4.1: Test convention.

Tables 4.2 and 4.3 contain all the input covariance information of the observation models used in the network adjustments.

With current technology, the precision of GPS positions is better ± 10 cm and that of the velocity is better than ± 0.01 m/s in the post-processing kinematic mode . In all the tests of this research, it has been considered an standard deviation of 5 cm for CUPT observation type (GPS positions) and 0.01 mm for VEL observation[1]

[1] Note that the value 0.01 mm for VEL observations must be interpreted as follows: instead of $0 = v - \dot{r}$, defined in Section 3.4.1 the functional model is $0 = r(t+1) - r(t) - \Delta t\, v(t)$.

IMU	Observation		v2	v9		Scenarios
LN200	FB-GG		2.2	2.2	10^{-3} m s^{-2}	(s) (t) (c)
	WIB		5.2	5.2	10^{-5} rad s^{-1}	(s) (t) (c)
	OB-O	(1)	4.9	4.9	10^{-6} rad s^{-1}	(s) (t) (c)
	AB-O	(1)	2.0	2.0	10^{-3} m s^{-2}	(s) (t) (c)
	OB	(2)	15.0	1.1	10^{-7} rad s^{-1}	(s) (t) (c)
	AB	(2)	130.0	8.9	10^{-4} m s^{-2}	(s) (t) (c)
LTN101	FB-GG		4.4	4.4	10^{-4} m s^{-2}	(s) (t) (c)
	WIB		1.3	1.3	10^{-6} rad s^{-1}	(s) (t) (c)
	OB-O	(1)	4.9	4.9	10^{-8} rad s^{-1}	(s) (t) (c)
	AB-O	(1)	4.9	4.9	10^{-4} m s^{-2}	(s) (t) (c)
	OB	(2)	61.0	4.3	10^{-12} rad s^{-1}	(s) (t) (c)
	AB	(2)	95.0	6.7	10^{-7} m s^{-2}	(s) (t) (c)

Table 4.2: Standard deviations of the IMU observations. Conventions: (1) Used when IMU calibration values are known. (2) Tests use random walk models described in Sections 3.4.8 and 3.4.10. (s) STATIC, (t) CIRCLE and (c) CTRA scenarios.

Observation	σ		Scenarios
GDT-GG	6.2	mGal	(s) (t) (c) (v2)
	0.016		(s) (t) (c) (v9)
GDT-GG-p	–	mGal	(s)
	6.2		(t)
	6.2		(c) (1 km)
	13.0		(c) (4 km)
DGUPT-GG	0.02	mGal	(s) (t) (c)
XOVER-GG	0.0003	mGal	(s) (t) (c)
AOFF-O	0.001	m	(s) (t) (c)
CUPT	0.05	m	(s) (t) (c)
VEL (1)	0.00001	m	(s) (t) (c)
Q-NORM	0.01	ppm	(s) (t) (c)
Q-O	0.01	ppm	(s) (t) (c)

Table 4.3: Standard deviations of the *geodetic*observations. Conventions: (1) Instead of $0 = \dot{r} - v$, $0 = r(t+1) - r(t) - \Delta t\, v(t)$ is used. s STATIC, t for CIRCLE and c CTRA scenarios.

To avoid computation problems and taking into account that some parameters have a slow variation in time, subsets of them can be grouped as a single one. Now the question is: how the parameter association has to be done?

Let the observation data be collected at Hz^{obs} rate and let $(\ell[n_{obs}])_{n_{obs}=1,\ldots,N^{obs}}$ be the observation model at time t_{obs} (where $\ell[n_{obs}] = \ell(t_{obs})$ and $t_{obs} = n_{obs}/Hz^{obs}$) be defined as

$$\ell[n_{obs}] = F(x_1(t_{obs}),\ldots,x_N(t_{obs})),$$

where $x_p(t_{obs})$ is the parameter to be computed at Hz^{x_p} rate. Then, each parameter $x_p(t_{obs})$ can be interpolated from $\left(x_p[n_{x_p}]\right)$, where $n_{x_p} = 1,\ldots,N^{x_p}$.

There are many interpolation methods that can be applied. Depending on the method, the associated functional model would be more or less complex. In this dissertation, for the sake of simplicity, a simple grouping rule has been considered.

Let t_{par} be the associated time of parameter $x_p[n_{x_p}]$, then

$$t_{par} = \frac{n_{x_p}}{Hz^{x_p}}$$

and $x_p(t_{obs}) = x_p(t_{par})$, if

$$t_{obs} \in \left] t_{par} - \frac{1}{2Hz^{x_p}}, t_{par} + \frac{1}{2Hz^{x_p}} \right].$$

4.3 Test STATIC

In order to validate the errorless signal and the implemented functional models, simulations begin by an static acquisition at 45 ° North latitude , 0 ° longitude and 0 m ellipsoidal height. The output of one of those simulations can be seen in Figure 4.2.

The static data of this simulation that has to be recovered is:

- $\underline{r}^{\mathsf{e}} = (4517590.879, 0.0, 4487348.409)^T$ m
- $\underline{v}^{\mathsf{e}} = (0.0, 0.0, 0.0)^T$ m/s
- $\underline{q} = (0.38268343, 0.0, 0.92387953, 0.0)^T$

The accelerations (FB-GG) and angular velocities (WIB) observations, computed using the simulator, are shown in Figure 4.2, respectively, where IMU tactical-grade (i.e. LN200) data are depicted in red and navigation-grade (i.e. LTN101) data in green.

Because there are no movements, if gravity is known at one event, then it is known for every time. So, for each event, a DGUPT-GG observation will be taken into account.

Furthermore, it is possible to consider that the attitude parameters — α, χ, η — are known from the beginning until the end of the mission.

Then, for each IMU sensor's configuration several network adjustments have been considered: STATIC-$\langle IMU \rangle$-v2a1, -v9a1, -vq2a1, -vq9a1 and -vqt9a1. Table 4.4 displays the dimensions that have to do with and the redundancy of each system, which obviously do not depend on the IMU type used. In $\langle IMU \rangle$-v9a1 and -vq9a1 configurations, where all the parameters are computed at IMU rate, a high redundancy number is obtained. The fact is that the auxiliary DGUPT-GG observations increase the number of equations, whereas the number of parameters remains the same.

version	Nrow	Ncol	Neq	Npar	r_b
v2a1	56 176	41 012	141 326	136 637	0.033
vq2a1	56 178	41 012	141 334	136 637	0.033
v9a1	137 368	81 608	384 902	258 425	0.329
vq9a1	137 370	81 608	384 910	258 425	0.329

Table 4.4: Test STATIC: network's dimensions.

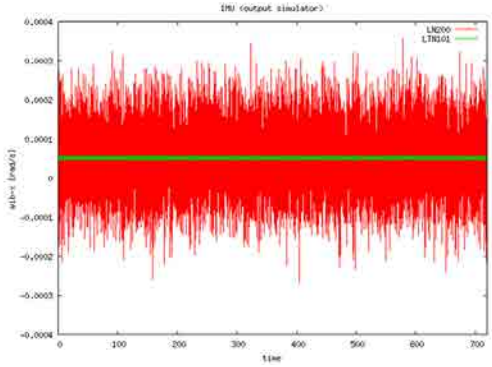

(a) X angular velocity (rad s^{-1})

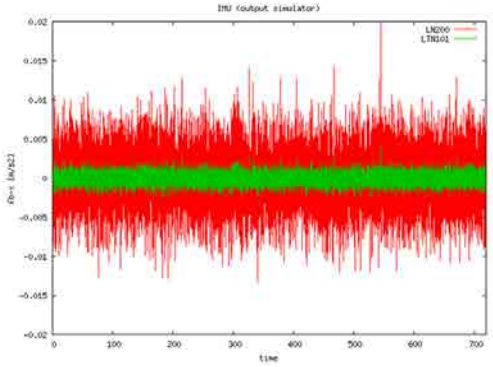

(b) X acceleration (m s^{-2})

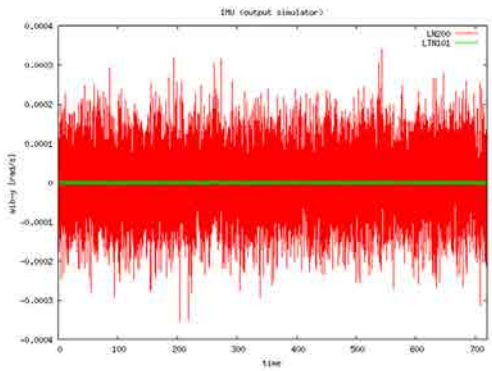

(c) Y angular velocity (rad s^{-1})

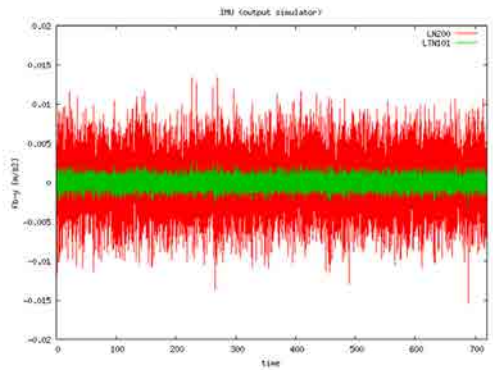

(d) Y acceleration (m s^{-2})

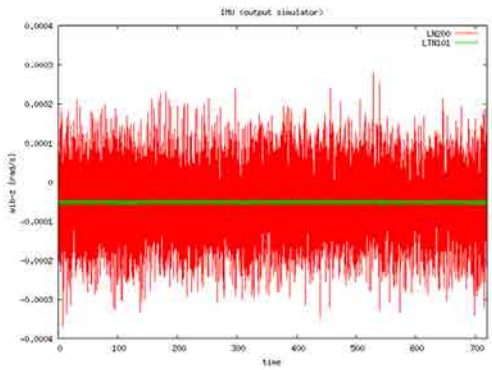

(e) Z angular velocity (rad s^{-1})

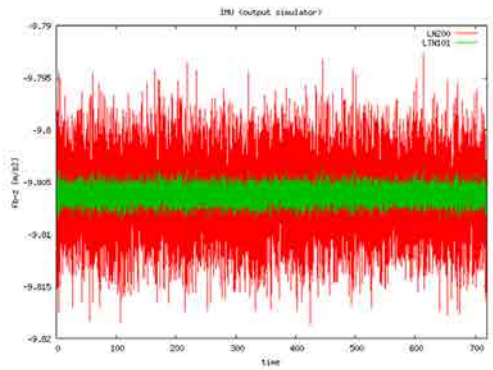

(f) Z acceleration (m s^{-2})

Figure 4.2: STATIC: IMU simulated data.

4.3.1 STATIC v2a1

As already discussed in Section 4.2, the codification this computation means:

- $\langle Hz \rangle = 2$: some subsets of parameters — $\underline{o}^{\mathsf{b}}$, $\underline{a}^{\mathsf{b}}$, δg or gg — has been grouped.
- $\langle \delta g_{NE} \rangle = a$: no prior knowledge of the horizontal gravity.
- $\langle method \rangle = 1$: basic network configuration similar to the Kalman filtering.

LN200

Table 4.5 summarises the network configuration used in this computation.

Model Name	Frequency		Equation	Standard Deviation	
FB-GG (3.4.5)	20.0 Hz	$\forall t$	(3.13)	2.2	10^{-3} m s^{-2}
WIB (3.4.2)	20.0 Hz	$\forall t$	(3.10)	5.2	10^{-5} rad s^{-1}
VEL (3.4.1)	20.0 Hz	$\forall t$	(3.4.1)	0.000 01	m
Q-NORM (3.4.6)	20.0 Hz	$\forall t$	(3.14)	0.01	ppm
OB-O (3.4.35)	0.1 Hz	$\forall t$	(3.48)	4.9	10^{-6} rad s^{-1}
AB-O (3.4.36)	0.1 Hz	$\forall t$	(3.49)	2.0	10^{-3} m s^{-2}
OB (3.4.8)	0.1 Hz	$\forall t$	(3.16)	15.0	10^{-7} rad s^{-1}
AB (3.4.10)	0.1 Hz	$\forall t$	(3.18)	130.0	10^{-4} m s^{-2}
AOFF-O (3.4.37)			(3.50)	0.001	m
CUPT (3.4.16)	1.0 Hz	$\forall t$	(3.26)	0.05	m
GDT-GG (3.4.13)	0.1 Hz	$\forall t$	(3.22)	6.2	mGal
DGUPT-GG (3.4.28)	0.1 Hz	$\forall t$	(3.41)	0.02	mGal

Table 4.5: Test STATIC-LN200-v2a1: network configuration.

Figure 4.3 proves that the functional models of the NA approach work succesfully:

- Figure 4.3a points out that the position has been recovered, especially heights — in Figure 4.3c — with a precision better than 0.6 cm. Longitude and latitude have been recovered with a precision of 0.00036 ".
- The navigation parameters — shown in Figure 4.3e — are recovered with a precision of 0.6 ' for roll (α) and pitch (χ) and 0.9 ' for heading (η).
- The IMU error parameters exhibited in Figures 4.3b and 4.3d are nearly constants within the defined tolerances (bias repeatability) of the IMU.
- Figure 4.3f also displays the gravity disturbance vector, that has to be zero, with a precision of 0.0000015 mGal.

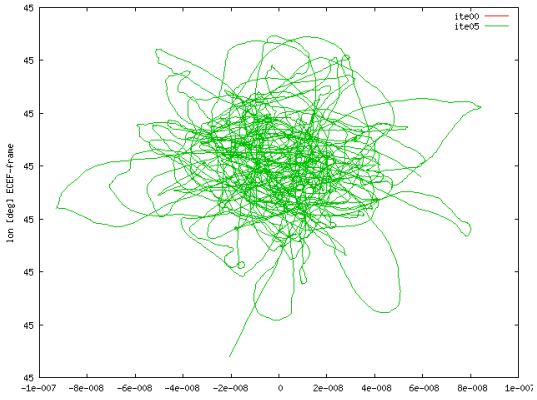

(a) Position (°)

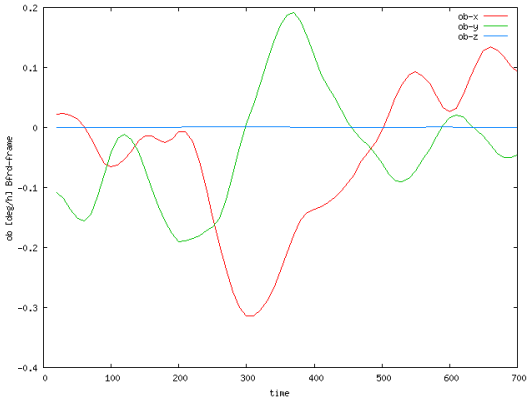

(b) Angular drift ($^\circ\,h^{-1}$)

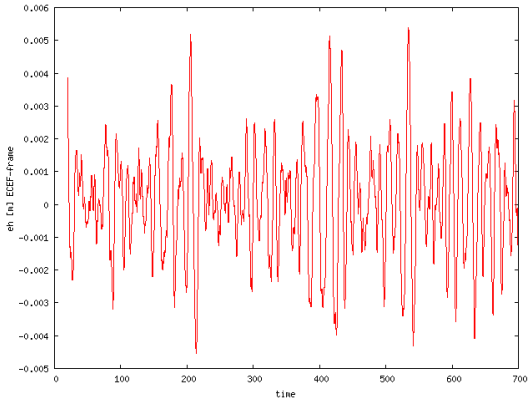

(c) Height (m)

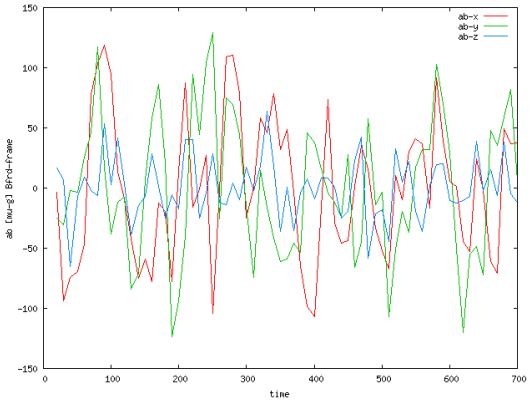

(d) Accelerometer bias (μg)

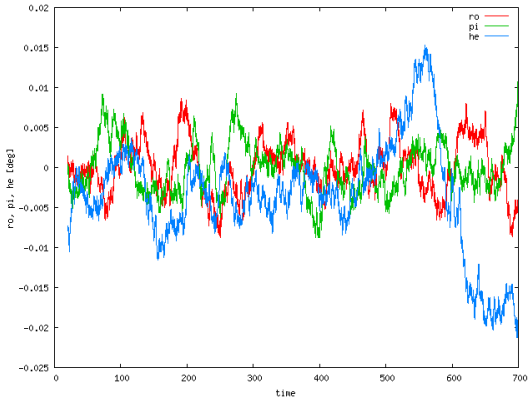

(e) Roll, Pitch and Heading (°)

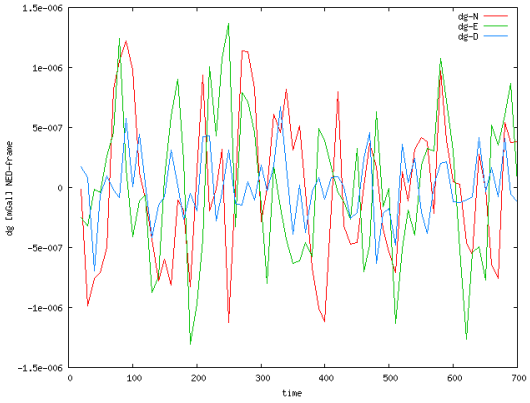

(f) Gravity disturbance (mGal)

Figure 4.3: STATIC LN200 v2a1: adjusted parameters.

LTN101

Table 4.6 summarises the network configuration used in this computation.

Model Name	Frequency		Equation	Standard Deviation	
FB-GG (3.4.5)	20.0 Hz	$\forall t$	(3.13)	4.4	10^{-4} m s^{-2}
WIB (3.4.2)	20.0 Hz	$\forall t$	(3.10)	1.3	10^{-6} rad s^{-1}
VEL (3.4.1)	20.0 Hz	$\forall t$	(3.4.1)	0.000 01	m
Q-NORM (3.4.6)	20.0 Hz	$\forall t$	(3.14)	0.01	ppm
OB-O (3.4.35)	0.1 Hz	$\forall t$	(3.48)	4.9	10^{-8} rad s^{-1}
AB-O (3.4.36)	0.1 Hz	$\forall t$	(3.49)	4.9	10^{-4} m s^{-2}
OB (3.4.8)	0.1 Hz	$\forall t$	(3.16)	61.0	10^{-12} rad s^{-1}
AB (3.4.10)	0.1 Hz	$\forall t$	(3.18)	95.0	10^{-7} m s^{-2}
AOFF-O (3.4.37)			(3.50)	0.001	m
CUPT (3.4.16)	1.0 Hz	$\forall t$	(3.26)	0.05	m
GDT-GG (3.4.13)	0.1 Hz	$\forall t$	(3.22)	6.2	mGal
DGUPT-GG (3.4.28)	0.1 Hz	$\forall t$	(3.41)	0.02	mGal

Table 4.6: Test STATIC-LTN101-v2a1: network configuration.

Figure 4.4 proves that the functional models of the NA approach work succesfully:

- Figure 4.4a points out that the position has been recovered, especially heights — in Figure 4.4c — with a precision better than 0.8 cm. Longitude and latitude have been recovered with a precision of 0.00036 ".
- The navigation parameters — shown in Figure 4.4e — are recovered with a precision of 7.2 " for roll (α) and pitch (χ) and 3.6 " for heading (η).
- The IMU error parameters exhibited in Figures 4.4b and 4.4d are nearly constants within the defined tolerances (bias repeatability) of the IMU.
- Figure 4.4f also displays the gravity disturbance vector, that has to be zero, with a precision of 0.00008 mGal.

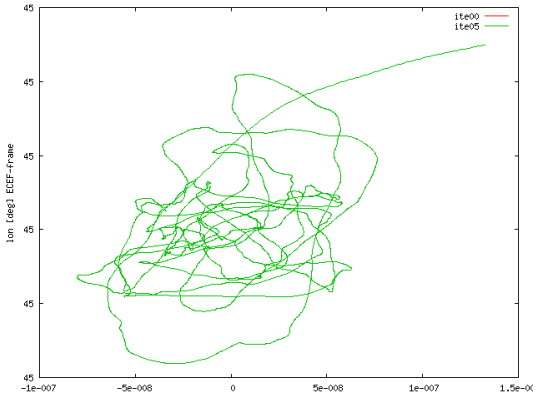

(a) Position (°)

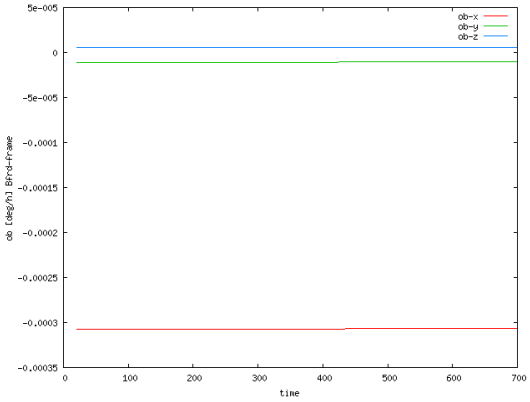

(b) Angular drift ($^\circ\,h^{-1}$)

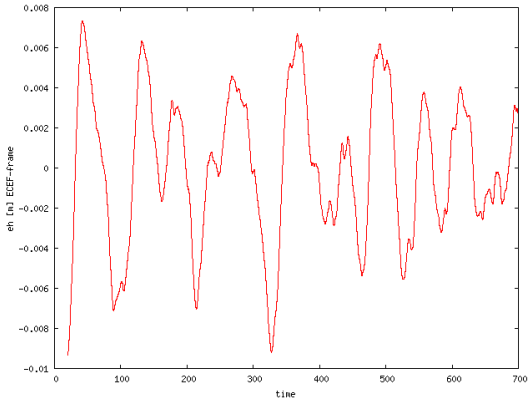

(c) Height (m)

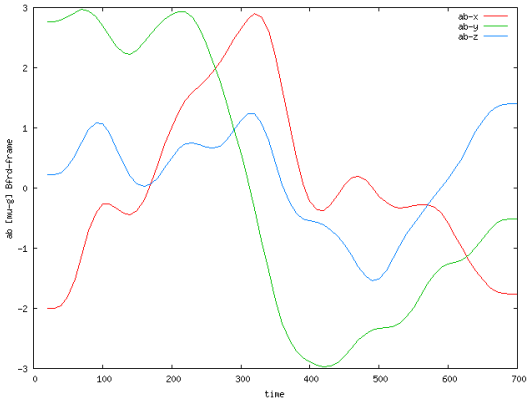

(d) Accelerometer bias (μg)

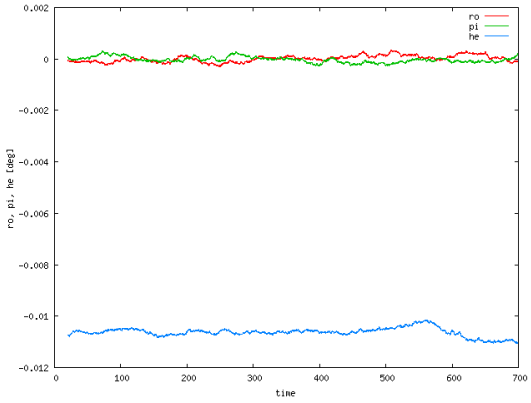

(e) Roll, Pitch and Heading (°)

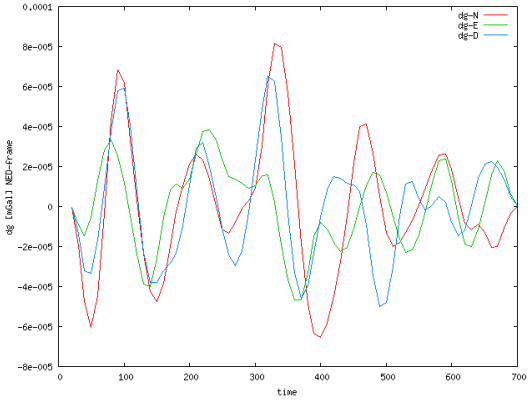

(f) Gravity disturbance (mGal)

Figure 4.4: STATIC LTN101b v2a1: adjusted parameters.

4.3.2 STATIC vq2a1

As already discussed in Section 4.2, the codification this computation means:

- $\langle q \rangle = q$, indicates that prior knowledge of the vehicle's attitude exists at the beginning (t_0) and at the end (t_N) of the mission.
- $\langle Hz \rangle = 2$: some subsets of parameters — $\underline{o}^{\mathsf{b}}$, $\underline{a}^{\mathsf{b}}$, δg or gg — has been grouped.
- $\langle \delta g_{NE} \rangle = a$: no prior knowledge of the horizontal gravity.
- $\langle method \rangle = 1$, indicates a basic network configuration similar to the Kalman filtering.

LN200

Table 4.7 summarises the network configuration used in this computation.

Model Name	Frequency		Equation	Standard Deviation	
FB-GG (3.4.5)	20.0 Hz	$\forall t$	(3.13)	2.2	10^{-3} m s^{-2}
WIB (3.4.2)	20.0 Hz	$\forall t$	(3.10)	5.2	10^{-5} rad s^{-1}
VEL (3.4.1)	20.0 Hz	$\forall t$	(3.4.1)	0.000 01	m
Q-NORM (3.4.6)	20.0 Hz	$\forall t$	(3.14)	0.01	ppm
OB-O (3.4.35)	0.1 Hz	$\forall t$	(3.48)	4.9	10^{-6} rad s^{-1}
AB-O (3.4.36)	0.1 Hz	$\forall t$	(3.49)	2.0	10^{-3} m s^{-2}
OB (3.4.8)	0.1 Hz	$\forall t$	(3.16)	15.0	10^{-7} rad s^{-1}
AB (3.4.10)	0.1 Hz	$\forall t$	(3.18)	130.0	10^{-4} m s^{-2}
AOFF-O (3.4.37)			(3.50)	0.001	m
CUPT (3.4.16)	1.0 Hz	$\forall t$	(3.26)	0.05	m
GDT-GG (3.4.13)	0.1 Hz	$\forall t$	(3.22)	6.2	mGal
DGUPT-GG (3.4.28)	0.1 Hz	$\forall t$	(3.41)	0.02	mGal
Q-O (3.4.34)		t_0, t_N	(3.47)	0.01	ppm

Table 4.7: Test STATIC-LN200-vq2a1: network configuration.

Figure 4.5 proves that the functional models of the NA approach work succesfully:

- Figure 4.5a points out that the position has been recovered, especially heights — in Figure 4.5c — with a precision better than 0.5 cm.
- The navigation parameters — shown in Figure 4.5e — are recovered with a precision of 18 " for roll (α) and pitch (χ) and 1.8 ' for heading (η).
- The IMU error parameters exhibited in Figures 4.5b and 4.5d are nearly constants within the defined tolerances (bias repeatability) of the IMU.
- Figure 4.5f also displays the gravity disturbance vector, that has to be zero, with a precision of 0.0000015 mGal.

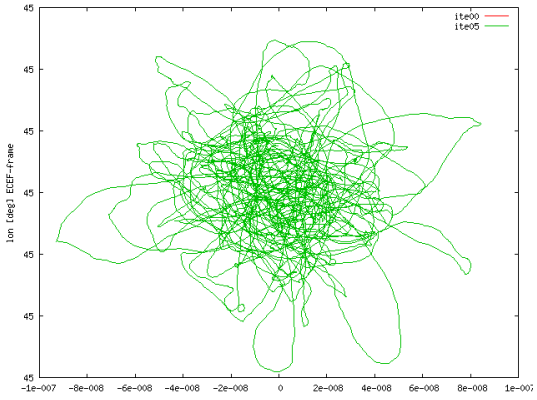

(a) Position (°)

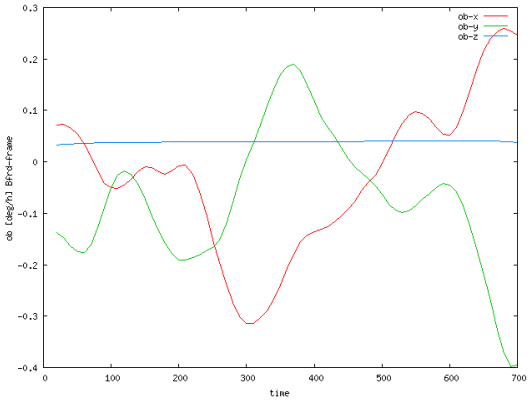

(b) Angular drift ($^\circ\,h^{-1}$)

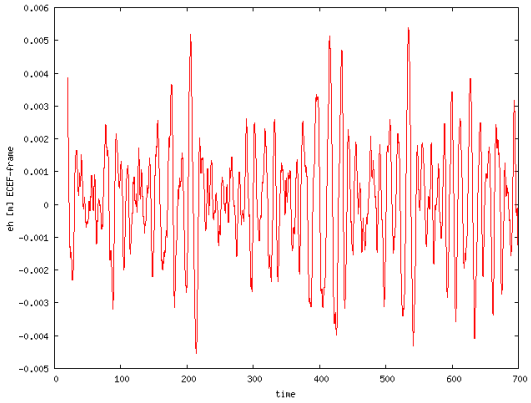

(c) Height (m)

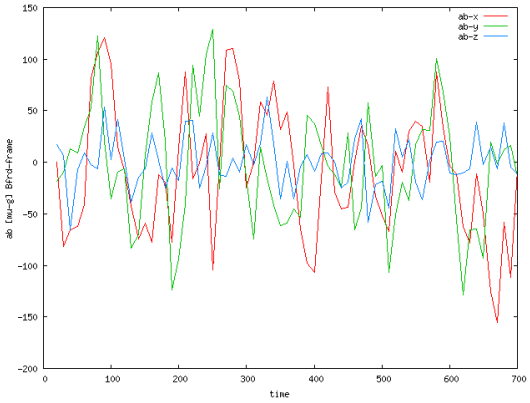

(d) Accelerometer bias (μg)

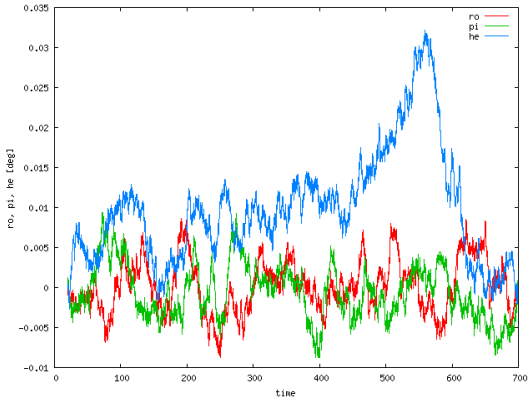

(e) Roll, Pitch and Heading (°)

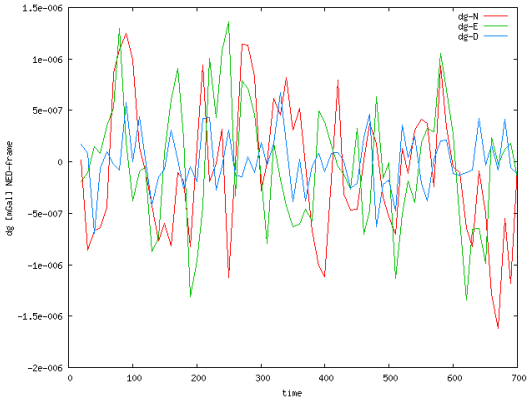

(f) Gravity disturbance (mGal)

Figure 4.5: STATIC LN200 vq2a1: adjusted parameters.

LTN101

Table 4.8 summarises the network configuration used in this computation.

Model Name	Frequency		Equation	Standard Deviation	
FB-GG (3.4.5)	20.0 Hz	$\forall t$	(3.13)	4.4	10^{-4} m s^{-2}
WIB (3.4.2)	20.0 Hz	$\forall t$	(3.10)	1.3	10^{-6} rad s^{-1}
VEL (3.4.1)	20.0 Hz	$\forall t$	(3.4.1)	0.000 01	m
Q-NORM (3.4.6)	20.0 Hz	$\forall t$	(3.14)	0.01	ppm
OB-O (3.4.35)	0.1 Hz	$\forall t$	(3.48)	4.9	10^{-8} rad s^{-1}
AB-O (3.4.36)	0.1 Hz	$\forall t$	(3.49)	4.9	10^{-4} m s^{-2}
OB (3.4.8)	0.1 Hz	$\forall t$	(3.16)	61.0	10^{-12} rad s^{-1}
AB (3.4.10)	0.1 Hz	$\forall t$	(3.18)	95.0	10^{-7} m s^{-2}
AOFF-O (3.4.37)			(3.50)	0.001	m
CUPT (3.4.16)	1.0 Hz	$\forall t$	(3.26)	0.05	m
GDT-GG (3.4.13)	0.1 Hz	$\forall t$	(3.22)	6.2	mGal
DGUPT-GG (3.4.28)	0.1 Hz	$\forall t$	(3.41)	0.02	mGal
Q-O (3.4.34)		t_0, t_N	(3.47)	0.01	ppm

Table 4.8: Test STATIC-LTN101-vq2a1: network configuration.

Figure 4.6 proves that the functional models of the NA approach work succesfully:

- Figure 4.6a points out that the position has been recovered, especially heights — in Figure 4.6c — with a precision better than 0.8 cm.
- The navigation parameters — shown in Figure 4.6e — are recovered with a precision of 0.72 " for roll (α) and pitch (χ) and 2.16 " for heading (η).
- The IMU error parameters exhibited in Figures 4.6b and 4.6d are nearly constants within the defined tolerances (bias repeatability) of the IMU.
- Figure 4.6f also displays the gravity disturbance vector, that has to be zero, with a precision of 0.00006 mGal.

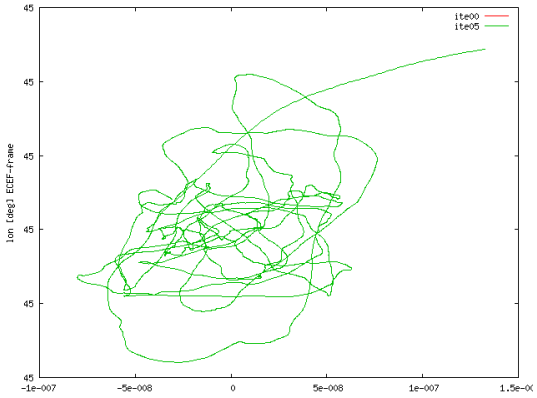

(a) Position (°)

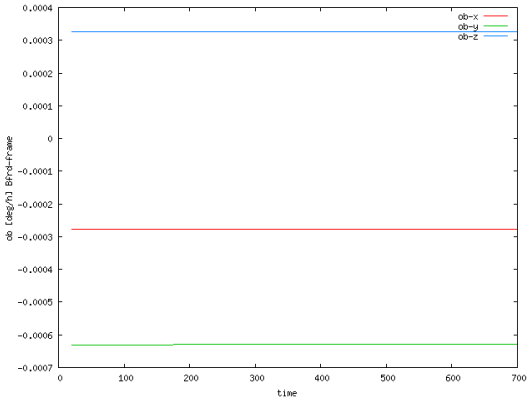

(b) Angular drift ($^\circ\,h^{-1}$)

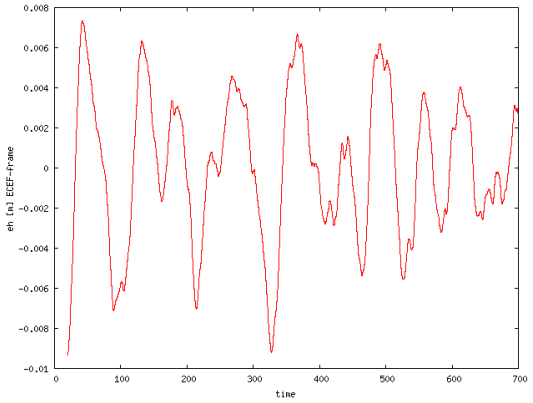

(c) Height (m)

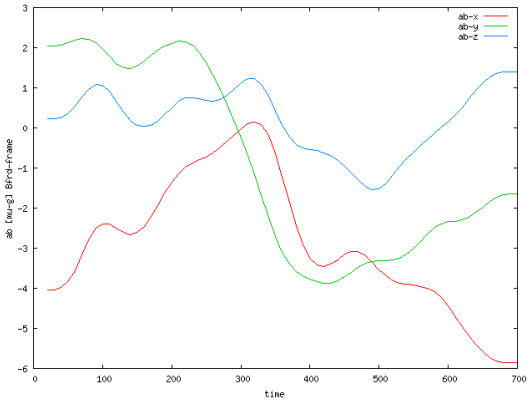

(d) Accelerometer bias (μg)

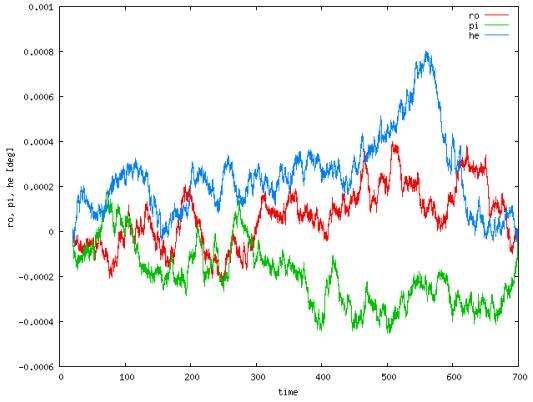

(e) Roll, Pitch and Heading (°)

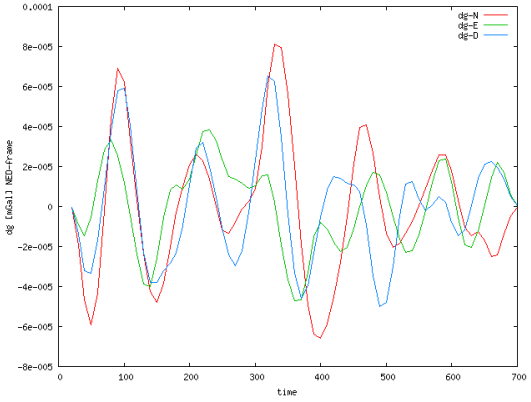

(f) Gravity disturbance (mGal)

Figure 4.6: STATIC LTN101b vq2a1: adjusted parameters.

4.3.3 STATIC v9a1

As already discussed in Section 4.2, the codification this computation means:

- $\langle Hz \rangle = 9$: all the parameters are computed at the IMU rate.
- $\langle \delta g_{NE} \rangle = a$: no prior knowledge of the horizontal gravity.
- $\langle method \rangle = 1$, indicates a basic network configuration similar to the Kalman filtering.

LN200

Table 4.9 summarises the network configuration used in this computation.

Model Name	Frequency		Equation	Standard Deviation	
FB-GG (3.4.5)	20.0 Hz	$\forall t$	(3.13)	2.2	10^{-3} m s^{-2}
WIB (3.4.2)	20.0 Hz	$\forall t$	(3.10)	5.2	10^{-5} rad s^{-1}
VEL (3.4.1)	20.0 Hz	$\forall t$	(3.4.1)	0.000 01	m
Q-NORM (3.4.6)	20.0 Hz	$\forall t$	(3.14)	0.01	ppm
OB-O (3.4.35)	20.0 Hz	$\forall t$	(3.48)	4.9	10^{-6} rad s^{-1}
AB-O (3.4.36)	20.0 Hz	$\forall t$	(3.49)	2.0	10^{-3} m s^{-2}
OB (3.4.8)	20.0 Hz	$\forall t$	(3.16)	1.1	10^{-7} rad s^{-1}
AB (3.4.10)	20.0 Hz	$\forall t$	(3.18)	8.9	10^{-4} m s^{-2}
AOFF-O (3.4.37)			(3.50)	0.001	m
CUPT (3.4.16)	1.0 Hz	$\forall t$	(3.26)	0.05	m
GDT-GG (3.4.13)	20.0 Hz	$\forall t$	(3.22)	0.016	mGal
DGUPT-GG (3.4.28)	20.0 Hz	$\forall t$	(3.41)	0.02	mGal

Table 4.9: Test STATIC-LN200-v9a1: network configuration.

Figure 4.7 proves that the functional models of the NA approach work succesfully:

- Figure 4.7a points out that the position has been recovered, especially heights — in Figure 4.7c — with a precision better than 1 cm.
- The navigation parameters — shown in Figure 4.7e — are recovered with a precision of 18 " for roll (α) and pitch (χ) and 1.5 ' for heading (η).
- The IMU error parameters exhibited in Figures 4.7b and 4.7d are nearly constants within the defined tolerances (bias repeatability) of the IMU.
- Figure 4.7f also displays the gravity disturbance vector, that has to be zero, with a precision of 0.00000015 mGal.

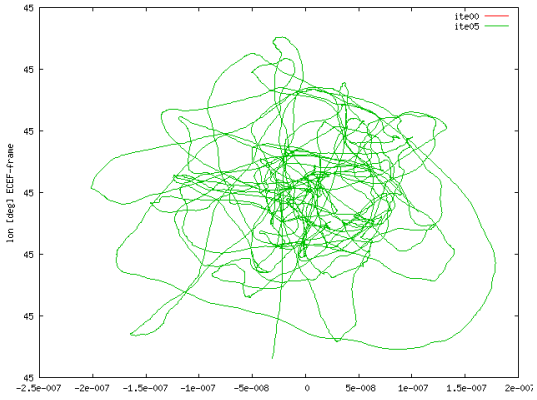

(a) Position (°)

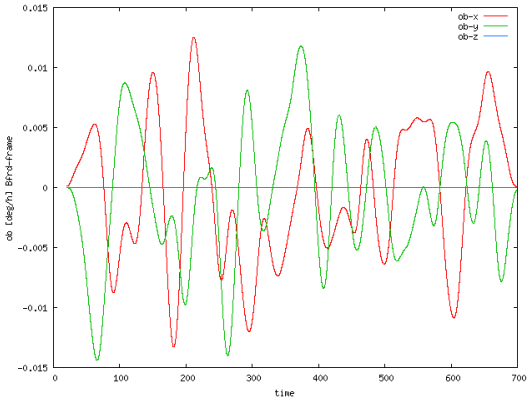

(b) Angular drift ($^\circ\,h^{-1}$)

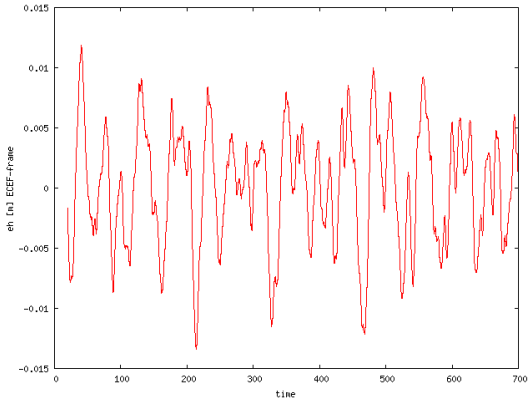

(c) Height (m)

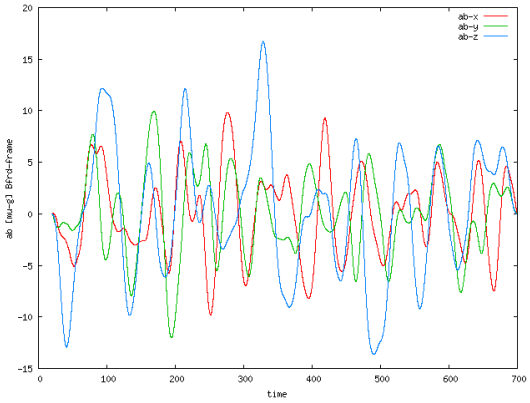

(d) Accelerometer bias (μg)

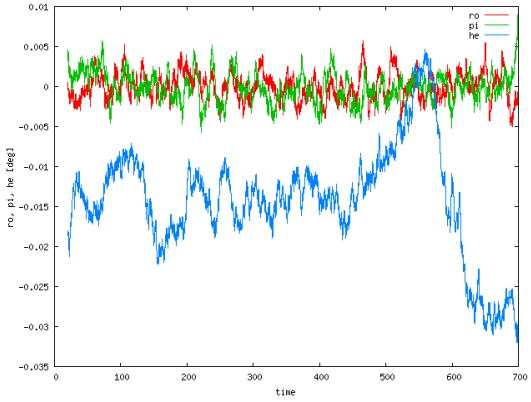

(e) Roll, Pitch and Heading (°)

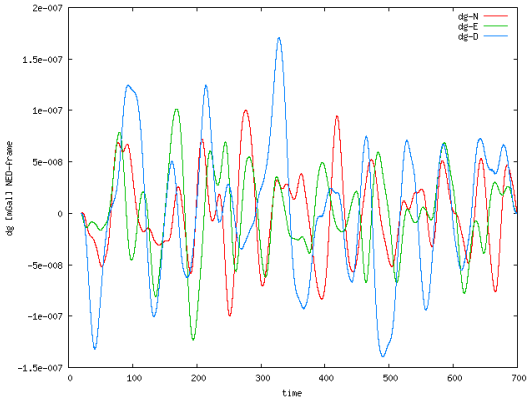

(f) Gravity disturbance (mGal)

Figure 4.7: STATIC LN200 v9a1: adjusted parameters.

LTN101

Table 4.10 summarises the network configuration used in this computation.

Model Name	Frequency		Equation	Standard Deviation	
FB-GG (3.4.5)	20.0 Hz	$\forall t$	(3.13)	4.4	10^{-4} m s^{-2}
WIB (3.4.2)	20.0 Hz	$\forall t$	(3.10)	1.3	10^{-6} rad s^{-1}
VEL (3.4.1)	20.0 Hz	$\forall t$	(3.4.1)	0.000 01	m
Q-NORM (3.4.6)	20.0 Hz	$\forall t$	(3.14)	0.01	ppm
OB-O (3.4.35)	20.0 Hz	$\forall t$	(3.48)	4.9	10^{-8} rad s^{-1}
AB-O (3.4.36)	20.0 Hz	$\forall t$	(3.49)	4.9	10^{-4} m s^{-2}
OB (3.4.8)	20.0 Hz	$\forall t$	(3.16)	4.3	10^{-12} rad s^{-1}
AB (3.4.10)	20.0 Hz	$\forall t$	(3.18)	6.7	10^{-7} m s^{-2}
AOFF-O (3.4.37)			(3.50)	0.001	m
CUPT (3.4.16)	1.0 Hz	$\forall t$	(3.26)	0.05	m
GDT-GG (3.4.13)	20.0 Hz	$\forall t$	(3.22)	0.016	mGal
DGUPT-GG (3.4.28)	20.0 Hz	$\forall t$	(3.41)	0.02	mGal

Table 4.10: Test STATIC-LTN101-v9a1: network configuration.

Figure 4.8 proves that the functional models of the NA approach work succesfully:

- Figure 4.8a points out that the position has been recovered, especially heights — in Figure 4.8c — with a precision better than 0.8 cm.
- The navigation parameters — shown in Figure 4.8e — are recovered with a precision of 7.2 " for roll (α), pitch (χ) and heading (η).
- The IMU error parameters exhibited in Figures 4.8b and 4.8d are nearly constants within the defined tolerances (bias repeatability) of the IMU.
- Figure 4.8f also displays the gravity disturbance vector, that has to be zero, with a precision of 0.0000004 mGal.

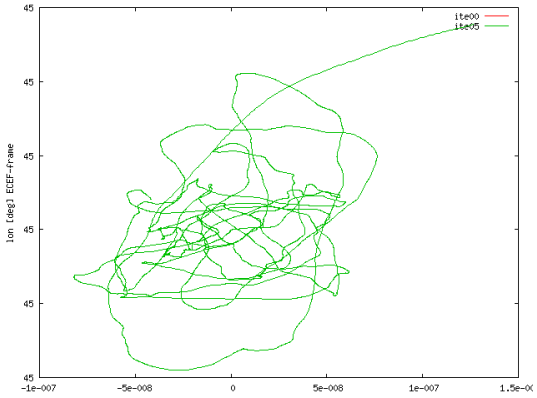

(a) Position (°)

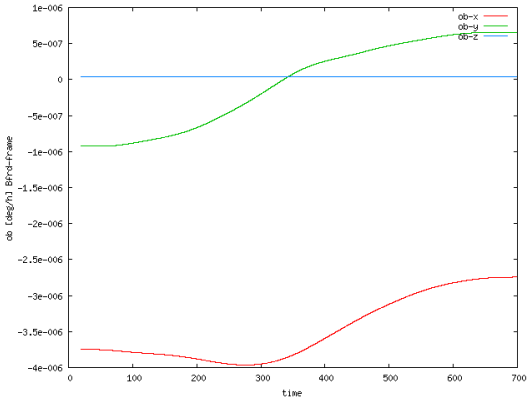

(b) Angular drift ($^\circ\,h^{-1}$)

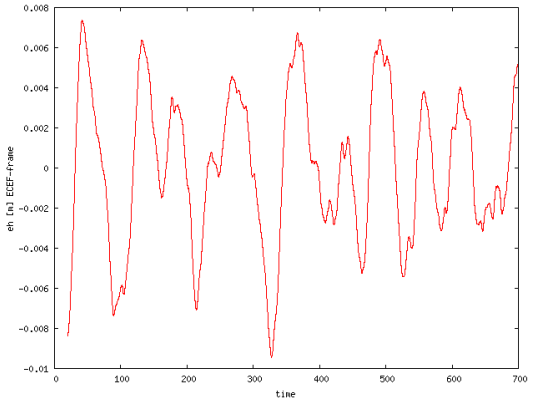

(c) Height (m)

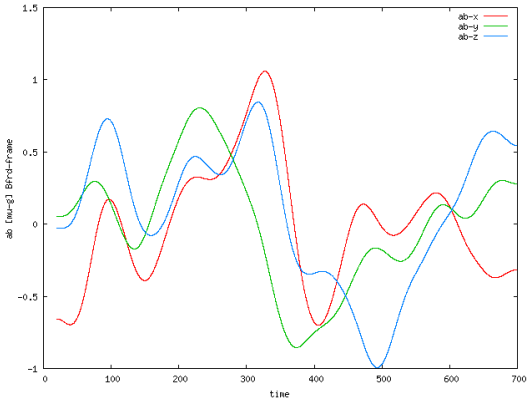

(d) Accelerometer bias (μg)

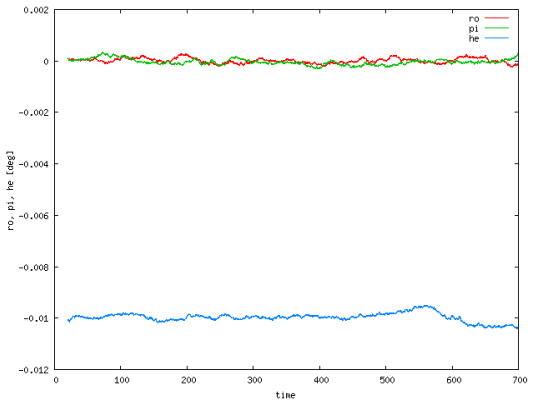

(e) Roll, Pitch and Heading (°)

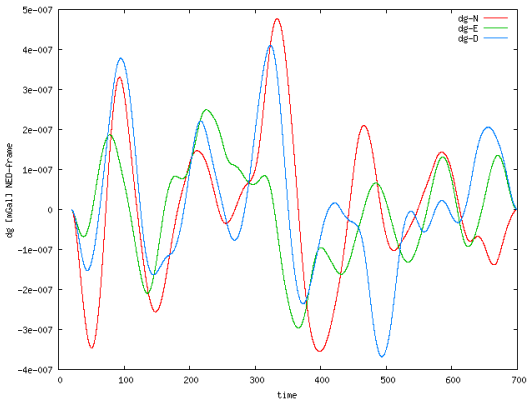

(f) Gravity disturbance (mGal)

Figure 4.8: STATIC LTN101b v9a1: adjusted parameters.

4.3.4 STATIC vq9a1

As already discussed in Section 4.2, the codification this computation means:

- $\langle q \rangle = q$, indicates if prior knowledge of the vehicle's attitude exists at the beginning (t_0) and at the end (t_N) of the mission.
- $\langle Hz \rangle = 9$: all the parameters are computed at the IMU rate.
- $\langle \delta g_{NE} \rangle = a$: no prior knowledge of the horizontal gravity.
- $\langle method \rangle = 1$, indicates a basic network configuration similar to the Kalman filtering.

LN200

Table 4.11 summarises the network configuration used in this computation.

Model Name	Frequency		Equation	Standard Deviation	
FB-GG (3.4.5)	20.0 Hz	$\forall t$	(3.13)	2.2	10^{-3} m s^{-2}
WIB (3.4.2)	20.0 Hz	$\forall t$	(3.10)	5.2	10^{-5} rad s^{-1}
VEL (3.4.1)	20.0 Hz	$\forall t$	(3.4.1)	0.000 01	m
Q-NORM (3.4.6)	20.0 Hz	$\forall t$	(3.14)	0.01	ppm
OB-O (3.4.35)	20.0 Hz	$\forall t$	(3.48)	4.9	10^{-6} rad s^{-1}
AB-O (3.4.36)	20.0 Hz	$\forall t$	(3.49)	2.0	10^{-3} m s^{-2}
OB (3.4.8)	20.0 Hz	$\forall t$	(3.16)	1.1	10^{-7} rad s^{-1}
AB (3.4.10)	20.0 Hz	$\forall t$	(3.18)	8.9	10^{-4} m s^{-2}
AOFF-O (3.4.37)			(3.50)	0.001	m
CUPT (3.4.16)	1.0 Hz	$\forall t$	(3.26)	0.05	m
GDT-GG (3.4.13)	20.0 Hz	$\forall t$	(3.22)	0.016	mGal
DGUPT-GG (3.4.28)	20.0 Hz	$\forall t$	(3.41)	0.02	mGal
Q-O (3.4.34)		t_0, t_N	(3.47)	0.01	ppm

Table 4.11: Test STATIC-LN200-vq9a1: network configuration.

Figure 4.9 proves that the functional models of the NA approach work succesfully:

- Figure 4.9a points out that the position has been recovered, especially heights — in Figure 4.9c — with a precision better than 1 cm.
- The navigation parameters — shown in Figure 4.9e — are recovered with a precision of 18 " for roll (α) and pitch (χ) and 1.8 ' for heading (η).
- The IMU error parameters exhibited in Figures 4.9b and 4.9d are nearly constants within the defined tolerances (bias repeatability) of the IMU.
- Figure 4.9f also displays the gravity disturbance vector, that has to be zero, with a precision of 0.0000001 mGal.

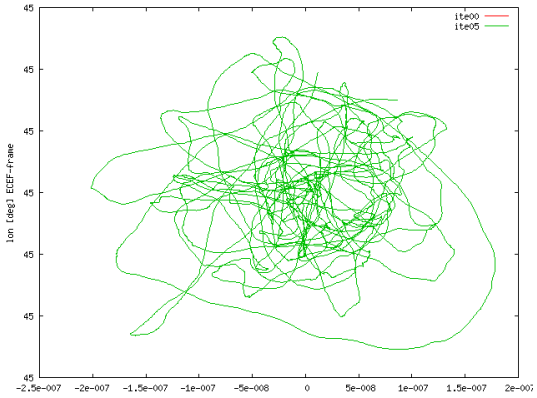

(a) Position (°)

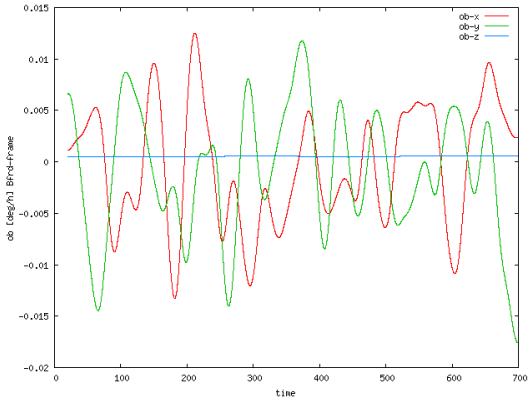

(b) Angular drift ($^\circ\,h^{-1}$)

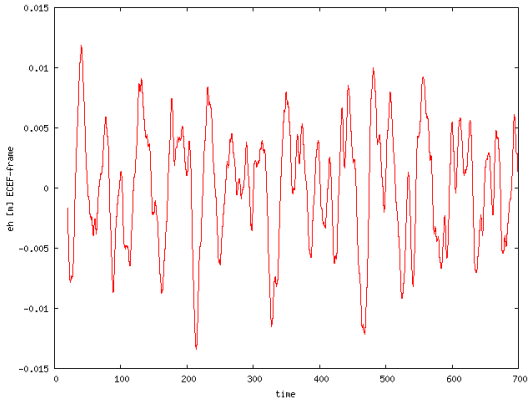

(c) Height (m)

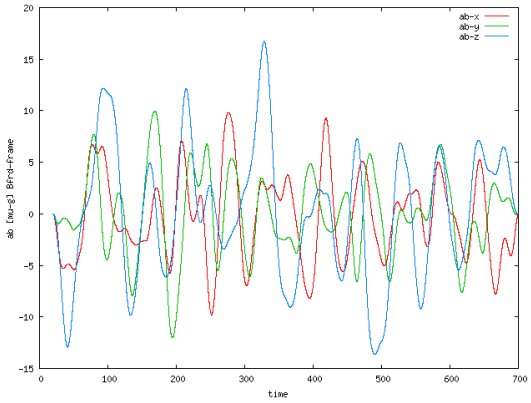

(d) Accelerometer bias (μg)

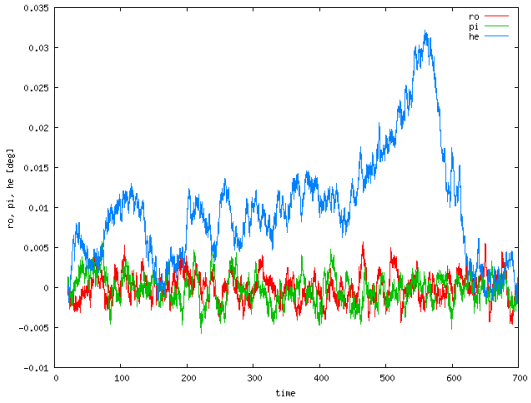

(e) Roll, Pitch and Heading (°)

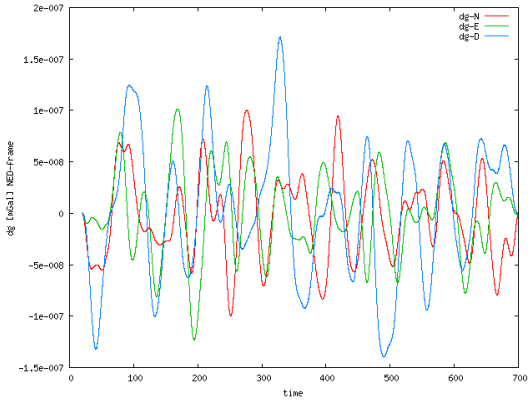

(f) Gravity disturbance (mGal)

Figure 4.9: STATIC LN200 vq9a1: adjusted parameters.

LTN101

Table 4.12 summarises the network configuration used in this computation.

Model Name	Frequency		Equation	Standard Deviation	
FB-GG (3.4.5)	20.0 Hz	$\forall t$	(3.13)	4.4	10^{-4} m s^{-2}
WIB (3.4.2)	20.0 Hz	$\forall t$	(3.10)	1.3	10^{-6} rad s^{-1}
VEL (3.4.1)	20.0 Hz	$\forall t$	(3.4.1)	0.000 01	m
Q-NORM (3.4.6)	20.0 Hz	$\forall t$	(3.14)	0.01	ppm
OB-O (3.4.35)	20.0 Hz	$\forall t$	(3.48)	4.9	10^{-8} rad s^{-1}
AB-O (3.4.36)	20.0 Hz	$\forall t$	(3.49)	4.9	10^{-4} m s^{-2}
OB (3.4.8)	20.0 Hz	$\forall t$	(3.16)	4.3	10^{-12} rad s^{-1}
AB (3.4.10)	20.0 Hz	$\forall t$	(3.18)	6.7	10^{-7} m s^{-2}
AOFF-O (3.4.37)			(3.50)	0.001	m
CUPT (3.4.16)	1.0 Hz	$\forall t$	(3.26)	0.05	m
GDT-GG (3.4.13)	20.0 Hz	$\forall t$	(3.22)	0.016	mGal
DGUPT-GG (3.4.28)	20.0 Hz	$\forall t$	(3.41)	0.02	mGal
Q-O (3.4.34)		t_0, t_N	(3.47)	0.01	ppm

Table 4.12: Test STATIC-LTN101-vq9a1: network configuration.

Figure 4.10 proves that the functional models of the NA approach work succesfully:

- Figure 4.10a points out that the position has been recovered, especially heights — in Figure 4.10c — with a precision better than 0.8 cm.
- The navigation parameters — shown in Figure 4.10e — are recovered with a precision of 0.72 " for roll (α) and pitch (χ) and 2.88 " for heading (η).
- The IMU error parameters exhibited in Figures 4.10b and 4.10d are nearly constants within the defined tolerances (bias repeatability) of the IMU.
- Figure 4.10f also displays the gravity disturbance vector, that has to be zero, with a precision of 0.0000004 mGal.

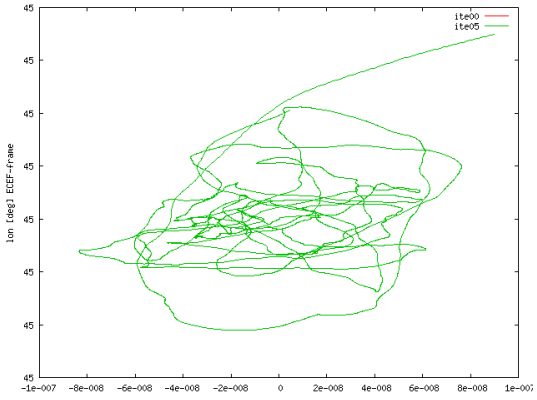

(a) Position (°)

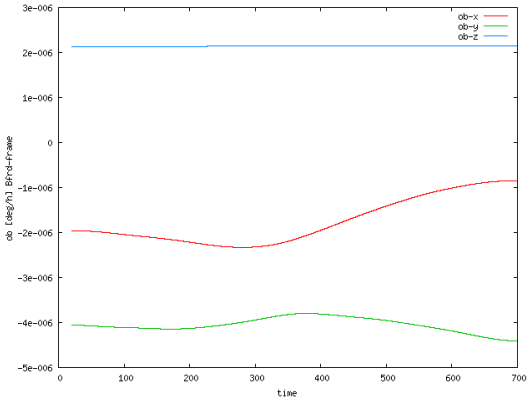

(b) Angular drift ($^\circ\,h^{-1}$)

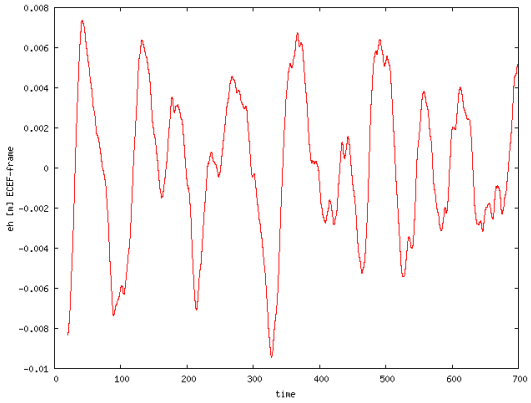

(c) Height (m)

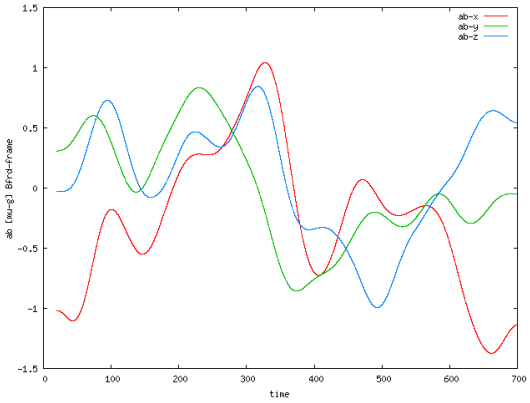

(d) Accelerometer bias (μg)

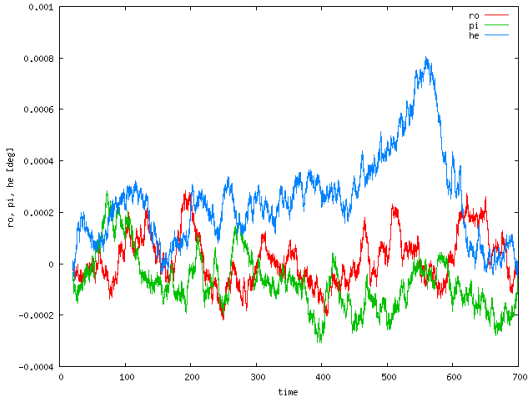

(e) Roll, Pitch and Heading (°)

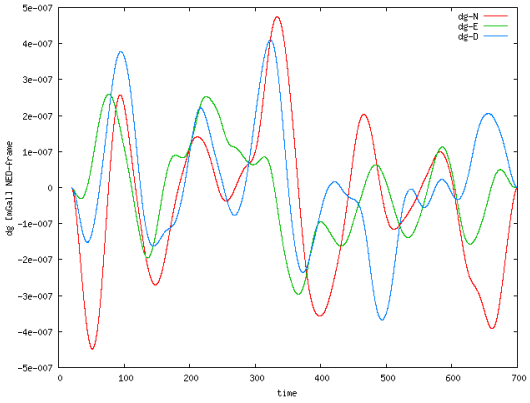

(f) Gravity disturbance (mGal)

Figure 4.10: STATIC LTN101b vq9a1: adjusted parameters.

4.3.5 STATIC vqt9a1

As already discussed in Section 4.2, the codification this computation means:

- $\langle q \rangle = qt$, indicates that prior knowledge of the vehicle's attitude exists, for all t.
- $\langle Hz \rangle = 9$: all the parameters are computed at the IMU rate.
- $\langle \delta g_{NE} \rangle = a$: no prior knowledge of the horizontal gravity.
- $\langle method \rangle = 1$, indicates a basic network configuration similar to the Kalman filtering.

LN200

Table 4.13 summarises the network configuration used in this computation.

Model Name	Frequency		Equation	Standard Deviation	
FB-GG (3.4.5)	20.0 Hz	$\forall t$	(3.13)	2.2	10^{-3} m s^{-2}
WIB (3.4.2)	20.0 Hz	$\forall t$	(3.10)	5.2	10^{-5} rad s^{-1}
VEL (3.4.1)	20.0 Hz	$\forall t$	(3.4.1)	0.000 01	m
Q-NORM (3.4.6)	20.0 Hz	$\forall t$	(3.14)	0.01	ppm
OB-O (3.4.35)	20.0 Hz	$\forall t$	(3.48)	4.9	10^{-6} rad s^{-1}
AB-O (3.4.36)	20.0 Hz	$\forall t$	(3.49)	2.0	10^{-3} m s^{-2}
OB (3.4.8)	20.0 Hz	$\forall t$	(3.16)	1.1	10^{-7} rad s^{-1}
AB (3.4.10)	20.0 Hz	$\forall t$	(3.18)	8.9	10^{-4} m s^{-2}
AOFF-O (3.4.37)			(3.50)	0.001	m
CUPT (3.4.16)	1.0 Hz	$\forall t$	(3.26)	0.05	m
GDT-GG (3.4.13)	20.0 Hz	$\forall t$	(3.22)	0.016	mGal
DGUPT-GG (3.4.28)	20.0 Hz	$\forall t$	(3.41)	0.02	mGal
Q-O (3.4.34)	20.0 Hz	$\forall t$	(3.47)	0.01	ppm

Table 4.13: Test STATIC-LN200-vqt9a1: network configuration.

Figure 4.11 proves that the functional models of the NA approach work succesfully:

- Figure 4.11a points out that the position has been recovered, especially heights — in Figure 4.11c — with a precision better than 1 cm.
- The navigation parameters — shown in Figure 4.11e — are recovered with a precision of 0.00036 " for roll (α), pitch (χ) and heading (η).
- The IMU error parameters exhibited in Figures 4.11b and 4.11d are nearly constants within the defined tolerances (bias repeatability) of the IMU.
- Figure 4.11f also displays the gravity disturbance vector, that has to be zero.

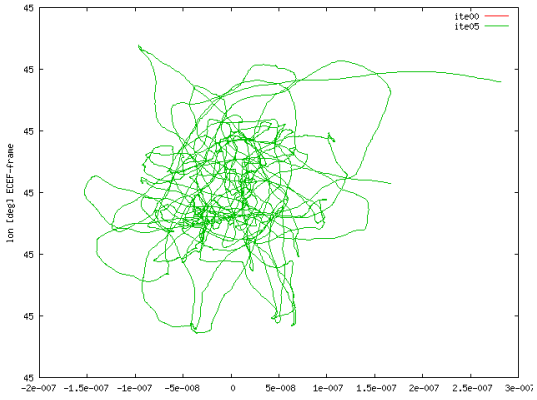

(a) Position (°)

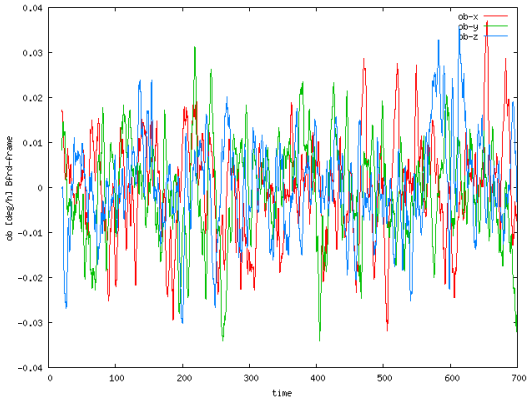

(b) Angular drift ($^\circ\,h^{-1}$)

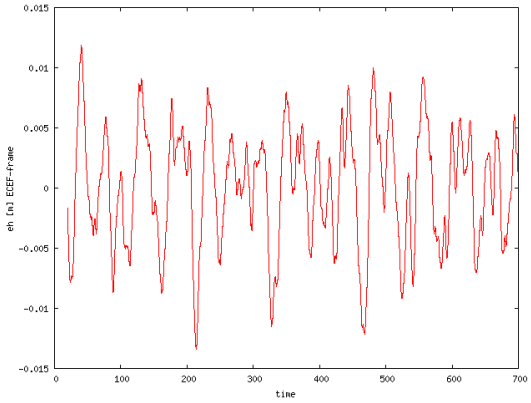

(c) Height (m)

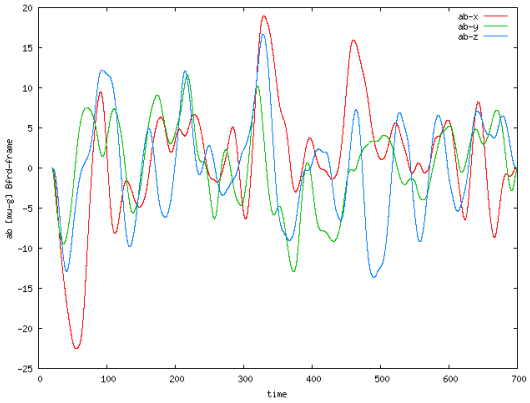

(d) Accelerometer bias (μg)

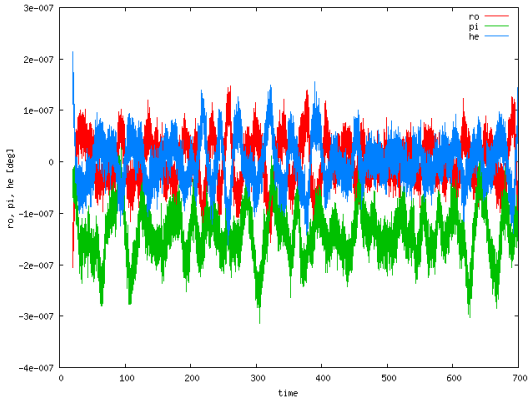

(e) Roll, Pitch and Heading (°)

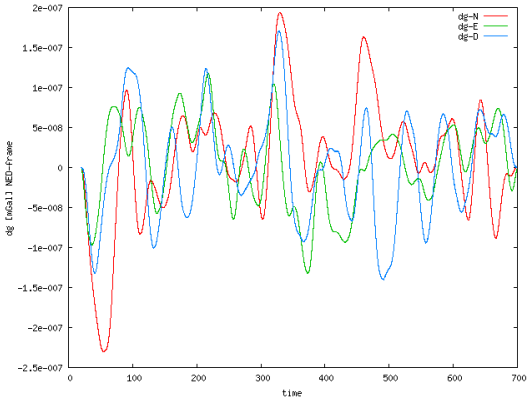

(f) Gravity disturbance (mGal)

Figure 4.11: STATIC LN200 vqt9a1: adjusted parameters.

LTN101

Table 4.14 summarises the network configuration used in this computation.

Model Name	Frequency		Equation	Standard Deviation	
FB-GG (3.4.5)	20.0 Hz	$\forall t$	(3.13)	4.4	10^{-4} m s^{-2}
WIB (3.4.2)	20.0 Hz	$\forall t$	(3.10)	1.3	10^{-6} rad s^{-1}
VEL (3.4.1)	20.0 Hz	$\forall t$	(3.4.1)	0.000 01	m
Q-NORM (3.4.6)	20.0 Hz	$\forall t$	(3.14)	0.01	ppm
OB-O (3.4.35)	20.0 Hz	$\forall t$	(3.48)	4.9	10^{-8} rad s^{-1}
AB-O (3.4.36)	20.0 Hz	$\forall t$	(3.49)	4.9	10^{-4} m s^{-2}
OB (3.4.8)	20.0 Hz	$\forall t$	(3.16)	4.3	10^{-12} rad s^{-1}
AB (3.4.10)	20.0 Hz	$\forall t$	(3.18)	6.7	10^{-7} m s^{-2}
AOFF-O (3.4.37)			(3.50)	0.001	m
CUPT (3.4.16)	1.0 Hz	$\forall t$	(3.26)	0.05	m
GDT-GG (3.4.13)	20.0 Hz	$\forall t$	(3.22)	0.016	mGal
DGUPT-GG (3.4.28)	20.0 Hz	$\forall t$	(3.41)	0.02	mGal
Q-O (3.4.34)	20.0 Hz	$\forall t$	(3.47)	0.01	ppm

Table 4.14: Test STATIC-LTN101-vqt9a1: network configuration.

Figure 4.12 proves that the functional models of the NA approach work succesfully:

- Figure 4.12a points out that the position has been recovered, especially heights — in Figure 4.12c — with a precision better than 0.8 cm.
- The navigation parameters — shown in Figure 4.12e — are recovered with a precision of 0.0072 " for roll (α), pitch (χ) and heading (η).
- The IMU error parameters exhibited in Figures 4.12b and 4.12d are nearly constants within the defined tolerances (bias repeatability) of the IMU.
- Figure 4.12f also displays the gravity disturbance vector, that has to be zero.

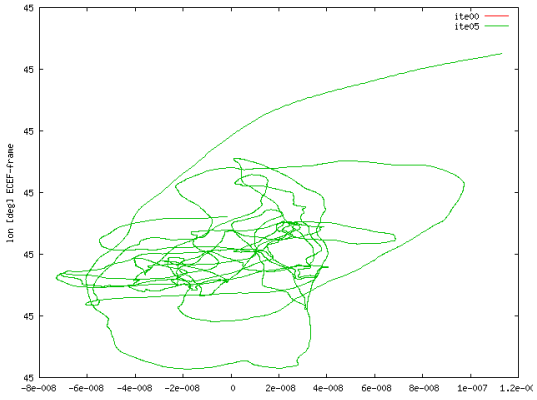

(a) Position (°)

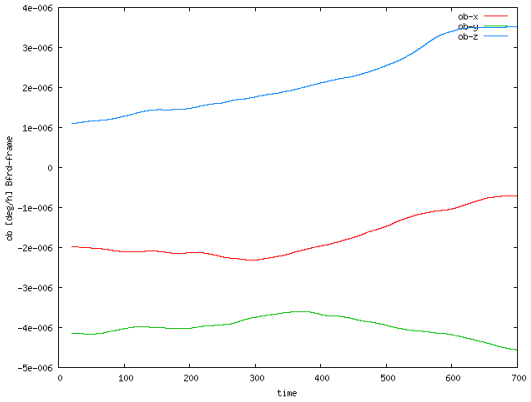

(b) Angular drift ($^\circ\,h^{-1}$)

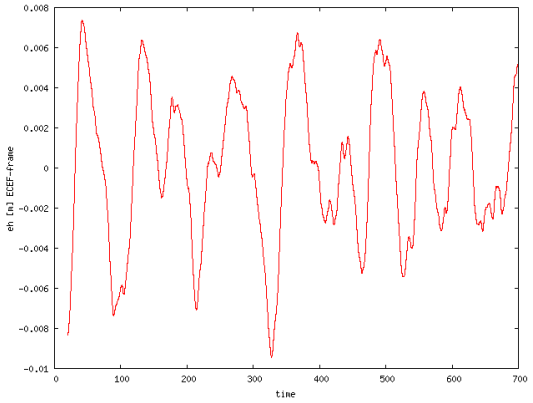

(c) Height (m)

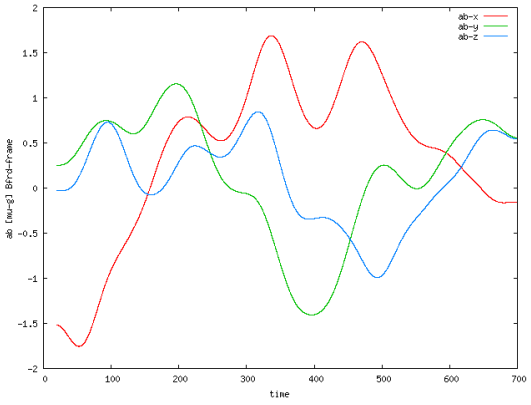

(d) Accelerometer bias (μg)

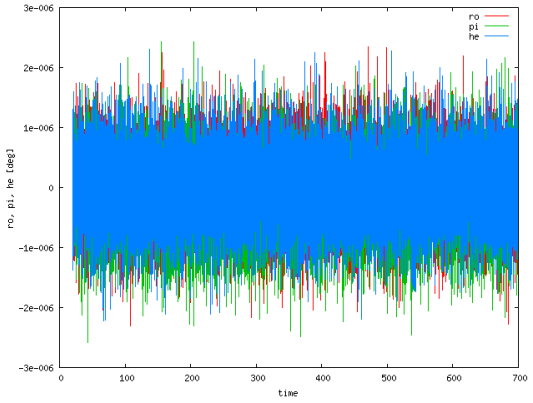

(e) Roll, Pitch and Heading (°)

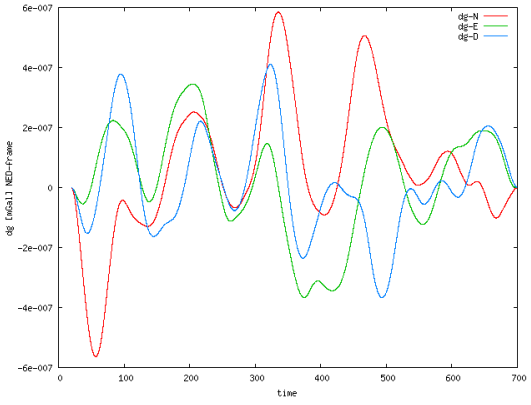

(f) Gravity disturbance (mGal)

Figure 4.12: STATIC LTN101b vqt9a1: adjusted parameters.

4.4 Test CIRCLE

After the static approximation, a new simple trajectory has to be considered. Now, a circular trajectory such as toy train is taken int account. In this case, it is supposed that the platform goes round a circuit 3 times.

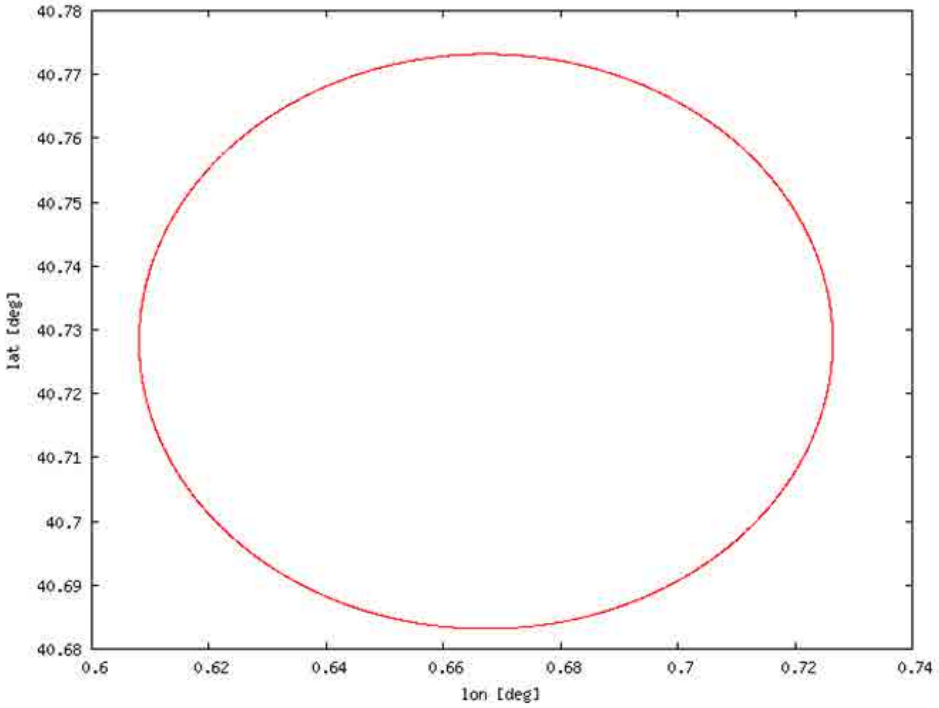

Figure 4.13: CIRCLE: input trajectory.

Now, the advantages of such as NA approach has to be demonstrated. As the train goes 3 times for each position, there is a gravity relationship of the type GDT between each pair of laps. These relationships result in additional GDT-GG observation equations, but in this case the related parameters have not to be correlative. Therefore the network redundancy number may increase substantially. In Table 4.15, for a *basic* configuration — v∗1 — a redundancy of 0.0318 is obtained, whereas a redundancy of 0.0459 for the *complex* configurations — v∗2x — that have been described above.

Like STATIC test,

- Figure 4.14 displays the output data of IG-IMU simulator (LN200 in red and LTN101 in green);
- several computations has been also done for each IMU configuration (v2a1, vq2a1, v2a2, vq2a2, v2a2x, vq2a2x, etc.), and

- Table 4.15 shows the associated dimensions for each system.

version	Nrow	Ncol	Neq	Npar	r_b
v2a1	56 111	41 012	141 131	136 637	0.031 8
vq2a1	56 113	41 012	141 139	136 637	0.031 9
v2a2	56 198	41 012	141 392	136 637	0.033 6
vq2a2	56 200	41 012	141 400	136 637	0.033 7
v2a2x	57 818	41 012	143 012	136 637	0.044 6
vq2a2x	57 820	41 012	143 020	136 637	0.044 6
v2b1	56 156	41 012	141 326	136 637	0.033 2
vq2b1	56 178	41 012	141 334	136 637	0.033 2
v2b2	56 263	41 012	141 587	136 637	0.035 0
vq2b2	56 265	41 012	141 595	136 637	0.035 0
v2b2x	57 883	41 012	143 207	136 637	0.045 9
vq2b2x	57 885	41 012	143 215	136 637	0.045 9

Table 4.15: Test CIRCLE: network's dimensions.

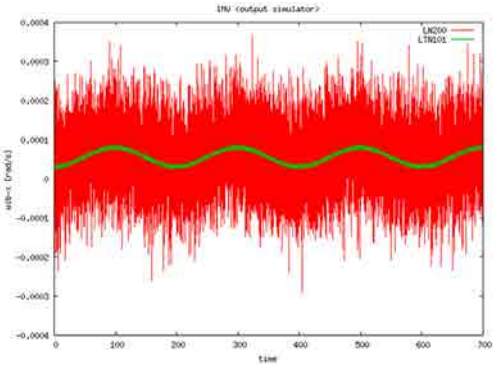

(a) X angular velocity (rad s^{-1})

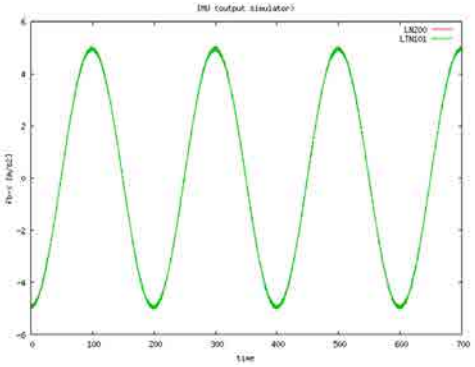

(b) X acceleration (m s^{-2})

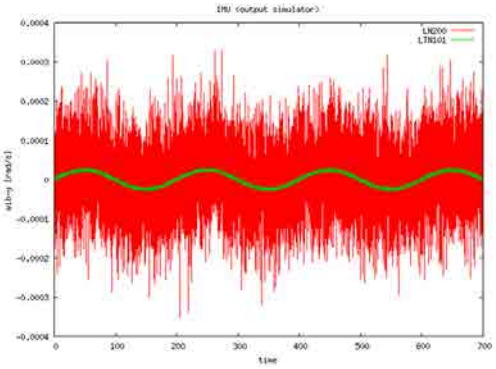

(c) Y angular velocity (rad s^{-1})

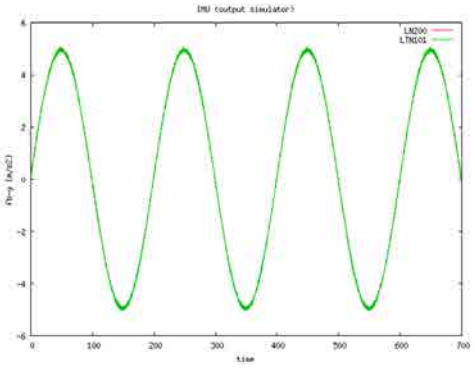

(d) Y acceleration (m s^{-2})

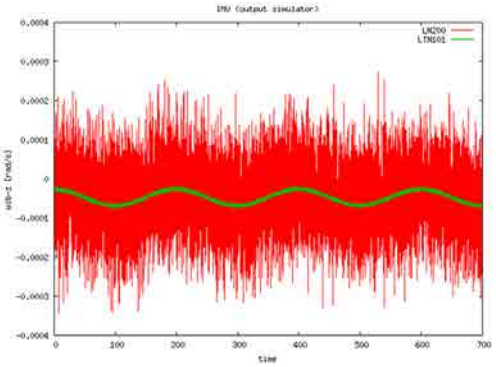

(e) Z angular velocity (rad s^{-1})

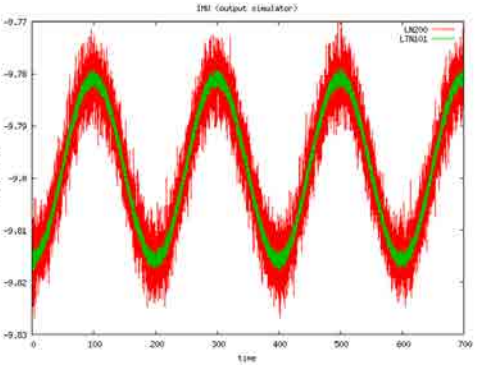

(f) Z acceleration (m s^{-2})

Figure 4.14: CIRCLE: simulated IMU data.

4.4.1 CIRCLE v2a1

As already discussed in Section 4.2, the codification this computation means:

- $\langle Hz \rangle = 2$: some subsets of parameters — $\underline{o}^{\mathsf{b}}$, $\underline{a}^{\mathsf{b}}$, δg or gg — has been grouped.
- $\langle \delta g_{NE} \rangle = a$: no prior knowledge of the horizontal gravity.
- $\langle method \rangle = 1$, indicates a basic network configuration similar to the Kalman filtering.

LN200

Table 4.16 summarises the network configuration used in this computation.

Model Name	Frequency		Equation	Standard Deviation	
FB-GG (3.4.5)	20.0 Hz	$\forall t$	(3.13)	2.2	10^{-3} m s^{-2}
WIB (3.4.2)	20.0 Hz	$\forall t$	(3.10)	5.2	10^{-5} rad s^{-1}
VEL (3.4.1)	20.0 Hz	$\forall t$	(3.4.1)	0.000 01	m
Q-NORM (3.4.6)	20.0 Hz	$\forall t$	(3.14)	0.01	ppm
OB-O (3.4.35)	0.1 Hz	$\forall t$	(3.48)	4.9	10^{-6} rad s^{-1}
AB-O (3.4.36)	0.1 Hz	$\forall t$	(3.49)	2.0	10^{-3} m s^{-2}
OB (3.4.8)	0.1 Hz	$\forall t$	(3.16)	15.0	10^{-7} rad s^{-1}
AB (3.4.10)	0.1 Hz	$\forall t$	(3.18)	130.0	10^{-4} m s^{-2}
AOFF-O (3.4.37)			(3.50)	0.001	m
CUPT (3.4.16)	1.0 Hz	$\forall t$	(3.26)	0.05	m
GDT-GG (3.4.13)	0.1 Hz	$\forall t$	(3.22)	6.2	mGal
DGUPT-GG (3.4.28)	$t_0^{v1} = t_0^{v2} = t_0^{v3} = t_N$		(3.41)	0.02	mGal

Table 4.16: Test CIRCLE-LN200-v2a1: network configuration.

Figure 4.15 proves that the functional models of the NA approach work succesfully:

- Figure 4.15a points out that the position has been recovered, especially heights — in Figure 4.15c — with a precision better than 0.6 cm.
- The navigation parameters — shown in Figure 4.15e — are recovered with a precision of 0.6 ' for roll (α) and pitch (χ) and 1.2 ' for heading (η).
- The IMU error parameters exhibited in Figures 4.15b and 4.15d are nearly constants within the defined tolerances (bias repeatability) of the IMU.
- Figure 4.15f also displays the gravity disturbance vector, that has to be zero, with a precision better than 1 mGal.

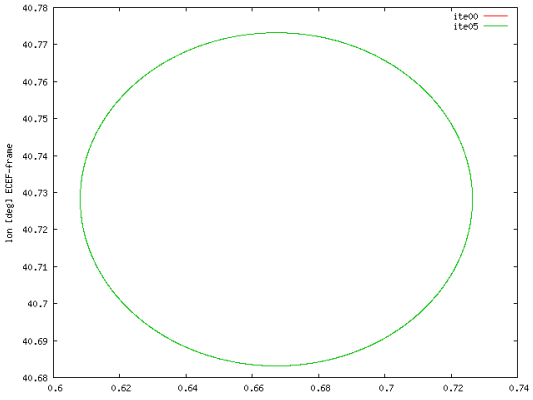

(a) Position (°)

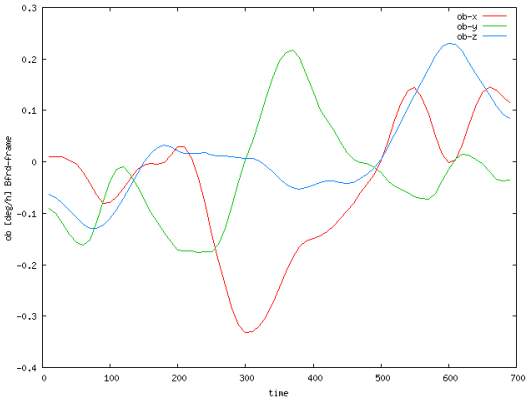

(b) Angular drift ($^\circ\,h^{-1}$)

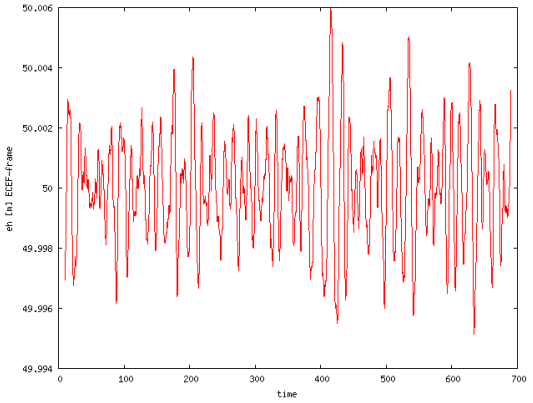

(c) Height (m)

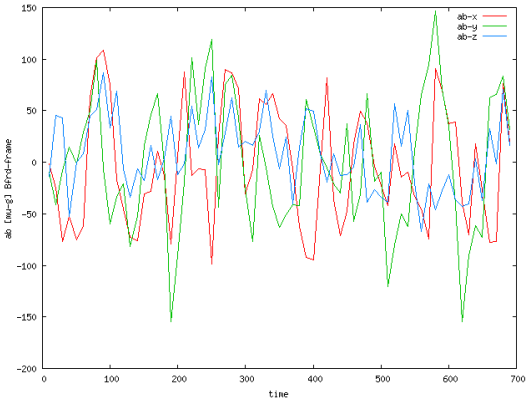

(d) Accelerometer bias (μg)

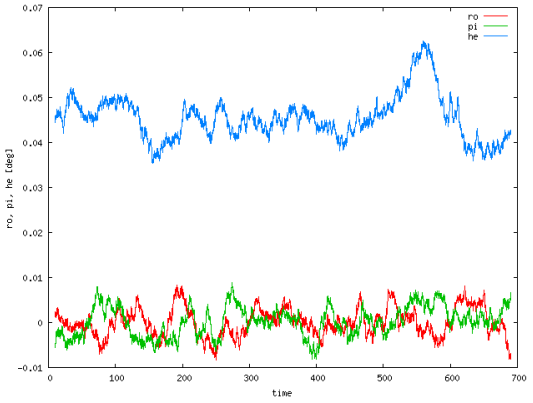

(e) Roll, Pitch and Heading (°)

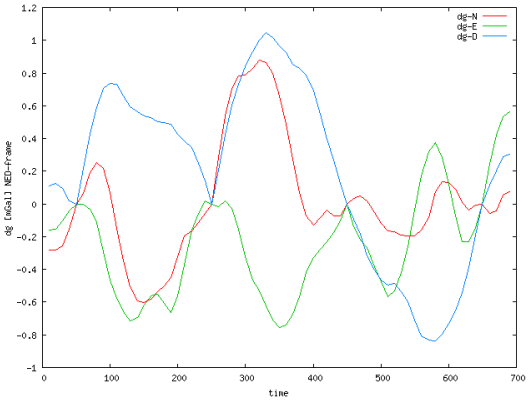

(f) Gravity disturbance (mGal)

Figure 4.15: CIRCLE LN200 v2a1: adjusted parameters.

LTN101

Table 4.17 summarises the network configuration used in this computation.

Model Name	Frequency		Equation	Standard Deviation	
FB-GG (3.4.5)	20.0 Hz	$\forall t$	(3.13)	4.4	10^{-4} m s^{-2}
WIB (3.4.2)	20.0 Hz	$\forall t$	(3.10)	1.3	10^{-6} rad s^{-1}
VEL (3.4.1)	20.0 Hz	$\forall t$	(3.4.1)	0.000 01	m
Q-NORM (3.4.6)	20.0 Hz	$\forall t$	(3.14)	0.01	ppm
OB-O (3.4.35)	0.1 Hz	$\forall t$	(3.48)	4.9	10^{-8} rad s^{-1}
AB-O (3.4.36)	0.1 Hz	$\forall t$	(3.49)	4.9	10^{-4} m s^{-2}
OB (3.4.8)	0.1 Hz	$\forall t$	(3.16)	61.0	10^{-12} rad s^{-1}
AB (3.4.10)	0.1 Hz	$\forall t$	(3.18)	95.0	10^{-7} m s^{-2}
AOFF-O (3.4.37)			(3.50)	0.001	m
CUPT (3.4.16)	1.0 Hz	$\forall t$	(3.26)	0.05	m
GDT-GG (3.4.13)	0.1 Hz	$\forall t$	(3.22)	6.2	mGal
DGUPT-GG (3.4.28)	$t_0^{v1} = t_0^{v2} = t_0^{v3} = t_N$		(3.41)	0.02	mGal

Table 4.17: Test CIRCLE-LTN101-v2a1: network configuration.

Figure 4.16 proves that the functional models of the NA approach work succesfully:

- Figure 4.16a points out that the position has been recovered, especially heights — in Figure 4.16c — with a precision better than 0.4 cm.
- The navigation parameters — shown in Figure 4.16e — are recovered with a precision of 18 " for roll (α), pitch (χ) and heading (η).
- The IMU error parameters exhibited in Figures 4.16b and 4.16d are nearly constants within the defined tolerances (bias repeatability) of the IMU.
- Figure 4.16f also displays the gravity disturbance vector, that has to be zero, with a precision better than 6 mGal.

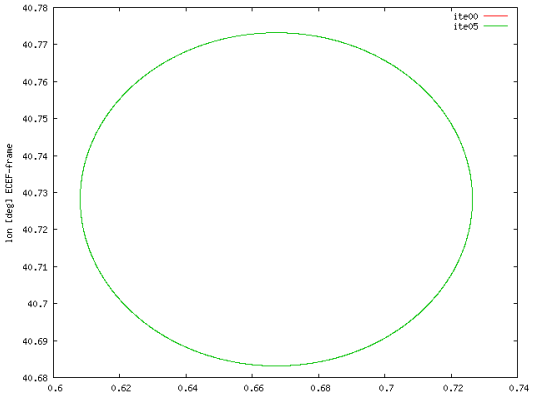

(a) Position (°)

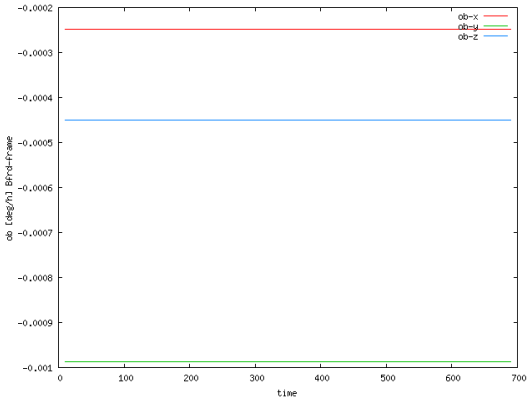

(b) Angular drift ($^\circ\,h^{-1}$)

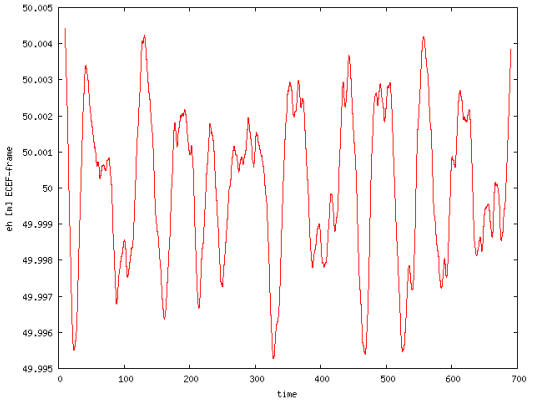

(c) Height (m)

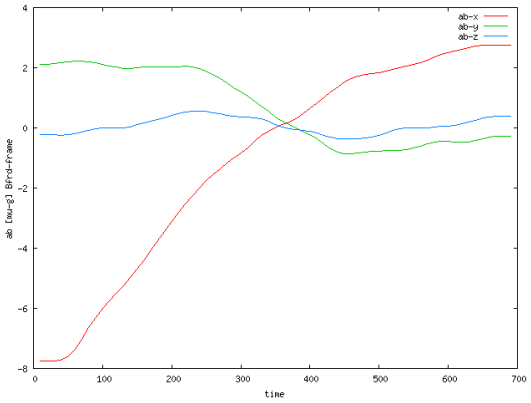

(d) Accelerometer bias (μg)

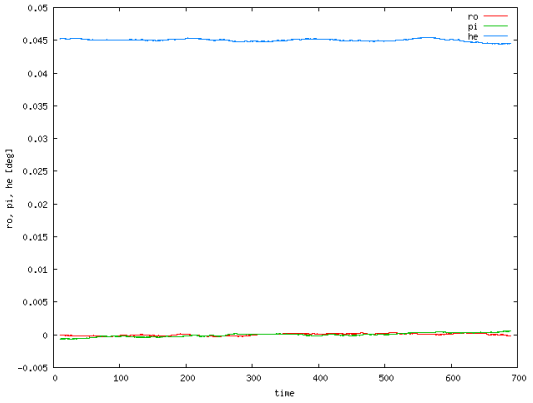

(e) Roll, Pitch and Heading (°)

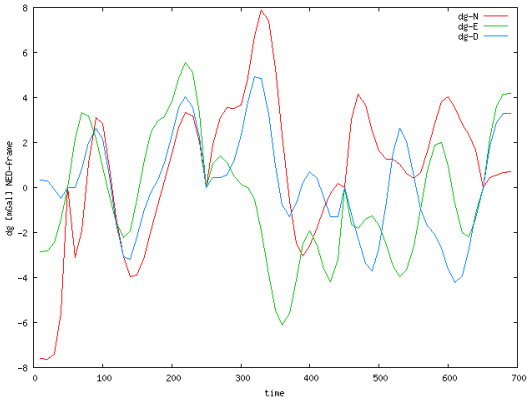

(f) Gravity disturbance (mGal)

Figure 4.16: CIRCLE LTN101b v2a1: adjusted parameters.

4.4.2 CIRCLE vq2a1

As already discussed in Section 4.2, the codification this computation means:

- $\langle q \rangle = q$, indicates that prior knowledge of the vehicle's attitude exists at the beginning (t_0) and at the end (t_N) of the mission.
- $\langle Hz \rangle = 2$: some subsets of parameters — $\underline{o}^{\mathsf{b}}$, $\underline{a}^{\mathsf{b}}$, δg or gg — has been grouped.
- $\langle \delta g_{NE} \rangle = a$: no prior knowledge of the horizontal gravity.
- $\langle method \rangle = 1$, indicates a basic network configuration similar to the Kalman filtering.

LN200

Table 4.18 summarises the network configuration used in this computation.

Model Name	Frequency		Equation	Standard Deviation	
FB-GG (3.4.5)	20.0 Hz	$\forall t$	(3.13)	2.2	10^{-3} m s^{-2}
WIB (3.4.2)	20.0 Hz	$\forall t$	(3.10)	5.2	10^{-5} rad s^{-1}
VEL (3.4.1)	20.0 Hz	$\forall t$	(3.4.1)	0.000 01	m
Q-NORM (3.4.6)	20.0 Hz	$\forall t$	(3.14)	0.01	ppm
OB-O (3.4.35)	0.1 Hz	$\forall t$	(3.48)	4.9	10^{-6} rad s^{-1}
AB-O (3.4.36)	0.1 Hz	$\forall t$	(3.49)	2.0	10^{-3} m s^{-2}
OB (3.4.8)	0.1 Hz	$\forall t$	(3.16)	15.0	10^{-7} rad s^{-1}
AB (3.4.10)	0.1 Hz	$\forall t$	(3.18)	130.0	10^{-4} m s^{-2}
AOFF-O (3.4.37)			(3.50)	0.001	m
CUPT (3.4.16)	1.0 Hz	$\forall t$	(3.26)	0.05	m
GDT-GG (3.4.13)	0.1 Hz	$\forall t$	(3.22)	6.2	mGal
DGUPT-GG (3.4.28)	$t_0^{v1} = t_0^{v2} = t_0^{v3} = t_N$		(3.41)	0.02	mGal
Q-O (3.4.34)		t_0, t_N	(3.47)	0.01	ppm

Table 4.18: Test CIRCLE-LN200-vq2a1: network configuration.

Figure 4.17 proves that the functional models of the NA approach work succesfully:

- Figure 4.17a points out that the position has been recovered, especially heights — in Figure 4.17c — with a precision better than 0.4 cm.
- The navigation parameters — shown in Figure 4.17e — are recovered with a precision of 36 " for roll (α) and pitch (χ) and with a range of 3 ' for heading (η).
- The IMU error parameters exhibited in Figures 4.17b and 4.17d are nearly constants within the defined tolerances (bias repeatability) of the IMU.
- Figure 4.17f also displays the gravity disturbance vector, that has to be zero.

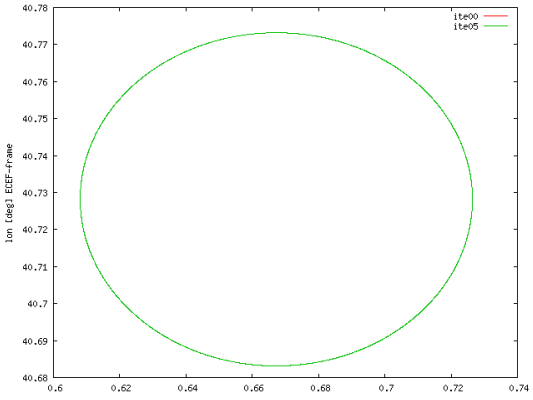

(a) Position (°)

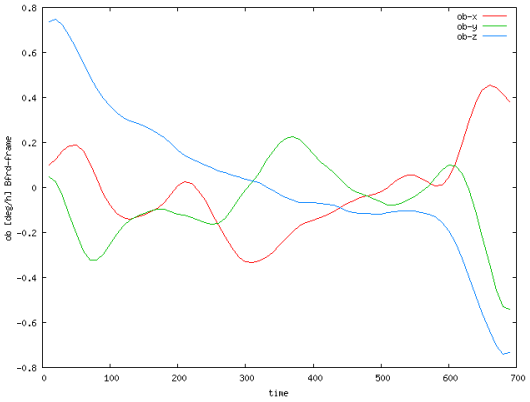

(b) Angular drift (° h^{-1})

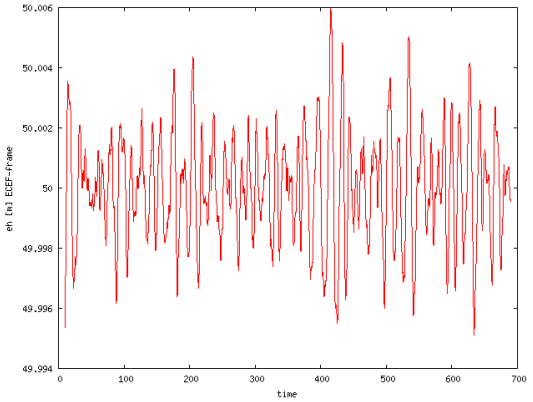

(c) Height (m)

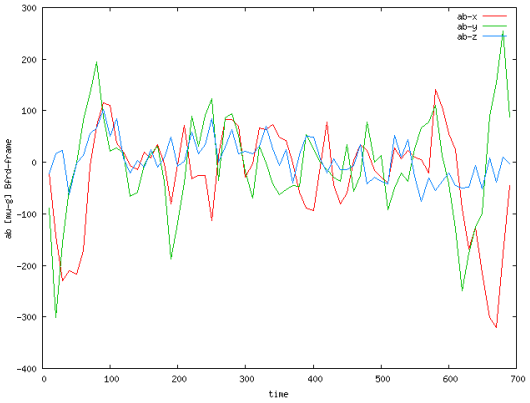

(d) Accelerometer bias (μg)

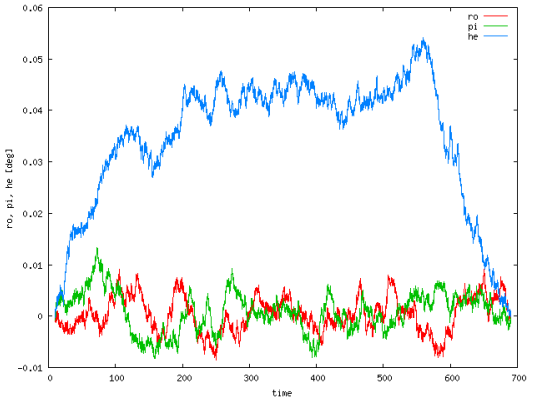

(e) Roll, Pitch and Heading (°)

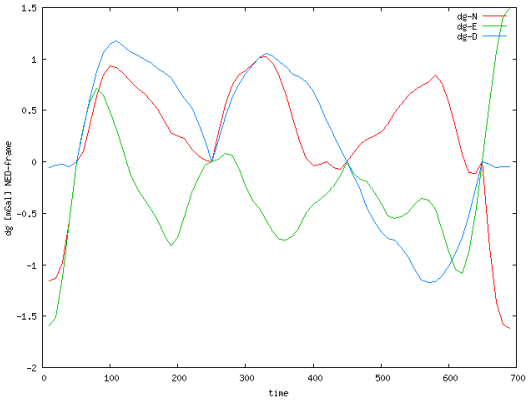

(f) Gravity disturbance (mGal)

Figure 4.17: CIRCLE LN200 vq2a1: adjusted parameters.

LTN101

Table 4.19 summarises the network configuration used in this computation.

Model Name	Frequency		Equation	Standard Deviation	
FB-GG (3.4.5)	20.0 Hz	$\forall t$	(3.13)	4.4	10^{-4} m s^{-2}
WIB (3.4.2)	20.0 Hz	$\forall t$	(3.10)	1.3	10^{-6} rad s^{-1}
VEL (3.4.1)	20.0 Hz	$\forall t$	(3.4.1)	0.000 01	m
Q-NORM (3.4.6)	20.0 Hz	$\forall t$	(3.14)	0.01	ppm
OB-O (3.4.35)	0.1 Hz	$\forall t$	(3.48)	4.9	10^{-8} rad s^{-1}
AB-O (3.4.36)	0.1 Hz	$\forall t$	(3.49)	4.9	10^{-4} m s^{-2}
OB (3.4.8)	0.1 Hz	$\forall t$	(3.16)	61.0	10^{-12} rad s^{-1}
AB (3.4.10)	0.1 Hz	$\forall t$	(3.18)	95.0	10^{-7} m s^{-2}
AOFF-O (3.4.37)			(3.50)	0.001	m
CUPT (3.4.16)	1.0 Hz	$\forall t$	(3.26)	0.05	m
GDT-GG (3.4.13)	0.1 Hz	$\forall t$	(3.22)	6.2	mGal
DGUPT-GG (3.4.28)	$t_0^{v1} = t_0^{v2} = t_0^{v3} = t_N$		(3.41)	0.02	mGal
Q-O (3.4.34)		t_0, t_N	(3.47)	0.01	ppm

Table 4.19: Test CIRCLE-LTN101-vq2a1: network configuration.

Figure 4.18 proves that the functional models of the NA approach work succesfully:

- Figure 4.18a points out that the position has been recovered, especially heights — in 4.18c — with a precision better than 0.4 cm.
- The navigation parameters — shown in Figure 4.18e — are recovered with a precision of 7.2 " for roll (α) and pitch (χ) and with a range of 7 ' for heading (η).
- The IMU error parameters exhibited in Figures 4.18b and 4.18d are nearly constants within the defined tolerances (bias repeatability) of the IMU.
- Figure 4.18f also displays the gravity disturbance vector, that has to be zero.

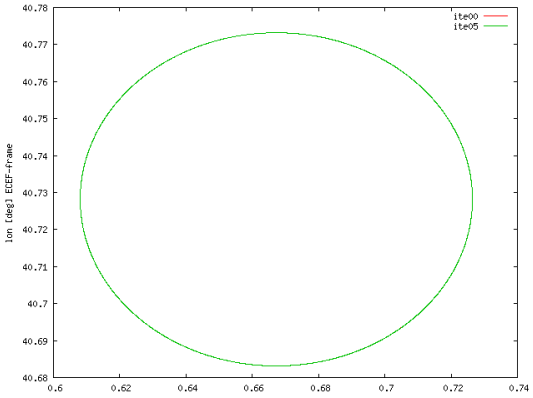

(a) Position (°)

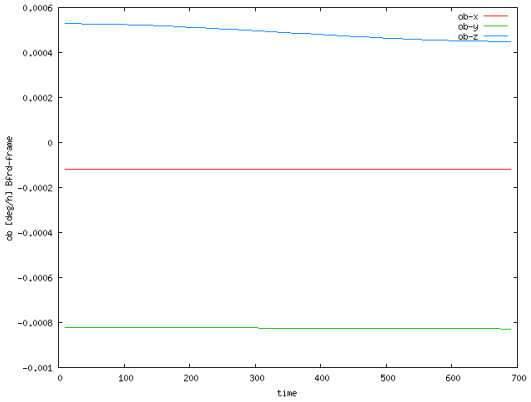

(b) Angular drift ($^\circ\,h^{-1}$)

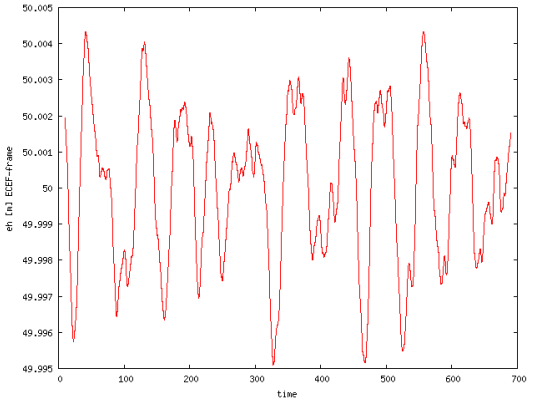

(c) Height (m)

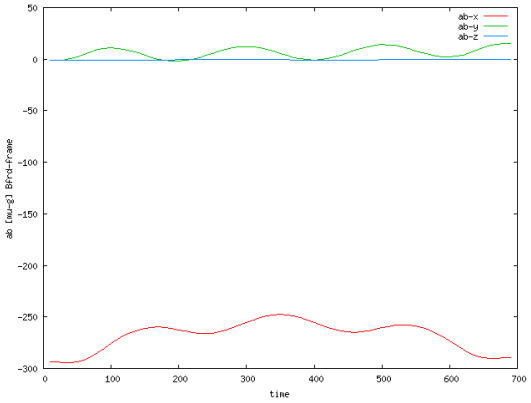

(d) Accelerometer bias (μg)

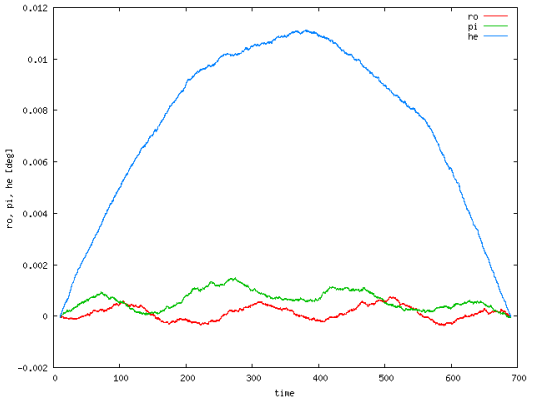

(e) Roll, Pitch and Heading (°)

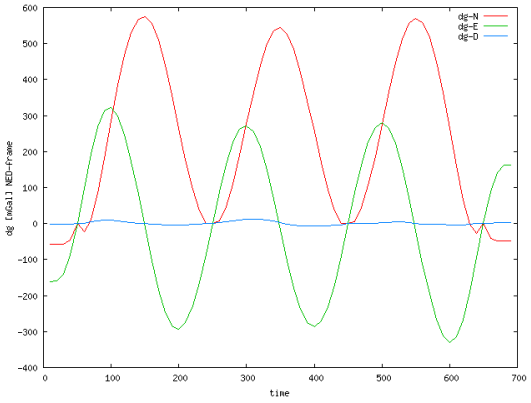

(f) Gravity disturbance (mGal)

Figure 4.18: CIRCLE LTN101b vq2a1: adjusted parameters.

4.4.3 CIRCLE v2a2

As already discussed in Section 4.2, the codification this computation means:

- $\langle Hz \rangle = 2$: some subsets of parameters — $\underline{o}^{\mathtt{b}}$, $\underline{a}^{\mathtt{b}}$, δg or gg — has been grouped.
- $\langle \delta g_{NE} \rangle = a$: no prior knowledge of the horizontal gravity.
- $\langle method \rangle = 2$: GDT-p (changes of the gravity disturbance of closed positions with respect to time) observations are added to the basic configuration.

LN200

Table 4.20 summarises the network configuration used in this computation.

Model Name	Frequency		Equation	Standard Deviation	
FB-GG (3.4.5)	20.0 Hz	$\forall t$	(3.13)	2.2	10^{-3} m s^{-2}
WIB (3.4.2)	20.0 Hz	$\forall t$	(3.10)	5.2	10^{-5} rad s^{-1}
VEL (3.4.1)	20.0 Hz	$\forall t$	(3.4.1)	0.000 01	m
Q-NORM (3.4.6)	20.0 Hz	$\forall t$	(3.14)	0.01	ppm
OB-O (3.4.35)	0.1 Hz	$\forall t$	(3.48)	4.9	10^{-6} rad s^{-1}
AB-O (3.4.36)	0.1 Hz	$\forall t$	(3.49)	2.0	10^{-3} m s^{-2}
OB (3.4.8)	0.1 Hz	$\forall t$	(3.16)	15.0	10^{-7} rad s^{-1}
AB (3.4.10)	0.1 Hz	$\forall t$	(3.18)	130.0	10^{-4} m s^{-2}
AOFF-O (3.4.37)			(3.50)	0.001	m
CUPT (3.4.16)	1.0 Hz	$\forall t$	(3.26)	0.05	m
GDT-GG (3.4.13)	0.1 Hz	$\forall t$	(3.22)	6.2	mGal
GDT-GG (3.4.13)	$v1 = v2 = v3$	$\forall t$	(3.22)	6.2	mGal
DGUPT-GG (3.4.28)	$t_0^{v1} = t_0^{v2} = t_0^{v3} = t_N$		(3.41)	0.02	mGal

Table 4.20: Test CIRCLE-LN200-v2a2: network configuration.

Figure 4.19 proves that the functional models of the NA approach work succesfully:

- Figure 4.19a points out that the position has been recovered, especially heights — in Figure 4.19c — with a precision better than 0.4 cm.
- The navigation parameters — shown in Figure 4.19e — are recovered with a precision better than 0.6 ' for roll (α) and pitch (χ) and 0.9 ' for heading (η).
- The IMU error parameters exhibited in Figures 4.19b and 4.19d are nearly constants within the defined tolerances (bias repeatability) of the IMU.
- Figure 4.19f also displays the gravity disturbance vector, that has to be zero, with a precision of 0.5 mGal.

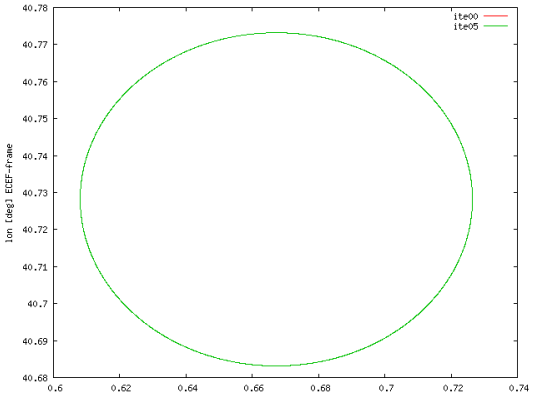

(a) Position (°)

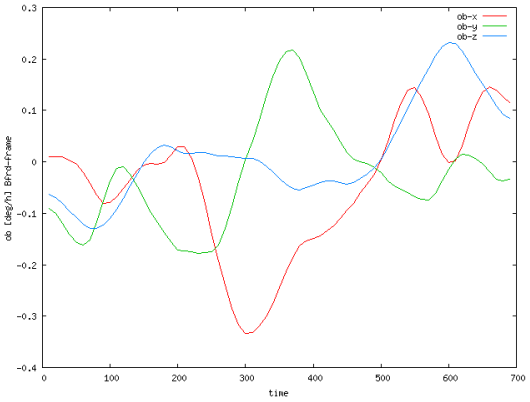

(b) Angular drift ($^\circ\,h^{-1}$)

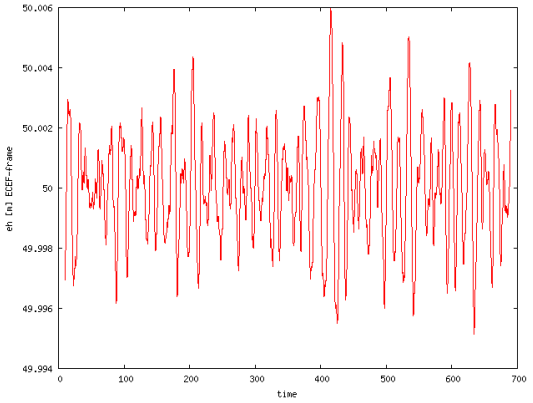

(c) Height (m)

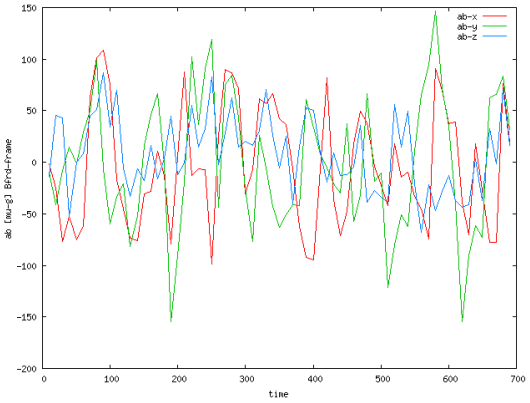

(d) Accelerometer bias (μg)

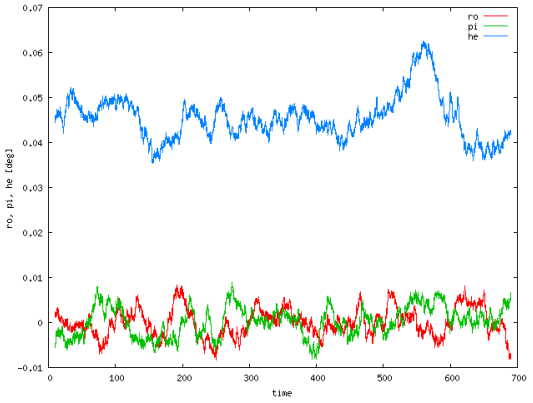

(e) Roll, Pitch and Heading (°)

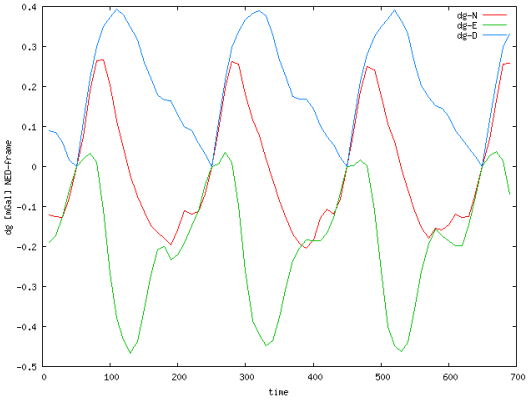

(f) Gravity disturbance (mGal)

Figure 4.19: CIRCLE LN200 v2a2: adjusted parameters.

LTN101

Table 4.21 summarises the network configuration used in this computation.

Model Name	Frequency		Equation	Standard Deviation	
FB-GG (3.4.5)	20.0 Hz	$\forall t$	(3.13)	4.4	10^{-4} m s^{-2}
WIB (3.4.2)	20.0 Hz	$\forall t$	(3.10)	1.3	10^{-6} rad s^{-1}
VEL (3.4.1)	20.0 Hz	$\forall t$	(3.4.1)	0.000 01	m
Q-NORM (3.4.6)	20.0 Hz	$\forall t$	(3.14)	0.01	ppm
OB-O (3.4.35)	0.1 Hz	$\forall t$	(3.48)	4.9	10^{-8} rad s^{-1}
AB-O (3.4.36)	0.1 Hz	$\forall t$	(3.49)	4.9	10^{-4} m s^{-2}
OB (3.4.8)	0.1 Hz	$\forall t$	(3.16)	61.0	10^{-12} rad s^{-1}
AB (3.4.10)	0.1 Hz	$\forall t$	(3.18)	95.0	10^{-7} m s^{-2}
AOFF-O (3.4.37)			(3.50)	0.001	m
CUPT (3.4.16)	1.0 Hz	$\forall t$	(3.26)	0.05	m
GDT-GG (3.4.13)	0.1 Hz	$\forall t$	(3.22)	6.2	mGal
GDT-GG (3.4.13)	$\upsilon 1 = \upsilon 2 = \upsilon 3$	$\forall t$	(3.22)	6.2	mGal
DGUPT-GG (3.4.28)	$t_0^{\upsilon 1} = t_0^{\upsilon 2} = t_0^{\upsilon 3} = t_N$		(3.41)	0.02	mGal

Table 4.21: Test CIRCLE-LTN101-v2a2: network configuration.

Figure 4.20 proves that the functional models of the NA approach work succesfully:

- Figure 4.20a points out that the position has been recovered, especially heights — in Figure 4.20c — with a precision better than 0.5 cm.
- The navigation parameters — shown in Figure 4.20e — are recovered with a precision better than 9 " for roll (α), pitch (χ). For heading (η), a constant value of 2.7 ', with a precision better than 9 ", has been recovered .
- The IMU error parameters exhibited in Figures 4.20b and 4.20d are nearly constants within the defined tolerances (bias repeatability) of the IMU.
- Figure 4.20f also displays the gravity disturbance vector, that has to be zero, with a precision of 3 mGal.

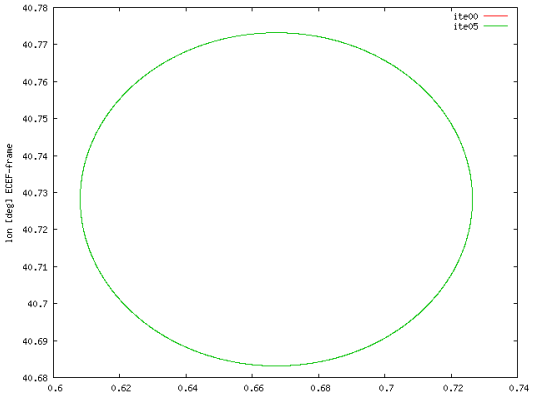

(a) Position (°)

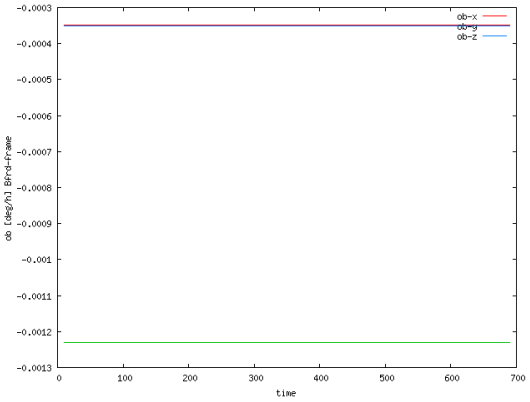

(b) Angular drift ($^\circ\,h^{-1}$)

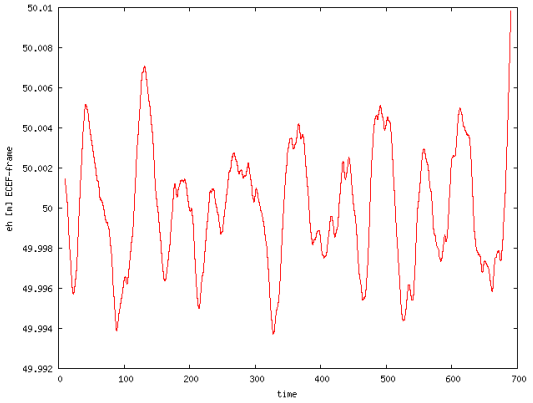

(c) Height (m)

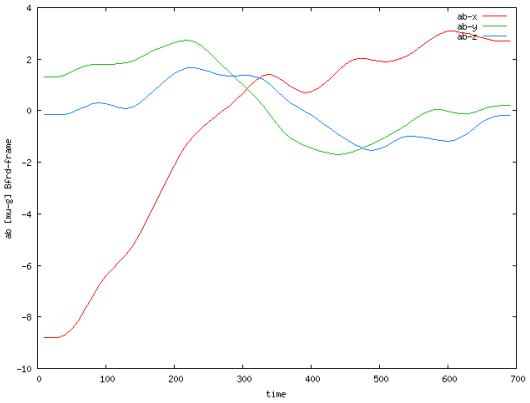

(d) Accelerometer bias (μg)

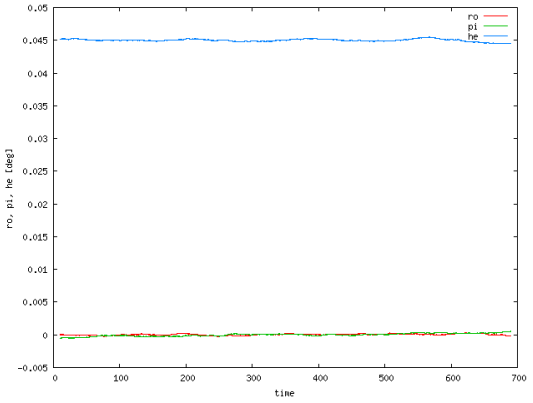

(e) Roll, Pitch and Heading (°)

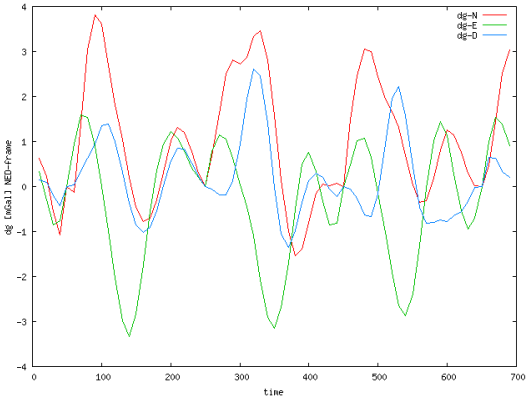

(f) Gravity disturbance (mGal)

Figure 4.20: CIRCLE LTN101b v2a2: adjusted parameters.

4.4.4 CIRCLE vq2a2

As already discussed in Section 4.2, the codification this computation means:

- $\langle q \rangle$,indicates that prior knowledge of the vehicle's attitude exists at the beginning (t_0) and at the end (t_N) of the mission.
- $\langle Hz \rangle = 2$: some subsets of parameters — $\underline{o}^{\mathsf{b}}$, $\underline{a}^{\mathsf{b}}$, δg or gg — has been grouped.
- $\langle \delta g_{NE} \rangle = a$: no prior knowledge of the horizontal gravity.
- $\langle method \rangle = 2$: GDT-p (changes of the gravity disturbance of closed positions with respect to time) observations are added to the basic configuration.

LN200

Table 4.22 summarises the network configuration used in this computation.

Model Name	Frequency		Equation	Standard Deviation	
FB-GG (3.4.5)	20.0 Hz	$\forall t$	(3.13)	2.2	10^{-3} m s^{-2}
WIB (3.4.2)	20.0 Hz	$\forall t$	(3.10)	5.2	10^{-5} rad s^{-1}
VEL (3.4.1)	20.0 Hz	$\forall t$	(3.4.1)	0.000 01	m
Q-NORM (3.4.6)	20.0 Hz	$\forall t$	(3.14)	0.01	ppm
OB-O (3.4.35)	0.1 Hz	$\forall t$	(3.48)	4.9	10^{-6} rad s^{-1}
AB-O (3.4.36)	0.1 Hz	$\forall t$	(3.49)	2.0	10^{-3} m s^{-2}
OB (3.4.8)	0.1 Hz	$\forall t$	(3.16)	15.0	10^{-7} rad s^{-1}
AB (3.4.10)	0.1 Hz	$\forall t$	(3.18)	130.0	10^{-4} m s^{-2}
AOFF-O (3.4.37)			(3.50)	0.001	m
CUPT (3.4.16)	1.0 Hz	$\forall t$	(3.26)	0.05	m
GDT-GG (3.4.13)	0.1 Hz	$\forall t$	(3.22)	6.2	mGal
GDT-GG (3.4.13)	$v1 = v2 = v3$	$\forall t$	(3.22)	6.2	mGal
DGUPT-GG (3.4.28)	$t_0^{v1} = t_0^{v2} = t_0^{v3} = t_N$		(3.41)	0.02	mGal
Q-O (3.4.34)		t_0, t_N	(3.47)	0.01	ppm

Table 4.22: Test CIRCLE-LN200-vq2a2: network configuration.

Figure 4.21 proves that the functional models of the NA approach work succesfully:

- Figures 4.21a and 4.21c point out that the position has been recovered, especially heights with a precision better than 0.5 cm.
- The navigation parameters — shown in Figure 4.21e — are recovered with a precision of 36 " for roll (α) and pitch (χ) and with a range of 3 ' for heading (η).
- The IMU error parameters exhibited in Figures 4.21b and 4.21d are nearly constants within the defined tolerances (bias repeatability) of the IMU.

- Figure 4.21f also displays the gravity disturbance vector, that has to be zero.

LTN101

Table 4.23 summarises the network configuration used in this computation.

Model Name	Frequency		Equation	Standard Deviation	
FB-GG (3.4.5)	20.0 Hz	$\forall t$	(3.13)	4.4	10^{-4} m s^{-2}
WIB (3.4.2)	20.0 Hz	$\forall t$	(3.10)	1.3	10^{-6} rad s^{-1}
VEL (3.4.1)	20.0 Hz	$\forall t$	(3.4.1)	0.000 01	m
Q-NORM (3.4.6)	20.0 Hz	$\forall t$	(3.14)	0.01	ppm
OB-O (3.4.35)	0.1 Hz	$\forall t$	(3.48)	4.9	10^{-8} rad s^{-1}
AB-O (3.4.36)	0.1 Hz	$\forall t$	(3.49)	4.9	10^{-4} m s^{-2}
OB (3.4.8)	0.1 Hz	$\forall t$	(3.16)	61.0	10^{-12} rad s^{-1}
AB (3.4.10)	0.1 Hz	$\forall t$	(3.18)	95.0	10^{-7} m s^{-2}
AOFF-O (3.4.37)			(3.50)	0.001	m
CUPT (3.4.16)	1.0 Hz	$\forall t$	(3.26)	0.05	m
GDT-GG (3.4.13)	0.1 Hz	$\forall t$	(3.22)	6.2	mGal
GDT-GG (3.4.13)	$v1 = v2 = v3$	$\forall t$	(3.22)	6.2	mGal
DGUPT-GG (3.4.28)	$t_0^{v1} = t_0^{v2} = t_0^{v3} = t_N$		(3.41)	0.02	mGal
Q-O (3.4.34)		t_0, t_N	(3.47)	0.01	ppm

Table 4.23: Test CIRCLE-LTN101-vq2a2: network configuration.

Figure 4.22 proves that the functional models of the NA approach work succesfully:

- Figures 4.22a and 4.22c point out that the position has been recovered, especially heights with a precision better than 1 cm.
- The navigation parameters — shown in Figure 4.22e — are recovered with a precision of 4 " for roll (α) and pitch (χ) and with a range of 0.6 ’ for heading (η).
- The IMU error parameters exhibited in Figures 4.22b and 4.22d are nearly constants within the defined tolerances (bias repeatability) of the IMU.
- Figure 4.22f also displays the gravity disturbance vector, that has to be zero.

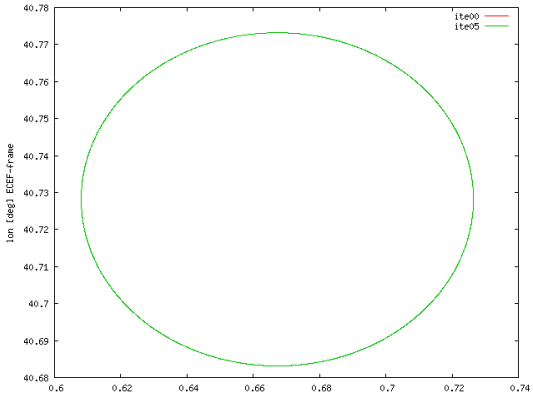

(a) Position (°)

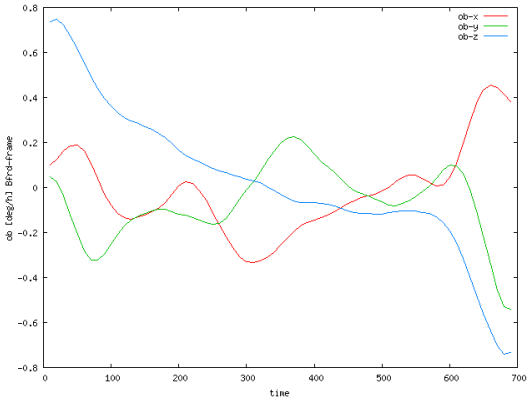

(b) Angular drift ($^\circ\,h^{-1}$)

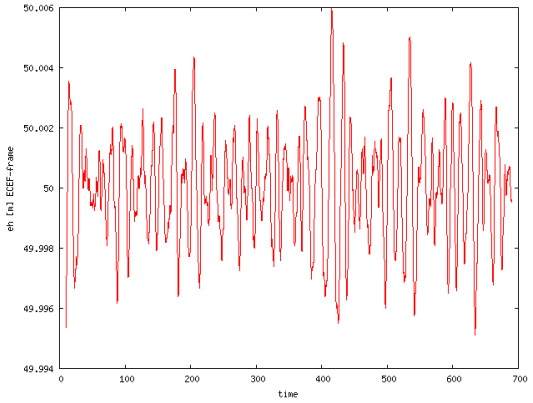

(c) Height (m)

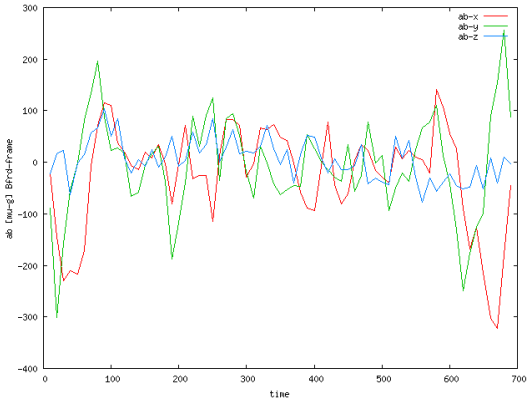

(d) Accelerometer bias (μg)

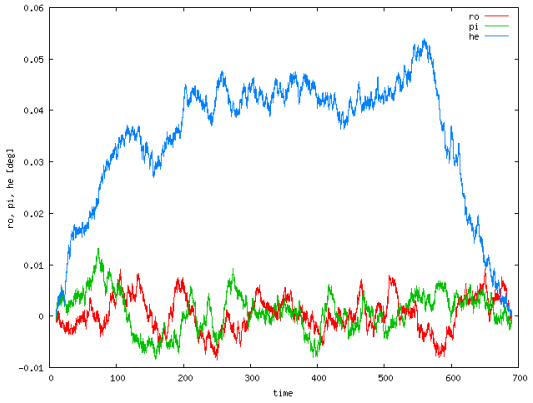

(e) Roll, Pitch and Heading (°)

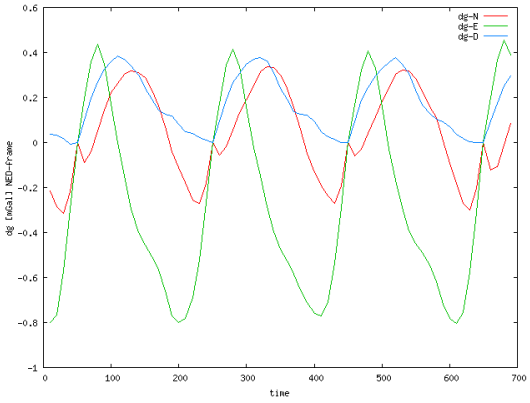

(f) Gravity disturbance (mGal)

Figure 4.21: CIRCLE LN200 vq2a2: adjusted parameters.

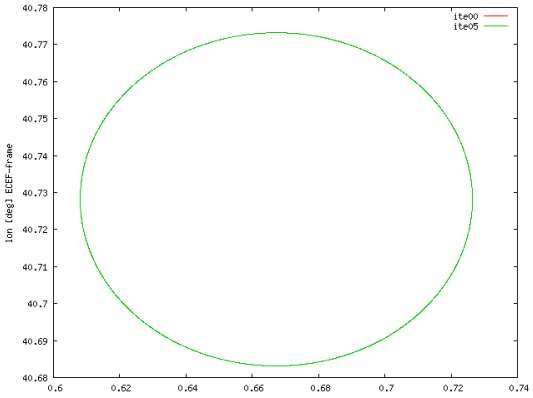

(a) Position (°)

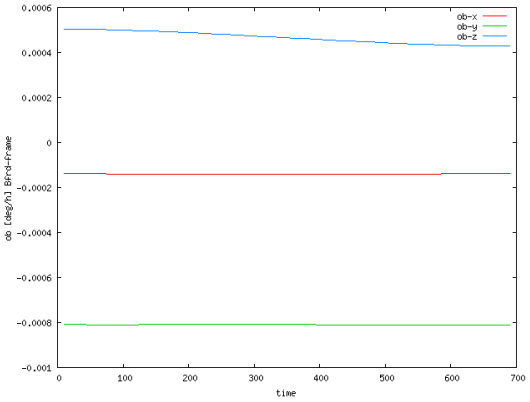

(b) Angular drift ($^\circ\,h^{-1}$)

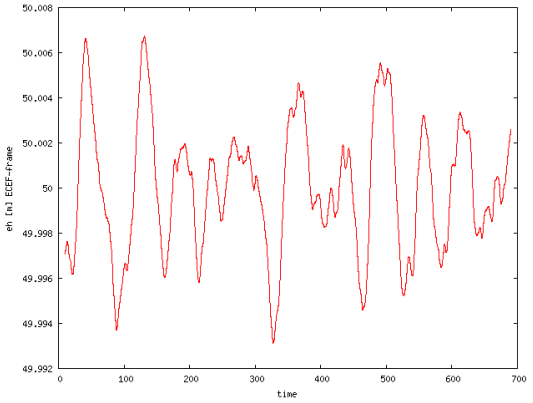

(c) Height (m)

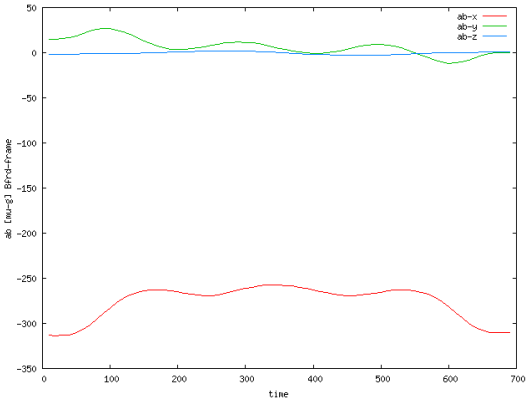

(d) Accelerometer bias (μg)

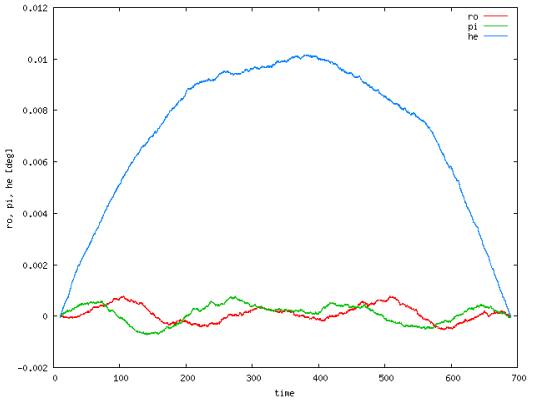

(e) Roll, Pitch and Heading (°)

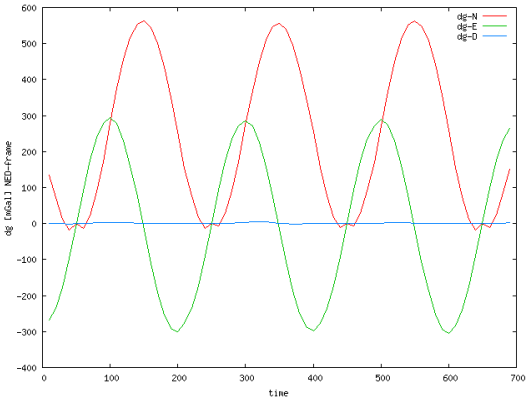

(f) Gravity disturbance (mGal)

Figure 4.22: CIRCLE LTN101b vq2a2: adjusted parameters.

4.4.5 CIRCLE v2b1

As already discussed in Section 4.2, the codification this computation means:

- $\langle Hz \rangle = 2$: some subsets of parameters — $\underline{o}^{\mathsf{b}}$, $\underline{a}^{\mathsf{b}}$, δg or gg — has been grouped.
- $\langle \delta g_{NE} \rangle = b$, indicates that, for all t, $\delta g_N(t) = \delta g_E(t) \approx 0$.
- $\langle method \rangle = 1$, indicates a basic network configuration similar to the Kalman filtering.

LN200

Table 4.24 summarises the network configuration used in this computation.

Model Name	Frequency		Equation	Standard Deviation	
FB-GG (3.4.5)	20.0 Hz	$\forall t$	(3.13)	2.2	10^{-3} m s^{-2}
WIB (3.4.2)	20.0 Hz	$\forall t$	(3.10)	5.2	10^{-5} rad s^{-1}
VEL (3.4.1)	20.0 Hz	$\forall t$	(3.4.1)	0.000 01	m
Q-NORM (3.4.6)	20.0 Hz	$\forall t$	(3.14)	0.01	ppm
OB-O (3.4.35)	0.1 Hz	$\forall t$	(3.48)	4.9	10^{-6} rad s^{-1}
AB-O (3.4.36)	0.1 Hz	$\forall t$	(3.49)	2.0	10^{-3} m s^{-2}
OB (3.4.8)	0.1 Hz	$\forall t$	(3.16)	15.0	10^{-7} rad s^{-1}
AB (3.4.10)	0.1 Hz	$\forall t$	(3.18)	130.0	10^{-4} m s^{-2}
AOFF-O (3.4.37)			(3.50)	0.001	m
CUPT (3.4.16)	1.0 Hz	$\forall t$	(3.26)	0.05	m
GDT-GG (3.4.13)	0.1 Hz	$\forall t$	(3.22)	6.2	mGal
DGUPT-GG (3.4.28)	0.1 Hz	$\forall t$	(3.41)	0.02	mGal

Table 4.24: Test CIRCLE-LN200-v2b1: network configuration.

Figure 4.23 proves that the functional models of the NA approach work succesfully:

- Figures 4.23a and 4.23c point out that the position has been recovered, especially heights with a precision better than 0.4 cm.
- The navigation parameters — shown in Figure 4.23e — are recovered with a precision better than 0.6 ' for roll (α) and pitch (χ). For heading (η), moreless a constant value of 2.7 ', with a precision of 0.6 ', has been recovered.
- The IMU error parameters exhibited in Figures 4.23b and 4.23d are nearly constants within the defined tolerances (bias repeatability) of the IMU.
- Figure 4.23f also displays the gravity disturbance vector, that has to be zero, with a precision of 1 mGal.

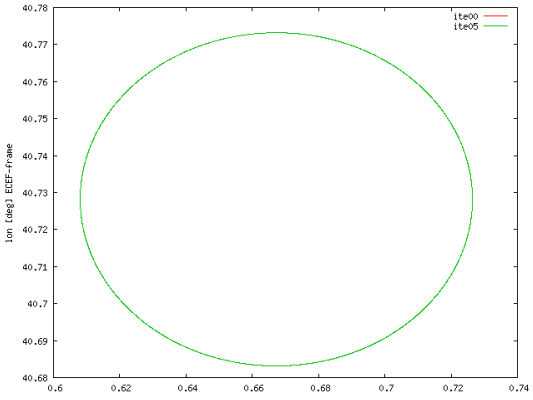

(a) Position (°)

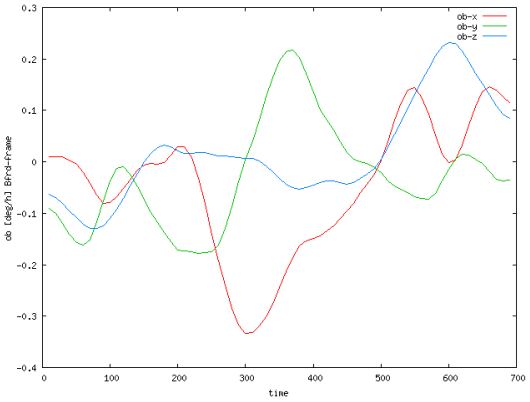

(b) Angular drift ($^\circ\,h^{-1}$)

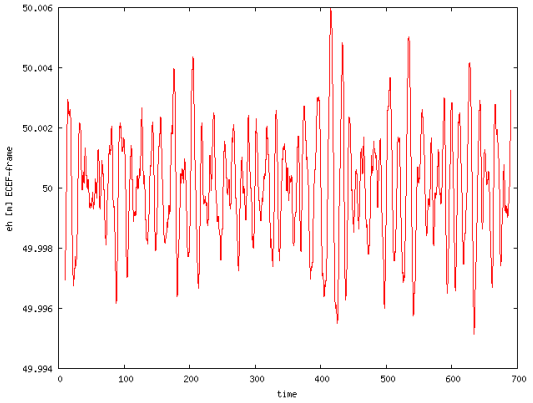

(c) Height (m)

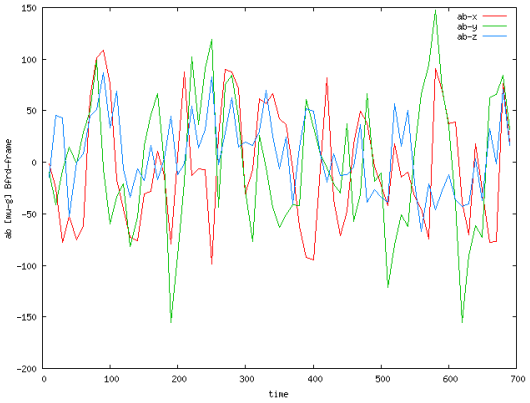

(d) Accelerometer bias (μg)

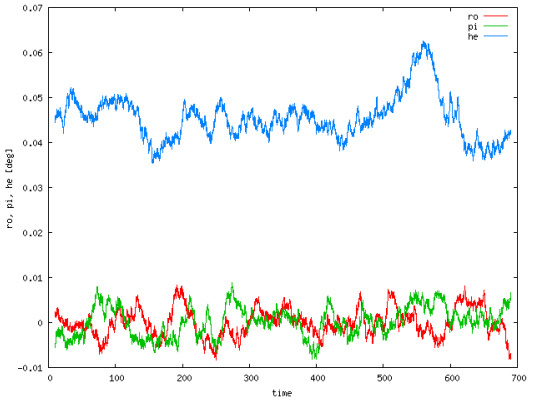

(e) Roll, Pitch and Heading (°)

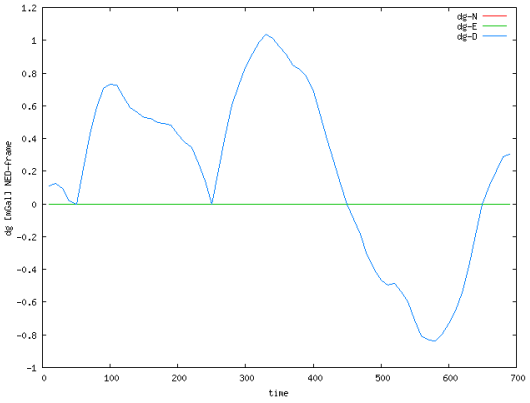

(f) Gravity disturbance (mGal)

Figure 4.23: CIRCLE LN200 v2b1: adjusted parameters.

LTN101

Table 4.25 summarises the network configuration used in this computation.

Model Name	Frequency		Equation	Standard Deviation	
FB-GG (3.4.5)	20.0 Hz	$\forall t$	(3.13)	4.4	10^{-4} m s^{-2}
WIB (3.4.2)	20.0 Hz	$\forall t$	(3.10)	1.3	10^{-6} rad s^{-1}
VEL (3.4.1)	20.0 Hz	$\forall t$	(3.4.1)	0.000 01	m
Q-NORM (3.4.6)	20.0 Hz	$\forall t$	(3.14)	0.01	ppm
OB-O (3.4.35)	0.1 Hz	$\forall t$	(3.48)	4.9	10^{-8} rad s^{-1}
AB-O (3.4.36)	0.1 Hz	$\forall t$	(3.49)	4.9	10^{-4} m s^{-2}
OB (3.4.8)	0.1 Hz	$\forall t$	(3.16)	61.0	10^{-12} rad s^{-1}
AB (3.4.10)	0.1 Hz	$\forall t$	(3.18)	95.0	10^{-7} m s^{-2}
AOFF-O (3.4.37)			(3.50)	0.001	m
CUPT (3.4.16)	1.0 Hz	$\forall t$	(3.26)	0.05	m
GDT-GG (3.4.13)	0.1 Hz	$\forall t$	(3.22)	6.2	mGal
DGUPT-GG (3.4.28)	0.1 Hz	$\forall t$	(3.41)	0.02	mGal

Table 4.25: Test CIRCLE-LTN101-v2b1: network configuration.

Figure 4.24 proves that the functional models of the NA approach work succesfully:

- Figures 4.24a and 4.24c point out that the position has been recovered, especially heights with a precision better than 0.4 cm.
- The navigation parameters — shown in Figure 4.24e — are recovered with a precision of 18 " for roll (α), pitch (χ) and heading (η).
- The IMU error parameters exhibited in Figures 4.24b and 4.24d are nearly constants within the defined tolerances (bias repeatability) of the IMU.
- Figure 4.24f also displays the gravity disturbance vector, that has to be zero.

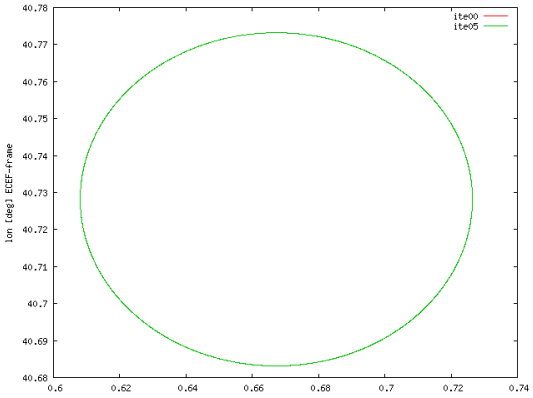

(a) Position (°)

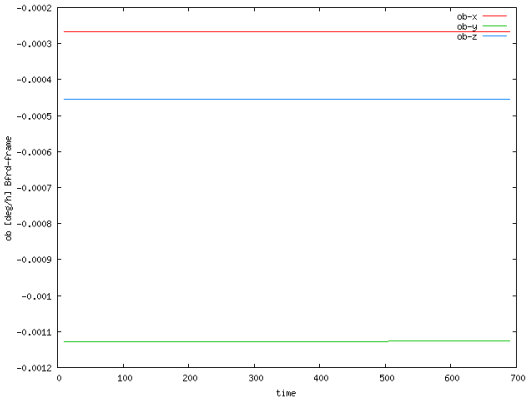

(b) Angular drift (° h^{-1})

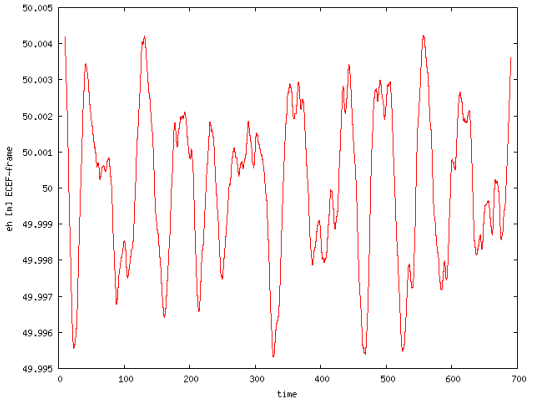

(c) Height (m)

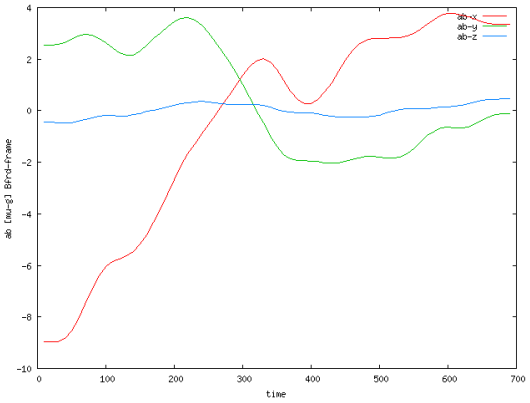

(d) Accelerometer bias (μg)

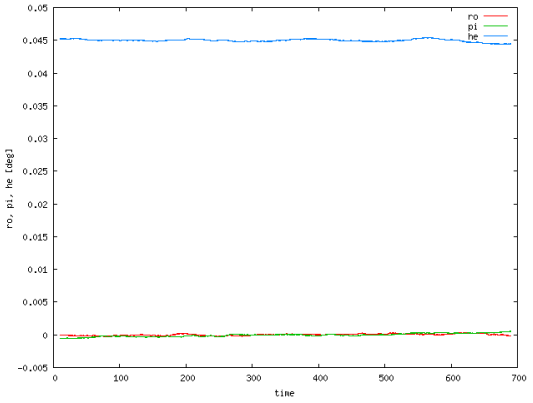

(e) Roll, Pitch and Heading (°)

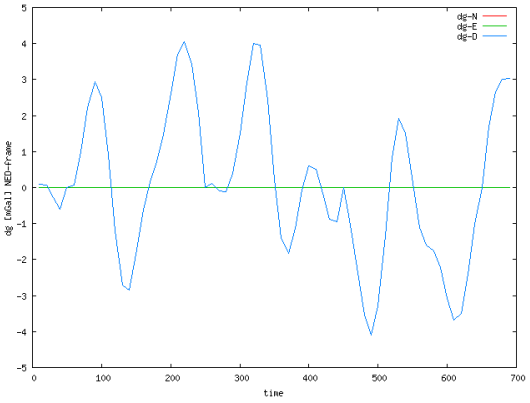

(f) Gravity disturbance (mGal)

Figure 4.24: CIRCLE LTN101b v2b1: adjusted parameters.

4.4.6 CIRCLE vq2b1

As already discussed in Section 4.2, the codification this computation means:

- $\langle q \rangle = q$, indicates that prior knowledge of the vehicle's attitude exists at the beginning (t_0) and at the end (t_N) of the mission.
- $\langle Hz \rangle = 2$: some subsets of parameters — $\underline{o}^{\mathsf{b}}$, $\underline{a}^{\mathsf{b}}$, δg or gg — has been grouped.
- $\langle \delta g_{NE} \rangle = b$, indicates that, for all t, $\delta g_N(t) = \delta g_E(t) \approx 0$.
- $\langle method \rangle = 1$, indicates a basic network configuration similar to the Kalman filtering.

LN200

Table 4.26 summarises the network configuration used in this computation.

Model Name	Frequency		Equation	Standard Deviation	
FB-GG (3.4.5)	20.0 Hz	$\forall t$	(3.13)	2.2	10^{-3} m s^{-2}
WIB (3.4.2)	20.0 Hz	$\forall t$	(3.10)	5.2	10^{-5} rad s^{-1}
VEL (3.4.1)	20.0 Hz	$\forall t$	(3.4.1)	0.000 01	m
Q-NORM (3.4.6)	20.0 Hz	$\forall t$	(3.14)	0.01	ppm
OB-O (3.4.35)	0.1 Hz	$\forall t$	(3.48)	4.9	10^{-6} rad s^{-1}
AB-O (3.4.36)	0.1 Hz	$\forall t$	(3.49)	2.0	10^{-3} m s^{-2}
OB (3.4.8)	0.1 Hz	$\forall t$	(3.16)	15.0	10^{-7} rad s^{-1}
AB (3.4.10)	0.1 Hz	$\forall t$	(3.18)	130.0	10^{-4} m s^{-2}
AOFF-O (3.4.37)			(3.50)	0.001	m
CUPT (3.4.16)	1.0 Hz	$\forall t$	(3.26)	0.05	m
GDT-GG (3.4.13)	0.1 Hz	$\forall t$	(3.22)	6.2	mGal
DGUPT-GG (3.4.28)	0.1 Hz	$\forall t$	(3.41)	0.02	mGal
Q-O (3.4.34)		t_0, t_N	(3.47)	0.01	ppm

Table 4.26: Test CIRCLE-LN200-vq2b1: network configuration.

Figure 4.25 proves that the functional models of the NA approach work succesfully:

- Figures 4.25a and 4.25c point out that the position has been recovered, especially heights with a precision better than 0.4 cm.
- The navigation parameters — shown in Figure 4.25e — are recovered with a precision of 36 " for roll (α) and pitch (χ) and with a range of 3 ' for heading (η).
- The IMU error parameters exhibited in Figures 4.25b and 4.25d are nearly constants within the defined tolerances (bias repeatability) of the IMU.
- Figure 4.25f also displays the gravity disturbance vector, that has to be zero.

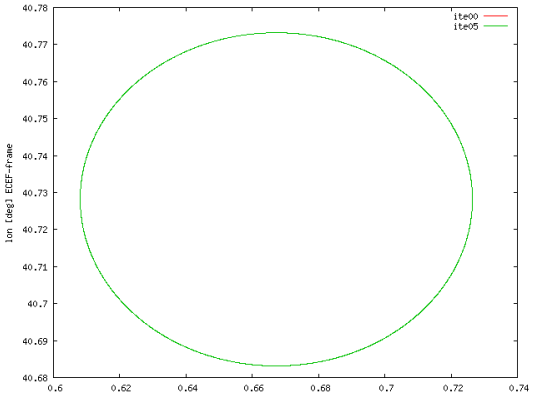

(a) Position (°)

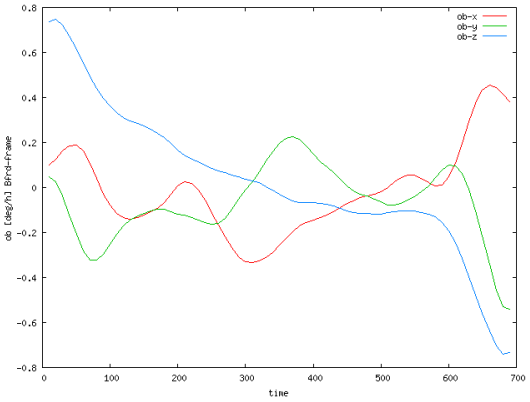

(b) Angular drift ($^\circ\,h^{-1}$)

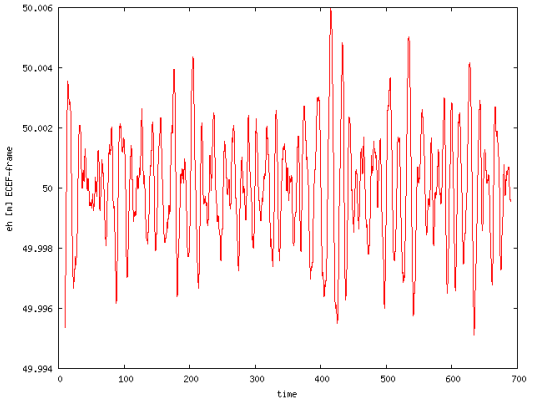

(c) Height (m)

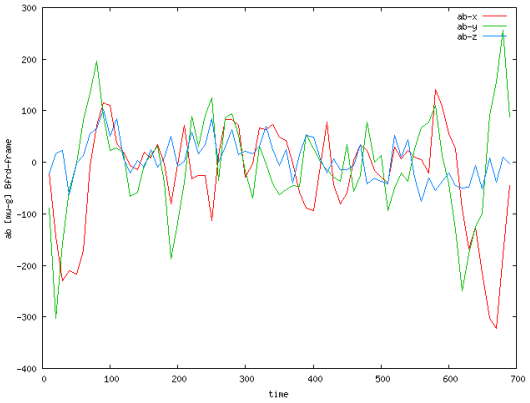

(d) Accelerometer bias (μg)

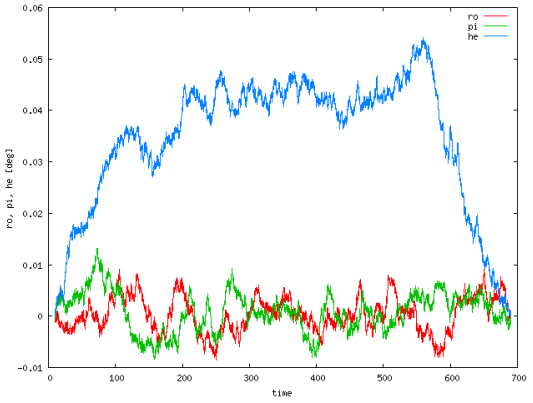

(e) Roll, Pitch and Heading (°)

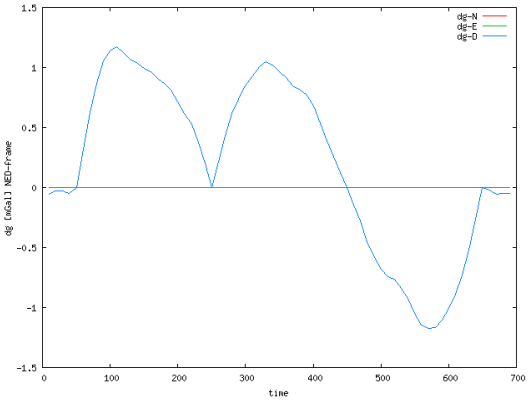

(f) Gravity disturbance (mGal)

Figure 4.25: CIRCLE LN200 vq2b1: adjusted parameters.

LTN101

Table 4.27 summarises the network configuration used in this computation.

Model Name	Frequency		Equation	Standard Deviation	
FB-GG (3.4.5)	20.0 Hz	$\forall t$	(3.13)	4.4	10^{-4} m s^{-2}
WIB (3.4.2)	20.0 Hz	$\forall t$	(3.10)	1.3	10^{-6} rad s^{-1}
VEL (3.4.1)	20.0 Hz	$\forall t$	(3.4.1)	0.000 01	m
Q-NORM (3.4.6)	20.0 Hz	$\forall t$	(3.14)	0.01	ppm
OB-O (3.4.35)	0.1 Hz	$\forall t$	(3.48)	4.9	10^{-8} rad s^{-1}
AB-O (3.4.36)	0.1 Hz	$\forall t$	(3.49)	4.9	10^{-4} m s^{-2}
OB (3.4.8)	0.1 Hz	$\forall t$	(3.16)	61.0	10^{-12} rad s^{-1}
AB (3.4.10)	0.1 Hz	$\forall t$	(3.18)	95.0	10^{-7} m s^{-2}
AOFF-O (3.4.37)			(3.50)	0.001	m
CUPT (3.4.16)	1.0 Hz	$\forall t$	(3.26)	0.05	m
GDT-GG (3.4.13)	0.1 Hz	$\forall t$	(3.22)	6.2	mGal
DGUPT-GG (3.4.28)	0.1 Hz	$\forall t$	(3.41)	0.02	mGal
Q-O (3.4.34)		t_0, t_N	(3.47)	0.01	ppm

Table 4.27: Test CIRCLE-LTN101-vq2b1: network configuration.

Figure 4.26 proves that the functional models of the NA approach work succesfully:

- Figures 4.26a and 4.26c point out that the position has been recovered, especially heights with a precision better than 0.5 cm.
- The navigation parameters — shown in Figure 4.26e — are recovered with a precision of 18 " for roll (α) and pitch (χ) and with a range of 2.4 ’ for heading (η).
- The IMU error parameters exhibited in Figures 4.26b and 4.26d are nearly constants within the defined tolerances (bias repeatability) of the IMU.
- Figure 4.26f also displays the gravity disturbance vector, that has to be zero.

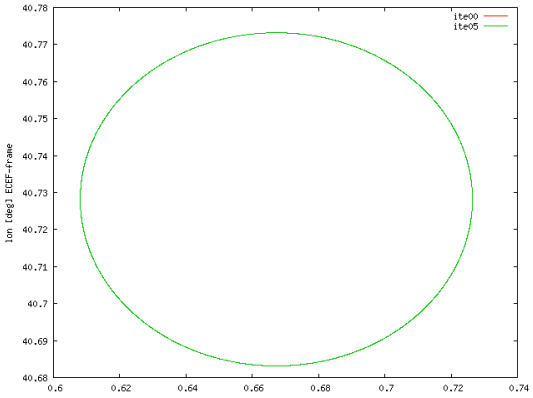

(a) Position (°)

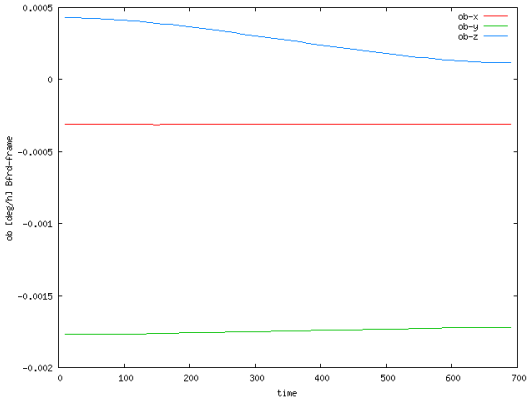

(b) Angular drift ($^\circ\,h^{-1}$)

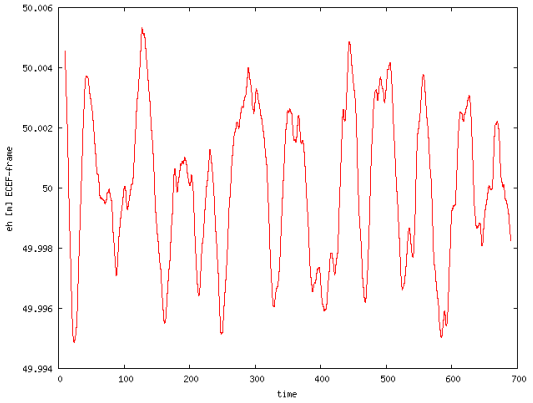

(c) Height (m)

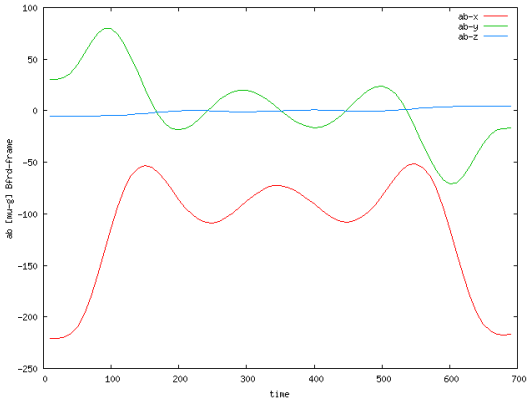

(d) Accelerometer bias (μg)

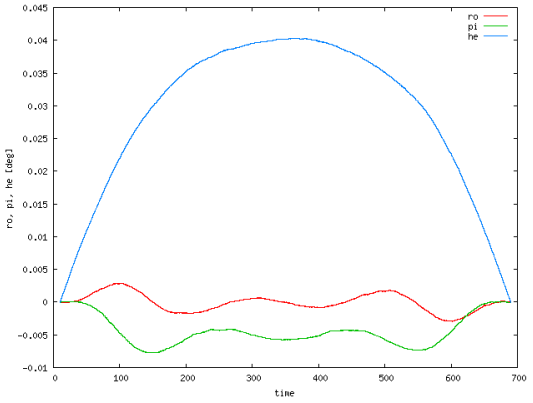

(e) Roll, Pitch and Heading (°)

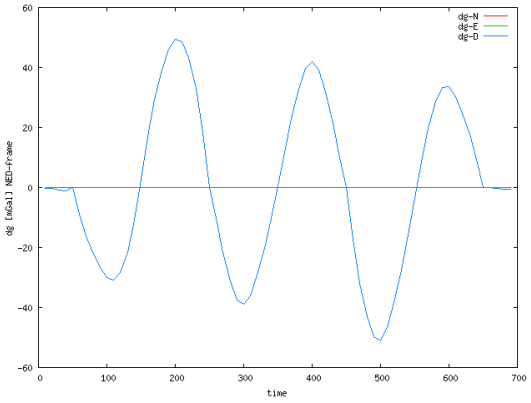

(f) Gravity disturbance (mGal)

Figure 4.26: CIRCLE LTN101b vq2b1: adjusted parameters.

4.4.7 CIRCLE v2b2

As already discussed in Section 4.2, the codification this computation means:

- $\langle Hz \rangle = 2$: some subsets of parameters — $\underline{o}^{\mathsf{b}}$, $\underline{a}^{\mathsf{b}}$, δg or gg — has been grouped.
- $\langle \delta g_{NE} \rangle = b$,indicates that, for all t, $\delta g_N(t) = \delta g_E(t) \approx 0$.
- $\langle method \rangle = 2$: GDT-p (changes of the gravity disturbance of closed positions with respect to time) observations are added to the basic configuration.

LN200

Table 4.28 summarises the network configuration used in this computation.

Model Name	Frequency		Equation	Standard Deviation	
FB-GG (3.4.5)	20.0 Hz	$\forall t$	(3.13)	2.2	10^{-3} m s^{-2}
WIB (3.4.2)	20.0 Hz	$\forall t$	(3.10)	5.2	10^{-5} rad s^{-1}
VEL (3.4.1)	20.0 Hz	$\forall t$	(3.4.1)	0.000 01	m
Q-NORM (3.4.6)	20.0 Hz	$\forall t$	(3.14)	0.01	ppm
OB-O (3.4.35)	0.1 Hz	$\forall t$	(3.48)	4.9	10^{-6} rad s^{-1}
AB-O (3.4.36)	0.1 Hz	$\forall t$	(3.49)	2.0	10^{-3} m s^{-2}
OB (3.4.8)	0.1 Hz	$\forall t$	(3.16)	15.0	10^{-7} rad s^{-1}
AB (3.4.10)	0.1 Hz	$\forall t$	(3.18)	130.0	10^{-4} m s^{-2}
AOFF-O (3.4.37)			(3.50)	0.001	m
CUPT (3.4.16)	1.0 Hz	$\forall t$	(3.26)	0.05	m
GDT-GG (3.4.13)	0.1 Hz	$\forall t$	(3.22)	6.2	mGal
GDT-GG (3.4.13)	$v1 = v2 = v3$	$\forall t$	(3.22)	6.2	mGal
DGUPT-GG (3.4.28)	0.1 Hz	$\forall t$	(3.41)	0.02	mGal

Table 4.28: Test CIRCLE-LN200-v2b2: network configuration.

Figure 4.27 proves that the functional models of the NA approach work succesfully:

- Figures 4.27a and 4.27c point out that the position has been recovered, especially heights with a precision better than 0.4 cm.
- The navigation parameters — shown in Figure 4.27e — are recovered with a precision better of 36 " for roll (α), pitch (χ) and heading (η).
- The IMU error parameters exhibited in Figures 4.27b and 4.27d are nearly constants within the defined tolerances (bias repeatability) of the IMU.
- Figure 4.27f also displays the gravity disturbance vector, that has to be zero.

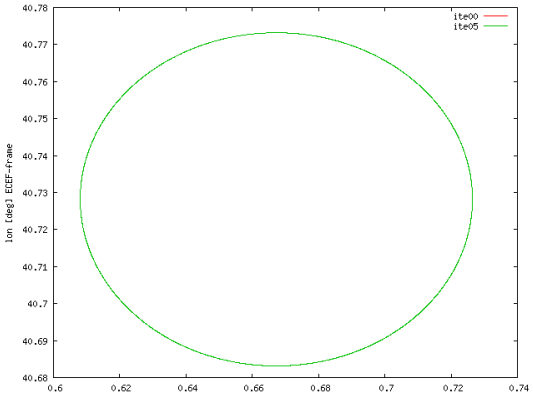

(a) Position (°)

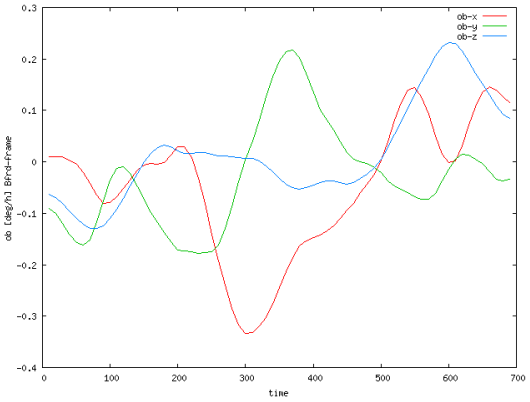

(b) Angular drift ($^\circ\,h^{-1}$)

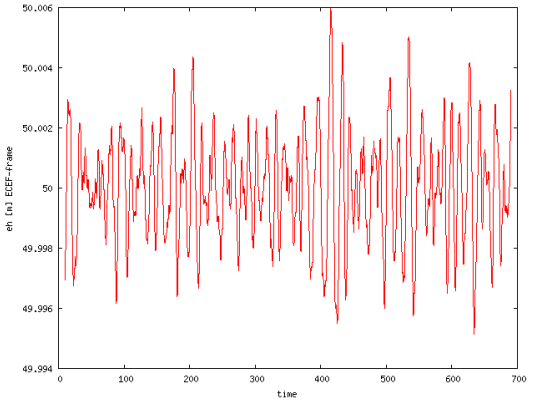

(c) Height (m)

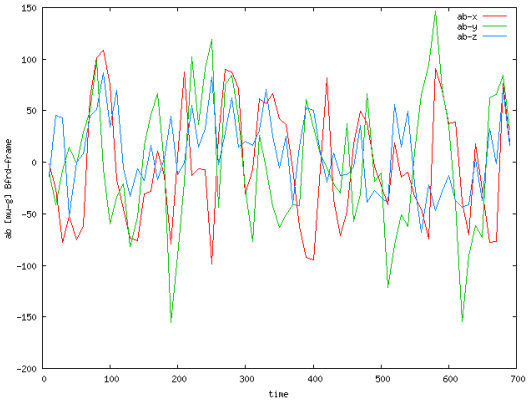

(d) Accelerometer bias (μg)

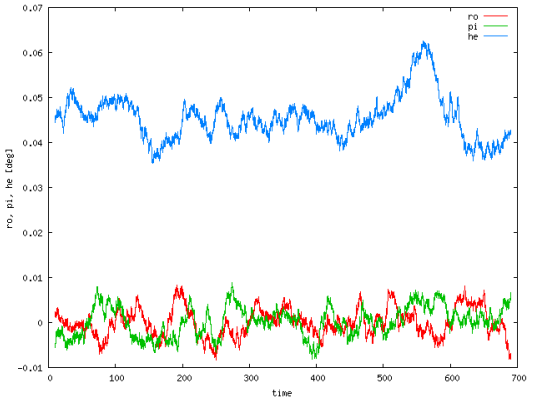

(e) Roll, Pitch and Heading (°)

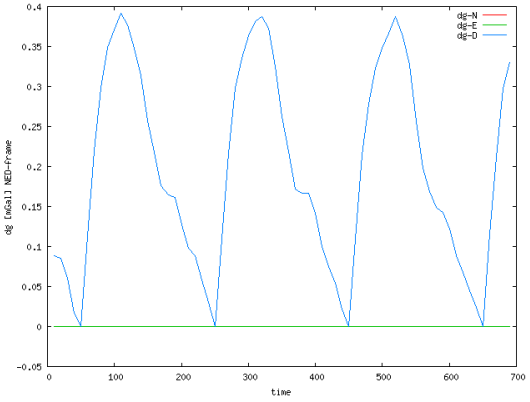

(f) Gravity disturbance (mGal)

Figure 4.27: CIRCLE LN200 v2b2: adjusted parameters.

LTN101

Table 4.29 summarises the network configuration used in this computation.

Model Name	Frequency		Equation	Standard Deviation	
FB-GG (3.4.5)	20.0 Hz	$\forall t$	(3.13)	4.4	10^{-4} m s^{-2}
WIB (3.4.2)	20.0 Hz	$\forall t$	(3.10)	1.3	10^{-6} rad s^{-1}
VEL (3.4.1)	20.0 Hz	$\forall t$	(3.4.1)	0.000 01	m
Q-NORM (3.4.6)	20.0 Hz	$\forall t$	(3.14)	0.01	ppm
OB-O (3.4.35)	0.1 Hz	$\forall t$	(3.48)	4.9	10^{-8} rad s^{-1}
AB-O (3.4.36)	0.1 Hz	$\forall t$	(3.49)	4.9	10^{-4} m s^{-2}
OB (3.4.8)	0.1 Hz	$\forall t$	(3.16)	61.0	10^{-12} rad s^{-1}
AB (3.4.10)	0.1 Hz	$\forall t$	(3.18)	95.0	10^{-7} m s^{-2}
AOFF-O (3.4.37)			(3.50)	0.001	m
CUPT (3.4.16)	1.0 Hz	$\forall t$	(3.26)	0.05	m
GDT-GG (3.4.13)	0.1 Hz	$\forall t$	(3.22)	6.2	mGal
GDT-GG (3.4.13)	$\nu 1 = \nu 2 = \nu 3$	$\forall t$	(3.22)	6.2	mGal
DGUPT-GG (3.4.28)	0.1 Hz	$\forall t$	(3.41)	0.02	mGal

Table 4.29: Test CIRCLE-LTN101-v2b2: network configuration.

Figure 4.28 proves that the functional models of the NA approach work succesfully:

- Figures 4.28a and 4.28c point out that the position has been recovered, especially heights with a precision better than 1 cm.
- The navigation parameters — shown in Figure 4.28e — are recovered with a precision of 9 " for roll (α), pitch (χ) and heading (η).
- The IMU error parameters exhibited in Figures 4.28b and 4.28d are nearly constants within the defined tolerances (bias repeatability) of the IMU.
- Figure 4.28f also displays the gravity disturbance vector, that has to be zero.

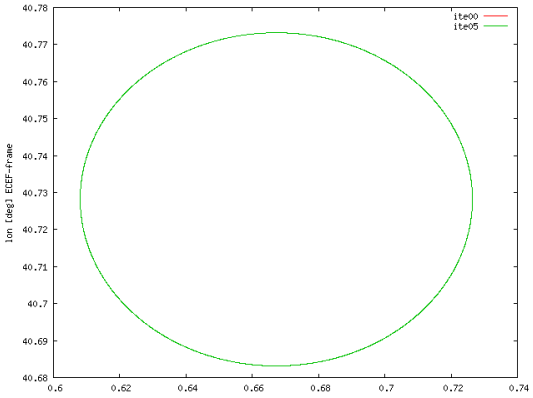

(a) Position (°)

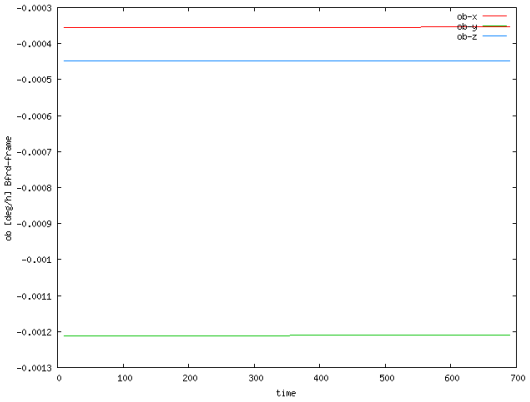

(b) Angular drift ($^\circ\,h^{-1}$)

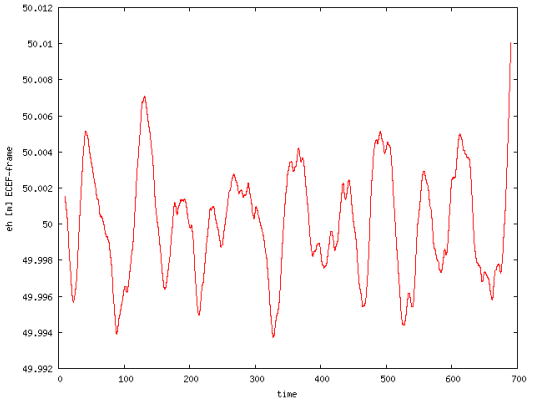

(c) Height (m)

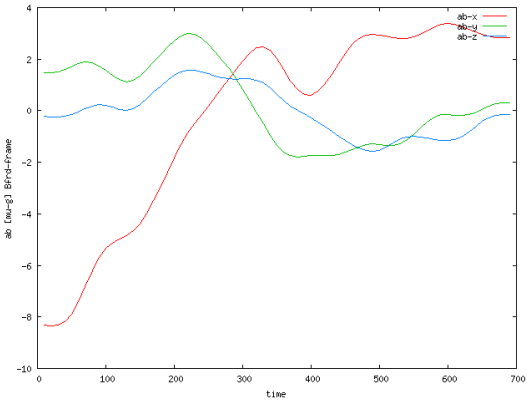

(d) Accelerometer bias (μg)

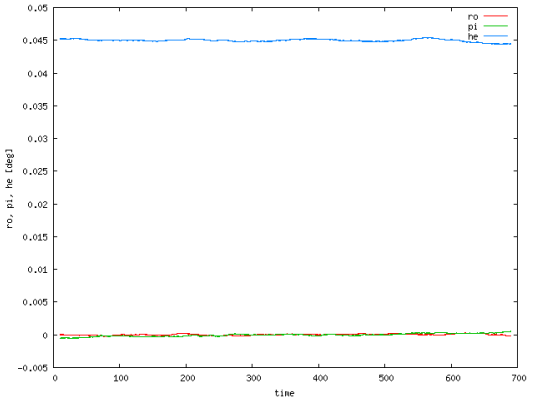

(e) Roll, Pitch and Heading (°)

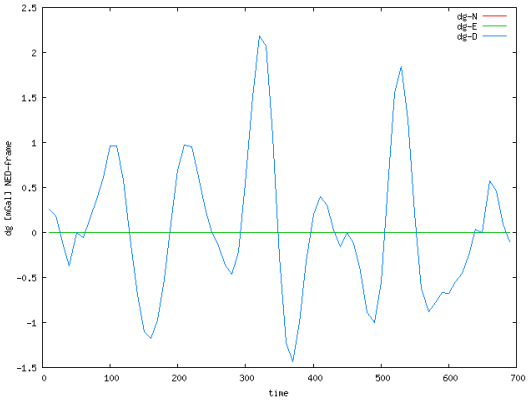

(f) Gravity disturbance (mGal)

Figure 4.28: CIRCLE LTN101b v2b2: adjusted parameters.

4.4.8 CIRCLE vq2b2

As already discussed in Section 4.2, the codification this computation means:

- $\langle q \rangle = q$, indicates that prior knowledge of the vehicle's attitude exists at the beginning (t_0) and at the end (t_N) of the mission.
- $\langle Hz \rangle = 2$: some subsets of parameters — $\underline{o}^{\mathtt{b}}$, $\underline{a}^{\mathtt{b}}$, δg or gg — has been grouped.
- $\langle \delta g_{NE} \rangle = b$, indicates that, for all t, $\delta g_N(t) = \delta g_E(t) \approx 0$.
- $\langle method \rangle = 2$: GDT-p (changes of the gravity disturbance of closed positions with respect to time) observations are added to the basic configuration.

LN200

Table 4.30 summarises the network configuration used in this computation.

Model Name	Frequency		Equation	Standard Deviation	
FB-GG (3.4.5)	20.0 Hz	$\forall t$	(3.13)	2.2	10^{-3} m s^{-2}
WIB (3.4.2)	20.0 Hz	$\forall t$	(3.10)	5.2	10^{-5} rad s^{-1}
VEL (3.4.1)	20.0 Hz	$\forall t$	(3.4.1)	0.000 01	m
Q-NORM (3.4.6)	20.0 Hz	$\forall t$	(3.14)	0.01	ppm
OB-O (3.4.35)	0.1 Hz	$\forall t$	(3.48)	4.9	10^{-6} rad s^{-1}
AB-O (3.4.36)	0.1 Hz	$\forall t$	(3.49)	2.0	10^{-3} m s^{-2}
OB (3.4.8)	0.1 Hz	$\forall t$	(3.16)	15.0	10^{-7} rad s^{-1}
AB (3.4.10)	0.1 Hz	$\forall t$	(3.18)	130.0	10^{-4} m s^{-2}
AOFF-O (3.4.37)			(3.50)	0.001	m
CUPT (3.4.16)	1.0 Hz	$\forall t$	(3.26)	0.05	m
GDT-GG (3.4.13)	0.1 Hz	$\forall t$	(3.22)	6.2	mGal
GDT-GG (3.4.13)	$v1 = v2 = v3$	$\forall t$	(3.22)	6.2	mGal
DGUPT-GG (3.4.28)	0.1 Hz	$\forall t$	(3.41)	0.02	mGal
Q-O (3.4.34)		t_0, t_N	(3.47)	0.01	ppm

Table 4.30: Test CIRCLE-LN200-vq2b2: network configuration.

Figure 4.29 proves that the functional models of the NA approach work succesfully:

- Figures 4.29a and 4.29c point out that the position has been recovered, especially heights with a precision better than 0.4 cm.
- The navigation parameters — shown in Figure 4.29e — are recovered with a precision of 36 " for roll (α) and pitch (χ) and with a range of 3 ' for heading (η).
- The IMU error parameters exhibited in Figures 4.29b and 4.29d are nearly constants within the defined tolerances (bias repeatability) of the IMU.

- Figure 4.29f also displays the gravity disturbance vector, that has to be zero.

LTN101

Table 4.31 summarises the network configuration used in this computation.

Model Name	Frequency		Equation	Standard Deviation	
FB-GG (3.4.5)	20.0 Hz	$\forall t$	(3.13)	4.4	10^{-4} m s^{-2}
WIB (3.4.2)	20.0 Hz	$\forall t$	(3.10)	1.3	10^{-6} rad s^{-1}
VEL (3.4.1)	20.0 Hz	$\forall t$	(3.4.1)	0.000 01	m
Q-NORM (3.4.6)	20.0 Hz	$\forall t$	(3.14)	0.01	ppm
OB-O (3.4.35)	0.1 Hz	$\forall t$	(3.48)	4.9	10^{-8} rad s^{-1}
AB-O (3.4.36)	0.1 Hz	$\forall t$	(3.49)	4.9	10^{-4} m s^{-2}
OB (3.4.8)	0.1 Hz	$\forall t$	(3.16)	61.0	10^{-12} rad s^{-1}
AB (3.4.10)	0.1 Hz	$\forall t$	(3.18)	95.0	10^{-7} m s^{-2}
AOFF-O (3.4.37)			(3.50)	0.001	m
CUPT (3.4.16)	1.0 Hz	$\forall t$	(3.26)	0.05	m
GDT-GG (3.4.13)	0.1 Hz	$\forall t$	(3.22)	6.2	mGal
GDT-GG (3.4.13)	$\nu 1 = \nu 2 = \nu 3$	$\forall t$	(3.22)	6.2	mGal
DGUPT-GG (3.4.28)	0.1 Hz	$\forall t$	(3.41)	0.02	mGal
Q-O (3.4.34)		t_0, t_N	(3.47)	0.01	ppm

Table 4.31: Test CIRCLE-LTN101-vq2b2: network configuration.

Figure 4.30 proves that the functional models of the NA approach work succesfully:

- Figures 4.30a and 4.30c point out that the position has been recovered, especially heights with a precision better than 1 cm.
- The navigation parameters — shown in Figure 4.30e — are recovered with a precision of 18 " for roll (α) and pitch (χ) and with a 2.4 ’ for heading (η).
- The IMU error parameters exhibited in Figures 4.30b and 4.30d are nearly constants within the defined tolerances (bias repeatability) of the IMU.
- Figure 4.30f also displays the gravity disturbance vector, that has to be zero.

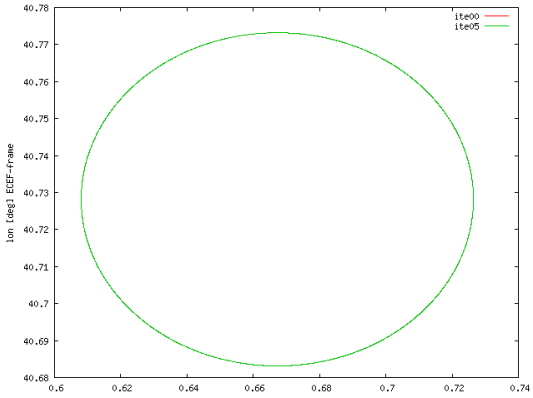

(a) Position (°)

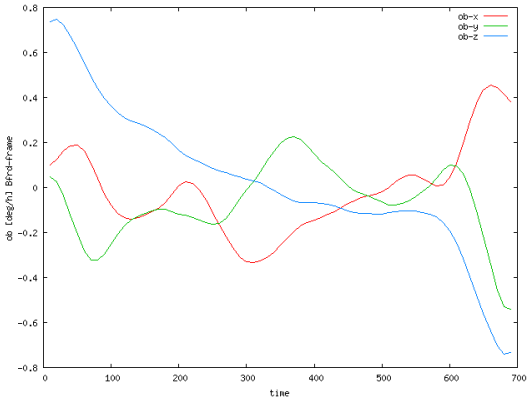

(b) Angular drift ($^\circ\,h^{-1}$)

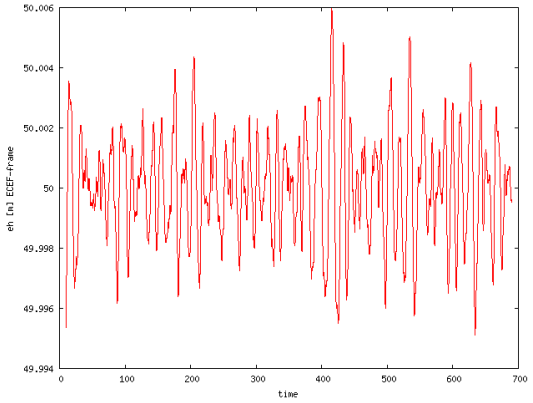

(c) Height (m)

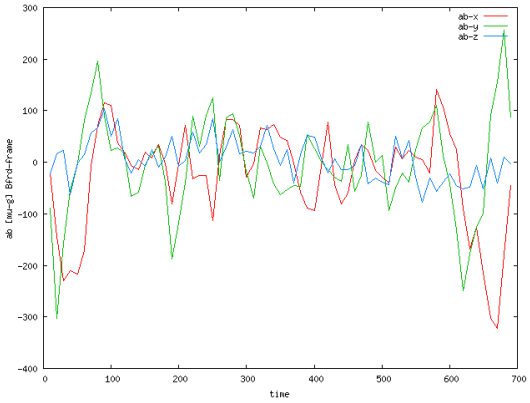

(d) Accelerometer bias (μg)

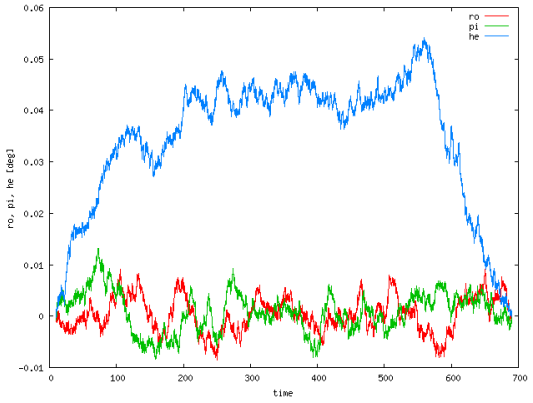

(e) Roll, Pitch and Heading (°)

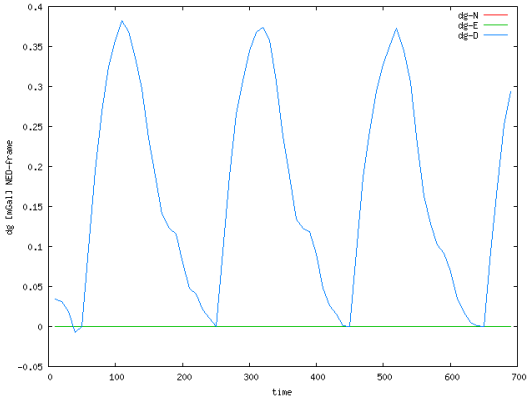

(f) Gravity disturbance (mGal)

Figure 4.29: CIRCLE LN200 vq2b2: adjusted parameters.

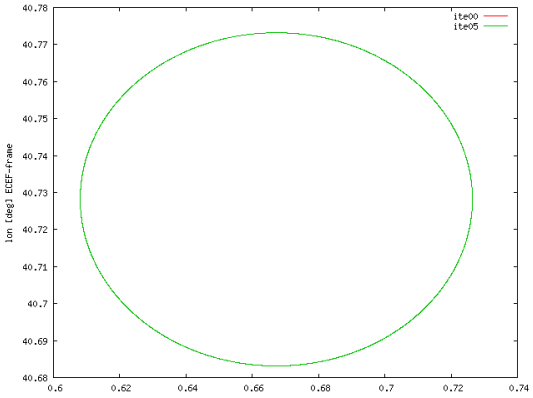

(a) Position (°)

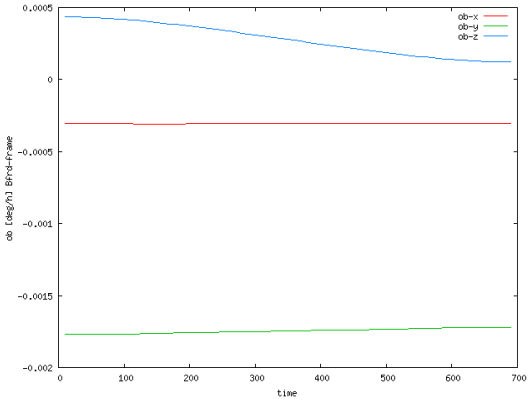

(b) Angular drift (° h^{-1})

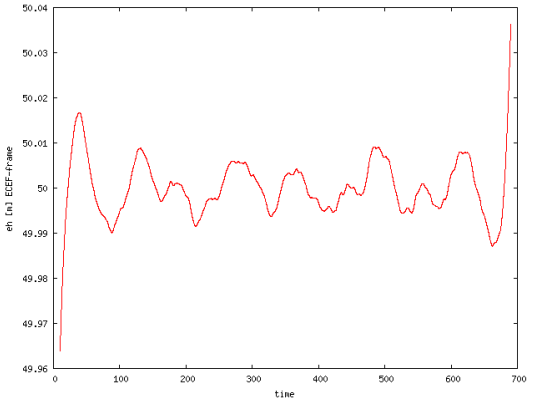

(c) Height (m)

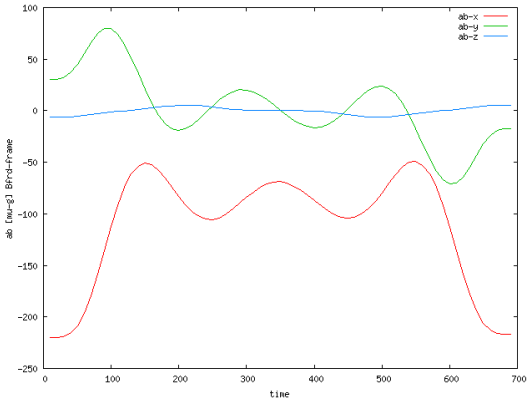

(d) Accelerometer bias (μg)

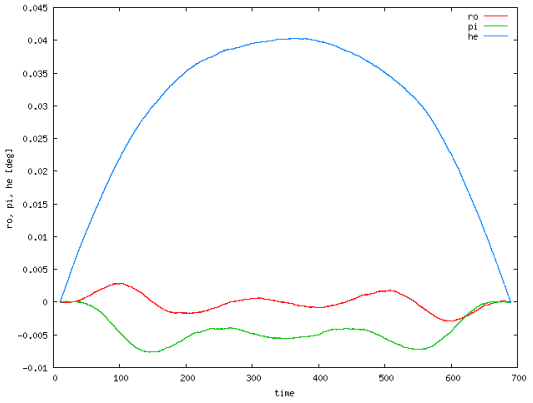

(e) Roll, Pitch and Heading (°)

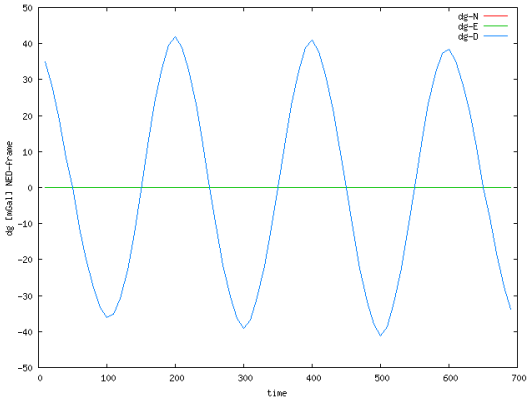

(f) Gravity disturbance (mGal)

Figure 4.30: CIRCLE LTN101b vq2b2: adjusted parameters.

4.4.9 CIRCLE v9a1

As already discussed in Section 4.2, the codification this computation means:

- $\langle Hz \rangle = 9$: all the parameters are computed at the IMU rate.
- $\langle \delta g_{NE} \rangle = a$: no prior knowledge of the horizontal gravity.
- $\langle method \rangle = 1$,indicates a basic network configuration similar to the Kalman filtering.

LN200

Table 4.32 summarises the network configuration used in this computation.

Model Name	Frequency		Equation	Standard Deviation	
FB-GG (3.4.5)	20.0 Hz	$\forall t$	(3.13)	2.2	10^{-3} m s^{-2}
WIB (3.4.2)	20.0 Hz	$\forall t$	(3.10)	5.2	10^{-5} rad s^{-1}
VEL (3.4.1)	20.0 Hz	$\forall t$	(3.4.1)	0.000 01	m
Q-NORM (3.4.6)	20.0 Hz	$\forall t$	(3.14)	0.01	ppm
OB-O (3.4.35)	20.0 Hz	$\forall t$	(3.48)	4.9	10^{-6} rad s^{-1}
AB-O (3.4.36)	20.0 Hz	$\forall t$	(3.49)	2.0	10^{-3} m s^{-2}
OB (3.4.8)	20.0 Hz	$\forall t$	(3.16)	1.1	10^{-7} rad s^{-1}
AB (3.4.10)	20.0 Hz	$\forall t$	(3.18)	8.9	10^{-4} m s^{-2}
AOFF-O (3.4.37)			(3.50)	0.001	m
CUPT (3.4.16)	1.0 Hz	$\forall t$	(3.26)	0.05	m
GDT-GG (3.4.13)	20.0 Hz	$\forall t$	(3.22)	0.016	mGal
DGUPT-GG (3.4.28)	$t_0^{v1} = t_0^{v2} = t_0^{v3} = t_N$		(3.41)	0.02	mGal

Table 4.32: Test CIRCLE-LN200-v9a1: network configuration.

Figure 4.31 proves that the functional models of the NA approach work succesfully:

- Figures 4.31a and 4.31c point out that the position has been recovered, especially heights with a precision better than 1 cm.
- The navigation parameters — shown in Figure 4.31e — are recovered with a precision better than 36 " for roll (α), pitch (χ) and heading (η).
- The IMU error parameters exhibited in Figures 4.31b and 4.31d are nearly constants within the defined tolerances (bias repeatability) of the IMU.
- Figure 4.31f also displays the gravity disturbance vector, that has to be zero, with a precision better than 0.03 mGal.

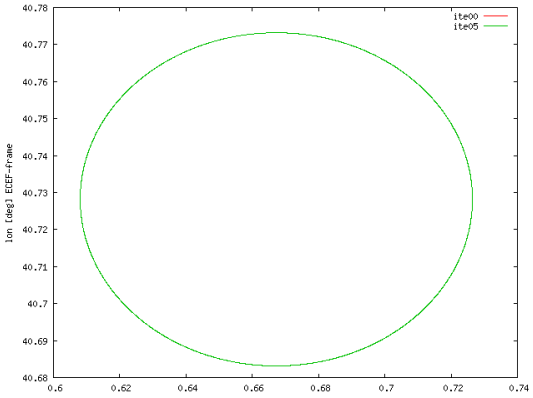

(a) Position (°)

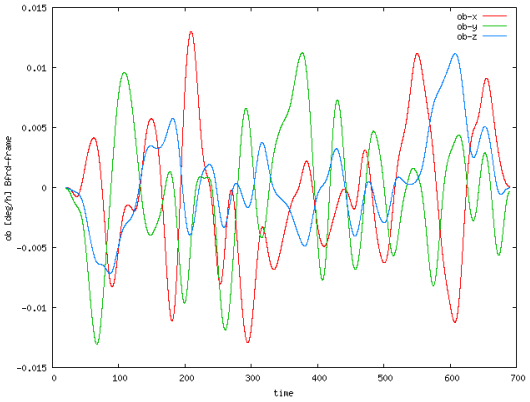

(b) Angular drift ($^\circ\,h^{-1}$)

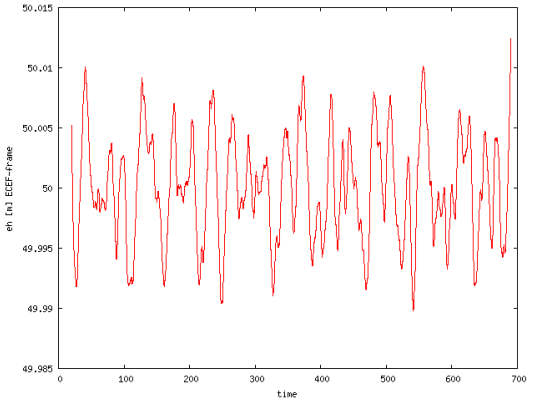

(c) Height (m)

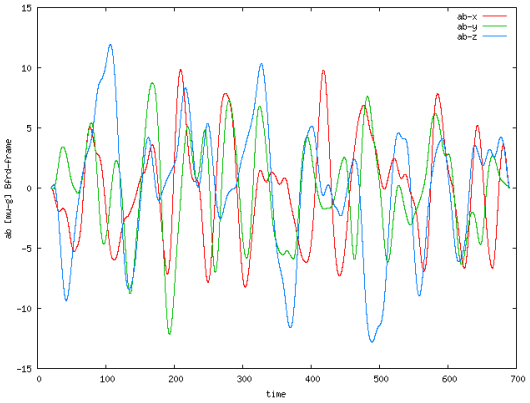

(d) Accelerometer bias (μg)

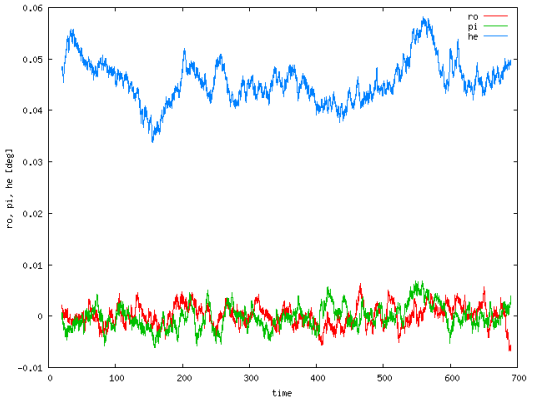

(e) Roll, Pitch and Heading (°)

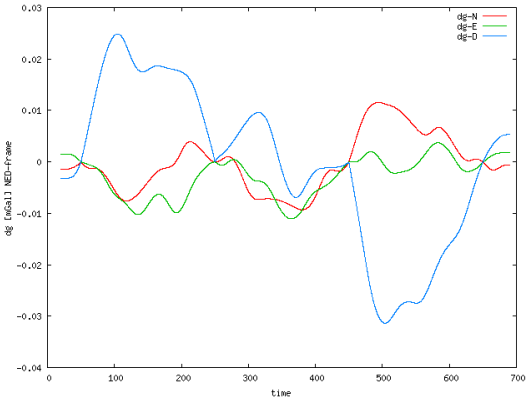

(f) Gravity disturbance (mGal)

Figure 4.31: CIRCLE LN200 v9a1: adjusted parameters.

LTN101

Table 4.33 summarises the network configuration used in this computation.

Model Name	Frequency		Equation	Standard Deviation	
FB-GG (3.4.5)	20.0 Hz	$\forall t$	(3.13)	4.4	10^{-4} m s^{-2}
WIB (3.4.2)	20.0 Hz	$\forall t$	(3.10)	1.3	10^{-6} rad s^{-1}
VEL (3.4.1)	20.0 Hz	$\forall t$	(3.4.1)	0.000 01	m
Q-NORM (3.4.6)	20.0 Hz	$\forall t$	(3.14)	0.01	ppm
OB-O (3.4.35)	20.0 Hz	$\forall t$	(3.48)	4.9	10^{-8} rad s^{-1}
AB-O (3.4.36)	20.0 Hz	$\forall t$	(3.49)	4.9	10^{-4} m s^{-2}
OB (3.4.8)	20.0 Hz	$\forall t$	(3.16)	4.3	10^{-12} rad s^{-1}
AB (3.4.10)	20.0 Hz	$\forall t$	(3.18)	6.7	10^{-7} m s^{-2}
AOFF-O (3.4.37)			(3.50)	0.001	m
CUPT (3.4.16)	1.0 Hz	$\forall t$	(3.26)	0.05	m
GDT-GG (3.4.13)	20.0 Hz	$\forall t$	(3.22)	0.016	mGal
DGUPT-GG (3.4.28)	$t_0^{v1} = t_0^{v2} = t_0^{v3} = t_N$		(3.41)	0.02	mGal

Table 4.33: Test CIRCLE-LTN101-v9a1: network configuration.

Figure 4.32 proves that the functional models of the NA approach work succesfully:

- Figures 4.32a and 4.32c point out that the position has been recovered, especially heights with a precision better than 1 cm.
- The navigation parameters — shown in Figure 4.32e — are recovered with a precision of 18 " for roll (α), pitch (χ) and heading (η).
- The IMU error parameters exhibited in Figures 4.32b and 4.32d are nearly constants within the defined tolerances (bias repeatability) of the IMU.
- Figure 4.32f also displays the gravity disturbance vector, that has to be zero.

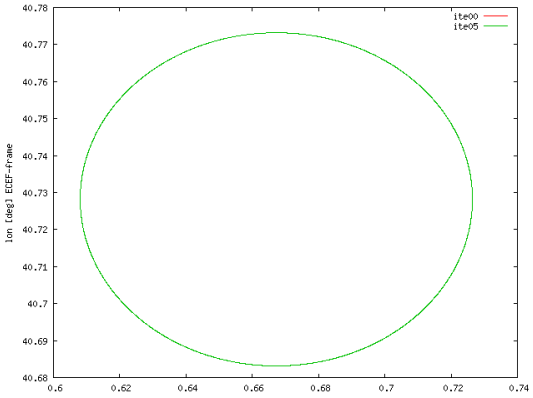

(a) Position (°)

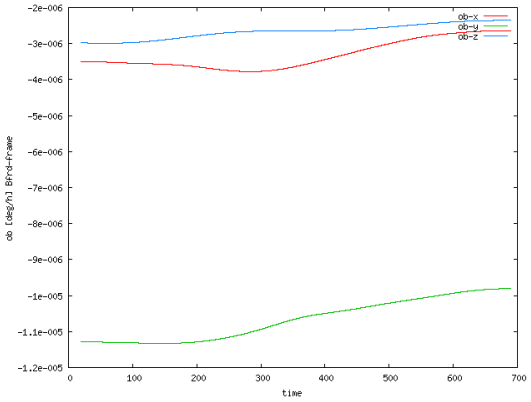

(b) Angular drift ($^\circ\,h^{-1}$)

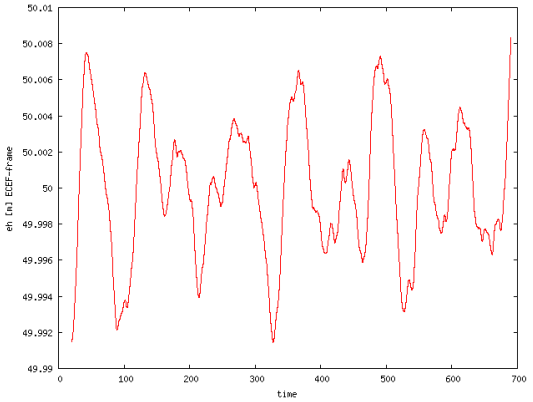

(c) Height (m)

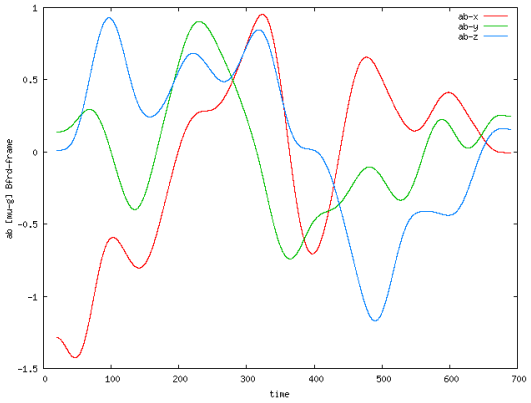

(d) Accelerometer bias (μg)

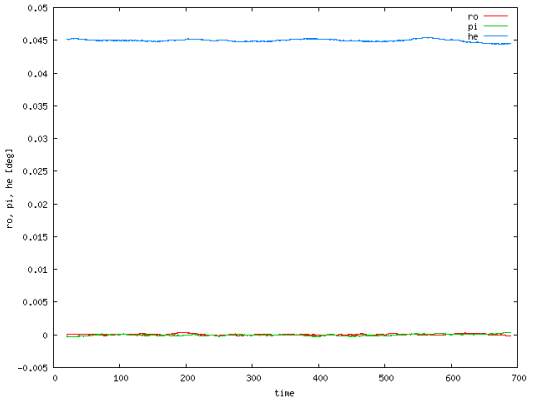

(e) Roll, Pitch and Heading (°)

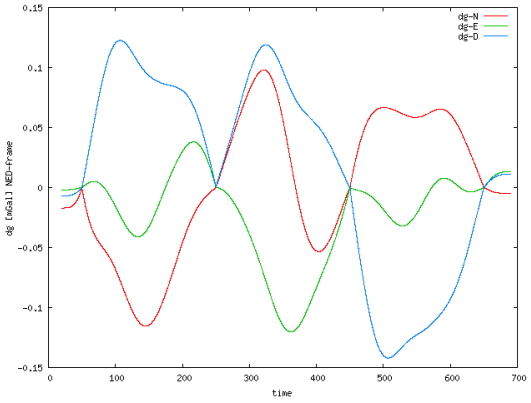

(f) Gravity disturbance (mGal)

Figure 4.32: CIRCLE LTN101b v9a1: adjusted parameters.

4.4.10 CIRCLE vq9a1

As already discussed in Section 4.2, the codification this computation means:

- $\langle q \rangle = q$: prior knowledge of the vehicle's attitude exists at the beginning (t_0) and at the end (t_N) of the mission.
- $\langle Hz \rangle = 9$: all the parameters are computed at the IMU rate.
- $\langle \delta g_{NE} \rangle = a$: no prior knowledge of the horizontal gravity.
- $\langle method \rangle = 1$, indicates a basic network configuration similar to the Kalman filtering.

LN200

Table 4.34 summarises the network configuration used in this computation.

Model Name	Frequency		Equation	Standard Deviation	
FB-GG (3.4.5)	20.0 Hz	$\forall t$	(3.13)	2.2	10^{-3} m s^{-2}
WIB (3.4.2)	20.0 Hz	$\forall t$	(3.10)	5.2	10^{-5} rad s^{-1}
VEL (3.4.1)	20.0 Hz	$\forall t$	(3.4.1)	0.000 01	m
Q-NORM (3.4.6)	20.0 Hz	$\forall t$	(3.14)	0.01	ppm
OB-O (3.4.35)	20.0 Hz	$\forall t$	(3.48)	4.9	10^{-6} rad s^{-1}
AB-O (3.4.36)	20.0 Hz	$\forall t$	(3.49)	2.0	10^{-3} m s^{-2}
OB (3.4.8)	20.0 Hz	$\forall t$	(3.16)	1.1	10^{-7} rad s^{-1}
AB (3.4.10)	20.0 Hz	$\forall t$	(3.18)	8.9	10^{-4} m s^{-2}
AOFF-O (3.4.37)			(3.50)	0.001	m
CUPT (3.4.16)	1.0 Hz	$\forall t$	(3.26)	0.05	m
GDT-GG (3.4.13)	20.0 Hz	$\forall t$	(3.22)	0.016	mGal
DGUPT-GG (3.4.28)	$t_0^{v1} = t_0^{v2} = t_0^{v3} = t_N$		(3.41)	0.02	mGal
Q-O (3.4.34)		t_0, t_N	(3.47)	0.01	ppm

Table 4.34: Test CIRCLE-LN200-vq9a1: network configuration.

Figure 4.33 proves that the functional models of the NA approach work succesfully:

- Figures 4.33a and 4.33c point out that the position has been recovered, especially heights with a precision better than 1 cm.
- The navigation parameters — shown in Figure 4.33e — are recovered with a precision of 36 " for roll (α) and pitch (χ) and with a range of 3 ' for heading (η).
- The IMU error parameters exhibited in Figures 4.33b and 4.33d are nearly constants within the defined tolerances (bias repeatability) of the IMU.
- Figure 4.33f also displays the gravity disturbance vector, that has to be zero, with a precision better than 0.04 mGal.

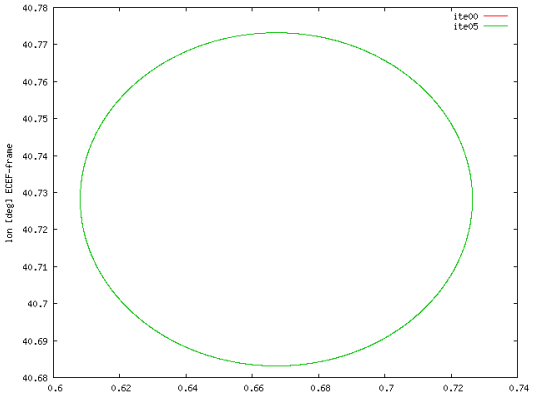

(a) Position (°)

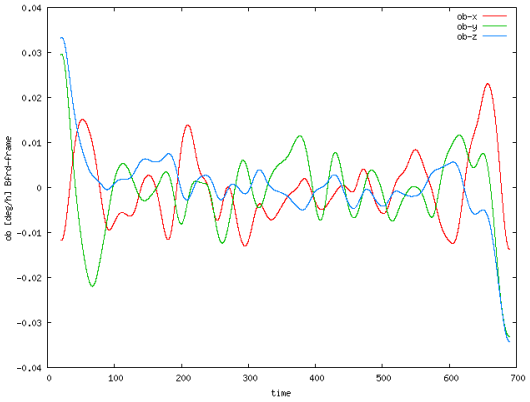

(b) Angular drift (° h^{-1})

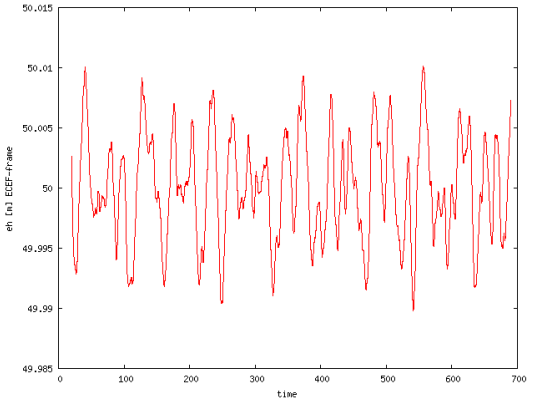

(c) Height (m)

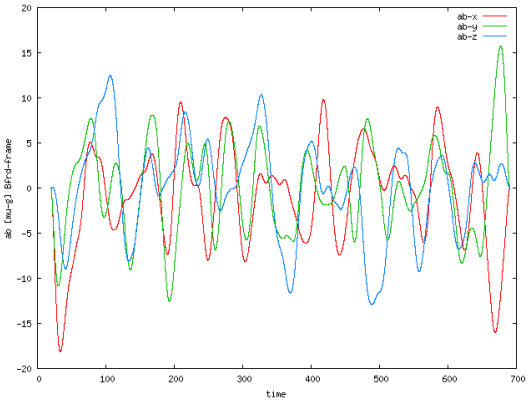

(d) Accelerometer bias (μg)

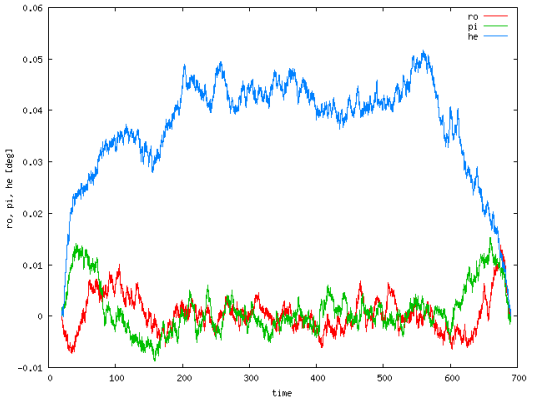

(e) Roll, Pitch and Heading (°)

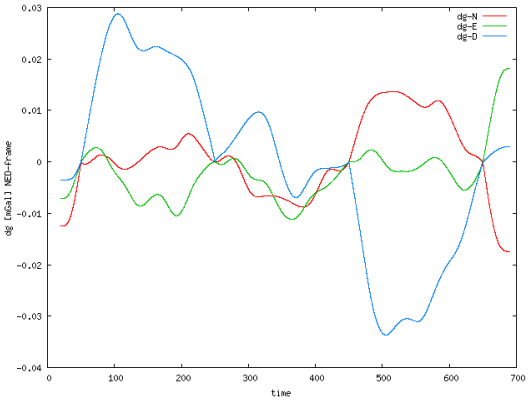

(f) Gravity disturbance (mGal)

Figure 4.33: CIRCLE LN200 vq9a1: adjusted parameters.

LTN101

Table 4.35 summarises the network configuration used in this computation.

Model Name	Frequency		Equation	Standard Deviation	
FB-GG (3.4.5)	20.0 Hz	$\forall t$	(3.13)	4.4	10^{-4} m s^{-2}
WIB (3.4.2)	20.0 Hz	$\forall t$	(3.10)	1.3	10^{-6} rad s^{-1}
VEL (3.4.1)	20.0 Hz	$\forall t$	(3.4.1)	0.000 01	m
Q-NORM (3.4.6)	20.0 Hz	$\forall t$	(3.14)	0.01	ppm
OB-O (3.4.35)	20.0 Hz	$\forall t$	(3.48)	4.9	10^{-8} rad s^{-1}
AB-O (3.4.36)	20.0 Hz	$\forall t$	(3.49)	4.9	10^{-4} m s^{-2}
OB (3.4.8)	20.0 Hz	$\forall t$	(3.16)	4.3	10^{-12} rad s^{-1}
AB (3.4.10)	20.0 Hz	$\forall t$	(3.18)	6.7	10^{-7} m s^{-2}
AOFF-O (3.4.37)			(3.50)	0.001	m
CUPT (3.4.16)	1.0 Hz	$\forall t$	(3.26)	0.05	m
GDT-GG (3.4.13)	20.0 Hz	$\forall t$	(3.22)	0.016	mGal
DGUPT-GG (3.4.28)	$t_0^{v1} = t_0^{v2} = t_0^{v3} = t_N$		(3.41)	0.02	mGal
Q-O (3.4.34)		t_0, t_N	(3.47)	0.01	ppm

Table 4.35: Test CIRCLE-LTN101-vq9a1: network configuration.

Figure 4.34 proves that the functional models of the NA approach work succesfully:

- Figures 4.34a and 4.34c point out that the position has been recovered, especially heights with a precision better than 1 cm.
- The navigation parameters — shown in Figure 4.34e — are recovered with a precision of 18 " for roll (α) and pitch (χ) and with a range of 3 ’ for heading (η).
- The IMU error parameters exhibited in Figures 4.34b and 4.34d are nearly constants within the defined tolerances (bias repeatability) of the IMU.
- Figure 4.34f also displays the gravity disturbance vector, that has to be zero.

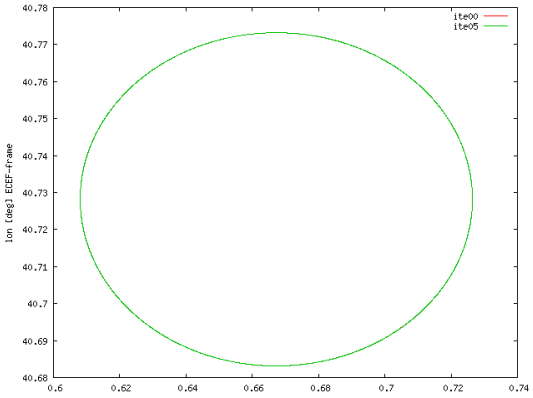

(a) Position (°)

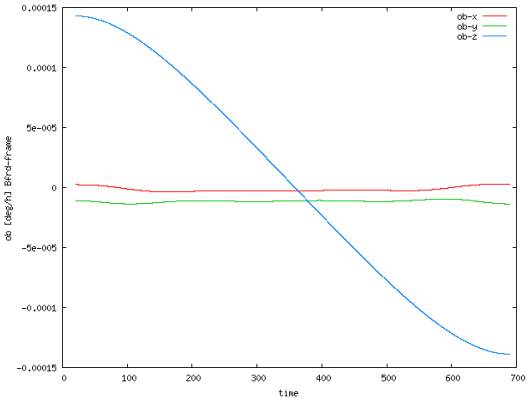

(b) Angular drift (° h^{-1})

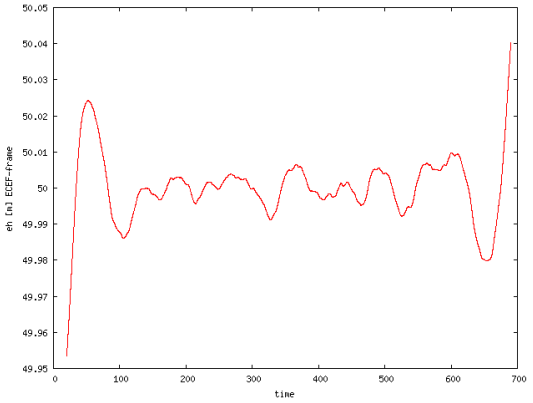

(c) Height (m)

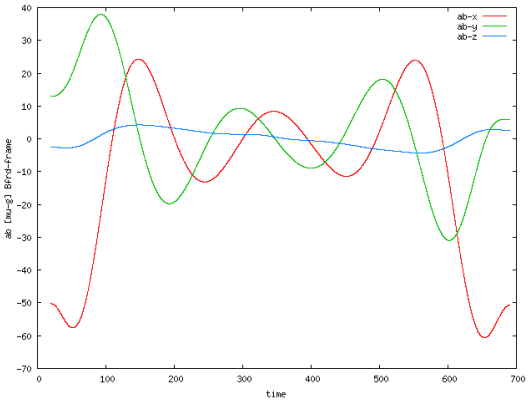

(d) Accelerometer bias (μg)

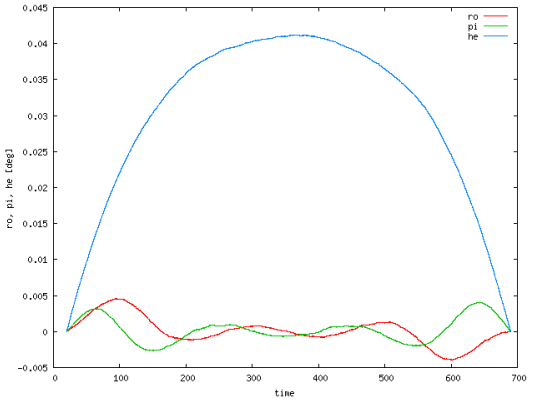

(e) Roll, Pitch and Heading (°)

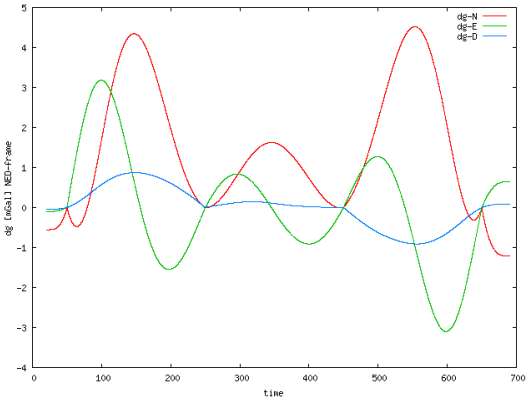

(f) Gravity disturbance (mGal)

Figure 4.34: CIRCLE LTN101b vq9a1: adjusted parameters.

4.4.11 CIRCLE v9b1

As already discussed in Section 4.2, the codification this computation means:

- $\langle Hz \rangle = 9$: all the parameters are computed at the IMU rate.
- $\langle \delta g_{NE} \rangle = b$, indicates that, for all t, $\delta g_N(t) = \delta g_E(t) \approx 0$.
- $\langle method \rangle = 1$, indicates a basic network configuration similar to the Kalman filtering.

LN200

Table 4.36 summarises the network configuration used in this computation.

Model Name	Frequency		Equation	Standard Deviation	
FB-GG (3.4.5)	20.0 Hz	$\forall t$	(3.13)	2.2	10^{-3} m s^{-2}
WIB (3.4.2)	20.0 Hz	$\forall t$	(3.10)	5.2	10^{-5} rad s^{-1}
VEL (3.4.1)	20.0 Hz	$\forall t$	(3.4.1)	0.000 01	m
Q-NORM (3.4.6)	20.0 Hz	$\forall t$	(3.14)	0.01	ppm
OB-O (3.4.35)	20.0 Hz	$\forall t$	(3.48)	4.9	10^{-6} rad s^{-1}
AB-O (3.4.36)	20.0 Hz	$\forall t$	(3.49)	2.0	10^{-3} m s^{-2}
OB (3.4.8)	20.0 Hz	$\forall t$	(3.16)	1.1	10^{-7} rad s^{-1}
AB (3.4.10)	20.0 Hz	$\forall t$	(3.18)	8.9	10^{-4} m s^{-2}
AOFF-O (3.4.37)			(3.50)	0.001	m
CUPT (3.4.16)	1.0 Hz	$\forall t$	(3.26)	0.05	m
GDT-GG (3.4.13)	20.0 Hz	$\forall t$	(3.22)	0.016	mGal
DGUPT-GG (3.4.28)	20.0 Hz	$\forall t$	(3.41)	0.02	mGal

Table 4.36: Test CIRCLE-LN200-v9b1: network configuration.

Figure 4.35 proves that the functional models of the NA approach work succesfully:

- Figures 4.35a and 4.35c point out that the position has been recovered, especially heights with a precision better than 1 cm.
- The navigation parameters — shown in Figure 4.35e — are recovered with a precision of 36 " for roll (α), pitch (χ) and heading (η).
- The IMU error parameters exhibited in Figures 4.35b and 4.35d are nearly constants within the defined tolerances (bias repeatability) of the IMU.
- Figure 4.35f also displays the gravity disturbance vector, that has to be zero, with a precision of 0.03 mGal.

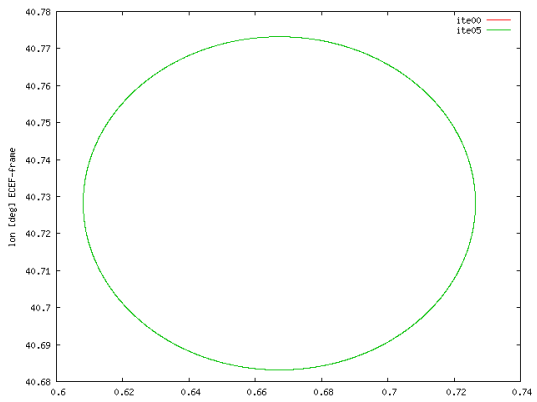

(a) Position (°)

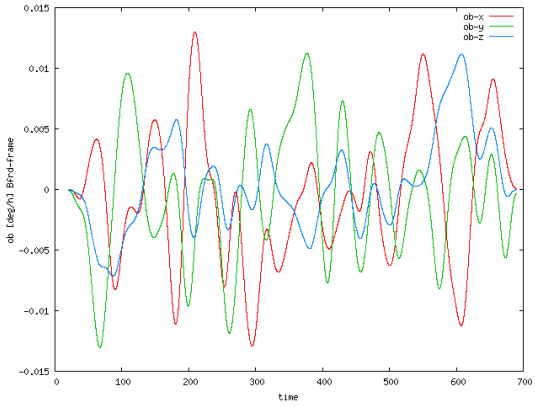

(b) Angular drift ($^\circ\,h^{-1}$)

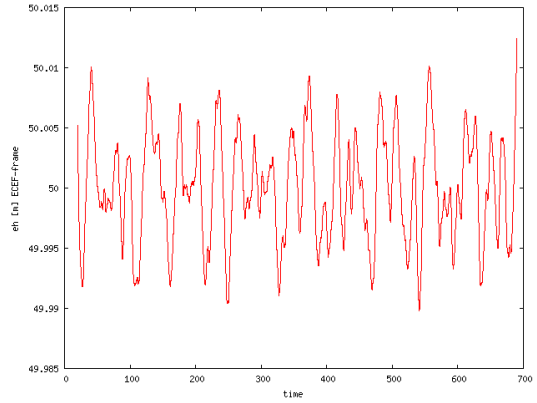

(c) Height (m)

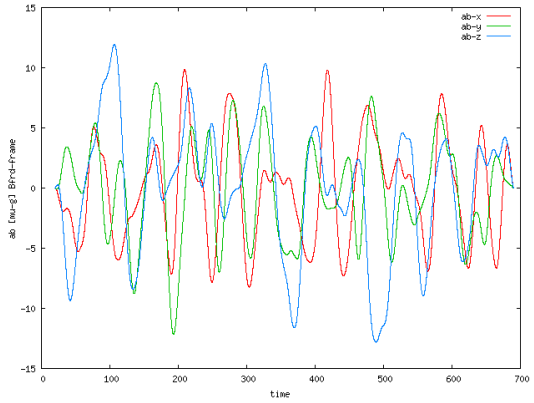

(d) Accelerometer bias (μg)

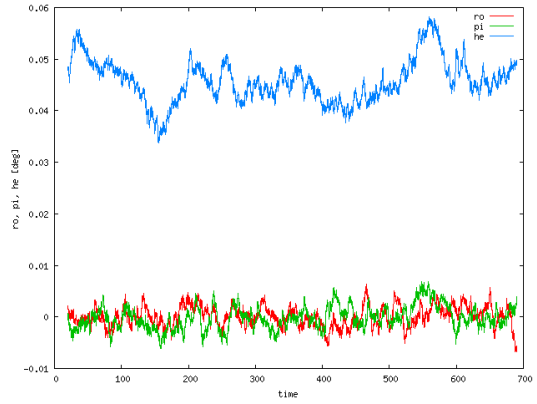

(e) Roll, Pitch and Heading (°)

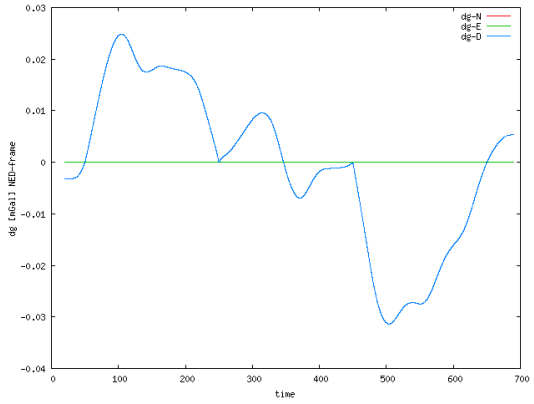

(f) Gravity disturbance (mGal)

Figure 4.35: CIRCLE LN200 v9b1: adjusted parameters.

LTN101

Table 4.37 summarises the network configuration used in this computation.

Model Name	Frequency		Equation	Standard Deviation	
FB-GG (3.4.5)	20.0 Hz	$\forall t$	(3.13)	4.4	10^{-4} m s^{-2}
WIB (3.4.2)	20.0 Hz	$\forall t$	(3.10)	1.3	10^{-6} rad s^{-1}
VEL (3.4.1)	20.0 Hz	$\forall t$	(3.4.1)	0.000 01	m
Q-NORM (3.4.6)	20.0 Hz	$\forall t$	(3.14)	0.01	ppm
OB-O (3.4.35)	20.0 Hz	$\forall t$	(3.48)	4.9	10^{-8} rad s^{-1}
AB-O (3.4.36)	20.0 Hz	$\forall t$	(3.49)	4.9	10^{-4} m s^{-2}
OB (3.4.8)	20.0 Hz	$\forall t$	(3.16)	4.3	10^{-12} rad s^{-1}
AB (3.4.10)	20.0 Hz	$\forall t$	(3.18)	6.7	10^{-7} m s^{-2}
AOFF-O (3.4.37)			(3.50)	0.001	m
CUPT (3.4.16)	1.0 Hz	$\forall t$	(3.26)	0.05	m
GDT-GG (3.4.13)	20.0 Hz	$\forall t$	(3.22)	0.016	mGal
DGUPT-GG (3.4.28)	20.0 Hz	$\forall t$	(3.41)	0.02	mGal

Table 4.37: Test CIRCLE-LTN101-v9b1: network configuration.

Figure 4.36 proves that the functional models of the NA approach work succesfully:

- Figures 4.36a and 4.36c point out that the position has been recovered, especially heights with a precision better than 0.8 cm.
- The navigation parameters — shown in Figure 4.36e — are recovered with a precision better than 9 " for roll (α), pitch (χ) and heading (η).
- The IMU error parameters exhibited in Figures 4.36b and 4.36d are nearly constants within the defined tolerances (bias repeatability) of the IMU.
- Figure 4.36f also displays the gravity disturbance vector, that has to be zero.

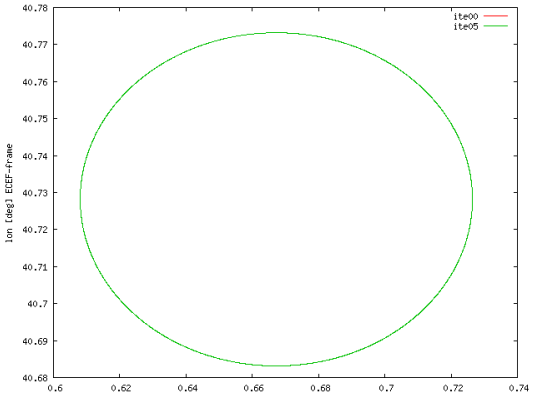

(a) Position (°)

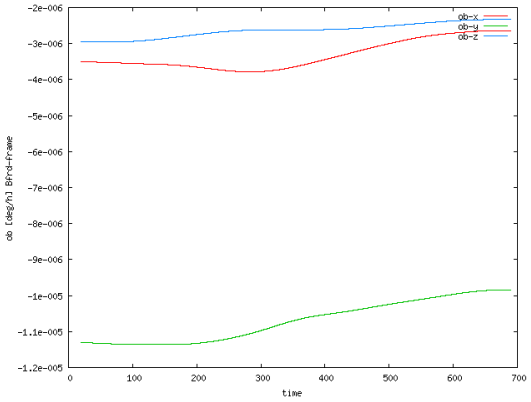

(b) Angular drift ($^\circ\,h^{-1}$)

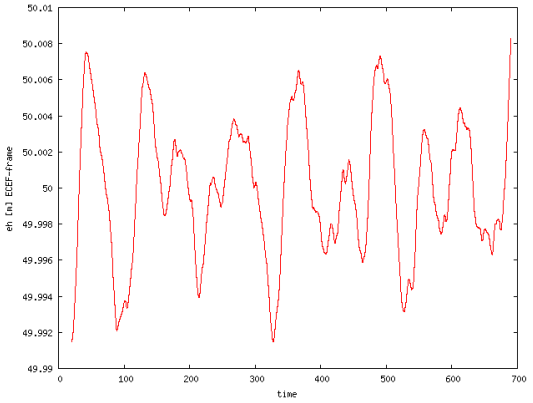

(c) Height (m)

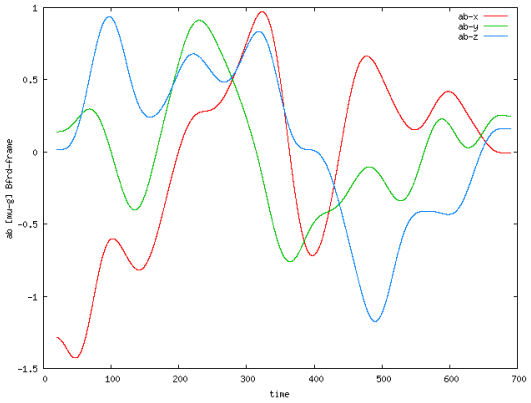

(d) Accelerometer bias (μg)

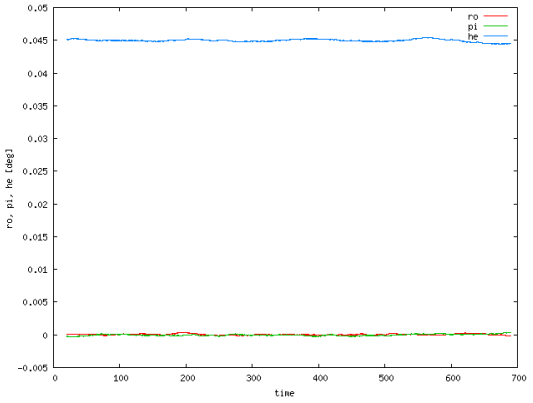

(e) Roll, Pitch and Heading (°)

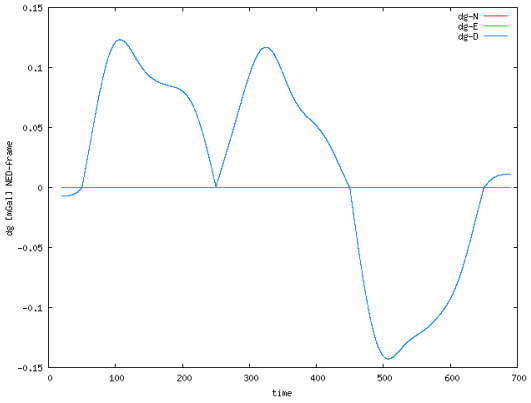

(f) Gravity disturbance (mGal)

Figure 4.36: CIRCLE LTN101b v9b1: adjusted parameters.

4.4.12 CIRCLE vq9b1

As already discussed in Section 4.2, the codification this computation means:

- $\langle q \rangle = q$: prior knowledge of the vehicle's attitude exists at the beginning (t_0) and at the end (t_N) of the mission.
- $\langle Hz \rangle = 9$: all the parameters are computed at the IMU rate.
- $\langle \delta g_{NE} \rangle = b$, indicates that, for all t, $\delta g_N(t) = \delta g_E(t) \approx 0$.
- $\langle method \rangle = 1$, indicates a basic network configuration similar to the Kalman filtering.

LN200

Table 4.38 summarises the network configuration used in this computation.

Model Name	Frequency		Equation	Standard Deviation	
FB-GG (3.4.5)	20.0 Hz	$\forall t$	(3.13)	2.2	10^{-3} m s^{-2}
WIB (3.4.2)	20.0 Hz	$\forall t$	(3.10)	5.2	10^{-5} rad s^{-1}
VEL (3.4.1)	20.0 Hz	$\forall t$	(3.4.1)	0.000 01	m
Q-NORM (3.4.6)	20.0 Hz	$\forall t$	(3.14)	0.01	ppm
OB-O (3.4.35)	20.0 Hz	$\forall t$	(3.48)	4.9	10^{-6} rad s^{-1}
AB-O (3.4.36)	20.0 Hz	$\forall t$	(3.49)	2.0	10^{-3} m s^{-2}
OB (3.4.8)	20.0 Hz	$\forall t$	(3.16)	1.1	10^{-7} rad s^{-1}
AB (3.4.10)	20.0 Hz	$\forall t$	(3.18)	8.9	10^{-4} m s^{-2}
AOFF-O (3.4.37)			(3.50)	0.001	m
CUPT (3.4.16)	1.0 Hz	$\forall t$	(3.26)	0.05	m
GDT-GG (3.4.13)	20.0 Hz	$\forall t$	(3.22)	0.016	mGal
DGUPT-GG (3.4.28)	20.0 Hz	$\forall t$	(3.41)	0.02	mGal
Q-O (3.4.34)		t_0, t_N	(3.47)	0.01	ppm

Table 4.38: Test CIRCLE-LN200-vq9b1: network configuration.

Figure 4.37 proves that the functional models of the NA approach work succesfully:

- Figure 4.37a points out that the position has been recovered, especially heights —in Figure 4.37c— with a precision better than 1 cm.
- The navigation parameters —shown in Figure 4.37e— are recovered with a precision of 36 " for roll (α) and pitch (χ) and with a range of 3 ' for heading (η).
- The IMU error parameters exhibited in Figures 4.37b and 4.37d are nearly constants within the defined tolerances (bias repeatability) of the IMU.
- Figure 4.37f also displays the gravity disturbance vector, that has to be zero, with a precision better than 0.04 mGal.

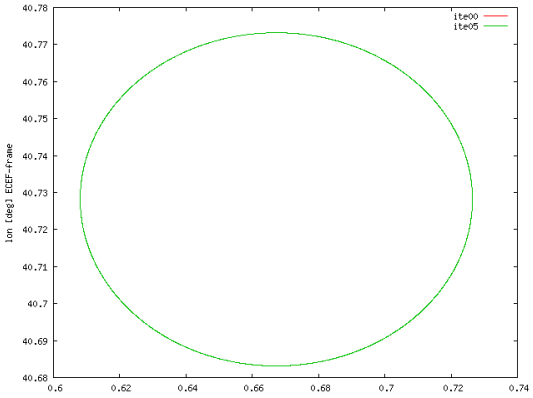

(a) Position (°)

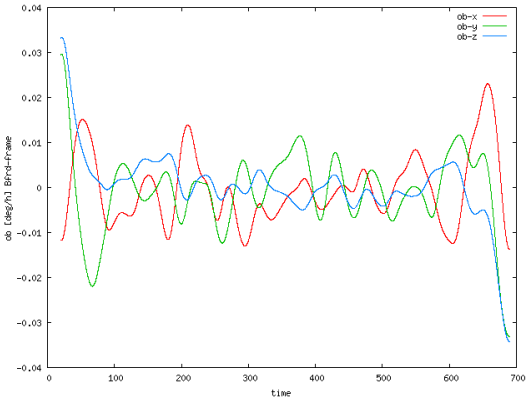

(b) Angular drift (° h^{-1})

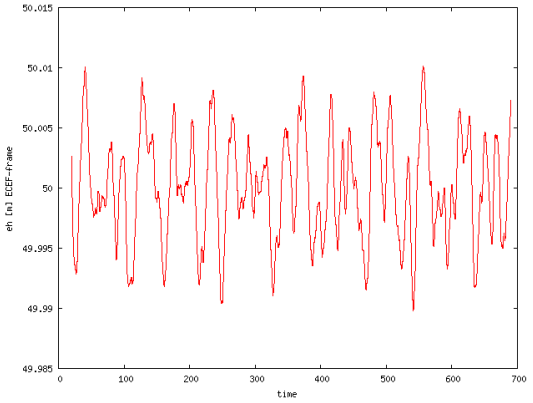

(c) Height (m)

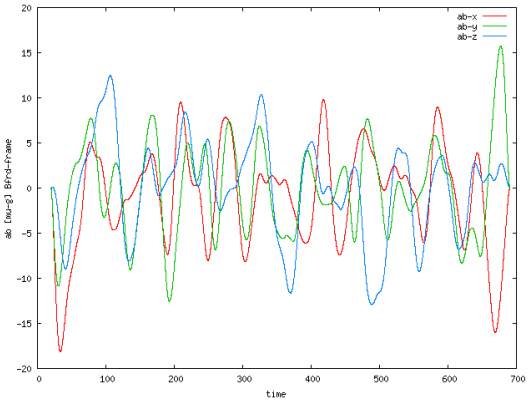

(d) Accelerometer bias (μg)

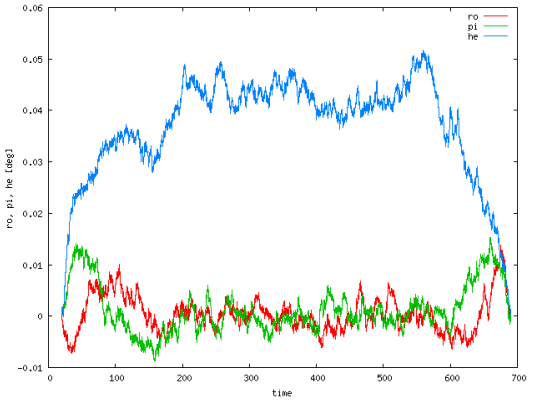

(e) Roll, Pitch and Heading (°)

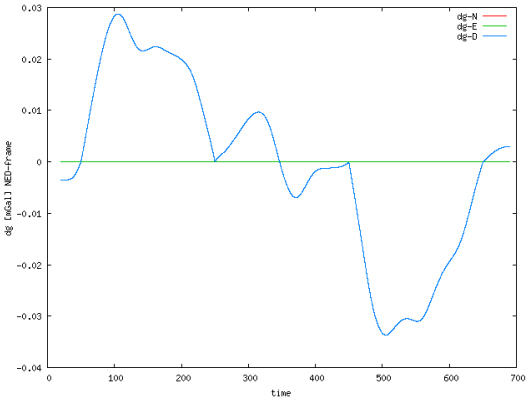

(f) Gravity disturbance (mGal)

Figure 4.37: CIRCLE LN200 vq9b1: adjusted parameters.

LTN101

Table 4.39 summarises the network configuration used in this computation.

Model Name	Frequency		Equation	Standard Deviation	
FB-GG (3.4.5)	20.0 Hz	$\forall t$	(3.13)	4.4	10^{-4} m s^{-2}
WIB (3.4.2)	20.0 Hz	$\forall t$	(3.10)	1.3	10^{-6} rad s^{-1}
VEL (3.4.1)	20.0 Hz	$\forall t$	(3.4.1)	0.000 01	m
Q-NORM (3.4.6)	20.0 Hz	$\forall t$	(3.14)	0.01	ppm
OB-O (3.4.35)	20.0 Hz	$\forall t$	(3.48)	4.9	10^{-8} rad s^{-1}
AB-O (3.4.36)	20.0 Hz	$\forall t$	(3.49)	4.9	10^{-4} m s^{-2}
OB (3.4.8)	20.0 Hz	$\forall t$	(3.16)	4.3	10^{-12} rad s^{-1}
AB (3.4.10)	20.0 Hz	$\forall t$	(3.18)	6.7	10^{-7} m s^{-2}
AOFF-O (3.4.37)			(3.50)	0.001	m
CUPT (3.4.16)	1.0 Hz	$\forall t$	(3.26)	0.05	m
GDT-GG (3.4.13)	20.0 Hz	$\forall t$	(3.22)	0.016	mGal
DGUPT-GG (3.4.28)	20.0 Hz	$\forall t$	(3.41)	0.02	mGal
Q-O (3.4.34)		t_0, t_N	(3.47)	0.01	ppm

Table 4.39: Test CIRCLE-LTN101-vq9b1: network configuration.

Figure 4.38 proves that the functional models of the NA approach work succesfully:

- Figures 4.38a and 4.38c point out that the position has been recovered, especially heights with a precision better than 1 cm.
- The navigation parameters —shown in Figure 4.38e— are recovered with a precision of 18 " for roll (α) and pitch (χ) and with a range of 3 ' for heading (η).
- The IMU error parameters exhibited in Figures 4.38b and 4.38d are nearly constants within the defined tolerances (bias repeatability) of the IMU.
- Figure 4.38f also displays the gravity disturbance vector, that has to be zero, with a precision better than 1 mGal.

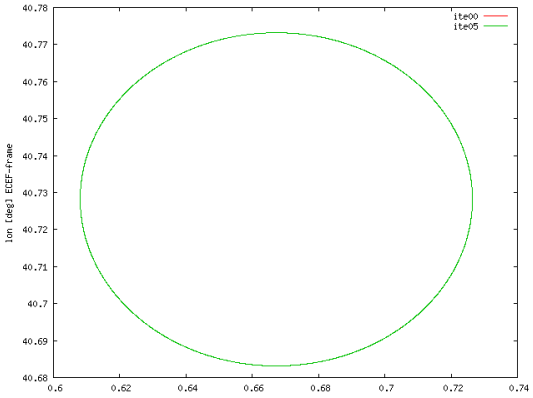

(a) Position (°)

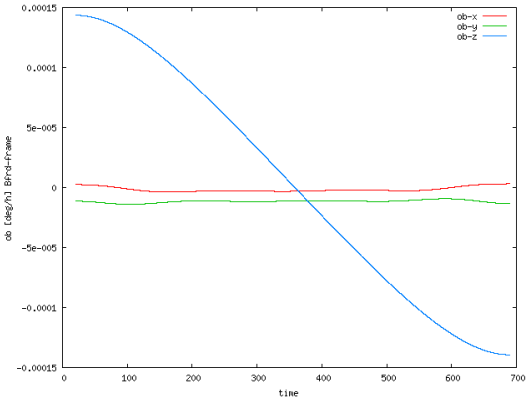

(b) Angular drift ($^\circ\,h^{-1}$)

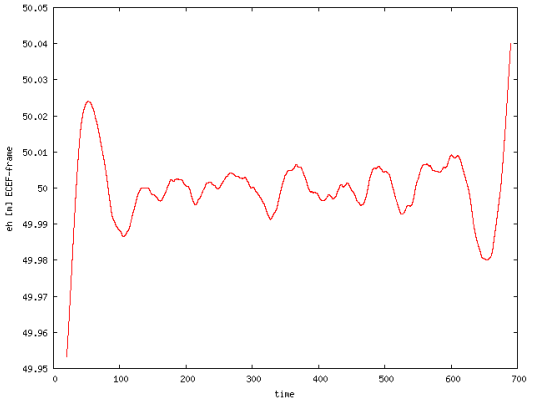

(c) Height (m)

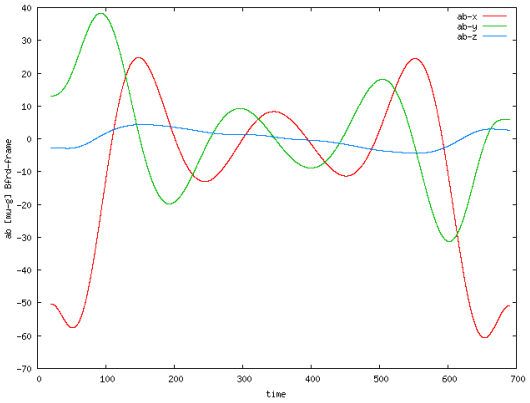

(d) Accelerometer bias (μg)

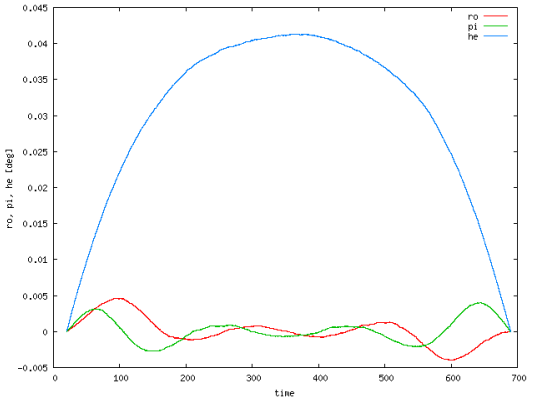

(e) Roll, Pitch and Heading (°)

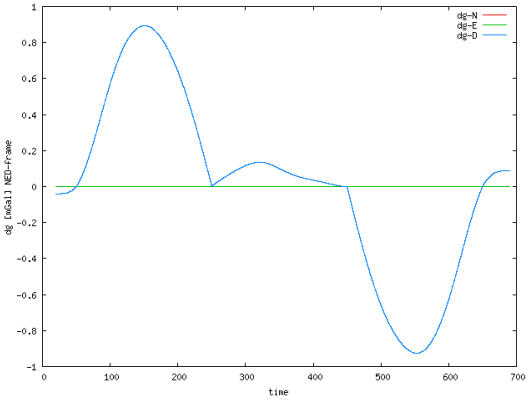

(f) Gravity disturbance (mGal)

Figure 4.38: CIRCLE LTN101b vq9b1: adjusted parameters.

4.5 Test CTRA

Finally, it is important to consider a trajectory as the one described in Figure 4.39. It simulates a vehicle that moves from a starting place, drives along the described trajectory and ends at the start point.

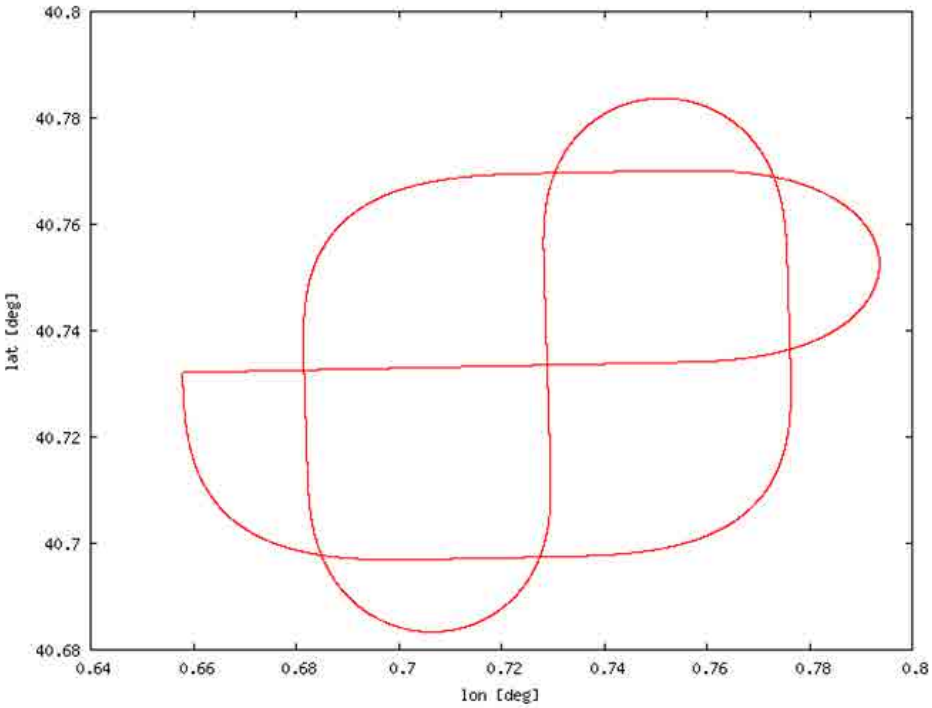

Figure 4.39: CTRA: input trajectory.

As it can be seen in such trajectory, there is additional information that has to be considered:

- the gravity disturbance is known at the start-end point;
- there are some crossovers; and
- there are also gravity space-relationship between lines.

As the preceding tests, the output simulator data are shown in Figure 4.40 and several computations have been also also done for each IMU configuration. Table 4.40 shows the associated dimensions and redundancy number for each network configuration.

version	Nrow	Ncol	Neq	Npar	r_b
v2a1	56 059	40 969	140 981	136 505	0.031 8
vq2a1	56 061	40 969	140 989	136 505	0.031 8
v2a2	56 066	40 969	141 002	136 505	0.031 9
vq2a2	56 068	40 969	141 010	136 505	0.032 0
v2a2x	56 206	40 969	141 142	136 505	0.032 9
vq2a2x	56 208	40 969	141 150	136 505	0.032 9
v2b1	56 092	40 969	141 080	136 505	0.032 4
vq2b1	56 094	40 969	141 088	136 505	0.032 5
v2b2	56 099	40 969	141 101	136 505	0.032 6
vq2b2	56 101	40 969	141 109	136 505	0.032 6
v2b2x	56 239	40 969	141 241	136 505	0.033 5
vq2b2x	56 241	40 969	141 249	136 505	0.033 6
v9a1	123 738	81 590	344 018	258 368	0.249 0
vq9a1	123 740	81 590	344 026	258 368	0.249 0
v9b1	137 334	81 590	384 806	258 368	0.328 6
vq9b1	137 336	81 590	384 814	258 368	0.328 6

Table 4.40: Test CTRA: network's dimensions.

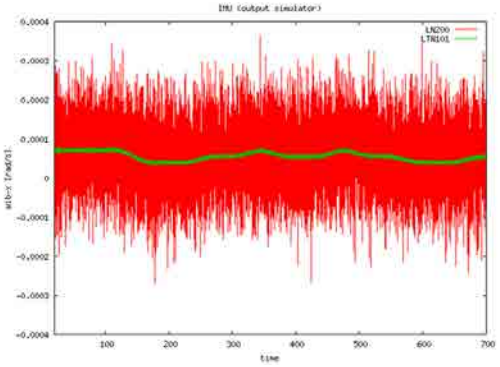

(a) X angular velocity (rad s^{-1})

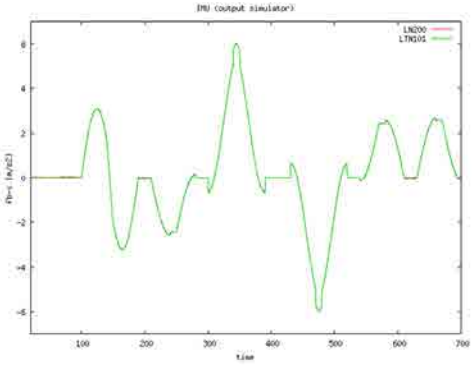

(b) X acceleration (m s^{-2})

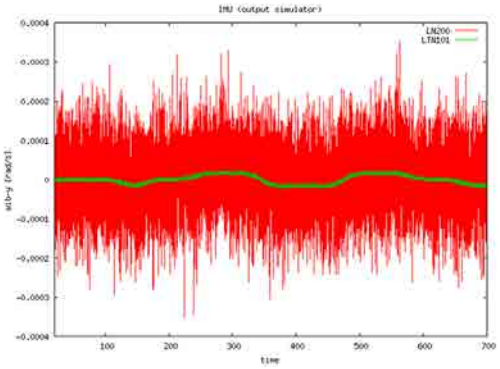

(c) Y angular velocity (rad s^{-1})

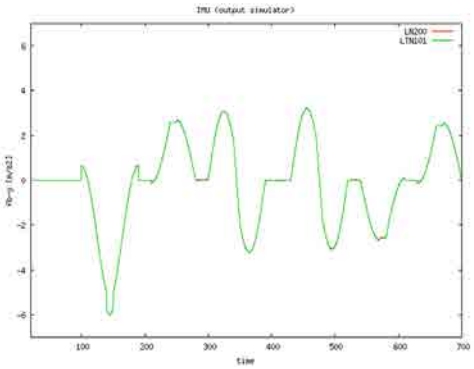

(d) Y acceleration (m s^{-2})

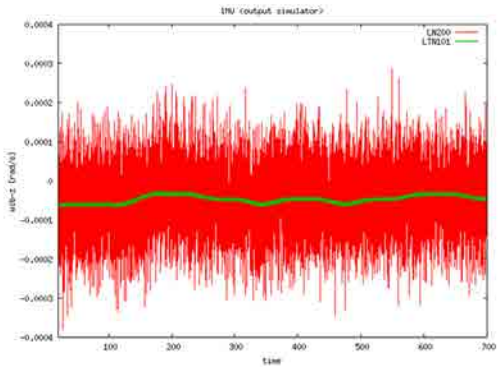

(e) Z angular velocity (rad s^{-1})

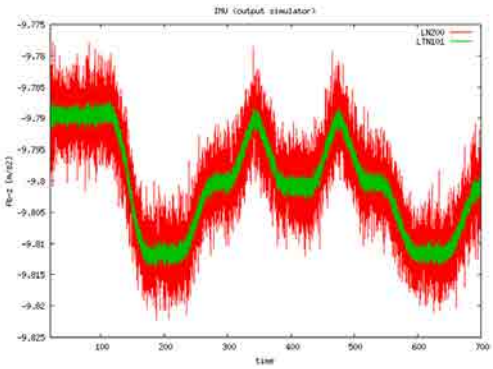

(f) Z acceleration (m s^{-2})

Figure 4.40: CTRA: simulated IMU data.

4.5.1 CTRA v2a1

As already discussed in Section 4.2, the codification this computation means:

- $\langle Hz \rangle = 2$: some subsets of parameters — $\underline{o}^{\mathsf{b}}$, $\underline{a}^{\mathsf{b}}$, δg or gg — has been grouped.
- $\langle \delta g_{NE} \rangle = a$: no prior knowledge of the horizontal gravity.
- $\langle method \rangle = 1$: basic network configuration similar to the Kalman filtering.

LN200

Table 4.41 summarises the network configuration used in this computation.

Model Name	Frequency		Equation	Standard Deviation	
FB-GG (3.4.5)	20.0 Hz	$\forall t$	(3.13)	2.2	10^{-3} m s^{-2}
WIB (3.4.2)	20.0 Hz	$\forall t$	(3.10)	5.2	10^{-5} rad s^{-1}
VEL (3.4.1)	20.0 Hz	$\forall t$	(3.4.1)	0.000 01	m
Q-NORM (3.4.6)	20.0 Hz	$\forall t$	(3.14)	0.01	ppm
OB-O (3.4.35)	0.1 Hz	$\forall t$	(3.48)	4.9	10^{-6} rad s^{-1}
AB-O (3.4.36)	0.1 Hz	$\forall t$	(3.49)	2.0	10^{-3} m s^{-2}
OB (3.4.8)	0.1 Hz	$\forall t$	(3.16)	15.0	10^{-7} rad s^{-1}
AB (3.4.10)	0.1 Hz	$\forall t$	(3.18)	130.0	10^{-4} m s^{-2}
AOFF-O (3.4.37)			(3.50)	0.001	m
CUPT (3.4.16)	1.0 Hz	$\forall t$	(3.26)	0.05	m
GDT-GG (3.4.13)	0.1 Hz	$\forall t$	(3.22)	6.2	mGal
DGUPT-GG (3.4.28)		t_0, t_N	(3.41)	0.02	mGal

Table 4.41: Test CTRA-LN200-v2a1: network configuration.

Figure 4.41 proves that the functional models of the NA approach work succesfully:

- Figure 4.41a points out that the position has been recovered, especially heights — in Figure 4.41c — with a precision better than 1 cm.
- The navigation parameters — shown in Figure 4.41e — are recovered with a precision of 1.2 ' for roll (α) and pitch (χ) and 4.2 ' for heading (η).
- The IMU error parameters exhibited in Figures 4.41b and 4.41d are nearly constants within the defined tolerances (bias repeatability) of the IMU.
- Figure 4.41f also displays the gravity disturbance vector, that has to be zero with a precision better than 2.5 mGal.

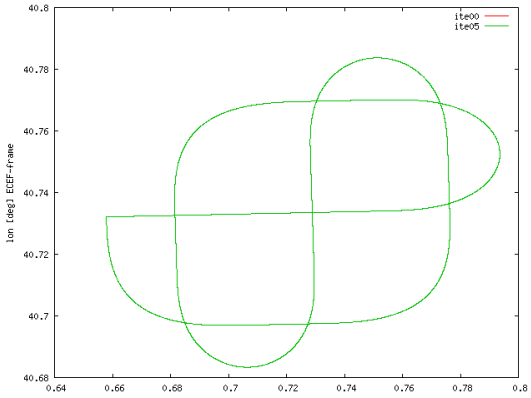

(a) Position (°)

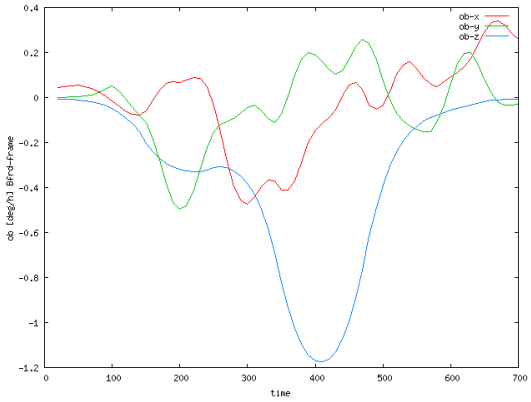

(b) Angular drift ($^\circ\,h^{-1}$)

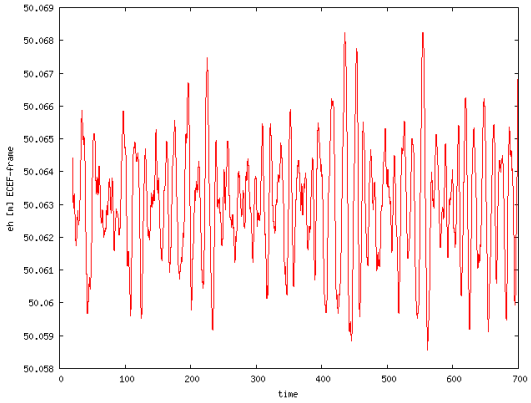

(c) Height (m)

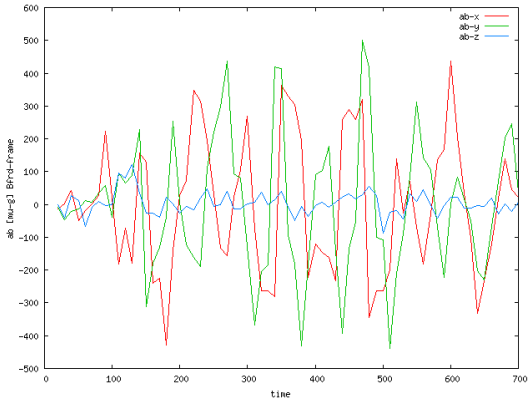

(d) Accelerometer bias (μg)

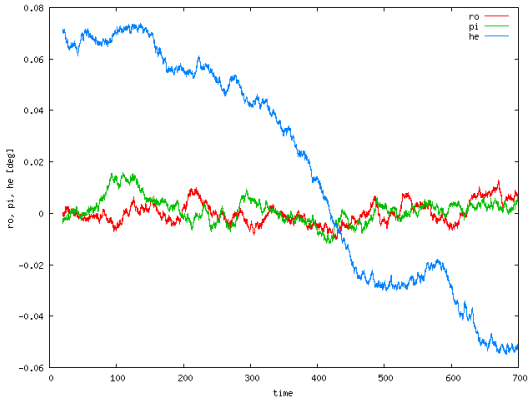

(e) Roll, Pitch and Heading (°)

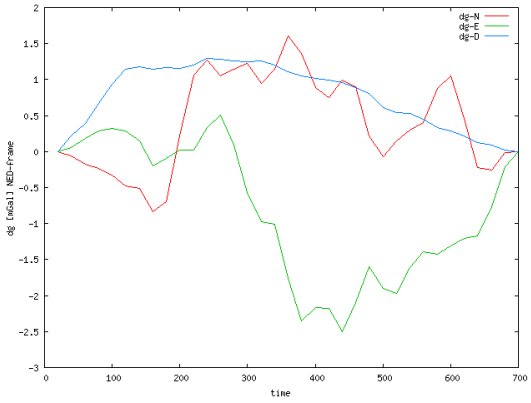

(f) Gravity disturbance (mGal)

Figure 4.41: CTRA LN200 v2a1: adjusted parameters.

LTN101

Table 4.42 summarises the network configuration used in this computation.

Model Name	Frequency		Equation	Standard Deviation	
FB-GG (3.4.5)	20.0 Hz	$\forall t$	(3.13)	4.4	10^{-4} m s^{-2}
WIB (3.4.2)	20.0 Hz	$\forall t$	(3.10)	1.3	10^{-6} rad s^{-1}
VEL (3.4.1)	20.0 Hz	$\forall t$	(3.4.1)	0.000 01	m
Q-NORM (3.4.6)	20.0 Hz	$\forall t$	(3.14)	0.01	ppm
OB-O (3.4.35)	0.1 Hz	$\forall t$	(3.48)	4.9	10^{-8} rad s^{-1}
AB-O (3.4.36)	0.1 Hz	$\forall t$	(3.49)	4.9	10^{-4} m s^{-2}
OB (3.4.8)	0.1 Hz	$\forall t$	(3.16)	61.0	10^{-12} rad s^{-1}
AB (3.4.10)	0.1 Hz	$\forall t$	(3.18)	95.0	10^{-7} m s^{-2}
AOFF-O (3.4.37)			(3.50)	0.001	m
CUPT (3.4.16)	1.0 Hz	$\forall t$	(3.26)	0.05	m
GDT-GG (3.4.13)	0.1 Hz	$\forall t$	(3.22)	6.2	mGal
DGUPT-GG (3.4.28)		t_0, t_N	(3.41)	0.02	mGal

Table 4.42: Test CTRA-LTN101-v2a1: network configuration.

Figure 4.42 proves that the functional models of the NA approach work succesfully:

- Figure 4.42a points out that the position has been recovered, especially heights — in Figure 4.42c — with a precision better than 1 cm.
- The navigation parameters — shown in Figure 4.42e — are recovered with a precision of 9 " for roll (α) and pitch (χ) and 1.5 ’ for heading (η).
- The IMU error parameters exhibited in Figures 4.42b and 4.42d are nearly constants within the defined tolerances (bias repeatability) of the IMU.
- Figure 4.42f also displays the gravity disturbance vector, that has to be zero.

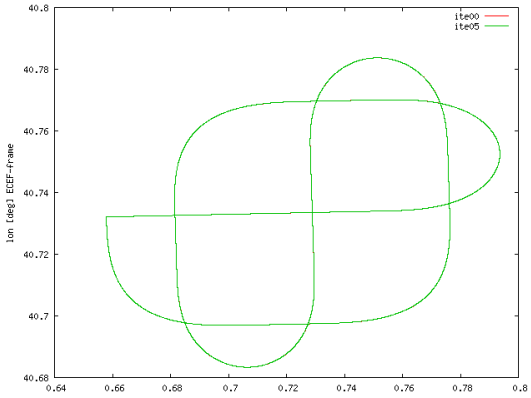

(a) Position (°)

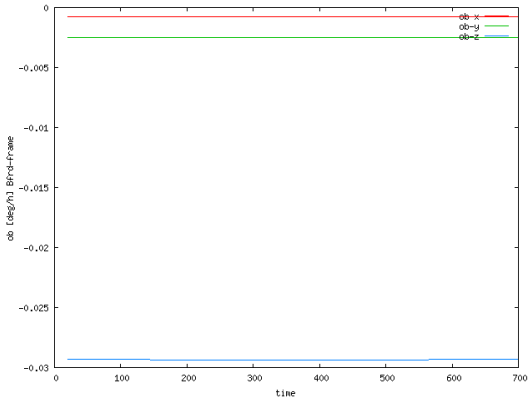

(b) Angular drift ($^\circ\,h^{-1}$)

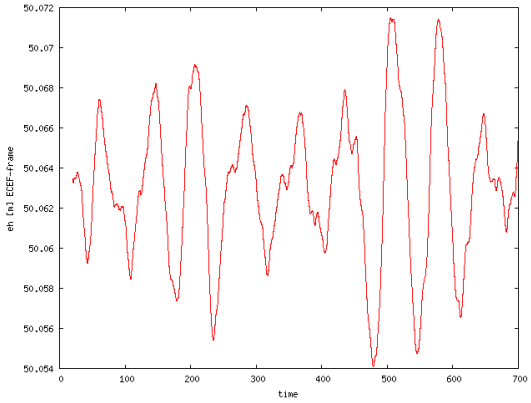

(c) Height (m)

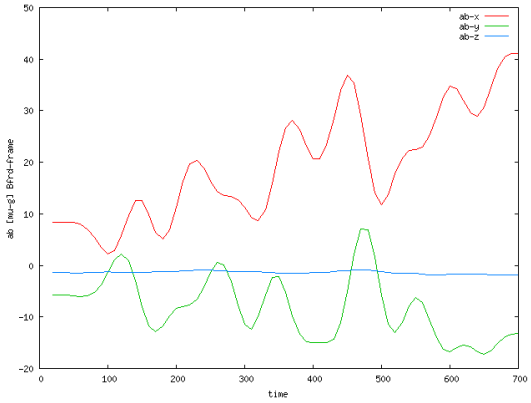

(d) Accelerometer bias (μg)

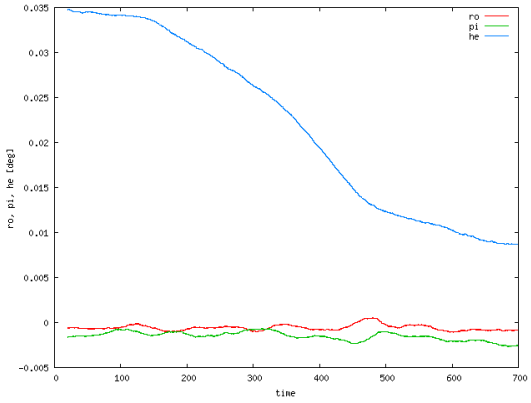

(e) Roll, Pitch and Heading (°)

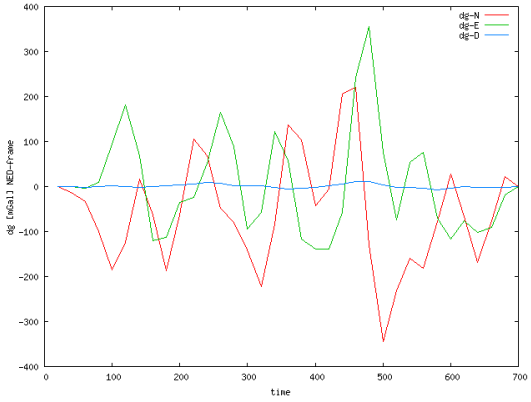

(f) Gravity disturbance (mGal)

Figure 4.42: CTRA LTN101b v2a1: adjusted parameters.

4.5.2 CTRA vq2a1

As already discussed in Section 4.2, the codification this computation means:

- $\langle q \rangle = q$, indicates that prior knowledge of the vehicle's attitude exists at the beginning (t_0) and at the end (t_N) of the mission.
- $\langle Hz \rangle = 2$: some subsets of parameters — $\underline{o}^{\mathsf{b}}$, $\underline{a}^{\mathsf{b}}$, δg or gg — has been grouped.
- $\langle \delta g_{NE} \rangle = a$: no prior knowledge of the horizontal gravity.
- $\langle method \rangle = 1$, indicates a basic network configuration similar to the Kalman filtering.

LN200

Table 4.43 summarises the network configuration used in this computation.

Model Name	Frequency		Equation	Standard Deviation	
FB-GG (3.4.5)	20.0 Hz	$\forall t$	(3.13)	2.2	10^{-3} m s^{-2}
WIB (3.4.2)	20.0 Hz	$\forall t$	(3.10)	5.2	10^{-5} rad s^{-1}
VEL (3.4.1)	20.0 Hz	$\forall t$	(3.4.1)	0.000 01	m
Q-NORM (3.4.6)	20.0 Hz	$\forall t$	(3.14)	0.01	ppm
OB-O (3.4.35)	0.1 Hz	$\forall t$	(3.48)	4.9	10^{-6} rad s^{-1}
AB-O (3.4.36)	0.1 Hz	$\forall t$	(3.49)	2.0	10^{-3} m s^{-2}
OB (3.4.8)	0.1 Hz	$\forall t$	(3.16)	15.0	10^{-7} rad s^{-1}
AB (3.4.10)	0.1 Hz	$\forall t$	(3.18)	130.0	10^{-4} m s^{-2}
AOFF-O (3.4.37)			(3.50)	0.001	m
CUPT (3.4.16)	1.0 Hz	$\forall t$	(3.26)	0.05	m
GDT-GG (3.4.13)	0.1 Hz	$\forall t$	(3.22)	6.2	mGal
DGUPT-GG (3.4.28)		t_0, t_N	(3.41)	0.02	mGal
Q-O (3.4.34)		t_0, t_N	(3.47)	0.01	ppm

Table 4.43: Test CTRA-LN200-vq2a1: network configuration.

Figure 4.43 proves that the functional models of the NA approach work succesfully:

- Figures 4.43a and 4.43c point out that the position has been recovered, especially heights with a precision better than 0.5 cm.
- The navigation parameters — shown in Figure 4.43e — are recovered with a precision of 6 ' for roll (α) and pitch (χ) and with a range of 4.2 ' for heading (η).
- The IMU error parameters exhibited in Figures 4.43b and 4.43d are nearly constants within the defined tolerances (bias repeatability) of the IMU.
- Figure 4.43f also displays the gravity disturbance vector, that has to be zero, with a precision better than 2 mGal.

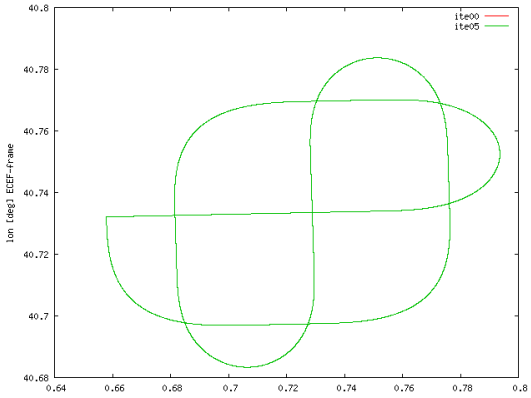

(a) Position (°)

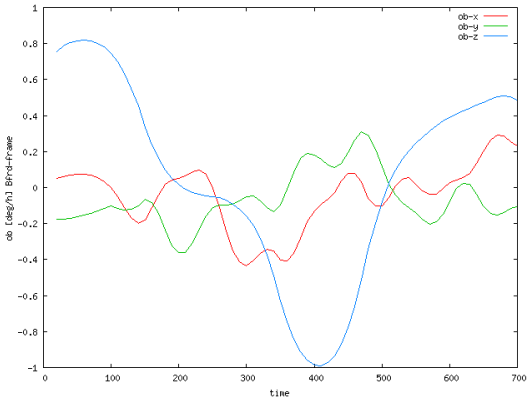

(b) Angular drift ($^\circ\,h^{-1}$)

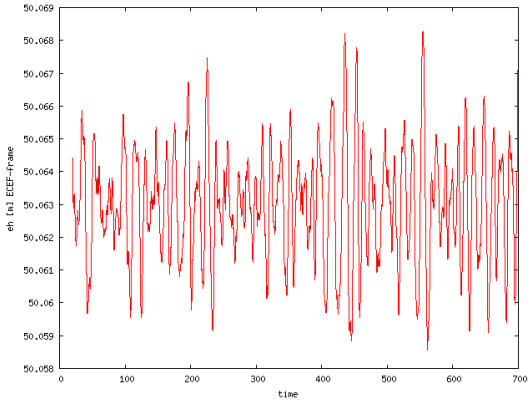

(c) Height (m)

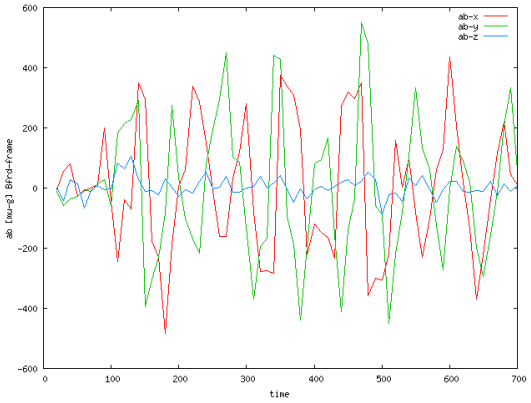

(d) Accelerometer bias (μg)

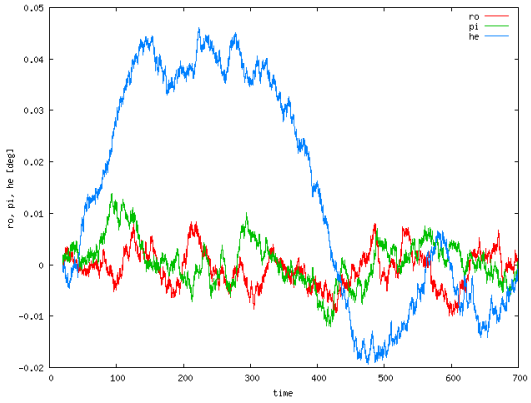

(e) Roll, Pitch and Heading (°)

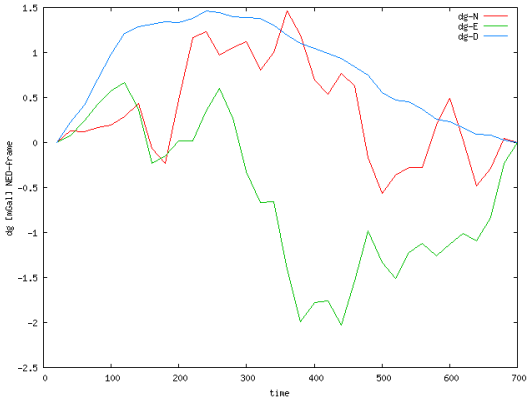

(f) Gravity disturbance (mGal)

Figure 4.43: CTRA LN200 vq2a1: adjusted parameters.

LTN101

Table 4.44 summarises the network configuration used in this computation.

Model Name	Frequency		Equation	Standard Deviation	
FB-GG (3.4.5)	20.0 Hz	$\forall t$	(3.13)	4.4	10^{-4} m s^{-2}
WIB (3.4.2)	20.0 Hz	$\forall t$	(3.10)	1.3	10^{-6} rad s^{-1}
VEL (3.4.1)	20.0 Hz	$\forall t$	(3.4.1)	0.000 01	m
Q-NORM (3.4.6)	20.0 Hz	$\forall t$	(3.14)	0.01	ppm
OB-O (3.4.35)	0.1 Hz	$\forall t$	(3.48)	4.9	10^{-8} rad s^{-1}
AB-O (3.4.36)	0.1 Hz	$\forall t$	(3.49)	4.9	10^{-4} m s^{-2}
OB (3.4.8)	0.1 Hz	$\forall t$	(3.16)	61.0	10^{-12} rad s^{-1}
AB (3.4.10)	0.1 Hz	$\forall t$	(3.18)	95.0	10^{-7} m s^{-2}
AOFF-O (3.4.37)			(3.50)	0.001	m
CUPT (3.4.16)	1.0 Hz	$\forall t$	(3.26)	0.05	m
GDT-GG (3.4.13)	0.1 Hz	$\forall t$	(3.22)	6.2	mGal
DGUPT-GG (3.4.28)		t_0, t_N	(3.41)	0.02	mGal
Q-O (3.4.34)		t_0, t_N	(3.47)	0.01	ppm

Table 4.44: Test CTRA-LTN101-vq2a1: network configuration.

Figure 4.44 proves that the functional models of the NA approach work succesfully:

- Figures 4.44a and 4.44c point out that the position has been recovered, especially heights with a precision better than 0.5 cm.
- The navigation parameters — shown in Figure 4.44e — are recovered with a precision of 3.6 " for roll (α) and pitch (χ) and with a range of 0.48 ’ for heading (η).
- The IMU error parameters exhibited in Figures 4.44b and 4.44d are nearly constants within the defined tolerances (bias repeatability) of the IMU.
- Figure 4.44f also displays the gravity disturbance vector, that has to be zero.

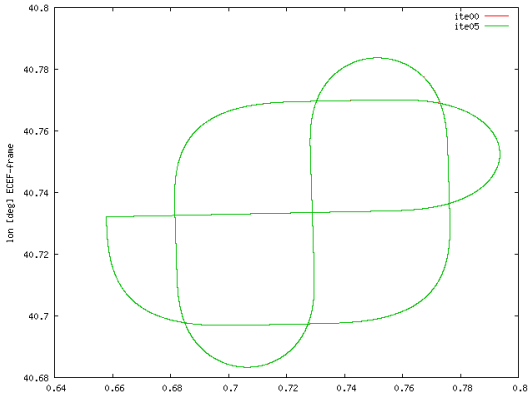

(a) Position (°)

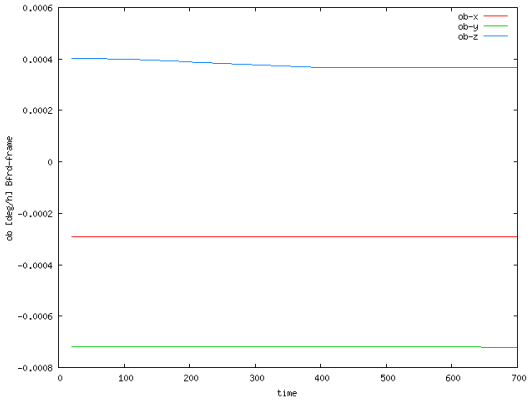

(b) Angular drift ($^\circ\,h^{-1}$)

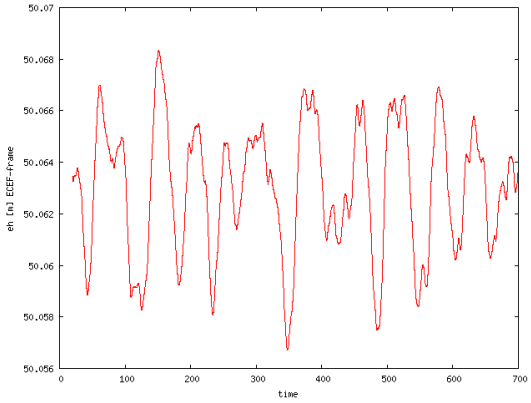

(c) Height (m)

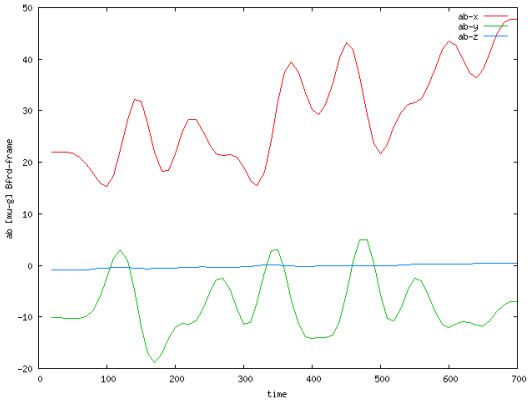

(d) Accelerometer bias (μg)

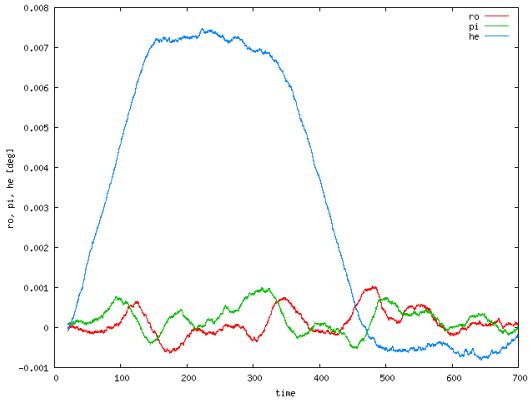

(e) Roll, Pitch and Heading (°)

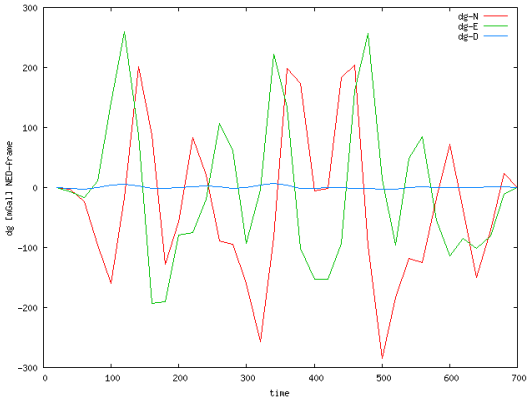

(f) Gravity disturbance (mGal)

Figure 4.44: CTRA LTN101b vq2a1: adjusted parameters.

4.5.3 CTRA v2a2

As already discussed in Section 4.2, the codification this computation means:

- $\langle Hz \rangle = 2$: some subsets of parameters — $\underline{o}^{\mathsf{b}}$, $\underline{a}^{\mathsf{b}}$, δg or gg — has been grouped.
- $\langle \delta g_{NE} \rangle = a$: no prior knowledge of the horizontal gravity.
- $\langle method \rangle = 2$: GDT-p (changes of the gravity disturbance of closed positions with respect to time) observations are added to the basic configuration.

LN200

Table 4.45 summarises the network configuration used in this computation.

Model Name	Frequency		Equation	Standard Deviation	
FB-GG (3.4.5)	20.0 Hz	$\forall t$	(3.13)	2.2	10^{-3} m s^{-2}
WIB (3.4.2)	20.0 Hz	$\forall t$	(3.10)	5.2	10^{-5} rad s^{-1}
VEL (3.4.1)	20.0 Hz	$\forall t$	(3.4.1)	0.000 01	m
Q-NORM (3.4.6)	20.0 Hz	$\forall t$	(3.14)	0.01	ppm
OB-O (3.4.35)	0.1 Hz	$\forall t$	(3.48)	4.9	10^{-6} rad s^{-1}
AB-O (3.4.36)	0.1 Hz	$\forall t$	(3.49)	2.0	10^{-3} m s^{-2}
OB (3.4.8)	0.1 Hz	$\forall t$	(3.16)	15.0	10^{-7} rad s^{-1}
AB (3.4.10)	0.1 Hz	$\forall t$	(3.18)	130.0	10^{-4} m s^{-2}
AOFF-O (3.4.37)			(3.50)	0.001	m
CUPT (3.4.16)	1.0 Hz	$\forall t$	(3.26)	0.05	m
GDT-GG (3.4.13)	0.1 Hz	$\forall t$	(3.22)	6.2	mGal
GDT-GG (3.4.13)	$\forall x_i, x_j : \left\|x_i - x_j\right\| = 1km$		(3.22)	6.2	mGal
GDT-GG (3.4.13)	$\forall x_i, x_j : \left\|x_i - x_j\right\| = 4km$		(3.22)	13.0	mGal
DGUPT-GG (3.4.28)		t_0, t_N	(3.41)	0.02	mGal

Table 4.45: Test CTRA-LN200-v2a2: network configuration.

Figure 4.45 proves that the functional models of the NA approach work succesfully:

- Figures 4.45a and 4.45c point out that the position has been recovered, especially heights with a precision better than 0.5 cm.
- The navigation parameters — shown in Figure 4.45e — are recovered with a precision better than 1.2 ' for roll (α) and pitch (χ) and with a range of 8.4 ' for heading (η).
- The IMU error parameters exhibited in Figures 4.45b and 4.45d are nearly constants within the defined tolerances (bias repeatability) of the IMU.
- Figure 4.45f also displays the gravity disturbance vector, that has to be zero with a precision of 1.5 mGal.

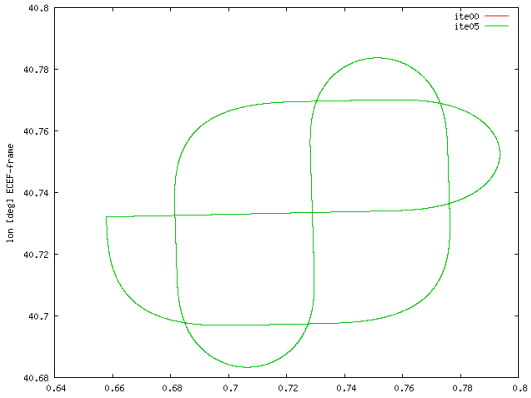

(a) Position (°)

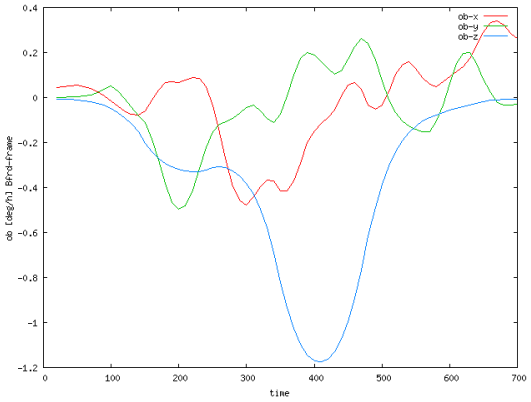

(b) Angular drift ($^\circ\,h^{-1}$)

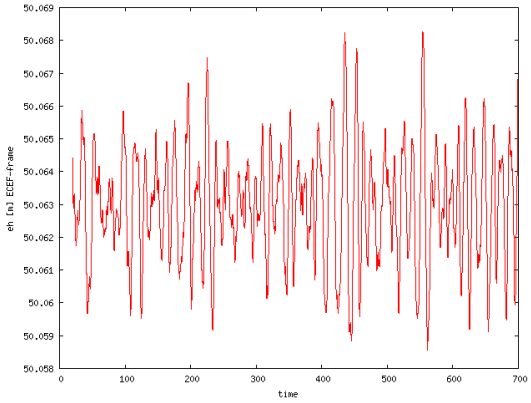

(c) Height (m)

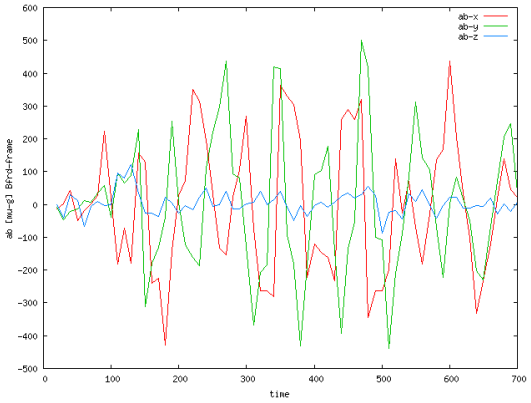

(d) Accelerometer bias (μg)

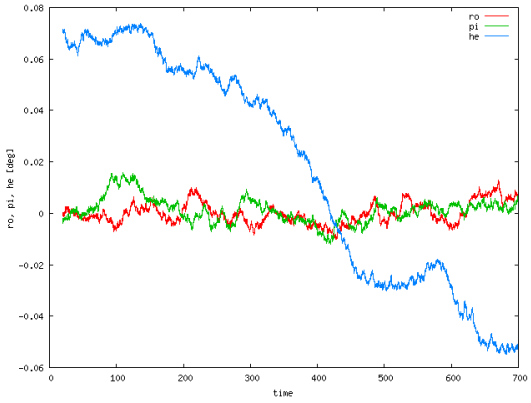

(e) Roll, Pitch and Heading (°)

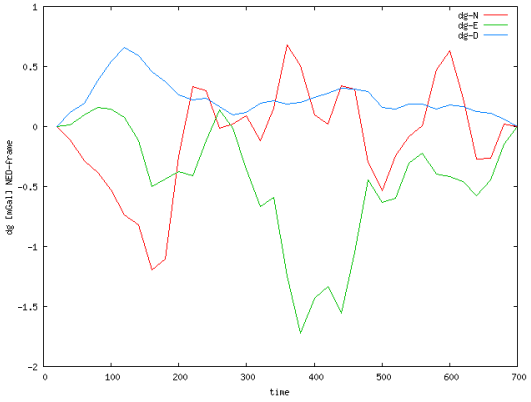

(f) Gravity disturbance (mGal)

Figure 4.45: CTRA LN200 v2a2: adjusted parameters.

LTN101

Table 4.46 summarises the network configuration used in this computation.

Model Name	Frequency		Equation	Standard Deviation	
FB-GG (3.4.5)	20.0 Hz	$\forall t$	(3.13)	4.4	10^{-4} m s^{-2}
WIB (3.4.2)	20.0 Hz	$\forall t$	(3.10)	1.3	10^{-6} rad s^{-1}
VEL (3.4.1)	20.0 Hz	$\forall t$	(3.4.1)	0.000 01	m
Q-NORM (3.4.6)	20.0 Hz	$\forall t$	(3.14)	0.01	ppm
OB-O (3.4.35)	0.1 Hz	$\forall t$	(3.48)	4.9	10^{-8} rad s^{-1}
AB-O (3.4.36)	0.1 Hz	$\forall t$	(3.49)	4.9	10^{-4} m s^{-2}
OB (3.4.8)	0.1 Hz	$\forall t$	(3.16)	61.0	10^{-12} rad s^{-1}
AB (3.4.10)	0.1 Hz	$\forall t$	(3.18)	95.0	10^{-7} m s^{-2}
AOFF-O (3.4.37)			(3.50)	0.001	m
CUPT (3.4.16)	1.0 Hz	$\forall t$	(3.26)	0.05	m
GDT-GG (3.4.13)	0.1 Hz	$\forall t$	(3.22)	6.2	mGal
GDT-GG (3.4.13)	$\forall x_i, x_j : \left\|x_i - x_j\right\| = 1km$		(3.22)	6.2	mGal
GDT-GG (3.4.13)	$\forall x_i, x_j : \left\|x_i - x_j\right\| = 4km$		(3.22)	13.0	mGal
DGUPT-GG (3.4.28)		t_0, t_N	(3.41)	0.02	mGal

Table 4.46: Test CTRA-LTN101-v2a2: network configuration.

Figure 4.46 proves that the functional models of the NA approach work succesfully:

- Figures 4.46a and 4.46c point out that the position has been recovered, especially heights with a precision better than 0.5 cm.
- The navigation parameters — shown in Figure 4.46e — are recovered with a precision better than 9 " for roll (α) and pitch (χ) and with a range of 1.8 ’ for heading (η).
- The IMU error parameters exhibited in Figures 4.46b and 4.46d are nearly constants within the defined tolerances (bias repeatability) of the IMU.
- Figure 4.46f also displays the gravity disturbance vector, that has to be zero.

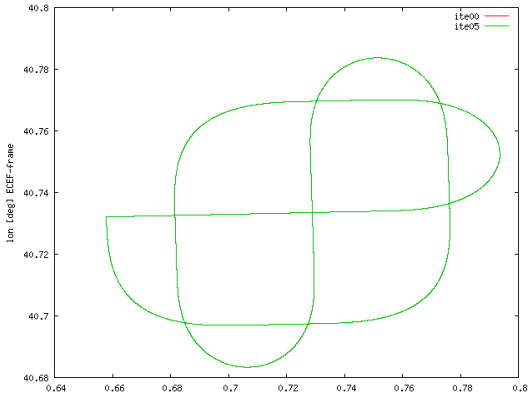

(a) Position (°)

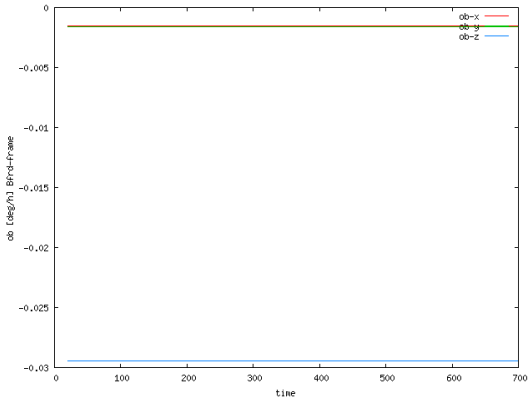

(b) Angular drift ($^\circ\,h^{-1}$)

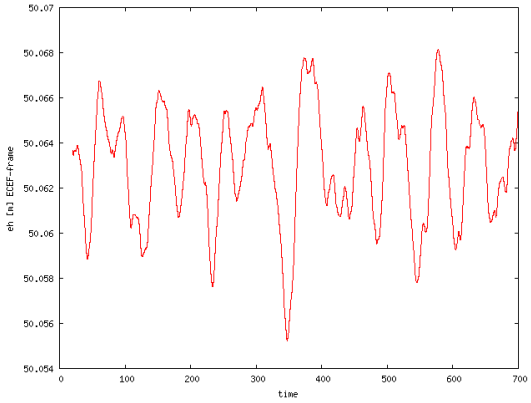

(c) Height (m)

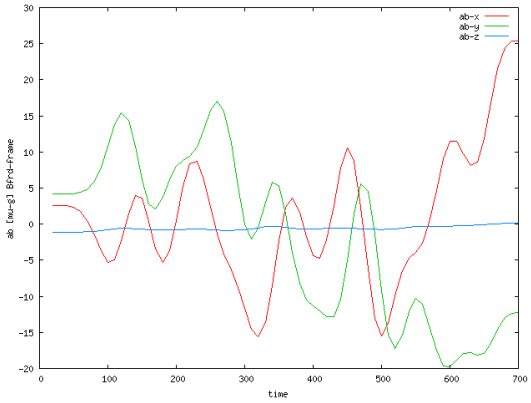

(d) Accelerometer bias (μg)

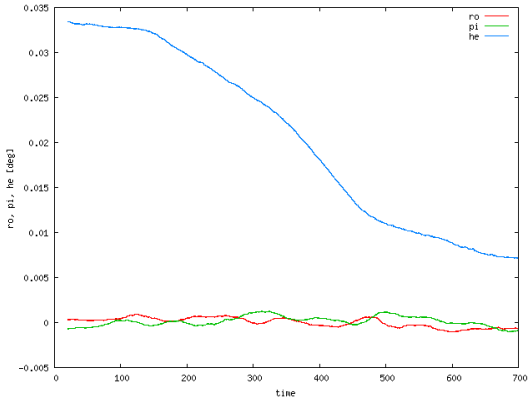

(e) Roll, Pitch and Heading (°)

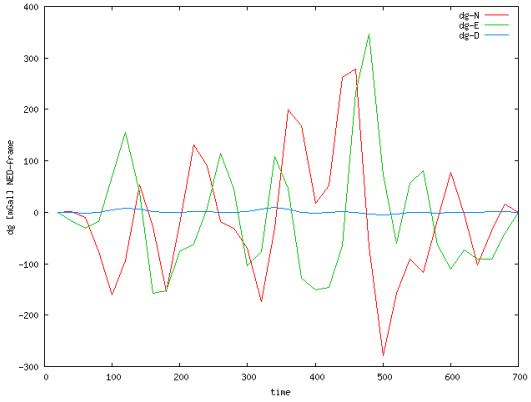

(f) Gravity disturbance (mGal)

Figure 4.46: CTRA LTN101b v2a2: adjusted parameters.

4.5.4 CTRA vq2a2

As already discussed in Section 4.2, the codification this computation means:

- $\langle q \rangle$,indicates that prior knowledge of the vehicle's attitude exists at the beginning (t_0) and at the end (t_N) of the mission.
- $\langle Hz \rangle = 2$: some subsets of parameters — $\underline{o}^{\mathsf{b}}$, $\underline{a}^{\mathsf{b}}$, δg or gg — has been grouped.
- $\langle \delta g_{NE} \rangle = a$: no prior knowledge of the horizontal gravity.
- $\langle method \rangle = 2$: GDT-p (changes of the gravity disturbance of closed positions with respect to time) observations are added to the basic configuration.

LN200

Table 4.47 summarises the network configuration used in this computation.

Model Name	Frequency		Equation	Standard Deviation	
FB-GG (3.4.5)	20.0 Hz	$\forall t$	(3.13)	2.2	10^{-3} m s^{-2}
WIB (3.4.2)	20.0 Hz	$\forall t$	(3.10)	5.2	10^{-5} rad s^{-1}
VEL (3.4.1)	20.0 Hz	$\forall t$	(3.4.1)	0.000 01	m
Q-NORM (3.4.6)	20.0 Hz	$\forall t$	(3.14)	0.01	ppm
OB-O (3.4.35)	0.1 Hz	$\forall t$	(3.48)	4.9	10^{-6} rad s^{-1}
AB-O (3.4.36)	0.1 Hz	$\forall t$	(3.49)	2.0	10^{-3} m s^{-2}
OB (3.4.8)	0.1 Hz	$\forall t$	(3.16)	15.0	10^{-7} rad s^{-1}
AB (3.4.10)	0.1 Hz	$\forall t$	(3.18)	130.0	10^{-4} m s^{-2}
AOFF-O (3.4.37)			(3.50)	0.001	m
CUPT (3.4.16)	1.0 Hz	$\forall t$	(3.26)	0.05	m
GDT-GG (3.4.13)	0.1 Hz	$\forall t$	(3.22)	6.2	mGal
GDT-GG (3.4.13)	$\forall x_i, x_j : \left\|x_i - x_j\right\| = 1km$		(3.22)	6.2	mGal
GDT-GG (3.4.13)	$\forall x_i, x_j : \left\|x_i - x_j\right\| = 4km$		(3.22)	13.0	mGal
DGUPT-GG (3.4.28)		t_0, t_N	(3.41)	0.02	mGal
Q-O (3.4.34)		t_0, t_N	(3.47)	0.01	ppm

Table 4.47: Test CTRA-LN200-vq2a2: network configuration.

Figure 4.47 proves that the functional models of the NA approach work succesfully:

- Figures 4.47a and 4.47c point out that the position has been recovered, especially heights with a precision better than 0.5 cm.
- The navigation parameters — shown in Figure 4.47e — are recovered with a precision of 0.6 ' for roll (α) and pitch (χ) and with a range of 4.2 ' for heading (η).

- The IMU error parameters exhibited in Figures 4.47b and 4.47d are nearly constants within the defined tolerances (bias repeatability) of the IMU.
- Figure 4.47f also displays the gravity disturbance vector, that has to be zero, with a precision better than 1.5 mGal.

LTN101

Table 4.48 summarises the network configuration used in this computation.

Model Name	Frequency		Equation	Standard Deviation	
FB-GG (3.4.5)	20.0 Hz	$\forall t$	(3.13)	4.4	10^{-4} m s^{-2}
WIB (3.4.2)	20.0 Hz	$\forall t$	(3.10)	1.3	10^{-6} rad s^{-1}
VEL (3.4.1)	20.0 Hz	$\forall t$	(3.4.1)	0.000 01	m
Q-NORM (3.4.6)	20.0 Hz	$\forall t$	(3.14)	0.01	ppm
OB-O (3.4.35)	0.1 Hz	$\forall t$	(3.48)	4.9	10^{-8} rad s^{-1}
AB-O (3.4.36)	0.1 Hz	$\forall t$	(3.49)	4.9	10^{-4} m s^{-2}
OB (3.4.8)	0.1 Hz	$\forall t$	(3.16)	61.0	10^{-12} rad s^{-1}
AB (3.4.10)	0.1 Hz	$\forall t$	(3.18)	95.0	10^{-7} m s^{-2}
AOFF-O (3.4.37)			(3.50)	0.001	m
CUPT (3.4.16)	1.0 Hz	$\forall t$	(3.26)	0.05	m
GDT-GG (3.4.13)	0.1 Hz	$\forall t$	(3.22)	6.2	mGal
GDT-GG (3.4.13)	$\forall x_i, x_j : \left\|x_i - x_j\right\| = 1km$		(3.22)	6.2	mGal
GDT-GG (3.4.13)	$\forall x_i, x_j : \left\|x_i - x_j\right\| = 4km$		(3.22)	13.0	mGal
DGUPT-GG (3.4.28)		t_0, t_N	(3.41)	0.02	mGal
Q-O (3.4.34)		t_0, t_N	(3.47)	0.01	ppm

Table 4.48: Test CTRA-LTN101-vq2a2: network configuration.

Figure 4.48 proves that the functional models of the NA approach work succesfully:

- Figures 4.48a and 4.48c point out that the position has been recovered, especially heights with a precision better than 1 cm.
- The navigation parameters — shown in Figure 4.48e — are recovered with a range of 10.8 " for roll (α) and pitch (χ) and 28.8 " for heading (η).
- The IMU error parameters exhibited in Figures 4.48b and 4.48d are nearly constants within the defined tolerances (bias repeatability) of the IMU.
- Figure 4.48f also displays the gravity disturbance vector, that has to be zero.

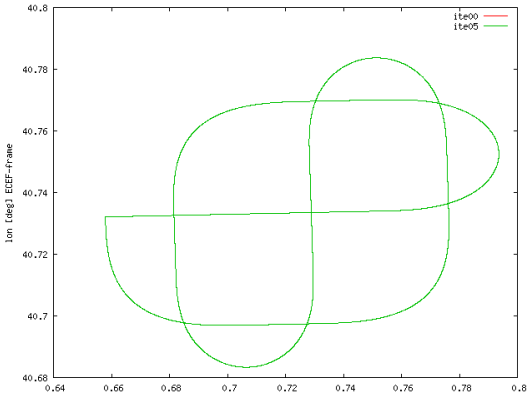

(a) Position (°)

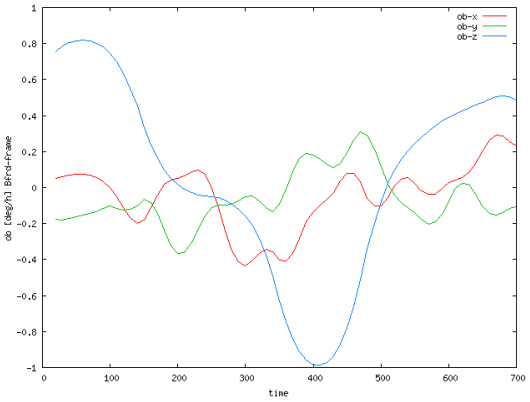

(b) Angular drift ($^\circ\,h^{-1}$)

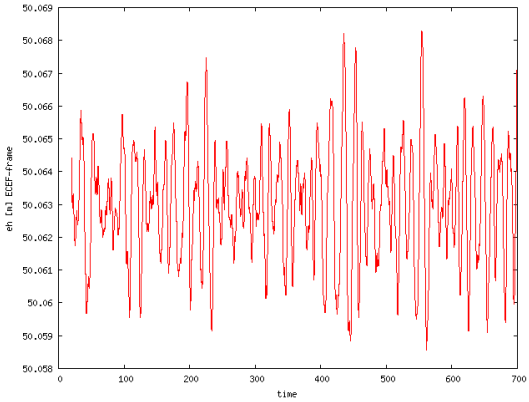

(c) Height (m)

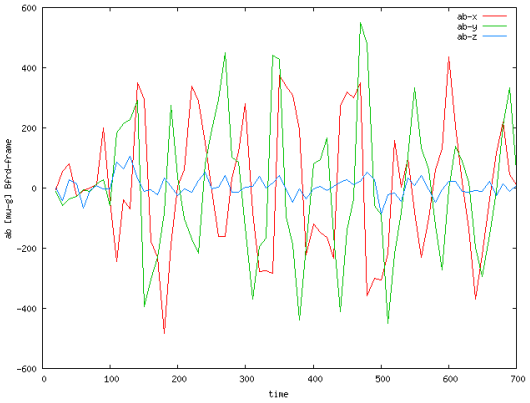

(d) Accelerometer bias (μg)

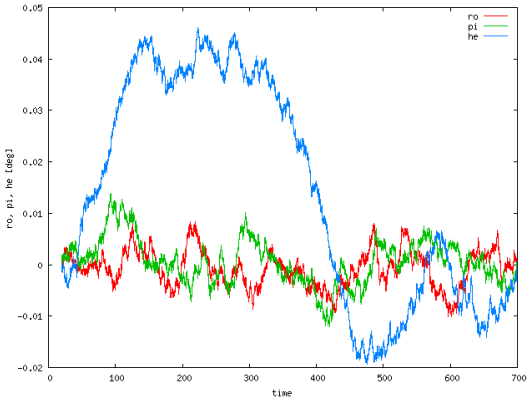

(e) Roll, Pitch and Heading (°)

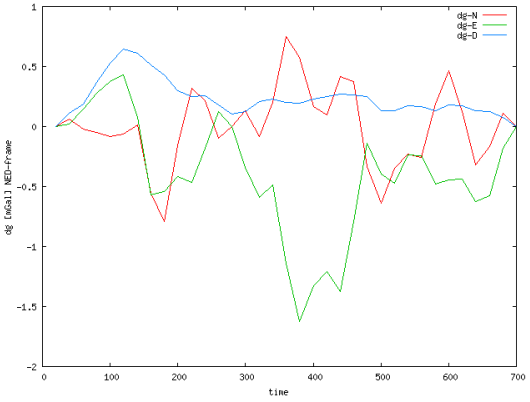

(f) Gravity disturbance (mGal)

Figure 4.47: CTRA LN200 vq2a2: adjusted parameters.

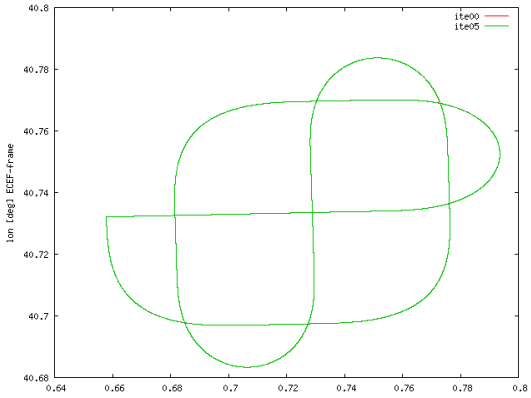

(a) Position (°)

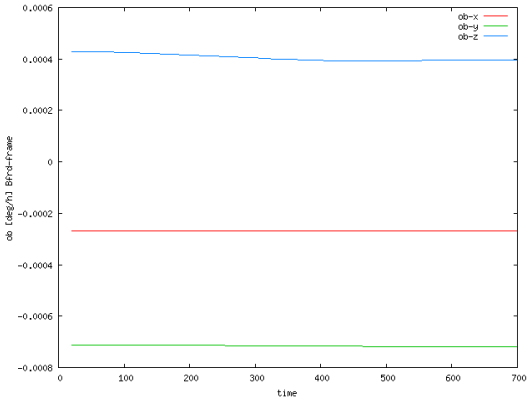

(b) Angular drift ($^\circ\,h^{-1}$)

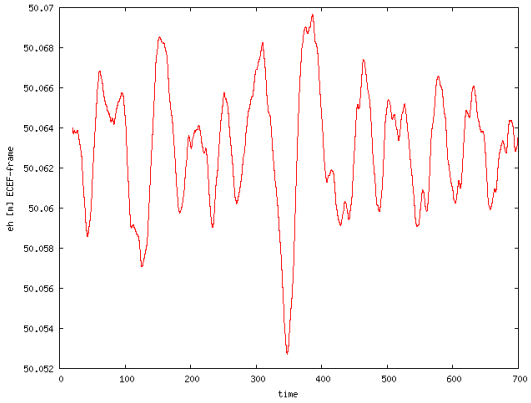

(c) Height (m)

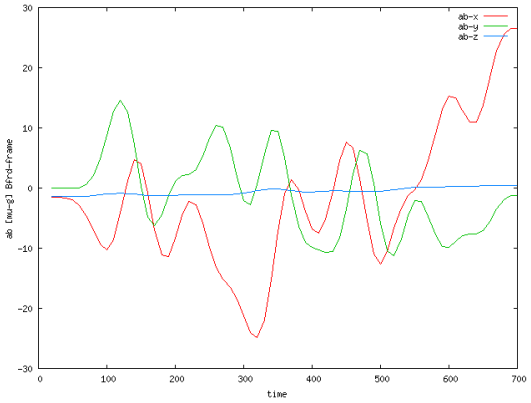

(d) Accelerometer bias (μg)

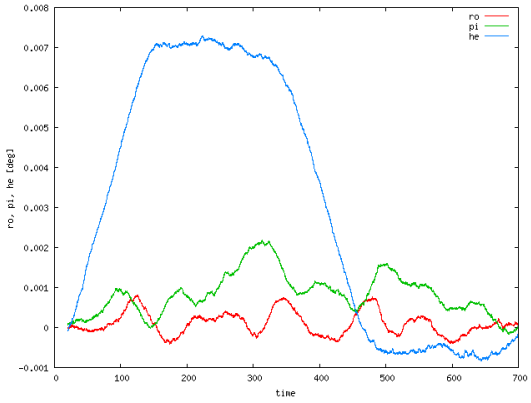

(e) Roll, Pitch and Heading (°)

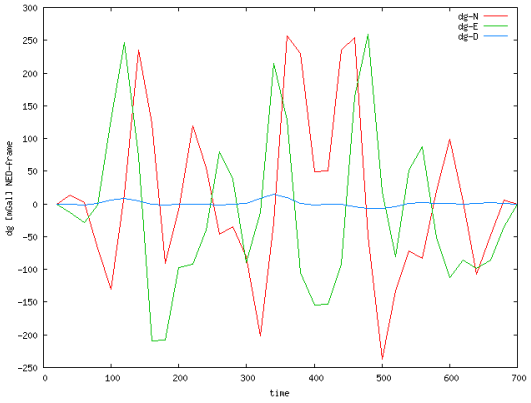

(f) Gravity disturbance (mGal)

Figure 4.48: CTRA LTN101b vq2a2: adjusted parameters.

4.5.5 CTRA v2a2x

As already discussed in Section 4.2, the codification this computation means:

- $\langle Hz \rangle = 2$: some subsets of parameters — $\underline{o}^{\mathsf{b}}$, $\underline{a}^{\mathsf{b}}$, δg or gg — has been grouped.
- $\langle \delta g_{NE} \rangle = a$: no prior knowledge of the horizontal gravity.
- $\langle method \rangle = 2x$: GDT-p (changes of the gravity disturbance of closed positions with respect to time) observations are added to the basic configuration and, moreover, XOVER observations are considered.

LN200

Table 4.49 summarises the network configuration used in this computation.

Model Name	Frequency		Equation	Standard Deviation	
FB-GG (3.4.5)	20.0 Hz	$\forall t$	(3.13)	2.2	10^{-3} m s^{-2}
WIB (3.4.2)	20.0 Hz	$\forall t$	(3.10)	5.2	10^{-5} rad s^{-1}
VEL (3.4.1)	20.0 Hz	$\forall t$	(3.4.1)	0.000 01	m
Q-NORM (3.4.6)	20.0 Hz	$\forall t$	(3.14)	0.01	ppm
OB-O (3.4.35)	0.1 Hz	$\forall t$	(3.48)	4.9	10^{-6} rad s^{-1}
AB-O (3.4.36)	0.1 Hz	$\forall t$	(3.49)	2.0	10^{-3} m s^{-2}
OB (3.4.8)	0.1 Hz	$\forall t$	(3.16)	15.0	10^{-7} rad s^{-1}
AB (3.4.10)	0.1 Hz	$\forall t$	(3.18)	130.0	10^{-4} m s^{-2}
AOFF-O (3.4.37)			(3.50)	0.001	m
CUPT (3.4.16)	1.0 Hz	$\forall t$	(3.26)	0.05	m
GDT-GG (3.4.13)	0.1 Hz	$\forall t$	(3.22)	6.2	mGal
GDT-GG (3.4.13)	$\forall x_i, x_j : \left\|x_i - x_j\right\| = 1km$		(3.22)	6.2	mGal
GDT-GG (3.4.13)	$\forall x_i, x_j : \left\|x_i - x_j\right\| = 4km$		(3.22)	13.0	mGal
DGUPT-GG (3.4.28)		t_0, t_N	(3.41)	0.02	mGal
XOVER-GG (3.4.31)			(3.44)	0.000 3	mGal

Table 4.49: Test CTRA-LN200-v2a2x: network configuration.

Figure 4.49 proves that the functional models of the NA approach work succesfully:

- Figures 4.49a and 4.49c point out that the position has been recovered, especially heights with a precision better than 0.5 cm.
- The navigation parameters — shown in Figure 4.49e — are recovered with a precision of 1.2 ' for roll (α) and pitch (χ) and 3.6 ' for heading (η).
- The IMU error parameters exhibited in Figures 4.49b and 4.49d are nearly constants within the defined tolerances (bias repeatability) of the IMU.

- Figure 4.49f also displays the gravity disturbance vector, that has to be zero, with a precision better than 1.5 mGal.

LTN101

Table 4.50 summarises the network configuration used in this computation.

Model Name	Frequency		Equation	Standard Deviation	
FB-GG (3.4.5)	20.0 Hz	$\forall t$	(3.13)	4.4	10^{-4} m s^{-2}
WIB (3.4.2)	20.0 Hz	$\forall t$	(3.10)	1.3	10^{-6} rad s^{-1}
VEL (3.4.1)	20.0 Hz	$\forall t$	(3.4.1)	0.000 01	m
Q-NORM (3.4.6)	20.0 Hz	$\forall t$	(3.14)	0.01	ppm
OB-O (3.4.35)	0.1 Hz	$\forall t$	(3.48)	4.9	10^{-8} rad s^{-1}
AB-O (3.4.36)	0.1 Hz	$\forall t$	(3.49)	4.9	10^{-4} m s^{-2}
OB (3.4.8)	0.1 Hz	$\forall t$	(3.16)	61.0	10^{-12} rad s^{-1}
AB (3.4.10)	0.1 Hz	$\forall t$	(3.18)	95.0	10^{-7} m s^{-2}
AOFF-O (3.4.37)			(3.50)	0.001	m
CUPT (3.4.16)	1.0 Hz	$\forall t$	(3.26)	0.05	m
GDT-GG (3.4.13)	0.1 Hz	$\forall t$	(3.22)	6.2	mGal
GDT-GG (3.4.13)	$\forall x_i, x_j : \left\|x_i - x_j\right\| = 1km$		(3.22)	6.2	mGal
GDT-GG (3.4.13)	$\forall x_i, x_j : \left\|x_i - x_j\right\| = 4km$		(3.22)	13.0	mGal
DGUPT-GG (3.4.28)		t_0, t_N	(3.41)	0.02	mGal
XOVER-GG (3.4.31)			(3.44)	0.000 3	mGal

Table 4.50: Test CTRA-LTN101-v2a2x: network configuration.

Figure 4.50 proves that the functional models of the NA approach work succesfully:

- Figures 4.50a and 4.50c point out that the position has been recovered, especially heights with a precision better than 0.2 cm.
- The navigation parameters — shown in Figure 4.50e — are recovered with a precision better than 9 " for roll (α) and pitch (χ) and 1.8 ' for heading (η).
- The IMU error parameters exhibited in Figures 4.50b and 4.50d are nearly constants within the defined tolerances (bias repeatability) of the IMU.
- Figure 4.50f also displays the gravity disturbance vector, that has to be zero.

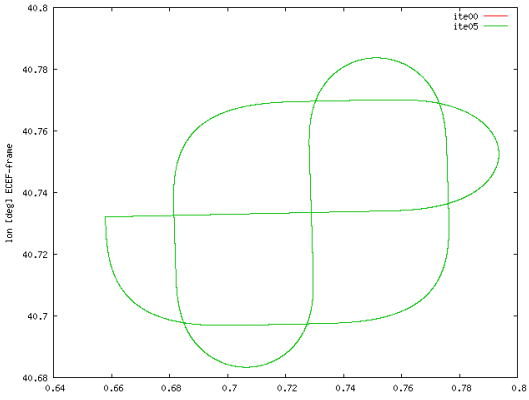

(a) Position (°)

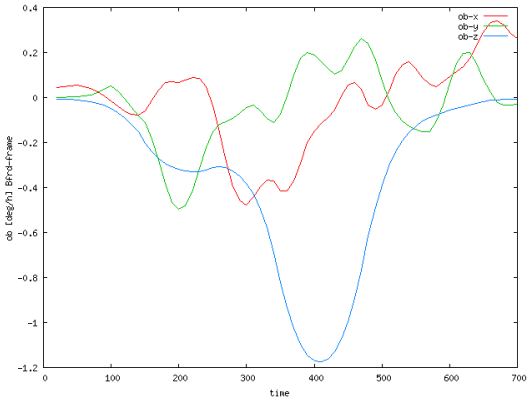

(b) Angular drift ($^\circ\,h^{-1}$)

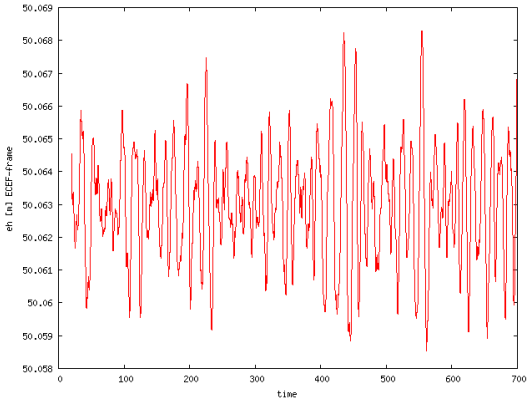

(c) Height (m)

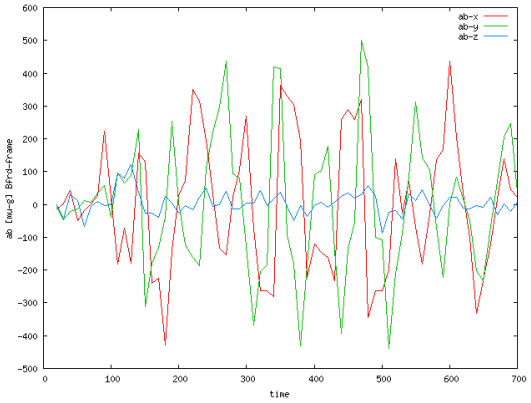

(d) Accelerometer bias (μg)

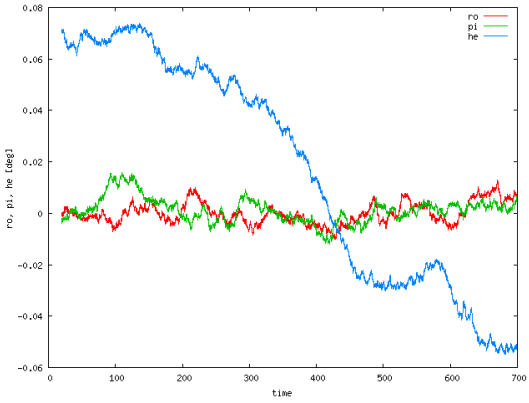

(e) Roll, Pitch and Heading (°)

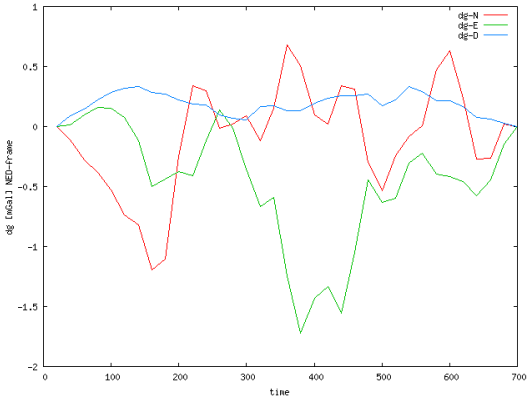

(f) Gravity disturbance (mGal)

Figure 4.49: CTRA LN200 v2a2x: adjusted parameters.

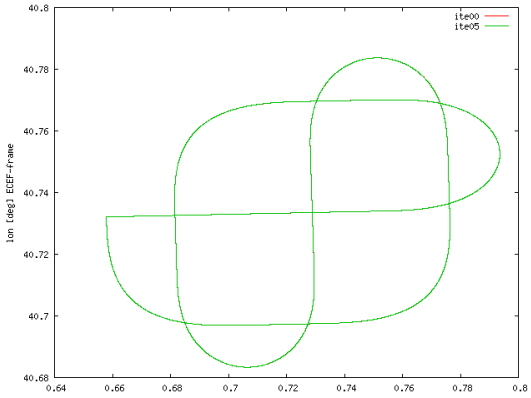

(a) Position (°)

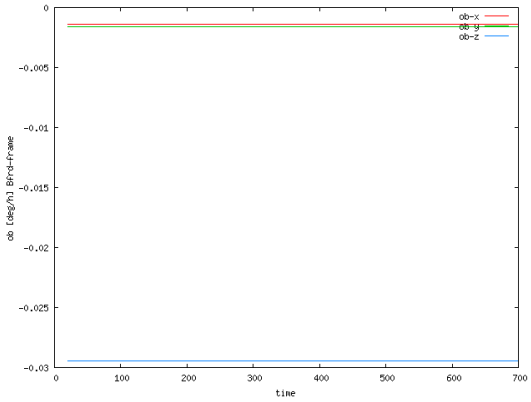

(b) Angular drift ($^\circ\,h^{-1}$)

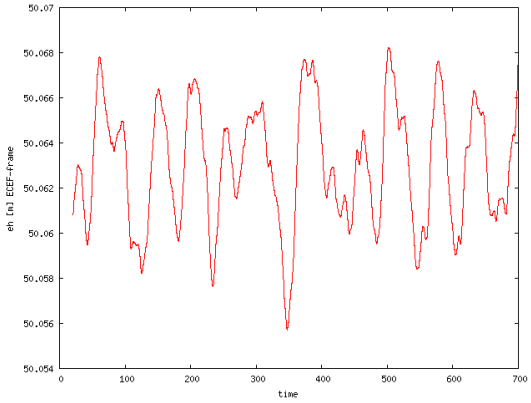

(c) Height (m)

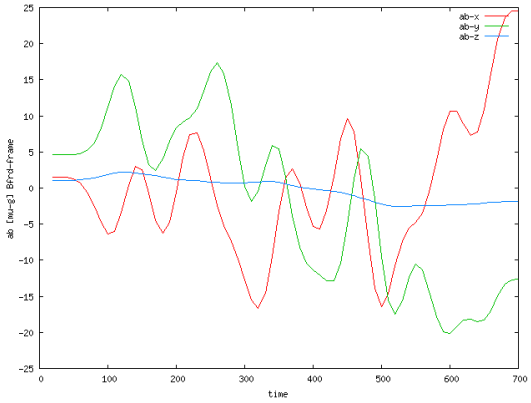

(d) Accelerometer bias (μg)

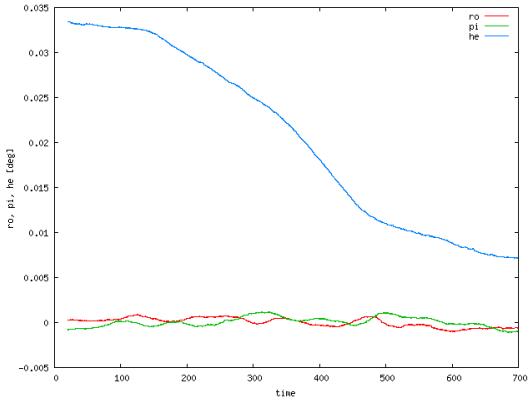

(e) Roll, Pitch and Heading (°)

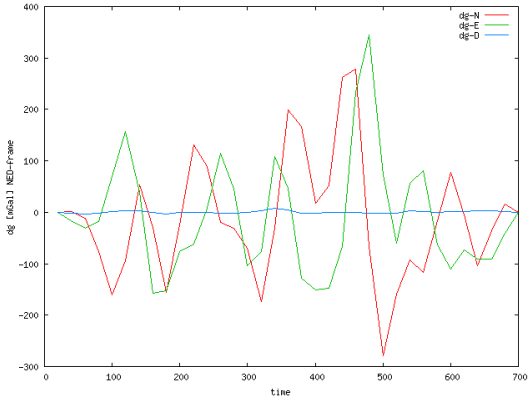

(f) Gravity disturbance (mGal)

Figure 4.50: CTRA LTN101b v2a2x: adjusted parameters.

4.5.6 CTRA vq2a2x

As already discussed in Section 4.2, the codification this computation means:

- $\langle q \rangle = q$: prior knowledge of the vehicle's attitude exists at the beginning (t_0) and at the end (t_N) of the mission.
- $\langle Hz \rangle = 2$: some subsets of parameters — $\underline{o}^{\mathsf{b}}$, $\underline{a}^{\mathsf{b}}$, δg or gg — has been grouped.
- $\langle \delta g_{NE} \rangle = a$: no prior knowledge of the horizontal gravity.
- $\langle method \rangle = 2x$: GDT-p (changes of the gravity disturbance of closed positions with respect to time) observations are added to the basic configuration and, moreover, XOVER observations are considered.

LN200

Table 4.51 summarises the network configuration used in this computation.

Model Name	Frequency		Equation	Standard Deviation	
FB-GG (3.4.5)	20.0 Hz	$\forall t$	(3.13)	2.2	10^{-3} m s^{-2}
WIB (3.4.2)	20.0 Hz	$\forall t$	(3.10)	5.2	10^{-5} rad s^{-1}
VEL (3.4.1)	20.0 Hz	$\forall t$	(3.4.1)	0.000 01	m
Q-NORM (3.4.6)	20.0 Hz	$\forall t$	(3.14)	0.01	ppm
OB-O (3.4.35)	0.1 Hz	$\forall t$	(3.48)	4.9	10^{-6} rad s^{-1}
AB-O (3.4.36)	0.1 Hz	$\forall t$	(3.49)	2.0	10^{-3} m s^{-2}
OB (3.4.8)	0.1 Hz	$\forall t$	(3.16)	15.0	10^{-7} rad s^{-1}
AB (3.4.10)	0.1 Hz	$\forall t$	(3.18)	130.0	10^{-4} m s^{-2}
AOFF-O (3.4.37)			(3.50)	0.001	m
CUPT (3.4.16)	1.0 Hz	$\forall t$	(3.26)	0.05	m
GDT-GG (3.4.13)	0.1 Hz	$\forall t$	(3.22)	6.2	mGal
GDT-GG (3.4.13)	$\forall x_i, x_j : \lvert x_i - x_j \rvert = 1km$		(3.22)	6.2	mGal
GDT-GG (3.4.13)	$\forall x_i, x_j : \lvert x_i - x_j \rvert = 4km$		(3.22)	13.0	mGal
DGUPT-GG (3.4.28)		t_0, t_N	(3.41)	0.02	mGal
Q-O (3.4.34)		t_0, t_N	(3.47)	0.01	ppm
XOVER-GG (3.4.31)			(3.44)	0.000 3	mGal

Table 4.51: Test CTRA-LN200-vq2a2x: network configuration.

Figure 4.51 proves that the functional models of the NA approach work succesfully:

- Figures 4.51a and 4.51c point out that the position has been recovered, especially heights with a precision better than 0.5 cm.
- The navigation parameters — shown in Figure 4.51e — are recovered with a precision of 0.6 ' for roll (α) and pitch (χ) and with a range of 3.6 ' for heading (η).

- The IMU error parameters exhibited in Figures 4.51b and 4.51d are nearly constants within the defined tolerances (bias repeatability) of the IMU.
- Figure 4.51f also displays the gravity disturbance vector, that has to be zero, with a precision better of 1.5 mGal.

LTN101

Table 4.52 summarises the network configuration used in this computation.

Model Name	Frequency		Equation	Standard Deviation	
FB-GG (3.4.5)	20.0 Hz	$\forall t$	(3.13)	4.4	10^{-4} m s^{-2}
WIB (3.4.2)	20.0 Hz	$\forall t$	(3.10)	1.3	10^{-6} rad s^{-1}
VEL (3.4.1)	20.0 Hz	$\forall t$	(3.4.1)	0.000 01	m
Q-NORM (3.4.6)	20.0 Hz	$\forall t$	(3.14)	0.01	ppm
OB-O (3.4.35)	0.1 Hz	$\forall t$	(3.48)	4.9	10^{-8} rad s^{-1}
AB-O (3.4.36)	0.1 Hz	$\forall t$	(3.49)	4.9	10^{-4} m s^{-2}
OB (3.4.8)	0.1 Hz	$\forall t$	(3.16)	61.0	10^{-12} rad s^{-1}
AB (3.4.10)	0.1 Hz	$\forall t$	(3.18)	95.0	10^{-7} m s^{-2}
AOFF-O (3.4.37)			(3.50)	0.001	m
CUPT (3.4.16)	1.0 Hz	$\forall t$	(3.26)	0.05	m
GDT-GG (3.4.13)	0.1 Hz	$\forall t$	(3.22)	6.2	mGal
GDT-GG (3.4.13)	$\forall x_i, x_j : \left\|x_i - x_j\right\| = 1km$		(3.22)	6.2	mGal
GDT-GG (3.4.13)	$\forall x_i, x_j : \left\|x_i - x_j\right\| = 4km$		(3.22)	13.0	mGal
DGUPT-GG (3.4.28)		t_0, t_N	(3.41)	0.02	mGal
Q-O (3.4.34)		t_0, t_N	(3.47)	0.01	ppm
XOVER-GG (3.4.31)			(3.44)	0.000 3	mGal

Table 4.52: Test CTRA-LTN101-vq2a2x: network configuration.

Figure 4.52 proves that the functional models of the NA approach work succesfully:

- Figures 4.52a and 4.52c point out that the position has been recovered, especially heights with a precision better than 1 cm.
- The navigation parameters — shown in Figure 4.52e — are recovered with a precision of 7.2 " for roll (α) and pitch (χ) and with a range of 28.8 " for heading (η).
- The IMU error parameters exhibited in Figures 4.52b and 4.52d are nearly constants within the defined tolerances (bias repeatability) of the IMU.
- Figure 4.52f also displays the gravity disturbance vector, that has to be zero.

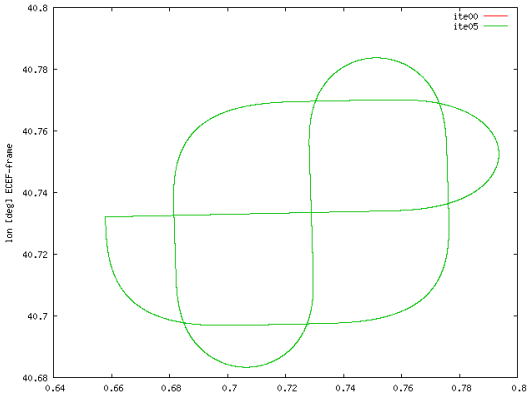

(a) Position (°)

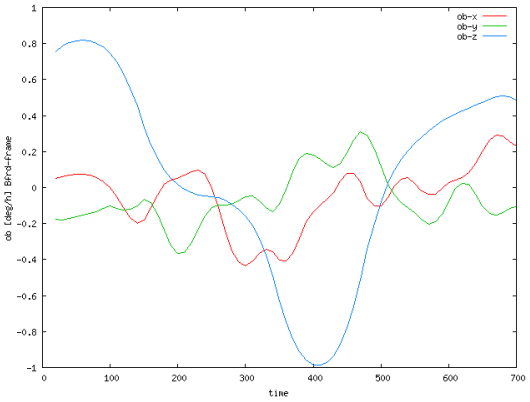

(b) Angular drift ($^\circ\,h^{-1}$)

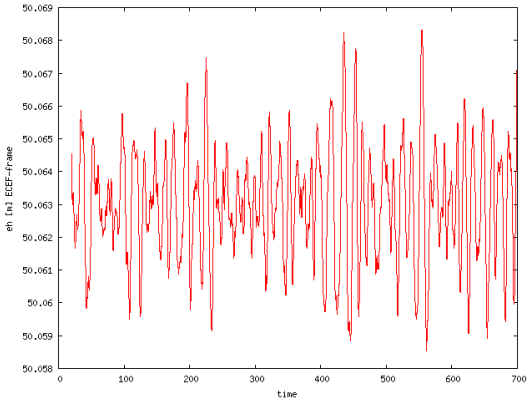

(c) Height (m)

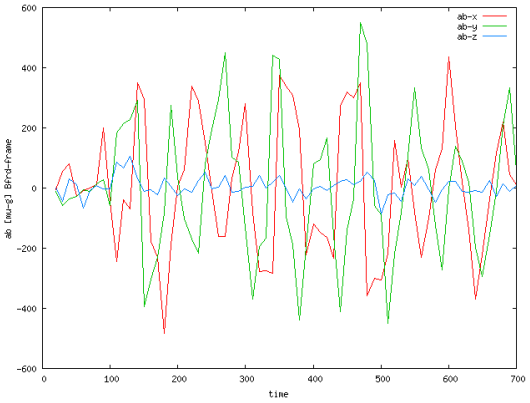

(d) Accelerometer bias (μg)

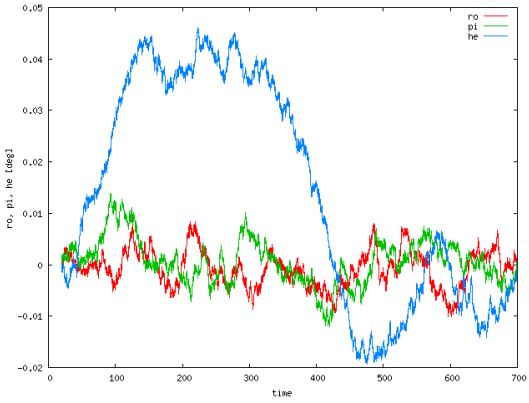

(e) Roll, Pitch and Heading (°)

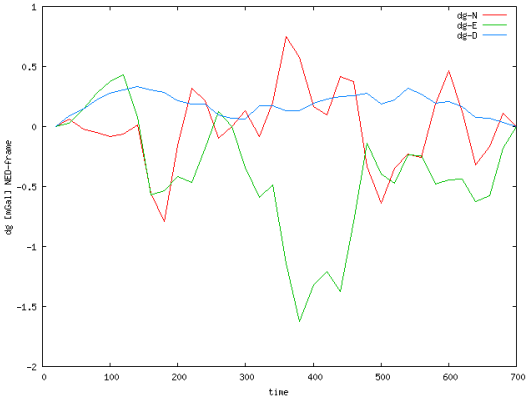

(f) Gravity disturbance (mGal)

Figure 4.51: CTRA LN200 vq2a2x: adjusted parameters.

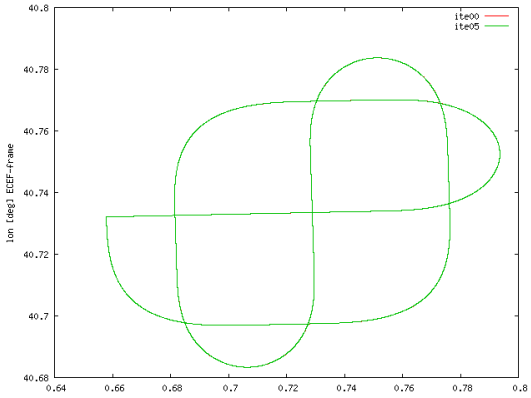

(a) Position (°)

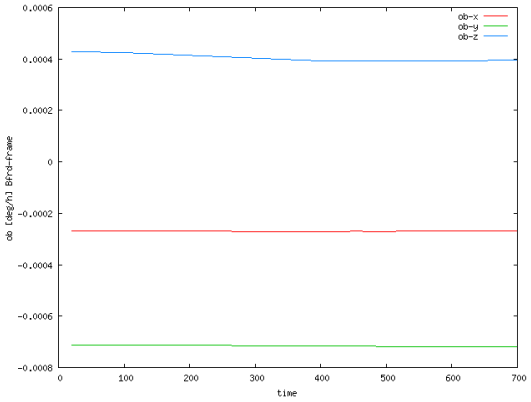

(b) Angular drift ($^\circ\,h^{-1}$)

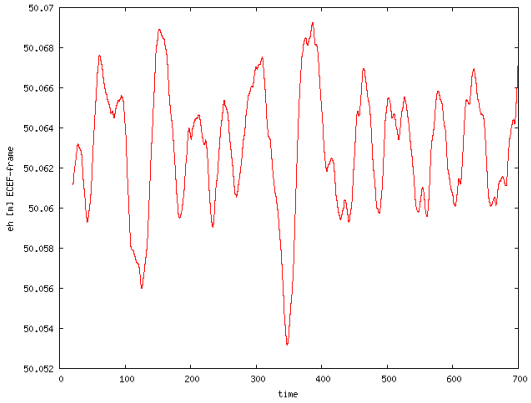

(c) Height (m)

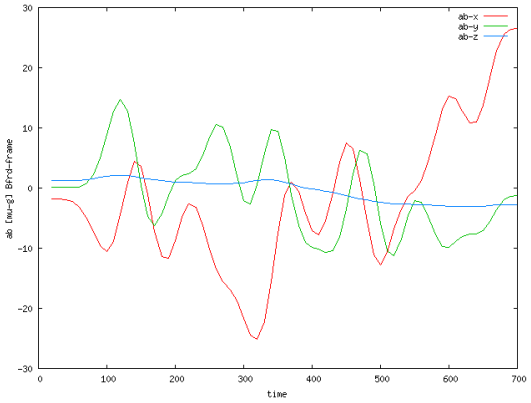

(d) Accelerometer bias (μg)

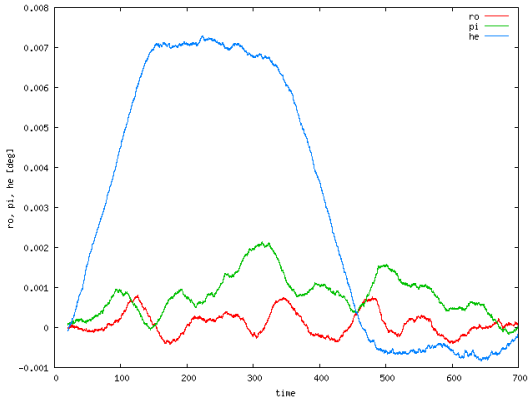

(e) Roll, Pitch and Heading (°)

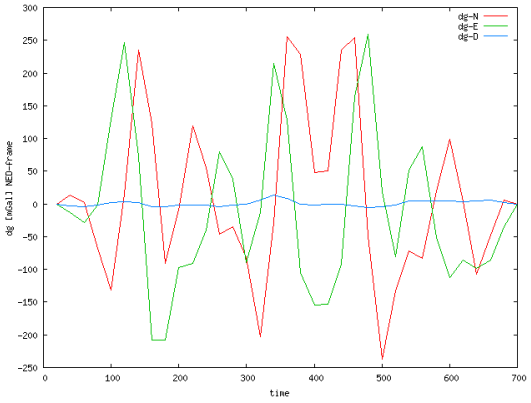

(f) Gravity disturbance (mGal)

Figure 4.52: CTRA LTN101b vq2a2x: adjusted parameters.

4.5.7 CTRA v2b1

As already discussed in Section 4.2, the codification this computation means:

- $\langle Hz \rangle = 2$: some subsets of parameters — $\underline{o}^{\mathsf{b}}$, $\underline{a}^{\mathsf{b}}$, δg or gg — has been grouped.
- $\langle \delta g_{NE} \rangle = b$, indicates that, for all t, $\delta g_N(t) = \delta g_E(t) \approx 0$.
- $\langle method \rangle = 1$, indicates a basic network configuration similar to the Kalman filtering.

LN200

Table 4.53 summarises the network configuration used in this computation.

Model Name	Frequency		Equation	Standard Deviation	
FB-GG (3.4.5)	20.0 Hz	$\forall t$	(3.13)	2.2	10^{-3} m s^{-2}
WIB (3.4.2)	20.0 Hz	$\forall t$	(3.10)	5.2	10^{-5} rad s^{-1}
VEL (3.4.1)	20.0 Hz	$\forall t$	(3.4.1)	0.000 01	m
Q-NORM (3.4.6)	20.0 Hz	$\forall t$	(3.14)	0.01	ppm
OB-O (3.4.35)	0.1 Hz	$\forall t$	(3.48)	4.9	10^{-6} rad s^{-1}
AB-O (3.4.36)	0.1 Hz	$\forall t$	(3.49)	2.0	10^{-3} m s^{-2}
OB (3.4.8)	0.1 Hz	$\forall t$	(3.16)	15.0	10^{-7} rad s^{-1}
AB (3.4.10)	0.1 Hz	$\forall t$	(3.18)	130.0	10^{-4} m s^{-2}
AOFF-O (3.4.37)			(3.50)	0.001	m
CUPT (3.4.16)	1.0 Hz	$\forall t$	(3.26)	0.05	m
GDT-GG (3.4.13)	0.1 Hz	$\forall t$	(3.22)	6.2	mGal
DGUPT-GG (3.4.28)	0.1 Hz	$\forall t$	(3.41)	0.02	mGal

Table 4.53: Test CTRA-LN200-v2b1: network configuration.

Figure 4.53 proves that the functional models of the NA approach work succesfully:

- Figures 4.53a and 4.53c point out that the position has been recovered, especially heights with a precision better than 0.2 cm.
- The navigation parameters — shown in Figure 4.53e — are recovered with a precision of 1.2 ' for roll (α) and pitch (χ) and 3.6 ' for heading (η).
- The IMU error parameters exhibited in Figures 4.53b and 4.53d are nearly constants within the defined tolerances (bias repeatability) of the IMU.
- Figure 4.53f also displays the gravity disturbance vector, that has to be zero.

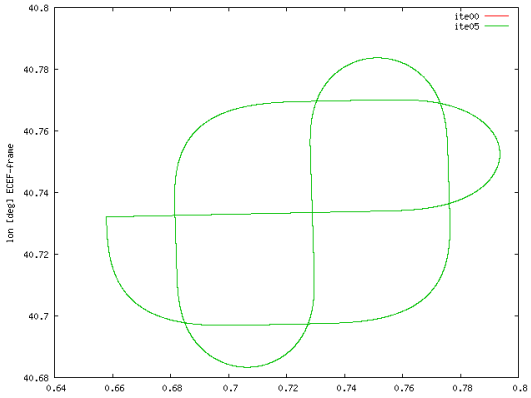

(a) Position (°)

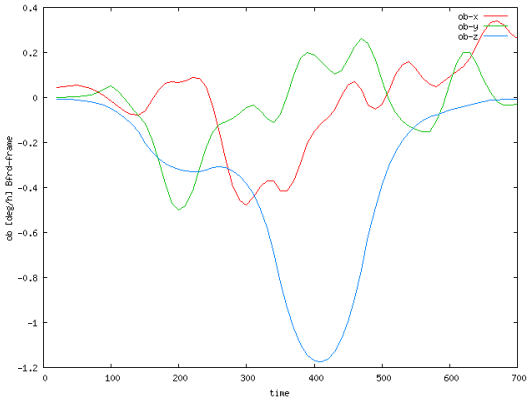

(b) Angular drift ($^\circ\,h^{-1}$)

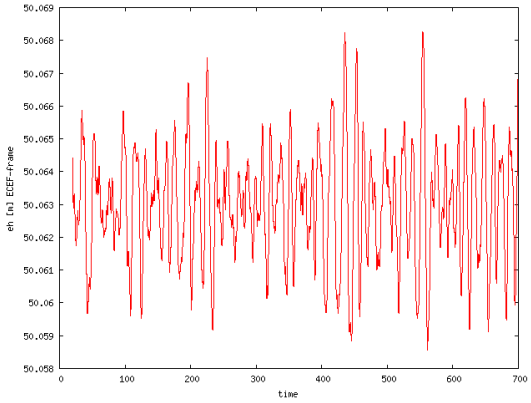

(c) Height (m)

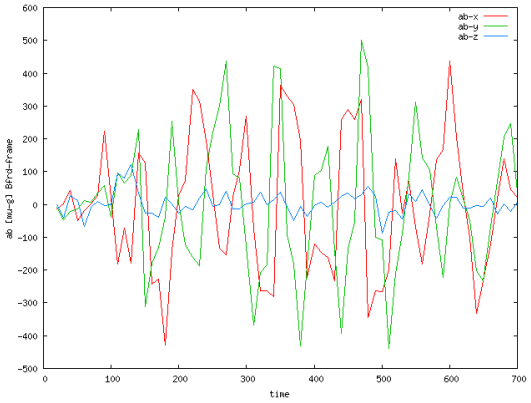

(d) Accelerometer bias (μg)

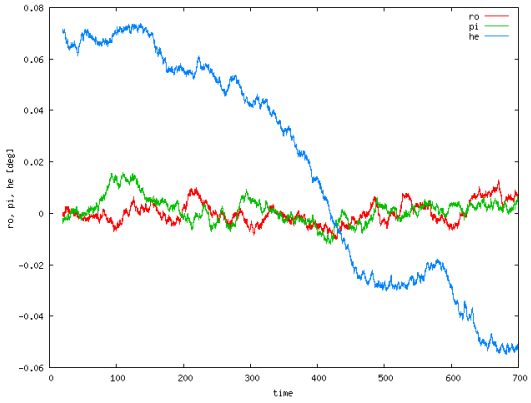

(e) Roll, Pitch and Heading (°)

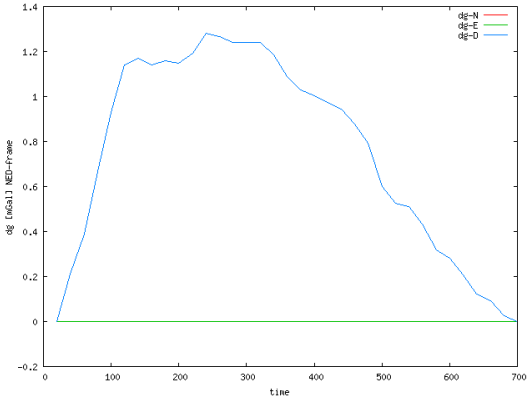

(f) Gravity disturbance (mGal)

Figure 4.53: CTRA LN200 v2b1: adjusted parameters.

Model Name	Frequency		Equation	Standard Deviation	
FB-GG (3.4.5)	20.0 Hz	$\forall t$	(3.13)	4.4	10^{-4} m s^{-2}
WIB (3.4.2)	20.0 Hz	$\forall t$	(3.10)	1.3	10^{-6} rad s^{-1}
VEL (3.4.1)	20.0 Hz	$\forall t$	(3.4.1)	0.000 01	m
Q-NORM (3.4.6)	20.0 Hz	$\forall t$	(3.14)	0.01	ppm
OB-O (3.4.35)	0.1 Hz	$\forall t$	(3.48)	4.9	10^{-8} rad s^{-1}
AB-O (3.4.36)	0.1 Hz	$\forall t$	(3.49)	4.9	10^{-4} m s^{-2}
OB (3.4.8)	0.1 Hz	$\forall t$	(3.16)	61.0	10^{-12} rad s^{-1}
AB (3.4.10)	0.1 Hz	$\forall t$	(3.18)	95.0	10^{-7} m s^{-2}
AOFF-O (3.4.37)			(3.50)	0.001	m
CUPT (3.4.16)	1.0 Hz	$\forall t$	(3.26)	0.05	m
GDT-GG (3.4.13)	0.1 Hz	$\forall t$	(3.22)	6.2	mGal
DGUPT-GG (3.4.28)	0.1 Hz	$\forall t$	(3.41)	0.02	mGal

Table 4.54: Test CTRA-LTN101-v2b1: network configuration.

LTN101

Table 4.54 summarises the network configuration used in this computation.

Figure 4.54 proves that the functional models of the NA approach work succesfully:

- Figures 4.54a and 4.54c point out that the position has been recovered, especially heights with a precision better than 1 cm.
- The navigation parameters — shown in Figure 4.54e — are recovered with a precision of 0.3 ' for roll (α) and pitch (χ) and with a range of 2.4 ' for heading (η).
- The IMU error parameters exhibited in Figures 4.54b and 4.54d are nearly constants within the defined tolerances (bias repeatability) of the IMU.
- Figure 4.54f also displays the gravity disturbance vector, that has to be zero.

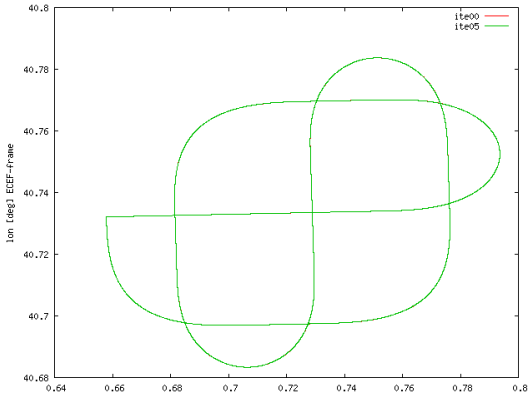

(a) Position (°)

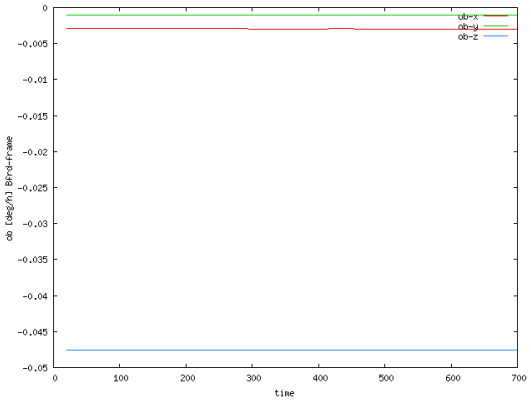

(b) Angular drift ($^\circ\,h^{-1}$)

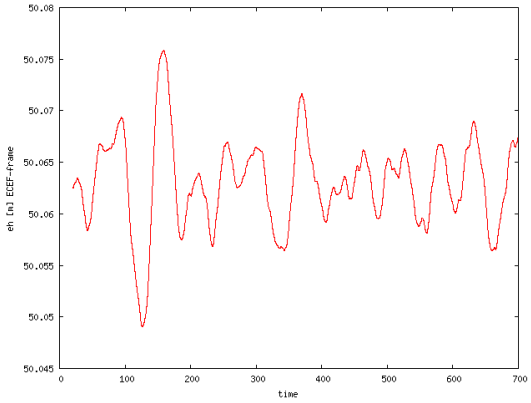

(c) Height (m)

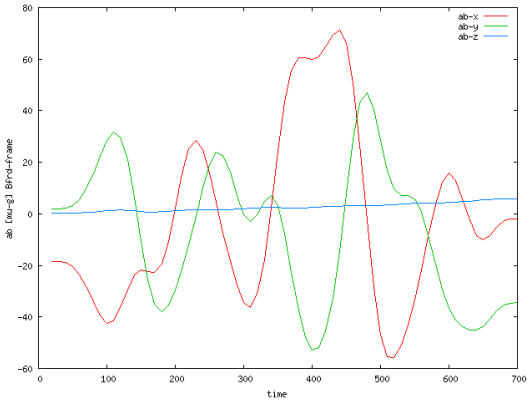

(d) Accelerometer bias (μg)

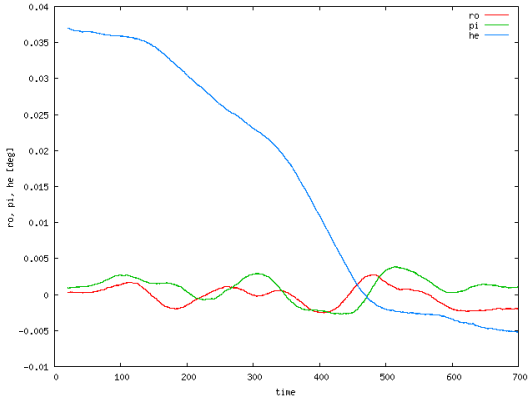

(e) Roll, Pitch and Heading (°)

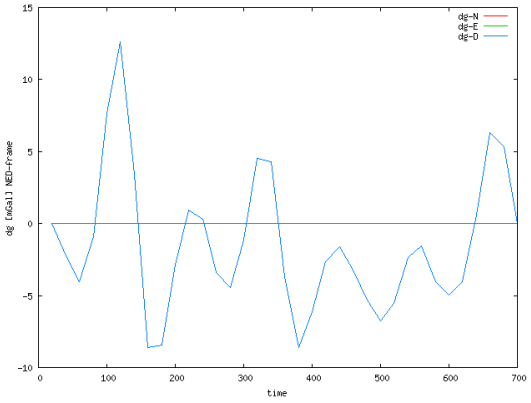

(f) Gravity disturbance (mGal)

Figure 4.54: CTRA LTN101b v2b1: adjusted parameters.

4.5.8 CTRA vq2b1

As already discussed in Section 4.2, the codification this computation means:

- $\langle q \rangle = q$, indicates that prior knowledge of the vehicle's attitude exists at the beginning (t_0) and at the end (t_N) of the mission.
- $\langle Hz \rangle = 2$: some subsets of parameters — $\underline{o}^{\mathsf{b}}$, $\underline{a}^{\mathsf{b}}$, δg or gg — has been grouped.
- $\langle \delta g_{NE} \rangle = b$, indicates that, for all t, $\delta g_N(t) = \delta g_E(t) \approx 0$.
- $\langle method \rangle = 1$, indicates a basic network configuration similar to the Kalman filtering.

LN200

Table 4.55 summarises the network configuration used in this computation.

Model Name	Frequency		Equation	Standard Deviation	
FB-GG (3.4.5)	20.0 Hz	$\forall t$	(3.13)	2.2	10^{-3} m s^{-2}
WIB (3.4.2)	20.0 Hz	$\forall t$	(3.10)	5.2	10^{-5} rad s^{-1}
VEL (3.4.1)	20.0 Hz	$\forall t$	(3.4.1)	0.000 01	m
Q-NORM (3.4.6)	20.0 Hz	$\forall t$	(3.14)	0.01	ppm
OB-O (3.4.35)	0.1 Hz	$\forall t$	(3.48)	4.9	10^{-6} rad s^{-1}
AB-O (3.4.36)	0.1 Hz	$\forall t$	(3.49)	2.0	10^{-3} m s^{-2}
OB (3.4.8)	0.1 Hz	$\forall t$	(3.16)	15.0	10^{-7} rad s^{-1}
AB (3.4.10)	0.1 Hz	$\forall t$	(3.18)	130.0	10^{-4} m s^{-2}
AOFF-O (3.4.37)			(3.50)	0.001	m
CUPT (3.4.16)	1.0 Hz	$\forall t$	(3.26)	0.05	m
GDT-GG (3.4.13)	0.1 Hz	$\forall t$	(3.22)	6.2	mGal
DGUPT-GG (3.4.28)	0.1 Hz	$\forall t$	(3.41)	0.02	mGal
Q-O (3.4.34)		t_0, t_N	(3.47)	0.01	ppm

Table 4.55: Test CTRA-LN200-vq2b1: network configuration.

Figure 4.55 proves that the functional models of the NA approach work succesfully:

- Figures 4.55a and 4.55c point out that the position has been recovered, especially heights with a precision better than 0.4 cm.
- The navigation parameters — shown in Figure 4.55e — are recovered with a precision of 0.6 ' for roll (α) and pitch (χ) and with a range of 3.6 ' for heading (η).
- The IMU error parameters exhibited in Figures 4.55b and 4.55d are nearly constants within the defined tolerances (bias repeatability) of the IMU.
- Figure 4.55f also displays the gravity disturbance vector, that has to be zero.

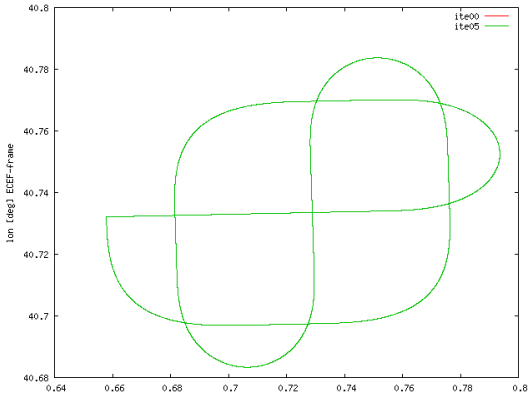

(a) Position (°)

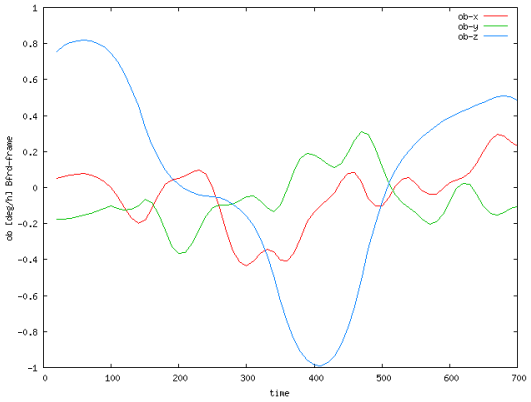

(b) Angular drift ($^\circ\,h^{-1}$)

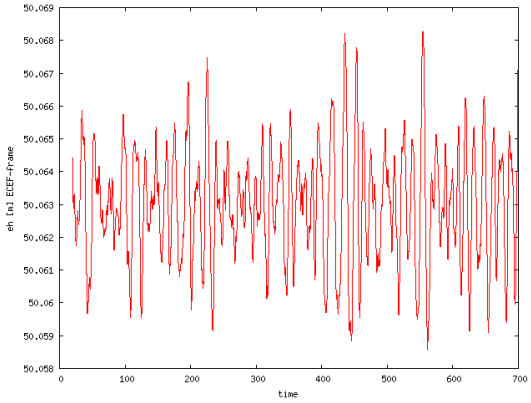

(c) Height (m)

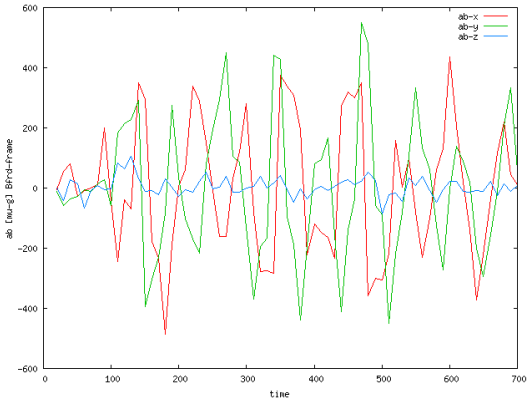

(d) Accelerometer bias (μg)

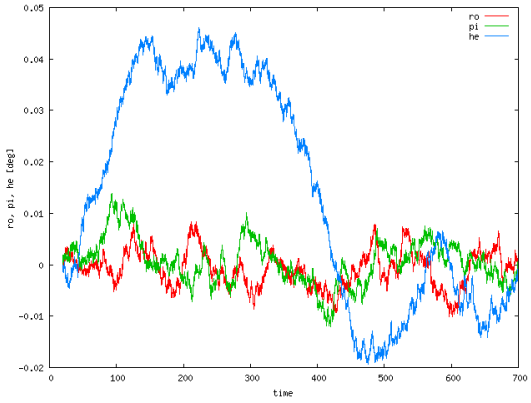

(e) Roll, Pitch and Heading (°)

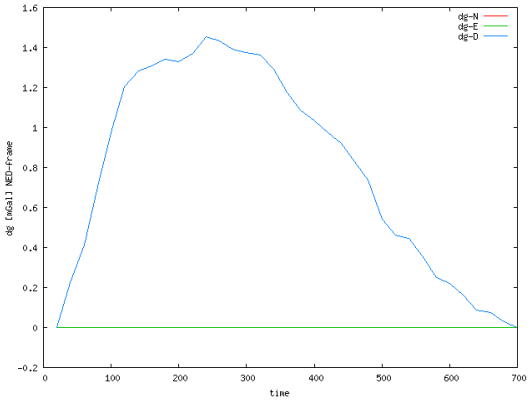

(f) Gravity disturbance (mGal)

Figure 4.55: CTRA LN200 vq2b1: adjusted parameters.

LTN101

Table 4.56 summarises the network configuration used in this computation.

Model Name	Frequency		Equation	Standard Deviation	
FB-GG (3.4.5)	20.0 Hz	$\forall t$	(3.13)	4.4	10^{-4} m s^{-2}
WIB (3.4.2)	20.0 Hz	$\forall t$	(3.10)	1.3	10^{-6} rad s^{-1}
VEL (3.4.1)	20.0 Hz	$\forall t$	(3.4.1)	0.000 01	m
Q-NORM (3.4.6)	20.0 Hz	$\forall t$	(3.14)	0.01	ppm
OB-O (3.4.35)	0.1 Hz	$\forall t$	(3.48)	4.9	10^{-8} rad s^{-1}
AB-O (3.4.36)	0.1 Hz	$\forall t$	(3.49)	4.9	10^{-4} m s^{-2}
OB (3.4.8)	0.1 Hz	$\forall t$	(3.16)	61.0	10^{-12} rad s^{-1}
AB (3.4.10)	0.1 Hz	$\forall t$	(3.18)	95.0	10^{-7} m s^{-2}
AOFF-O (3.4.37)			(3.50)	0.001	m
CUPT (3.4.16)	1.0 Hz	$\forall t$	(3.26)	0.05	m
GDT-GG (3.4.13)	0.1 Hz	$\forall t$	(3.22)	6.2	mGal
DGUPT-GG (3.4.28)	0.1 Hz	$\forall t$	(3.41)	0.02	mGal
Q-O (3.4.34)		t_0, t_N	(3.47)	0.01	ppm

Table 4.56: Test CTRA-LTN101-vq2b1: network configuration.

Figure 4.56 proves that the functional models of the NA approach work succesfully:

- Figures 4.56a and 4.56c point out that the position has been recovered, especially heights with a precision better than 0.5 cm.
- The navigation parameters — shown in Figure 4.56e — are recovered with a precision of 0.12 ' for roll (α) and pitch (χ) and with a range of 1.08 ' for heading (η).
- The IMU error parameters exhibited in Figures 4.56b and 4.56d are nearly constants within the defined tolerances (bias repeatability) of the IMU.
- Figure 4.56f also displays the gravity disturbance vector, that has to be zero.

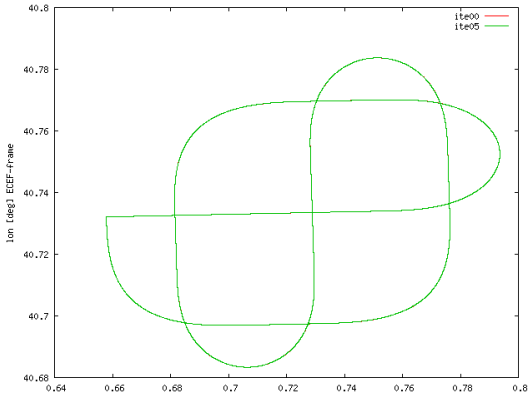

(a) Position (°)

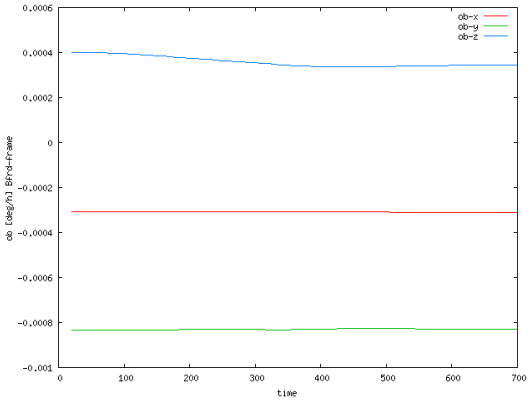

(b) Angular drift ($^\circ\,h^{-1}$)

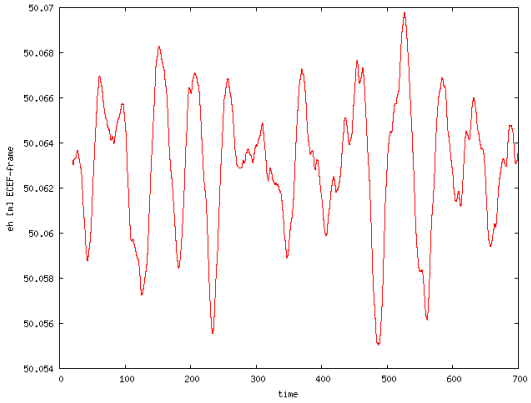

(c) Height (m)

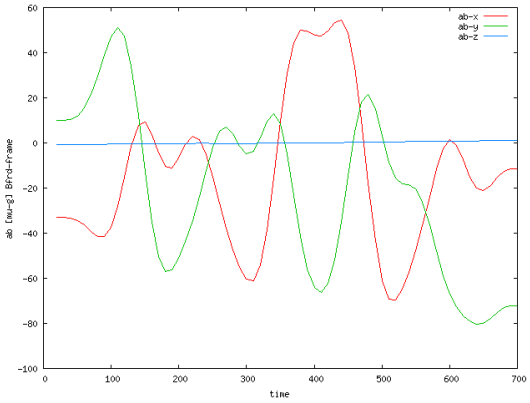

(d) Accelerometer bias (μg)

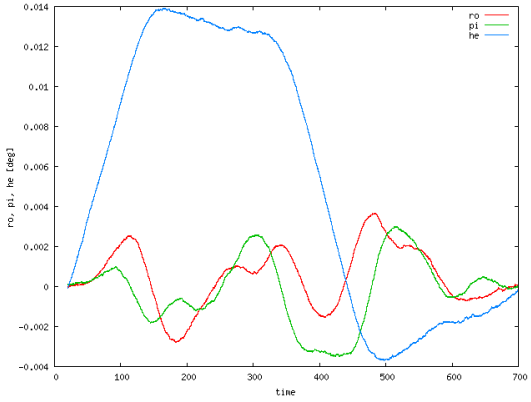

(e) Roll, Pitch and Heading (°)

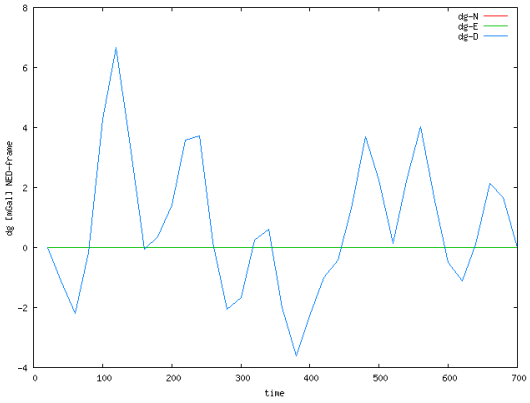

(f) Gravity disturbance (mGal)

Figure 4.56: CTRA LTN101b vq2b1: adjusted parameters.

4.5.9 CTRA v2b2

As already discussed in Section 4.2, the codification this computation means:

- $\langle Hz \rangle = 2$: some subsets of parameters — $\underline{o}^{\mathsf{b}}$, $\underline{a}^{\mathsf{b}}$, δg or gg — has been grouped.
- $\langle \delta g_{NE} \rangle = b$,indicates that, for all t, $\delta g_N(t) = \delta g_E(t) \approx 0$.
- $\langle method \rangle = 2$: GDT-p (changes of the gravity disturbance of closed positions with respect to time) observations are added to the basic configuration.

LN200

Table 4.57 summarises the network configuration used in this computation.

Model Name	Frequency		Equation	Standard Deviation	
FB-GG (3.4.5)	20.0 Hz	$\forall t$	(3.13)	2.2	10^{-3} m s^{-2}
WIB (3.4.2)	20.0 Hz	$\forall t$	(3.10)	5.2	10^{-5} rad s^{-1}
VEL (3.4.1)	20.0 Hz	$\forall t$	(3.4.1)	0.000 01	m
Q-NORM (3.4.6)	20.0 Hz	$\forall t$	(3.14)	0.01	ppm
OB-O (3.4.35)	0.1 Hz	$\forall t$	(3.48)	4.9	10^{-6} rad s^{-1}
AB-O (3.4.36)	0.1 Hz	$\forall t$	(3.49)	2.0	10^{-3} m s^{-2}
OB (3.4.8)	0.1 Hz	$\forall t$	(3.16)	15.0	10^{-7} rad s^{-1}
AB (3.4.10)	0.1 Hz	$\forall t$	(3.18)	130.0	10^{-4} m s^{-2}
AOFF-O (3.4.37)			(3.50)	0.001	m
CUPT (3.4.16)	1.0 Hz	$\forall t$	(3.26)	0.05	m
GDT-GG (3.4.13)	0.1 Hz	$\forall t$	(3.22)	6.2	mGal
GDT-GG (3.4.13)	$\forall x_i, x_j : \lvert x_i - x_j \rvert = 1km$		(3.22)	6.2	mGal
GDT-GG (3.4.13)	$\forall x_i, x_j : \lvert x_i - x_j \rvert = 4km$		(3.22)	13.0	mGal
DGUPT-GG (3.4.28)	0.1 Hz	$\forall t$	(3.41)	0.02	mGal

Table 4.57: Test CTRA-LN200-v2b2: network configuration.

Figure 4.57 proves that the functional models of the NA approach work succesfully:

- Figures 4.57a and 4.57c point out that the position has been recovered, especially heights with a precision better than 0.5 cm.
- The navigation parameters — shown in Figure 4.57e — are recovered with a precision of 1.2 ' for roll (α) and pitch (χ) and 3.6 ' for heading (η).
- The IMU error parameters exhibited in Figures 4.57b and 4.57d are nearly constants within the defined tolerances (bias repeatability) of the IMU.
- Figure 4.57f also displays the gravity disturbance vector, that has to be zero.

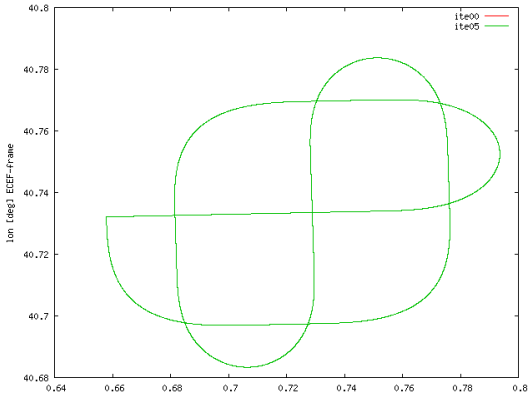

(a) Position (°)

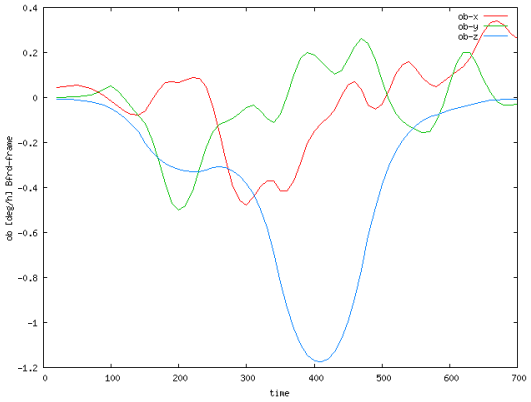

(b) Angular drift ($^\circ\,h^{-1}$)

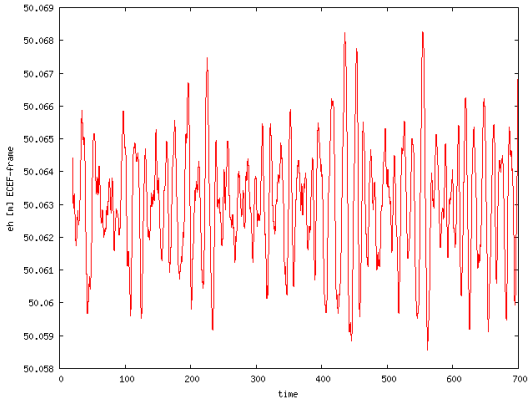

(c) Height (m)

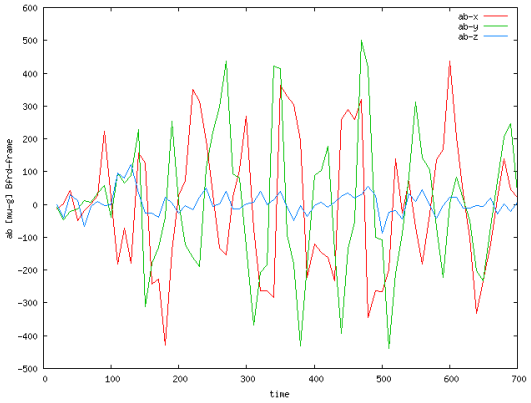

(d) Accelerometer bias (μg)

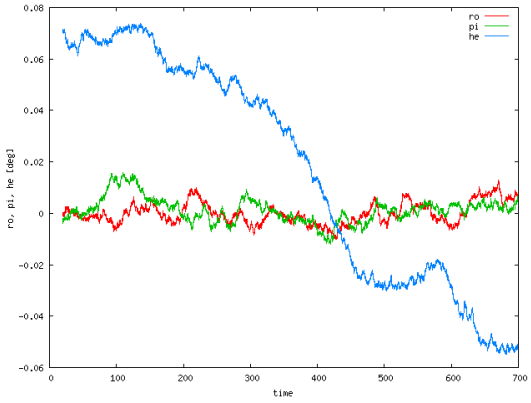

(e) Roll, Pitch and Heading (°)

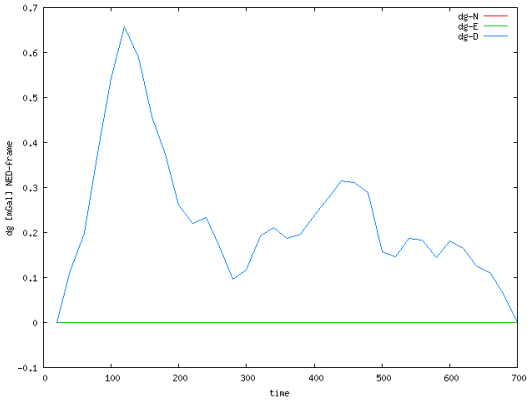

(f) Gravity disturbance (mGal)

Figure 4.57: CTRA LN200 v2b2: adjusted parameters.

LTN101

Table 4.58 summarises the network configuration used in this computation.

Model Name	Frequency		Equation	Standard Deviation	
FB-GG (3.4.5)	20.0 Hz	$\forall t$	(3.13)	4.4	10^{-4} m s^{-2}
WIB (3.4.2)	20.0 Hz	$\forall t$	(3.10)	1.3	10^{-6} rad s^{-1}
VEL (3.4.1)	20.0 Hz	$\forall t$	(3.4.1)	0.000 01	m
Q-NORM (3.4.6)	20.0 Hz	$\forall t$	(3.14)	0.01	ppm
OB-O (3.4.35)	0.1 Hz	$\forall t$	(3.48)	4.9	10^{-8} rad s^{-1}
AB-O (3.4.36)	0.1 Hz	$\forall t$	(3.49)	4.9	10^{-4} m s^{-2}
OB (3.4.8)	0.1 Hz	$\forall t$	(3.16)	61.0	10^{-12} rad s^{-1}
AB (3.4.10)	0.1 Hz	$\forall t$	(3.18)	95.0	10^{-7} m s^{-2}
AOFF-O (3.4.37)			(3.50)	0.001	m
CUPT (3.4.16)	1.0 Hz	$\forall t$	(3.26)	0.05	m
GDT-GG (3.4.13)	0.1 Hz	$\forall t$	(3.22)	6.2	mGal
GDT-GG (3.4.13)	$\forall x_i, x_j : \left\|x_i - x_j\right\| = 1km$		(3.22)	6.2	mGal
GDT-GG (3.4.13)	$\forall x_i, x_j : \left\|x_i - x_j\right\| = 4km$		(3.22)	13.0	mGal
DGUPT-GG (3.4.28)	0.1 Hz	$\forall t$	(3.41)	0.02	mGal

Table 4.58: Test CTRA-LTN101-v2b2: network configuration.

Figure 4.58 proves that the functional models of the NA approach work succesfully:

- Figures 4.58a and 4.58c point out that the position has been recovered, especially heights with a precision better than 1 cm.
- The navigation parameters — shown in Figure 4.58e — are recovered with a precision better than 0.3 ' for roll (α) and pitch (χ) and with a range of 2.4 ' for heading (η).
- The IMU error parameters exhibited in Figures 4.58b and 4.58d are nearly constants within the defined tolerances (bias repeatability) of the IMU.
- Figure 4.58f also displays the gravity disturbance vector, that has to be zero.

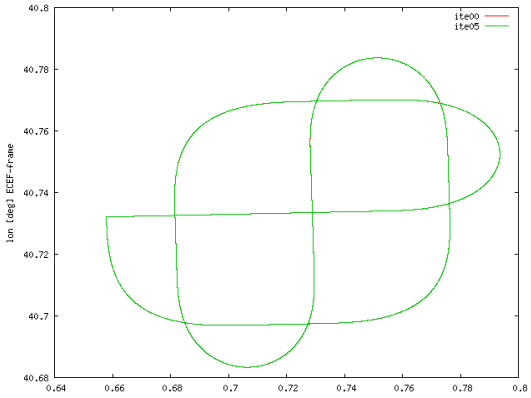

(a) Position (°)

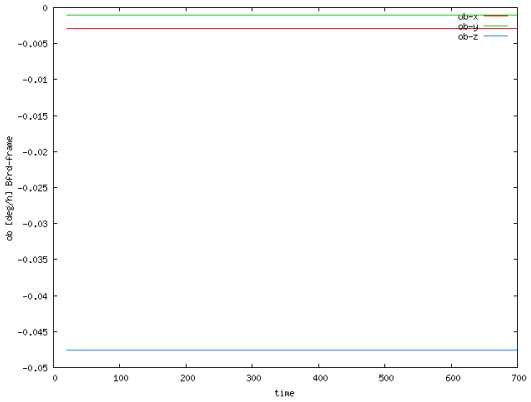

(b) Angular drift ($^\circ\,h^{-1}$)

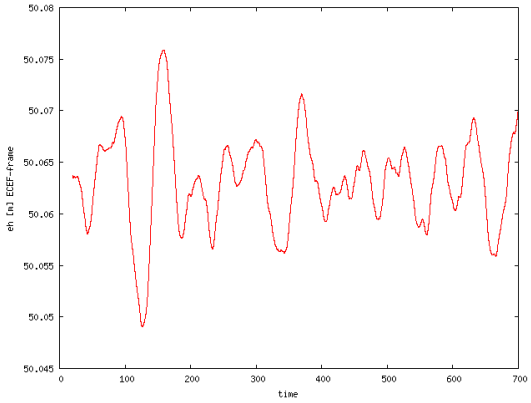

(c) Height (m)

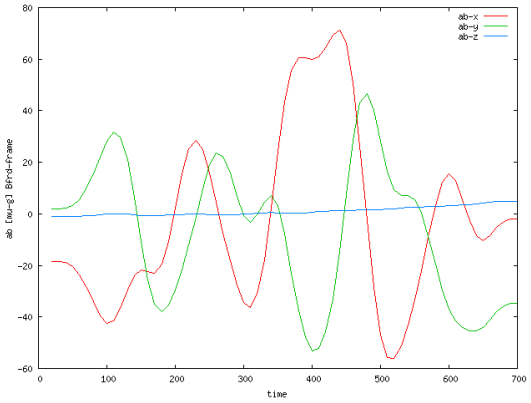

(d) Accelerometer bias (μg)

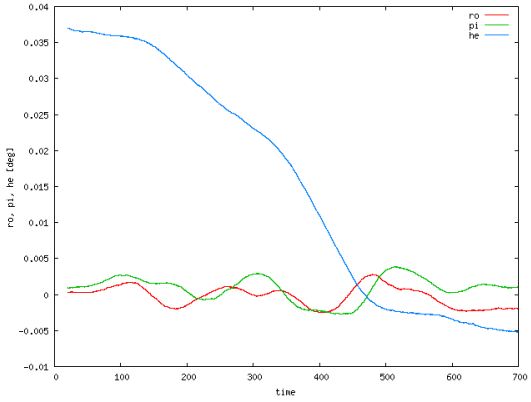

(e) Roll, Pitch and Heading (°)

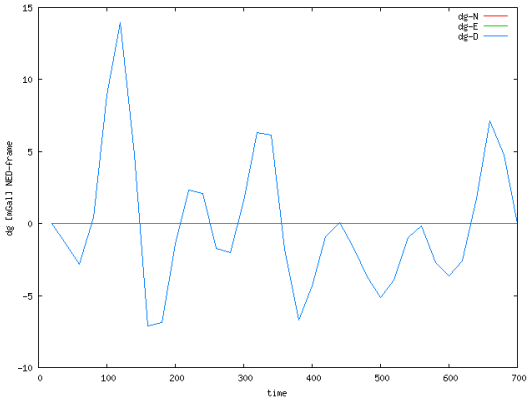

(f) Gravity disturbance (mGal)

Figure 4.58: CTRA LTN101b v2b2: adjusted parameters.

4.5.10 CTRA vq2b2

As already discussed in Section 4.2, the codification this computation means:

- $\langle q \rangle = q$, indicates that prior knowledge of the vehicle's attitude exists at the beginning (t_0) and at the end (t_N) of the mission.
- $\langle Hz \rangle = 2$: some subsets of parameters — $\underline{o}^{\mathsf{b}}$, $\underline{a}^{\mathsf{b}}$, δg or gg — has been grouped.
- $\langle \delta g_{NE} \rangle = b$, indicates that, for all t, $\delta g_N(t) = \delta g_E(t) \approx 0$.
- $\langle method \rangle = 2$: GDT-p (changes of the gravity disturbance of closed positions with respect to time) observations are added to the basic configuration.

LN200

Table 4.59 summarises the network configuration used in this computation.

Model Name	Frequency		Equation	Standard Deviation	
FB-GG (3.4.5)	20.0 Hz	$\forall t$	(3.13)	2.2	10^{-3} m s^{-2}
WIB (3.4.2)	20.0 Hz	$\forall t$	(3.10)	5.2	10^{-5} rad s^{-1}
VEL (3.4.1)	20.0 Hz	$\forall t$	(3.4.1)	0.000 01	m
Q-NORM (3.4.6)	20.0 Hz	$\forall t$	(3.14)	0.01	ppm
OB-O (3.4.35)	0.1 Hz	$\forall t$	(3.48)	4.9	10^{-6} rad s^{-1}
AB-O (3.4.36)	0.1 Hz	$\forall t$	(3.49)	2.0	10^{-3} m s^{-2}
OB (3.4.8)	0.1 Hz	$\forall t$	(3.16)	15.0	10^{-7} rad s^{-1}
AB (3.4.10)	0.1 Hz	$\forall t$	(3.18)	130.0	10^{-4} m s^{-2}
AOFF-O (3.4.37)			(3.50)	0.001	m
CUPT (3.4.16)	1.0 Hz	$\forall t$	(3.26)	0.05	m
GDT-GG (3.4.13)	0.1 Hz	$\forall t$	(3.22)	6.2	mGal
GDT-GG (3.4.13)	$\forall x_i, x_j : \lvert x_i - x_j \rvert = 1km$		(3.22)	6.2	mGal
GDT-GG (3.4.13)	$\forall x_i, x_j : \lvert x_i - x_j \rvert = 4km$		(3.22)	13.0	mGal
DGUPT-GG (3.4.28)	0.1 Hz	$\forall t$	(3.41)	0.02	mGal
Q-O (3.4.34)		t_0, t_N	(3.47)	0.01	ppm

Table 4.59: Test CTRA-LN200-vq2b2: network configuration.

Figure 4.59 proves that the functional models of the NA approach work succesfully:

- Figures 4.59a and 4.59c point out that the position has been recovered, especially heights with a precision better than 0.4 cm.
- The navigation parameters — shown in Figure 4.59e — are recovered with a precision of 0.6 ' for roll (α) and pitch (χ) and with a range of 3.9 ' for heading (η).

- The IMU error parameters exhibited in Figures 4.59b and 4.59d are nearly constants within the defined tolerances (bias repeatability) of the IMU.
- Figure 4.59f also displays the gravity disturbance vector, that has to be zero, with a precision of 0.65 mGal.

LTN101

Table 4.60 summarises the network configuration used in this computation.

Model Name	Frequency		Equation	Standard Deviation	
FB-GG (3.4.5)	20.0 Hz	$\forall t$	(3.13)	4.4	10^{-4} m s^{-2}
WIB (3.4.2)	20.0 Hz	$\forall t$	(3.10)	1.3	10^{-6} rad s^{-1}
VEL (3.4.1)	20.0 Hz	$\forall t$	(3.4.1)	0.000 01	m
Q-NORM (3.4.6)	20.0 Hz	$\forall t$	(3.14)	0.01	ppm
OB-O (3.4.35)	0.1 Hz	$\forall t$	(3.48)	4.9	10^{-8} rad s^{-1}
AB-O (3.4.36)	0.1 Hz	$\forall t$	(3.49)	4.9	10^{-4} m s^{-2}
OB (3.4.8)	0.1 Hz	$\forall t$	(3.16)	61.0	10^{-12} rad s^{-1}
AB (3.4.10)	0.1 Hz	$\forall t$	(3.18)	95.0	10^{-7} m s^{-2}
AOFF-O (3.4.37)			(3.50)	0.001	m
CUPT (3.4.16)	1.0 Hz	$\forall t$	(3.26)	0.05	m
GDT-GG (3.4.13)	0.1 Hz	$\forall t$	(3.22)	6.2	mGal
GDT-GG (3.4.13)	$\forall x_i, x_j : \left\|x_i - x_j\right\| = 1km$		(3.22)	6.2	mGal
GDT-GG (3.4.13)	$\forall x_i, x_j : \left\|x_i - x_j\right\| = 4km$		(3.22)	13.0	mGal
DGUPT-GG (3.4.28)	0.1 Hz	$\forall t$	(3.41)	0.02	mGal
Q-O (3.4.34)		t_0, t_N	(3.47)	0.01	ppm

Table 4.60: Test CTRA-LTN101-vq2b2: network configuration.

Figure 4.60 proves that the functional models of the NA approach work succesfully:

- Figures 4.60a and 4.60c point out that the position has been recovered, especially heights with a precision better than 0.5 cm.
- The navigation parameters — shown in Figure 4.60e — are recovered with a precision of 7.2 " for roll (α) and pitch (χ) and with a range of 1.08 ' for heading (η).
- The IMU error parameters exhibited in Figures 4.60b and 4.60d are nearly constants within the defined tolerances (bias repeatability) of the IMU.
- Figure 4.60f also displays the gravity disturbance vector, that has to be zero.

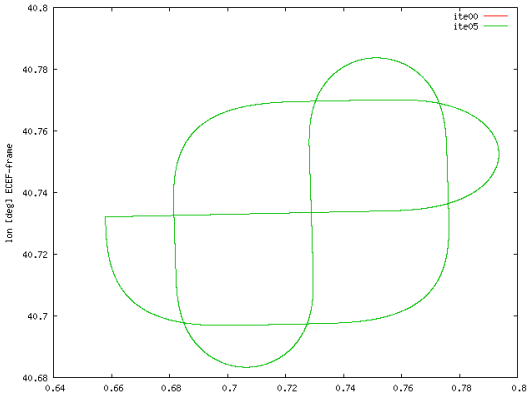

(a) Position (°)

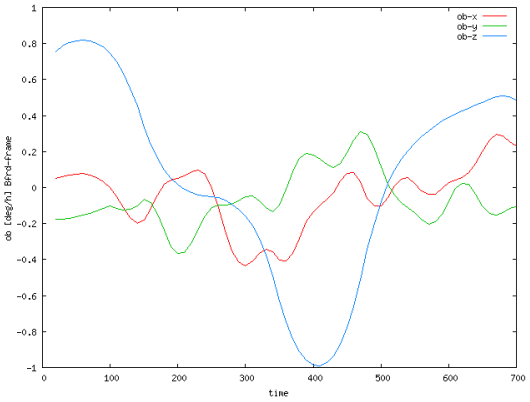

(b) Angular drift ($^\circ\,h^{-1}$)

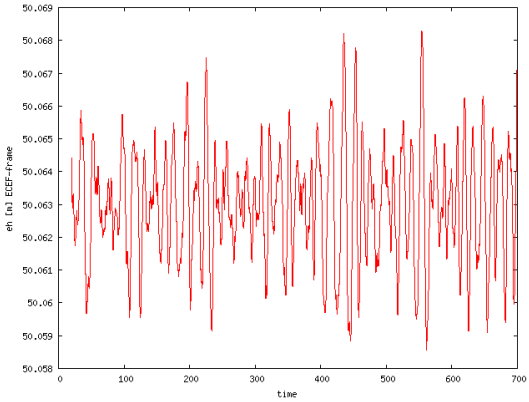

(c) Height (m)

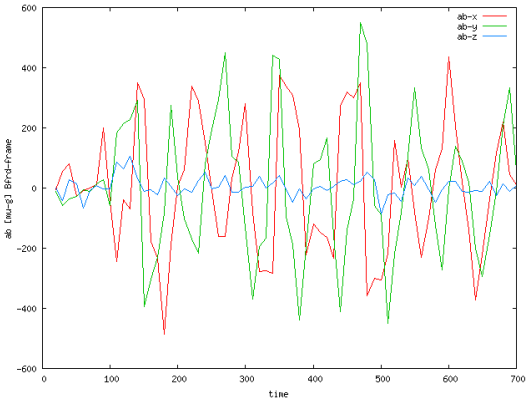

(d) Accelerometer bias (μg)

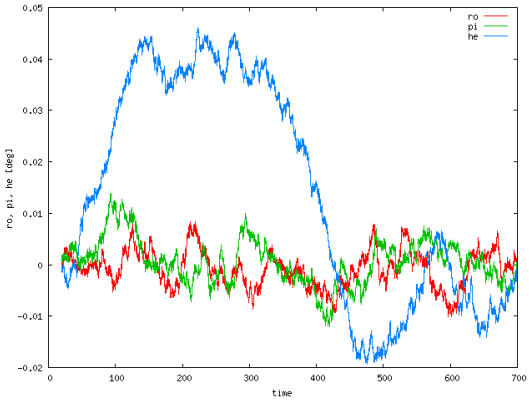

(e) Roll, Pitch and Heading (°)

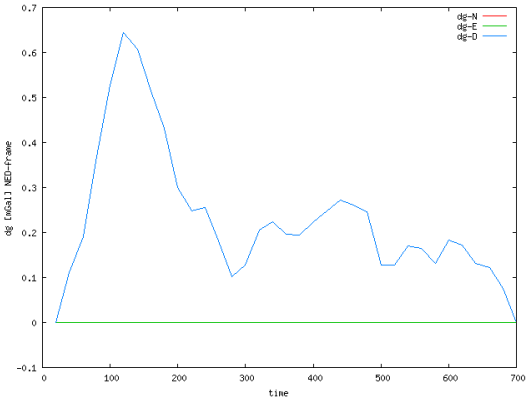

(f) Gravity disturbance (mGal)

Figure 4.59: CTRA LN200 vq2b2: adjusted parameters.

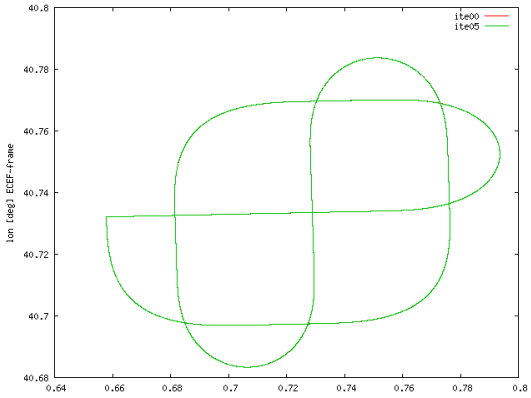

(a) Position (°)

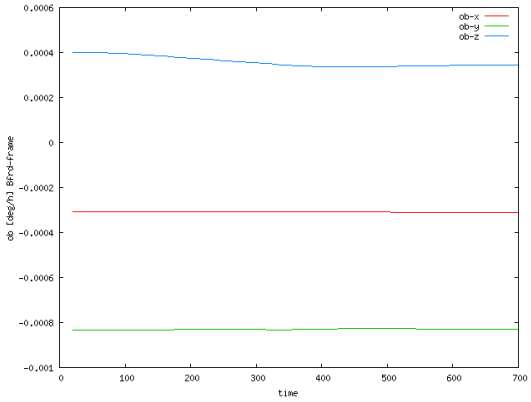

(b) Angular drift ($^\circ\,h^{-1}$)

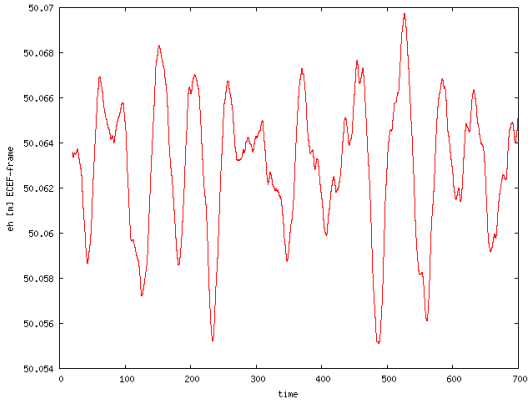

(c) Height (m)

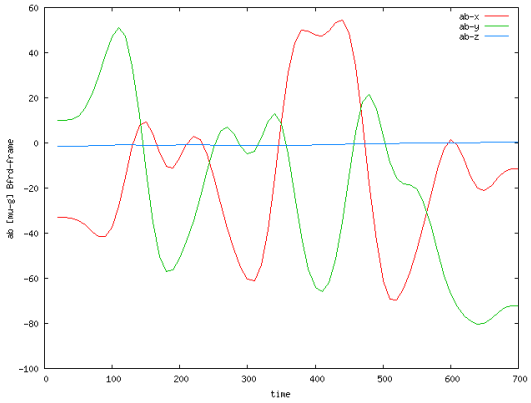

(d) Accelerometer bias (μg)

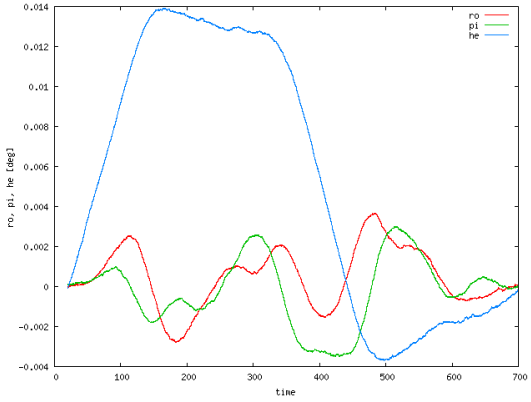

(e) Roll, Pitch and Heading (°)

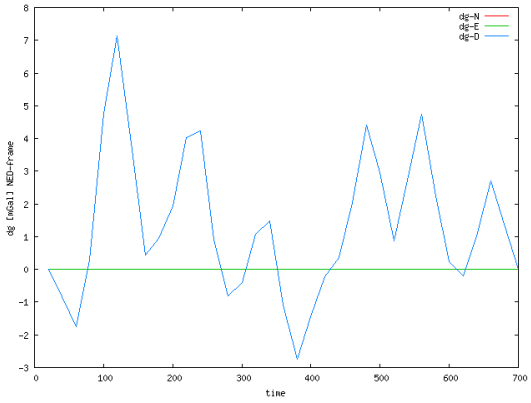

(f) Gravity disturbance (mGal)

Figure 4.60: CTRA LTN101b vq2b2: adjusted parameters.

4.5.11 CTRA v2b2x

As already discussed in Section 4.2, the codification this computation means:

- $\langle Hz \rangle = 2$: some subsets of parameters — $\underline{o}^{\mathsf{b}}$, $\underline{a}^{\mathsf{b}}$, δg or gg — has been grouped.
- $\langle \delta g_{NE} \rangle = b$, indicates that, for all t, $\delta g_N(t) = \delta g_E(t) \approx 0$.
- $\langle method \rangle = 2x$: GDT-p (changes of the gravity disturbance of closed positions with respect to time) observations are added to the basic configuration and, moreover, XOVER observations are considered $\langle method \rangle = 2x$.

LN200

Table 4.61 summarises the network configuration used in this computation.

Model Name	Frequency		Equation	Standard Deviation	
FB-GG (3.4.5)	20.0 Hz	$\forall t$	(3.13)	2.2	10^{-3} m s^{-2}
WIB (3.4.2)	20.0 Hz	$\forall t$	(3.10)	5.2	10^{-5} rad s^{-1}
VEL (3.4.1)	20.0 Hz	$\forall t$	(3.4.1)	0.000 01	m
Q-NORM (3.4.6)	20.0 Hz	$\forall t$	(3.14)	0.01	ppm
OB-O (3.4.35)	0.1 Hz	$\forall t$	(3.48)	4.9	10^{-6} rad s^{-1}
AB-O (3.4.36)	0.1 Hz	$\forall t$	(3.49)	2.0	10^{-3} m s^{-2}
OB (3.4.8)	0.1 Hz	$\forall t$	(3.16)	15.0	10^{-7} rad s^{-1}
AB (3.4.10)	0.1 Hz	$\forall t$	(3.18)	130.0	10^{-4} m s^{-2}
AOFF-O (3.4.37)			(3.50)	0.001	m
CUPT (3.4.16)	1.0 Hz	$\forall t$	(3.26)	0.05	m
GDT-GG (3.4.13)	0.1 Hz	$\forall t$	(3.22)	6.2	mGal
GDT-GG (3.4.13)	$\forall x_i, x_j : \left\|x_i - x_j\right\| = 1km$		(3.22)	6.2	mGal
GDT-GG (3.4.13)	$\forall x_i, x_j : \left\|x_i - x_j\right\| = 4km$		(3.22)	13.0	mGal
DGUPT-GG (3.4.28)	0.1 Hz	$\forall t$	(3.41)	0.02	mGal
XOVER-GG (3.4.31)			(3.44)	0.000 3	mGal

Table 4.61: Test CTRA-LN200-v2b2x: network configuration.

Figure 4.61 prove that the functional models of the NA approach work succesfully:

- Figures 4.61a and 4.61c point out that the position has been recovered, especially heights with a precision better than 0.5 cm.
- The navigation parameters — shown in Figure 4.61e — are recovered with a precision of 1.2 ' for roll (α) and pitch (χ) and 3.6 ' for heading (η).
- The IMU error parameters exhibited in Figures 4.61b and 4.61d are nearly constants within the defined tolerances (bias repeatability) of the IMU.

- Figure 4.61f also displays the gravity disturbance vector, that has to be zero.

LTN101

Table 4.62 summarises the network configuration used in this computation.

Model Name	Frequency		Equation	Standard Deviation	
FB-GG (3.4.5)	20.0 Hz	$\forall t$	(3.13)	4.4	10^{-4} m s^{-2}
WIB (3.4.2)	20.0 Hz	$\forall t$	(3.10)	1.3	10^{-6} rad s^{-1}
VEL (3.4.1)	20.0 Hz	$\forall t$	(3.4.1)	0.000 01	m
Q-NORM (3.4.6)	20.0 Hz	$\forall t$	(3.14)	0.01	ppm
OB-O (3.4.35)	0.1 Hz	$\forall t$	(3.48)	4.9	10^{-8} rad s^{-1}
AB-O (3.4.36)	0.1 Hz	$\forall t$	(3.49)	4.9	10^{-4} m s^{-2}
OB (3.4.8)	0.1 Hz	$\forall t$	(3.16)	61.0	10^{-12} rad s^{-1}
AB (3.4.10)	0.1 Hz	$\forall t$	(3.18)	95.0	10^{-7} m s^{-2}
AOFF-O (3.4.37)			(3.50)	0.001	m
CUPT (3.4.16)	1.0 Hz	$\forall t$	(3.26)	0.05	m
GDT-GG (3.4.13)	0.1 Hz	$\forall t$	(3.22)	6.2	mGal
GDT-GG (3.4.13)	$\forall x_i, x_j : \left\|x_i - x_j\right\| = 1km$		(3.22)	6.2	mGal
GDT-GG (3.4.13)	$\forall x_i, x_j : \left\|x_i - x_j\right\| = 4km$		(3.22)	13.0	mGal
DGUPT-GG (3.4.28)	0.1 Hz	$\forall t$	(3.41)	0.02	mGal
XOVER-GG (3.4.31)			(3.44)	0.000 3	mGal

Table 4.62: Test CTRA-LTN101-v2b2x: network configuration.

Figure 4.62 proves that the functional models of the NA approach work succesfully:

- Figures 4.62a and 4.62c point out that the position has been recovered, especially heights with a precision better than 2 cm.
- The navigation parameters — shown in Figure 4.62e — are recovered with a precision better than 0.3 ' for roll (α) and pitch (χ) and with a range of 2.4 ' for heading (η).
- The IMU error parameters exhibited in Figures 4.62b and 4.62d are nearly constants within the defined tolerances (bias repeatability) of the IMU.
- Figure 4.62f also displays the gravity disturbance vector, that has to be zero.

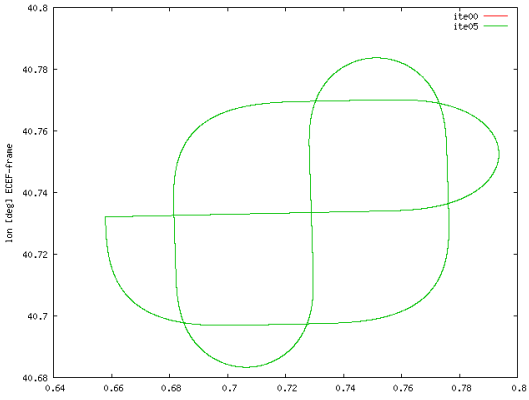

(a) Position (°)

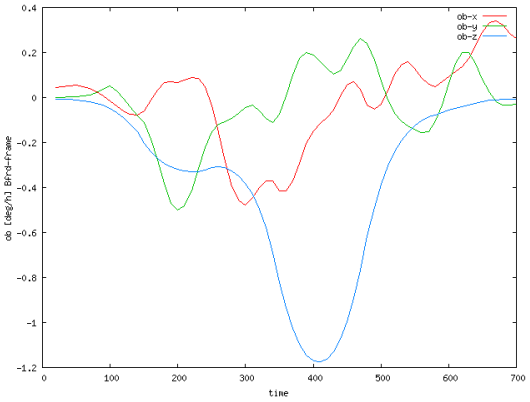

(b) Angular drift (° h^{-1})

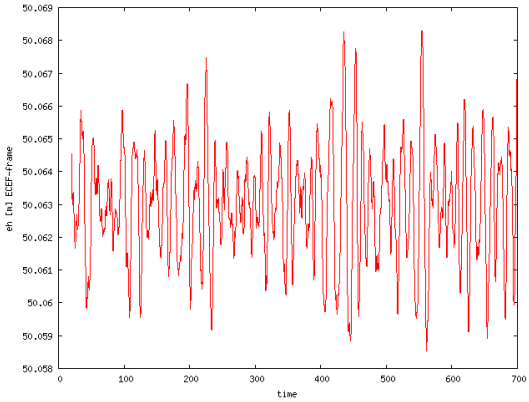

(c) Height (m)

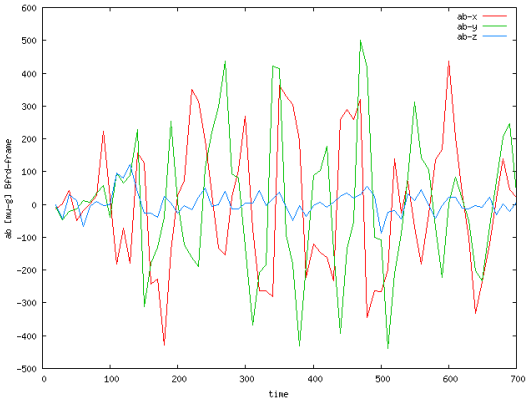

(d) Accelerometer bias (μg)

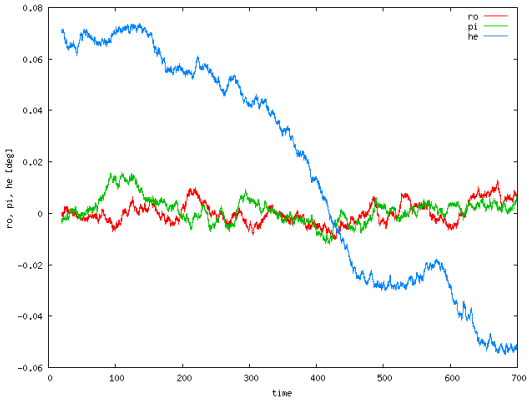

(e) Roll, Pitch and Heading (°)

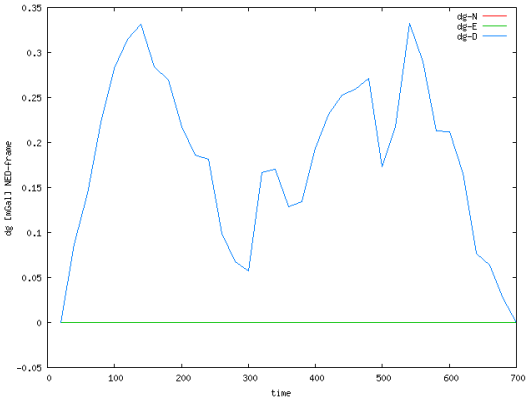

(f) Gravity disturbance (mGal)

Figure 4.61: CTRA LN200 v2b2x: adjusted parameters.

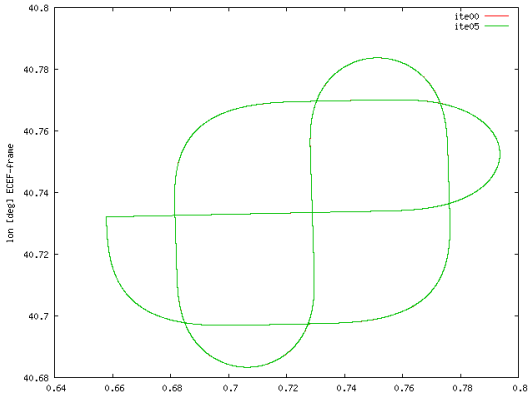

(a) Position (°)

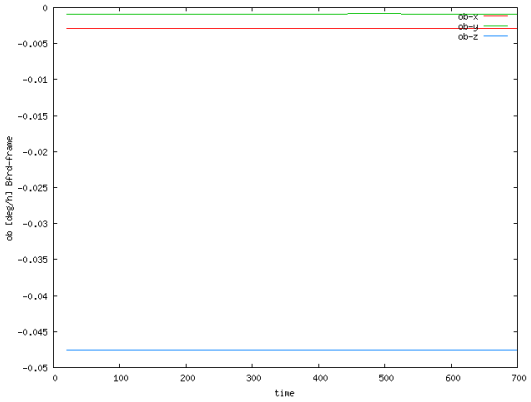

(b) Angular drift ($^\circ\,h^{-1}$)

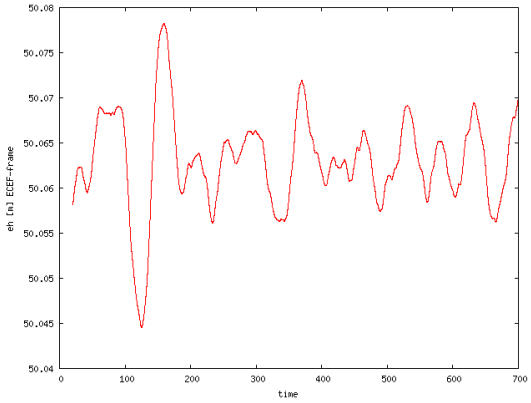

(c) Height (m)

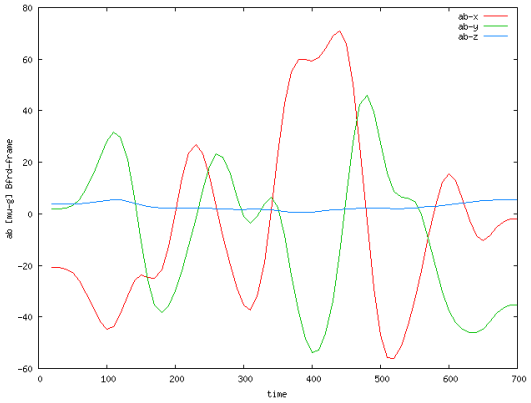

(d) Accelerometer bias (μg)

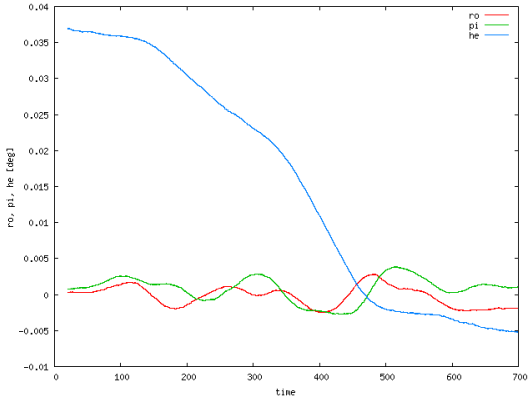

(e) Roll, Pitch and Heading (°)

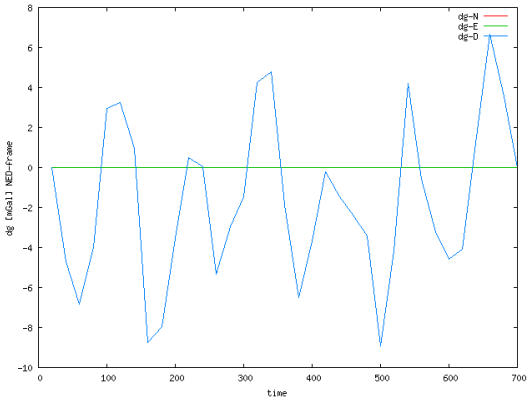

(f) Gravity disturbance (mGal)

Figure 4.62: CTRA LTN101b v2b2x: adjusted parameters.

4.5.12 CTRA vq2b2x

As already discussed in Section 4.2, the codification this computation means:

- $\langle q \rangle = q$: no prior knowledge of the vehicle's attitude exists at the beginning (t_0) and at the end (t_N) of the mission.
- $\langle Hz \rangle = 2$: some subsets of parameters — $\underline{o}^{\mathsf{b}}$, $\underline{a}^{\mathsf{b}}$, δg or gg — has been grouped.
- $\langle \delta g_{NE} \rangle = b$, indicates that, for all t, $\delta g_N(t) = \delta g_E(t) \approx 0$.
- $\langle method \rangle = 2x$: GDT-p (changes of the gravity disturbance of closed positions with respect to time) observations are added to the basic configuration and moreover, XOVER observations are considered $\langle method \rangle = 2x$.

LN200

Table 4.63 summarises the network configuration used in this computation.

Model Name	Frequency		Equation	Standard Deviation	
FB-GG (3.4.5)	20.0 Hz	$\forall t$	(3.13)	2.2	10^{-3} m s^{-2}
WIB (3.4.2)	20.0 Hz	$\forall t$	(3.10)	5.2	10^{-5} rad s^{-1}
VEL (3.4.1)	20.0 Hz	$\forall t$	(3.4.1)	0.000 01	m
Q-NORM (3.4.6)	20.0 Hz	$\forall t$	(3.14)	0.01	ppm
OB-O (3.4.35)	0.1 Hz	$\forall t$	(3.48)	4.9	10^{-6} rad s^{-1}
AB-O (3.4.36)	0.1 Hz	$\forall t$	(3.49)	2.0	10^{-3} m s^{-2}
OB (3.4.8)	0.1 Hz	$\forall t$	(3.16)	15.0	10^{-7} rad s^{-1}
AB (3.4.10)	0.1 Hz	$\forall t$	(3.18)	130.0	10^{-4} m s^{-2}
AOFF-O (3.4.37)			(3.50)	0.001	m
CUPT (3.4.16)	1.0 Hz	$\forall t$	(3.26)	0.05	m
GDT-GG (3.4.13)	0.1 Hz	$\forall t$	(3.22)	6.2	mGal
GDT-GG (3.4.13)	$\forall x_i, x_j : \lvert x_i - x_j \rvert = 1km$		(3.22)	6.2	mGal
GDT-GG (3.4.13)	$\forall x_i, x_j : \lvert x_i - x_j \rvert = 4km$		(3.22)	13.0	mGal
DGUPT-GG (3.4.28)	0.1 Hz	$\forall t$	(3.41)	0.02	mGal
Q-O (3.4.34)		t_0, t_N	(3.47)	0.01	ppm
XOVER-GG (3.4.31)			(3.44)	0.000 3	mGal

Table 4.63: Test CTRA-LN200-vq2b2x: network configuration.

Figure 4.63 proves that the functional models of the NA approach work succesfully:

- Figures 4.63a and 4.63c point out that the position has been recovered, especially heights with a precision better than 0.5 cm.
- The navigation parameters — shown in Figure 4.63e — are recovered with a precision of 0.6 ' for roll (α) and pitch (χ) and with a range of 4.2 ' for heading (η).

- The IMU error parameters exhibited in Figures 4.63b and 4.63d are nearly constants within the defined tolerances (bias repeatability) of the IMU.
- Figure 4.63f also displays the gravity disturbance vector, that has to be zero, with a precision of 0.35 mGal

LTN101

Table 4.64 summarises the network configuration used in this computation.

Model Name	Frequency		Equation	Standard Deviation	
FB-GG (3.4.5)	20.0 Hz	$\forall t$	(3.13)	4.4	10^{-4} m s^{-2}
WIB (3.4.2)	20.0 Hz	$\forall t$	(3.10)	1.3	10^{-6} rad s^{-1}
VEL (3.4.1)	20.0 Hz	$\forall t$	(3.4.1)	0.000 01	m
Q-NORM (3.4.6)	20.0 Hz	$\forall t$	(3.14)	0.01	ppm
OB-O (3.4.35)	0.1 Hz	$\forall t$	(3.48)	4.9	10^{-8} rad s^{-1}
AB-O (3.4.36)	0.1 Hz	$\forall t$	(3.49)	4.9	10^{-4} m s^{-2}
OB (3.4.8)	0.1 Hz	$\forall t$	(3.16)	61.0	10^{-12} rad s^{-1}
AB (3.4.10)	0.1 Hz	$\forall t$	(3.18)	95.0	10^{-7} m s^{-2}
AOFF-O (3.4.37)			(3.50)	0.001	m
CUPT (3.4.16)	1.0 Hz	$\forall t$	(3.26)	0.05	m
GDT-GG (3.4.13)	0.1 Hz	$\forall t$	(3.22)	6.2	mGal
GDT-GG (3.4.13)	$\forall x_i, x_j : \lvert x_i - x_j \rvert = 1km$		(3.22)	6.2	mGal
GDT-GG (3.4.13)	$\forall x_i, x_j : \lvert x_i - x_j \rvert = 4km$		(3.22)	13.0	mGal
DGUPT-GG (3.4.28)	0.1 Hz	$\forall t$	(3.41)	0.02	mGal
Q-O (3.4.34)		t_0, t_N	(3.47)	0.01	ppm
XOVER-GG (3.4.31)			(3.44)	0.000 3	mGal

Table 4.64: Test CTRA-LTN101-vq2b2x: network configuration.

Figure 4.64 proves that the functional models of the NA approach work succesfully:

- Figures 4.64a and 4.64c point out that the position has been recovered, especially heights with a precision better than 0.5 cm.
- The navigation parameters — shown in Figure 4.64e — are recovered with a precision of 7.2 " for roll (α) and pitch (χ) and with a range of 1.08 ' for heading (η).
- The IMU error parameters exhibited in Figures 4.64b and 4.64d are nearly constants within the defined tolerances (bias repeatability) of the IMU.
- Figure 4.64f also displays the gravity disturbance vector, that has to be zero, with a precision of 3 mGal.

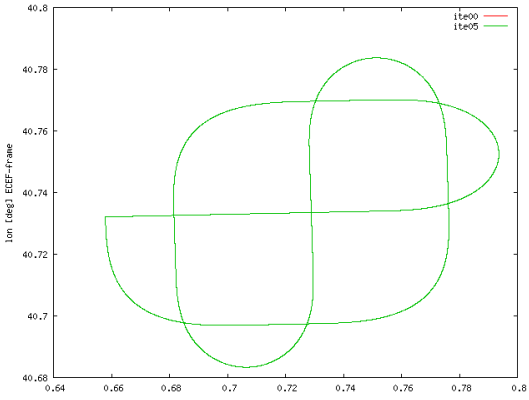

(a) Position (°)

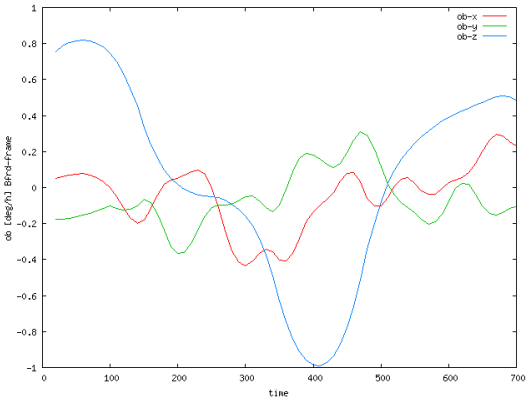

(b) Angular drift ($^\circ\,h^{-1}$)

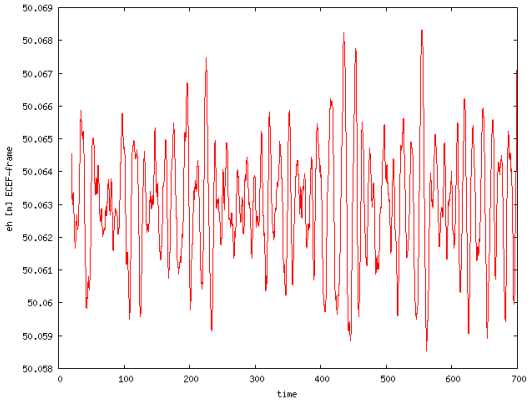

(c) Height (m)

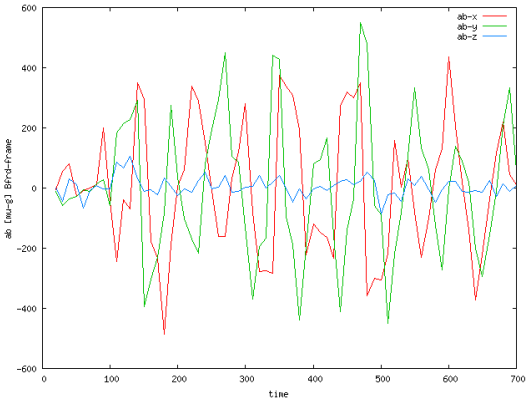

(d) Accelerometer bias (μg)

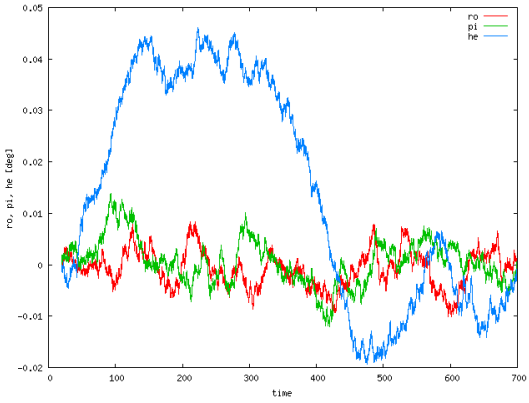

(e) Roll, Pitch and Heading (°)

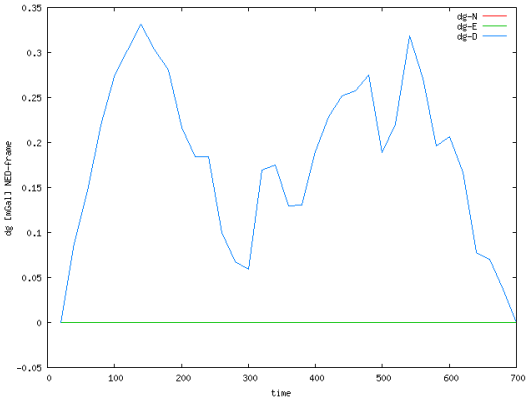

(f) Gravity disturbance (mGal)

Figure 4.63: CTRA LN200 vq2b2x: adjusted parameters.

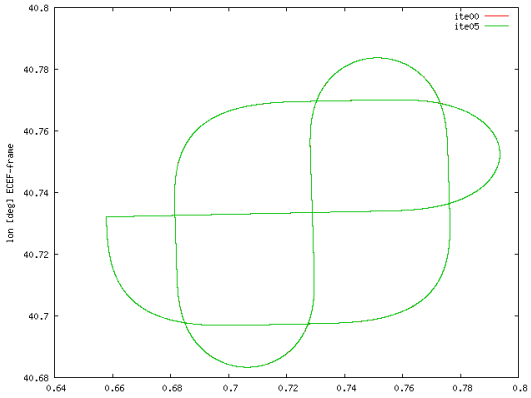

(a) Position (°)

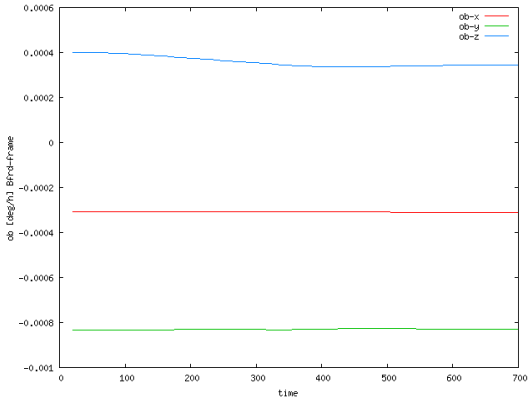

(b) Angular drift ($^\circ\,h^{-1}$)

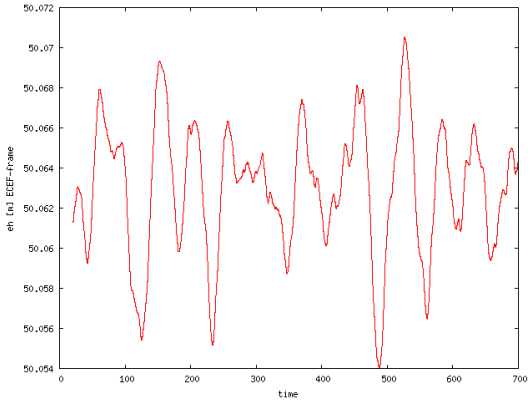

(c) Height (m)

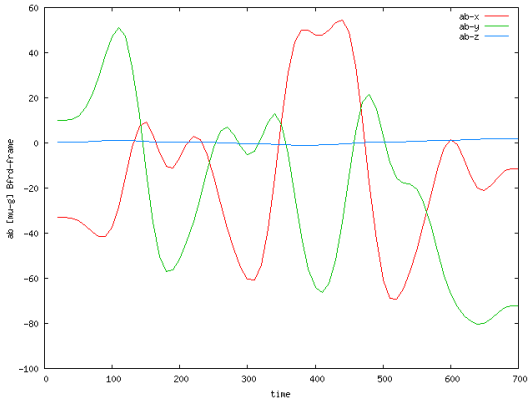

(d) Accelerometer bias (μg)

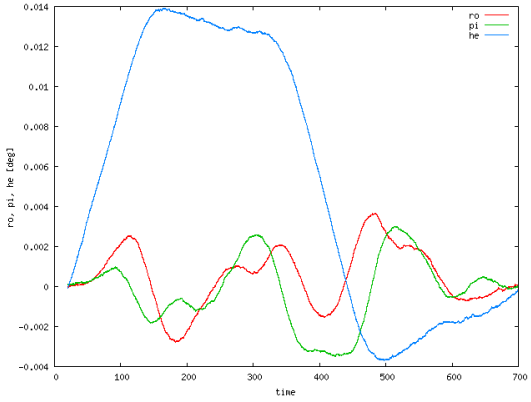

(e) Roll, Pitch and Heading (°)

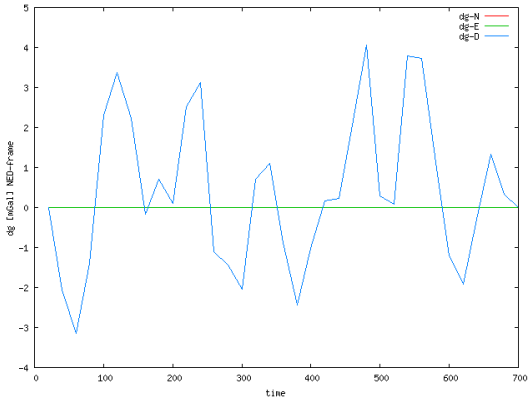

(f) Gravity disturbance (mGal)

Figure 4.64: CTRA LTN101b vq2b2x: adjusted parameters.

4.5.13 CTRA v9a1

As already discussed in Section 4.2, the codification this computation means:

- $\langle Hz \rangle = 9$: all the parameters are computed at the IMU rate.
- $\langle \delta g_{NE} \rangle = a$: no prior knowledge of the horizontal gravity.
- $\langle method \rangle = 1$,indicates a basic network configuration similar to the Kalman filtering.

LN200

Table 4.65 summarises the network configuration used in this computation.

Model Name	Frequency		Equation	Standard Deviation	
FB-GG (3.4.5)	20.0 Hz	$\forall t$	(3.13)	2.2	10^{-3} m s^{-2}
WIB (3.4.2)	20.0 Hz	$\forall t$	(3.10)	5.2	10^{-5} rad s^{-1}
VEL (3.4.1)	20.0 Hz	$\forall t$	(3.4.1)	0.000 01	m
Q-NORM (3.4.6)	20.0 Hz	$\forall t$	(3.14)	0.01	ppm
OB-O (3.4.35)	20.0 Hz	$\forall t$	(3.48)	4.9	10^{-6} rad s^{-1}
AB-O (3.4.36)	20.0 Hz	$\forall t$	(3.49)	2.0	10^{-3} m s^{-2}
OB (3.4.8)	20.0 Hz	$\forall t$	(3.16)	1.1	10^{-7} rad s^{-1}
AB (3.4.10)	20.0 Hz	$\forall t$	(3.18)	8.9	10^{-4} m s^{-2}
AOFF-O (3.4.37)			(3.50)	0.001	m
CUPT (3.4.16)	1.0 Hz	$\forall t$	(3.26)	0.05	m
GDT-GG (3.4.13)	20.0 Hz	$\forall t$	(3.22)	0.016	mGal
DGUPT-GG (3.4.28)		t_0, t_N	(3.41)	0.02	mGal

Table 4.65: Test CTRA-LN200-v9a1: network configuration.

Figure 4.65 proves that the functional models of the NA approach work succesfully:

- Figures 4.65a and 4.65c point out that the position has been recovered, especially heights with a precision better than 2 cm.
- The navigation parameters — shown in Figure 4.65e — are recovered with a precision of 1.2 ' for roll (α) and pitch (χ) and 6 ' for heading (η).
- The IMU error parameters exhibited in Figures 4.65b and 4.65d are nearly constants within the defined tolerances (bias repeatability) of the IMU.
- Figure 4.65f also displays the gravity disturbance vector, that has to be zero, with a precision better than 0.5 mGal.

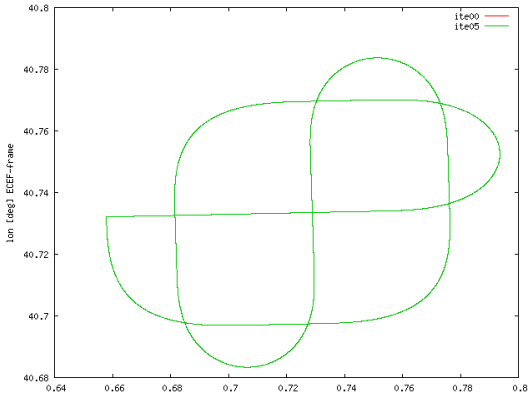

(a) Position (°)

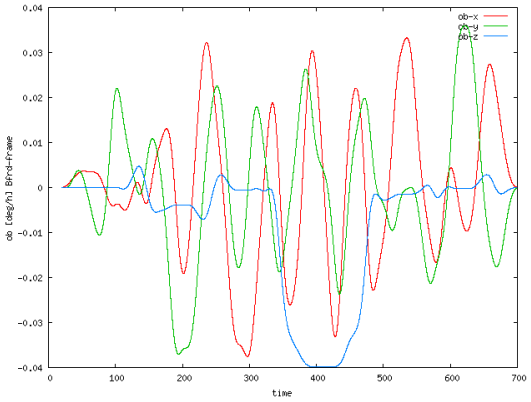

(b) Angular drift ($^\circ\,h^{-1}$)

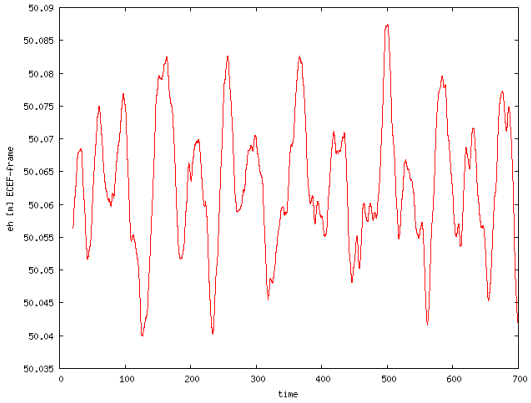

(c) Height (m)

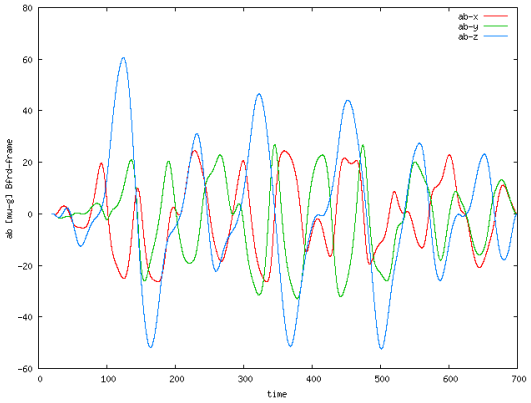

(d) Accelerometer bias (μg)

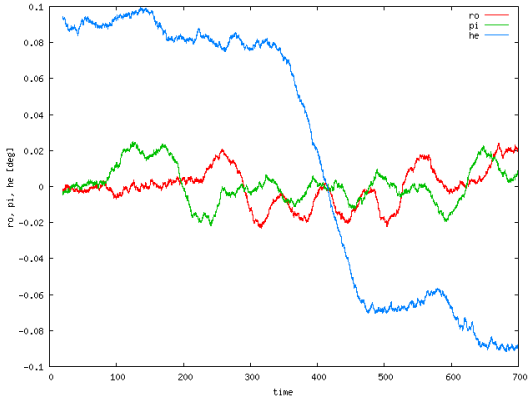

(e) Roll, Pitch and Heading (°)

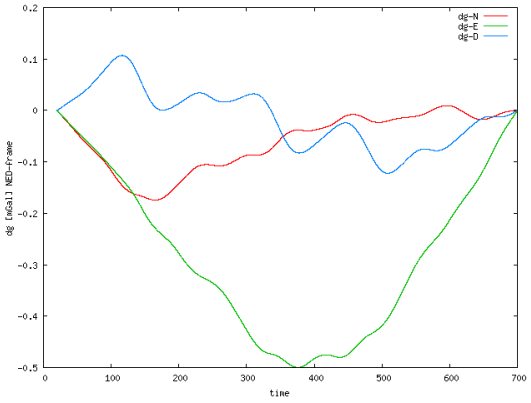

(f) Gravity disturbance (mGal)

Figure 4.65: CTRA LN200 v9a1: adjusted parameters.

LTN101

Table 4.66 summarises the network configuration used in this computation.

Model Name	Frequency		Equation	Standard Deviation	
FB-GG (3.4.5)	20.0 Hz	$\forall t$	(3.13)	4.4	10^{-4} m s^{-2}
WIB (3.4.2)	20.0 Hz	$\forall t$	(3.10)	1.3	10^{-6} rad s^{-1}
VEL (3.4.1)	20.0 Hz	$\forall t$	(3.4.1)	0.000 01	m
Q-NORM (3.4.6)	20.0 Hz	$\forall t$	(3.14)	0.01	ppm
OB-O (3.4.35)	20.0 Hz	$\forall t$	(3.48)	4.9	10^{-8} rad s^{-1}
AB-O (3.4.36)	20.0 Hz	$\forall t$	(3.49)	4.9	10^{-4} m s^{-2}
OB (3.4.8)	20.0 Hz	$\forall t$	(3.16)	4.3	10^{-12} rad s^{-1}
AB (3.4.10)	20.0 Hz	$\forall t$	(3.18)	6.7	10^{-7} m s^{-2}
AOFF-O (3.4.37)			(3.50)	0.001	m
CUPT (3.4.16)	1.0 Hz	$\forall t$	(3.26)	0.05	m
GDT-GG (3.4.13)	20.0 Hz	$\forall t$	(3.22)	0.016	mGal
DGUPT-GG (3.4.28)		t_0, t_N	(3.41)	0.02	mGal

Table 4.66: Test CTRA-LTN101-v9a1: network configuration.

Figure 4.66 proves that the functional models of the NA approach work succesfully:

- Figures 4.66a and 4.66c point out that the position has been recovered, especially heights with a precision better than 3 cm.
- The navigation parameters — shown in Figure 4.66e — are recovered with a precision of 0.3 ' for roll (α) and pitch (χ) and with a range of 2.4 ' for heading (η).
- The IMU error parameters exhibited in Figures 4.66b and 4.66d are nearly constants within the defined tolerances (bias repeatability) of the IMU.
- Figure 4.66f also displays the gravity disturbance vector, that has to be zero.

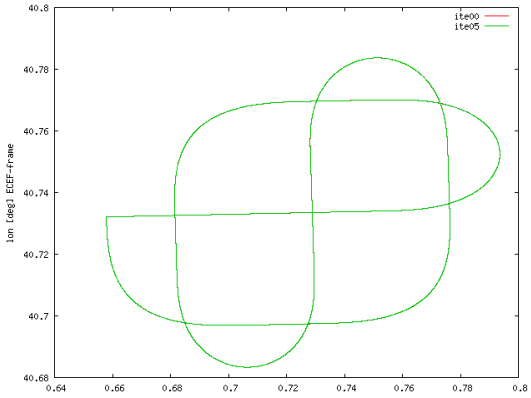

(a) Position (°)

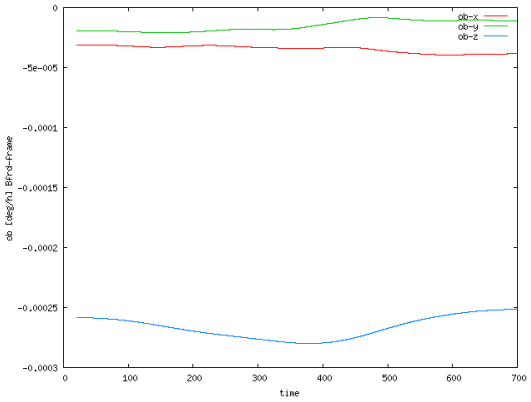

(b) Angular drift ($^\circ\,h^{-1}$)

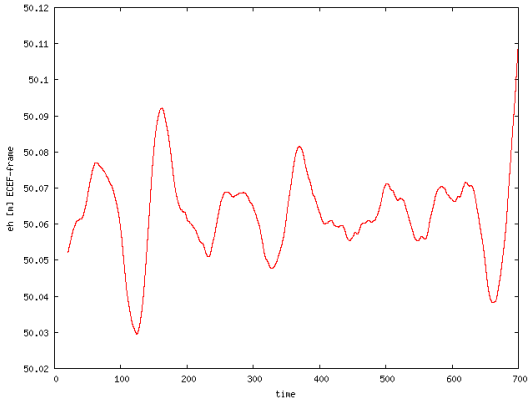

(c) Height (m)

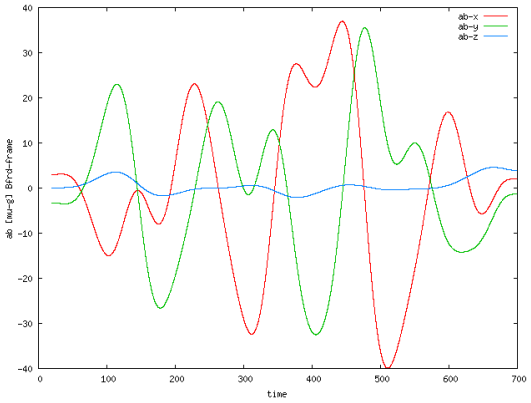

(d) Accelerometer bias (μg)

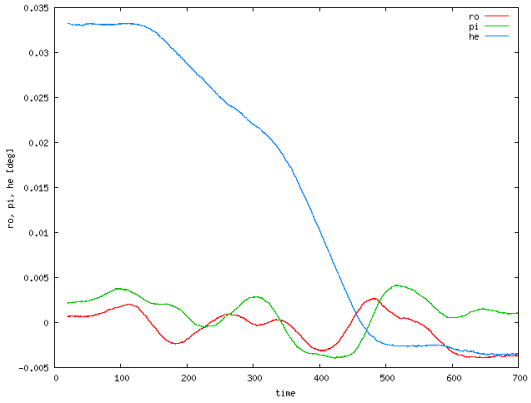

(e) Roll, Pitch and Heading (°)

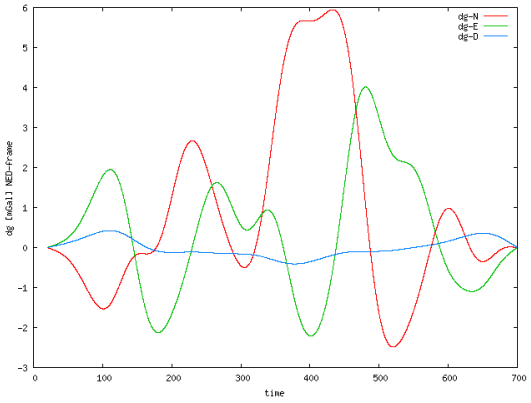

(f) Gravity disturbance (mGal)

Figure 4.66: CTRA LTN101b v9a1: adjusted parameters.

4.5.14 CTRA vq9a1

As already discussed in Section 4.2, the codification this computation means:

- $\langle q \rangle = q$: prior knowledge of the vehicle's attitude exists at the beginning (t_0) and at the end (t_N) of the mission.
- $\langle Hz \rangle = 9$: all the parameters are computed at the IMU rate.
- $\langle \delta g_{NE} \rangle = a$: no prior knowledge of the horizontal gravity.
- $\langle method \rangle = 1$, indicates a basic network configuration similar to the Kalman filtering.

LN200

Table 4.67 summarises the network configuration used in this computation.

Model Name	Frequency		Equation	Standard Deviation	
FB-GG (3.4.5)	20.0 Hz	$\forall t$	(3.13)	2.2	10^{-3} m s^{-2}
WIB (3.4.2)	20.0 Hz	$\forall t$	(3.10)	5.2	10^{-5} rad s^{-1}
VEL (3.4.1)	20.0 Hz	$\forall t$	(3.4.1)	0.000 01	m
Q-NORM (3.4.6)	20.0 Hz	$\forall t$	(3.14)	0.01	ppm
OB-O (3.4.35)	20.0 Hz	$\forall t$	(3.48)	4.9	10^{-6} rad s^{-1}
AB-O (3.4.36)	20.0 Hz	$\forall t$	(3.49)	2.0	10^{-3} m s^{-2}
OB (3.4.8)	20.0 Hz	$\forall t$	(3.16)	1.1	10^{-7} rad s^{-1}
AB (3.4.10)	20.0 Hz	$\forall t$	(3.18)	8.9	10^{-4} m s^{-2}
AOFF-O (3.4.37)			(3.50)	0.001	m
CUPT (3.4.16)	1.0 Hz	$\forall t$	(3.26)	0.05	m
GDT-GG (3.4.13)	20.0 Hz	$\forall t$	(3.22)	0.016	mGal
DGUPT-GG (3.4.28)		t_0, t_N	(3.41)	0.02	mGal
Q-O (3.4.34)		t_0, t_N	(3.47)	0.01	ppm

Table 4.67: Test CTRA-LN200-vq9a1: network configuration.

Figure 4.67 proves that the functional models of the NA approach work succesfully:

- Figures 4.67a and 4.67c point out that the position has been recovered, especially heights with a precision better than 2 cm.
- The navigation parameters — shown in Figure 4.67e — are recovered with a precision of 1.2 ' for roll (α) and pitch (χ) and 4.2 ' for heading (η).
- The IMU error parameters exhibited in Figures 4.67b and 4.67d are nearly constants within the defined tolerances (bias repeatability) of the IMU.
- Figure 4.67f also displays the gravity disturbance vector, that has to be zero, with a precision better than 1 mGal.

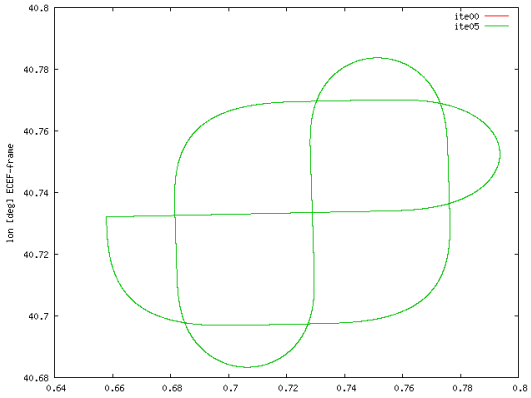

(a) Position (°)

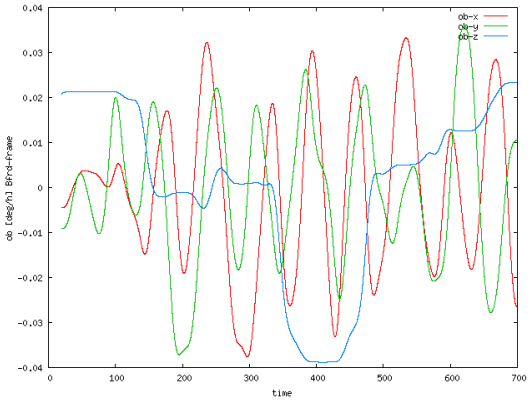

(b) Angular drift ($^\circ\,h^{-1}$)

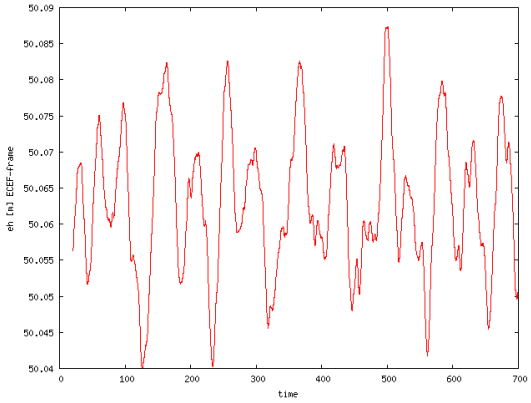

(c) Height (m)

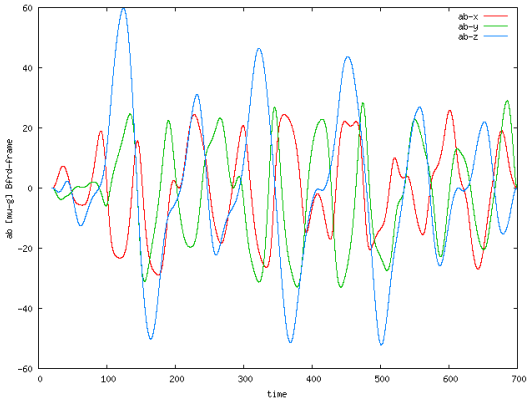

(d) Accelerometer bias (μg)

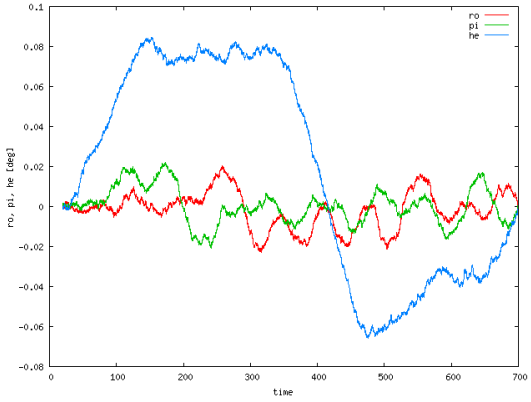

(e) Roll, Pitch and Heading (°)

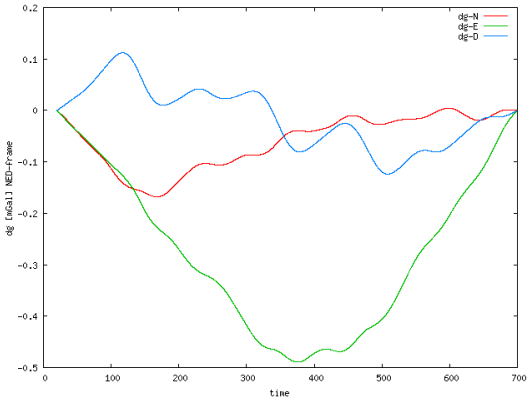

(f) Gravity disturbance (mGal)

Figure 4.67: CTRA LN200 vq9a1: adjusted parameters.

LTN101

Table 4.68 summarises the network configuration used in this computation.

Model Name	Frequency		Equation	Standard Deviation	
FB-GG (3.4.5)	20.0 Hz	$\forall t$	(3.13)	4.4	10^{-4} m s^{-2}
WIB (3.4.2)	20.0 Hz	$\forall t$	(3.10)	1.3	10^{-6} rad s^{-1}
VEL (3.4.1)	20.0 Hz	$\forall t$	(3.4.1)	0.000 01	m
Q-NORM (3.4.6)	20.0 Hz	$\forall t$	(3.14)	0.01	ppm
OB-O (3.4.35)	20.0 Hz	$\forall t$	(3.48)	4.9	10^{-8} rad s^{-1}
AB-O (3.4.36)	20.0 Hz	$\forall t$	(3.49)	4.9	10^{-4} m s^{-2}
OB (3.4.8)	20.0 Hz	$\forall t$	(3.16)	4.3	10^{-12} rad s^{-1}
AB (3.4.10)	20.0 Hz	$\forall t$	(3.18)	6.7	10^{-7} m s^{-2}
AOFF-O (3.4.37)			(3.50)	0.001	m
CUPT (3.4.16)	1.0 Hz	$\forall t$	(3.26)	0.05	m
GDT-GG (3.4.13)	20.0 Hz	$\forall t$	(3.22)	0.016	mGal
DGUPT-GG (3.4.28)		t_0, t_N	(3.41)	0.02	mGal
Q-O (3.4.34)		t_0, t_N	(3.47)	0.01	ppm

Table 4.68: Test CTRA-LTN101-vq9a1: network configuration.

Figure 4.68 proves that the functional models of the NA approach work succesfully:

- Figures 4.68a and 4.68c point out that the position has been recovered, especially heights with a precision better than 1.5 cm.
- The navigation parameters — shown in Figure 4.68e — are recovered with a precision of 14.4 " for roll (α) and pitch (χ) and 1.2 ' for heading (η).
- The IMU error parameters exhibited in Figures 4.68b and 4.68d are nearly constants within the defined tolerances (bias repeatability) of the IMU.
- Figure 4.68f also displays the gravity disturbance vector, that has to be zero, with a precision of 1 mGal.

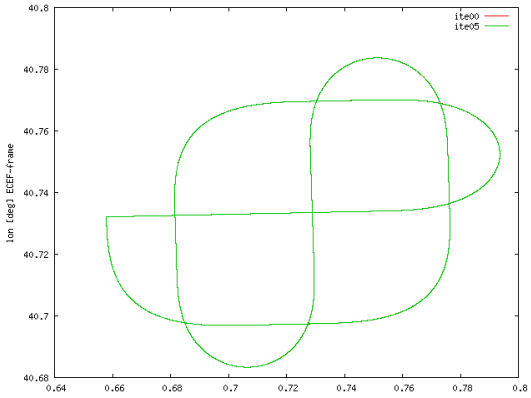

(a) Position (°)

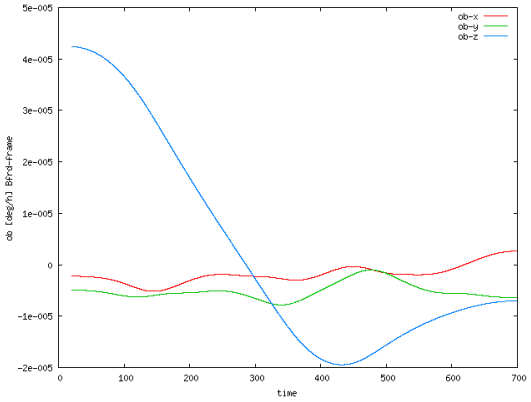

(b) Angular drift ($^\circ\,h^{-1}$)

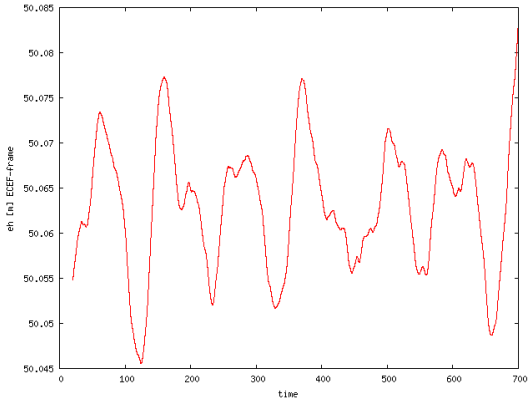

(c) Height (m)

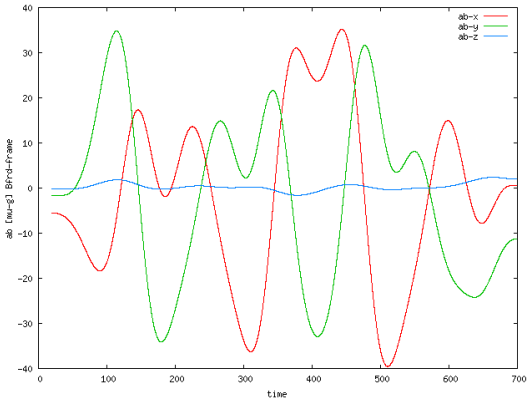

(d) Accelerometer bias (μg)

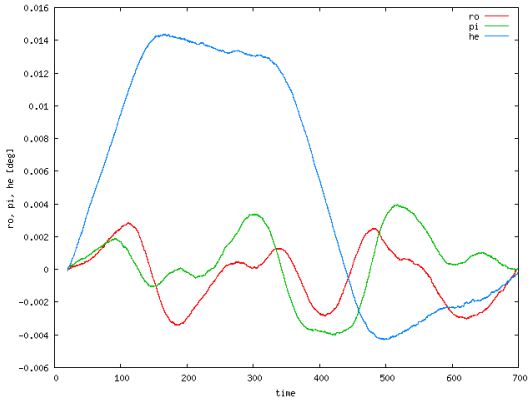

(e) Roll, Pitch and Heading (°)

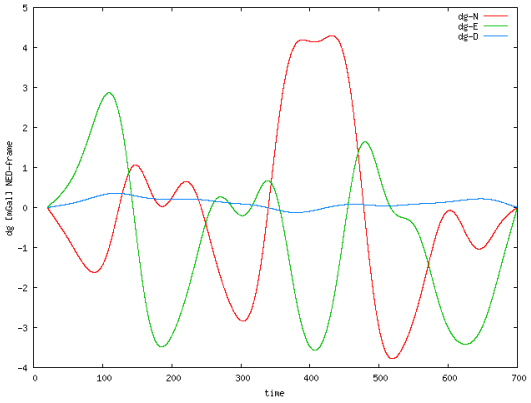

(f) Gravity disturbance (mGal)

Figure 4.68: CTRA LTN101b vq9a1: adjusted parameters.

4.5.15 CTRA v9b1

As already discussed in Section 4.2, the codification this computation means:

- $\langle Hz \rangle = 9$: all the parameters are computed at the IMU rate.
- $\langle \delta g_{NE} \rangle = b$, indicates that, for all t, $\delta g_N(t) = \delta g_E(t) \approx 0$.
- $\langle method \rangle = 1$, indicates a basic network configuration similar to the Kalman filtering.

LN200

Table 4.69 summarises the network configuration used in this computation.

Model Name	Frequency		Equation	Standard Deviation	
FB-GG (3.4.5)	20.0 Hz	$\forall t$	(3.13)	2.2	10^{-3} m s^{-2}
WIB (3.4.2)	20.0 Hz	$\forall t$	(3.10)	5.2	10^{-5} rad s^{-1}
VEL (3.4.1)	20.0 Hz	$\forall t$	(3.4.1)	0.000 01	m
Q-NORM (3.4.6)	20.0 Hz	$\forall t$	(3.14)	0.01	ppm
OB-O (3.4.35)	20.0 Hz	$\forall t$	(3.48)	4.9	10^{-6} rad s^{-1}
AB-O (3.4.36)	20.0 Hz	$\forall t$	(3.49)	2.0	10^{-3} m s^{-2}
OB (3.4.8)	20.0 Hz	$\forall t$	(3.16)	1.1	10^{-7} rad s^{-1}
AB (3.4.10)	20.0 Hz	$\forall t$	(3.18)	8.9	10^{-4} m s^{-2}
AOFF-O (3.4.37)			(3.50)	0.001	m
CUPT (3.4.16)	1.0 Hz	$\forall t$	(3.26)	0.05	m
GDT-GG (3.4.13)	20.0 Hz	$\forall t$	(3.22)	0.016	mGal
DGUPT-GG (3.4.28)	20.0 Hz	$\forall t$	(3.41)	0.02	mGal

Table 4.69: Test CTRA-LN200-v9b1: network configuration.

Figure 4.69 proves that the functional models of the NA approach work succesfully:

- Figures 4.69a and 4.69c point out that the position has been recovered, especially heights with a precision better than 2 cm.
- The navigation parameters —shown in Figure 4.69e— are recovered with a precision of 1.2 ' for roll (α) and pitch (χ) and 6 ' for heading (η).
- The IMU error parameters exhibited in Figures 4.69b and 4.69d are nearly constants within the defined tolerances (bias repeatability) of the IMU.
- Figure 4.69f also displays the gravity disturbance vector, that has to be zero, with a precision of 0.15 mGal.

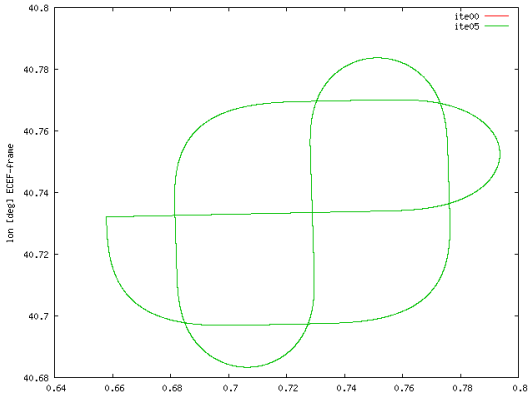

(a) Position (°)

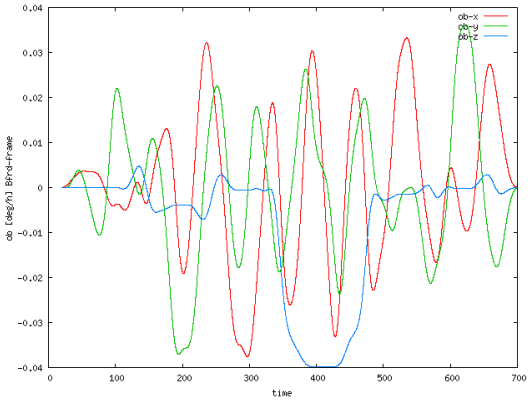

(b) Angular drift ($^\circ\,h^{-1}$)

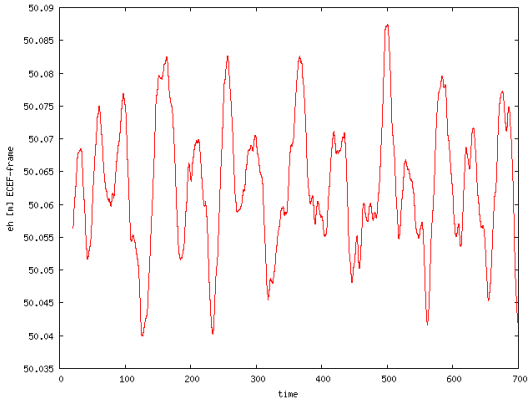

(c) Height (m)

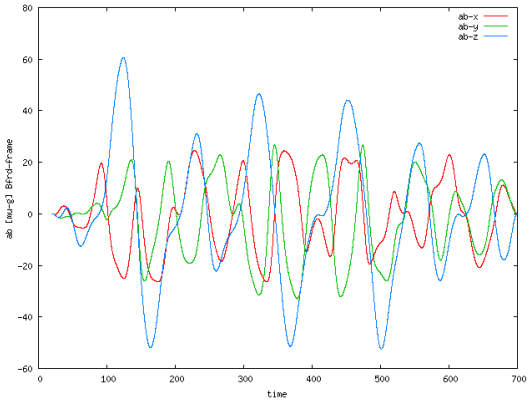

(d) Accelerometer bias (μg)

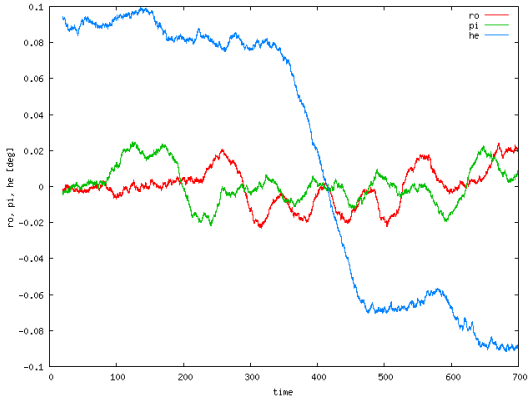

(e) Roll, Pitch and Heading (°)

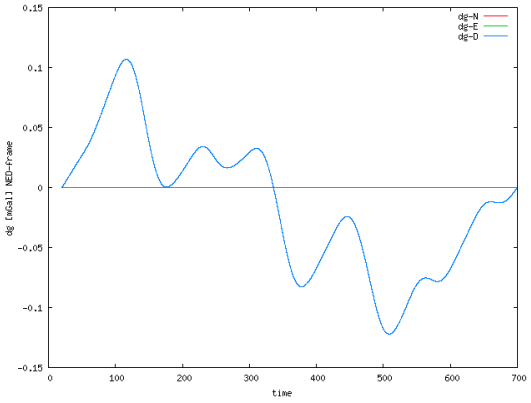

(f) Gravity disturbance (mGal)

Figure 4.69: CTRA LN200 v9b1: adjusted parameters.

LTN101

Table 4.70 summarises the network configuration used in this computation.

Model Name	Frequency		Equation	Standard Deviation	
FB-GG (3.4.5)	20.0 Hz	$\forall t$	(3.13)	4.4	10^{-4} m s^{-2}
WIB (3.4.2)	20.0 Hz	$\forall t$	(3.10)	1.3	10^{-6} rad s^{-1}
VEL (3.4.1)	20.0 Hz	$\forall t$	(3.4.1)	0.000 01	m
Q-NORM (3.4.6)	20.0 Hz	$\forall t$	(3.14)	0.01	ppm
OB-O (3.4.35)	20.0 Hz	$\forall t$	(3.48)	4.9	10^{-8} rad s^{-1}
AB-O (3.4.36)	20.0 Hz	$\forall t$	(3.49)	4.9	10^{-4} m s^{-2}
OB (3.4.8)	20.0 Hz	$\forall t$	(3.16)	4.3	10^{-12} rad s^{-1}
AB (3.4.10)	20.0 Hz	$\forall t$	(3.18)	6.7	10^{-7} m s^{-2}
AOFF-O (3.4.37)			(3.50)	0.001	m
CUPT (3.4.16)	1.0 Hz	$\forall t$	(3.26)	0.05	m
GDT-GG (3.4.13)	20.0 Hz	$\forall t$	(3.22)	0.016	mGal
DGUPT-GG (3.4.28)	20.0 Hz	$\forall t$	(3.41)	0.02	mGal

Table 4.70: Test CTRA-LTN101-v9b1: network configuration.

Figure 4.70 proves that the functional models of the NA approach work succesfully:

- Figures 4.70a and 4.70c point out that the position has been recovered, especially heights with a precision better than 2.5 cm.
- The navigation parameters —shown in Figure 4.70e— are recovered with a precision of 0.3 ' for roll (α) and pitch (χ) and with a range of 2.4 ' for heading (η).
- The IMU error parameters exhibited in Figures 4.70b and 4.70d are nearly constants within the defined tolerances (bias repeatability) of the IMU.
- Figure 4.70f also displays the gravity disturbance vector, that has to be zero, with a precision of 0.5 mGal.

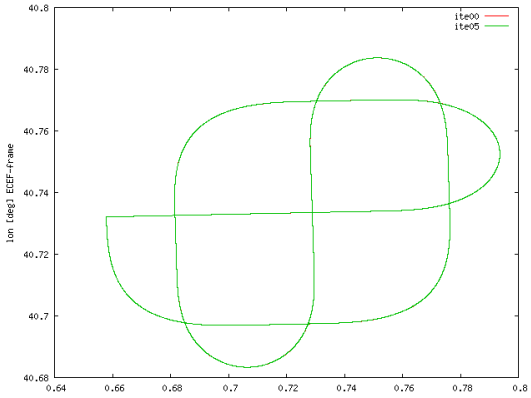

(a) Position (°)

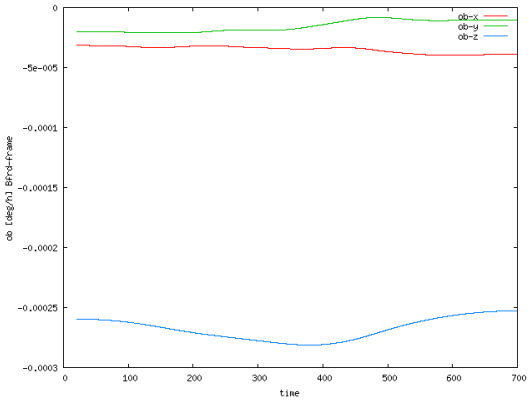

(b) Angular drift ($^\circ\,h^{-1}$)

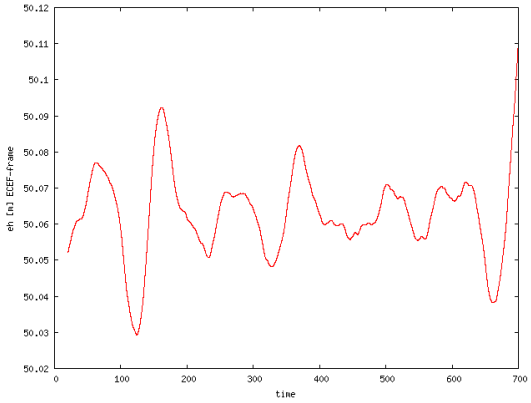

(c) Height (m)

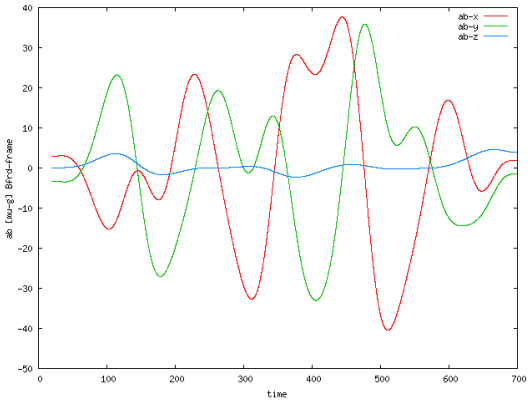

(d) Accelerometer bias (μg)

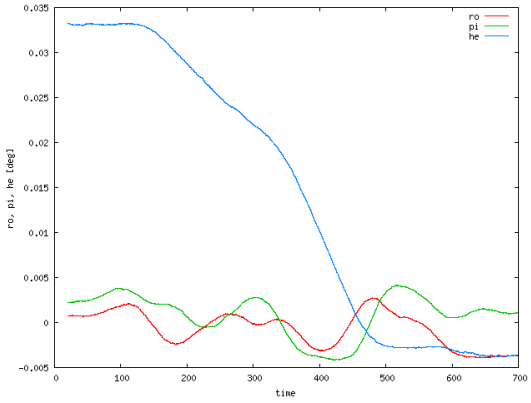

(e) Roll, Pitch and Heading (°)

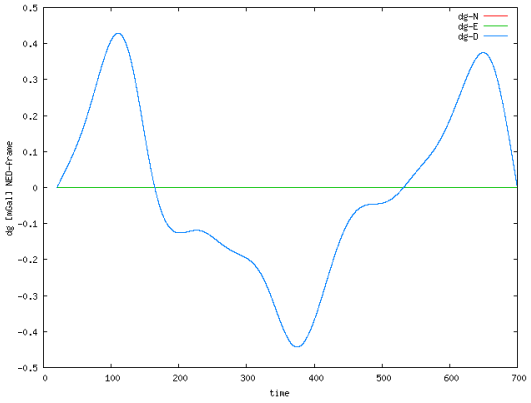

(f) Gravity disturbance (mGal)

Figure 4.70: CTRA LTN101b v9b1: adjusted parameters.

4.5.16 CTRA vq9b1

As already discussed in Section 4.2, the codification this computation means:

- $\langle q \rangle = q$: prior knowledge of the vehicle's attitude exists at the beginning (t_0) and at the end (t_N) of the mission.
- $\langle Hz \rangle = 9$: all the parameters are computed at the IMU rate.
- $\langle \delta g_{NE} \rangle = b$, indicates that, for all t, $\delta g_N(t) = \delta g_E(t) \approx 0$.
- $\langle method \rangle = 1$, indicates a basic network configuration similar to the Kalman filtering.

LN200

Table 4.71 summarises the network configuration used in this computation.

Model Name	Frequency		Equation	Standard Deviation	
FB-GG (3.4.5)	20.0 Hz	$\forall t$	(3.13)	2.2	10^{-3} m s^{-2}
WIB (3.4.2)	20.0 Hz	$\forall t$	(3.10)	5.2	10^{-5} rad s^{-1}
VEL (3.4.1)	20.0 Hz	$\forall t$	(3.4.1)	0.000 01	m
Q-NORM (3.4.6)	20.0 Hz	$\forall t$	(3.14)	0.01	ppm
OB-O (3.4.35)	20.0 Hz	$\forall t$	(3.48)	4.9	10^{-6} rad s^{-1}
AB-O (3.4.36)	20.0 Hz	$\forall t$	(3.49)	2.0	10^{-3} m s^{-2}
OB (3.4.8)	20.0 Hz	$\forall t$	(3.16)	1.1	10^{-7} rad s^{-1}
AB (3.4.10)	20.0 Hz	$\forall t$	(3.18)	8.9	10^{-4} m s^{-2}
AOFF-O (3.4.37)			(3.50)	0.001	m
CUPT (3.4.16)	1.0 Hz	$\forall t$	(3.26)	0.05	m
GDT-GG (3.4.13)	20.0 Hz	$\forall t$	(3.22)	0.016	mGal
DGUPT-GG (3.4.28)	20.0 Hz	$\forall t$	(3.41)	0.02	mGal
Q-O (3.4.34)		t_0, t_N	(3.47)	0.01	ppm

Table 4.71: Test CTRA-LN200-vq9b1: network configuration.

Figure 4.71 proves that the functional models of the NA approach work succesfully:

- Figures 4.71a and 4.71c point out that the position has been recovered, especially heights with a precision better than 2 cm.
- The navigation parameters — shown in Figure 4.71e — are recovered with a precision of 1.2 ' for roll (α) and pitch (χ) and 4.8 ' for heading (η).
- The IMU error parameters exhibited in Figures 4.71b and 4.71d are nearly constants within the defined tolerances (bias repeatability) of the IMU.
- Figure 4.71f also displays the gravity disturbance vector, that has to be zero, with a precision of 0.15 mGal.

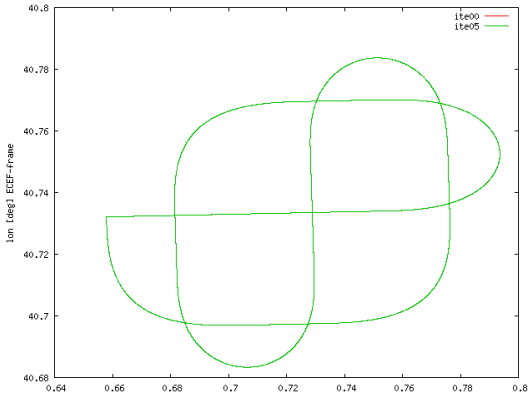

(a) Position (°)

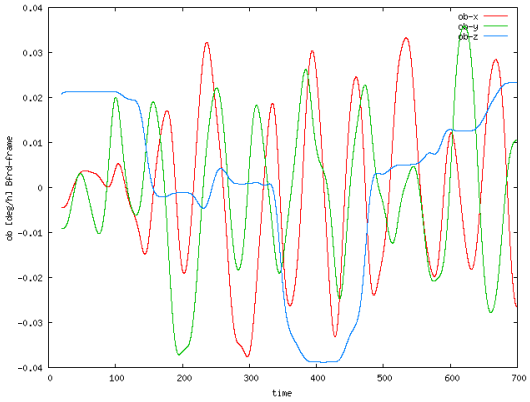

(b) Angular drift ($^\circ\,h^{-1}$)

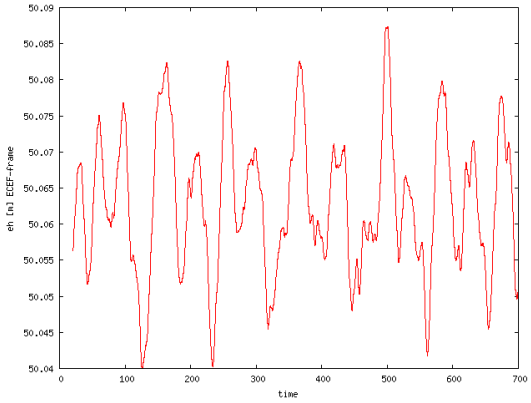

(c) Height (m)

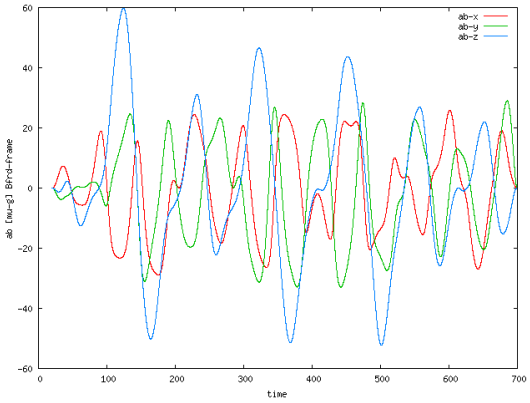

(d) Accelerometer bias (μg)

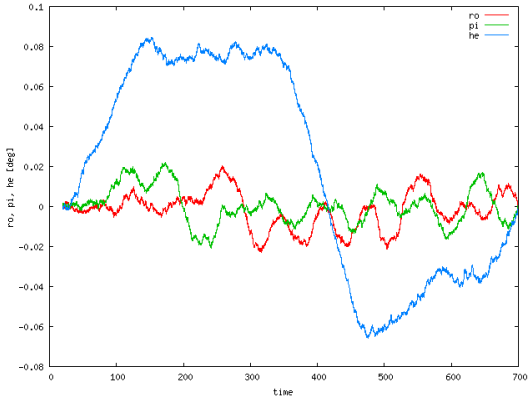

(e) Roll, Pitch and Heading (°)

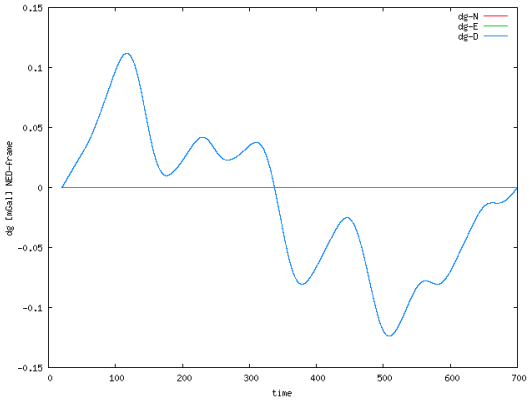

(f) Gravity disturbance (mGal)

Figure 4.71: CTRA LN200 vq9b1: adjusted parameters.

LTN101

Table 4.72 summarises the network configuration used in this computation.

Model Name	Frequency		Equation	Standard Deviation	
FB-GG (3.4.5)	20.0 Hz	$\forall t$	(3.13)	4.4	10^{-4} m s^{-2}
WIB (3.4.2)	20.0 Hz	$\forall t$	(3.10)	1.3	10^{-6} rad s^{-1}
VEL (3.4.1)	20.0 Hz	$\forall t$	(3.4.1)	0.000 01	m
Q-NORM (3.4.6)	20.0 Hz	$\forall t$	(3.14)	0.01	ppm
OB-O (3.4.35)	20.0 Hz	$\forall t$	(3.48)	4.9	10^{-8} rad s^{-1}
AB-O (3.4.36)	20.0 Hz	$\forall t$	(3.49)	4.9	10^{-4} m s^{-2}
OB (3.4.8)	20.0 Hz	$\forall t$	(3.16)	4.3	10^{-12} rad s^{-1}
AB (3.4.10)	20.0 Hz	$\forall t$	(3.18)	6.7	10^{-7} m s^{-2}
AOFF-O (3.4.37)			(3.50)	0.001	m
CUPT (3.4.16)	1.0 Hz	$\forall t$	(3.26)	0.05	m
GDT-GG (3.4.13)	20.0 Hz	$\forall t$	(3.22)	0.016	mGal
DGUPT-GG (3.4.28)	20.0 Hz	$\forall t$	(3.41)	0.02	mGal
Q-O (3.4.34)		t_0, t_N	(3.47)	0.01	ppm

Table 4.72: Test CTRA-LTN101-vq9b1: network configuration.

Figure 4.72 proves that the functional models of the NA approach work succesfully:

- Figures 4.72a and 4.72c point out that the position has been recovered, especially heights with a precision better than 2 cm.
- The navigation parameters — shown in Figure 4.72e — are recovered with a precision of 0.24 ' for roll (α) and pitch (χ) and 1.2 ' for heading (η).
- The IMU error parameters exhibited in Figures 4.72b and 4.72d are nearly constants within the defined tolerances (bias repeatability) of the IMU.
- Figure 4.72f also displays the gravity disturbance vector, that has to be zero, with a precision better than 0.5 mGal.

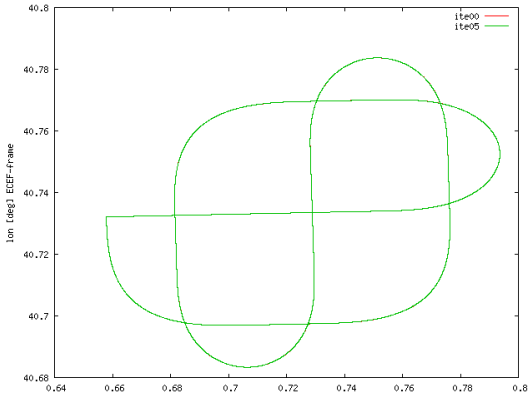

(a) Position (°)

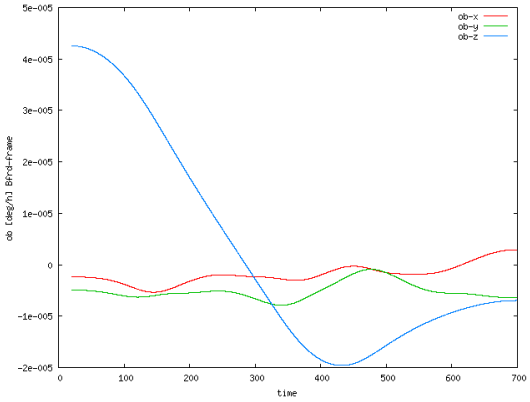

(b) Angular drift ($^\circ\,h^{-1}$)

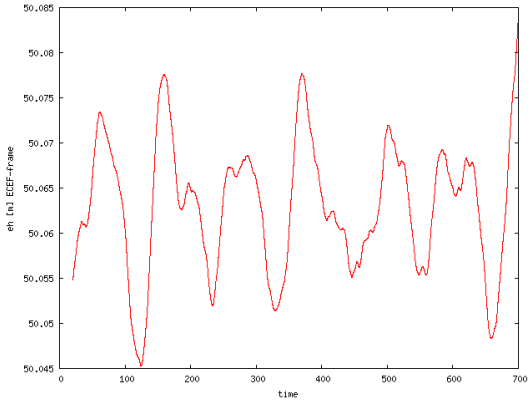

(c) Height (m)

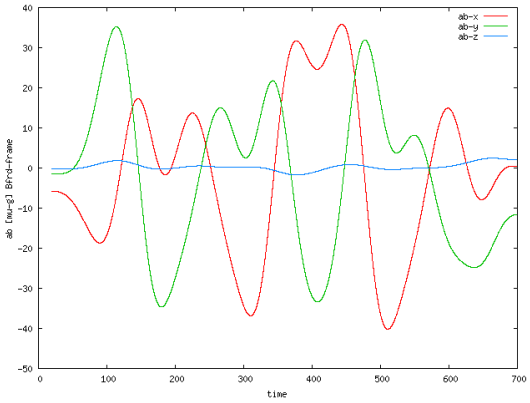

(d) Accelerometer bias (μg)

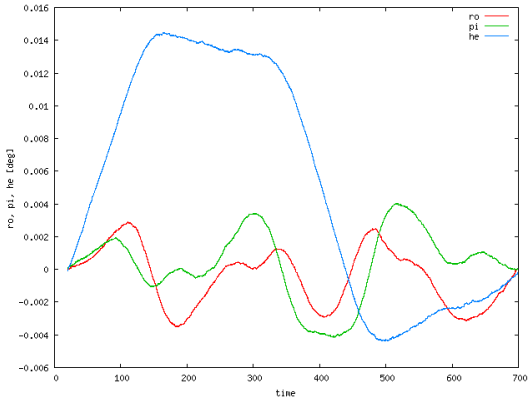

(e) Roll, Pitch and Heading (°)

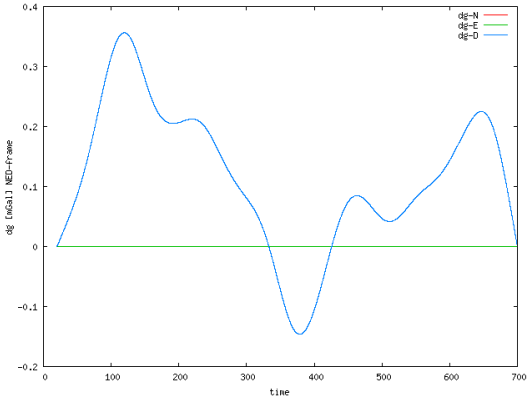

(f) Gravity disturbance (mGal)

Figure 4.72: CTRA LTN101b vq9b1: adjusted parameters.

5 Results

In the previous chapter, all the computations have been discussed in detail one by one. From them, mainly, it follows that the NA approach models work succesfully. But it is hard to tell which type of network configuration is the most appropiate.

In this chapter the outcome of the most relevant adjustments of the chapter before are discussed together, in order to examine which network configuration is best suited for each simulation test. The evaluation of different network configurations allows also to study how they can influence the determination of INS parameters — angular drifts and accelerometer bias — and the gravity field.

The tables and figures that display the results of these comparisons are located, usually, at the end of each test.

5.1 Test STATIC

Figures 5.1, 5.2 and 5.3 show the results of tests STATIC-LN200-vq2a1 and STATIC-LN200-vq9a1, with a tactical-grade IMU. Figures 5.4, 5.5 and 5.6 display the same comparisons but for the navigation-grade IMU: STATIC-LTN101-vq2a1 and STATIC-LTN101-vq9a1.

The above figures prove that the functional models of the NA approach work succesfully:

- Figure 5.1 points out that the position has been recovered, especially heights with a precision better than 2 cm.
- The navigation parameters — shown in Figure 5.1 — are recovered with a precision of 35 " for roll (α) and pitch (χ) and 2 ’ for heading (η).
- The IMU error parameters exhibited in Figure 5.2 are nearly constants within the defined tolerances (bias repeatability) of the IMU.
- Figure 5.3 displays the gravity disturbance vector, that has to be zero.

The same conclusions of the computations can be deduced from the navigation-grade LTN101 tests (see Figures 5.4, 5.5 and 5.6).

Results seem to confirm that it is always better to compute with highest rate parameters than grouped ones. But often this can entail computation problems.

Remember that to perform a least-squares adjustment is to know the expectation of the parameters and their covariance. The position parameters $\underline{r}^{\mathsf{e}}$ have been determined with an standard deviation better than of 6 mm for the LN200 IMU and 3 mm for the LTN101 one. The adjusted attitude parameters — roll, pitch and heading — have an accuracy better than 36 " in roll-pitch) and 2.4 ’ in heading for the LN200. For the Litton LTN101, 1.44 " in roll-pitch and 3.6 " in heading.

The IMU error parameters — $\underline{o}^{\mathsf{b}}$ and $\underline{a}^{\mathsf{b}}$ — have been determined with a mean standard deviation of 0.19 $^{\circ}\,\mathrm{h}^{-1}$ and 31 μg respectively for the Litton LN200. For the LTN101, 0.008 $^{\circ}\,\mathrm{h}^{-1}$ for $\underline{o}^{\mathsf{b}}$ and 1 μg for $\underline{a}^{\mathsf{b}}$.

The gravity g have been determined with an accuracy of 0.01 mGal, and 0.002" for the deflections of the vertical.

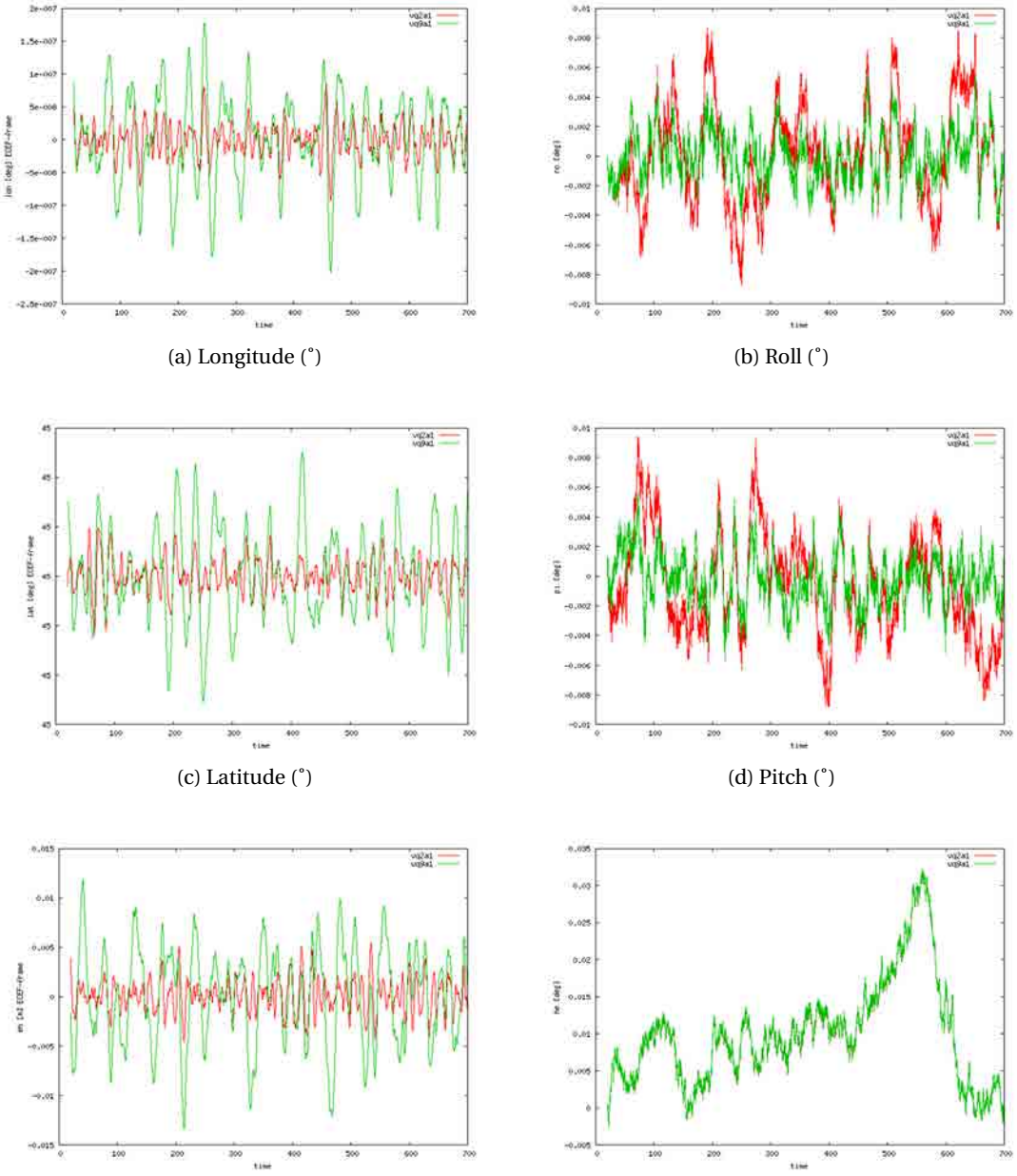

(a) Longitude (°)

(b) Roll (°)

(c) Latitude (°)

(d) Pitch (°)

(e) Height (m)

(f) Heading (°)

Figure 5.1: STATIC LN200: vq2a1 and vq9a1. Position and Attitude.

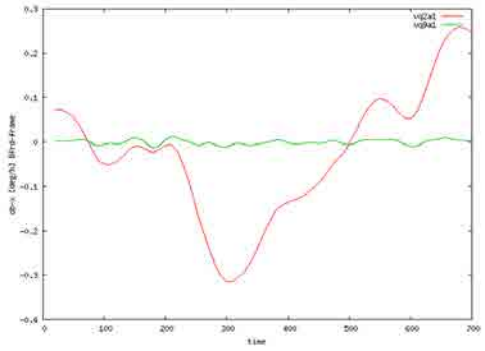

(a) X angular drift ($^\circ$ h^{-1})

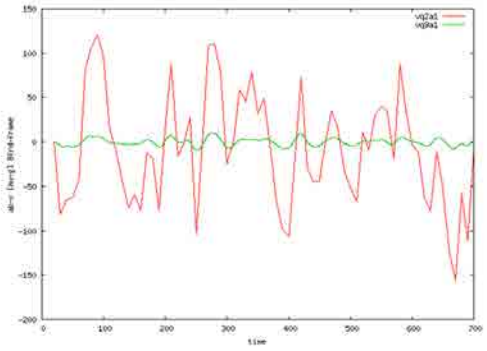

(b) X accelerometer bias (μg)

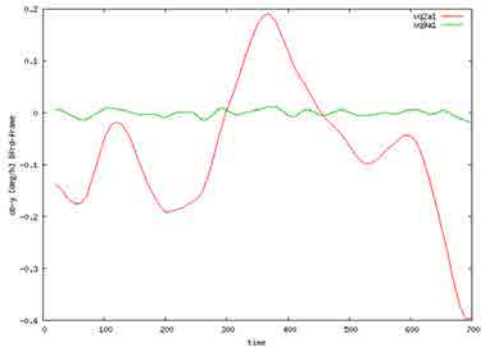

(c) Y angular drift ($^\circ$ h^{-1})

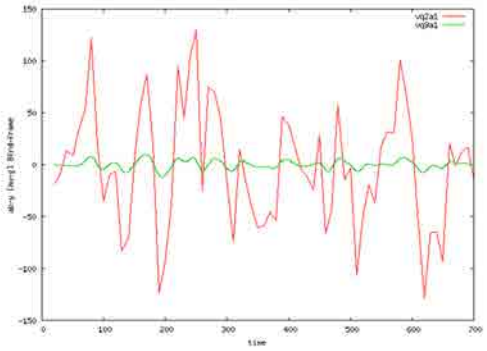

(d) Y accelerometer bias (μg)

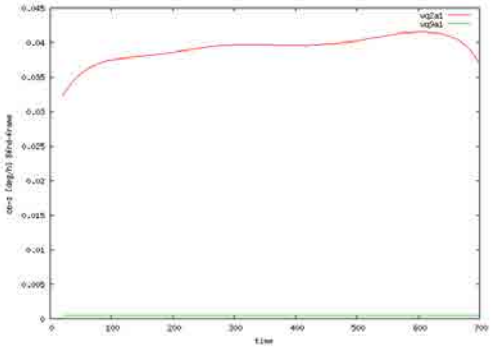

(e) Z angular drift ($^\circ$ h^{-1})

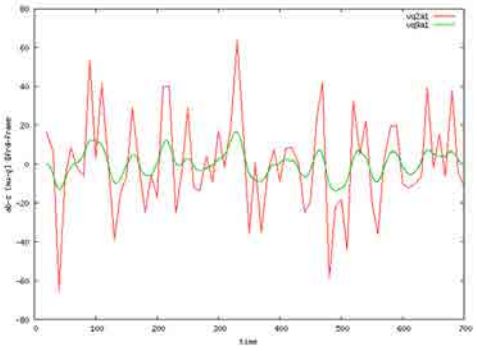

(f) Z accelerometer bias (μg)

Figure 5.2: STATIC LN200: vq2a1 and vq9a1. Angular drift and Accelerometer bias.

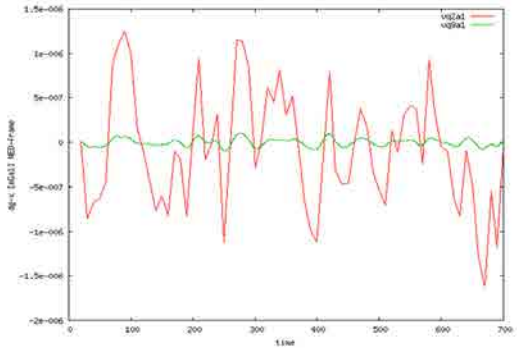

(a) N component (mGal)

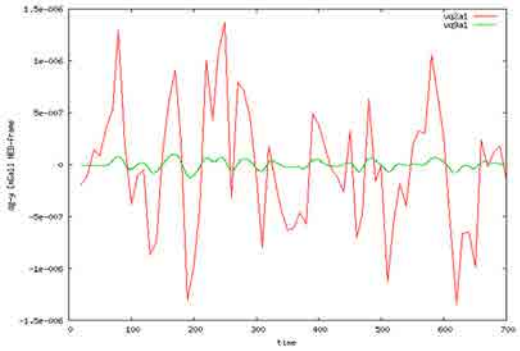

(b) E component (mGal)

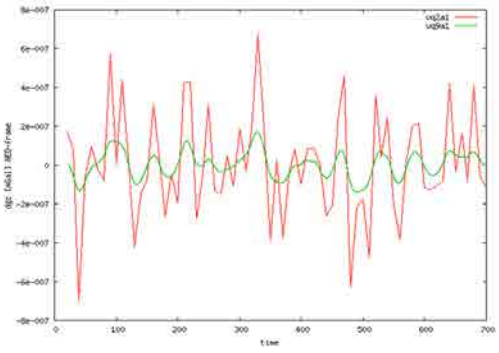

(c) D component (mGal)

Figure 5.3: STATIC LN200: vq2a1 and vq9a1. Gravity disturbance.

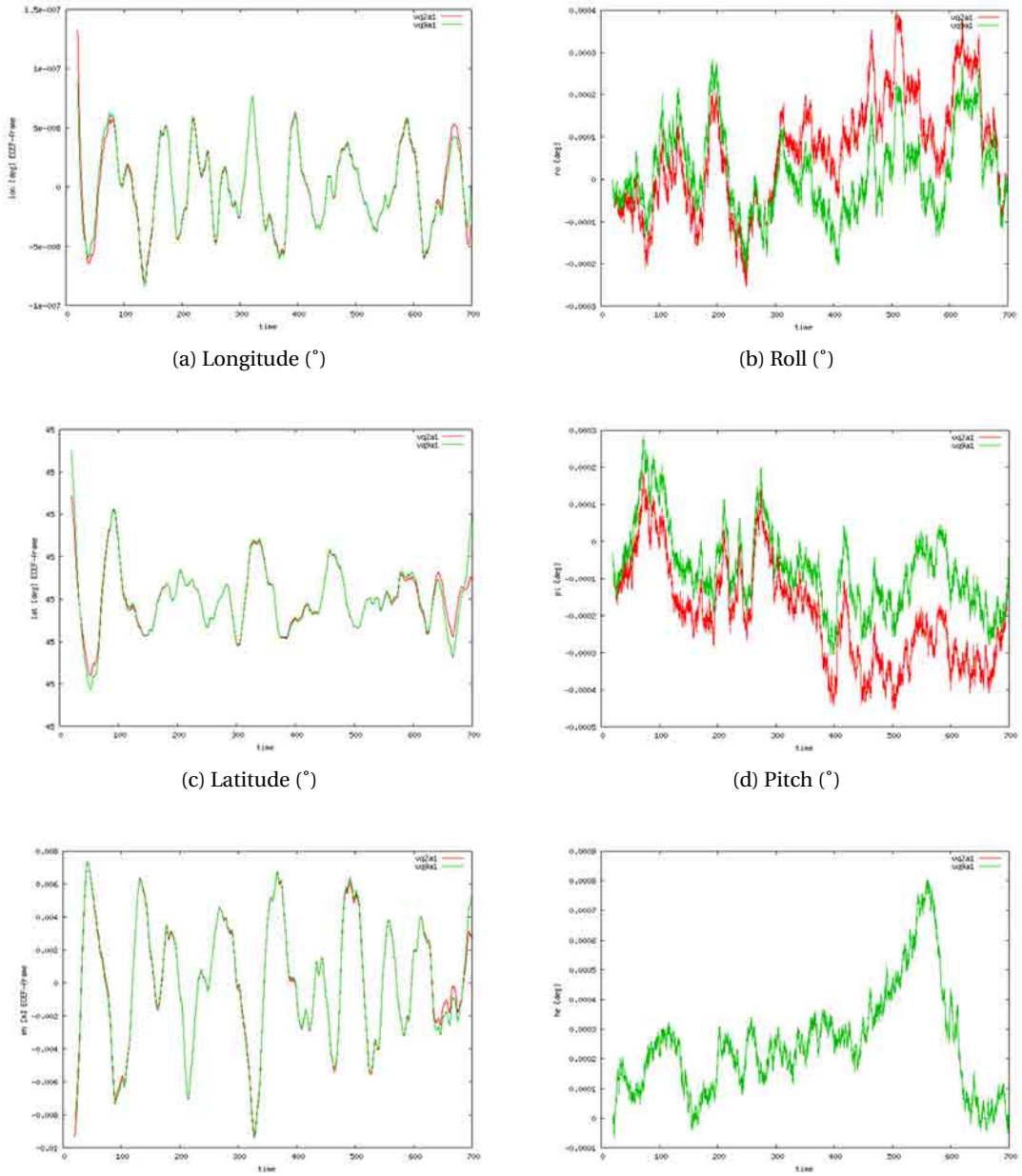

(a) Longitude (°)

(b) Roll (°)

(c) Latitude (°)

(d) Pitch (°)

(e) Height (m)

(f) Heading (°)

Figure 5.4: STATIC LTN101: vq2a1 and vq9a1. Position and Attitude.

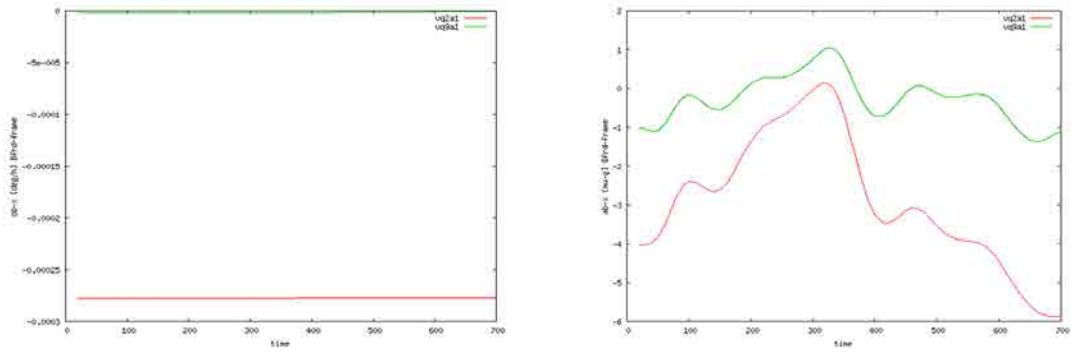

(a) X angular drift ($^\circ\,h^{-1}$)

(b) X accelerometer bias (μg)

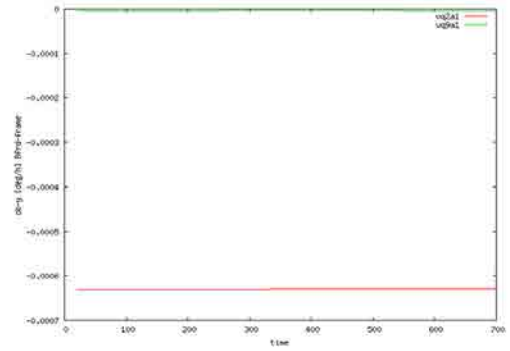

(c) Y angular drift ($^\circ\,h^{-1}$)

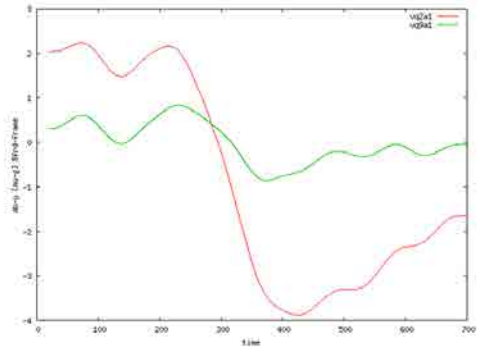

(d) Y accelerometer bias (μg)

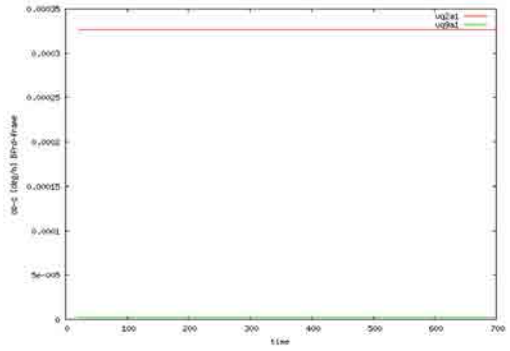

(e) Z angular drift ($^\circ\,h^{-1}$)

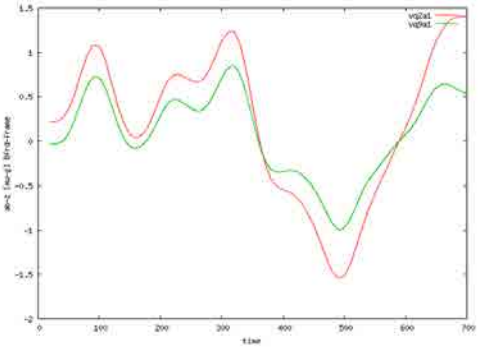

(f) Z accelerometer bias (μg)

Figure 5.5: STATIC LTN101: vq2a1 and vq9a1. Angular drift and Accelerometer bias.

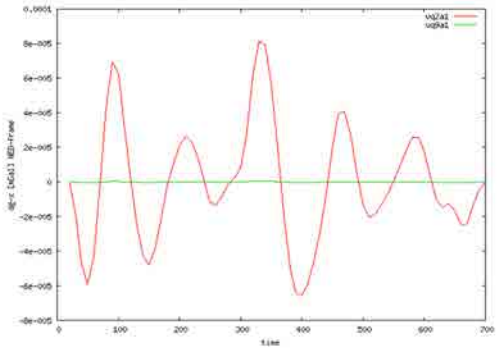

(a) N component (mGal)

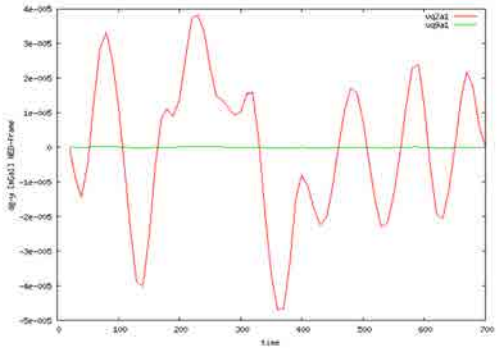

(b) E component (mGal)

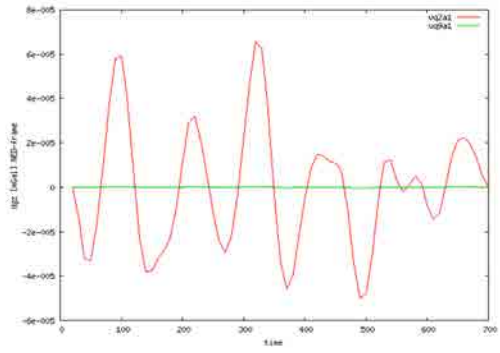

(c) D component (mGal)

Figure 5.6: STATIC LTN101: vq2a1 and vq9a1. Gravity disturbance.

5.2 Test CIRCLE

Figures 5.7, 5.8 and 5.9 show the results of tests CIRCLE-LN200-v2a1 and CIRCLE-LN200-v2a2. Figures 5.10, 5.11 and 5.12 show similar computations but for the IMU LTN101: CIRCLE-LTN101-v2a1 and CIRCLE-LTN101-v2a2.

At that point, it is important to remember that v2a1 cases are the *basic* configurations (equivalent to the SSA approach) and v2a2 cases are a simple example of the NA approach. In fact, v2a2 cases are made up of the v2a1 case plus only the additional GDT-GG observations connecting each pair of laps.

The position parameters $\underline{r}^{\mathsf{e}}$ have been determined with an standard deviation better than of 1.5 cm. The adjusted attitude parameters have an accuracy better than 36 " in roll-pitch and 3 ' in heading for the LN200. For the LTN101, 3.6 " in roll-pitch and 36 " in heading.

The IMU error parameters — $\underline{o}^{\mathsf{b}}$ and $\underline{a}^{\mathsf{b}}$ — have been determined with a mean standard deviation of 0.02 $^{\circ}\,\mathrm{h}^{-1}$ and 40 μg respectively for the LN200. For the LTN101, 0.008 $^{\circ}\,\mathrm{h}^{-1}$ for $\underline{o}^{\mathsf{b}}$ and 8 μg for $\underline{a}^{\mathsf{b}}$.

The gravity g has been determined with an accuracy of 12 mGal (maximum of all cases), and 2.5 " maximum for the deflections of the vertical.

Figures 5.7 and 5.10 prove that the navigation parameters haven been recovered and that there is no difference between SSA and NA approaches.

For the IMU error parameters, the situation is quite different. Figures 5.8 prove that for tactical-grade IMUs such as the LN200, v2a1 and v2a2 solutions are equivalent, but no constant values as they were expected. For navigation-grade IMUs as the LTN101, Figures 5.11 show that expected values have been recovered.

But here, the most important, is the gravity field (i.e. disturbance gravity vector) determination. Both cases — shown in Figures 5.9 and 5.12 — prove the improvement obtained if some additional observations are considered. In this case, the additional GDT-GG observations relate that gravity information in a place is time-invariant. For the SSA approach (v$*$1 cases) only the consecutive time-relations are considered and the gravity disturbance respect the trajectory is interpreted like a corkscrew.

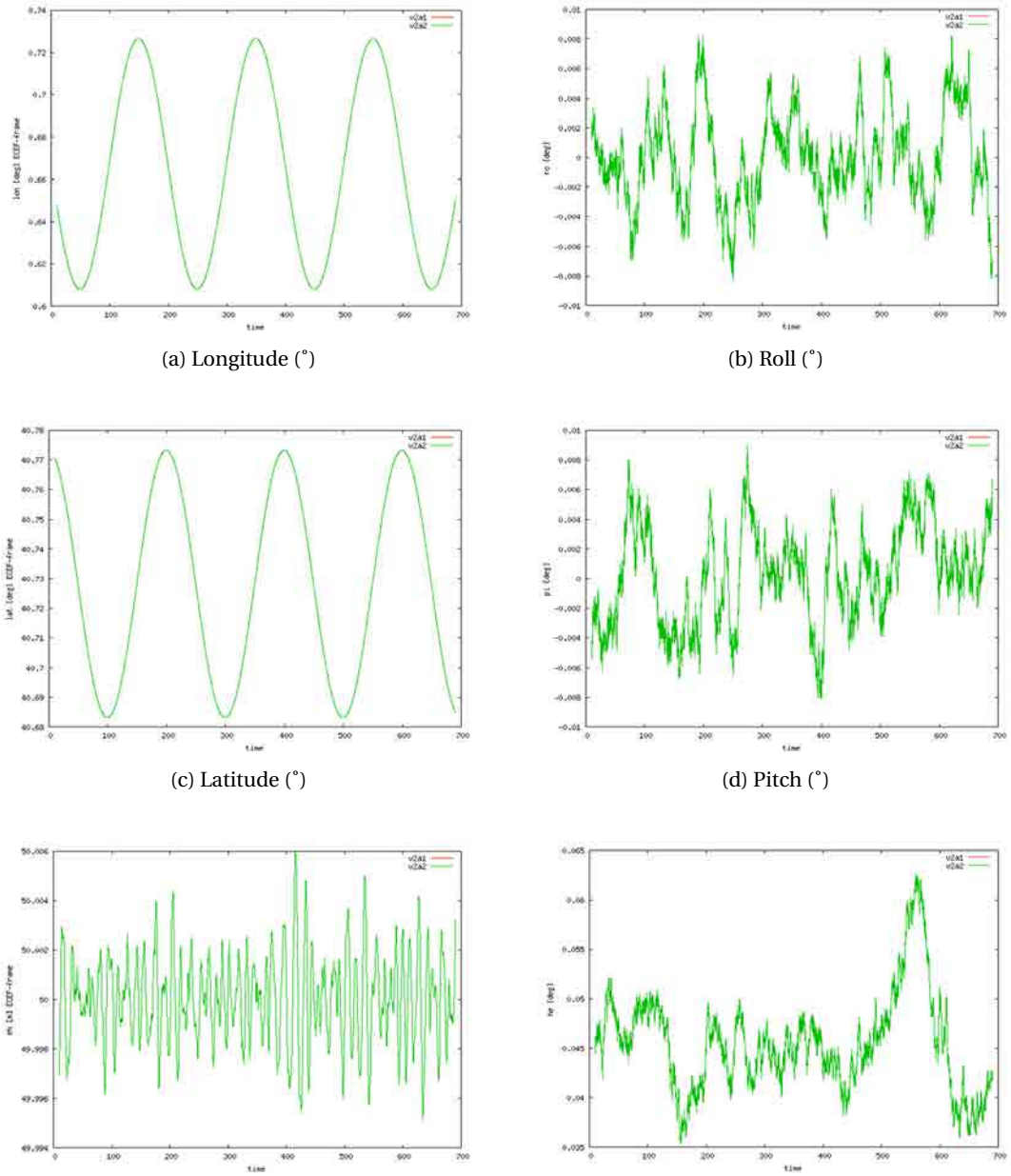

(a) Longitude (°)

(b) Roll (°)

(c) Latitude (°)

(d) Pitch (°)

(e) Height (m)

(f) Heading (°)

Figure 5.7: CIRCLE LN200: v2a1 and v2a2. Position and Attitude.

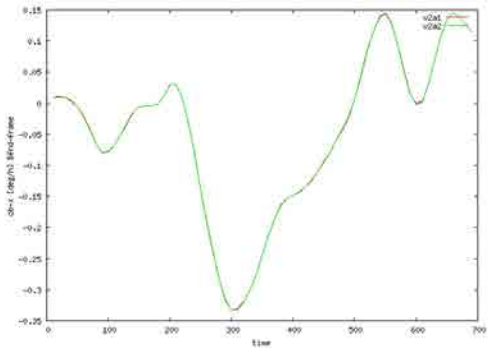

(a) X angular drift ($^\circ\,h^{-1}$)

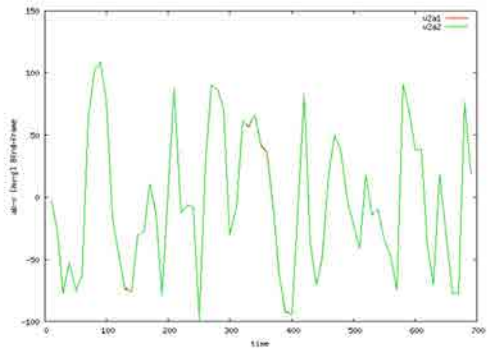

(b) X accelerometer bias (μg)

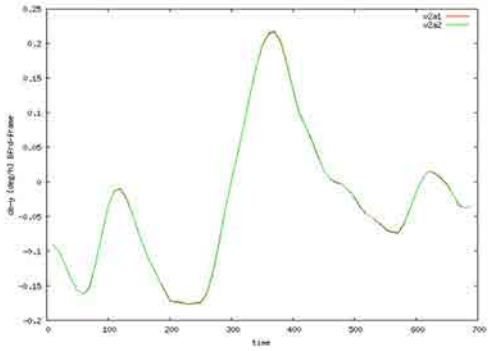

(c) Y angular drift ($^\circ\,h^{-1}$)

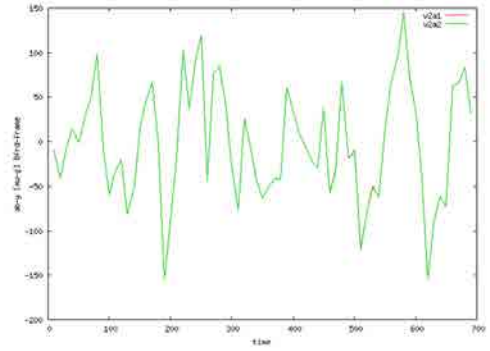

(d) Y accelerometer bias (μg)

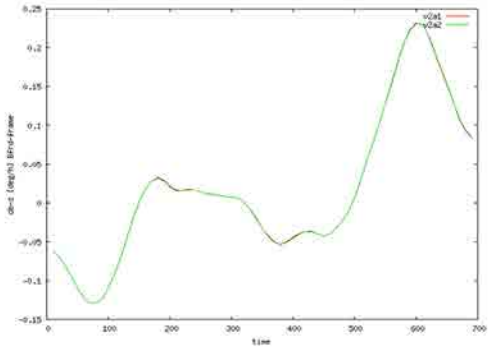

(e) Z angular drift ($^\circ\,h^{-1}$)

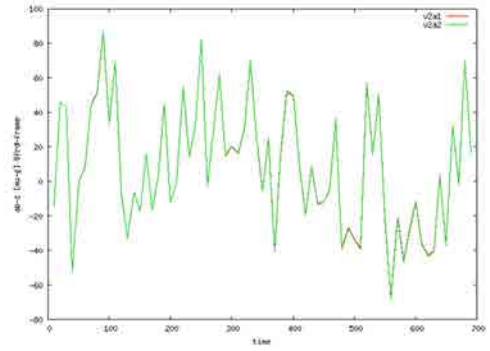

(f) Z accelerometer bias (μg)

Figure 5.8: CIRCLE LN200: v2a1 and v2a2. Angular drift and Accelerometer bias.

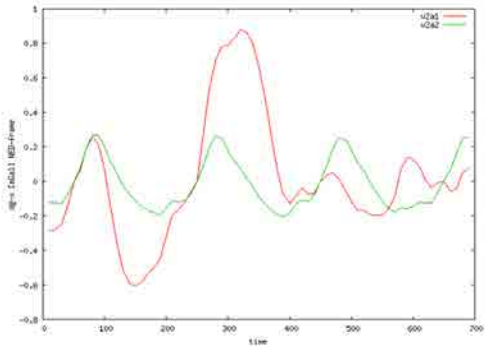

(a) N component (mGal)

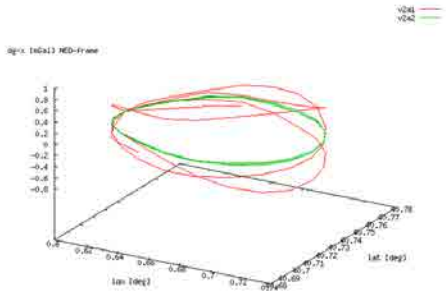

(b) N component (mGal)

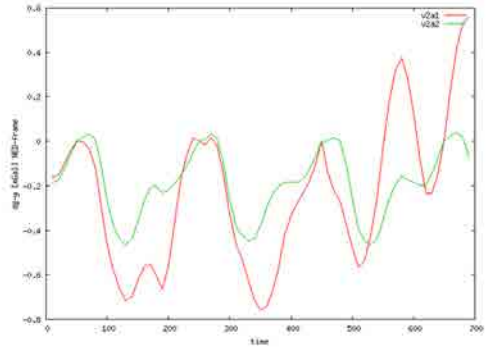

(c) E component (mGal)

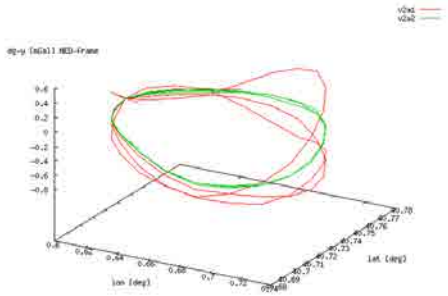

(d) E component (mGal)

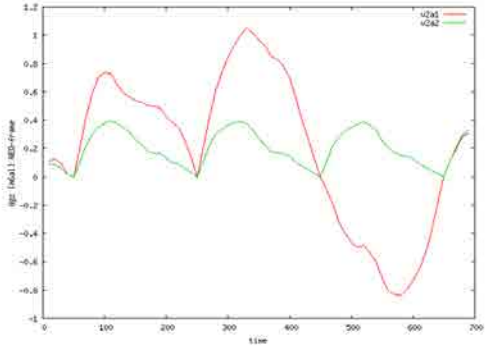

(e) D component (mGal)

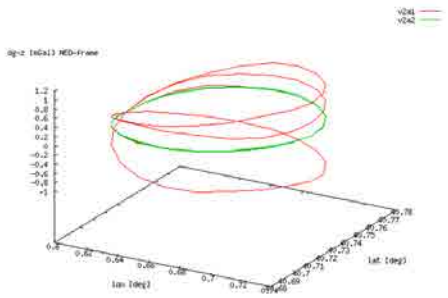

(f) D component (mGal)

Figure 5.9: CIRCLE LN200: v2a1 and v2a2. Gravity disturbances.

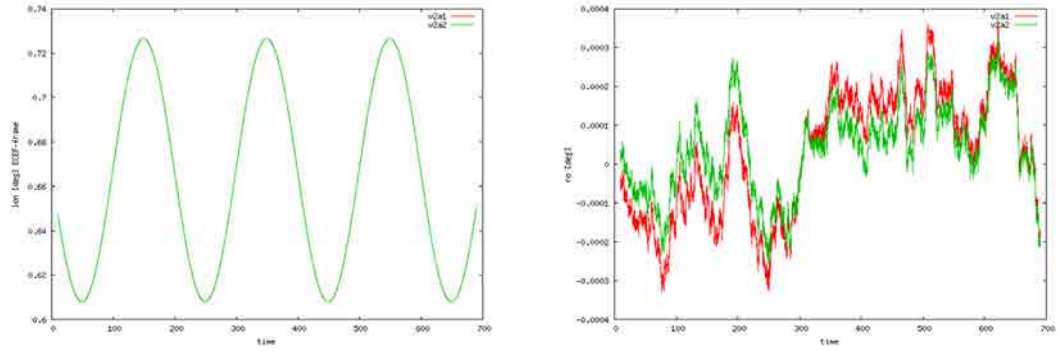

(a) Longitude (°)

(b) Roll (°)

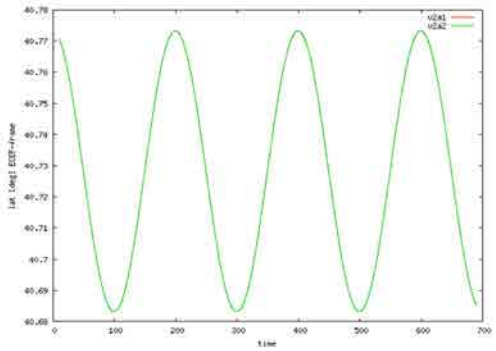

(c) Latitude (°)

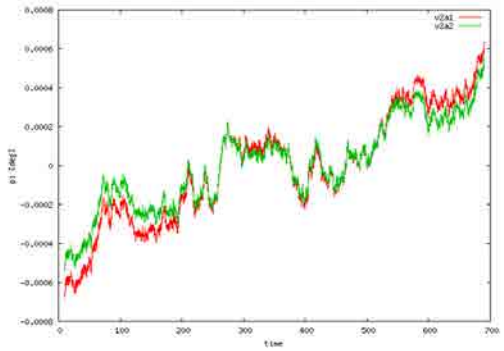

(d) Pitch (°)

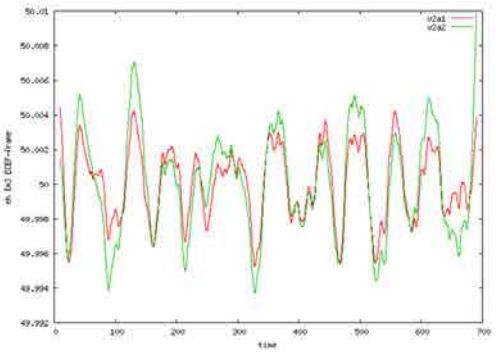

(e) Height (m)

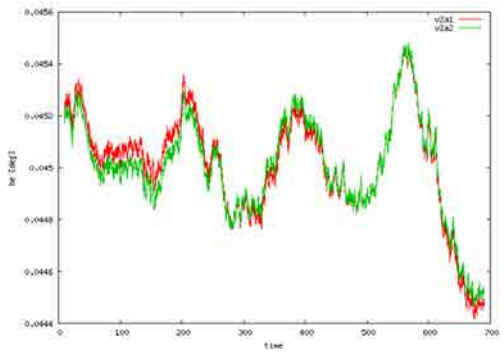

(f) Heading (°)

Figure 5.10: CIRCLE LTN101: v2a1 and v2a2. Position and attitude.

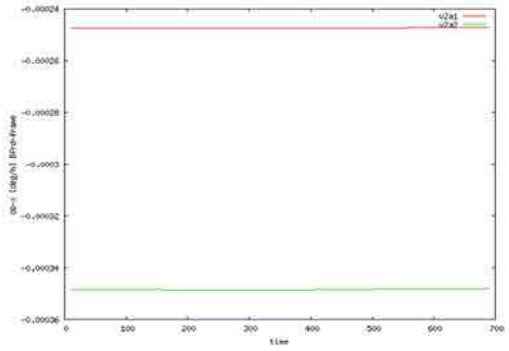

(a) X angular drift ($^\circ$ h^{-1})

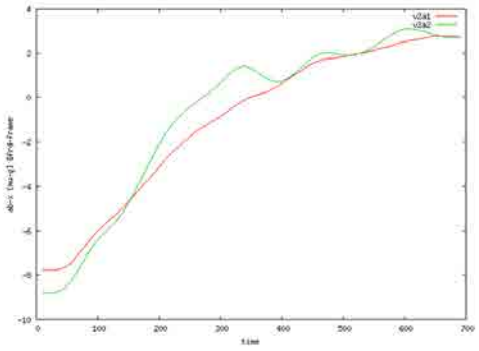

(b) X accelerometer bias (μg)

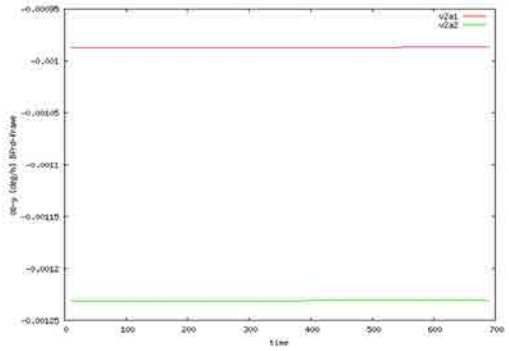

(c) Y angular drift ($^\circ$ h^{-1})

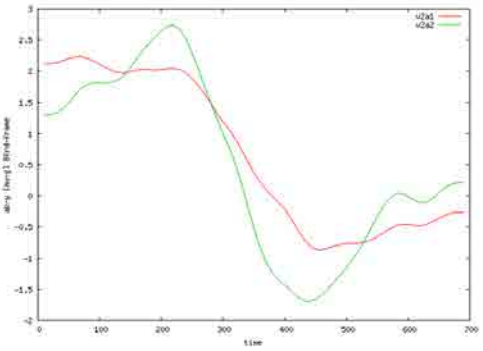

(d) Y accelerometer bias (μg)

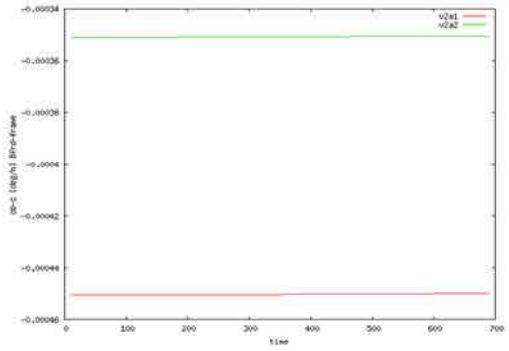

(e) Z angular drift ($^\circ$ h^{-1})

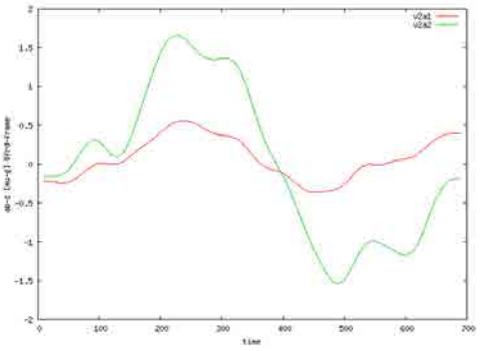

(f) Z accelerometer bias (μg)

Figure 5.11: CIRCLE LTN101: v2a1 and v2a2. Angular drift and Accelerometer bias.

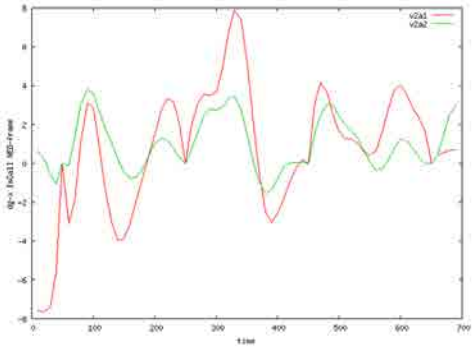

(a) N component (mGal)

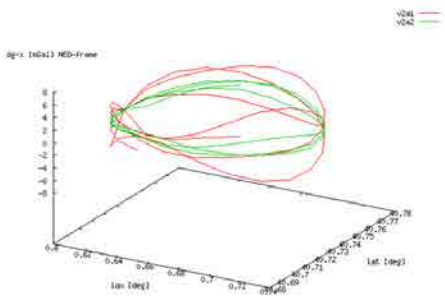

(b) N component (mGal)

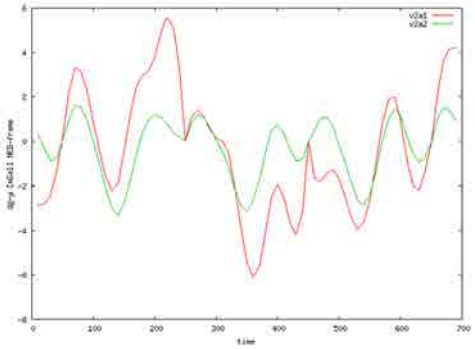

(c) E component (mGal)

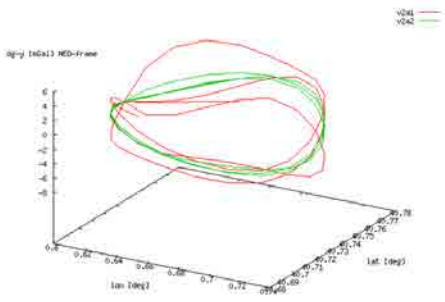

(d) E component (mGal)

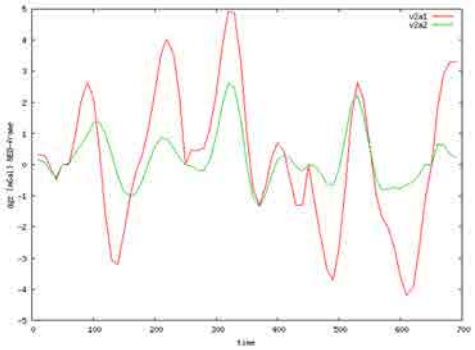

(e) D component (mGal)

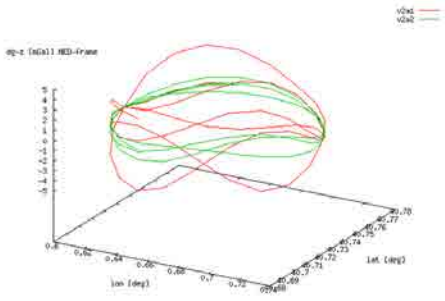

(f) D component (mGal)

Figure 5.12: CIRCLE LTN101: v2a1 and v2a2. Gravity disturbance.

5.3 Test CTRA

Figures 5.13, 5.14 and 5.15 show the differences between CTRA-LN200-v9a1 (computing at navigation rate) and CTRA-LN200-v2a1 (with grouped parameters).

Because of the software capacity limitations (see Table 4.40) and the adjusted parameters shown in the above Figures, the study of CTRA configuration — on an equal basis as it has been done in CIRCLE — is focused only on *reduced* or *grouped* cases v2.

The study of CTRA test starts computing CTRA-$*$-v2a1, a network configuration similar to SSA approach. Knowing that gravity disturbance vector in NED-frame is moreless of the form $(0,0,\delta g)^T$, a new configuration has to be considered: CTRA-$*$-v2b1, where additional observations of the type DGUPT-GG are considered: the horizontal components are fix to 0 and only the vertical component will be determined.

Figures 5.16, 5.17 and 5.18 show the differences encountered between test CTRA-LN200-v2a1 and test CTRA-LN200-v2b1. They display that vb case only improves the horizontal components of the gravity disturbance vector (the equations added). Contrary to this the horizontal components of the accelerometer biases $\underline{a}^{\mathsf{b}}$ are worse. It corroborates that $\underline{a}^{\mathsf{b}}$ and δg are completely correlated.

Figures 5.19, 5.20 and 5.21 show similar computations but for the LTN101.

The behavior of the LTN101 results is very similar to the LN200 one. In both configurations, the v2a1 determination is more stable that v2b1 one, except for the horizontal components of the gravity disturbance vector. Jekeli ([65]) describes in detail this behavior and these adjustment results only corroborate it. So, as a result of that, only the v2a cases have to been considered in the test study.

Now the knowledge of attitude parameters at the beginning and at the end of the campaign are considered (case vq2a1). Then differences respect v2a1 cases for the LN200 are found in Figures 5.22, 5.23 and 5.24. The same comparison but for the LTN101 are shown in Figures 5.25, 5.26 and 5.27.

Here, after analysing the plots, only an improvement in the attitude determination is shown. For the other parameters, the behavior is quite similar. Then, we are ready to include more additional information into the network system.

If some relations between lines (vq2a2 cases) and crossover information (vq2a2x) are considered, we obtain the results that are considered, for the LN200, in Figures 5.28, 5.29 and 5.30.

Here, if all three cases are analyzed, it is possible to see that position and attitude parameters are equally determined. The same for the gyro drifts parameters $\underline{o}^{\mathsf{b}}$ and accelerometer bias $\underline{a}^{\mathsf{b}}$. They seem to be normal, because only information about gravity relations has been added.

Respect to the results of the gravity disturbance vector, a little improvement in cases vq2a2 and va2a2x has been done, but the known unstable behavior continues. But the great improvement it has been noticed in the vertical component, as it was expected.

For the LTN101, Figures 5.31, 5.32 and 5.33 show the adjusted parameters for vq2a1, vq2a2 and vq2ax cases.

Here the improvement is not so large and these IMU configurations show that the stochastic error model for gravity has not been chosen suitably. The random error GDT model is inadequate to model the gravity disturbance parameters.

With regard to the adjusted covariance data it is important to note that position parameters have been determined with an accuracy better than 3 cm for both IMUs. For the adjusted attitudes, the accuracy is 1.2 ’ in roll-pitch and 4.8 ’ in heading for the LN200 configurations. For the LTN101 ones, 18 " in roll-pitch and 1.8 ’ in heading.

The IMU error parameters — $\underline{o}^{\mathsf{b}}$ and $\underline{a}^{\mathsf{b}}$ — have been determined with a mean standard deviation of 0.10 $^{\circ}\,\mathrm{h}^{-1}$ and 20 μg respectively for the LN200. For the LTN101, 0.008 $^{\circ}\,\mathrm{h}^{-1}$ for $\underline{o}^{\mathsf{b}}$ and 15 μg for $\underline{a}^{\mathsf{b}}$.

The gravity g have been determined with an accuracy of 20 mGal (maximum of all cases), and 5 " maximum for the deflections of the vertical. It has to be noticed that the standard deviations related to the LN200 are less than the LTN101 ones. All this confirms that the stochastic gravity models (the random walk GDT-DGE, GDT-DGN or GDT-GG) work properly with tactical-grade IMUs — such as the LN200 — but they have to be improved for navigation-grade ones as the LTN101.

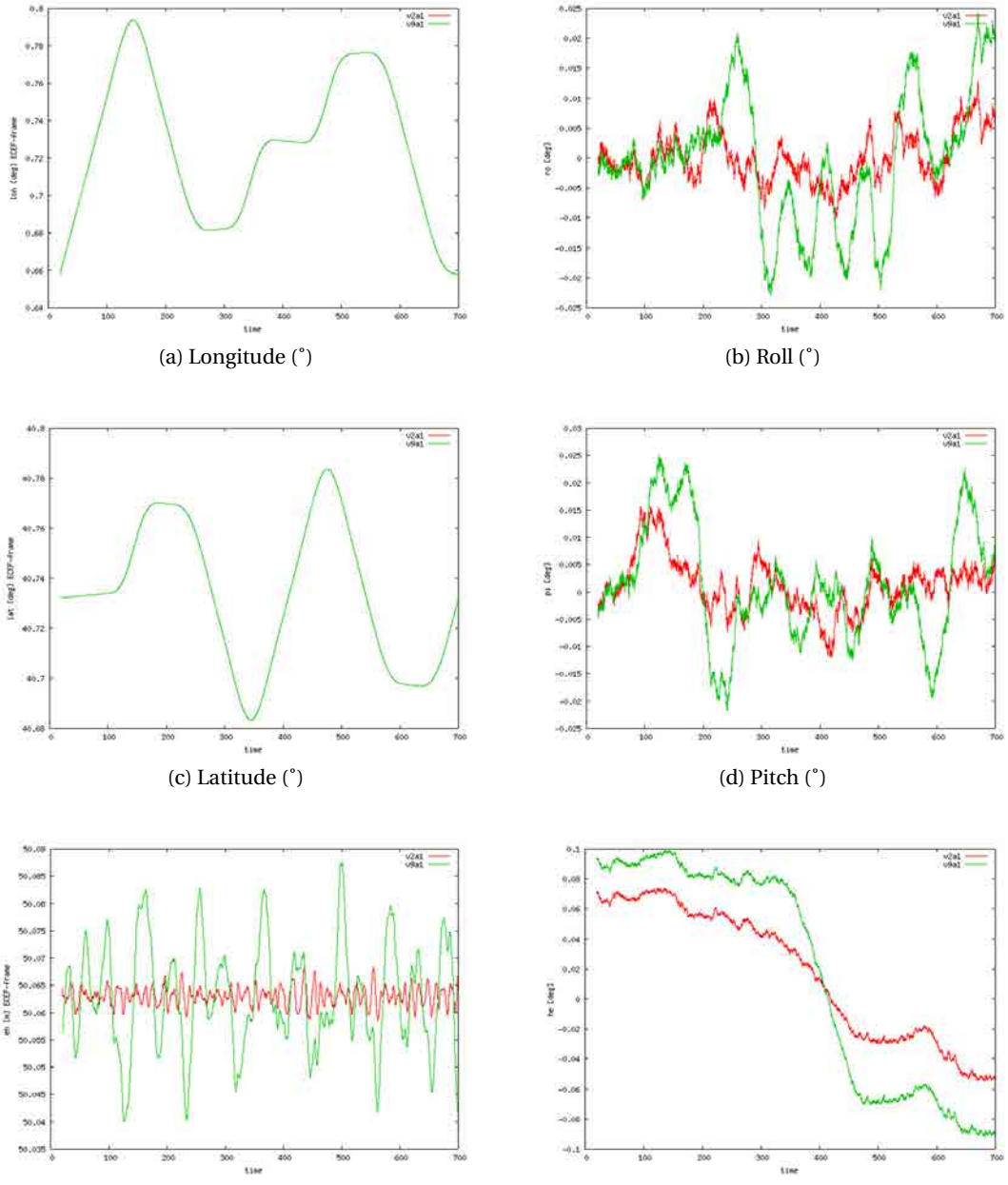

(a) Longitude (°)

(b) Roll (°)

(c) Latitude (°)

(d) Pitch (°)

(e) Height (m)

(f) Heading (°)

Figure 5.13: CTRA LN200: v2a1 and v9a1. Position and Attitude.

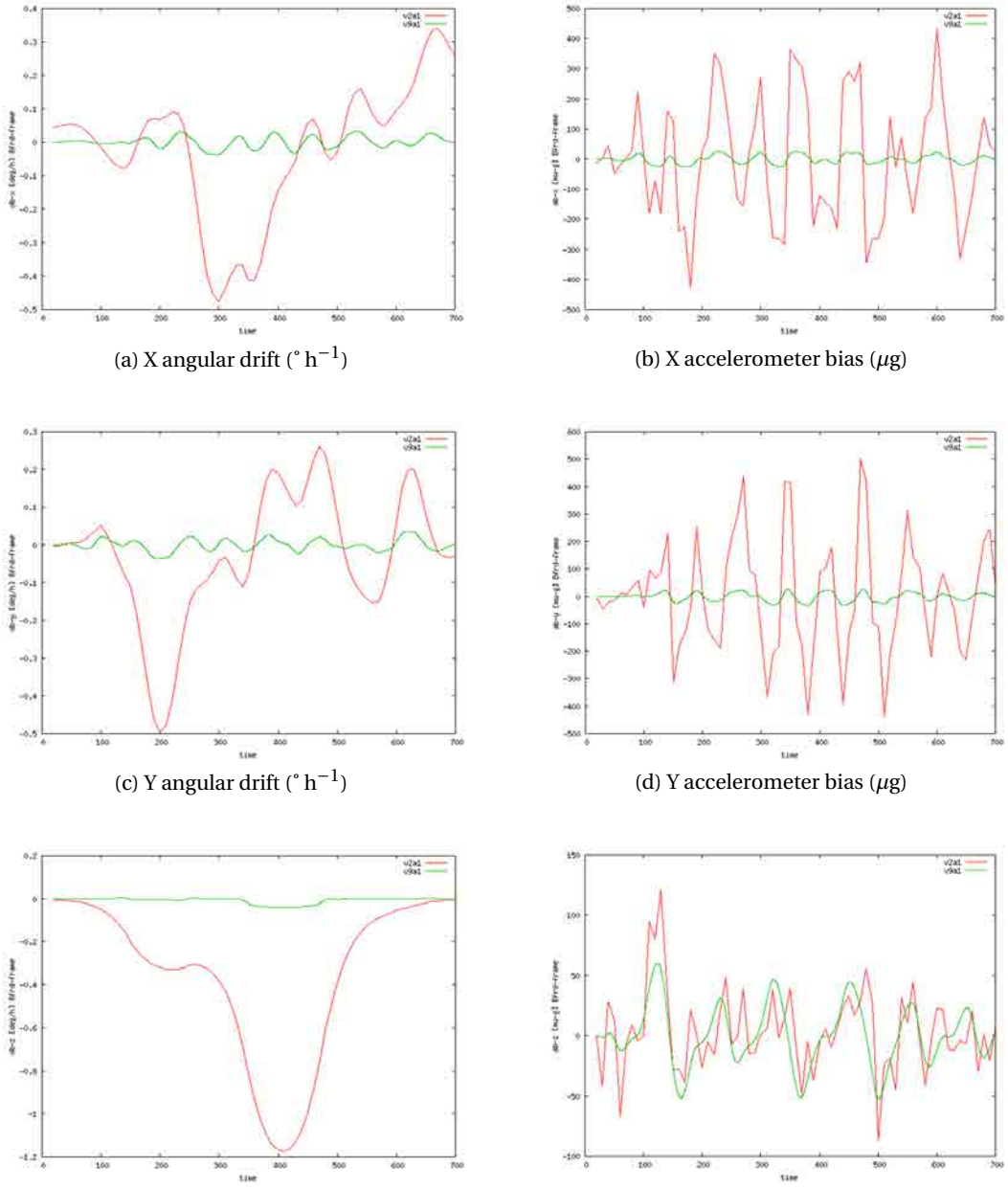

(a) X angular drift ($^\circ\,h^{-1}$)

(b) X accelerometer bias (μg)

(c) Y angular drift ($^\circ\,h^{-1}$)

(d) Y accelerometer bias (μg)

(e) Z angular drift ($^\circ\,h^{-1}$)

(f) Z accelerometer bias (μg)

Figure 5.14: CTRA LN200: v2a1 and v9a1. Angular drift and Accelerometer bias.

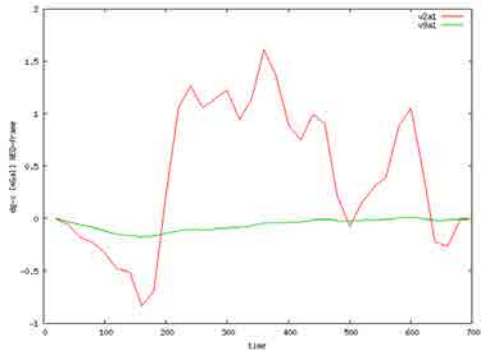

(a) N component (mGal)

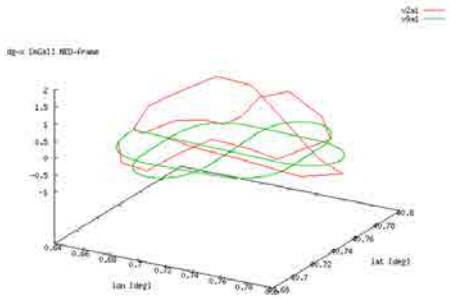

(b) N component (mGal)

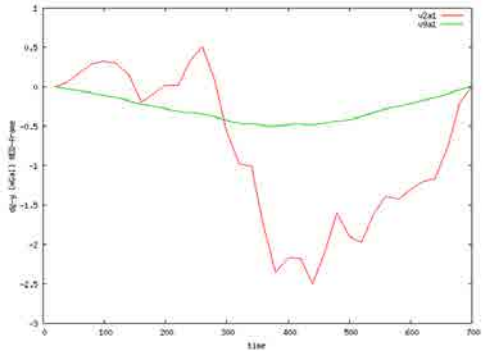

(c) E component (mGal)

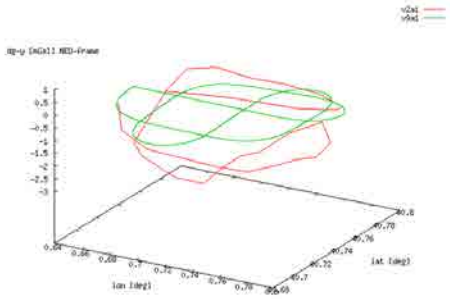

(d) E component (mGal)

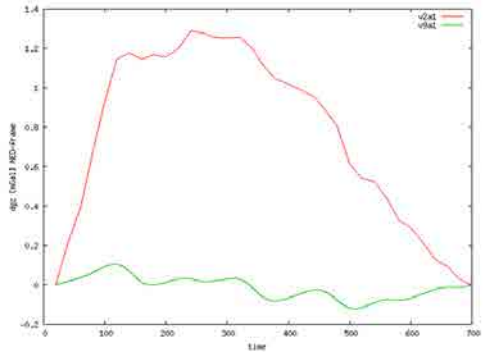

(e) D component (mGal)

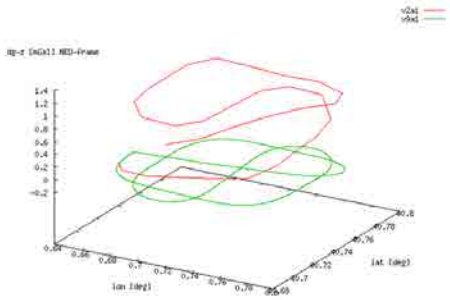

(f) D component (mGal)

Figure 5.15: CTRA LN200: v2a1 and v9a1. Gravity disturbances.

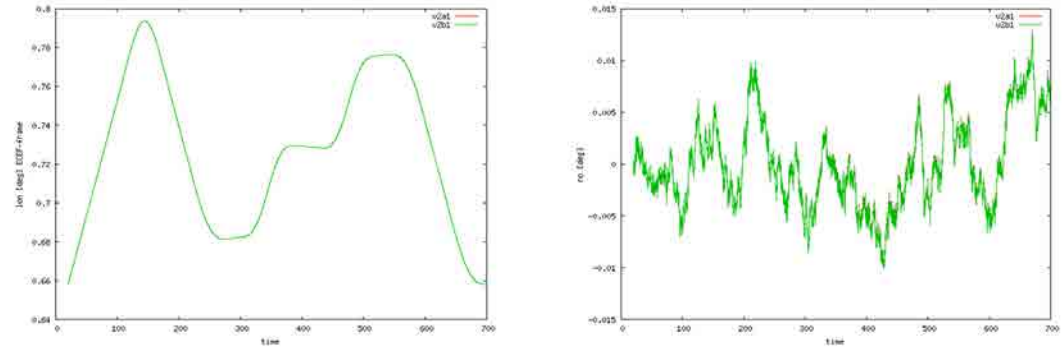

(a) Longitude (°)

(b) Roll (°)

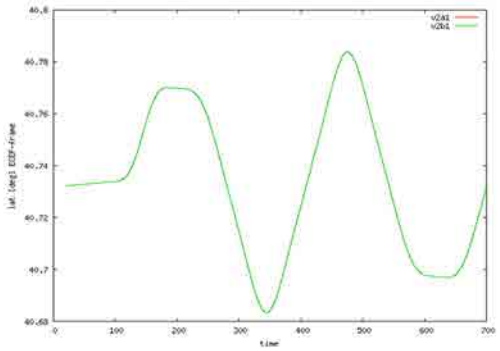

(c) Latitude (°)

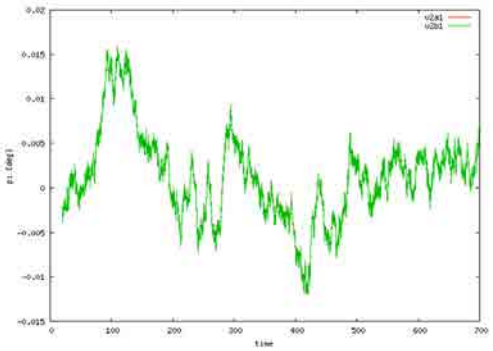

(d) Pitch (°)

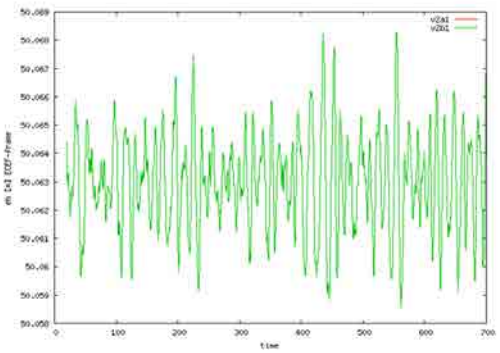

(e) Height (m)

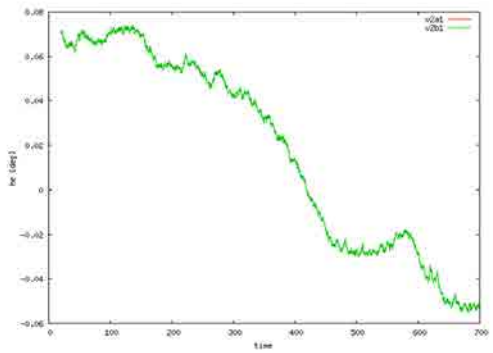

(f) Heading (°)

Figure 5.16: CTRA LN200: v2a1 and v2b1. Position and Attitude.

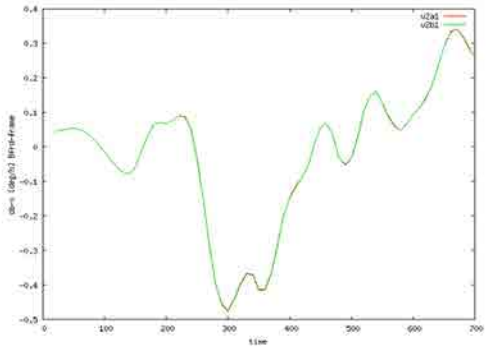

(a) X angular drift ($^\circ$ h^{-1})

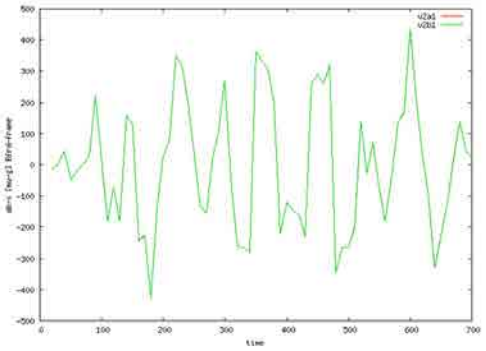

(b) X accelerometer bias (μg)

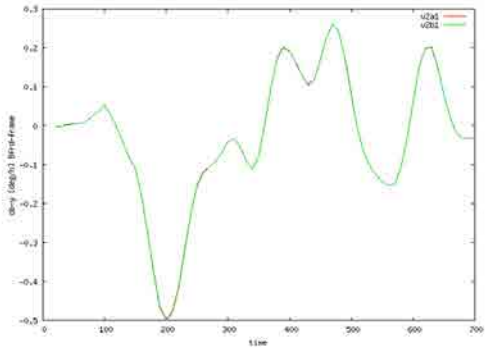

(c) Y angular drift ($^\circ$ h^{-1})

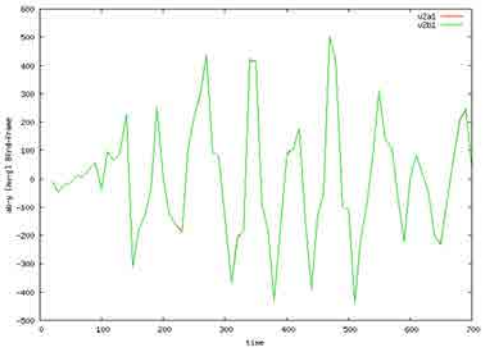

(d) Y accelerometer bias (μg)

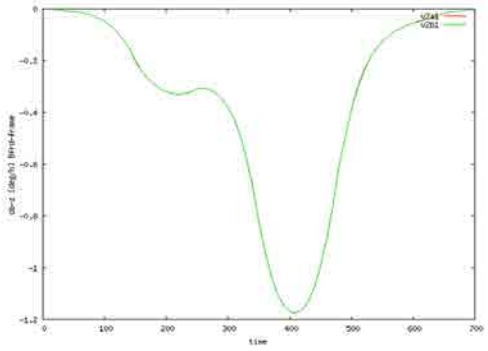

(e) Z angular drift ($^\circ$ h^{-1})

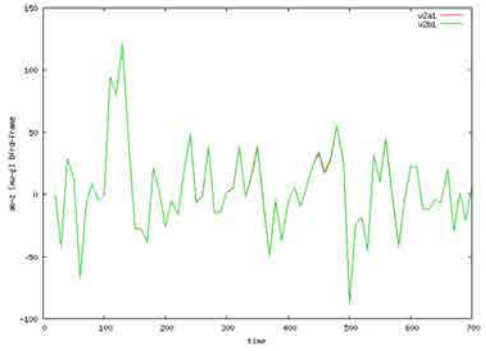

(f) Z accelerometer bias (μg)

Figure 5.17: CTRA LN200: v2a1 and v2b1. Angular drift and Accelerometer bias.

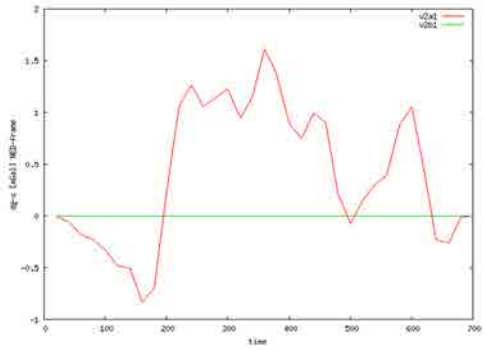

(a) N component (mGal)

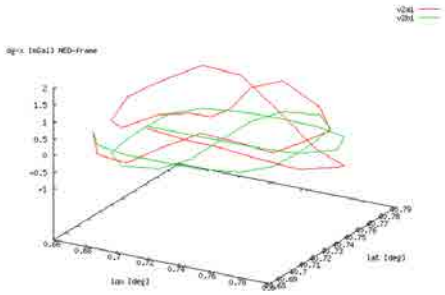

(b) N component (mGal)

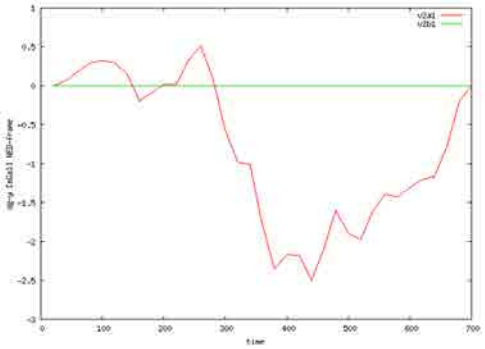

(c) E component (mGal)

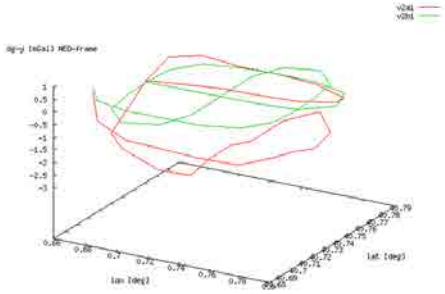

(d) E component (mGal)

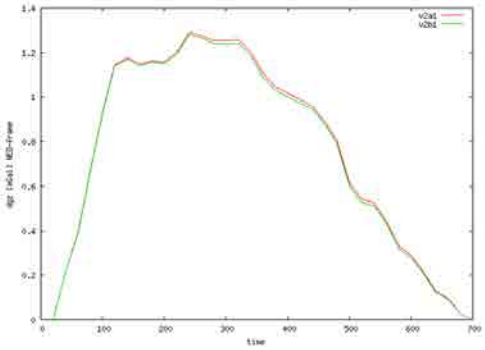

(e) D component (mGal)

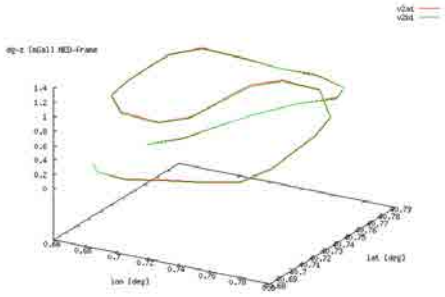

(f) D component (mGal)

Figure 5.18: CTRA LN200: v2a1 and v2b1. Gravity disturbances.

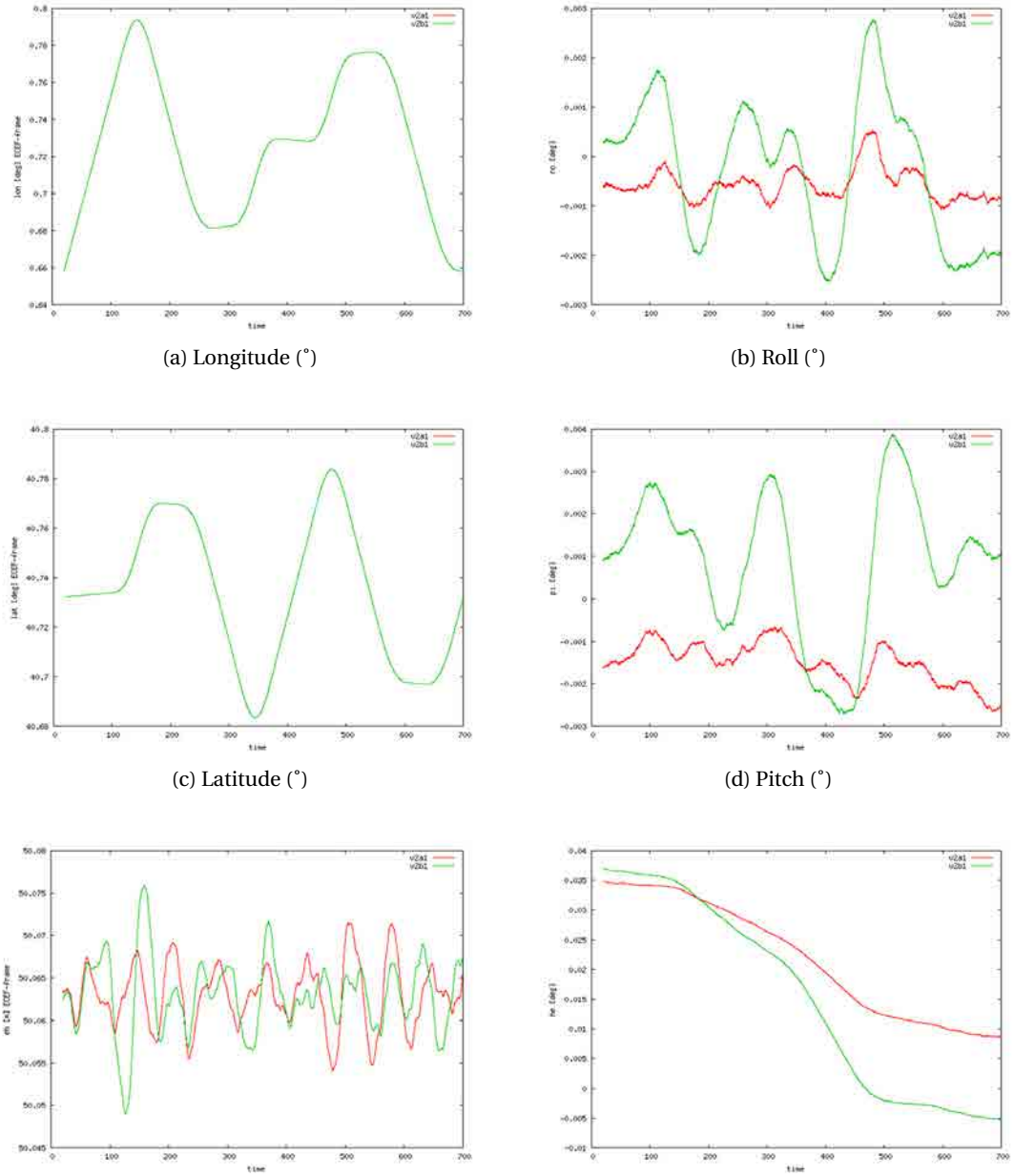

(a) Longitude (°)

(b) Roll (°)

(c) Latitude (°)

(d) Pitch (°)

(e) Height (m)

(f) Heading (°)

Figure 5.19: CTRA LTN101: v2a1 and v2b1. Position and Attitude.

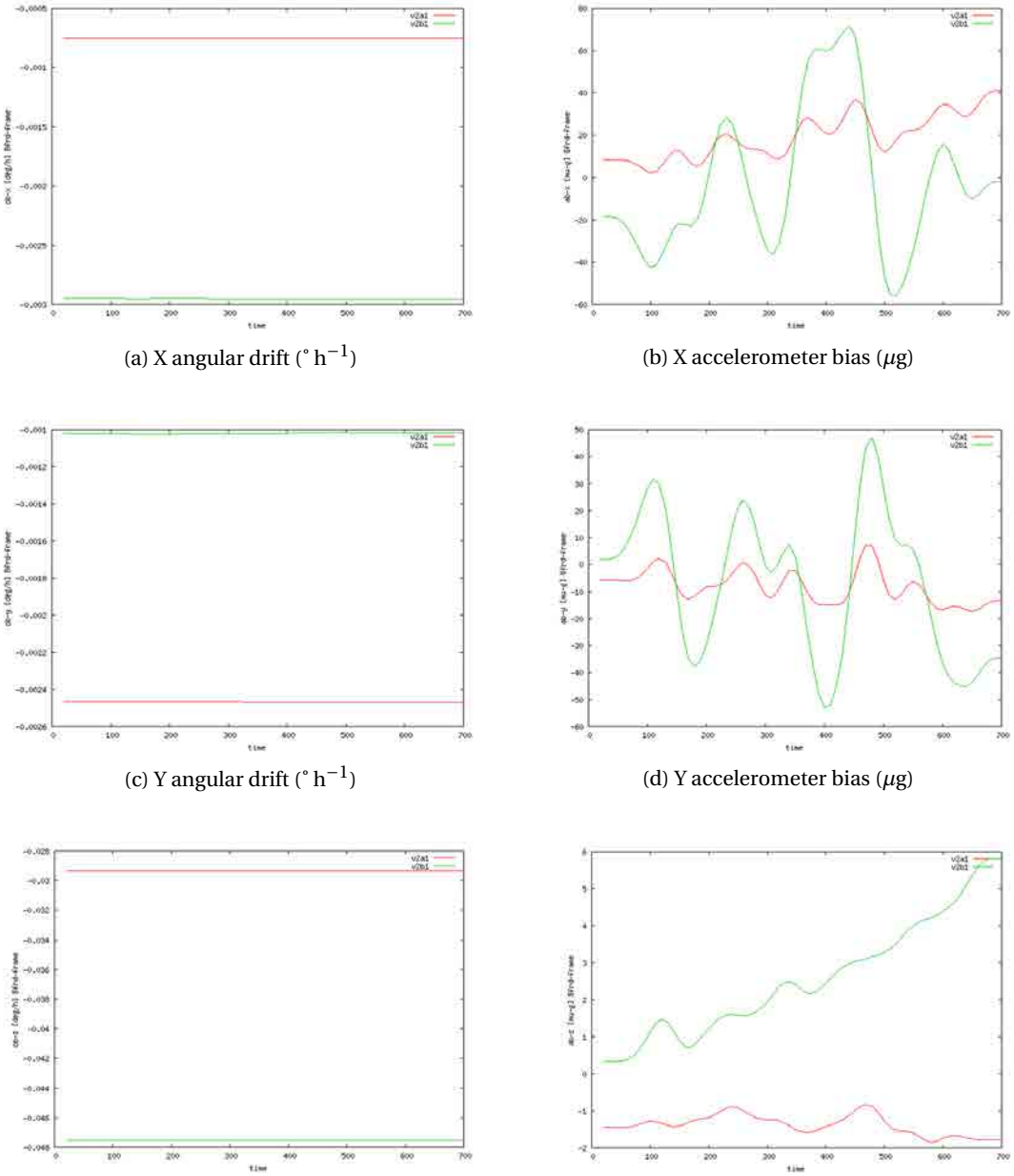

(a) X angular drift ($^\circ\,h^{-1}$)

(b) X accelerometer bias (μg)

(c) Y angular drift ($^\circ\,h^{-1}$)

(d) Y accelerometer bias (μg)

(e) Z angular drift ($^\circ\,h^{-1}$)

(f) Z accelerometer bias (μg)

Figure 5.20: CTRA LTN101: v2a1 and v2b1. Angular drift and Accelerometer bias.

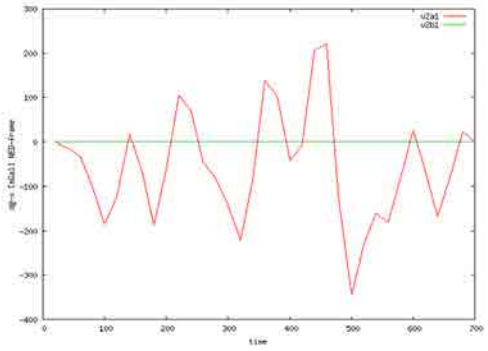

(a) N component (mGal)

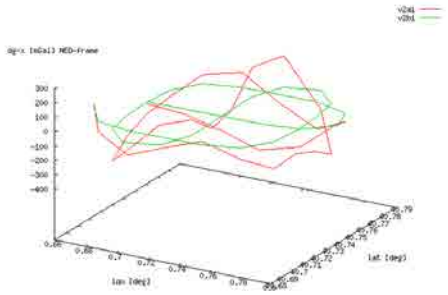

(b) N component (mGal)

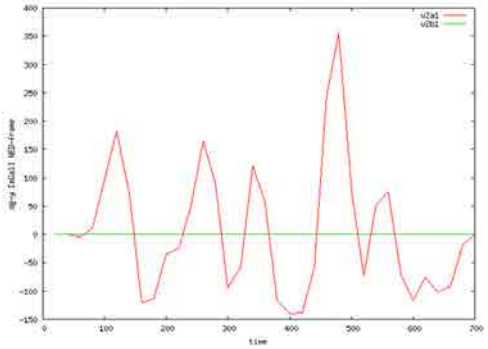

(c) E component (mGal)

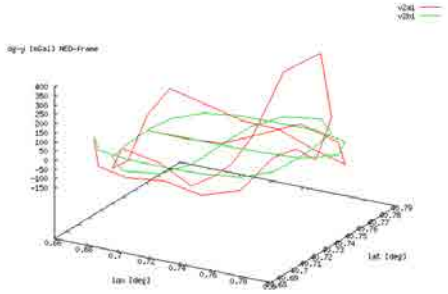

(d) E component (mGal)

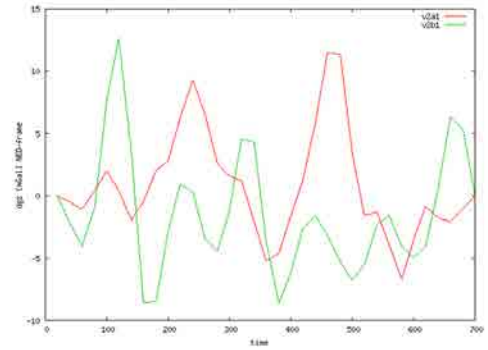

(e) D component (mGal)

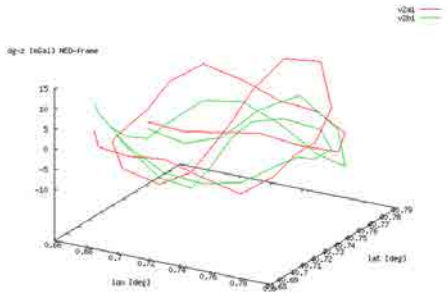

(f) D component (mGal)

Figure 5.21: CTRA LTN101: v2a1 and v2b1. Gravity disturbances.

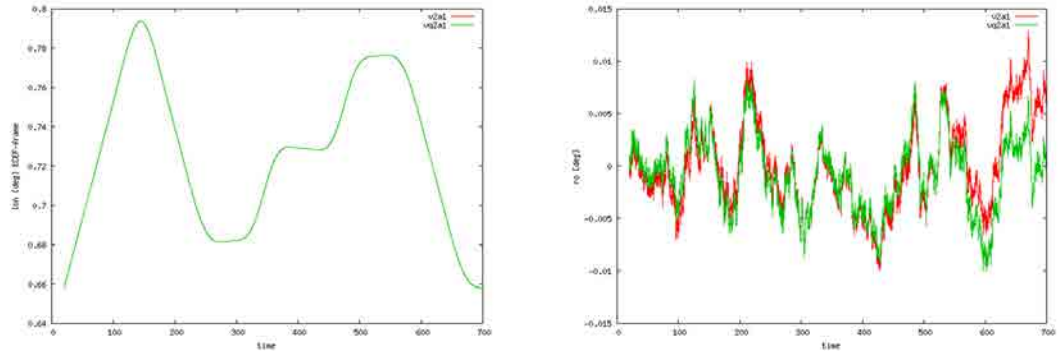

(a) Longitude (°)

(b) Roll (°)

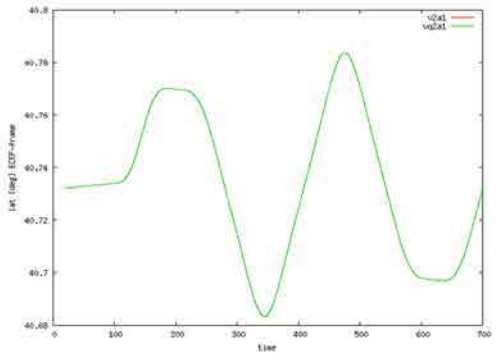

(c) Latitude (°)

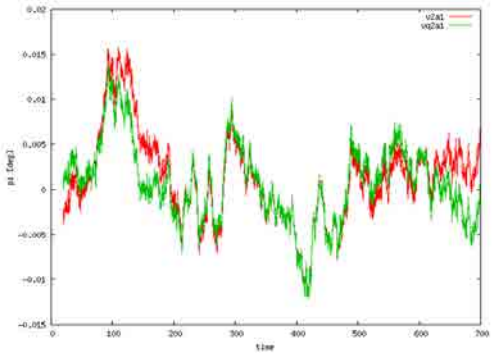

(d) Pitch (°)

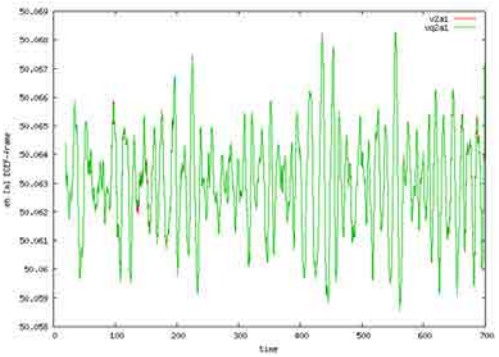

(e) Height (m)

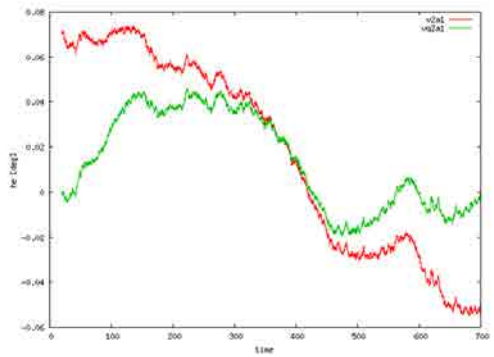

(f) Heading (°)

Figure 5.22: CTRA LN200: v2a1 and vq2a1. Position and Attitude.

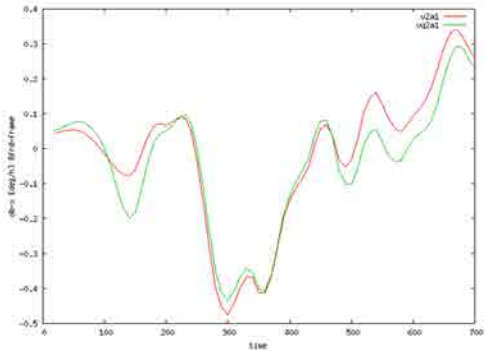

(a) X angular drift ($^\circ$ h^{-1})

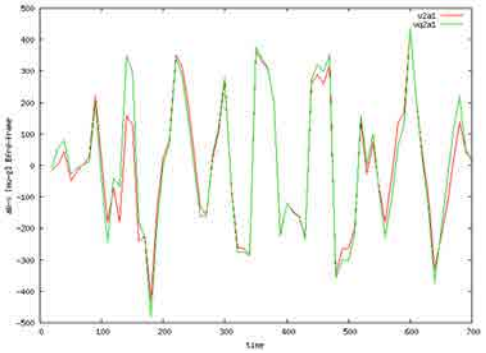

(b) X accelerometer bias (μg)

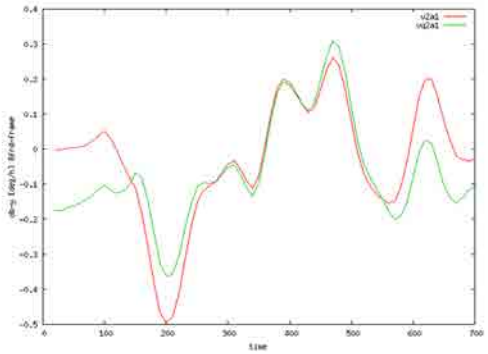

(c) Y angular drift ($^\circ$ h^{-1})

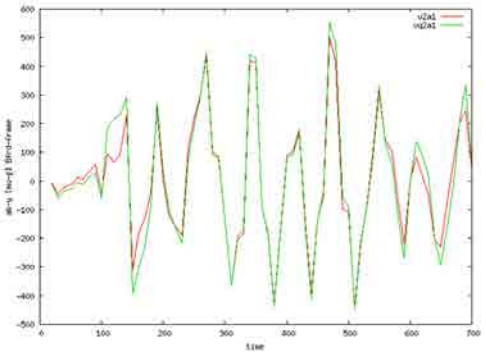

(d) Y accelerometer bias (μg)

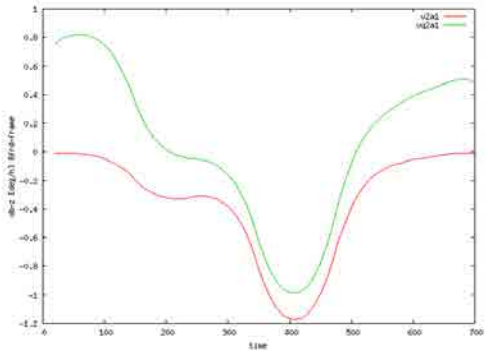

(e) Z angular drift ($^\circ$ h^{-1})

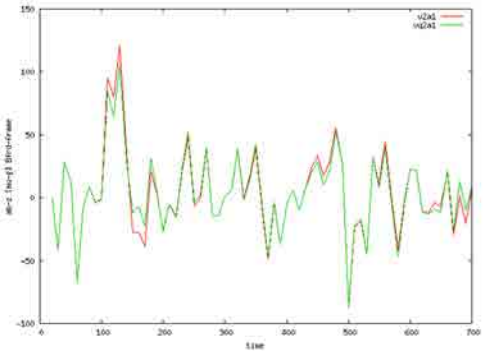

(f) Z accelerometer bias (μg)

Figure 5.23: CTRA LN200: v2a1 and vq2a1. Angular drift and Accelerometer bias.

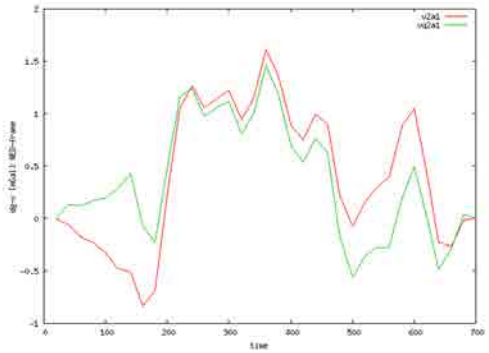

(a) N component (mGal)

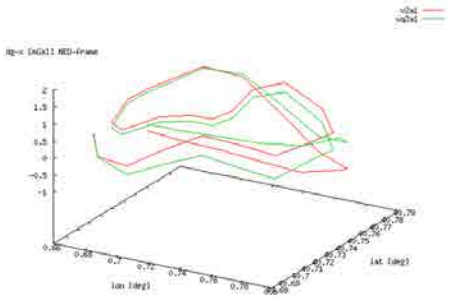

(b) N component (mGal)

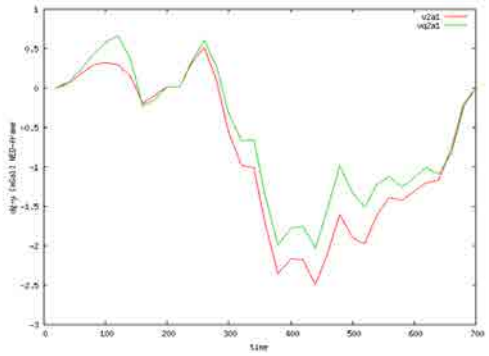

(c) E component (mGal)

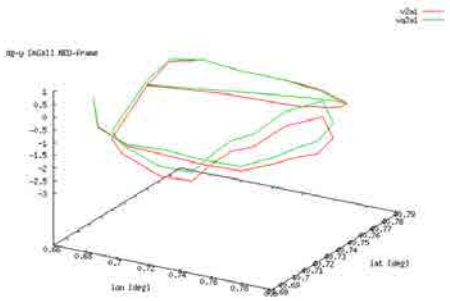

(d) E component (mGal)

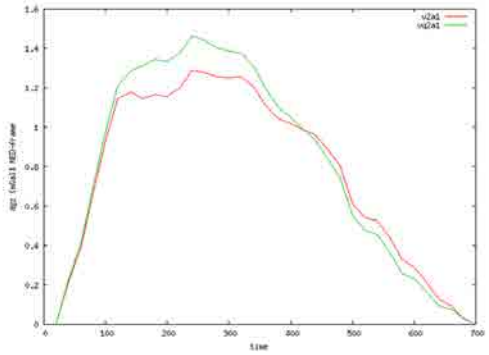

(e) D component (mGal)

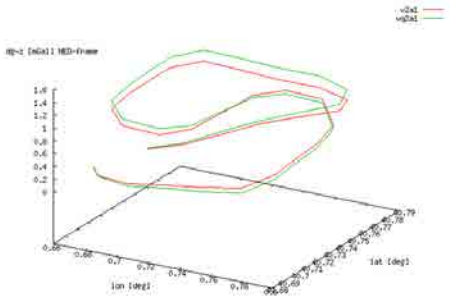

(f) D component (mGal)

Figure 5.24: CTRA LN200: v2a1 and vq2a1. Gravity disturbances.

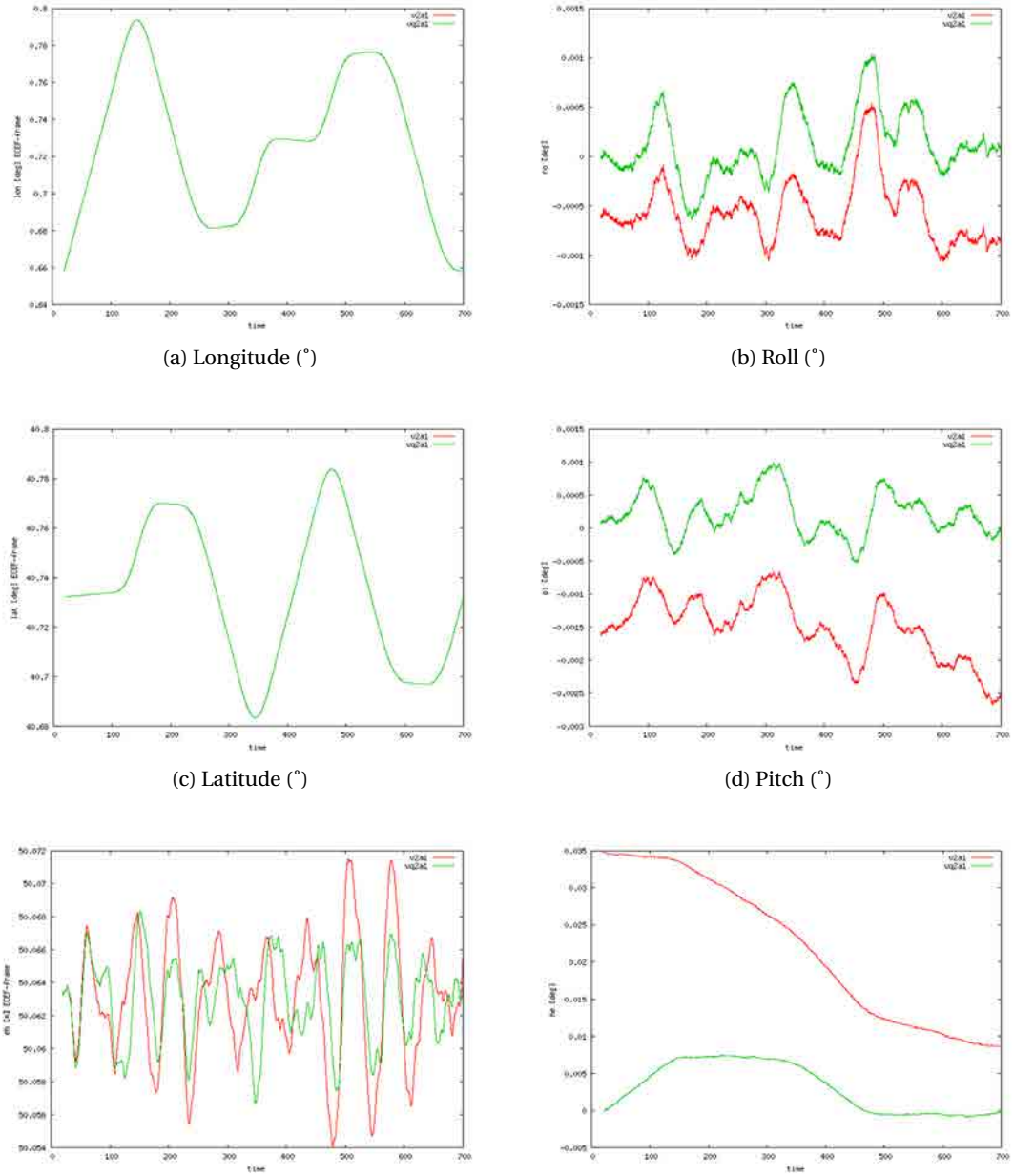

(a) Longitude (°)

(b) Roll (°)

(c) Latitude (°)

(d) Pitch (°)

(e) Height (m)

(f) Heading (°)

Figure 5.25: CTRA LTN101: v2a1 and vq2a1. Position and Attitude.

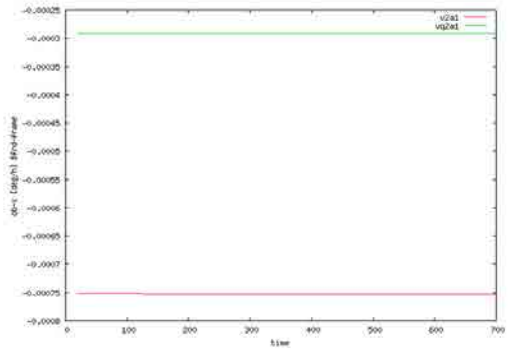

(a) X angular drift ($^\circ\,h^{-1}$)

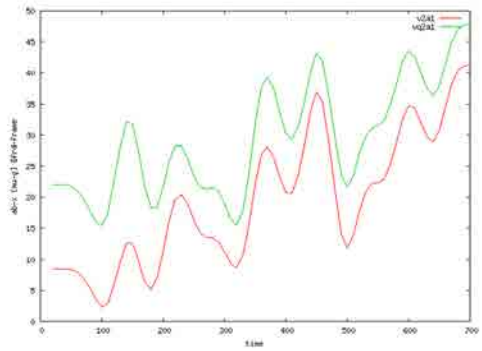

(b) X accelerometer bias (μg)

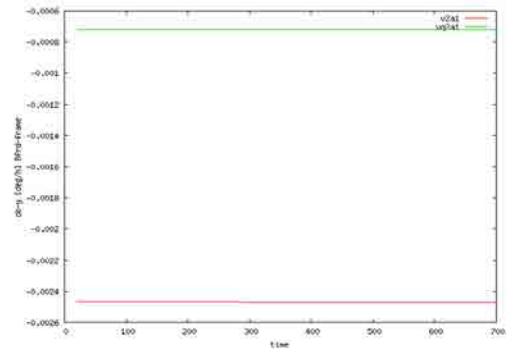

(c) Y angular drift ($^\circ\,h^{-1}$)

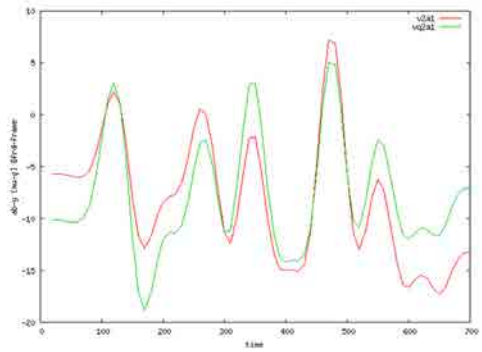

(d) Y accelerometer bias (μg)

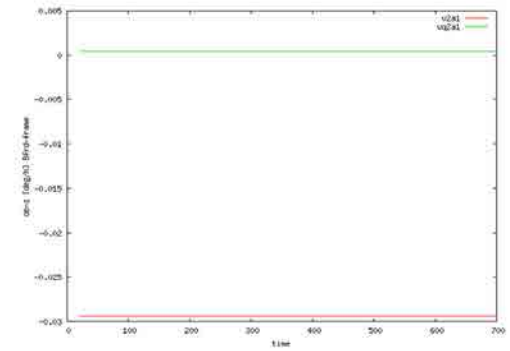

(e) Z angular drift ($^\circ\,h^{-1}$)

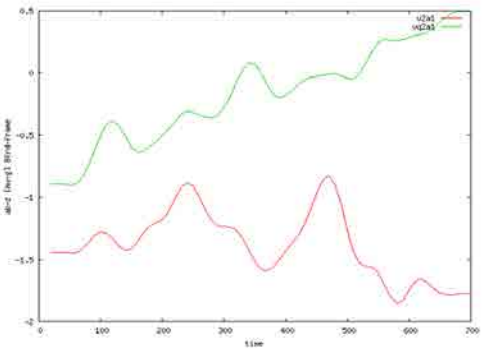

(f) Z accelerometer bias (μg)

Figure 5.26: CTRA LTN101: v2a1 and vq2a1. Angular drift and Accelerometer bias.

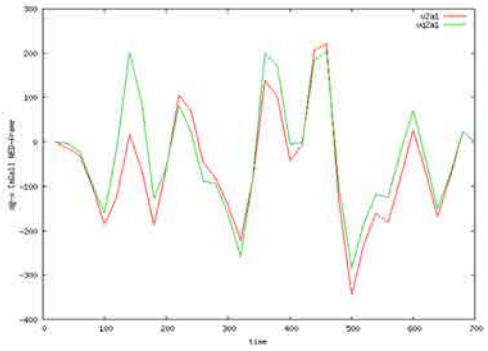

(a) N component (mGal)

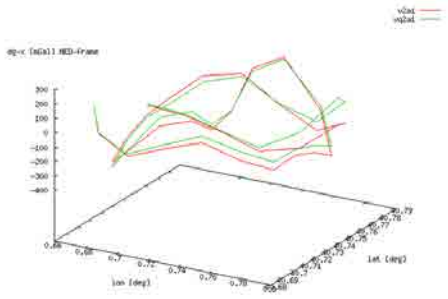

(b) N component (mGal)

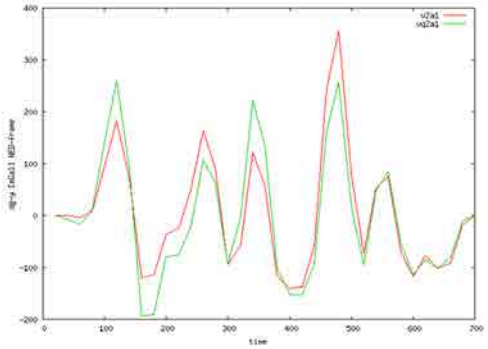

(c) E component (mGal)

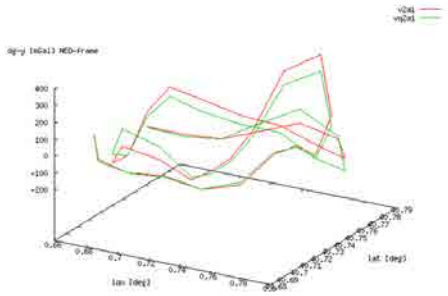

(d) E component (mGal)

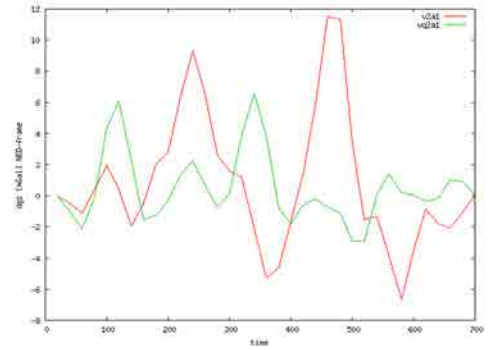

(e) D component (mGal)

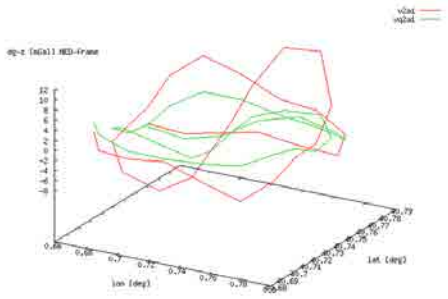

(f) D component (mGal)

Figure 5.27: CTRA LTN101: v2a1 and vq2a1. Gravity disturbances.

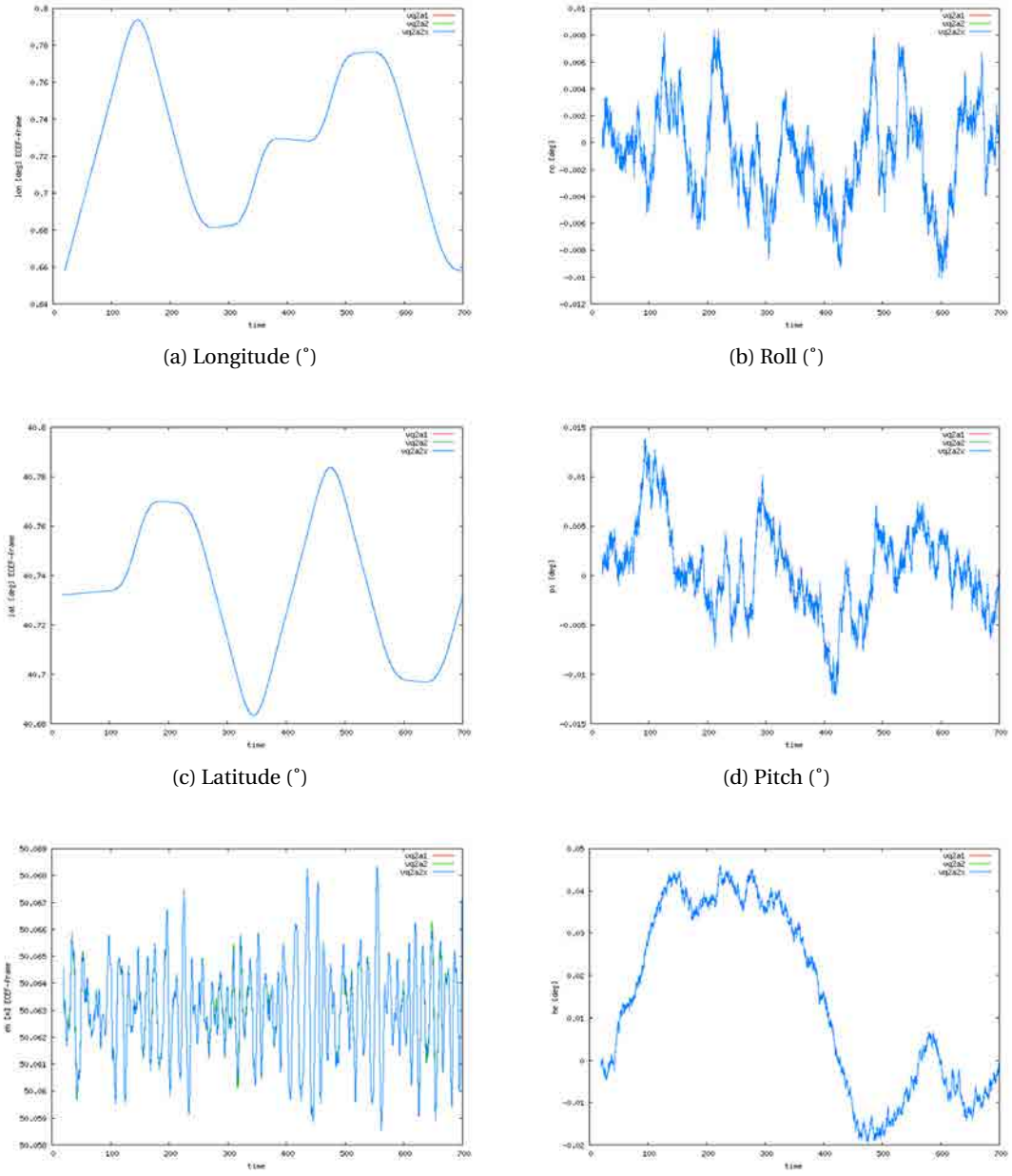

(a) Longitude (°)

(b) Roll (°)

(c) Latitude (°)

(d) Pitch (°)

(e) Height (m)

(f) Heading (°)

Figure 5.28: CTRA LN200: vq2a1, vq2a2 and vq2a2x. Position and Attitude.

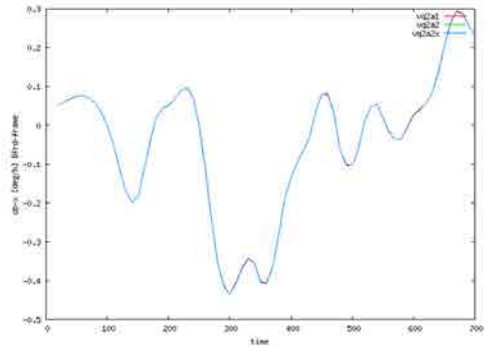

(a) X angular drift ($^\circ$ h^{-1})

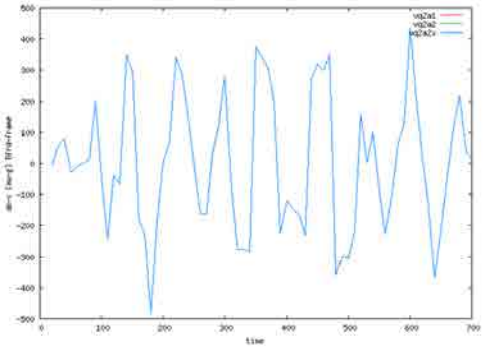

(b) X accelerometer bias (μg)

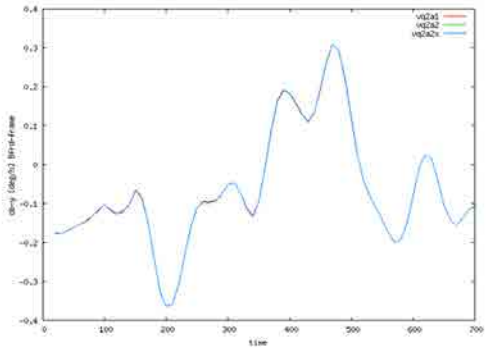

(c) Y angular drift ($^\circ$ h^{-1})

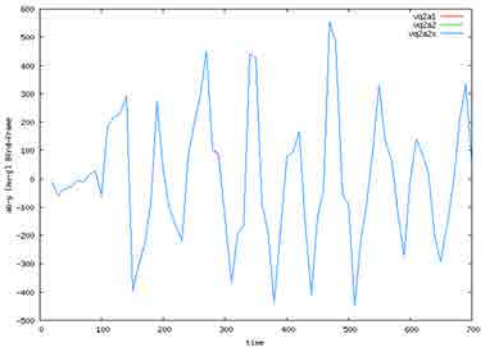

(d) Y accelerometer bias (μg)

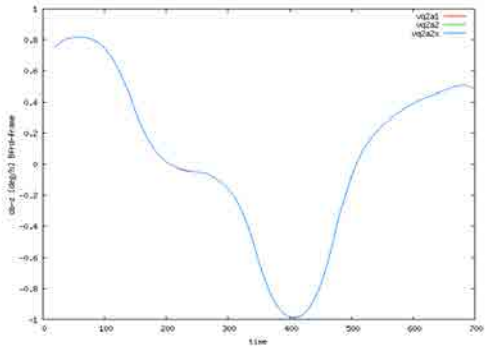

(e) Z angular drift ($^\circ$ h^{-1})

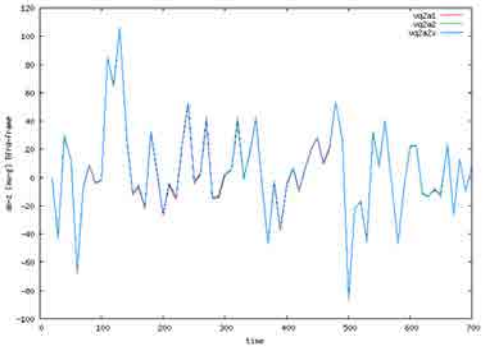

(f) Z accelerometer bias (μg)

Figure 5.29: CTRA LN200: vq2a1, vq2a2 and vq2a2x. Angular drift and Accelerometer bias.

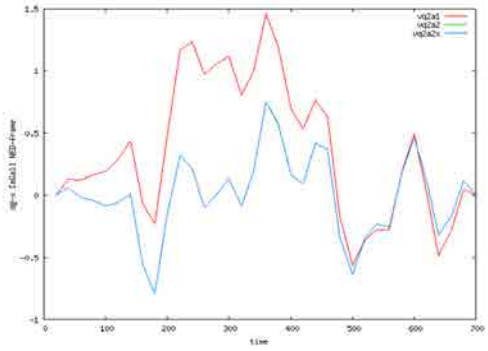

(a) N component (mGal)

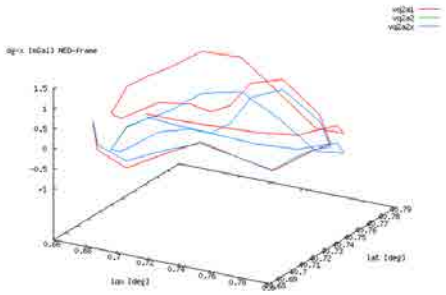

(b) N component (mGal)

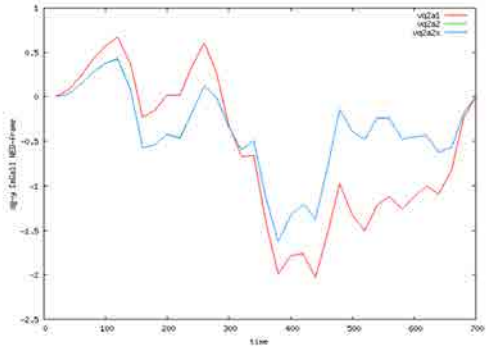

(c) E component (mGal)

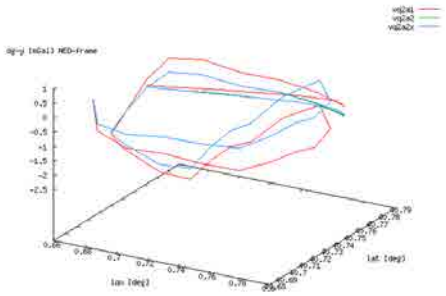

(d) E component (mGal)

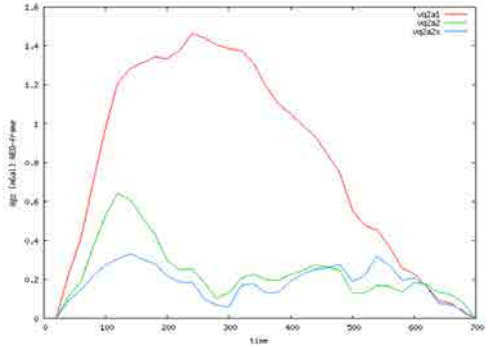

(e) D component (mGal)

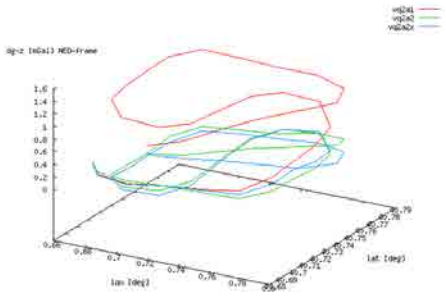

(f) D component (mGal)

Figure 5.30: CTRA LN200: vq2a1, vq2a2 and vq2a2x. Gravity disturbances.

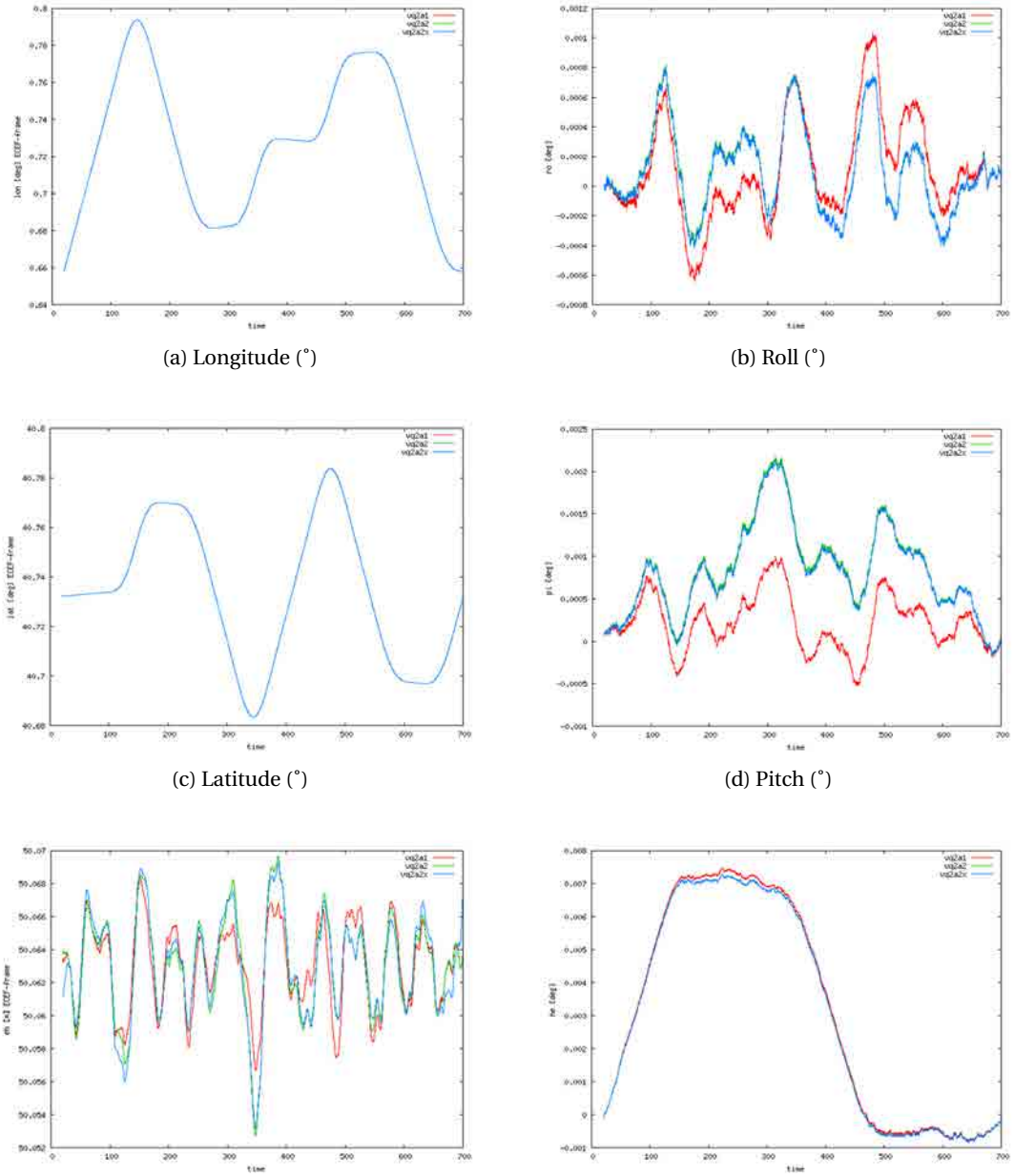

(a) Longitude (°)

(b) Roll (°)

(c) Latitude (°)

(d) Pitch (°)

(e) Height (m)

(f) Heading (°)

Figure 5.31: CTRA LTN101: vq2a1, vq2a2 and vq2a2x. Position and Attitude.

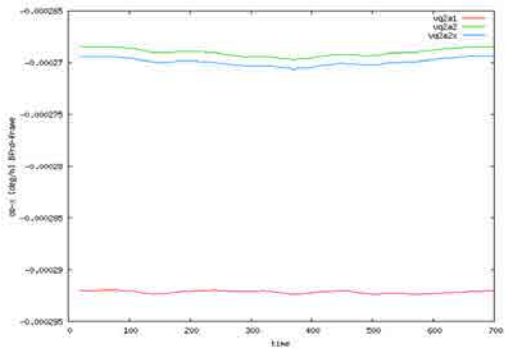

(a) X angular drift ($^\circ\,h^{-1}$)

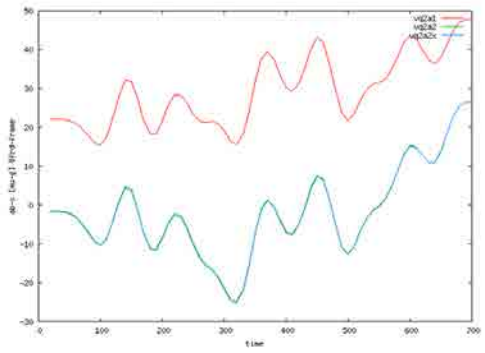

(b) X accelerometer bias (μg)

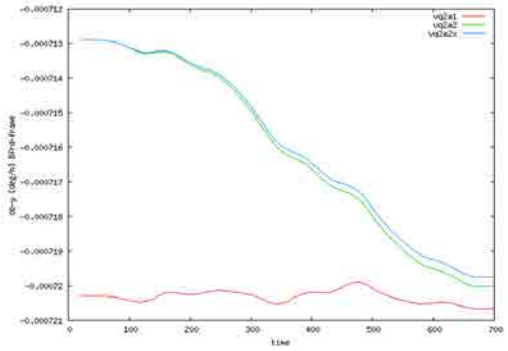

(c) Y angular drift ($^\circ\,h^{-1}$)

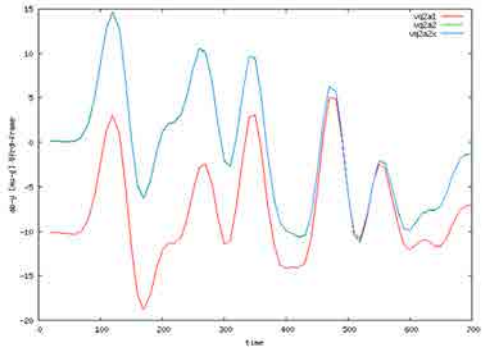

(d) Y accelerometer bias (μg)

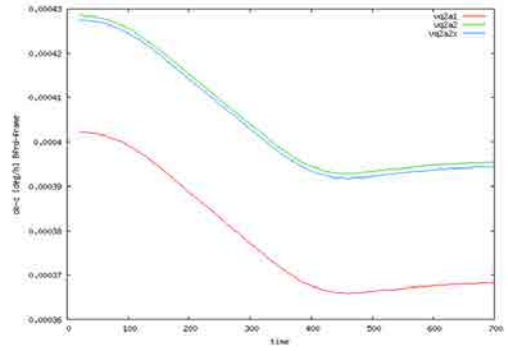

(e) Z angular drift ($^\circ\,h^{-1}$)

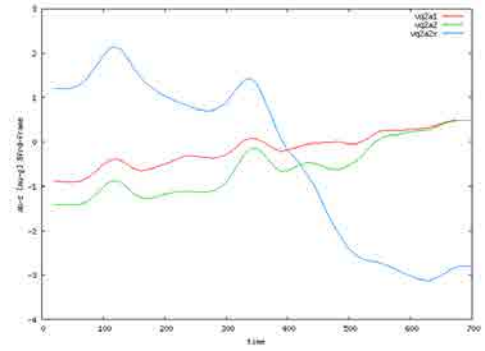

(f) Z accelerometer bias (μg)

Figure 5.32: CTRA LTN101: vq2a1, vq2a2 and vq2a2x. Angular drift and Accelerometer bias.

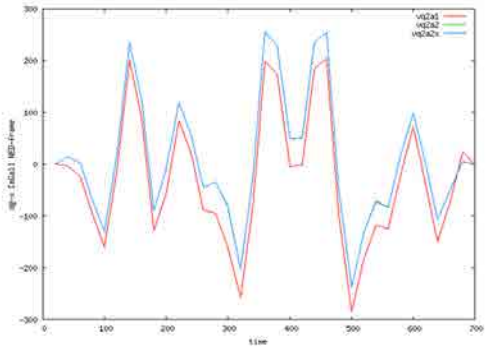

(a) N component (mGal)

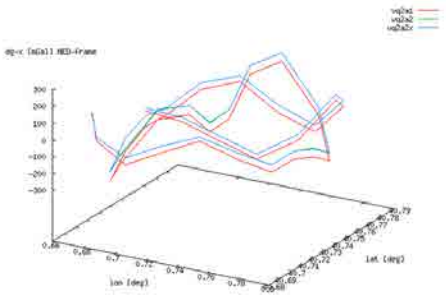

(b) N component (mGal)

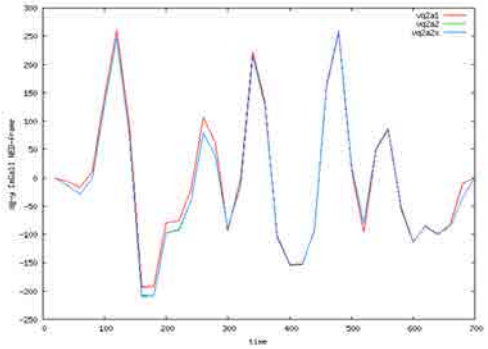

(c) E component (mGal)

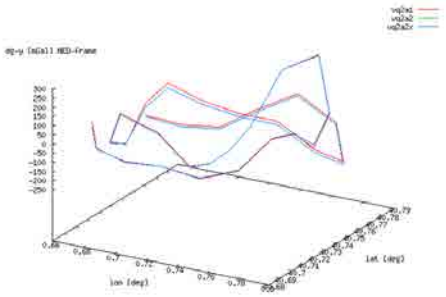

(d) E component (mGal)

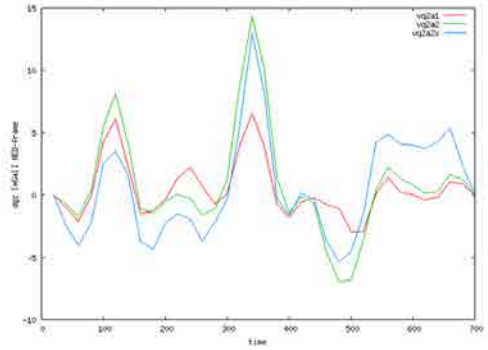

(e) D component (mGal)

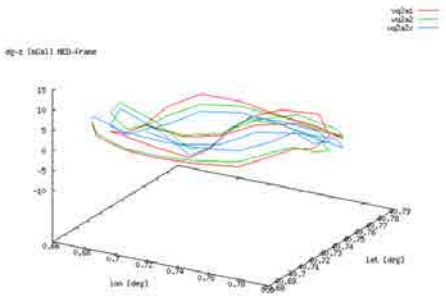

(f) D component (mGal)

Figure 5.33: CTRA LTN101: vq2a1, vq2a2 and vq2a2x. Gravity disturbances.

6 Concluding Remarks

The main objectives of the research described in this dissertation are:

- to prove the feasibility of the NA for the rigorous determination of the gravity field using INS/GNSS techniques;
- to show that the above use of NA methodology shall provide, within the essential limitations of the technology, a procedure to simultaneously calibrate the INS sensors and estimate the anomalous gravity field.

Despite of the simple stochastic error models used, both goals have been met.

In the following, more detailed comments are made about the above contributions and improvements resulting from the research. Important results are highlighted, conclusions are drawn and recommendations are given.

6.1 Specific contributions

- It has been demonstrated that the NA approach allows the use of information — observations — that the SSA cannot take and facilitating the achievement of the two above objectives. The development of an adjustment method in genuinely geodetic post-process, with the explicit purpose to determine precise gravity anomalies taking advantage at maximum the space characteristics of the gravitational field, has been validated with simulated data and configurations.
- It has been also demonstrated that gravity determination is considerably improved when additional observation models (DGUPT, GDT and XOVER) are taken into account. These models are related to previous knowledge of the gravity field that SSA approach can not handle with.
- Several implementations of the same observation equation have been considered depending on the parameters. At this moment, gravity parameters can be computed

directly as gravity disturbance vector expressed in ECEF-frame, expressed in NED-frame or as gravity and deflections of the vertical.

The gravity parameters, that have been computed in all the adjustments described in Chapter 4 are expressed as

$$gg = (g, \eta, \zeta)^T,$$

where g is the gravity and (η,ζ) are the deflections of the vertical and later transform into NED-framed gravity vector using Equation (C.20):

$$\begin{aligned} \text{gg}[1] &= g \sin\zeta \\ \text{gg}[2] &= g \sin\eta \\ \text{gg}[3] &= g \cos\theta \end{aligned}$$

and

$$\theta = \left(\eta^2 + \zeta^2\right)^{\frac{1}{2}}.$$

- The INS mechanisation equations and additional observation equations studied in this research have been implemented into the existing GeoTeX system of the ICC (the GeoTeX/ACX program), which is used since 1988 for both research and production projects.
- With GeoTeX/ACX development, different number of IMU and GNSS data can be managed at the same time. As a consequence, it is possible to validate one sensor from the knowledge of another one.
- The NA approach used in this dissertation — random walk stochastic error models — works properly for tactical-grade IMU sensors. It has been proved by the LN200 data.

6.2 Recommendations

- The NA approach works properly for small networks and simulated data. However this work should continue with the validation using real data. This goal is highly related with the improvements of computer hardware technology, and with further research of numerical and geodetic methods to handle large amount of data and also to increase the redundancy of the resulting network.
- In the future, many modelling and estimation problems in geomatics may benefit from the concept of time dependent network. All the research that is now being carried on in this direction promise to obtain better results than the ones presented here.
- In this dissertation, the INS mechanisation equations in e-frame have been considered. It could be interesting to study the network adjustment if the NED-frame mechanisations

are implemented. The same reasoning will be done for the parameters. Now position is expressed in cartesian coordinates and quaternions are used to express the attitude parameters. Consequently, the development of the observation equations with geodetic coordinates and with roll, pitch and heading angles should be studied.

- In spite of the fact that all the gravity data computed in Chapter 4 are expressed as

$$gg = (g, \eta, \zeta)^T$$

—where g is the gravity and (η,ζ) are the deflections of the vertical— they have not been studied in depth. As mentioned before, g is transformed later into `NED`-framed gravity vector using Equation (C.20 and used in the results analysis.

With respect to usually applied gravimetric techniques for geoid computation, the deflections of the vertical (η,ζ) — usually astrogeodetically determined — represent an independent complementary data set that can be used for validation purposes and combined computations. So, further research work about vertical deflection data determination can be done.

- It is recommended to fully exploit the statistical and geometric information that the NA provides like covariances, correlations, redundancy numbers, etc. In this dissertation, it has not been studied in depth, but further research work should be done.

- The random walk stochastic error model for gravity data has to be improved. Further studies using Gauss-Markov models of different order and other stochastic models have to be carried out to investigate gravity models based on stochastic differential equations that are symmetric with respect to time as opposed to the Gauss-Markov model. This is a work for one o more dissertations (or Ph.D. thesis).

- It is recommended to continue the research on IMU error modeling as done since long by various groups.

- `GeoTeX/ACX` software is able to handle with different types of IMU and GNSS data jointly. Thus, it is possible to study and to determine (i.e*to calibrate*) an IMU error model through the knowledge of another IMU model. Although this IMU *calibration* has not been studied in this dissertation, it is recommended to perform further research work about it.

Bibliography

[1] Bastos, L., Cunha, S., Forsberg, R., Olesen, A. V., Gidskehaug, A., Mayer, U., Boebel, T., Timmen, L., Xu, G., Nesemann, M., Hehl, K. (1997). An airborne geoid mapping system for regional sea-surface topography: applications to the Skagerrak and Azores areas. IAG Symposia Series 119: Geodesy on the Move — gravity, geoid, geodynamics and Antarctica, pp. 30–36

[2] Bastos, L., Cunha, S., Forsberg, R., Olesen, A., Gidskehaug, A., Timmen, L., Meyer, U. (1999). On the use of airborne gravimetry in gravity field modeling: experiences from the AGMASCO project. Physics and Chemistry of the Earth 25(1):1–7

[3] Boedecker, G., Böder, Völksen, C. (2002). Precise GPS-Positioning and Acceleration for Airborne Gravimetry: A Case Study. IGGC Meeting Thessaloniki.

[4] Boedecker,G., Meyer,U. (2007). Airborne gravimetry. Deutsche Geodaetische Kommission, Reihe B, Nr. 315, pp. 41–44

[5] Brezezowski, S., Heller, W. (1988). Gravity Gradiometer Survey System Errors. Geophysics, 53(10):1355–1361

[6] Brown, J. M., Niebauer, T. M., Klingele, E. E. (2000). Towards a Dynamic Absolute Gravity System. IAG Symposia Series 123: Vistas for geodesy in the new millenium.

[7] Brozena, J. M., Peters, M. F. (1988). An airborne gravity study of eastern North Carolina. Geophysics, 53:245–253

[8] Brozena, J. M., Mader, G. L., Peters, M. F. (1989). Interferometric Global Positioning System: Three-Dimensional Positioning Source for Airborne Gravimetry. Journal of Geophysical Research 94(B9):12153–12162

[9] Brozena, J. M. (1991). GPS and airborne gravimetry: recent progress and future plans. Bulletin Géodésique, 65:116–121

[10] Brozena, J. M. (1992). Airborne Gravimetry. Chapter 4 in R.A. Geyer (ed): CRC Handbook of Geophysical Exploration at Sea, Hard Minerals, second edition, CRC Press, Boca Raton, 1992, pp. 117–136

[11] Brozena, J. M. (1992). The Greenland Aerogeophysics Project: Airborne Gravity, Topographic and Magnetic Mapping of an Entire Continent. IAG Symposia G3: Determination of the Gravity Field by Space and Airborne Methods, Vienna, Aug. 1991.

[12] Brozena, J. M., Peters, M. F. (1992). The Greenland Aerogeophysics Project: Year 1. ION 48th Annual Meeting, 1992.

[13] Brozena, J. M., Peters, M. F. (1994). Airborne Gravity Measurement at NRL. International Symposium on Kinematic Systems in Geodesy, Geomatics and Navigation, Banff, Canada, August 30 – September 2, pp. 495–506

[14] Brozena, J. M., Peters, M. F., Salman, R. (1997). Arctic airborne gravity measurement program. IAG Symposia GRAGEOMAR, Tokyo 1996. IAG Symposia Series 117: Gravity, Geoid and Marine Geodesy, pp. 131–138

[15] Brozena, J. M., Childers, V. (1999). The NRL Airborne Gravity Program. IAG General Assembly, July 19–30 1999, Birmingham, UK. IAG Symposia Series 121: Geodesy Beyond 2000, pp. 125–130

[16] Bruton, A. M., Schwarz, K. P. (1997). Airborne gravity estimation using adaptive filters. M.E. Cannon and G. Lachapelle (eds.), International Symposium on Kinematic System in Geodesy, Geomatics and Navigation, Banff, Canada, June 3–6, 1997, pp. 605–612

[17] Bruton, A. M., Glennie, C. L., Schwarz, K. P. (1999). Differentation for High Precision GPS Velocity and Acceleration Determination. GPS Solutions, 2(4):7–21

[18] Bruton, A. M. (2000). Improving the Accuracy and Resolution of SINS/DGPS Airborne Gravimetry. UCGE Reports Number 20145. Department of Geomatics Engineering, University of Calgary.

[19] Bruton, A. M., Hammada, Y., Ferguson, S., Schwarz, K. P., Wei, M., Halpenny, J. (2001). A Comparison of Inertial Platform, Damped 2-axis Platform and Strapdown Airborne Gravimetry. International Symposium on Kinematic Systems in Geodesy, Geomatics and Navigation, KISS-2001, Banff, Canada, June 5–8, 2001.

[20] Bruton, A. M., Schwarz, K. P., Ferguson, S., Kern, M., Wei, M. (2002). Deriving acceleration from DGPS: towards higher resolution applications for airborne gravimetry. GPS Solutions, Vol. 5, No. 3

[21] Colomina, I., Navarro, J., Térmens, A. (1992). GeoTeX: a general point determination system. International Archives of Photogrammetry and Remote Sensing, Vol.29–B3, International Society for Photogrammetry and Remote Sensing, pp. 656–664

[22] Colomina, I., Blázquez, M. (2004). A unified approach to static and dynamic modelling in photogrammetry and remote sensing. ISPRS International Archives at Photogrammetry, Remote Sensing and Spatial Information Sciences, Vol.35–B1, Comm. I, pp. 178–183

[23] Colomina, I., Blázquez, M. (2005). On the stochastic modeling and solution of time dependent networks. Geomatics Week, Barcelona.

[24] Czompo, J. (1994). Airborne Scalar Gravimetry System Errors in the Spectral Domain. Ph.D. Thesis, UCGE Reports Number 20067, Department of Geomatics Engineering, University of Calgary.

[25] $http://earth-info.nga.mil/GandG/wgs84/gravitymod/egm2008$

[26] $http://op.gfz-potsdam.de/grace/results/index_RESULTS.html$

[27] Eissfeller, B., Spietz, P. (1989). Shaping Filter Design for the Anomalous Gravity Field by Means of Spectral Factorization. Manuscripta Geodaetica 14:183–192

[28] Eissfeller, B. (1990). Mathematical Analysis of the Geodetic Space-Stabilized INS. IAG Symposium 107 "Kinematic Systems in Geodesy, Surveying and Remote Sensing", pp. 47–58.

[29] Farrell, J. L. (2008). Robust Design for GNSS Integration. ION GNSS 2008, 16–18 September 2008, Savannah, Georgia.

[30] Ferguson, S. T., Hammada, Y. (2000). Experiences with AIRGrav: Results from a New Airborne Gravimeter. IAG Symposia Series 123: Vistas for geodesy in the new millenium.

[31] Fernandes, M. J., Gidskehaug, A., Solheim, D., Mork, M., Jaccard, P., Catalão, J. (1998). Gravimetric and hydrographic campaign in the Azores region. I Assembleia Luso Espanhola de Geodesia e Geofísica, Almeria, Spain, February 1998.

[32] Forsberg, R., Vassiliou, A. A., Schwarz, K. P., Wong, R. V. C. (1986). Inertial Gravimetry — a Comparison of Kalman Filtering-smoothing and Post-mission Adjustment Techniques. Bulletin Géodésique 60:129–142

[33] Forsberg, R. (1987). A New Covariance Model for Inertial Gravimetry and Gradiometry. Journal of Geophysical Research 92(B2):1305–1310

[34] Forsberg, R., Kenyon, S. (1994). Evaluation and Downward Continuation of Airborne Gravity Data — the Greenland Example. International Symposium on Kinematic Systems in Geodesy, Geomatics and Navigation, Banff, Canada, August 30 – September 2, pp. 531–538

[35] Forsberg, R., Brozena, J. M. (1997). Airborne geoid measurements in the arctic ocean. IAG Symposia GRAGEOMAR, Tokyo 1996. IAG Symposia Series 117: Gravity, Geoid and Marine Geodesy, pp. 139–146

[36] Forsberg, R., Olesen, A. V., Keller, K. (1999). Airborne gravity survey of the north Greenland Shelf 1998. Technical Report N.10, National Survey and Cadastre, Denmark, 1999.

[37] Forsberg, R., Olesen, A., Bastos, L., Gidskehaug, A., Meyer, U., Timmen, L. (2000). Airborne geoid determination. Earth, Planets and Space, 52:863–866

[38] Forsberg, R., Olesen, A. V., Keller, K. (2000). Airborne Gravity Survey of the North Greenland Continental Shelf. IAG Symposia Series 123: Vistas for geodesy in the new millenium, pp. 235–240

[39] Forsberg, R., Andersen, O. B., Knudsen, P., Laxon, S. W., Johannesen, J., Tscherning, C. C., Braun, A. (2004). ARCGICE — Combination of Spaceborne, Airborne and In-Situ Gravity Measurements in Support of Arctic Sea-Ice Mapping. A proposal for ESA EOP-SM/1090 (1/6/04).

[40] Forsberg, R., Olesen, A., Vest, A., Solheim, D., Hipkin, R., Omang, O., Knudsen, P. (2004). Gravity Field Improvements in the North Atlantic Region. GOCE Workshop, ESA-ESRIN, March 2004.

[41] Friedland (1978).

[42] $http://ec.europa.eu/enterprise/policies/satnav/galileo/index_en.htm$

[43] Glennie, C., Schwarz, K. P. (1997). Airborne Gravity by Strapdown INS/DGPS in a 100 km by 100 km Area of the Rocky Mountains. M.E. Cannon and G. Lachapelle (eds.), International Symposium on Kinematic System in Geodesy, Geomatics and Navigation, Banff, Canada, June 3–6, 1997, pp. 619–624

[44] Glennie, C., Schwarz, K. P., Bruton, A. M., Tennant, J. K. A Combined DGPS/INS and Synthetic Aperture Radar System for Geoid Referenced Elevation Models and Ortho-Rectified Image Maps.

[45] Glennie, C., Schwarz, K. P. (1999). A comparision and analysis of airborne gravimetry results from two strapdown inertial/DGPS systems. Journal of Geodesy, 73:311–321

[46] Glennie, C., Schwarz, K. P., Bruton, A. M., Forsberg, R., Olesen, A. V., Keller, K. (1999). A comparison of stable platform and strapdown airborne gravity. IAG General Assembly, July 19–30 1999, Birmingham, UK.

[47] Glennie, C. (1999). An analysis of Airborne Gravity by Strapdown INS/GPS. UCGE Reports Number 20125.

[48] Glennie, C., Schwarz, K. P., Bruton, A. M., Forsberg, R., Olesen, A. V., Keller, K. (2000). A comparison of stable platform and strapdwon airborne gravity. Journal of Geodesy, 74:383–389

[49] Grejner-Brzezinska, D. A., Wang, J. (1998). Gravity Modeling for High-Accuracy GPS/INS Integration. Navigation, 45(3):209–220

[50] Gumert, W. R. (1992). Airborne Gravity Measurements. Chapter 6 in R.A. Geyer (ed): CRC Handbook of Geophysical Exploration at Sea, Hydrocarbons, CRC Press, Boca Raton, 1992, pp. 125–139

[51] Gumert, W. R. (1995). Third Generation Aerogravity System. Airborne Gravimetry, IAG Symposia G4, IUGG XXI General Assembly, Boulder, Colorado, pp. 153–161

[52] Hammada, Y. (1996). A Comparison of Filtering Techniques for Airborne Gravimetry. M.Sc. Thesis, University of Calgary, UCGE Reports Number 20089.

[53] Hammada, Y., Schwarz, K.P. (1997). Airborne Gravimetry Model-based versus Frequency-domain Filtering Approaches. M.E. Cannon and G. Lachapelle (eds.), International Symposium on Kinematic System in Geodesy, Geomatics and Navigation, Banff, Canada, June 3–6, 1997, pp. 581–595

[54] Hammer, S. (1983). Airborne Gravity is Here! Geophysics, 48:213–223

[55] Hein, G. W. (1995). Progress in Airborne Gravimetry: Solved, Open and Critical Problems. Airborne Gravimetry, IAG Symposia G4, IUGG XXI General Assembly, Boulder, Colorado, pp. 3–11

[56] Heiskanen, W. A., Moritz, H. (1967). Physical Geodesy. W.H.Freeman and Company.

[57] Hwang, C., Hsiao, Y. S., Shih, H. C., Wang, C. G., Forsberg, R., Olesen, A. V. (2005). Geodetic and geophysical results from a Taiwan airborne gravity survey. IAG General Assembly Dynamic Planet 2005, August 22–26 2005, Cairns, Australia.

[58] Jekeli, C. (1988). The Gravity Gradiometer Survey System (GGSS). EOS, Transactions American Geophysical Union, 69(8), 105 pp.

[59] Jekeli, C. (1992). Does a gravimeter sense gravitation? Manuscripta Geodaetica, 17:365–372

[60] Jekeli, C. (1992). Vector gravimetry using GPS in free-fall and in an earth-fixed frame. Bulletin Géodésique, 66:54–61

[61] Jekeli, C. (1995). Airborne Vector Gravimetry Using Precise Position-Aided Inertial Measurement Units. Bulletin Géodésique, 69:1–11

[62] Jekeli, C. (1995). GPS/INS Positioning and the Earth's Gravitational Field. 1995 Mobile Mapping Symposium, American Society for Photogrammetry and Remote Sensing, Bethesda, Maryland, pp. 163–172.

[63] Jekeli, C., Garcia, R. (1997). GPS phase accelerations for moving-base vector gravimetry. Journal of Geodesy, 71:630–639

[64] Jekeli, C. (1999). An Analysis of vertical deflections derived from high-degree spherical harmonic models. Journal of Geodesy, 73:10–22

[65] Jekeli, C. (2001). Inertial navigation systems with geodetic applications. Berlin; New York: de Gruyter.

[66] Jekeli, C., Kwon, J. (2002). Geoid profile determination by direct integration of GPS/INS vector gravimetry. Journal of Geophysical Research 107(B10), DOI: 101029/2001 JBod626.

[67] Jones, P. C., Johnson, A. C. (1995). Airborne Gravity Survey in Southern Palmer Land, Antarctica. Airborne Gravimetry, IAG Symposia G4, IUGG XXI General Assembly, Boulder, Colorado, pp. 117–124

[68] Jones, P. (1997). Towards a new free air anomaly map of the Antarctic Peninsula. IAG Scientific Assembly, September 3–9 1997, Rio de Janeiro, Brazil. IAG Symposia Series 119: Geodesy on the Move — gravity, geoid, geodynamics and Antarctica, pp. 517–522

[69] Kleusberg, A., Peyton, D., Wells, D. (1990). Airborne Gravity and the Global Positioning System. IEEE PLANS 1990, pp. 273–278

[70] Klingelé, E. E., Baganaschi, L., Halliday, M., Cocard, M., Kahle, H. G. (1994). Airborne Gravimetric Survey of Switzerland. First results. Bericht N.239. Institut für Geodäsie und Photogrammetrie. Eidgenössische Technische Hochschule Zürich.

[71] Klingelé, E. E., Halliday, M., Cocard, M., Kahle, H. G. (1995). Airborne Gravimetric Survey of Switzerland. VPK 4/95:248–253

[72] Klingelé, E. E.,Halliday, M. (1995). Airborne gravity survey in Switzerland. Airborne Gravimetry, IAG Symposia G4, IUGG XXI General Assembly, Boulder, Colorado, pp. 109–116

[73] Klingelé, E. E., Cocard, M., Halliday, M., Kahle, H. G. (1996). The Airborne Gravimetric Survey of Switzerland. Matériaux pour la Géologie de la Suisse, Geophysique,N. 31, 104 pp.

[74] Klingelé, E. E., Cocard, M., Kahle, H. G., Halliday, M. (1997). Kinematic GPS as a source for airborne gravity reduction: The airborne gravity survey of Switzerland. Journal of Geophysical Research, 102(B4):7705–7715

[75] Kloeden, P. E., Platen, E. (1999). Numerical solution of Stochastic Differential Equations. Springer Verlag, New York, US.

[76] Knickmeyer, E. T. (1990). Vector Gravimetry by a combination of INS and GPS measurements. Phd. Thesis. UCGE Reports Number 20035. University of Calgary.

[77] Lemoine, F. G., Kenyon, S. C., Factor, J. K., Trimmer, R. G., Palvis, N. K., Chinn, D. S., Cox, C. M., Klosko, S. M., Luthcke, S. B., Torrence, M. H., Wang, Y. M., Williamson, R. G., Palvis, E. C., Rapp, R. H., Olson, T. R. (1998). The Development of the Joint NASA GSFC and the National Imagery and Mapping Agency (NIMA) Geopotential Model EGM96. NASA/TP, 1998-206861, Goddard Space Flight Center, Greenbelt, Maryland.

[78] Marchenko, D. A., Meyer, U., Bastos, L. (2004). Airborne gravity disturbances in sequential multipole analysis for geoid determination and its test over the Azores. Bolletino di Geodesia e Scienze Affini, 63(2004)2:101–114

[79] Moritz, H. (1967). Kinematical Geodesy. Report No 92, Department of Geodetic Science and Surveying, Ohio State University, Columbus.

[80] Moritz, H. (1971). Kinematical Geodesy II. Report No 165, Department of Geodetic Science and Surveying, Ohio State University, Columbus.

[81] Nassar, S., Schwarz, K. P., Noureldin, A., El-Sheimy, N. (2003). Modeling Inertial Sensor Errors using Autoregressive (AR) Models. ION NTM-2003, Annaheim, USA, January 22–24, 2003, pp. 116–125

[82] Nettleton, L. L., LaCoste, L. J. B., Harrison, J. C. (1960). Tests of an Airborne Gravity Meter. Geophysics, 25(1):181–202

[83] Nettleton, L. L., LaCoste, L. J. B., Harrison, J. C. (1962). Quantitative evaluation of Precision of Airborne Gravity Meter. JGR, 67(11):4395–4410

[84] Novák, P., Kern, M., Schwarz, K. P. (2000). On the Determination of the Relative Geoid from Airborne Gravimetry. IAG Symposia Series 123: Vistas for geodesy in the new millenium.

[85] Novák, P., Heck, B. (2002). Downward continuation and geoid determination based on band-limited airborne gravity data. Journal of Geodesy, 76:269–278

[86] ⊘ksendal, B. (1993). Stochastic differential equations: an introduction with applications. Universitext, third edn, Springer Verlag.

[87] Olesen, A. V., Forsberg, R., Keller, K., Gidskehaug, A. (2000). Airborne gravity survey of the Lincoln Sea and Wandel Sea, North Greenland. Physics and Chemistry of the Earth, 25(1):25–29

[88] Parés, M. E., Rosales, J. J., Colomina, I. (2008). Yet another IMU simulator: validation and applications. EUROCOW "International Calibration and Orientation Workshop", January 30 – February 1, Castelldefels, Spain.

[89] Pavlis,N.K., Holmes,S.A., Kenyon,S.C., Factor,J.K. (2008). Earth gravitational model to degree 2160: EGM2008. Paper presented to the European Geosciences Union General Assembly, Vienna, Austria. April 2008.

[90] Rapp, R. H., Pavlis, N. K. (1990). The Development and Analysis of Geopotential Coefficient Models to Spherical Harmonic Degree 360. Journal of Geophysical Research, B95:21885–21911

[91] Reigber, C., King., Z., Konig, R., Schwinter, P. (1997). CHAMP, a minisatellite mission for geopotential and atmospheric research. AGU Spring Meeting, Baltimore.

[92] Rummel, R. (1999). Gravity Field and Steady-State Ocean Circulation Mission. Earth Explorer Mission Selection Workshop, ESA, Granada, Spain, October 12–15, 1999.

[93] Salychev, O. S., Bykovsky, A. V., Voronov, V. V., Schwarz, K. P., Liu, Z., Wei, M., Panenka, J. (1994). Determination of Gravity and Deflections of the Vertical for Geophysical Applications using the ITC-2 Platform. International Symposium on Kinematic Systems in Geodesy, Geomatics and Navigation, Banff, Canada, August 30 – September 2, pp. 521–529

[94] Salychev, O. S., Schwarz, K. P. (1995). Airborne Gravimetric Results Obtained with the ITC-2 Inertial Platform System. Airborne Gravimetry, IAG Symposia G4, IUGG XXI General Assembly, Boulder, Colorado, pp. 125–142

[95] Salychev, O. S. (1998). Inertial Systems in Navigation and Geophysics (chapter 10). Bauman MSTU Press, Moscow, Russia.

[96] Schwarz, K. P. (1985). A Unified Approach to Post-mission Processing of Inertial Data. Bulletin Géodésique, 59:33–54

[97] Schwarz, K. P. (1987). Approaches to Kinematic Geodesy. In: Geodetic Theory and Methodology. Publ. N.60006. Department of Surveying Engineering, University of Calgary.

[98] Schwarz, K. P., Cannon, M. E., Wong, R. V. C. (1989). A Comparison of GPS Kinematic Models for the Determination of Position and Velocity along a Trajectory. Manuscripta Geodaetica, 14:345–353

[99] Schwarz, K. P., Sideris, M., Forsberg, R. (1990). The Use of FFT Techniques in Physical Geodesy. Geophys. J. Int. 100:485–514

[100] Schwarz, K. P., Wei, M. (1990). A framework for modelling the gravity vector by kinematic measurements. Bulletin Géodésique, 64(4):331–346

[101] Schwarz, K. P., Lachapelle, G. (1991). Kinematic Systems in Geodesy, Surveying, and Remote Sensing. IAG Symposia Series 107: Kinematic Systems in Geodesy, Surveying and Remote Sensing.

[102] Schwarz, K. P., Colombo, O., Hein, G., Knickmeyer, E. T. (1991). Requirements of Airborne Vector Gravimetry. IAG Symposia G3 "From Mars to Greenland: Charting Gravity with Space and Airborne Instruments", pp. 273–283

[103] Schwarz, K. P., Li, Y. C., Wei, M. (1994). The Spectral Window for Airborne Gravity and Geoid Determination. International Symposium on Kinematic Systems in Geodesy, Geomatics and Navigation, Banff, Canada, August 30 – September 2, pp. 445–456

[104] Schwarz, K. P., Li, Y. C. (1995). What can airborne gravimetry contribute to geoid determination? Airborne Gravimetry, IAG Symposia G4, IUGG XXI General Assembly, Boulder, Colorado, pp. 143–152

[105] Schwarz, K. P., Wei, M. (1995). Inertial Geodesy and INS/GPS Integration (partial lecture notes for ENGO623). Department of Geomatics Engineering, University of Calgary.

[106] Schwarz, K. P., Wei, M. (1995). Some unsolved problems in airborne gravimetry. IAG Symposia Series 113: Gravity and Geoid, pp. 131–150

[107] Schwarz, K. P., Li, Y. C. (1996). What can airborne gravimetry contribute to geoid determination? Journal of Geophysical Research, 101(B8):17873–17882

[108] Schwarz, K. P. (1996). Airborne gravimetry — an assessment of the current state and future potential of the technology. International Symposium Geoinformatics'96, Wuhan, PRC, October 16–19,1996, pp. 367–376

[109] Schwarz, K. P., Wei, M. (1998). Flight test results from a strapdown airborne gravity system. Journal of Geodesy, 72:323–332

[110] Schwarz, K. P. (ed.). Geodesy Beyond 2000. The Challenges of the First Decade. International Association of Geodesy Symposia, Vol.121, Springer, 2000.

[111] Schwarz, K. P., Li, Y. C. (2000). How well can the gravimetric geoid be determined by airborne gravity? IAG Symposia Series 123: Vistas for geodesy in the new millenium.

[112] Serpas,J.G., Jekeli,C. (2005). Local geoid determination from airborne gravimetry. Journal of Geodesy, 78:577–587

[113] Tapley, B., Reigber, C., Melbourne, W. (1997). Gravity Recovery And Climate Experiment (GRACE) mission. AGU Spring Meeting, Baltimore.

[114] Termens, A., Colomina, I. (2003). Sobre la corrección de errores sistemáticos en gravimetría aerotransportada. 5. Geomatics Week, Barcelona.

[115] Thompson, L. G. D., LaCoste, L. J. B. (1960). Aerial Gravity Measurements. Journal of Geophysical Research, 65(1):305–322

[116] Timmen, L., Bastos, L., Forsberg, R., Gidskehaug, A., Meyer, U. (1999). Airborne Gravity Surveying for Oceanography, Geology and Geodesy — the Experiences from AGMASCO. IAG General Assembly, July 19–30 1999, Birmingham, UK. IAG Symposia Series 121: Geodesy Beyond 2000, pp. 118–123

[117] Tomé, P. (2002). Integration of Inertial and Satellite Navigation Systems for Aircraft Attitude Determination. Ph.D. Thesis. Department Applied Mathematics. Faculty of Sciences. University of Oporto.

[118] Torge, W. (1989). Gravimetry. Berlin; New York: de Gruyter.

[119] Vasco, D. W. (1989). Inversion of Airborne Gravity Gradient Data, Southwestern Oklahoma. Geophysics, 56, 1.

[120] Verdun, J., Klingelé, E. E., Bayer, R., Cocard, M., Geiger, A., Kahle, H. (2003). The Alpine Swiss French airborne gravity survey. Geoph. J. Int., 152:8–19

[121] Wang, J. (1997). Gravity Recovery by LN-93 Strapdown Airborne Gravity System — A Comparison of DifferentGravimetry Approaches Based on Simulation. Report No. 439, Department of Geodetic Science and Surveying, Ohio State University, Columbus.

[122] Wang, J., Jekeli, C. (1998). Stochastic Model Versus Deterministic Model in INS/GPS Positioning. ISPRS, Commission III Symposium, 6–10 July, Columbus Ohio, USA.

[123] Wei, M., Schwarz, K. P. (1990). A strapdown inertial algorithm using an Earth-fixed cartesian frame. Navigation, 37(2):153–167

[124] Wei, M., Schwarz, K. P. (1994). An Error Analysis of Airborne Vector Gravimetry. International Symposium on Kinematic Systems in Geodesy, Geomatics and Navigation, Banff, Canada, August 30 – September 2, pp. 509–520

[125] Wei, M., Schwarz, K. P. (1995). Analysis of GPS-derived Acceleration from Airborne Tests. Airborne Gravimetry, IAG Symposia G4, IUGG XXI General Assembly, Boulder, Colorado, pp. 175–188

[126] Wei, M., Schwarz, K. P. (1996). Comparison of Different Approaches to Airborne Gravimetry by Strapdown INS/DGPS. IAG Symposia Series 117: Gravity, Geoid and Marine Geodesy, pp. 155–162

[127] Wei, M., Schwarz, K. P. (1998). Flight test results from a strapdown airborne gravity system. Journal of Geodesy, 72:323–332

[128] Wei, M., Tennant, J. K. (2000). STAR-3i Airborne Gravity and Geoid Mapping System. IAG Symposia Series 123: Vistas for geodesy in the new millenium.

A Notation

Here, mathematical notation and coordinate frames used in the dissertation are introduced:

- Vectors are represented by letters that are lowercase and underlined. The most common uses of vectors herein are for the representation of position, velocity, angular velocity and gravity anomaly.
- A superscript is used to indicate the coordinate frame in which the components of a vector are given. For example, the position of an object with respect to the b-frame is given by:

$$\underline{r}^{\mathtt{b}} = \begin{pmatrix} x^{\mathtt{b}} \\ y^{\mathtt{b}} \\ z^{\mathtt{b}} \end{pmatrix}$$

- Matrices are represented by letters that are uppercase and underlined. The most common use of matrices herein is to represent the rotation from one coordinate frame to another, and to represent Jacobian matrices associated to mathematical models.
- Rotation matrices between coordinate systems are defined by a subscript and a superscript denoting the two coordinate systems. For example, the representation of a coordinate in the e-frame — $\underline{r}^{\mathtt{e}}$ — can be computed from its representation in the b-frame — $\underline{r}^{\mathtt{b}}$ — as follows:

$$\underline{r}^{\mathtt{e}} = \underline{R}^{\mathtt{e}}_{\mathtt{b}} \cdot \underline{r}^{\mathtt{b}}$$

- Angular velocity between two coordinate systems may be expressed either by an angular velocity vector (e.g. $\underline{\omega}^{\mathtt{b}}_{\mathtt{ib}}$ describes the rotation between the inertial and body frames expressed in the body frame) or by the corresponding skew-symmetric matrix:

$$\left[\underline{\omega}^{\mathtt{b}}_{\mathtt{ib}}\times\right] = \underline{\Omega}^{\mathtt{b}}_{\mathtt{ib}} = \begin{pmatrix} 0 & -\omega_z & \omega_y \\ \omega_z & 0 & -\omega_x \\ -\omega_y & \omega_x & 0 \end{pmatrix}$$

B A note on reference frames

To describe locations of points on or near Earth's surface, a reference system[1] should be defined. Although one could describe the whereabouts of objects and places using a relational or synthetic database, it is necessary to assign an algebraic reference system if one wants to know more than the location information such as the measure of distance, area, volume and direction. In navigation, it is also necessary to measure the progress and determine the course and destination of a vehicle based on the selected coordinate system.

It should be noted that the term reference system and reference frame do not have the same meaning. The reference system includes the description of the physical theories and their approximations that are used to define the coordinate axes, while frame denotes the accessible realisation of the system through, usually, a set of points whose coordinates are monumented or otherwise observable. A coordinate system is a mathematical parametrisation. The most common coordinate system in use is the Cartesian coordinate system whose axes are mutually orthogonal. To define a Cartesian coordinate system, three elements such as origin, orientation and scale factors should be determined.

There are several reference frames in use in the field of geodesy. Those frames can be divided into global and local frames. While the global Cartesian frames are fixed either to the Earth or the celestial sphere, the local Cartesian frames are defined by local directions; for example north, east and down. The curvilinear coordinate system, defined by the geodetic latitude, longitude and height, is also used for its appropriateness of representing the motion and position on the sphere or ellipsoid. For an inertial navigation system, one has to deal with a couple of more coordinate frames related to the navigation instruments, the platform on which those are installed and the vehicle carrying the platform.

The obvious problem when dealing with several different reference frames is to establish the mutual relationship of a frame to all other frames so that the measurements in a frame can

[1] A *reference system* is a definition. A *reference frame* is a realisation of the definition. A *coordinate system* is a mathematical parametrisation. Derived concepts are *reference coordinate system = reference system + coordinate system*; and *reference coordinate frame = reference frame + coordinate system.*

be transferred to the other frames. This is called reference frame transformations. Before describing the transformations, each coordinate system will be defined.

B.1 Inertial Frame

The inertial frame — noted as i-frame — is non-rotating and non-accelerating with respect to a true inertial frame within the accuracy of the sensors used to define it. For the applications considered in this dissertation, the definition of the i-frame is the following:

- origin: assumed at the center of mass of the Earth,
- x-axis: pointing toward the mean equinoctial colure,
- y-axis: being orthogonal to the two other axes to complete a right-handed frame.
- z-axis: being parallel to the mean spin axis of the Earth,

B.2 Conventional Terrestrial Frame

The Conventional Terrestrial frame is an Earth-centered-Earth-fixed (ECEF) frame, or e-frame, and it is defined as followings:

- origin: at the center of mass of the Earth,
- x-axis: pointing toward the mean meridian of Greenwich,
- y-axis: completing a right-handed orthogonal frame.
- z-axis: parallel to the mean spin axis of the Earth,

Another set of ECEF coordinates being used in geodesy is the conventional geodetic coordinate system. It consists of the curvilinear coordinates latitude and longitude — (φ,λ) — and the normal height (h) of and adopted ellipsoid of revolution. The angles φ and λ determine the horizontal positions and h does the vertical position. With a geocentric ellipsoid, the geodetic coordinate system could be used in place of the Cartesian ECEF coordinate system.

The i-frame and the e-frame differ by a constant angular rotation, equal to the mean rotation of the Earth $\omega_{\mathtt{e}}$, about the common z-axis:

$$\underline{\omega}^{\mathtt{e}}_{\mathtt{ie}} = \begin{pmatrix} 0 \\ 0 \\ \omega_{\mathtt{e}} \end{pmatrix}.$$

The transformation matrix from i-frame to e-frame is simply a rotation about the 3-axis by $\omega_{\mathtt{e}} t$

$$R_{\mathtt{i}}^{\mathtt{e}} = \begin{pmatrix} \cos\omega_{\mathtt{e}} t & \sin\omega_{\mathtt{e}} t & 0 \\ -\sin\omega_{\mathtt{e}} t & \cos\omega_{\mathtt{e}} t & 0 \\ 0 & 0 & 1 \end{pmatrix},$$

where t is time.

B.3 Local-level Frame or Navigation Frame

The frame that is commonly used to describe the navigation of a vehicle is a local coordinate frame (l-frame) or navigation frame (n-frame).

The local system of coordinates may be defined as a set of Cartesian coordinate axes, where the third axis is aligned with the ellipsoidal normal at a point, in the *down* direction, the first axis points due north (parallel to the tangent to the meridian), and the second axis points east. The north-east-down (NED) frame, adopted here and conventionally implemented in the field of inertial navigation, is known as the navigation frame or the n-frame. The origin of the n-frame is local, either on the ellipsoid, or at the location of the navigation system. In this dissertation , we only refer this local or navigation frame as l-frame.

Note that the 3-axis of the l-frame does not pass through the Earth's center of mass. This adds a complication to the transformation of coordinates of points between the l-frame and the e-frame.

It should be noted that this l-frame is not used to represent a vehicle's position because the l-frame itself moves with the vehicle carrying the navigation system. Therefore, only the third component of the coordinate could be non-zero by definition. The advantage of the l-frame is that it provides the local direction of the vehicle motion through north, east and down velocities. Because the inertial sensors are always aligned with the local horizontal and vertical either mechanically or computationally, this frame is the one to which the platform or the sensor frame is directly related.

Because the e-frame and the l-frame are not concentric, the transformation is more or less complicated. The orientation transformation needs two successive rotations; first rotate about the local east axis by the angle $(\pi/2+\phi)$; then rotate about the new 3-axis by the angle $-\lambda$:

$$R_{\mathtt{l}}^{\mathtt{e}} = \begin{pmatrix} -\sin\varphi\cos\lambda & -\sin\lambda & -\cos\varphi\cos\lambda \\ -\sin\varphi\sin\lambda & \cos\lambda & -\cos\varphi\sin\lambda \\ \cos\varphi & 0 & -\sin\varphi \end{pmatrix}$$

B.4 Body Frame

The body frame, or `b`-frame, generally refers to the vehicle itself. Conventionally, the axes are defined along the forward, right, and through-the-floor directions (`Bfrd`).

The transformation between the `b`-frame and `l`-frame is also represented by the three successive rotations: about 1-axis by the negative roll angle , $-\alpha$ (positive if the right wing of the airplane is inclined down); about 2-axis by the negative pitch angle, $-\chi$ (positive if the aircraft point upwards); and about 3-axis by the negative yaw angle, $-\eta$ (clockwise angle respect North):

$$R_{\mathtt{b}}^{\mathtt{l}} = R_3(-\eta) \cdot R_2(-\chi) \cdot R_1(-\alpha).$$

$$R_{\mathtt{b}}^{\mathtt{l}} = \begin{pmatrix} \cos\eta & -\sin\eta & 0 \\ \sin\eta & \cos\eta & 0 \\ 0 & 0 & 1 \end{pmatrix} \cdot \begin{pmatrix} \cos\chi & 0 & \sin\chi \\ 0 & 1 & 0 \\ -\sin\chi & 0 & \cos\chi \end{pmatrix} \cdot \begin{pmatrix} 1 & 0 & 0 \\ 0 & \cos\alpha & -\sin\alpha \\ 0 & \sin\alpha & \cos\alpha \end{pmatrix}$$

And inversely, the angles α, χ and η can be obtained by

$$\begin{aligned} \alpha &= \arctan(R_{\mathtt{b}}^{\mathtt{l}}(3,2)/R_{\mathtt{b}}^{\mathtt{l}}(3,3)) \\ \chi &= \arcsin(-R_{\mathtt{b}}^{\mathtt{l}}(3,1)) \\ \eta &= \arctan(R_{\mathtt{b}}^{\mathtt{l}}(2,1)/R_{\mathtt{b}}^{\mathtt{l}}(1,1)) \end{aligned}$$

C The Earth and its gravity field

The physical surface of the Earth is the border between the solid or fluid masses and the atmosphere. The mathematical figure of the Earth is represented by the geoid, which is defined as a particular level surface of the Earth's gravity field. Under certain assumptions, the ocean surface is part of this level surface. The geoid is used as a fundamental reference for many geodetic measurements. But the geoid has no simple analytical expression due to the irregular change of the Earth's gravity field.

For many practical applications, the geometric figure of the Earth is approximated by a rotational ellipsoid flattened at the poles because of its simple equation. This rotational ellipsoid is called the reference ellipsoid.

Based on the reference ellipsoid a point on and outside the ellipsoid can be determined by the geodetic coordinates $(\lambda, \varphi, h)^T$. The relationship between the geodetic coordinates and the cartesian coordinates in the e-frame, can be obtained using the following transformation formulas

$$\begin{aligned} X^{\mathsf{e}} &= (N+h)\cos\lambda\cos\varphi \\ Y^{\mathsf{e}} &= (N+h)\sin\lambda\cos\varphi \\ Z^{\mathsf{e}} &= ((1-e^2)N+h)\sin\varphi \end{aligned}$$

where $e^2 = b^2/a^2$ and N is the prime (east–west) radius of curvature of the ellipsoid.

The principal radii of curvature, the meridian radius M and the radius of curvature in the prime vertical N are given by

$$\begin{aligned} M &= a\,(1-e^2)\,(1-e^2\sin^2\varphi)^{-3/2} \\ N &= a\,(1-e^2\sin^2\varphi)^{-1/2} \end{aligned}$$

Equation (C) allows us to compute cartesian coordinates $(X^{\mathsf{e}}, Y^{\mathsf{e}}, Z^{\mathsf{e}})^T$ from geodetic coordinates $(\lambda, \varphi, h)^T$.

The inverse procedure for the computation of geodetic coordinates $(\lambda,\varphi,h)^T$ from given cartesian coordinates $(X^{\mathsf{e}},Y^{\mathsf{e}},Z^{\mathsf{e}})^T$ is more complicated because no direct closed form to convert $(X^{\mathsf{e}},Y^{\mathsf{e}},Z^{\mathsf{e}})^T$ to $(\lambda,\varphi,h)^T$ can be used. In [56] an iterative algorithm is discussed.

C.1 `getogc` model

`getogc`:

$$\begin{array}{lcl} R^3 & \longrightarrow & R^3 \\ \underline{lph} & \longmapsto & \underline{XYZ} \end{array}$$

$$\begin{array}{rcl} X^{\mathsf{e}} &=& (N+h)\cos\lambda\cos\varphi \\ Y^{\mathsf{e}} &=& (N+h)\sin\lambda\cos\varphi \\ Z^{\mathsf{e}} &=& ((1-e^2)N+h)\sin\varphi \end{array} \tag{C.1}$$

Concept	#	Notation	Constants
Observables	1	$\underline{XYZ}$	a,e^2
$\underline{XYZ}$	3	$(X^{\mathsf{e}},Y^{\mathsf{e}},Z^{\mathsf{e}})^T$	
Parameter Groups	1	$\underline{lph}$	
$\underline{lph}$	3	$(\lambda,\varphi,h)^T$	

Table C.1: Function `getogc`.

Derivatives

To compute D`getogc`, first we have to compute $\dot{N}$. As N is only a function of φ, then the derivative is:

$$\dot{N} = e^2 N \sin\varphi\cos\varphi(1-e^2\sin^2\varphi)^{-1}$$

Then

$$D\texttt{getogc} = \begin{pmatrix} -Y^{\mathsf{e}} & \left(\dot{N}\cos\varphi-(N+h)\sin\varphi\right)\cos\lambda & \cos\lambda\cos\varphi \\ X^{\mathsf{e}} & \left(\dot{N}\cos\varphi-(N+h)\sin\varphi\right)\sin\lambda & \sin\lambda\cos\varphi \\ 0 & (1-e^2)\dot{N}\sin\varphi+((1-e^2)N+h)\cos\varphi & \sin\varphi \end{pmatrix}$$

C.2 Earth's gravitational and gravity field

Because the vehicle motion is in the gravitational field of the Earth, an inertial sensor measures the difference between the inertially referenced accelerations and the gravitational accelerations. Thus, the Earth's gravitational field and its effect on the inertial sensor has to be known.

C.2.1 Earth's gravitational field

The Earth's gravitational field is usually described by the gravitational potential V of the body of the Earth, expressed by the integral formula

$$V(P) = k \int\int\int \rho(Q)/l \, dv_Q \tag{C.2}$$

where P is the point at which the gravitational potential is computed, Q is the point within the Earth's body, dv_Q is the volume element with the center Q, l is the distance between P and Q, $\rho(Q)$ is the mass density at Q, and k is the Newtonian gravitational constant.

We can also describe the gravitational field using a vector field, i.e. the field of the gravitational vector $\underline{gg}$. The gravitational vector is defined as the gradient of V of the form

$$\underline{gg} = \text{grad}\, V = \frac{\partial V}{\partial r} = \begin{pmatrix} V_X \\ V_Y \\ V_Z \end{pmatrix} \tag{C.3}$$

Its components are the partial derivatives of the gravitational potential V with respect to the coordinates (X,Y,Z) of the reference frame.

The second-order gravitational gradients are defined as second-order partial derivatives of the gravitational potential V with respect to the position vector r and form a symmetric matrix $\underline{G}$ as follows

$$\underline{G}^{\mathsf{e}} = \frac{\partial^2 V}{\partial \underline{r}^{\mathsf{e}} \partial \underline{r}^{\mathsf{e}}} = \begin{pmatrix} V_{XX} & V_{XY} & V_{XZ} \\ V_{YX} & V_{YY} & V_{YZ} \\ V_{ZX} & V_{ZY} & V_{ZZ} \end{pmatrix} \tag{C.4}$$

where the matrix $\underline{G}^{\mathsf{e}}$ is called the gravitational gradient tensor and elements in the bracket are the second-order gravitational gradients with respect to the coordinates (X,Y,Z) of the reference frame.

If the gravitational vector $\underline{gg}$ is given in an arbitrary frame, say the b-frame, the transformation of the gravitational vector $\underline{gg}$ into the e-frame is given by

$$\underline{gg}^{\mathtt{e}} = \underline{R}^{\mathtt{e}}_{\mathtt{b}}\, \underline{gg}^{\mathtt{b}} \tag{C.5}$$

Usually, the gravitational gradients are given in the local-level frame (l). The transformation of the gradient tensor $\bar{G}$ from the l-frame to the e-frame makes use of the following transformation

$$\underline{G}^{\mathtt{e}} = \underline{R}^{\mathtt{e}}_{\mathtt{l}}\, \underline{G}^{\mathtt{l}}\, \underline{R}^{\mathtt{l}}_{\mathtt{e}} \tag{C.6}$$

C.2.2 Time derivative of the gravitational vector

The change of $\underline{gg}^{\mathtt{e}}$ between two points P and Q is obtained by a Taylor expansion which involves the gravitational gradient tensor $\underline{G}^{\mathtt{e}}$ as the linear term in the expansion, i.e.

$$\underline{gg}^{\mathtt{e}}(P) = \underline{gg}^{\mathtt{e}}(Q) + \underline{G}^{\mathtt{e}}\, \Delta\underline{r}^{\mathtt{e}} \tag{C.7}$$

where $\underline{gg}^{\mathtt{e}}(P)$ is the gravitational vector at point P, $\underline{gg}^{\mathtt{e}}(Q)$ is the gravitational vector at point Q, and $\Delta\underline{r}^{\mathtt{e}}$ is the vector of position differences between points P and Q.

The gravitational field discussed above is considered as an invariant field in terms of time. Then, both the gravitational vector $\underline{gg}$ and the gravitational gradient tensor $\underline{G}$ are stationary in terms of time, but are position dependent. Now consider the changes of the gravitational vectors $\underline{gg}$ along the trajectory of a moving vehicle with respect to time.

Since Equation (C.7) gives the change of $\underline{gg}^{\mathtt{e}}$ in terms of the position changes, the time derivatives of $\underline{gg}^{\mathtt{e}}$ in terms of products of the gravitational gradients and vehicle velocities can be obtained by

$$\underline{\dot{gg}}^{\mathtt{e}} = lim_{\substack{\Delta t \to 0 \\ P \to Q}} \left(\underline{gg}^{\mathtt{e}}(P) - \underline{gg}^{\mathtt{e}}(Q)\right) (\Delta t)^{-1} = \underline{G}^{\mathtt{e}}\, \dot{\underline{r}}^{\mathtt{e}} \tag{C.8}$$

Equation (C.8) indicates that the gravitational vector along a trajectory can be obtained by integrating the gravitational gradient tensor $\underline{G}$ along the trajectory.

C.2.3 Earth gravity field

Due to Earth rotation the gravity field is more frequently used. The gravity vector is defined by

$$\underline{g} = \underline{gg} - \Omega_{\mathtt{ie}}\, \Omega_{\mathtt{ie}}\, \underline{r} \tag{C.9}$$

where $\underline{gg}$ is the gravitational vector, $\Omega_{\mathtt{ie}}$ is skew-symmetric matrix of the angular velocity of Earth's rotation $\omega_{\mathtt{ie}}$, $\underline{r}$ is the geocentric position vector and the second term represents the centripetal acceleration vector due to the Earth's rotation.

Usually, the gravity vector is given in the local-level frame and can be expressed as

$$\underline{g}^{\mathtt{l}} = \begin{pmatrix} \gamma\eta \\ \gamma\zeta \\ -(\gamma + \delta g_u) \end{pmatrix} \tag{C.10}$$

where η is the prime deflection of the vertical (positive about east), ζ is the meridian deflection of the vertical (positive about north), γ is normal gravity, and δg_u is the vertical component of the gravity disturbance vector and almost the same as the gravity anomaly Δg.

C.3 Normal gravity formulas

The gravity model used in standard mechanisations of inertial systems is based on an approximation of the actual gravity field of the Earth, the so-called normal gravity field.

The normal gravity field is derived from the gravity potential of the rotational level ellipsoid and can be expressed by simple analytic formulas (see [56] for details).

The normal gravity vector in a reference frame is obtained by differentiating the normal gravity potential with respect to the respective frame. Since the normal gravity vector on the ellipsoid coincides with the ellipsoidal normal, only the third component of the normal gravity vector appears in the $\mathtt{l}$-frame. Normal gravity on the ellipsoid, which is the magnitude of the normal gravity vector, can be computed using a closed formula, the formula of Somigliana, as follows

$$\gamma_0 = \left(a\gamma_e \cos^2\varphi + b\gamma_p \sin^2\varphi\right) \cdot \left(a^2\cos^2\varphi + b^2\sin^2\varphi\right)^{-1/2} \tag{C.11}$$

where a and b are the major and minor semi-axes of the ellipsoid; γ_e and γ_p are normal gravity at the equator and the pole, respectively; and φ is the geodetic latitude.

This formula is not well suited for high speed computations and it is therefore rewritten as

$$\gamma_0 = \gamma_e\left(1 + k\sin^2\varphi\right)\left(1 - e^2\sin^2\varphi\right)^{-1/2} \tag{C.12}$$

where e is the first eccentricity of the ellipsoid and

$$k = \frac{b\gamma_p}{a\gamma_e} - 1$$

By expanding Equation (C.11) into a power series with respect to e^2 and truncating it after the third term, a formula more convenient for numerical computations is obtained:

$$\gamma_0 = a_1 \left(1 + a_2 \sin^2 \varphi + a_3 \sin^4 \varphi\right) \tag{C.13}$$

The normal gravity γ outside the ellipsoid can also be computed using a Taylor series expansion with respect to the ellipsoidal height h. The Equation (C.13) can be extended by adding terms which are linear and quadratic in height, i.e.

$$\gamma(\varphi, h) = a_1 \left(1 + a_2 \sin^2 \varphi + a_3 \sin^4 \varphi\right) + \left(a_4 + a_5 \sin^2 \varphi\right) h + a_6 h^2 \tag{C.14}$$

where h is the height above the ellipsoid, for details see again [56]. The coefficients in Equation (C.14) for the GRS80 are

$$\begin{array}{lcrl} a_1 & = & 9.7803267715 & m/s^2 \\ a_2 & = & 0.0052790414 & m/s^2 \\ a_3 & = & 0.0000232718 & m/s^2 \\ a_4 & = & -0.0000030876910891 & /s^2 \\ a_5 & = & 0.0000000043977311 & /s^2 \\ a_6 & = & 0.0000000000007211 & /(ms^2) \end{array} \tag{C.15}$$

When the earth-fixed Cartesian frame — e-frame — is used as reference frame for the strapdown inertial mechanisations, the normal gravity vector γ is required to be given in the e-frame. The derivation of accurate and efficient formulas for normal gravity in the e-frame is obviously more involved because none of the vector elements will be equal to zero and no closed expressions can be obtained. After some additional operations, the normal gravity vector in the e-frame is obtained as

$$\underline{\gamma}^{\mathsf{e}} = \underline{R}_{\mathsf{l}}^{\mathsf{e}} \cdot \underline{\gamma}^{\mathsf{l}} = \begin{pmatrix} -\sin\varphi\cos\lambda & -\sin\lambda & -\cos\varphi\cos\lambda \\ -\sin\varphi\sin\lambda & \cos\lambda & -\cos\varphi\sin\lambda \\ \cos\varphi & 0 & -\sin\varphi \end{pmatrix} \cdot \begin{pmatrix} \gamma_N \\ 0 \\ \gamma_D \end{pmatrix} \tag{C.16}$$

where

- $\underline{R}_{\mathsf{l}}^{\mathsf{e}}$ is the transformation matrix from the l-frame to the e-frame,
- γ_N is the (North) horizontal component of normal gravity given approximately by ([56]):

  $$\gamma_N(\varphi, h) \approx -8.08 \times 10^{-9} h \sin 2\varphi \; [m/s^2].$$

  This formula is accurate to better than 1×10^{-6} m/s^2 at an altitude of 20 km and more accurate at lower altitudes.

- $-\gamma_D \approx \gamma(\varphi, h)$ is computed from Equation (C.14).

Finally, the normal gravity vector in the e-frame has the following expression

$$\underline{\gamma}^{\mathsf{e}} = \begin{pmatrix} -\left(\gamma_N \sin\varphi + \gamma_D \cos\varphi\right)\cos\lambda \\ -\left(\gamma_N \sin\varphi + \gamma_D \cos\varphi\right)\sin\lambda \\ \left(\gamma_N \cos\varphi - \gamma_D \sin\varphi\right) \end{pmatrix} \tag{C.17}$$

C.3.1 gnl model

$$\begin{array}{l}\texttt{gnl}: \\ \quad \begin{array}{ccc} R^3 & \longrightarrow & R^3 \\ \underline{r}^{\texttt{e}} & \longmapsto & \underline{\gamma}^{\texttt{l}} \end{array}\end{array}$$

As it has been defined in Equation (C.16):

$$\underline{\gamma}^{\texttt{l}} = \begin{pmatrix} \gamma_N \\ 0 \\ \gamma_D \end{pmatrix} \tag{C.18}$$

Concept	#	Notation	Constants	Frame
Observables	1	$\underline{\gamma}^{\texttt{l}}$		
$\underline{\gamma}^{\texttt{l}}$	3	$\texttt{gnl}[i]$		$\texttt{l}$
Parameter Groups	1	$\underline{r}^{\texttt{e}}$		
$\underline{r}^{\texttt{e}}$	3	$\texttt{re}[i]$		$\texttt{e}$

Table C.2: Function gnl.

Derivatives

$$D\texttt{gnl} = \begin{pmatrix} D\langle \gamma_N, \texttt{re}[1] \rangle & D\langle \gamma_N, \texttt{re}[2] \rangle & D\langle \gamma_N, \texttt{re}[3] \rangle \\ 0 \quad 0 & 0 & \\ D\langle \gamma_D, \texttt{re}[1] \rangle & D\langle \gamma_D, \texttt{re}[2] \rangle & D\langle \gamma_D, \texttt{re}[3] \rangle \end{pmatrix}$$

To compute $D\texttt{gnl}$, first we compute $D\gamma_N$ and $D\gamma_D$. They are only functions of φ and h (computed using the model gctoge), and $\forall k = 1, \div 3$:

$$\begin{aligned} D\langle \gamma_N, \texttt{re}[k] \rangle &= -16.16 \times 10^{-9} h \cos 2\varphi D\langle \varphi, \texttt{re}[k] \rangle - \\ &- 8.08 \times 10^{-9} \sin 2\varphi D\langle h, \texttt{re}[k] \rangle \end{aligned}$$

$$\begin{aligned} D\langle \gamma_D, \texttt{re}[k] \rangle &= -2a_1 a_2 \sin\varphi\cos\varphi D\langle \varphi, \texttt{re}[k] \rangle - \\ &- 4a_1 a_3 \sin^3\varphi\cos\varphi D\langle \varphi, \texttt{re}[k] \rangle - 2a_5 \sin\varphi\cos\varphi h D\langle \varphi, \texttt{re}[k] \rangle - \\ &- a_4 D\langle h, \texttt{re}[k] \rangle - a_5 \sin^2\varphi D\langle h, \texttt{re}[k] \rangle - 2a_6 h D\langle h, \texttt{re}[k] \rangle \end{aligned}$$

C.3.2 gne model

$$\begin{array}{l} \texttt{gne}: \\ \quad R^3 \longrightarrow R^3 \\ \quad \underline{lph} \longmapsto \underline{\gamma}^{\mathsf{e}} \end{array}$$

$$\begin{array}{lcl} \texttt{gne}[1] & = & -\left(\gamma_N \sin\varphi + \gamma_D \cos\varphi\right)\cos\lambda \\ \texttt{gne}[2] & = & -\left(\gamma_N \sin\varphi + \gamma_D \cos\varphi\right)\sin\lambda \\ \texttt{gne}[3] & = & \gamma_N \cos\varphi - \gamma_D \sin\varphi \end{array} \tag{C.19}$$

where

$$\begin{array}{lcl} \gamma_N & \approx & -8.08\times 10^{-9} h \sin 2\varphi \\ \gamma_D & \approx & -a_1\left(1 + a_2 \sin^2\varphi + a_3 \sin^4\varphi\right) - \left(a_4 + a_5 \sin^2\varphi\right) h - a_6 h^2 \end{array}$$

Concept	#	Notation	Constants
Observables	1	$\underline{\gamma}^{\mathsf{e}}$	$a_i, i = 1 \div 6$
$\underline{\gamma}^{\mathsf{e}}$	3	$\texttt{gne}[i]$	
Parameter Groups	1	$\underline{lph}$	
$\underline{lph}$	3	$(\lambda, \varphi, h)^T$	

Table C.3: Function gne.

Derivatives

$$D\texttt{gne} = \begin{pmatrix} D\langle \texttt{gne}[1], \lambda\rangle & D\langle \texttt{gne}[1], \varphi\rangle & D\langle \texttt{gne}[1], h\rangle \\ D\langle \texttt{gne}[2], \lambda\rangle & D\langle \texttt{gne}[2], \varphi\rangle & D\langle \texttt{gne}[2], h\rangle \\ D\langle \texttt{gne}[3], \lambda\rangle & D\langle \texttt{gne}[3], \varphi\rangle & D\langle \texttt{gne}[3], h\rangle \end{pmatrix}$$

To compute $D\texttt{gne}$, first we compute $D\gamma_N$ and $D\gamma_D$. They are only functions of φ and h:

$$\begin{array}{lcl} D\gamma_N[1] & \approx & 0 \\ D\gamma_N[2] & \approx & -16.16\times 10^{-9} h \cos 2\varphi \\ D\gamma_N[3] & \approx & -8.08\times 10^{-9} \sin 2\varphi \end{array}$$

$$\begin{array}{lcl} D\gamma_D[1] & \approx & 0 \\ D\gamma_D[2] & \approx & -a_1 \sin 2\varphi \left(a_2 + 2a_3 \sin\varphi\right) - 2a_5 h \sin\varphi\cos\varphi \\ D\gamma_D[3] & \approx & -\left(a_4 + a_5 \sin^2\varphi\right) - 2a_6 h \end{array}$$

Then, finally, we have

$$
\begin{aligned}
D\langle \mathrm{gne}[1], \lambda \rangle &= \gamma_N \sin\varphi \sin\lambda + \gamma_D \cos\varphi \sin\lambda \\
D\langle \mathrm{gne}[1], \varphi \rangle &= -D\gamma_N[2] \sin\varphi \cos\lambda - \gamma_N \cos\varphi \cos\lambda - \\
&- D\gamma_D[2] \cos\varphi \cos\lambda + \gamma_D \sin\varphi \cos\lambda \\
D\langle \mathrm{gne}[1], h \rangle &= -D\gamma_N[3] \sin\varphi \cos\lambda - D\gamma_D[3] \cos\varphi \cos\lambda
\end{aligned}
$$

$$
\begin{aligned}
D\langle \mathrm{gne}[2], \lambda \rangle &= -\gamma_N \sin\varphi \cos\lambda - \gamma_D \cos\varphi \cos\lambda \\
D\langle \mathrm{gne}[2], \varphi \rangle &= -D\gamma_N[2] \sin\varphi \sin\lambda - \gamma_N \cos\varphi \sin\lambda - \\
&- D\gamma_D[2] \cos\varphi \sin\lambda + \gamma_D \sin\varphi \sin\lambda \\
D\langle \mathrm{gne}[2], h \rangle &= -D\gamma_N[3] \sin\varphi \sin\lambda - D\gamma_D[3] \cos\varphi \sin\lambda
\end{aligned}
$$

$$
\begin{aligned}
D\langle \mathrm{gne}[3], \lambda \rangle &= 0 \\
D\langle \mathrm{gne}[3], \varphi \rangle &= D\gamma_N[2] \cos\varphi - \gamma_N \sin\varphi - D\gamma_D[2] \sin\varphi - \gamma_D \cos\varphi \\
D\langle \mathrm{gne}[3], h \rangle &= D\gamma_N[3] \cos\varphi - D\gamma_D[3] \sin\varphi
\end{aligned}
$$

C.3.3 gg model

$$\begin{array}{l} \mathrm{gg}: \\ \quad R^3 \longrightarrow R^3 \\ \quad gg \longmapsto \underline{g}^{\mathtt{l}} \end{array}$$

$$\begin{array}{lcl} \mathrm{gg}[1] & = & g\sin\zeta \\ \mathrm{gg}[2] & = & g\sin\eta \\ \mathrm{gg}[3] & = & g\cos\theta \end{array} \tag{C.20}$$

where $\theta = \left(\eta^2+\zeta^2\right)^{\frac{1}{2}}$, $gg = (g,\eta,\zeta)^T$, g is the gravity and (η,ζ) are the deflections of the vertical.

Concept	#	Notation	Constants
Observables	1	$\underline{g}^{\mathtt{l}}$	
$\underline{g}^{\mathtt{l}}$	3	$(\mathrm{gg}[i])$	
Parameter Groups	1	gg	
gg	3	$(g,\eta,\zeta)^T$	

Table C.4: Function gg.

Derivatives

$$D\mathrm{gg} = \begin{pmatrix} D\langle \mathrm{gg}[1], g\rangle & D\langle \mathrm{gg}[1], \eta\rangle & D\langle \mathrm{gg}[1], \zeta\rangle \\ D\langle \mathrm{gg}[2], g\rangle & D\langle \mathrm{gg}[2], \eta\rangle & D\langle \mathrm{gg}[2], \zeta\rangle \\ D\langle \mathrm{gg}[3], g\rangle & D\langle \mathrm{gg}[3], \eta\rangle & D\langle \mathrm{gg}[3], \zeta\rangle \end{pmatrix}$$

$$= \begin{pmatrix} \sin\zeta & 0 & g\cos\zeta \\ \sin\eta & g\cos\eta & 0 \\ \cos\theta & -g\theta^{-1}\eta\sin\theta & -g\theta^{-1}\zeta\sin\theta \end{pmatrix}$$

D A note on the differentiation

A discrete-time differentiator operates on a uniformly sample sequence in such a way as to produce a corresponding output sequence that, after suitable band-limiting, approximates the actual continuous-time derivative of the input signal.

According to general bibliography, the frequency response of an ideal uniformly-sampled discrete-time differentiator, $H(e^{j\omega T})$, is given by

$$H(e^{j\omega T}) = j\omega, \tag{D.1}$$

for $0 \leq |\omega| < \omega_s/2$, where ω is the frequency of the spectrum of the signal, $\omega_s \equiv 2\pi/T$ is the sampling frequency, and T is the corresponding sampling period. The task of differentiating a discrete-time signal can therefore be seen as approximating this idealisation and applying it to some signal of interest.

The differentiator discussed in this appendix is a type of FIR filter. Practically, such a filter is applied to a discrete data set, $\underline{x}(nT)$, using a convolution as follows

$$\underline{\dot{x}}(nT) = \sum_{k=0}^{N-1} h(nT)\, \underline{x}(nT - nk), \tag{D.2}$$

where in this case, $\underline{\dot{x}}(nT)$ is the derivative of the input sequence $\underline{x}(nT)$, and $h(nT)$ is the impulse response of the system, having length N.

The relationship between the discrete-time unit impulse response, $h(nT)$, and the frequency response of the discrete-time differentiator, $H(e^{j\omega T})$, is given by the Inverse Fourier Transform. Then, the design of a digital differentiator becomes the problem of designing an impulse response, $h(nT)$, that can be applied to a data using Equation (D.2) and that has a frequency response as close as possible to that in Equation (D.1), within the frequency band of interest.

Consider the first-order difference approximation to the derivative that is given by

$$\underline{\dot{x}}(nT) = T^{-1}\left(\underline{x}(nT) - \underline{x}(nT-T)\right) \tag{D.3}$$

so that the derivative of $\underline{x}$ at time nT is estimated using data at two epochs (times nT and $nT-T$).

Higher order central difference equations are often presented in the literature as an alternative to this simple first-order approximation (because it is intuitive that using more data on either side of time nT will provide a better estimate of the derivative). These higher order derivations are also based on Taylor series.

In the network approach used in all this dissertation, this simple approximation is considered, in order to simplify the associated mathematical models.

The expression of this basic equation as FIR filter is relatively straightforward and useful; the impulse response corresponding to the first-order differentiators given above is represented as a vector as follows

$$\underline{h} = \begin{bmatrix} 1 & -1 \end{bmatrix}^T \tag{D.4}$$

D.1 deriva1 model

$$\begin{array}{l} \underline{\texttt{deriva1}}: \\ \quad R^m \times R^m \longrightarrow R^m \\ \quad \underline{x}[n-1], \underline{x}[n] \longmapsto \underline{\dot{x}}[n] \end{array}$$

$$\underline{\dot{x}}[n] = \Delta t \begin{pmatrix} -1_m & 1_m \end{pmatrix} \begin{pmatrix} \underline{x}[n-1] \\ \underline{x}[n] \end{pmatrix} \tag{D.5}$$

where

$$\Delta t = t[n] - t[n-1]$$

Derivatives

$$D\underline{\texttt{deriva1}} = (\Delta t)^{-1} \left(\begin{array}{c|c} -1_m & 1_m \end{array} \right)$$

Concept	#	Notation	Constants
Observables	1	$\underline{\dot{x}}[n]$	
$\underline{\dot{x}}[n]$	m	$\dot{x}[n\|i]$	
Parameter Groups	2	$\underline{x}[n-1]$,$\underline{x}[n+1]$	
$\underline{x}[n-1]$	m	$x[n-1\|i]$	$t[n-1]$
$\underline{x}[n]$	m	$x[n\|i]$	$t[n]$

Table D.1: Function `deriva1`.

E A note on the interpolation

In this section, the interpolation of data has been considered. Starting with the lineal interpolation, in a general form, let's be $(\underline{x}[n])_{n=1}^{N}$ and $(t[n])_{n=1}^{N}$, for each time T the value of $\underline{x}[T]$ has the following form:

$$\underline{x}[T] = I1[n] \cdot \underline{x}[n] + I2[n] \cdot \underline{x}[n+1] \tag{E.1}$$

where

$$\begin{aligned}
&I1[n] = (\Delta t)^{-1} \cdot (t[n+1] - T)\,, \\
&I2[n] = (\Delta t)^{-1} \cdot (T - t[n]) \text{ and} \\
&\Delta t = t[n+1] - t[n].
\end{aligned}$$

E.1 $\underline{\texttt{intp}}$ model

$$\begin{array}{lll}
\underline{\texttt{intp}} & : & \\
R^m \times R^m & \longrightarrow & R^m \\
\underline{x}[n], \underline{x}[n+1] & \longmapsto & \underline{x}[T]
\end{array}$$

The associated Equation (E.1) is represented by

$$\underline{x}[T] = \begin{pmatrix} I1[n] \cdot 1_m & I2[n] \cdot 1_m \end{pmatrix} \cdot \begin{pmatrix} \underline{x}[n] \\ \underline{x}[n+1] \end{pmatrix} \tag{E.2}$$

The derivatives matrices respect every parameter group are

$$D\underline{\texttt{intp}} = \left(\begin{array}{c|c} I1[n] \cdot 1_m & I2[n] \cdot 1_m \end{array} \right) \tag{E.3}$$

F Rotation $\underline{\mathtt{rbe}}$-matrix

The differential equations describing continuous change in the transformation from the body frame (b-frame) to a computational frame (e-frame) is given in

$$\underline{\dot{R}}_{\mathtt{b}}^{\mathtt{e}} = \underline{R}_{\mathtt{b}}^{\mathtt{e}}\,\underline{\Omega}_{\mathtt{eb}}^{\mathtt{b}} = \underline{R}_{\mathtt{b}}^{\mathtt{e}}\left[\underline{\omega}_{\mathtt{eb}}^{\mathtt{b}}\times\right] \tag{F.1}$$

For the general case, this equation will be written without the superscript and the subscript, i.e.

$$\underline{\dot{R}} = \underline{R}\,\underline{\Omega} = \underline{R}\left[\underline{\omega}\times\right] \tag{F.2}$$

where $\underline{R}$ represents the transformation from the body frame to the computational frame and $\underline{\Omega}$ is the skew-symmetric matrix of angular velocities $\underline{\omega} = (\omega_x, \omega_y, \omega_z)^T$ of the body frame with respect to the computational frame.

To obtain the transformation matrix from the angular velocity data the nine differential equations in (F.2) must be solved.

F.1 Quaternion equation

The most popular method to obtain the coordinate transformation matrix is the quaternion approach. By Euler's theorem, rotation of a rigid body, represented by the body frame, with respect to a reference frame, represented by the computational frame, can be expressed in terms of the rotation angle θ about a fixed axis and the direction cosine of the rotation axis to define the rotation direction. Thus, quaternion parameters — $q = (q_1, q_2, q_3, q_4)^T$ — are introduced to describe the rotation of the body frame with respect to the computational frame

as follows

$$\begin{array}{lcl} q_1 & = & \theta^{-1}\,\theta_x\,\sin\frac{\theta}{2} \\ q_2 & = & \theta^{-1}\,\theta_y\,\sin\frac{\theta}{2} \\ q_3 & = & \theta^{-1}\,\theta_z\,\sin\frac{\theta}{2} \\ q_4 & = & \cos\frac{\theta}{2} \end{array} \tag{F.3}$$

where $\theta = (\theta_x^2 + \theta_y^2 + \theta_z^2)^{1/2}$ is the rotation angle and $\theta^{-1}\,\theta_x$, $\theta^{-1}\,\theta_y$, $\theta^{-1}\,\theta_z$ are the three direction cosines of the rotation axis with respect to the computational frame.

The definition of the quaternion parameters in Equation (F.3) implies that the four quaternion components (q_1, q_2, q_3, q_4) are not independent, because the following equation for the quaternion parameters holds

$$q_1^2 + q_2^2 + q_3^2 + q_4^2 = 1 \tag{F.4}$$

Equation (F.3) indicates that three independent parameters are sufficient to describe rigid body rotation.

The quaternion parameters are also functions of time. The associated differential equations for the quaternion parameters is given by

$$\dot{q} = \frac{1}{2}\,\Omega(\omega)\,q \tag{F.5}$$

where $\Omega(\omega)$ is a skew-symmetric matrix of the form

$$\Omega(\omega) = \begin{pmatrix} 0 & \omega_z & -\omega_y & \omega_x \\ -\omega_z & 0 & \omega_x & \omega_y \\ \omega_y & -\omega_x & 0 & \omega_z \\ -\omega_x & -\omega_y & -\omega_z & 0 \end{pmatrix} = \begin{pmatrix} -\Omega & \omega \\ -\omega^T & 0 \end{pmatrix} \tag{F.6}$$

and $\omega = (\omega_x, \omega_y, \omega_z)$ is the angular velocity of body rotation, Ω is the skew-symmetric form of ω, the same as in Equation (F.2).

F.2 rbe model

Equivalence of the differential equations for the transformation matrix defined by Equation (F.2) and the quaternion parameters defined in Equation (F.5) is proved by Friedland in [41]. Thus, the transformation matrix resulting from Equations (F.2) and (F.5) can be expressed by each other.

The transformation matrix in Equation (F.2) is expressed in terms of the quaternion parameters by

$$\begin{array}{lll} \underline{\mathtt{rbe}} & : & \\ & R^4 & \longrightarrow \quad R^9 \\ & \underline{q} & \longmapsto \quad \underline{R}_{\mathsf{b}}^{\mathsf{e}} \end{array}$$

$$\underline{R}_{\mathsf{b}}^{\mathsf{e}} = \left(\mathtt{rbe}\left[i,j\right]\right) \tag{F.7}$$

$$\begin{aligned}
&\mathtt{rbe}\left[1,1\right] = q_1^2 + q_2^2 - q_3^2 - q_4^2 \\
&\mathtt{rbe}\left[1,2\right] = 2\left(q_2\, q_3 + q_1\, q_4\right) \\
&\mathtt{rbe}\left[1,3\right] = 2\left(q_2\, q_4 - q_1\, q_3\right) \\
&\\
&\mathtt{rbe}\left[2,1\right] = 2\left(q_2\, q_3 - q_1\, q_4\right) \\
&\mathtt{rbe}\left[2,2\right] = q_1^2 - q_2^2 + q_3^2 - q_4^2 \\
&\mathtt{rbe}\left[2,3\right] = 2\left(q_3\, q_4 + q_1\, q_2\right) \\
&\\
&\mathtt{rbe}\left[3,1\right] = 2\left(q_2\, q_4 + q_1\, q_3\right) \\
&\mathtt{rbe}\left[3,2\right] = 2\left(q_3\, q_4 - q_1\, q_2\right) \\
&\mathtt{rbe}\left[3,3\right] = q_1^2 - q_2^2 - q_3^2 + q_4^2
\end{aligned}$$

Concept	#	Notation	Constants
Observables	1	$\underline{R}_{\mathsf{b}}^{\mathsf{e}}$	
$\underline{R}_{\mathsf{b}}^{\mathsf{e}}$	9	$\left(\mathtt{rbe}\left[i,j\right]\right)_{i,j=1\div3}$	
Parameter Groups	1	$\underline{q}$	
$\underline{q}$	4	q_i	t

Table F.1: Function $\underline{\mathtt{rbe}}$.

On the other hand, if the transformation matrix is known, the quaternion parameters can be obtained from

$$\begin{aligned}
q_1 &= \tfrac{1}{2}\left(1 + \mathtt{rbe}\left[1,1\right] + \mathtt{rbe}\left[2,2\right] + \mathtt{rbe}\left[3,3\right]\right)^{1/2} \\
q_2 &= \left(4q_1\right)^{-1}\left(\mathtt{rbe}\left[2,3\right] - \mathtt{rbe}\left[3,2\right]\right) \\
q_3 &= \left(4q_1\right)^{-1}\left(\mathtt{rbe}\left[1,3\right] - \mathtt{rbe}\left[3,1\right]\right) \\
q_4 &= \left(4q_1\right)^{-1}\left(\mathtt{rbe}\left[1,2\right] - \mathtt{rbe}\left[2,1\right]\right)
\end{aligned} \tag{F.8}$$

Derivatives

The derivatives matrices associated to Equation (F.8) respect every quaternion component are

$$D\left\langle \underline{\underline{R}}_{\mathsf{b}}^{\mathsf{e}}, q_1 \right\rangle = 2\begin{pmatrix} q_1 & q_4 & -q_3 \\ -q_4 & q_1 & q_2 \\ q_3 & -q_2 & q_1 \end{pmatrix}$$

$$D\left\langle \underline{\underline{R}}_{\mathsf{b}}^{\mathsf{e}}, q_2 \right\rangle = 2\begin{pmatrix} q_2 & q_3 & q_4 \\ q_3 & -q_2 & q_1 \\ q_4 & -q_1 & -q_2 \end{pmatrix}$$

$$D\left\langle \underline{\underline{R}}_{\mathsf{b}}^{\mathsf{e}}, q_3 \right\rangle = 2\begin{pmatrix} -q_3 & q_2 & -q_1 \\ q_2 & q_3 & q_4 \\ q_1 & q_4 & -q_3 \end{pmatrix}$$

$$D\left\langle \underline{\underline{R}}_{\mathsf{b}}^{\mathsf{e}}, q_4 \right\rangle = 2\begin{pmatrix} -q_4 & q_1 & q_2 \\ -q_1 & -q_4 & q_3 \\ q_2 & q_3 & q_4 \end{pmatrix}$$

G $\underline{\texttt{mq}}$-MATRIX

It has been note in Appendix F.1 that quaternion parameters are also functions of time and the associated differential equations for quaternion is given by

$$\underline{\dot{q}} = \frac{1}{2}\,\underline{\Omega}(\underline{\omega})\,\underline{q} \tag{G.1}$$

Then

$$\begin{aligned}
\underline{\Omega}(\underline{\omega})\,\underline{q} &= \begin{pmatrix} 0 & \omega_z & -\omega_y & \omega_x \\ -\omega_z & 0 & \omega_x & \omega_y \\ \omega_y & -\omega_x & 0 & \omega_z \\ -\omega_x & -\omega_y & -\omega_z & 0 \end{pmatrix} \begin{pmatrix} q[1] \\ q[2] \\ q[3] \\ q[4] \end{pmatrix} \\
&= \begin{pmatrix} q[4] & -q[3] & q[2] \\ q[3] & q[4] & -q[1] \\ -q[2] & q[1] & q[4] \\ -q[1] & -q[2] & -q[3] \end{pmatrix} \begin{pmatrix} \omega_x \\ \omega_y \\ \omega_z \end{pmatrix} \\
&= \underline{M}_{\underline{q}}\,\underline{\omega}
\end{aligned}$$

where $\underline{M}_{\underline{q}}$ matrix satisfies

$$\underline{M}_{\underline{q}}^{T}\,\underline{M}_{\underline{q}} = 1_3 \tag{G.2}$$

G.1 $\underline{\texttt{mq}}$ model

$\underline{\texttt{mq}}$:

$$\begin{array}{ccc} R^4 & \longrightarrow & R^{12} \\ \underline{q} & \longmapsto & \underline{M}_{\underline{q}} \end{array}$$

$$\underline{\underline{M}}_{\underline{q}} = \left(\texttt{mq}[i,j]\right) = \begin{pmatrix} q[4] & -q[3] & q[2] \\ q[3] & q[4] & -q[1] \\ -q[2] & q[1] & q[4] \\ -q[1] & -q[2] & -q[3] \end{pmatrix} \tag{G.3}$$

Concept	#	Notation	Constants
Observables	1	$\underline{\underline{M}}_{\underline{q}}$	
$\underline{\underline{M}}_{\underline{q}}$	12	$(\texttt{mq}[i,j])_{i=1\div4,j=1\div3}$	
Parameter Groups	1	$\underline{q}$	
$\underline{q}$	4	$q[i]$	t

Table G.1: Function $\underline{\texttt{mq}}$.

Derivatives

$$D\left\langle \underline{\underline{M}}_{\underline{q}}, q_1 \right\rangle = \begin{pmatrix} 0 & 0 & 0 \\ 0 & 1 & -1 \\ 0 & 0 & 0 \\ -1 & 0 & 0 \end{pmatrix}$$

$$D\left\langle \underline{\underline{M}}_{\underline{q}}, q_2 \right\rangle = \begin{pmatrix} 0 & 0 & 1 \\ 0 & 0 & 0 \\ -1 & 0 & 0 \\ 0 & -1 & 0 \end{pmatrix}$$

$$D\left\langle \underline{\underline{M}}_{\underline{q}}, q_3 \right\rangle = \begin{pmatrix} 0 & -1 & 0 \\ 1 & 0 & 0 \\ 0 & 0 & 0 \\ 0 & 0 & -1 \end{pmatrix}$$

$$D\left\langle \underline{\underline{M}}_{\underline{q}}, q_4 \right\rangle = \begin{pmatrix} 1 & 0 & 0 \\ 0 & 1 & 0 \\ 0 & 0 & 1 \\ 0 & 0 & 0 \end{pmatrix}$$

H INS/GNSS general formulas

GNSS (now GPS) and INS are integrated primarily for applications in positioning and navigation because of their complementary error characteristics and consequent mutual aiding abilities. There is another type of integration that has attracted the geodetic and geophysical communities in their efforts to measure the gravity field. It is based directly on Newton's second law of motion

$$\underline{g}^{\mathtt{i}} = \ddot{\underline{x}}^{\mathtt{i}} - \underline{a}^{\mathtt{i}} \tag{H.1}$$

where $\ddot{\underline{x}}^{\mathtt{i}}$ is obtained from GNSS and $\underline{a}^{\mathtt{i}}$ from INS.

Gravitational vector is the difference between the total acceleration (as determined kinematically by differentiating GNSS-derived positions) and the specific force (as measured by an accelerometer).

In fact, this is not an integration or blending of GNSS and INS, but a collocation of two distinct sensors whose functional dissimilarity is the essence of the combination that, at the same time, suffers from their contrasting error characteristics. That is, since neither system aids the other, their error combine.

We know that INS errors accumulate with time and thus are significant primarily in the long term. Assuming GNSS position errors are mostly white, the corresponding errors in the derived acceleration are large at high frequencies, or in the short term. Consequently, there is only a potentially small window within which the gravitational signal may be discerned. The window depends also on the speed of the vehicle and moves to the right relative to the gravity signal with decreasing speed.

The acceleration (specific force) of the platform is taken from the output of the INS. The kinematic acceleration must be calculated independently by numerical differentiation with respect to time of positions determined by GNSS. Subsequently, gravitational components are estimated from the difference of these two types of accelerations.

One aspect of vector gravimetry is the strong coupling of uncompensated gyro errors into the horizontal acceleration components, but there is no inherent dependence on a stochastic interpretation or modelling of the gravity disturbance vector.

In terms of the specific force, $\underline{f}^{\mathtt{b}}$, in the sensor frame and the kinematic acceleration, $\underline{\ddot{x}}^{\mathtt{i}}$, the gravitation vector is expressed in the e-frame as follows:

$$\underline{g}^{\mathtt{e}} = \underline{R}^{\mathtt{e}}_{\mathtt{i}} \left(\underline{\ddot{x}}^{\mathtt{i}} - \underline{R}^{\mathtt{i}}_{\mathtt{b}} \, \underline{f}^{\mathtt{b}} \right) \tag{H.2}$$

The gravity disturbance vector is obtained by removing from $\underline{g}^{\mathtt{e}}$ the normal gravity vector corrected for Earth's centrifugal acceleration:

$$\begin{aligned} \delta \underline{g}^{\mathtt{e}} &= \underline{g}^{\mathtt{e}} - \underline{\gamma}^{\mathtt{e}} = \underline{g}^{\mathtt{e}} - \underline{\Omega}^{\mathtt{e}}_{\mathtt{ie}} \, \underline{\Omega}^{\mathtt{e}}_{\mathtt{ie}} \, \underline{x}^{\mathtt{e}} - \underline{\gamma}^{\mathtt{e}} = \\ &= \underline{R}^{\mathtt{e}}_{\mathtt{i}} \left(\underline{\ddot{x}}^{\mathtt{i}} - \underline{R}^{\mathtt{i}}_{\mathtt{b}} \, \underline{f}^{\mathtt{b}} \right) - \left(\underline{\gamma}^{\mathtt{e}} + \underline{R}^{\mathtt{e}}_{\mathtt{i}} \, \underline{\Omega}^{\mathtt{i}}_{\mathtt{ie}} \, \underline{\Omega}^{\mathtt{i}}_{\mathtt{ie}} \, \underline{x}^{\mathtt{i}} \right) \end{aligned}$$

where $\underline{\Omega}^{\mathtt{e}}_{\mathtt{ie}} = \underline{R}^{\mathtt{e}}_{\mathtt{i}} \, \underline{\Omega}^{\mathtt{i}}_{\mathtt{ie}} \, \underline{R}^{\mathtt{i}}_{\mathtt{e}}$ and all quantities of the right side are measured or computed.

We remark that gyro errors here will affect the computation of $\underline{R}^{\mathtt{i}}_{\mathtt{b}} \, \underline{f}^{\mathtt{b}}$.

If we want to use the l-frame form, it should be noted that the transformation matrix $\underline{R}^{\mathtt{l}}_{\mathtt{i}} = \underline{R}^{\mathtt{l}}_{\mathtt{e}} \, \underline{R}^{\mathtt{e}}_{\mathtt{i}}$ is readily calculated from the position of the vehicle using the transformation from cartesian Earth-fixed to geodetic coordinates. An error in these coordinates represents a misregistration error of the gravity disturbance vector.

All positioning requirements for registration of computed and estimated quantities are easily achieved with GPS (or GNSS).

What demands much more precision, however, is the position $\underline{x}^{\mathtt{i}}$ that must be differentiated to obtain kinematic acceleration $\underline{\ddot{x}}^{\mathtt{i}}$.

It may be desirable or even necessary to estimate the major errors associated with the INS. A Kalman filter can be formulated very simply in which the kinematic acceleration from GPS serves as external update. The error states of the system are now limited to the INS error parameters and the orientation errors, which link to the gyro and accelerometer errors, and one may include the gravity disturbance in the state vector.

In all the bibliography consulted note that for illustrative purposes, they restrict the sensor errors to biases and accelerometer scale factors errors; however, in actual situations, a different set of parameters may be chosen depending on their estimability.

The coordinate errors further fall into two categories: associated with control points coordinates, and without any external control.

It is assumed that the remaining systematic error parameters, though stochastic, do not behave as stochastic processes, since only a single adjustment will be performed. As such, the remaining errors are essentially empirical in nature, being represented by simple functions thought to describe their variation along the traverse.

A typical set of systematic error parameters may be based on gyro drift biases and initial velocity errors.

The most rigorous and straightforward approach is to estimate the control point coordinates and system parameter errors for all traverses simultaneously using observations of all control point coordinates in the network.

	GPS	INS
meas. principle	dist. from time delays	inertial accel.
system operation	reliance on space segment	autonomous
output variables	position, time	position, orientation
long-wave. errors	low	high
short-wave. errors	high	low
data rate	low (1 Hz)	high (≥ 25 Hz)
instrument cost	low	high

Table H.1: Characteristics of GPS versus INS.

From the geodetic point of view, we may consider INS as aiding GPS positioning, both as an interpolator and as a stopgap device. In addition, because of the orientation output from an INS, the possibility exists to determine the complete rotational motion of the vehicle.

The only drawback is the cost of the INS that ultimately is a function of the required accuracy.

Geodetic applications of the integrated INS/GNSS for enhanced positioning capability have focused on the mobile mapping system and similar systems that perform remote sensing and land data acquisition through multispectral imaging.

In geodetic application, we are less concerned with real-time kinematic positioning and usually are able to integrate systems only off-the-shelf, that is, without significant hardware coupling between them. Furthermore, most applications are in a dynamically benign environment and it is enough to concentrate on integrating the data processing algorithms.

H.1 Detailed equations in the e-frame

We start with

$$\underline{x}^{\mathsf{e}} = \underline{r}^{\mathsf{e}} + \underline{R}^{\mathsf{e}}_{\mathsf{b}}\, \underline{a}^{\mathsf{b}} \tag{H.3}$$

where $\underline{x}^{\mathtt{e}}$ is the GNSS antenna position in e-frame (earth frame), $\underline{r}^{\mathtt{e}}$ is the IMU position in e-frame and $\underline{a}^{\mathtt{b}}$ is the offset antenna between IMU and GNSS in b-frame (body frame).

We know that

$$\underline{a}^{\mathtt{e}} = \underline{x}^{\mathtt{e}} - \underline{r}^{\mathtt{e}} \tag{H.4}$$

and if they are combined, the following equation results

$$\underline{a}^{\mathtt{e}} = \underline{R}^{\mathtt{e}}_{\mathtt{b}}\, \underline{a}^{\mathtt{b}} \tag{H.5}$$

We know that

$$\underline{\Omega}^{\mathtt{b}}_{\mathtt{eb}} = \underline{\Omega}^{\mathtt{b}}_{\mathtt{ei}} + \underline{\Omega}^{\mathtt{b}}_{\mathtt{ib}} = \underline{\Omega}^{\mathtt{b}}_{\mathtt{ib}} - \underline{\Omega}^{\mathtt{b}}_{\mathtt{ie}} = \underline{\Omega}^{\mathtt{b}}_{\mathtt{ib}} - \underline{R}^{\mathtt{b}}_{\mathtt{e}}\, \underline{\Omega}^{\mathtt{e}}_{\mathtt{ie}}\, \underline{R}^{\mathtt{e}}_{\mathtt{b}} \tag{H.6}$$

where $\underline{\Omega}^{\mathtt{b}}_{\mathtt{ib}}$ is measured, $\underline{\Omega}^{\mathtt{e}}_{\mathtt{ie}}$ is known, and $\underline{R}^{\mathtt{b}}_{\mathtt{e}}$ and $\underline{R}^{\mathtt{e}}_{\mathtt{b}}$ are computed.

So, we have

$$\underline{\dot{\Omega}}^{\mathtt{b}}_{\mathtt{eb}} = \underline{\dot{\Omega}}^{\mathtt{b}}_{\mathtt{ib}} - \underline{\dot{R}}^{\mathtt{b}}_{\mathtt{e}}\, \underline{\Omega}^{\mathtt{e}}_{\mathtt{ie}}\, \underline{R}^{\mathtt{e}}_{\mathtt{b}} - \underline{R}^{\mathtt{b}}_{\mathtt{e}}\, \underline{\dot{\Omega}}^{\mathtt{e}}_{\mathtt{ie}}\, \underline{R}^{\mathtt{e}}_{\mathtt{b}} - \underline{R}^{\mathtt{b}}_{\mathtt{e}}\, \underline{\Omega}^{\mathtt{e}}_{\mathtt{ie}}\, \underline{\dot{R}}^{\mathtt{e}}_{\mathtt{b}} \tag{H.7}$$

and

$$\underline{\dot{R}}^{\mathtt{e}}_{\mathtt{b}} = \underline{R}^{\mathtt{e}}_{\mathtt{b}}\, \underline{\Omega}^{\mathtt{b}}_{\mathtt{eb}} = \underline{R}^{\mathtt{e}}_{\mathtt{b}}\, \underline{\Omega}^{\mathtt{b}}_{\mathtt{ib}} - \underline{\Omega}^{\mathtt{e}}_{\mathtt{ie}}\, \underline{R}^{\mathtt{e}}_{\mathtt{b}} \tag{H.8}$$

$$\underline{\dot{R}}^{\mathtt{b}}_{\mathtt{e}} = \underline{R}^{\mathtt{b}}_{\mathtt{e}}\, \underline{\Omega}^{\mathtt{e}}_{\mathtt{be}} = -\underline{\Omega}^{\mathtt{b}}_{\mathtt{eb}}\, \underline{R}^{\mathtt{b}}_{\mathtt{e}} \tag{H.9}$$

Then applying these relationships to

$$\underline{a}^{\mathtt{e}} = \underline{R}^{\mathtt{e}}_{\mathtt{b}}\, \underline{a}^{\mathtt{b}} \tag{H.10}$$

we obtain

$$\underline{\dot{a}}^{\mathtt{e}} = \underline{\dot{R}}^{\mathtt{e}}_{\mathtt{b}}\, \underline{a}^{\mathtt{b}} + \underline{R}^{\mathtt{e}}_{\mathtt{b}}\, \underline{\dot{a}}^{\mathtt{b}} \tag{H.11}$$

$$\underline{\ddot{a}}^{\mathtt{e}} = \underline{R}^{\mathtt{e}}_{\mathtt{b}} \left(\underline{\ddot{a}}^{\mathtt{b}} + 2\, \underline{\Omega}^{\mathtt{b}}_{\mathtt{eb}}\, \underline{\dot{a}}^{\mathtt{b}} + \underline{\dot{\Omega}}^{\mathtt{b}}_{\mathtt{eb}}\, \underline{a}^{\mathtt{b}} + \underline{\Omega}^{\mathtt{b}}_{\mathtt{eb}}\, \underline{\Omega}^{\mathtt{b}}_{\mathtt{eb}}\, \underline{a}^{\mathtt{b}} \right) \tag{H.12}$$

where $2\, \underline{\Omega}^{\mathtt{b}}_{\mathtt{eb}}\, \underline{\dot{a}}^{\mathtt{b}}$ is the *Coriolis* term; $\underline{\dot{\Omega}}^{\mathtt{b}}_{\mathtt{eb}}\, \underline{a}^{\mathtt{b}}$ is the *tangential* term and $\underline{\Omega}^{\mathtt{b}}_{\mathtt{eb}}\, \underline{\Omega}^{\mathtt{b}}_{\mathtt{eb}}\, \underline{a}^{\mathtt{b}}$ is the *centripetal* part.

We also know from [105, Equation (4–10)] that

$$\underline{g}^{\mathtt{e}} = \underline{\ddot{r}}^{\mathtt{e}} - \underline{R}^{\mathtt{e}}_{\mathtt{b}}\,\underline{f}^{\mathtt{b}} + 2\,\underline{\Omega}^{\mathtt{e}}_{\mathtt{ie}}\,\underline{\dot{r}}^{\mathtt{e}} \tag{H.13}$$

and we have

$$\begin{array}{rcl} \underline{r}^{\mathtt{e}} & = & \underline{x}^{\mathtt{e}} - \underline{a}^{\mathtt{e}} \\ \underline{\dot{r}}^{\mathtt{e}} & = & \underline{x}^{\mathtt{e}} - \underline{\dot{a}}^{\mathtt{e}} \\ \underline{\ddot{r}}^{\mathtt{e}} & = & \underline{\ddot{x}}^{\mathtt{e}} - \underline{\ddot{a}}^{\mathtt{e}} \end{array} \tag{H.14}$$

Then

$$\underline{g}^{\mathtt{e}} = \underline{\ddot{x}}^{\mathtt{e}} - \underline{\ddot{a}}^{\mathtt{e}} - \underline{R}^{\mathtt{e}}_{\mathtt{b}}\,\underline{f}^{\mathtt{b}} + 2\,\underline{\Omega}^{\mathtt{e}}_{\mathtt{ie}}\,\underline{\dot{x}}^{\mathtt{e}} - 2\,\underline{\Omega}^{\mathtt{e}}_{\mathtt{ie}}\,\underline{\dot{a}}^{\mathtt{e}} \tag{H.15}$$

Finally

$$\begin{array}{rcl} \underline{g}^{\mathtt{e}} & = & \underline{\ddot{x}}^{\mathtt{e}} - \underline{R}^{\mathtt{e}}_{\mathtt{b}}\,\underline{f}^{\mathtt{b}} + 2\,\underline{\Omega}^{\mathtt{e}}_{\mathtt{ie}}\,\underline{\dot{x}}^{\mathtt{e}} - \underline{R}^{\mathtt{e}}_{\mathtt{b}}\,\underline{\ddot{a}}^{\mathtt{b}} + 2\,\underline{R}^{\mathtt{e}}_{\mathtt{b}}\,\underline{\Omega}^{\mathtt{b}}_{\mathtt{eb}}\,\underline{\dot{a}}^{\mathtt{b}} + \\ & + & \underline{R}^{\mathtt{e}}_{\mathtt{b}}\,\underline{\dot{\Omega}}^{\mathtt{b}}_{\mathtt{eb}}\,\underline{a}^{\mathtt{b}} + \underline{R}^{\mathtt{e}}_{\mathtt{b}}\,\underline{\Omega}^{\mathtt{b}}_{\mathtt{eb}}\,\underline{\Omega}^{\mathtt{b}}_{\mathtt{eb}}\,\underline{a}^{\mathtt{b}} + 2\,\underline{\Omega}^{\mathtt{e}}_{\mathtt{ie}}\,\underline{\dot{R}}^{\mathtt{e}}_{\mathtt{b}}\,\underline{a}^{\mathtt{b}} + \\ & + & 2\,\underline{\Omega}^{\mathtt{e}}_{\mathtt{ie}}\,\underline{R}^{\mathtt{e}}_{\mathtt{b}}\,\underline{\dot{a}}^{\mathtt{b}} = \\ & = & \underline{\ddot{x}}^{\mathtt{e}} - \underline{R}^{\mathtt{e}}_{\mathtt{b}}\,\underline{f}^{\mathtt{b}} + 2\,\underline{\Omega}^{\mathtt{e}}_{\mathtt{ie}}\,\underline{\dot{x}}^{\mathtt{e}} - \underline{R}^{\mathtt{e}}_{\mathtt{b}}\,\underline{\ddot{a}}^{\mathtt{b}} - 2\,\underline{R}^{\mathtt{e}}_{\mathtt{b}}\,\underline{\Omega}^{\mathtt{b}}_{\mathtt{ib}}\,\underline{\dot{a}}^{\mathtt{b}} - \\ & - & \underline{R}^{\mathtt{e}}_{\mathtt{b}}\,\underline{\Omega}^{\mathtt{b}}_{\mathtt{ib}}\,\underline{\Omega}^{\mathtt{b}}_{\mathtt{ib}}\,\underline{a}^{\mathtt{b}} + \underline{R}^{\mathtt{e}}_{\mathtt{b}}\,\underline{\dot{\Omega}}^{\mathtt{b}}_{\mathtt{ib}}\,\underline{a}^{\mathtt{b}} + \underline{\Omega}^{\mathtt{e}}_{\mathtt{ie}}\,\underline{\Omega}^{\mathtt{e}}_{\mathtt{ie}}\,\underline{R}^{\mathtt{e}}_{\mathtt{b}}\,\underline{a}^{\mathtt{b}} + \\ & + & \underline{\dot{\Omega}}^{\mathtt{e}}_{\mathtt{ie}}\,\underline{R}^{\mathtt{e}}_{\mathtt{b}}\,\underline{a}^{\mathtt{b}} \end{array}$$

It is supposed that $\underline{\Omega}^{\mathtt{e}}_{\mathtt{ie}}$ is constant, so $\underline{\dot{\Omega}}^{\mathtt{e}}_{\mathtt{ie}} = 0$ and then

$$\begin{array}{rcl} \underline{g}^{\mathtt{e}} & = & \underline{\ddot{x}}^{\mathtt{e}} - \underline{R}^{\mathtt{e}}_{\mathtt{b}}\,\underline{f}^{\mathtt{b}} + 2\,\underline{\Omega}^{\mathtt{e}}_{\mathtt{ie}}\,\underline{\dot{x}}^{\mathtt{e}} - \underline{R}^{\mathtt{e}}_{\mathtt{b}}\,\underline{\ddot{a}}^{\mathtt{b}} - 2\,\underline{R}^{\mathtt{e}}_{\mathtt{b}}\,\underline{\Omega}^{\mathtt{b}}_{\mathtt{ib}}\,\underline{\dot{a}}^{\mathtt{b}} + \\ & + & \underline{\Omega}^{\mathtt{e}}_{\mathtt{ie}}\,\underline{\Omega}^{\mathtt{e}}_{\mathtt{ie}}\,\underline{R}^{\mathtt{e}}_{\mathtt{b}}\,\underline{a}^{\mathtt{b}} - \underline{R}^{\mathtt{e}}_{\mathtt{b}}\,\underline{\dot{\Omega}}^{\mathtt{b}}_{\mathtt{ib}}\,\underline{a}^{\mathtt{b}} - \underline{R}^{\mathtt{e}}_{\mathtt{b}}\,\underline{\Omega}^{\mathtt{b}}_{\mathtt{ib}}\,\underline{\Omega}^{\mathtt{b}}_{\mathtt{ib}}\,\underline{a}^{\mathtt{b}} \end{array}$$

By linearisation of this equation and neglecting the second order terms, one can derive an error model as follows:

$$\begin{aligned}
d\underline{g}^{\mathrm{e}} &= d\ddot{\underline{x}}^{\mathrm{e}} - \underline{R}_{\mathrm{b}}^{\mathrm{e}}\, d\underline{f}^{\mathrm{b}} + 2\,\underline{\Omega}_{\mathrm{ie}}^{\mathrm{e}}\, d\dot{\underline{x}}^{\mathrm{e}} + \underline{R}_{\mathrm{b}}^{\mathrm{e}}\,(\underline{a}^{\mathrm{b}})^{*}\, d\dot{\underline{\omega}}_{\mathrm{ib}}^{\mathrm{b}} + \\
&+ \left[2\,\underline{R}_{\mathrm{b}}^{\mathrm{e}}\,(\dot{\underline{a}}^{\mathrm{b}})^{\star} + \underline{R}_{\mathrm{b}}^{\mathrm{e}}\,(\underline{a}^{\mathrm{b}})^{\star}\,\underline{\Omega}_{\mathrm{ib}}^{\mathrm{b}} + 2\,\underline{R}_{\mathrm{b}}^{\mathrm{e}}\,\underline{\Omega}_{\mathrm{ib}}^{\mathrm{b}}\,(\underline{a}^{\mathrm{b}})^{\star}\right] d\underline{\omega}_{\mathrm{ib}}^{\mathrm{b}} - \\
&- \underline{R}_{\mathrm{b}}^{\mathrm{e}}\, d\ddot{\underline{a}}^{\mathrm{b}} - 2\,\underline{R}_{\mathrm{b}}^{\mathrm{e}}\,\underline{\Omega}_{\mathrm{ib}}^{\mathrm{b}}\, d\dot{\underline{a}}^{\mathrm{b}} + \\
&+ \left[\underline{\Omega}_{\mathrm{ie}}^{\mathrm{e}}\,\underline{\Omega}_{\mathrm{ie}}^{\mathrm{e}}\,\underline{R}_{\mathrm{b}}^{\mathrm{e}} - \underline{R}_{\mathrm{b}}^{\mathrm{e}}\left(\dot{\underline{\Omega}}_{\mathrm{ib}}^{\mathrm{b}} + \underline{\Omega}_{\mathrm{ib}}^{\mathrm{b}}\,\underline{\Omega}_{\mathrm{ib}}^{\mathrm{b}}\right)\right] \dot{\underline{a}}^{\mathrm{b}} + \\
&+ \left[\left(\underline{R}_{\mathrm{b}}^{\mathrm{e}}\,\underline{f}^{\mathrm{b}}\right)^{\star} + \left(\underline{R}_{\mathrm{b}}^{\mathrm{e}}\,\ddot{\underline{a}}^{\mathrm{b}}\right)^{\star} + 2\left(\underline{R}_{\mathrm{b}}^{\mathrm{e}}\,\underline{\Omega}_{\mathrm{ib}}^{\mathrm{b}}\,\dot{\underline{a}}^{\mathrm{b}}\right)^{\star} - \right. \\
&- \left.\underline{\Omega}_{\mathrm{ie}}^{\mathrm{e}}\,\underline{\Omega}_{\mathrm{ie}}^{\mathrm{e}}\left(\underline{R}_{\mathrm{b}}^{\mathrm{e}}\underline{a}^{\mathrm{b}}\right)^{\star} + \left(\underline{R}_{\mathrm{b}}^{\mathrm{e}}\,\underline{\Omega}_{\mathrm{ib}}^{\mathrm{b}}\,\underline{\Omega}_{\mathrm{ib}}^{\mathrm{b}}\,\underline{a}^{\mathrm{b}}\right)^{\star} + \left(\underline{R}_{\mathrm{b}}^{\mathrm{e}}\,\dot{\underline{\Omega}}_{\mathrm{ib}}^{\mathrm{b}}\,\underline{a}^{\mathrm{b}}\right)^{\star}\right] \underline{\varepsilon}^{\mathrm{e}}
\end{aligned}$$

Up to this point, it has been assumed that the two measurement system INS and GNSS are perfectly sinchronised. In reality this can never be achieved and therefore a small synchronisation error dT has to be added to the equation. Thus, we obtain

$$\begin{aligned}
d\underline{g}^{\mathrm{e}} &= d\ddot{\underline{x}}^{\mathrm{e}} - \underline{R}_{\mathrm{b}}^{\mathrm{e}}\, d\underline{f}^{\mathrm{b}} + 2\,\underline{\Omega}_{\mathrm{ie}}^{\mathrm{e}}\, d\dot{\underline{x}}^{\mathrm{e}} + \underline{R}_{\mathrm{b}}^{\mathrm{e}}\,(\underline{a}^{\mathrm{b}})^{*}\, d\dot{\underline{\omega}}_{\mathrm{ib}}^{\mathrm{b}} + \\
&+ \left[2\,\underline{R}_{\mathrm{b}}^{\mathrm{e}}\,(\dot{\underline{a}}^{\mathrm{b}})^{\star} + \underline{R}_{\mathrm{b}}^{\mathrm{e}}\,(\underline{a}^{\mathrm{b}})^{\star}\,\underline{\Omega}_{\mathrm{ib}}^{\mathrm{b}} + 2\,\underline{R}_{\mathrm{b}}^{\mathrm{e}}\underline{\Omega}_{\mathrm{ib}}^{\mathrm{b}}(\underline{a}^{\mathrm{b}})^{\star}\right] d\underline{\omega}_{\mathrm{ib}}^{\mathrm{b}} - \\
&- \underline{R}_{\mathrm{b}}^{\mathrm{e}}\, d\ddot{\underline{a}}^{\mathrm{b}} - 2\,\underline{R}_{\mathrm{b}}^{\mathrm{e}}\,\underline{\Omega}_{\mathrm{ib}}^{\mathrm{b}}\, d\dot{\underline{a}}^{\mathrm{b}} + \\
&+ \left[\underline{\Omega}_{\mathrm{ie}}^{\mathrm{e}}\,\underline{\Omega}_{\mathrm{ie}}^{\mathrm{e}}\,\underline{R}_{\mathrm{b}}^{\mathrm{e}} - \underline{R}_{\mathrm{b}}^{\mathrm{e}}\left(\dot{\underline{\Omega}}_{\mathrm{ib}}^{\mathrm{b}} + \underline{\Omega}_{\mathrm{ib}}^{\mathrm{b}}\,\underline{\Omega}_{\mathrm{ib}}^{\mathrm{b}}\right)\right] d\underline{a}^{\mathrm{b}} + \\
&+ \left[\left(\underline{R}_{\mathrm{b}}^{\mathrm{e}}\,\underline{f}^{\mathrm{b}}\right)^{\star} + \left(\underline{R}_{\mathrm{b}}^{\mathrm{e}}\,\ddot{\underline{a}}^{\mathrm{b}}\right)^{\star} + 2\left(\underline{R}_{\mathrm{b}}^{\mathrm{e}}\,\underline{\Omega}_{\mathrm{ib}}^{\mathrm{b}}\,\dot{\underline{a}}^{\mathrm{b}}\right)^{\star} - \right. \\
&- \underline{\Omega}_{\mathrm{ie}}^{\mathrm{e}}\,\underline{\Omega}_{\mathrm{ie}}^{\mathrm{e}}\left(\underline{R}_{\mathrm{b}}^{\mathrm{e}}\,\underline{a}^{\mathrm{b}}\right)^{\star} + \left(\underline{R}_{\mathrm{b}}^{\mathrm{e}}\underline{\Omega}_{\mathrm{ib}}^{\dot{\mathrm{b}}}\,\underline{\Omega}_{\mathrm{ib}}^{\mathrm{b}}\,\underline{a}^{\mathrm{b}}\right)^{\star} + \\
&+ \left.\left(\underline{R}_{\mathrm{b}}^{\mathrm{e}}\,\dot{\underline{\Omega}}_{\mathrm{ib}}^{\mathrm{b}}\,\underline{a}^{\mathrm{b}}\right)^{\star}\right] \underline{\varepsilon}^{\mathrm{e}} + \left(\dot{\underline{R}}_{\mathrm{b}}^{\mathrm{e}}\,\underline{f}^{\mathrm{b}} + \underline{R}_{\mathrm{b}}^{\mathrm{e}}\,\dot{\underline{f}}^{\mathrm{b}}\right) dT
\end{aligned}$$

Usually it is also supposed that $\dot{\underline{a}}^{\mathrm{b}} = \ddot{\underline{a}}^{\mathrm{b}} = 0$, then

$$\begin{aligned}
\underline{g}^{\mathrm{e}} &= \ddot{\underline{x}}^{\mathrm{e}} - \underline{R}_{\mathrm{b}}^{\mathrm{e}}\,\underline{f}^{\mathrm{b}} + 2\,\underline{\Omega}_{\mathrm{ie}}^{\mathrm{e}}\,\dot{\underline{x}}^{\mathrm{e}} - \underline{\Omega}_{\mathrm{ie}}^{\mathrm{e}}\,\underline{\Omega}_{\mathrm{ie}}^{\mathrm{e}}\,\underline{R}_{\mathrm{b}}^{\mathrm{e}}\,\underline{a}^{\mathrm{b}} + \underline{R}_{\mathrm{b}}^{\mathrm{e}}\,\dot{\underline{\Omega}}_{\mathrm{ib}}^{\mathrm{b}}\,\underline{a}^{\mathrm{b}} + \\
&+ \underline{R}_{\mathrm{b}}^{\mathrm{e}}\,\underline{\Omega}_{\mathrm{ib}}^{\mathrm{b}}\,\underline{\Omega}_{\mathrm{ib}}^{\mathrm{b}}\,\underline{a}^{\mathrm{b}}
\end{aligned}$$

$$
\begin{aligned}
d\underline{g}^{\mathtt{e}} &= d\underline{\ddot{x}}^{\mathtt{e}} - \underline{R}^{\mathtt{e}}_{\mathtt{b}}\, d\underline{f}^{\mathtt{b}} + 2\,\underline{\Omega}^{\mathtt{e}}_{\mathtt{ie}}\, d\underline{\dot{x}}^{\mathtt{e}} + \underline{R}^{\mathtt{e}}_{\mathtt{b}}\, (\underline{a}^{\mathtt{b}})^{*}\, d\underline{\dot{\omega}}^{\mathtt{b}}_{\mathtt{ib}} + \\
&+ \underline{R}^{\mathtt{e}}_{\mathtt{b}}\, (\underline{a}^{\mathtt{b}})^{\star}\, \underline{\Omega}^{\mathtt{b}}_{\mathtt{ib}}\, d\underline{\omega}^{\mathtt{b}}_{\mathtt{ib}} + 2\,\underline{R}^{\mathtt{e}}_{\mathtt{b}}\, \underline{\Omega}^{\mathtt{b}}_{\mathtt{ib}}\, (\underline{a}^{\mathtt{b}})^{\star}\, d\underline{\omega}^{\mathtt{b}}_{\mathtt{ib}} - \\
&- \underline{\Omega}^{\mathtt{e}}_{\mathtt{ie}}\, \underline{\Omega}^{\mathtt{e}}_{\mathtt{ie}}\, \underline{R}^{\mathtt{e}}_{\mathtt{b}}\, d\underline{a}^{\mathtt{b}} + \underline{R}^{\mathtt{e}}_{\mathtt{b}}\, \underline{\dot{\Omega}}^{\mathtt{b}}_{\mathtt{ib}}\, d\underline{a}^{\mathtt{b}} + \\
&+ \underline{R}^{\mathtt{e}}_{\mathtt{b}}\, \underline{\Omega}^{\mathtt{b}}_{\mathtt{ib}}\, \underline{\Omega}^{\mathtt{b}}_{\mathtt{ib}}\, d\underline{a}^{\mathtt{b}} + \left(\underline{R}^{\mathtt{e}}_{\mathtt{b}}\, \underline{f}^{\mathtt{b}}\right)^{\star}\, \varepsilon^{\mathtt{e}} - \underline{\Omega}^{\mathtt{e}}_{\mathtt{ie}}\, \underline{\Omega}^{\mathtt{e}}_{\mathtt{ie}}\, \left(\underline{R}^{\mathtt{e}}_{\mathtt{b}}\, \underline{a}^{\mathtt{b}}\right)^{\star}\, \varepsilon^{\mathtt{e}} + \\
&+ \left(\underline{R}^{\mathtt{e}}_{\mathtt{b}}\, \underline{\Omega}^{\mathtt{b}}_{\mathtt{ib}}\, \underline{\Omega}^{\mathtt{b}}_{\mathtt{ib}}\, \underline{a}^{\mathtt{b}}\right)^{\star}\, \varepsilon^{\mathtt{e}} + \left(\underline{R}^{\mathtt{e}}_{\mathtt{b}}\, \underline{\dot{\Omega}}^{\mathtt{b}}_{\mathtt{ib}}\, \underline{a}^{\mathtt{b}}\right)^{\star}\, \varepsilon^{\mathtt{e}} + \\
&+ \underline{\dot{R}}^{\mathtt{e}}_{\mathtt{b}}\, \underline{f}^{\mathtt{b}}\, dT + \underline{R}^{\mathtt{e}}_{\mathtt{b}}\, \dot{f}^{\mathtt{b}}\, dT
\end{aligned}
$$

I IG-IMU simulator data

As it has been introduced in Chapter 4, IMU simulator used in this research is a computer program developed at the Institute of Geomatics (IG) in the frame of the `Navega` system for testing and validating navigation algorithms. This tool, which has been described by Parés in [88], emulates the behavior of standard IMUs with three linear accelerometers and three angular rate sensors in an orthogonal configuration. Also, it has been mainly developed to validate methods involving inertial technology.

The fundamentals of the IG-IMU simulator are the functional model that characterise the inertial motion (INS mechanisation equations), the stochastic models that characterise the IMU errors and the *geodetic* model that contextualises the previous models.

As any real IMU, the simulator computes angular velocities and linear accelerations for a trajectory. Given a set of times, positions, velocities and attitudes, the system provides the signal that an IMU measures as if it were in that situation. After that, the signal is modified by adding a variety of errors, such as biases or scale factors. The order in which these errors are introduced to IMU data — $IMU = (\omega, f)^T$ — is:

- scale factor

  $$IMU_{out} = \left(1 + S_c + S_{rc} + S_{gm} + S_{rw}\right) \cdot IMU_{in}$$

  where IMU_{out} is the output data, IMU_{in} is the original data, S_c is the constant component of the scale factor, S_{rc} is a random constant stochastic process, S_{gm} is a Gauss-Markov stochastic process and S_{rw} is a random walk stochastic process.

- bias

  $$IMU_{out} = B_c + B_{rc} + B_{gm} + B_{rw} + \begin{pmatrix} 1 & B_{gs} \\ 0 & 1 \end{pmatrix} \cdot IMU_{in}$$

  where IMU_{out} is the output data, IMU_{in} is the original data, B_c is the constant component of the bias, B_{rc} is a random constant stochastic process, B_{gm} is a Gauss-Markov

stochastic process, B_{rw} is a random walk stochastic process and B_{gs} is a component depending on linear accelerations.

- misalignment

$$IMU_{out} = \begin{pmatrix} 1 & -y_z & z_y \\ x_z & 1 & -z_x \\ -x_y & y_x & 1 \end{pmatrix} \cdot IMU_{in}$$

where IMU_{out} is the output data, IMU_{in} is the original data, x_y, x_z, y_x, y_z, z_x, z_y are the misalignments between axis.

- random noise

$$IMU_{out} = \alpha \cdot SENSOR(PSD_{noise}) + IMU_{in}$$

where IMU_{out} is the output data, IMU_{in} is the original data, α is a random number, $SENSOR_NOISE$ is the covariance of the data noise, that is a function of PSD_{noise}.

- quantisation

$$IMU_{out} = \left\lfloor \frac{IMU_{in}}{quant} \right\rfloor \cdot quant$$

where IMU_{out} is the output data, IMU_{in} is the original data, $quant$ is the number of quantisation and $\lfloor \cdot \rfloor$ means the integer part of a real number.

The parameters that define each errors are introduced in a XML file. Later on, the structure of this file is:

```
<?xml version="1.0" encoding="UTF-8"?>
<imu_file
    xmlns:xsi="http://www.w3.org/2001/XMLSchema-instance
    xsi:noNamespaceSchemaLocation='err_file.xsd'>

  <lineage>
    <id> ... </id>
    <author><item> ... </item></author>
    <organization> ... </organization>
    <department> ... </department>
    <date_time> ... </date_time>
    <ref_documents><item> doc IMU's </item></ref_documents>
    <project> TE-AT </project>
    <task> IMU simulator </task>
```

```
  <remarks> ... </remarks>
</lineage>

<imu_info>
  <model> ... </model>
  <manufacturer> ... </manufacturer>
  <country> -- </country>
  <ref_frame> XYZ </ref_frame>
  <coord_system> geo </coord_system>
  <frequency> 50 </frequency>
</imu_info>

<gyros_info>
  <bias>
    <Constant> B_{c} <\Constant>
    <R_constant> B_{rc} <\R_constant>
    <G_Markov>
      <initial_val> B_{gm}  <\initial_val>
      <corr_time> t_{c} <\corr_time>
      <proc_noise> W_{x} <\proc_noise>
    <\G_Markov>
    <R_walk>  B_{rw} <\R_walk>
    <G_dependant> B_{gs} <\G_dependant>
  </bias>
  <scale_factor><Repeatibility> S_{rc} </Repeatibility></scale_factor>
  <misalignment><Angles> 0 0 0 </Angles></misalignment>
  <noise> <RW-PSD> W_{noise} </RW-PSD></noise>
  <quantization><Step> quant </Step></quantization>
</gyros_info>

<accel_info>
  <bias>
    <Constant> B_{c} <\Constant>
    <R_constant> B_{rc} <\R_constant>
    <G_Markov>
      <initial_val> B_{gm} <\initial_val>
      <corr_time> t_{c} <\corr_time>
      <proc_noise> W_{x} <\proc_noise>
    <\G_Markov>
    <R_walk> B_{rc} <\R_walk>
  </bias>
  <scale_factor><Repeatibility> S_{rc} </Repeatibility></scale_factor>
```

```
    <misalignment><Angles> 0 0 0 </Angles></misalignment>
    <noise><RW-PSD> PSD_{noise} </RW-PSD></noise>
    <quantization><Step> quant </Step></quantization>
  </accel_info>

</imu_file>
```

Now the data used in the computations correspond only to the prior knowledge of LTN101 and LN200 IMUs.

I.0.1 LTN101 data

```
<?xml version="1.0" encoding="UTF-8"?>
<imu_file
  xmlns:xsi="http://www.w3.org/2001/XMLSchema-instance"
  xsi:noNamespaceSchemaLocation='err_file.xsd'>

  <lineage>
    <id> 005 </id>
    <author><item> ATermens </item></author>
    <organization> ICC </organization>
    <department> Geodesia </department>
    <date_time> 07/10/2006 </date_time>
    <ref_documents>
      <item> doc IMU's </item>
    </ref_documents>
    <project> TE-AT </project>
    <task> IMU simulator </task>
    <remarks> perturbat </remarks>
  </lineage>

  <imu_info>
    <model> LTN-101 </model>
    <manufacturer> Litton </manufacturer>
    <country> ??? </country>
    <ref_frame> XYZ </ref_frame>
    <coord_system> geo </coord_system>
    <frequency> 50 </frequency>
  </imu_info>

  <gyros_info>
    <bias>
      <Constant>   0.0   0.0   0.0 <\Constant>
      <R_constant> 0.0   0.0   0.0 <\R_constant>
      <G_Markov>
        <initial_val> 0  0  0  <\initial_val>
        <corr_time>   0  0  0 <\corr_time>
        <proc_noise>  0  0  0 <\proc_noise>
      <\G_Markov>
      <R_walk>        0  0  0 <\R_walk>
      <G_dependant>   0  0  0 <\G_dependant>
    </bias>
```

```
    <scale_factor> <Repeatibility> 0 0 0 </Repeatibility> </scale_factor>
    <misalignment> <Angles> 0 0 0 </Angles> </misalignment>
    <noise> <RW-PSD> 0.001 0.001 0.001  </RW-PSD> </noise>
    <quantization> <Step> 0 0 0 </Step> </quantization>
  </gyros_info>

  <accel_info>
    <bias>
      <Constant>    0  0  0 <\Constant>
      <R_constant>  0  0  0 <\R_constant>
      <G_Markov>
        <initial_val> 0  0  0 <\initial_val>
        <corr_time>   0  0  0 <\corr_time>
        <proc_noise>  0  0  0 <\proc_noise>
      <\G_Markov>
      <R_walk> 0  0  0 <\R_walk>
    </bias>
    <scale_factor> <Repeatibility> 0 0 0 </Repeatibility> </scale_factor>
    <misalignment> <Angles> 0 0 0 </Angles> </misalignment>
    <noise> <RW-PSD> 10.0 10.0 10.0 </RW-PSD> </noise>
    <quantization> <Step> 0 0 0 </Step> </quantization>
  </accel_info>

</imu_file>
```

I.0.2 LN200 data

```
<?xml version="1.0" encoding="UTF-8"?>
<imu_file
    xmlns:xsi="http://www.w3.org/2001/XMLSchema-instance"
    xsi:noNamespaceSchemaLocation='err_file.xsd'>

  <lineage>
    <id> 005 </id>
    <author><item> ATermens </item></author>
    <organization> ICC </organization>
    <department> Geodesia </department>
    <date_time> 07/10/2006 </date_time>
    <ref_documents>
      <item> doc IMU's </item>
    </ref_documents>
    <project> TE-AT </project>
    <task> IMU simulator </task>
    <remarks> perturbacio LN200A1 segons Skaloud </remarks>
  </lineage>

  <imu_info>
    <model> LN-200 A1 </model>
    <manufacturer> Litton </manufacturer>
    <country> -- </country>
    <ref_frame> XYZ </ref_frame>
    <coord_system> geo </coord_system>
    <frequency> 50 </frequency>
  </imu_info>

  <gyros_info>
    <bias>
      <Constant> 0.0 0.0 0.0 <\Constant>
      <R_constant> 0.0 0.0 0.0 <\R_constant>
      <G_Markov>
        <initial_val> 0 0 0 <\initial_val>
        <corr_time> 0 0 0 <\corr_time>
        <proc_noise> 0 0 0 <\proc_noise>
      <\G_Markov>
      <R_walk> 0.0 0.0 0.0 <\R_walk>
      <G_dependant> 0 0 0 <\G_dependant>
    </bias>
```

```
    <scale_factor> <Repeatibility> 0 0 0 </Repeatibility> </scale_factor>
    <misalignment> <Angles> 0 0 0 </Angles> </misalignment>
    <noise> <RW-PSD> 0.04 0.04 0.04 </RW-PSD> </noise>
    <quantization> <Step> 0 0 0 </Step> </quantization>
  </gyros_info>

  <accel_info>
    <bias>
      <Constant> 0 0 0 <\Constant>
      <R_constant> 0 0 0 <\R_constant>
      <G_Markov>
        <initial_val> 0 0 0 <\initial_val>
        <corr_time> 0 0 0 <\corr_time>
        <proc_noise> 0 0 0 <\proc_noise>
      <\G_Markov>
      <R_walk> 0 0 0 <\R_walk>
    </bias>
    <scale_factor> <Repeatibility> 0 0 0 </Repeatibility> </scale_factor>
    <misalignment> <Angles> 0 0 0 </Angles> </misalignment>
    <noise> <RW-PSD> 50.0 50.0 50.0 </RW-PSD> </noise>
    <quantization> <Step> 0 0 0 </Step> </quantization>
  </accel_info>

</imu_file>
```